Richard H. Enns

It's a Nonlinear World

Springer Undergraduate Texts
in Mathematics and Technology

Richard H. Enns

It's a Nonlinear World

Richard H. Enns
Department of Physics
Simon Fraser University
Burnaby, BC V5A 1S6
Canada
renns@sfu.ca

Printed on acid-free paper

*This text is dedicated
to my loving wife,
Karen,
who lights my path
through
this nonlinear world.*

Contents

Preface

The purpose of this text, **It's a Nonlinear World**, is to prepare science and engineering students for the "real" world where problems and issues on the frontiers of modern scientific, technological, economic, and social research are often nonlinear in nature. In this nonlinear world, many of the mathematical concepts and tools learned and applied in traditional undergraduate, and even graduate, science courses are simply inadequate and new mathematical tools must be introduced. This text will supply these tools and then illustrate how they are used, drawing examples from diverse fields in the physical, chemical, biological, engineering, medical, and social sciences.

The book is divided into two parts, the first section introducing the reader to nonlinear dynamical (evolving with time) systems in the **World of Mathematics**. In the opening chapter of this section, we examine what is meant by a nonlinear mathematical system, providing a variety of historically important, as well as current, examples formulated in terms of ordinary differential equations (ODEs) and finite difference equations ("maps"). Since exact analytic solutions to nonlinear ODE model equations of importance in the real world generally do not exist, the reader is introduced to some of the more common numerical algorithms for solving these equations on the computer.

In the subsequent three chapters of the **World of Mathematics**, we systematically present the mathematical framework of nonlinear dynamics. The material is organized according to mathematical structure, namely, nonlinear ODEs, nonlinear maps, and similarity and soliton solutions of nonlinear PDE (partial differential equation) models. In these chapters, the reader is introduced to such nonlinear concepts as fixed points, bifurcations, limit cycles, fractals, chaos, solitons, etc., and nonlinear diagnostic tools such as fixed point analysis, bifurcation diagrams, Lyapunov exponents, and so on.

The second part (**Our Nonlinear World**) of the book presents illustrative examples of nonlinear dynamics in the real world grouped in the following seven chapters:

- **World of Motion**

- **World of Sports**

- **World of Electromagnetism**

- **World of Weather Prediction**

- **World of Chemistry**

- **World of Disease**

- **World of War**

Each chapter provides topics which are highly relevant to the contemporary world and makes extensive use of the ideas and methods introduced in the first part of the text. Such a selection of topics and examples is inherently bound to be uneven, reflecting not only the background and knowledge of the author but also the fact that the nonlinear universe is vast and we are able to sample only a small portion of it. The examples range from the flight of a major baseball league curve ball, to the origin of the earth's magnetic field, to the spread of an epidemic, to the conflict between different ant colonies, and to the inherent difficulty in long-range weather forecasting, to mention just a few of the intellectual treats that will be presented. All the examples are fully referenced to the published literature or the Internet so that they can be more fully explored if desired. The Internet is becoming a rich source of information with many nonlinear scientists making copies of their published (and refereed) papers available online. Journals, on the other hand, do not provide online copies of published papers free of charge, so a visit to a university or college library may be necessary to view these papers.

The mathematical level of the text assumes a good working knowledge of basic calculus (ordinary and partial derivatives, integrals, etc.) and a reasonable familiarity with differential equations. To keep the text as mathematically simple as possible, the overwhelming number of examples are formulated in terms of nonlinear ODEs and maps. With the exception of seeking soliton and similarity solutions in certain cases by reducing PDEs to ODEs, the coverage of most PDE models in this text tends to generally be more qualitative than quantitative.

It's a Nonlinear World may be used as a course text or for self-study, but is written in such a way that the more casual mathematically literate reader can simply read the book for intellectual enjoyment and enlightenment. A wide variety of exercises and problems are provided at the end of each chapter which allow the reader to explore other nonlinear models and, if desired, to test his or her mastery of the subject matter.

This book is intended to be open-ended, aimed at whetting the appetite of the reader to more fully explore our nonlinear world. Entire regions of this world, such as nonlinear modeling in economics, have not been traversed in this text and remain for you to discover what treats lie therein.

Part I

WORLD OF MATHEMATICS

To most outsiders, modern mathematics is unknown territory.
Its borders are protected by dense thickets of technical terms;
its landscapes are a mass of indecipherable equations
and incomprehensible concepts.
Few realize that the
world of modern mathematics
is rich
with
vivid images
and
provocative ideas.

Ivars Peterson,
Award-winning
mathematics writer

Chapter 1

World of Nonlinear Systems

Linear mathematical systems tend to dominate even moderately advanced university courses. The mathematical intuition so developed ill equips the student to confront the bizarre behavior exhibited by the simplest of nonlinear systems. Yet nonlinear systems are surely the rule, not the exception, not only in research, but also in the everyday world.
Robert M. May, mathematical biologist, *Nature*, Vol. 261, 459 (1976),
an abbreviated version of the original quote.

The aim of this text is to illustrate how scientists and engineers are using nonlinear dynamical (evolving with time) equations to mathematically model many of the more interesting and important phenomena that are observed in the world around us. If the time variable can be treated as continuous, these model systems are described by ordinary or partial *differential equations* (ODEs or PDEs). If the time is regarded as discrete (e.g., due to measurements or observations being made at finite time intervals), the models then involve *difference equations*. If this sounds mathematically formidable, don't panic! If you have a working knowledge of basic calculus (derivatives, integrals, Taylor expansions, etc.) and been introduced to linear ODEs, you should have no difficulty in following the mathematical treatment in this book.

In ensuing chapters, the nonlinear phenomena will range from the flight of a spinning golf ball to the spread of infectious diseases to the arms race between nations to the difficulties in accurate long-range weather forecasting. You will see that simple nonlinear models can generate very complex and often unexpected results, the possible outcomes often being sensitive to the parameter values in the model and/or the initial conditions. This has profound implications for the predictions of more complicated nonlinear models such as those used in weather forecasting and, on a longer time scale, in attempting to predict future climate change.

Our exploration of the nonlinear world will necessarily be somewhat uneven. This is not only because there are only so many topics that can be covered in a book of this length, but also because the more complicated nonlinear models involve mathematical treatments that are either too lengthy or too complex for this elementary text. For the latter models, our coverage will tend to be more qualitative than quantitative, our goal being to provide you with the flavor of the topic and how it fits into the nonlinear world.

1.1   Introduction to Nonlinear ODE Models

The mathematically simplest dynamical models are those which involve only one independent[1] variable, the time t. If the time can be regarded as continuous, these systems are governed by one or more *ordinary* differential equations (ODEs) describing the temporal evolution of various quantities depending on t.

A system of *linear* differential equations is one for which the dependent quantities or variables only appear to the first power. If terms are present which involve products of the dependent variables, or other powers, or other mathematical forms, the system is said to be *nonlinear*. A similar classification applies to difference equations, discussed in the following section.

To amplify on these ideas, let us briefly consider two historically important models of population growth, the dependent variable being the population number or population density (number per unit area) $P(t)$ at time t. The governing ODE for the rate of population growth is quite generally

$$\frac{dP}{dt} = F(P, t), \tag{1.1}$$

where the form of the population growth function F remains to be specified.

In his book entitled *An Essay on the Principle of Population*,[2] the English demographer and political economist Thomas Malthus (1766 − 1834) assumed that

$$F(P) = r\,P, \tag{1.2}$$

with the constant r called the *intrinsic growth rate*. This leads to the *Malthus* ODE,

$$\frac{dP}{dt} = r\,P, \tag{1.3}$$

which is linear (first-order) in the dependent variable P. This ODE is easily solved by *separating* the dependent and independent variables. That is to say, we rewrite the equation as

$$\frac{dP}{P} = r\,dt$$

and then integrate both sides of the equation. If P_0 and P are the population numbers at time $t = 0$ and time $t > 0$, respectively, integration yields

$$\ln\left(\frac{P}{P_0}\right) = r\,t,$$

where ln is the *natural logarithm*. Solving for P then yields the solution

$$P(t) = P_0\,e^{r\,t}, \tag{1.4}$$

---

[1]If the system also evolves in space as well as time, thus increasing the number of independent variables, *partial* differential equations must be invoked.

[2]The first edition was published anonymously in London in 1798, but Malthus was identified as the author in subsequent editions. The sixth and last edition appeared in 1826.

where e is the *exponential* function.

For $r > 0$ (births exceed deaths), the population grows exponentially with increasing time, while decaying to zero as $t \to +\infty$ if $r < 0$. Based on the conjectured exponential growth of the world's population, Malthus incorrectly predicted that the world's food supply would not keep pace with the population increase by the middle of the 19th century.

The Belgian mathematician Pierre-Francois Verhulst (1804–1849) generalized the Malthusian model to account for a slowing in the growth rate due to overcrowding or limited resources. Specifically, he assumed that the growth function had the mathematical form

$$F(P) = r P \left(1 - \frac{P}{K}\right), \tag{1.5}$$

with K a positive constant. This leads to the *Verhulst* ODE,

$$\frac{dP}{dt} = r P \left(1 - \frac{P}{K}\right) = r P - \frac{r}{K} P^2, \tag{1.6}$$

which is nonlinear since it contains the quadratic term, P^2. The constant K represents the maximum sustainable value of P and is called the *carrying capacity*. In the limit $K \to \infty$ (unlimited resources), Verhulst's ODE reduces to that of Malthus.

Verhulst's ODE can be cast into a simpler *dimensionless* form, by introducing the new dimensionless variables $x = P/K$ and $\tau = r\,t$. Adopting the standard shorthand *dot notation*, $\dot{x}(\tau) \equiv dx(\tau)/d\tau$, Verhulst's ODE then becomes

$$\dot{x}(\tau) = x\,(1 - x), \tag{1.7}$$

which is commonly referred to as the *logistic* ODE. Although nonlinear, the logistic equation can also be solved by separating variables, the solution (called the *logistic curve*) being

$$x(\tau) = \frac{1}{1 + \left(\dfrac{1 - x_0}{x_0}\right) e^{-\tau}}, \tag{1.8}$$

with $x_0 > 0$ the initial value of x. As $\tau \to +\infty$, $x(\tau) \to 1$. That is to say, in dimensional terms, the population number P approaches the carrying capacity K.

The following example illustrates a successful application of the logistic curve by the Russian microbiologist, Georgy Frantsevitch Gause (1910–1986).

Example 1-1: *Saccharomyces cerevisiae*

In a set of carefully controlled experiments, Gause ([Gau69]) applied the logistic model to the growth of various yeasts in a test tube with a fixed amount of nutrient. For the yeast *Saccharomyces cerevisiae*, he obtained $x_0 = 0.04099$ and $r = 0.2183$ for the best-fitting logistic curve to the experimental data.

    a. Plot the logistic curve for the first 50 hours of growth and discuss the shape.

    b. At what time T was the growth of *Saccharomyces cerevisiae* a maximum?

Solution: a. Noting that $\tau = r t$, and substituting the values of x_0 and r into Equation (1.8), the logistic curve is plotted in Figure 1.1 as a function of t. The curve is S-shaped, the inflection point where the curvature changes from concave upwards to concave downwards occurring about the 15-hour mark.
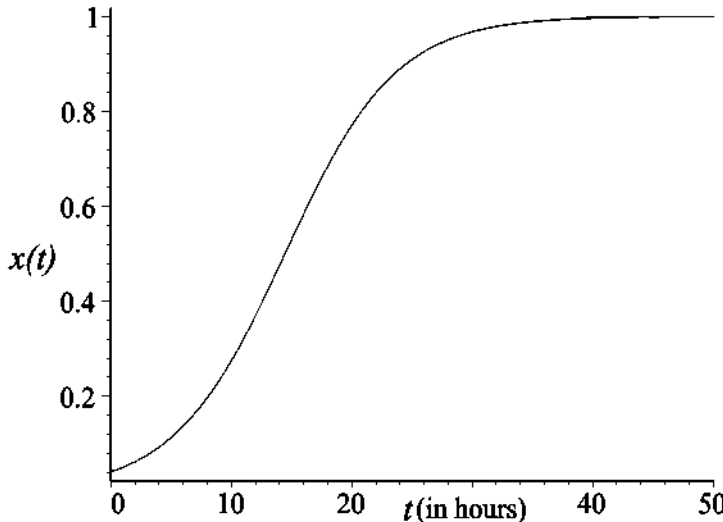
Figure 1.1: Growth of cerevisiae yeast as a function of time t.

b. The growth is a maximum at the inflection point which, as already mentioned, occurs at about 15 hours. The precise time T at which maximum growth occurs can be obtained by calculating the second time derivative of the logistic curve (proportional to the curvature), setting the result equal to zero, and solving for the time. Leaving the detailed calculation as a problem at the end of the chapter, this yields the general result in real time units,

$$T = -\frac{\ln\left(\dfrac{x_0}{1 - x_0}\right)}{r}. \tag{1.9}$$

Substituting the x_0 and r values, we obtain $T \approx 14.44$ hours as the time of maximum growth.

<div align="center">***</div>

The logistic curve may be applied to growth situations outside the laboratory as well. It has been successfully used to predict the oil production in the so-called US–48 (the lower 48 United States excluding Alaska and Hawaii) by the American geologist Dr. M. King Hubbert.

Hubbert was Chief Consultant (General Geology) for Shell's Exploration and Production Research Division and later worked for the U.S. Geological Survey. He became famous in the popular press for his peak oil "theory" in which he successfully predicted in 1956 that the peak in oil production in the US–48 would occur around 1970 and decline thereafter.

He modeled the cumulative oil production Q in the US–48 up to year t with a logistic curve of the form

$$Q = \frac{U}{1 + e^{-b(t - t_m)}}, \tag{1.10}$$

where U is the *ultimate recovery* (the maximum value of Q), t_m is the year of the midpoint, i.e., when one-half the oil ($Q = U/2$) has been recovered, and b is a positive coefficient which controls the slope of the curve.

The time derivative of the logistic curve (1.10) then models the annual oil production, the resulting so-called *Hubbert curve* given by

$$P = \frac{2 P_m}{1 + \cosh(b(t - t_m))}, \tag{1.11}$$

with $P = dQ/dt$, $P_m = bU/2$ the peak production occurring at the midpoint, and cosh the hyperbolic cosine function.[3] As t spans the range from $-\infty$ to $+\infty$, the Hubbert curve starts and ends at zero, with a single peak in between.

It is important to emphasize that the Hubbert curve does not apply to an individual oil field's production, which is characterized by a gradual increase to maximum output, then a long regime of steady output, followed by a gradual decrease as the field "dries up." In oil exploration, one typically has a small number of large fields discovered near the beginning of the discovery cycle and a large number of small fields found near the end. For example, nearing the end of its discovery cycle, the US–48 had 240,000 wells in 2002 with an average output of 20 barrels per day. At the same time, Saudi Arabia had only 1560 wells, but each well produced an average of 4150 barrels per day. When the outputs of many fields are combined, they produce a bell-shaped curve which can be approximated by the Hubbert function (1.11).

Example 1-2: Peak Oil Theory and the Hubbert Curve

The annual production in the US–48 up to 1997 showed a good fit to the Hubbert curve with $t_m = 1970$, $P_m = 3.5$ Gb/year (gigabarrels per year), and $b = 5/68$.

- **a.** What is the predicted annual production in the US–48 in the year 2030?
- **b.** Plot the Hubbert curve for the period 1900 to 2030.
- **c.** Carry out an Internet search to determine if there have been any noticeable deviations away from the Hubbert curve.
- **d.** Using the Internet, give examples of oil field regions where the Hubbert curve does not work well. Explain why this is the case.

Solution: a. Using the given parameter values, the predicted annual production in the year 2030 should be

$$P = \frac{2 \times 3.5}{1 + \cosh\left(\dfrac{5}{68} \times (2030 - 1970)\right)} \approx 0.17 \ \text{Gb/year}.$$

---

[3] As a function of x, the hyperbolic cosine function is $\cosh(x) = (e^x + e^{-x})/2$.
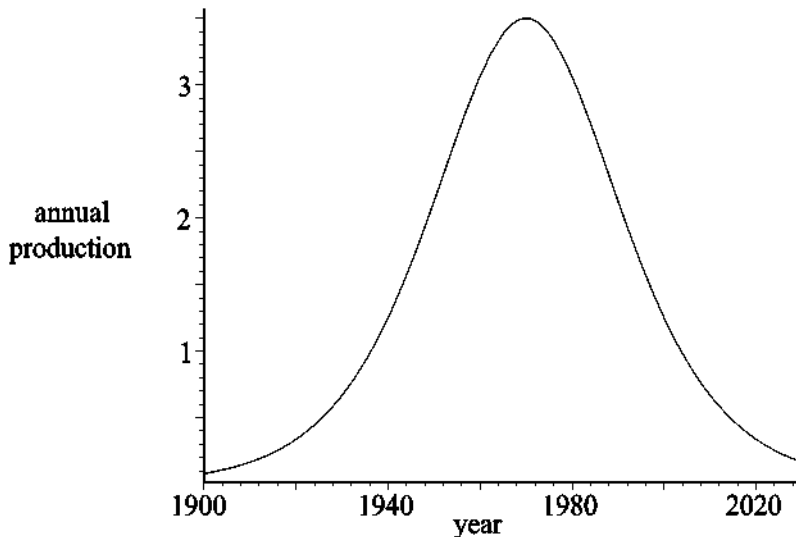
Figure 1.2: Hubbert curve showing annual oil production (Gb/year) in the US–48.

b. The Hubbert curve over the time interval 1900 to 2030 is shown in Figure 1.2.

c. Deviations from the Hubbert curve occurred in the Great Depression of the 1930s, in the late 1950s due to prorationing, and in the early 1980s due to price rises.

d. Although successful for the US–48, the Hubbert curve does not work well for

- Alaska and the North Sea where a few giant fields came online simultaneously;

- the Persian Gulf states where OPEC (Organization of Petroleum Exporting Countries) artificially controls oil production;

- fields where oil production is interrupted by wars and revolutions, e.g., Iran.

Another difficulty with applying peak oil theory in practice and using the Hubbert curve to estimate the peak oil production is that the ultimate recovery U that is usually cited is not the absolute quantity of oil remaining to be tapped but the estimated quantity of oil that can be extracted with current technology and at current market prices. A case in point is the Alberta (Canada) oil sands, where U has been progressively pushed higher.

<center>***</center>

As another real-world example, the giant retailer Walmart assumes that the sales of goods are modeled by the logistic curve. For each item they check monthly to see if the inflection point in the logistic curve has been reached. When it has, they discontinue stocking the goods. As a result, Walmart rarely has sales on discontinued items.

1.2 Introduction to Difference Equation Models

In many situations, data is recorded at regular time intervals rather than continuously. In the world of finance, for example, the Dow Jones industrial average[4] and the prices of stocks are recorded at the end of each day and reported in the financial pages of daily newspapers. Similarly, the population of a given country is not recorded at every instant in time, but rather at finite time intervals dictated by the national census. In such instances, the model equations should take the form of difference equations. Let's look at both the Malthus and Verhulst models from this mathematical viewpoint.

Suppose that time is divided into equal finite intervals and the population number at the end of the nth interval is $P_n = P(n)$. The change ΔP in population number from the end of the nth interval to the end of interval $n + 1$ is, according to the Malthus assumption, given by the linear *difference equation*

$$\Delta P = P_{n+1} - P_n = r\,P_n, \text{ or } P_{n+1} = (1+r)\,P_n \equiv a\,P_n. \tag{1.12}$$

Starting with an initial population P_0 at $n = 0$, *iterating* Equation (1.12) yields

$$P_1 = a\,P_0,$$

$$P_2 = a\,P_1 = a^2\,P_0,$$

$$P_3 = a\,P_2 = a^3\,P_0,$$

$$P_n = a\,P_{n-1} = a^n\,P_0.$$

For $a > 1$ (i.e., $r > 0$), the population grows *geometrically* with time (increasing n). In his famous *Essay*, Malthus actually referred to this geometrical growth, rather than the ODE-based exponential growth mentioned in the previous section. His prediction of "catastrophe" was based on an assumed *arithmetic* growth in the food supply. For $a < 1$, the population number decays to zero as $n \to \infty$.

Uncontrolled geometric growth of the bacterium *Escherichia coli (E. coli)* is the theme of the following quote taken from the best-selling author Michael Crichton's science fiction thriller ([Chr69]), *The Andromeda Strain*:

The mathematics of uncontrolled growth are frightening. A single cell of the bacterium E. coli would, under ideal circumstances, divide every twenty minutes. That is not particularly disturbing until you think about it, but the fact is that bacteria multiply geometrically: one becomes two, two become four, four become eight, and so on. In this way it can be shown that in a single day, one cell of E. coli could produce a super-colony equal in size and weight to the entire planet Earth.

The following example examines Crichton's claim.

---

[4]A price-weighted average based on the stock prices of 30 of the largest and most widely held public companies (e.g., Boeing, Coca-Cola, General Electric, General Motors, Walmart) in the U.S.

Example 1-3: The Andromeda Strain

If a single cell of the bacterium *E. coli* divides every 20 minutes, how many *E. coli* would there be at the end of 24 hours? The mass of an *E. coli* bacterium ([MPD$^+$07]) is 1.7×10^{-12} g, while the mass of the Earth is 6.0×10^{27} g. Is Crichton's claim accurate? How many hours should he have allowed for his statement to be correct?

Solution: In this case, $P_0 = 1$ and $a = 2$. Since the time for cell division is $1/3$ hour, in 24 hours there would be $3 \times 24 = 72$ doublings. If the Malthus model applied, at the end of 24 hours, there would be

$$2^{72} \times 1 \approx 0.47 \times 10^{22} \quad E. \; coli.$$

At this time, the mass of the super-colony would be

$$(0.47 \times 10^{22}) \times (1.7 \times 10^{-12}) = 0.8 \times 10^{10} \quad \text{grams,}$$

considerably less than the mass of the Earth.

The number x of hours needed for the *E. coli* mass to equal that of the Earth is obtained by solving the equation

$$2^{3x} \times (1.7 \times 10^{-12}) = 6.0 \times 10^{27} \quad \Longrightarrow \quad x \approx 44 \quad \text{hours.}$$

The time needed is closer to 2 days than 1.

<div align="center">***</div>

Turning our attention to the Verhulst model, the finite difference version is

$$P_{n+1} = P_n + r \, P_n \left(1 - P_n/K\right) \tag{1.13}$$

which, on setting

$$P_n = (1 + r) \, K \, x_n / r \quad \text{and} \quad 1 + r = a,$$

yields the nonlinear *logistic difference equation*

$$x_{n+1} = a \, x_n \left(1 - x_n\right) \equiv a \, F(x_n), \quad \text{with } 0 < x_0 < 1. \tag{1.14}$$

Noting that $F(x) = x \, (1 - x)$ is an inverted parabola with a maximum value of $1/4$ at $x = 1/2$, for positive a the value of a must be restricted to between 0 and 4 to ensure that x always stays between 0 and 1. In this a range, an exact closed-form solution doesn't exist except for $a = 2$ and 4. See Lauwerier ([Lau86]) and Wolfram's *MathWorld* (mathworld.wolfram.com) for a discussion of this point. Of course, the value of x_n can be obtained for any $n > 0$ by numerically iterating Equation (1.14) n times, starting with the initial value x_0.

The mathematical biologist Robert May ([May76]) championed the introduction of the logistic difference equation into elementary mathematics courses because, despite its very simple mathematical form, it can exhibit unexpectedly complicated dynamics. This is illustrated in the following example.

Example 1-4: Period Doubling

Taking $x_0 = 0.1$ and $N = 60$ iterations, solve Equation (1.14) for **(a)** $a = 2.8$; **(b)** $a = 3.2$. In each case plot x_n versus n (using a point format) and discuss the result.

Solution: Independent of the particular programming language chosen, the logistic (or any other difference) equation is easy to solve numerically on the computer, viz.,

- Specify the coefficient value(s) (e.g., $a = 2.8$), initial condition(s) ($x_0 = 0.1$), and number ($N = 60$) of iterations.

- Iterate the difference equation(s) N times, storing the result of each iteration.

- Using a suitable plotting routine, plot the stored numerical values.

a. For $a = 2.8$, we obtain the result shown on the left of Figure 1.3. After a transient interval, the curve approaches a plateau value $x \approx 0.643$. This growth to a plateau is similar to that for the logistic ODE, although the plateau now is not at $x = 1$.
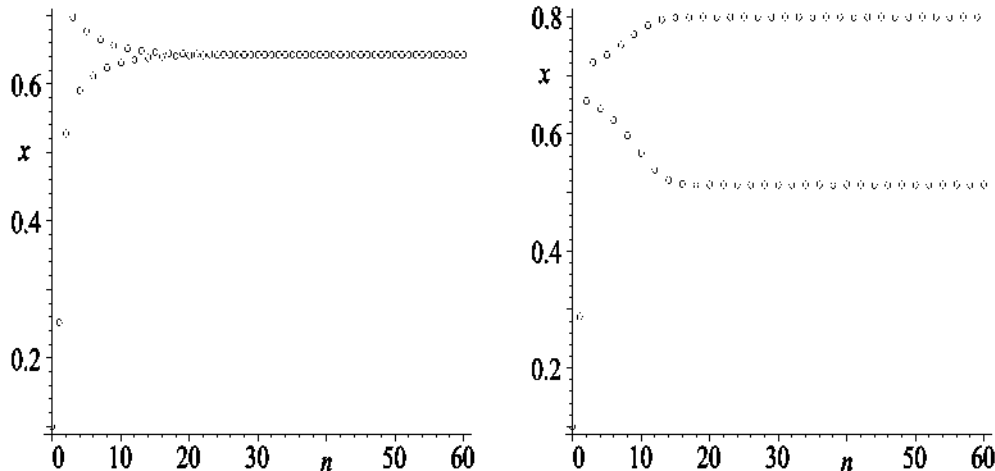
Figure 1.3: Left: solution for $a = 2.8$. Right: solution for $a = 3.2$.

b. Taking $a = 3.2$ generates the result shown on the right of Figure 1.3. After a transient interval, x_n oscillates between two "branches," with (approximate) values 0.513 and 0.799, the repeat interval between branches being $\Delta n = 2$. This surprising result is referred to as a *period-2* solution. The repeat interval in part **(a)** in steady state was $\Delta n = 1$, so this was a *period-1* solution.

If a is further increased from 3.2, a *period-4* (repeat interval $\Delta n = 4$) steady-state oscillation (4 branches) occurs, then *period-8, period-16,* and so on. This *period doubling* continues until there is no discernible repeat pattern, at which point the solution becomes *chaotic*. For larger a, the chaotic regime is interspersed with periodic "windows."

***

1.3   Solving Nonlinear ODEs on the Computer

Most nonlinear dynamical ODE (and PDE) equations that are formulated to model the "real" world cannot be solved analytically, so a computer must be used to obtain a numerical solution. The basic approach is to first replace the differential equation(s) by some *finite difference approximation* and then proceed in the same manner as in the last example. We will confine ourself here to ODEs, leaving PDEs for later discussion.

Since an nth-order ODE can always be rewritten as a system of n first-order ODEs,[5] our discussion will be for a typical first-order time-dependent ODE of the form

$$\frac{dx}{dt} = f(t, x), \tag{1.15}$$

where f is a known function. The extension to a system of first-order ODEs is straight-forward.

Historically, the *forward Euler* algorithm has served as the starting point for more sophisticated numerical schemes. Divide the continuous time t into small equal time steps of size $\Delta t \ll 1$. Let x_n be the value of x at time t_n and x_{n+1} the value at time $t_{n+1} = t_n + \Delta t$. To advance forward in time from t_n to t_{n+1}, the first derivative dx/dt is approximated by the *forward difference* approximation $(x_{n+1} - x_n)/\Delta t$. In the Euler scheme, f is evaluated at the "old" time step, i.e., we use $f(t_n, x_n) \equiv f_n$. Putting it all together, Equation (1.15) is replaced with the *Euler algorithm*

$$\frac{(x_{n+1} - x_n)}{\Delta t} = f_n,$$

or

$$x_{n+1} = x_n + f_n \, \Delta t. \tag{1.16}$$

Since this is just a (finite) difference equation, a typical computer program will involve the same steps as in Example 1-4, except the time interval Δt must be also specified.

Example 1-5: Spruce Budworm

A major problem in Canadian forests is the outbreak of the voracious spruce budworm which can defoliate a balsam tree forest in about 4 years, causing the trees to die and thus be commercially useless. Don Ludwig and co-workers ([LJH78]) have considered the normalized budworm population density x to be governed by the logistic equation with a predation term $p(x)$ due to consumption of budworms by birds, viz.,

$$\dot{x} = x\,(1 - x) - p(x). \tag{1.17}$$

Noting that for small budworm densities the predation drops rapidly as the birds tend to seek food elsewhere and at very large densities the predation saturates as the birds can only eat so much, Ludwig et al. suggested a predation term of the form

$$p(x) = \frac{b\,x^2}{(a^2 + x^2)}, \qquad \text{with } b > 0, a > 0.$$

---

[5]E.g., for $n = 2$ and f some function, the ODE $d^2x/dt^2 = f(t, x, dx/dt)$ can be rewritten as the coupled *2-dimensional system*, $dx/dt = y$, $dy/dt = f(t, x, y)$.

Taking $t_0 = 0$, $x_0 = 0.5$, $a = 0.1$, time step $\Delta t = 0.01$, and total time $T = 20$, use the Euler method to numerically solve the budworm ODE for $b = 0.1$, 0.2, 0.3, 0.4 and plot the results in the same figure. Discuss the effect of changing b.

Solution: The following procedure is carried out for each value of b:

- specify the numerical values of t_0, x_0, a, b, Δt, and T;

- calculate the number of steps $N = T/\Delta t = 20/0.01 = 2000$ that the algorithm is to be iterated;

- iterate the following Euler algorithm N times:

$$t_{n+1} = t_n + \Delta t, \qquad x_{n+1} = x_n + \Delta t \left[x_n (1 - x_n) - b\, x_n^2 / (a^2 + x_n^2) \right];$$

- form plotting points (t_n, x_n) on each time step;

- use a plotting routine to join the time-ordered sequence of plotting points.

The result is shown in Figure 1.4, the curves ordered from $b = 0.1$ at the top to $b = 0.4$ at the bottom. For small b (top two curves for $b = 0.1$ and $b = 0.2$), the predation is
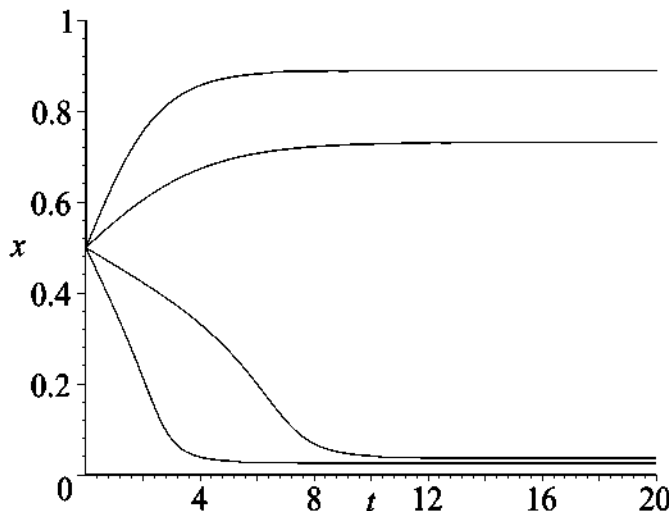
Figure 1.4: Budworm population density x versus time t.

not sufficient to prevent an "outbreak" in the budworm population. As b is increased slightly to $b = 0.3$, the outbreak is dramatically suppressed.

<center>***</center>

In some population dynamic models, there is a time delay before the system reacts. The Euler algorithm is easily modified to handle this situation as illustrated in the following example.

Example 1-6: Regulation of Hematopoiesis

The regulation of *hematopoiesis* refers to the formation of blood cell elements (white and red blood cells, platelets, etc.) in the body. The blood cells are produced in the bone marrow and then enter the bloodstream. When the level of oxygen in the blood decreases, a substance is released which causes a time-delayed increase in the release of blood elements from the marrow. Leon Glass and Michael Mackey ([MG77], [GM79]) have formulated a simple model equation for this process.

Let $C(t)$ be the concentration of cells (number of cells/mm^3) in the circulating blood at time t (measured in days). The concentration is governed by the ODE

$$\dot{C}(t) = -g\,C(t) + P(C(t-\tau)), \tag{1.18}$$

the first term on the right-hand side representing the rate at which blood cells are lost, the positive coefficient g having the units (day)$^{-1}$. The second term represents the concentration-dependent time-delayed production of blood cells by the marrow, τ being the time delay. After the reduction of cells in the bloodstream there is about a $\tau = 6$ day time delay before the marrow releases further blood cells to make up the deficit. The production P depends on the concentration at the earlier time $t - \tau$. One mathematical form for P considered by Mackey and Glass is

$$P(C(t-\tau)) = \frac{\lambda\,a^m\,C(t-\tau)}{a^m + (C(t-\tau))^m}, \tag{1.19}$$

with λ, a, and m being positive constants. Combining equations, and setting $x \equiv C/a$, yields the nonlinear *delay-differential* equation

$$\dot{x}(t) = -g\,x(t) + \frac{\lambda\,x(t-\tau)}{1 + (x(t-\tau))^m}. \tag{1.20}$$

a. Taking $g = 0.1\,\mathrm{day}^{-1}$, $\lambda = 0.2\,\mathrm{day}^{-1}$, $m = 10$, $\tau = 6$ days, and $x(0) = 0.1$, numerically solve (1.20) using the Euler method with $\Delta t = 0.01$ and a total time $T = 600$ days. Plot x versus t and $x(t - \tau)$ versus $x(t)$ and discuss the graphs.

b. How would the behavior of the solution change if the time delay were $\tau = 20$ days, all other parameter values remaining unchanged?

Solution: a. The following steps are carried out:

- specify $t_0 = 0$, $\Delta t = 0.01$, $\tau = 6$, $\lambda = 0.2$, $g = 0.1$, and $m = 10$;

- calculate the total integer number N of time steps, $N = T/\Delta t = 60000$;

- calculate the integer number d of time steps associated with the time delay, $d = \tau/\Delta t = 600$;

- for integer n from $-d$ to 0 set $x_n = 0.1$; note: in order to integrate forward in time from $t_0 = 0$, it is necessary to make some assumption about the values of x between $-\tau$ and 0;

- for integer n from 0 to N iterate

$$t_{n+1} = t_n + \Delta t, \quad x_{n+1} = x_n + \left[-g\,x_n + \frac{\lambda\,x_{n-d}}{1 + x_{n-d}^m} \right] \Delta t;$$

- form plotting points (t_n, x_n) and (x_n, x_{n-d}) on each time step and use a plotting routine to join the time-ordered sequence of plotting points.

Carrying out the above steps, we find that for $\tau = 6$ days the normalized blood cell concentration varies with time as shown on the left of Figure 1.5.
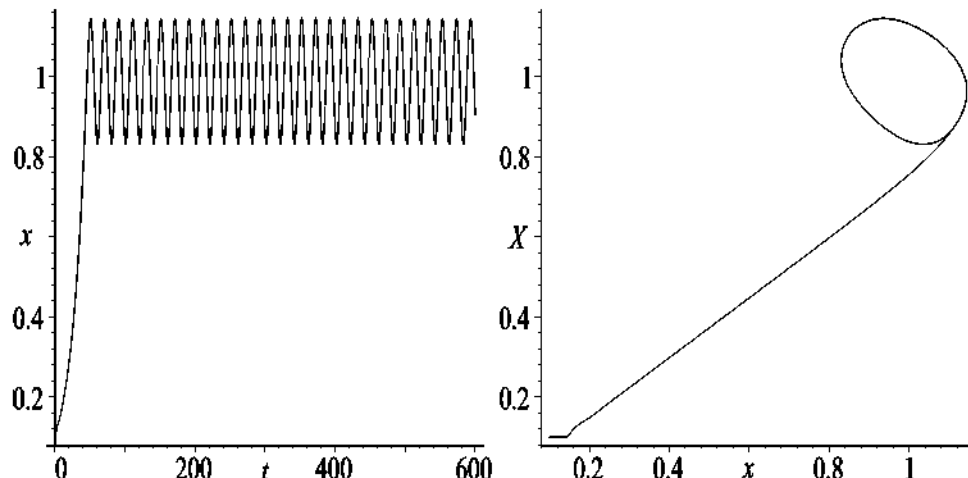
Figure 1.5: Left: x vs. t for $\tau = 6$ days. Right: $X \equiv x(t - \tau)$ vs. $x(t)$.
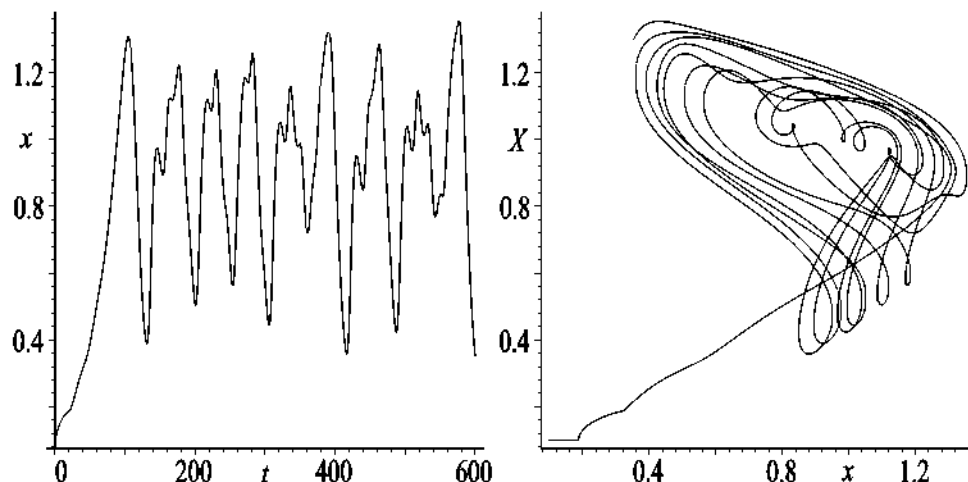
Figure 1.6: Left: x vs. t for $\tau = 20$ days. Right: $X \equiv x(t - \tau)$ vs. $x(t)$.

After a short transient interval, the concentration settles down to a steady-state, low-amplitude, periodic oscillation. The period of the oscillation is about 20 days.

Turning to the figure on the right of Figure 1.5, the ODE system traces out a *trajectory* in the $x(t - \tau)$ vs. $x(t)$ plane (referred to as the *phase plane*). After the transient interval, the phase-plane trajectory settles down on a single closed loop indicative of a periodic solution.

(b) When the time delay is increased from 6 days to 20 days, a nonrepeating pattern of oscillations occurs as shown on the left of Figure 1.6. Taking even longer times confirms that we are not just looking at the transient, but that the oscillations are indeed *aperiodic* or *chaotic*. The nonrepeating chaotic trajectory in the $x(t - \tau)$ versus $x(t)$ phase plane is shown on the right.

<div align="center">***</div>

To obtain a numerically accurate answer with the Euler algorithm, the step size must be taken to be quite small. If the time interval under consideration is not short, such as in this last example, this leads to a very large number of time and, therefore, computational steps. This becomes a problem for many nonlinear models involving systems of ordinary or partial differential equations such as those used in numerically predicting the weather. Obviously, one wants the computation to be sufficiently fast so as to predict the weather before it actually occurs. Even with a supercomputer, computationally accurate and fast algorithms are required.

So computer scientists over the decades have devised more sophisticated algorithms which combine high accuracy with fewer time steps thus leading to greater computational speed. A discussion of these numerical schemes is found in standard numerical analysis texts such as the one by Burden and Faires ([BF89]).

For a fixed time step Δt, the algorithm which best combines accuracy and speed is the *fourth-order Runge–Kutta* (abbreviated RK4) scheme. The phrase "fourth-order" refers to the accuracy of the algorithm, RK4 having an accuracy of order $(\Delta t)^4$. The Euler method, on the other hand, is only a "first-order" algorithm, the accuracy being of order Δt.

The fourth-order Runge–Kutta approximation to Equation (1.15) is

$$x_{n+1} = x_n + \frac{1}{6}\left(k_1 + 2\,k_2 + 2\,k_3 + k_4\right)\Delta t, \tag{1.21}$$

with

$$k_1 = f(t_n, x_n), \quad k_2 = f(t_n + \Delta t/2, x_n + k_1/2),$$

$$k_3 = f(t_n + \Delta t/2, x_n + k_2/2), \quad k_4 = f(t_n + \Delta t, x_n + k_3). \tag{1.22}$$

Example 1-7: Lotka–Volterra Predator–Prey Equations

Extending the ideas on population dynamics for a single species to interacting species, the mathematicians Vito Volterra (1860–1940) and Alfred Lotka (1880–1949) independently ([Vol26b], [Vol26a], [Lot56]) formulated a simple nonlinear model of the interaction between predators and their prey. Volterra's work was motivated by the cyclic

variation in predator (sharks, skates, etc.) numbers in fish catches in the Adriatic sea during the early 20th century observed by his biologist son-in-law Humberto D'Ancona. Assuming that the predators (population number or density, y) only survive by eating the prey (x), while the prey have abundant space and food over the time interval being considered, the Lotka–Volterra (LV) predator–prey equations are

$$\dot{x} = a\,x\,(1 - b\,y/a) = a\,x - b\,x\,y \equiv f(x,y), \quad a > 0,\, b > 0,$$

$$\dot{y} = -c\,y\,(1 - d\,x/c) = -c\,y + d\,x\,y \equiv g(x,y), \quad c > 0,\, d > 0.$$

(1.23)

a. Discuss the structure of the Lotka–Volterra equations.

b. On the planet Erehwon, the rat (the prey) and feral cat (predator) population densities, $R(t)$ and $C(t)$ respectively, evolve with time according to the LV equations with $a = 3$, $b = 1/2$, $c = 1$, $d = 1/10$, $R(0) = 10$, $C(0) = 5$, and the time in years. Taking $\Delta t = 0.01$ year, solve the LV ODEs over a time interval of 50 years with (i) the forward Euler method; (ii) the RK4 method. In each case, plot and discuss the trajectory in the $C(t)$ versus $R(t)$ (phase) plane.

c. For the RK4 method, plot $R(t)$ and $C(t)$ in the same figure and discuss the result.

Solution: a. In the absence of any interaction between predator and prey, the predators would starve to death, their population number decreasing to zero according to the Malthus ODE, $\dot{y} = -c\,y$, with $c > 0$. On the other hand, the prey population would grow according to the Malthus ODE, $\dot{x} = a\,x$, with $a > 0$. The presence of the predators will reduce the growth rate of prey, the constant a being replaced (in the spirit of Verhulst) with the predator-dependent term $a\,(1 - b\,y/a)$ with b positive. Similarly, the presence of prey will reduce the negative growth rate of predators, the constant $-c$ being replaced with the prey-dependent term $-c\,(1 - d\,x/c)$, with d positive.

b. i. In the forward Euler approximation, the rats–cats Lotka–Volterra ODE system

$$\dot{R} = 3\,R - \frac{1}{2}\,R\,C \equiv f(R,C), \quad \dot{C} = -C + \frac{1}{10}\,R\,C \equiv g(R,C)$$

is replaced with the finite difference equation system

$$R_{n+1} = R_n + f(R_n, C_n)\,\Delta t,$$

$$C_{n+1} = C_n + g(R_n, G_n)\,\Delta t,$$

$$t_{n+1} = t_n + \Delta t.$$

With $R(0) = 10$, $C(0) = 5$, and $\Delta t = 0.01$, the finite difference equations are iterated from $n = 0$ up to $n = N = 50/\Delta t = 5000$. Plotting points (R, C) are formed on each time step. Joining the plotting points, the solution curve in the $C(t)$ versus $R(t)$ phase

plane is plotted on the left of Figure 1.7. Time evolves counterclockwise around the
solution curve from the starting point $R(0) = 10$, $C(0) = 5$. The solution curve spirals
outwards with increasing time, not displaying a closed loop which would be expected if
the population densities were cyclic.
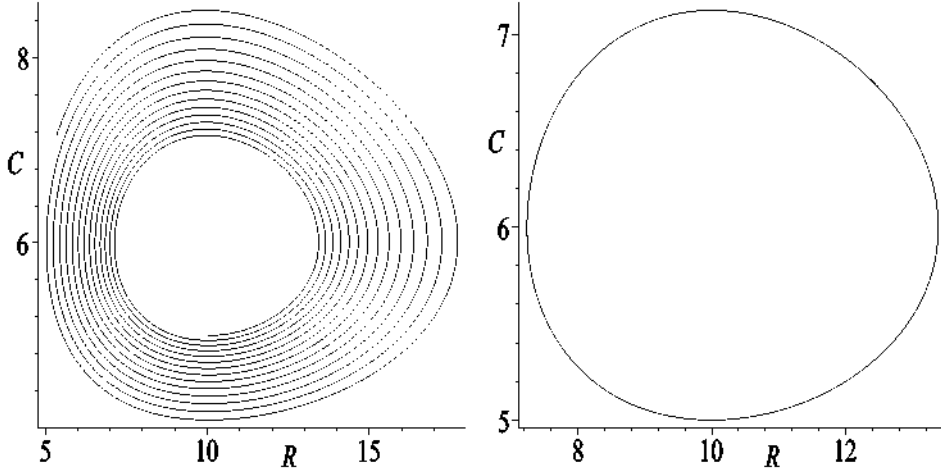
Figure 1.7: Left: Forward Euler solution of rats–cats ODEs. Right: RK4 solution.

ii. To show that the outward spiral is an artifact of the not-very-accurate Euler method,
let's now use the RK4 scheme with exactly the same time step. For the RK4 method,
the finite difference equations for the rats and cats are

$$R_{n+1} = R_n + \frac{1}{6}\left(k_1 + 2\,k_2 + 2\,k_3 + k_4\right)\Delta t,$$

$$C_{n+1} = C_n + \frac{1}{6}\left(m_1 + 2\,m_2 + 2\,m_3 + m_4\right)\Delta t, \tag{1.24}$$

$$t_{n+1} = t_n + \Delta t,$$

with

$$k_1 = f(R_n, C_n), \quad m_1 = g(R_n, C_n),$$

$$k_2 = f(R_n + k_1/2, C_n + m_1/2), \quad m_2 = g(R_n + k_1/2, C_n + m_1/2),$$

$$k_3 = f(R_n + k_2/2, C_n + m_2/2), \quad m_3 = g(R_n + k_2/2, C_n + m_2/2),$$

$$k_4 = f(R_n + k_3, C_n + m_3), \quad m_4 = g(R_n + k_3, C_n + m_3).$$

$$\tag{1.25}$$

Iterating the finite difference system (1.24) from $n = 0$ to $n = N = 5000$ with the same
initial values and time step produces the correct cyclic behavior displayed on the right
of Figure 1.7.

c. Forming plotting points (t, R) and (t, C) on each time step and plotting each solution curve as a solid line, the periodic behavior of the rat and cat population densities with time t is shown in Figure 1.8. The lower curve is for the cats, the upper curve for the rats. Note that the cycles are slightly out of phase, the rat population not being a minimum when the cat population is a maximum.
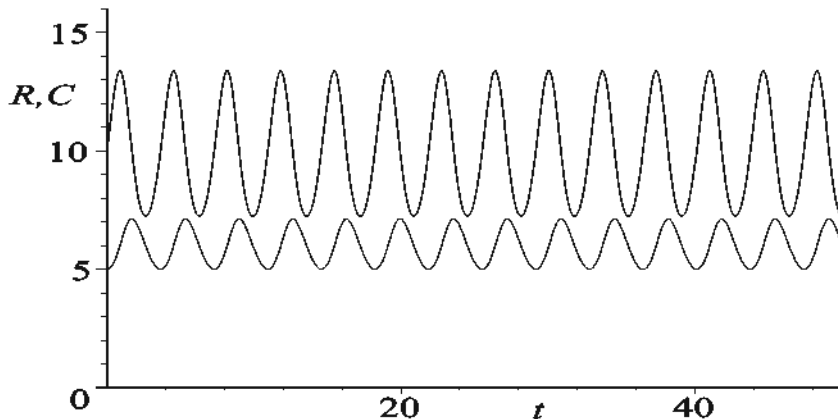
Figure 1.8: Periodic behavior of rat and cat population densities.

***

Although the above example involved a fictitious planet, it should be noted that cyclic variations in population numbers due to predator–prey interaction have been observed here on Earth. Figure 1.9 shows the trading records of fur catches of lynx (the
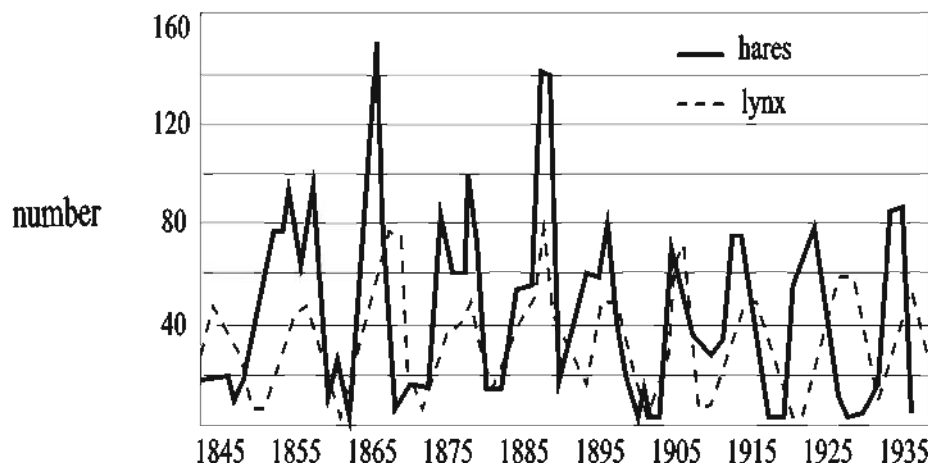
Figure 1.9: Trading records of fur catches for the Hudson's Bay Company.

predator) and snowshoe hares (the prey) for the Hudson's Bay Company in the Canadian north for the period 1845 to 1935.

Turning back to our discussion of numerical schemes, the RK4 algorithm involves more computations on each time step than the Euler method, but this is compensated for by the fact that the step size can be taken to be larger. However, Δt cannot be taken too large or the numerical solution will display wild oscillations (referred to as *numerical instability*) which bear no resemblance to the real solution. Numerical instability is a potential problem for all *explicit*[6] schemes built on the forward difference approximation to the time derivative.

To save even more computer time, *variable step* algorithms are very popular and are usually the default numerical solver in most computer software packages. These algorithms change the step size according to the numerical "terrain" being encountered, taking larger steps when the terrain is relatively flat and smaller steps when the solution curve begins to get steep. One of the best known of these numerical schemes is the *Runge–Kutta–Fehlberg 45 (RKF45)* algorithm (see [BF89] for the details) which on each step compares the RK4 solution with that obtained with a fifth-order accurate Runge–Kutta (RK5) scheme. When the difference between the RK4 and RK5 answers exceeds a specified tolerance, the step size is reduced. If the difference is smaller than some specified value, the step size is increased.

Completing this very brief introduction to solving ODEs on the computer, let us turn to the issue of programming languages. Historically, computer programming languages such as Fortran and C have evolved to perform the necessary number crunching. However, over the last several years more powerful programming languages have been developed which not only can perform numerical calculations but also can carry out complicated symbolic manipulations (differentiation, integration, Taylor expansion, etc.) as well, including finding analytical solutions to nonlinear ODEs and difference equations, when such solutions exist. Computer software systems which can perform symbolic as well as numerical calculations are referred to as *computer algebra systems* (CASs). Currently, the two predominant CASs are *Maple* and *Mathematica*. *Mathcad*, another system popular with engineers for doing numerical calculations, uses the *Maple* kernel to perform symbolic manipulations. Conversely, *Maple* has the capability of accessing *Mathcad*. Most colleges and universities have site licenses for one or more of these computer algebra systems, and (relatively) inexpensive student versions are also available.

In this book, we will present some dynamical problems which must be solved numerically. The choice of programming language or computer software is left up to you. The standard source book for Fortran and C programming is *Numerical Recipes* by Press et al. ([PFTV89]). If you are interested in seeing *Maple* or *Mathematica* programming applied to nonlinear physics and other areas of science, consult one of the computer algebra "recipe" texts by Enns and McGuire ([EM00], [EM01], [EM06], [EM07]).

We finish this chapter with the following example which is solved using the RKF45 algorithm.

---

[6]So-called *implicit* schemes, built on a *backward difference* approximation to the time derivative (dx/dt replaced with $(x_n - x_{n-1})/\Delta t$), avoid numerical instability but one must solve a set of simultaneous (in general, nonlinear) equations on each time step. See [BF89].

Example 1-8: More Realistic Predator–Prey Model

The Lotka–Volterra predator–prey model assumes that the prey growth is unbounded in the absence of predation. More realistically, a finite carrying capacity K should be included. Also assuming that the predation term shows some saturation, Jim Murray ([Mur02]) has suggested a prey equation of the form

$$\dot{X} = r\,X\left(1 - \frac{X}{K}\right) - \frac{k\,X\,Y}{(X + C)}, \tag{1.26}$$

with X and Y the prey and predator population densities and r, K, k, and C all positive constants. Assuming that the carrying capacity for the predator is directly proportional to the prey density, he also suggested the predator equation (with s, $h > 0$)

$$\dot{Y} = s\,Y\left(1 - \frac{h\,Y}{X}\right). \tag{1.27}$$

a. By rewriting the two nonlinear ODEs in dimensionless form, show that the number of parameters may be reduced from six to three.

Solution: Setting

$$\tau = r\,t, \quad x(\tau) = \frac{X(t)}{K}, \quad y(\tau) = \frac{h\,Y(t)}{K},$$

and

$$a = \frac{k}{h\,r}, \quad b = \frac{s}{r}, \quad c = \frac{C}{K},$$

the coupled ODE system becomes

$$\dot{x} = x\,(1 - x) - \frac{a\,x\,y}{x + c},$$
$$\dot{y} = b\,y\left(1 - \frac{y}{x}\right), \tag{1.28}$$

with three dimensionless parameters a, b, and c.

b. Using the RKF45 method, numerically solve the dimensionless ODE system (1.28) for $a = 0.75$, $b = 0.15$, $c = 0.05$ and the two initial conditions:

(i) $x(0) = 0.3$, $y(0) = 0.3$;
(ii) $x(0) = 0.75$, $y(0) = 0.5$.

Create phase-plane (y vs. x) plots for both solution curves and plot them in the same figure. Discuss the results.

Solution: Using the RKF45 numerical method, the solution curves are generated for the two initial conditions and plotted in the y vs. x phase plane as shown in Figure 1.10. For both initial conditions, the solution curves eventually wind onto the same closed loop. This is an example of a stable *limit cycle*, a periodic solution which is approached as $t \to +\infty$, irrespective of the initial conditions.
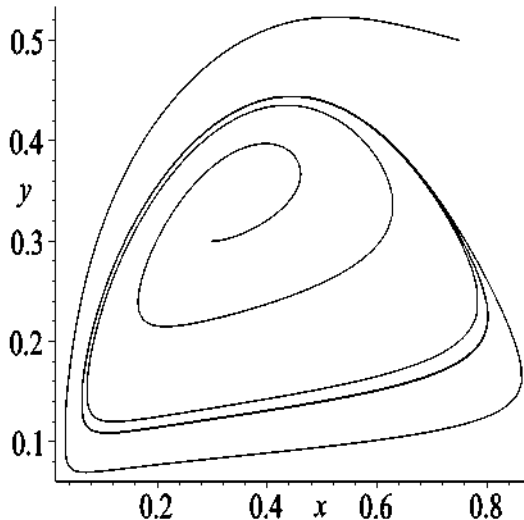
Figure 1.10: Two solution curves evolving onto a stable limit cycle.

***

As will be illustrated later in the text, such stable limit cycles are observed in the real world for electronic, chemical, and biological oscillators.

PROBLEMS

Problem 1-1: The logistic curve
By separating variables, explicitly derive the mathematical form, Equation (1.8), of the logistic curve.

Problem 1-2: Time of maximum growth
Derive the general formula, Equation (1.9), for the time of maximum growth of the logistic curve.

Problem 1-3: The Hubbert curve
Derive the mathematical form, Equation (1.11), of the Hubbert curve.

Problem 1-4: *Schizosaccharomyces kephir*
In another of his pioneering yeast experiments, Gause ([Gau69]) found that the growth of the yeast *Schizosaccharomyces kephir* satisfied the logistic ODE with $x_0 = 0.0919$ and $r = 0.0607$. Plot $x(t)$ over the first 160 hours of growth and compare with that for the yeast *Saccharomyces cerevisiae*. Determine the time at which the growth was a maximum.

Problem 1-5: Myxomatosis
Myxomatosis is a disease caused by the *myxoma virus* which infects and kills rabbits. First observed in Uruguay in the 1900s, it was deliberately introduced into Australia in 1950 in an attempt to control the vast hordes of rabbits which were causing crop

damage. Within 2 years, the population of 600 million rabbits was reduced to 100 million. The surviving population acquired partial immunity, so that in 1996 a second virus (rabbit calcivirus) was introduced.

Suppose that the growth of the rabbit population number N is governed by the Verhulst ODE, $\dot{N} = r\,N\,(1 - N/N_0)$, where N_0 is the equilibrium number (carrying capacity). After an epidemic of myxomatosis has suddenly reduced the rabbit population number to 2% of N_0, the rabbits grow according to the logistic equation with a rate constant $r = 0.25$, time being measured in months. How many months does it take for N to climb back up to 50% of N_0? Plot $N(t)/N_0$ over this time interval.

Problem 1-6: Pella–Tomlinson model for yellowfin tuna

In order to describe the time evolution of the yellowfin tuna (*Thunnus albacares*) fish population in the eastern Pacific, Pella and Tomlinson ([PT69]) proposed the following modified logistic model for the normalized fish population number x:

$$\dot{x} = r\,x\,(1 - x^m), \quad \text{with } r > 0,\, m \geq 1,\, \text{and } x(0) = x_0.$$

a. By separating variables, analytically determine $x(t)$ for arbitrary $m \geq 1$.

b. Determine the time T at which $x(t)$ grows fastest.

c. Taking $r = 3$, $x_0 = 1/2$, plot $x(t)$ and calculate T for $m = 1$ and 2 and compare the results.

Problem 1-7: Symbiosis

When the interaction of two species is to the advantage of both, this situation is referred to as *symbiosis* or *mutualism*. A simple model ([Mur02]) of symbiosis for two species with normalized population densities x and y is given by the following ODE system:

$$\dot{x} = x\,(1 - x + a\,y),$$

$$\dot{y} = r\,y\,(1 - y + b\,x),$$

with the dimensionless parameters a, b, and r all positive. Using the forward Euler method with $r = 0.1$ and $\Delta t = 0.01$ and plotting $x(t)$ and $y(t)$, investigate and discuss the change in behavior of the solution curves as the product $a\,b$ is increased through the critical value $a\,b = 1$. Include several different initial conditions for each plot.

Problem 1-8: Regulation of hematopoiesis

In the regulation of hematopoiesis example,

a. show by plotting x vs. t that a period-two oscillation occurs for $x(0) = 0.1$, $g = 1$, $\lambda = 2$, $T = 2$, and $m = 10$. Take $\Delta t = 1/100$ and a total time 80.

b. plot $x(t - T)$ vs. $x(t)$ for the time interval $t = 60$ to $t = 80$ and discuss the result.

c. explore the periodicity (period-1, period-2, or ?) for the interval $m = 7$ to 20, all other parameter values remaining unchanged.

Problem 1-9: White dwarf ODE
In his theory of white dwarf stars, the 1983 Nobel physics laureate Subrahmanyan Chandrasekhar (1910–1995) introduced ([Cha39]) the second-order nonlinear ODE

$$x \frac{d^2 y}{dx^2} + 2 \frac{dy}{dx} + x (y^2 - C)^{3/2} = 0,$$

with C a positive parameter and boundary conditions $y(0) = 1$, $dy(0)/dx = 0$.

   a. Write the second-order ODE as a system of two first-order ODEs.

   b. Taking $C = 0.1$ and $\Delta t = 0.01$, use the forward Euler method to numerically compute $y(x)$ over the range $0 \le x \le 4$. To avoid any problem at the origin, start at $x = 0.01$.

   c. Plot $y(x)$.

Problem 1-10: Australian sheep blowfly
Robert May ([May75]) has applied the normalized logistic delay-differential equation

$$\dot{x}(t) = x(t) \left(1 - x(t - \tau)\right)$$

to experimental data ([Nic57]) on the Australian sheep blowfly (*Lucilia cuprina*), a pest of considerable importance in Australian sheep farming. Here x is the normalized population number at time t and the normalized delay time τ is approximately the time for a larva to mature into an adult.

   Taking $x(0) = 0.1$, $\tau = 2.1$, $\Delta t = 0.01$, and a total time $T = 80$, use the Euler algorithm to numerically solve the logistic delay-differential equation for $x(t)$. Plot and discuss the result.

Problem 1-11: A fish harvesting model
To take into account the effect of fishing on a single species of fish, a *harvesting term* can be added to the dimensionless logistic equation describing population growth, viz.,

$$\frac{dx(t)}{dt} = x (1 - x) - \frac{h\,x}{(a + x)}.$$

The harvesting coefficient h and the parameter a are both positive.

   a. Discuss the structure of the harvesting term.

   b. Taking $x(0) = 0.1$, $a = 0.2$, and $\Delta t = 0.1$, use the RK4 method to numerically solve this ODE for the following increasing values of the harvesting coefficient, $h = 0.1, 0.2, 0.3, \ldots$.

   c. Plot $x(t)$ versus t for each h value.

   d. Discuss the change in behavior of the solution as h is increased.

Problem 1-12: Only the lonely
On the bucolic planet of Erehwon, gnus and their genetically modified relatives, the sung, are put together in a large enclosed pasture where they munch on the clover, their

only food supply. Suppose that the dynamical equations describing the gnu number $g(t)$ and sung number $s(t)$ (per unit area) at time t are

$$\frac{dg}{dt} = g\left(\frac{5}{2} - g\right) - 2gs,$$

$$\frac{ds}{dt} = s(2 - s) - \frac{3}{2}gs.$$

a. Interpret the mathematical structure of these equations. For example, why do the gnu–sung interaction terms have the same sign here?

b. Assume that $g(0) = 5$ and $s(0) = 5$. Solving the ODE system numerically using the RK4 method with time step $\Delta t = 0.01$, create a phase-plane portrait (plot of s versus g) for the gnus and sung and describe what happens.

c. By making a suitable plot, determine the approximate time at which the sung population is a minimum.

d. Try some other initial conditions. What can you conclude? Can the gnus and sung ever coexist?

Problem 1-13: Competing for the same resources
A simple model ([Mur02]) for two species with normalized population densities x and y competing for the same limited resources is given by the following ODE system:

$$\dot{x} = x(1 - x - ay),$$

$$\dot{y} = ry(1 - y - bx),$$

with the dimensionless parameters a, b, and r all positive.

Taking $x(0) = y(0) = 0.1$, $b = 0.2$, $r = 0.3$, and $\Delta t = 0.1$, numerically solve for $x(t)$ and $y(t)$ using the RK4 method for:

(i) $a = 0.5$; **(ii)** $a = 1.0$; **(iii)** $a = 1.5$.

Plot $x(t)$ and $y(t)$ in the same figure for each case and discuss the results.

Problem 1-14: More realistic predator–prey model
Using the RKF45 method, investigate the effect of increasing the value of b in the more realistic predator–prey model, holding the initial conditions and all other parameter values fixed at the same values as in the text example. Discuss the resulting plots.

Problem 1-15: Biochemical switch
Explaining such biological patterns as those on the wings of a butterfly is an area of much scientific interest. A simple model of a biochemical switch for turning on a gene, which is normally inactive, to produce a pigment has been suggested by Mitchison ([Mit77]), used by Lewis et al. ([LSW77]), and discussed in detail in Murray ([Mur02]).

The dimensionless model equation is

$$\dot{x}(\tau) = s - \gamma x + \frac{x^2}{1 + x^2},$$

where $x(\tau)$ is the normalized concentration of pigment at time τ, $s > 0$ the normalized concentration of biochemical signal substance which activates the gene, and $\gamma > 0$ the degradation coefficient. Numerically explore this model equation for different values of s and γ using the Euler algorithm with $\Delta\tau = 0.01$ and $x(0) = 0$. Plot the results and discuss them.

Problem 1-16: Baleen whales
Robert May ([May80]) has proposed the following normalized equation to describe the population number x of sexually mature adult baleen whales at time t:

$$\dot{x}(t) = -a\,x(t) + b\,x(t - \tau)(1 - (x(t - \tau))^n).$$

Here a and b are the mortality and reproduction coefficients, τ the time lag necessary to achieve sexual maturity, and n a positive parameter. If the term $1 - (x(t - \tau))^n < 0$, then this term is to be set equal to zero.

Taking $a = 1$, $b = 2$, $\tau = 2$, and step size $\Delta t = 0.01$, use the Euler method to numerically solve for $x(t - \tau)$ versus $x(t)$ and for $x(t)$ over the time interval $t = 0$ to 40 for (a) $n = 3.0$, (b) $n = 3.5$. Plot the results and interpret the figures.

Problem 1-17: FitzHugh–Nagumo equations for nerve cell firing
The FitzHugh–Nagumo equations ([Fit61], [NAY62]) capture the important aspects of electrical impulse transmission in nerve cells. With v the voltage across the cell membrane and w a recovery variable, the model equations are

$$\dot{v} = i(t) - v\,(v - a)\,(v - 1) - w,$$

$$\dot{w} = b\,(v - c\,w).$$

Here a, b, and c are positive constants and $i(t)$ is the stimulus current injected into the cell at time t.

Taking the values

$$a = 0.139, \quad b = 0.008, \quad c = 2.54, \quad v(0) = w(0) = 0, \quad i(t) = \begin{cases} A, & 10 \le t < 20, \\ 0, & \text{otherwise,} \end{cases}$$

use the RK4 method to determine $v(t)$ for t up to 120 seconds for

(i) $A = 0.02$; (ii) $A = 0.03$, (iii) $A = 0.10$.

Plot $v(t)$ and comment on the change of behavior as A is varied.

The sequence of firing and returning to rest in the 0.03 and 0.10 cases are examples of an *action potential*.

Problem 1-18: The Andromeda Strain revisited

How many *E. coli* would there be after 48 hours? The diameter of an *E. coli* bacterium is about 10^{-6} m. How would the volume of *E. coli* after 48 hours compare with the volume of the Earth which is about 10^{21} m^3?

Problem 1-19: Exploring the logistic difference equation

Consider the logistic difference equation (1.14) with $x_0 = 0.1$ and the following a values: (i) $a = 3.40$, (ii) $a = 3.50$, (iii) $a = 3.70$, and (iv) $a = 3.83$. In each case, calculate x_n up to $n = N = 150$ and plot x_n versus n. By examining the repeat interval, determine the period of each solution. Which one of the a values probably corresponds to chaos?

Problem 1-20: Predator–prey difference equations

Lauwerier ([Lau86]) has suggested the following predator–prey difference equation model for the population numbers of two species:

$$x_{n+1} = a\,x_n\,(1 - x_n - y_n), \quad 2 < a \leq 4,$$

$$y_{n+1} = b\,x_n\,y_n, \quad 2 < b \leq 4.$$

a. Explain the structure of these difference equations, identifying which is the predator and which is the prey.

b. Taking $a = b = 3.0$, $x_0 = 0.5$, $y_0 = 0.2$, iterate the difference equation system $n = N = 2000$ times. Taking only the last 100 points to eliminate any possible transient, separately plot x_n vs. n and y_n vs. n and interpret the results. Hint: how many branches are there?

c. Explore other values of a and b in the allowed ranges and in each case discuss the graphical results.

Problem 1-21: Propagation of annual plants ([EK88])

Certain annual plants produce seeds at the end of their growth season in September and then wither and die. A fraction of these seeds survive the winter and some of these germinate at the beginning of the following growing season in May, producing a new generation of plants. The fraction that germinates depends on the age of the seeds, but seeds older than 2 years do not germinate.

Letting

- γ be the number of seeds produced per plant in September;

- σ be the fraction of seeds that survive the winter;

- α be the fraction of 1-year-old seeds that germinate in May;

- β be the fraction of 2-year-old seeds that germinate in May;

derive a single difference equation for the number N_n of plants in generation n. Is the difference equation linear or nonlinear? Explain.

Problem 1-22: Population growth
For a population of size P, the birth and death rates (i.e., the number of births and deaths as fractions of the population) per year are equal to $(0.72 - 0.000051\,P)$ and $(0.22 + 0.00016\,P)$, respectively.

a. Write down the difference equation for the growth of this population.

b. Plot the population number P as a function of year for $P(0) = 10^4$.

c. At what minimum time will the population number be within 1% of the steady-state value?

Problem 1-23: Nonlinear models of social systems
V. P. Jain Karmeshu ([Kar03]) has discussed the use of non-linear modelling to capture the intricate dynamics of social systems. Present the main ideas and associated examples contained in this article. A reprint is available online at:

www.scribd.com/doc/22989/Nonlinear-Models-of-Social-Systems.

Problem 1-24: Nonlinear acoustics in cicada mating calls
The cicada emits one of the loudest sounds in all of the insect population, generating a sound intensity disproportionate to its small size. An explanation of why has been given by Derke Hughes ([HNKC09]) and coworkers in a journal article entitled "Nonlinear acoustics in cicada mating calls enhance sound propagation." A reprint of this paper is available online at:

www.dtic.mil/cgi-bin/GetTRDoc?AD=ADA502955&Location=U2
&doc=GetTRDoc.pdf.

Discuss in detail the nature of the nonlinearity associated with enhancing the cicada mating call.

Chapter 2

World of Nonlinear ODEs

Not only in research, but also in the everyday world..., we would all be better off if more people realized that simple nonlinear systems do not necessarily possess simple dynamic properties.
Robert M. May, mathematical biologist, *Nature*, Vol. 261, 459 (1976)

In the next three chapters some of the more important mathematical properties of nonlinear dynamical systems as well as the diagnostic tools for analyzing such systems will be introduced. This is a vast subject, so we will only present enough so that you can appreciate and understand the various topics that will be presented in subsequent chapters as we explore the various domains of our nonlinear world. Where needed to further our understanding, we will later expand on these nonlinear mathematical concepts, and even introduce some new ones. In this chapter the properties of nonlinear ODE systems are examined, the subsequent two chapters dealing with nonlinear difference equations (commonly referred to as nonlinear *maps*) and, much more briefly, with nonlinear PDEs and cellular automata.

We will begin by discussing the "breakdown" of the linear superposition principle for nonlinear ODEs. Because of this breakdown, many of the "bread and butter" mathematical techniques (such as Laplace transforms and Fourier analysis) for solving linear ODEs no longer work or are useful for attempting to solve nonlinear ODEs. This necessitates the introduction of new mathematical approaches, many of which apply only to certain classes of nonlinear equations. Some of these mathematical methods are beyond the scope and level of this introductory text and will not be covered. Our intention here is to provide a simple, yet sufficient, mathematical framework that the reader can understand and analyze the various nonlinear models that will be presented in ensuing chapters. Our goal is to give you a glimpse of the nonlinear world, not to teach you all the mathematical tricks that exist for solving nonlinear dynamical equations.

It should also be mentioned that the frontiers of nonlinear dynamics are constantly being pushed out with new ideas and applications continually appearing on a regular basis in various research publications. At present there is a somewhat "piecemeal" approach to tackling nonlinear dynamical equations, but, undoubtedly, as the subject matures, new mathematical techniques and concepts will be discovered and further "unification" will occur.

2.1   Breakdown of Linear Superposition

A general feature of all nonlinear dynamical equations, including nonlinear ODEs, is the "breakdown" of linear additivity or superposition. In the nonlinear world, two plus two can sometimes make five and doubling the stimulus may not double the response. In the world of nonlinear dynamics, a linear combination of two solutions to a nonlinear ODE will generally produce a *nonsolution*.

As a simple example of these ideas, let's look at the amount x of stretching of a spring fixed at one end which has a force F applied to the other. If the force is not too large, a very good approximation to experimental reality is to assume that there is a linear relationship between x and F, viz.,

$$F = k\,x, \tag{2.1}$$

a relationship which is referred to as *Hooke's law* after its discoverer Robert Hooke.[1] The positive proportionality constant k is called the *spring constant* and is a measure of the stretchability of the spring.

However, if the applied force is sufficiently large (but not large enough to permanently deform the spring) or if the "spring" is actually is a clever assembly of a collection of springs, Hooke's law may be inadequate, the relationship between amount of stretching and applied force being nonlinear. For example, if the stretching is symmetric about the equilibrium point, the nonlinear force law

$$F_{NL} = k\,x + k_2\,x^3 \tag{2.2}$$

is often found to be a good approximation to reality.

If the constant $k_2 > 0$, the spring is referred to as a *hard spring* since it is harder to stretch the spring by a given amount x than if only Hooke's law prevailed ($k_2 = 0$). Doubling the nonlinear force doesn't double the amount of stretching.

For $k_2 < 0$, the spring is referred to as *soft*. Experimentally, "hard" and "soft spring" situations can be created in the laboratory and many of the nonlinear dynamical properties discussed in this chapter can be verified. The interested reader is referred to Enns and McGuire's *Nonlinear Physics* ([EM00]) where various simple experimental activities involving hard and soft springs may be found.

Now consider a mass m which is displaced from equilibrium by an amount x and which experiences a restoring force given by $F = -F_{NL}$, no other forces (such as friction) being present. Newton's second law of motion (force=mass × acceleration) then yields the following second-order nonlinear ODE for the motion of the mass:

$$m\,\ddot{x} = F = -k\,x - k_2\,x^3,$$

or, on rearranging and setting $\alpha \equiv k/m$ and $\beta \equiv k_2/m$,

$$\ddot{x} + \alpha\,x + \beta\,x^3 = 0. \tag{2.3}$$

---

[1] Although now best remembered for this law, Robert Hooke (1635−1703) was the inventor of the iris diaphragm in cameras, the universal joint in cars, the balance wheel in a watch, and the person who introduced the word "cell" in biology.

If the coefficient $\beta = 0$ (i.e., Hooke's law prevails), this ODE reduces to the well-known linear *simple harmonic oscillator* (SHO) equation,

$$\ddot{x} + \omega^2 x = 0, \tag{2.4}$$

where $\omega = \sqrt{\alpha}$. It is well known that $x_1 = \sin \omega t$ and $x_2 = \cos \omega t$ are independent solutions of the SHO, i.e., substitution of either x_1 or x_2 into the left-hand side (lhs) of the SHO yields 0. An arbitrary linear combination of x_1 and x_2 also yields zero on the lhs, thus confirming the principle of linear superposition.

On the other hand, the linear superposition principle does not hold for the nonlinear ODE (2.3), as shown in the following example.

Example 2-1: Breakdown of Linear Superposition

If x_1 and x_2 are independent solutions of Equation (2.3), show that the linear combination $x_1 + x_2$ doesn't satisfy the equation.

Solution: Since x_1 and x_2 are both solutions of Equation (2.3), then

$$\ddot{x}_1 + \alpha\, x_1 + \beta\, x_1^3 = 0, \quad \text{and} \quad \ddot{x}_2 + \alpha\, x_2 + \beta\, x_2^3 = 0.$$

Substituting $x_1 + x_2$ into the lhs of (2.3) and using the above relations, we obtain

$$\ddot{x}_1 + \ddot{x}_2 + \alpha\,(x_1 + x_2) + \beta\,(x_1 + x_2)^3 = 3\,\beta\, x_1\, x_2\,(x_1 + x_2).$$

At an arbitrary time t, this result is not equal to zero, so the linear combination $x_1 + x_2$ doesn't satisfy the equation, i.e., linear superposition breaks down.

It should be mentioned that for some nonlinear ODEs a *nonlinear superposition* of the solutions may satisfy the original ODE. The form of the nonlinear superposition, however, varies from one nonlinear ODE to the next. An example of nonlinear superposition is left as a problem at the end of the chapter.

<p align="center">***</p>

As mentioned earlier, with the breakdown of linear superposition it is not too surprising that many of the standard mathematical methods such as Laplace transforms and Fourier series that are used for analytically solving linear ODEs are no longer useful. Specialized techniques (such as those summarized in Daniel Zwillinger's *Handbook of Differential Equations* ([Zwi89])) for obtaining exact analytic solutions exist, but they are not universal, applying to limited classes of nonlinear ODEs, most of which are not of physical interest. Zwillinger's book also outlines methods of obtaining approximate analytical solutions, for example, *perturbation theory* when the nonlinearity is small.
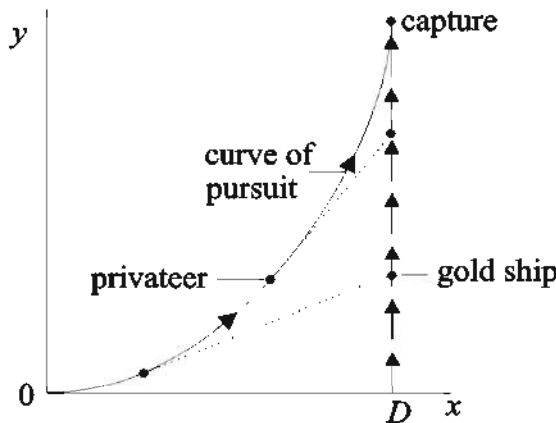
We shall not go into these exact and approximate analytic methods here, being content in the following section to give a few physically interesting examples which can be solved exactly by elementary mathematical techniques. Just because an analytic solution doesn't exist isn't the end of the world. As we shall see in later sections, there exist a host of approaches ranging from phase-plane analysis which can be used to analytically predict *all possible* solutions, to use of the computer to numerically solve *any* nonlinear ODE for given initial or boundary conditions.

2.2   Some Analytically Solvable Examples

According to Harold Davis ([Dav62]), the problem of attempting to determine *curves of pursuit* originated with Leonardo de Vinci but was not really tackled mathematically until the 1700s when the pursuit of heavily laden treasure ships by pirates and privateers[2] was a problem of much practical interest. In 1732, the French hydrographer Pierre Bouguer (1698−1758) solved the problem of *linear pursuit*, the subject of the following example.

Example 2-2: Linear Pursuit

An English privateer pursues a Spanish gold ship which flees along a straight line. The ratio $r > 1$ of the speeds of the two ships is fixed and the privateer always aims at the gold ship which is initially spotted a distance D km away. The geometry of the linear pursuit problem is summarized in the following figure:

a. Derive the nonlinear ODE governing the equation $y(x)$ of the curve of pursuit.

b. Analytically solve the ODE for $y(x)$.

c. If $r = 2$ and $d = 9$ km, at what value of y does capture take place?

Solution: a. The gold ship moves vertically along the line $x = D$. At some instant in time, let the gold ship and privateer coordinates be (D, Y) and (x, y), respectively. Since the line tangent to the privateer's instantaneous position must pass through the instantaneous position of the gold ship, we have the slope condition

$$\frac{dy}{dx} = \frac{Y - y}{D - x}, \quad \text{or, on rearranging,} \quad Y = (D - x)\frac{dy}{dx} + y. \tag{2.5}$$

The speed of the privateer is r times that of the gold ship. Letting $ds = \sqrt{(dx)^2 + (dy)^2}$

---

[2]A privateer was a private warship authorized by a country's government by letters of marque to attack foreign shipping.

be an element of arclength along the curve of pursuit, then $ds/dt = r\,(dY/dt)$. So,

$$ds = r\,dY, \quad \text{or}, \quad \sqrt{1 + \left(\frac{dy}{dx}\right)^2} = r\,\frac{dY}{dx}. \tag{2.6}$$

Differentiating Equation (2.5) with respect to x yields

$$\frac{dY}{dx} = -\frac{dy}{dx} + (D - x)\frac{d^2y}{dx^2} + \frac{dy}{dx} = (D - x)\frac{d^2y}{dx^2}.$$

Substituting this result into the right-hand side (rhs) of (2.6) yields the nonlinear ODE governing the equation of pursuit, viz.,

$$r\,(D - x)\frac{d^2y}{dx^2} = \sqrt{1 + \left(\frac{dy}{dx}\right)^2}. \tag{2.7}$$

b. To solve the ODE (2.7), we set $p = dy/dx$ and separate variables,

$$\frac{r\,dp}{\sqrt{1 + p^2}} = \frac{dx}{D - x}.$$

Integrating, we obtain

$$p = \frac{dy}{dx} = \frac{1}{2}\left[\frac{C}{(D - x)^{1/r}} - \frac{(D - x)^{1/r}}{C}\right], \tag{2.8}$$

where C is an arbitrary constant. Integrating a second time yields

$$y = \frac{1}{2}\left[\frac{r\,C}{(1 - r)}\,(D - x)^{1 - 1/r} + \frac{r}{C\,(1 + r)}\,(D - x)^{1 + 1/r}\right] + C', \tag{2.9}$$

where C' is a second arbitrary constant. Since both y and dy/dx are 0 when $x = 0$, then from (2.8) and (2.9), we have $C = D^{1/r}$ and $C' = r\,D/(r^2 - 1)$. Thus, from (2.9), the curve of pursuit is

$$y = \frac{r\,D}{(r^2 - 1)}\left[1 + \frac{1}{2}\,(r - 1)\left(1 - \frac{x}{D}\right)^{1 + 1/r} - \frac{1}{2}\,(r + 1)\left(1 - \frac{x}{D}\right)^{1 - 1/r}\right]. \tag{2.10}$$

c. Capture takes place when $x = D$, in which case $y = r\,D/(r^2 - 1)$. For $r = 2$ and $D = 9$ km, capture takes place at $y = 6$ km.

<div align="center">***</div>

A realm of mathematics which is a good source for analytically solvable nonlinear ODEs of physical interest is the so-called *calculus of variations*. The goal of problems in this realm is to determine the function $y(x)$ which maximizes or minimizes an integral I of the form

$$I = \int_a^b F(x, y(x), y'(x))\,dx, \tag{2.11}$$

where F is a known integrand and $y' \equiv dy/dx$. The form of $y(x)$ is found by solving the *Euler–Lagrange* equation ([GPS02]),

$$\frac{\partial F}{\partial y} - \frac{d}{dx}\frac{\partial F}{\partial y'} = 0, \tag{2.12}$$

subject to the boundary conditions at the end points a and b.

One of the oldest examples to which this mathematical framework has been applied is the *brachistochrone*[3] problem proposed and solved by Johann Bernoulli before posing it to readers of *Acta Eruditorum* in June 1696. The mathematicians Isaac Newton, Jacob Bernoulli (Johann's brother), Gottfried Leibniz, Ehrenfried Tschirnhaus, and Guillaume de l'Hôpital provided solutions, four (l'Hôpital's was left out) of which were published in the May 1697 edition of *Acta Eruditorum*.

Example 2-3: The Brachistochrone

Consider the smooth curve $y(x)$ in the following figure joining the origin O ($x = a = 0, y = 0$) and a lower point B ($x = b, y = c$). Starting from rest, a small mass m slides along the curve under the influence of gravity (gravitational acceleration g). What is
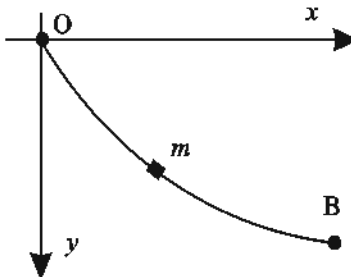
Figure 2.1: Geometry for the brachistochrone.

the equation of the curve which minimizes the time of travel between O and B? Neglect friction.

Solution: If v is the speed of the mass after falling a distance y, then equating the gain in kinetic energy to the decrease in potential energy yields

$$\frac{1}{2}mv^2 = mgy, \quad \text{so} \quad v = \sqrt{2gy}.$$

If ds is an element of arclength along the curve traced out in the time interval dt, then $v = ds/dt$. Noting that $ds = \sqrt{(dx)^2 + (dy)^2} = \sqrt{1 + (y')^2}\, dx$, the time for the mass to fall from O to B is

$$T = \int_O^B \frac{ds}{\sqrt{2gy}} = \int_0^b \left(\frac{1 + (y')^2}{2gy}\right)^{1/2} dx \equiv \int_0^b F\, dx. \tag{2.13}$$

---

[3]From the Greek: brachisto=shortest, chronos=time.

Substituting F into the Euler–Lagrange equation (2.12), and performing the mathematical operations, yields the nonlinear ODE

$$2y\frac{d^2y}{dx^2} + \left(\frac{dy}{dx}\right)^2 + 1 = 0. \tag{2.14}$$

To solve this ODE, we use the same approach as in the previous example. Setting $p = dy/dx$ and noting that $d^2y/dx^2 = p\,(dp/dy)$, Equation (2.14) then becomes

$$2yp\frac{dp}{dy} + p^2 + 1 = 0.$$

Integrating, substituting $p = dy/dx$, and separating variables yields

$$dx = \left(\frac{y}{C_1 - y}\right)^{1/2} dy, \tag{2.15}$$

where C_1 is an arbitrary constant. An *implicit solution* $x(y)$ is readily found but it cannot be inverted to give the *explicit solution* $y(x)$. A *parametric solution* may be obtained by introducing the parameter θ through the relation

$$y = \frac{C_1}{2}\,(1 - \cos\theta) = C_1\,\sin^2\left(\frac{\theta}{2}\right). \tag{2.16}$$

Then (2.15) becomes

$$dx = C_1\,\sin^2\left(\frac{\theta}{2}\right)\,d\theta,$$

which can be integrated to yield

$$x = \frac{C_1}{2}\,(\theta - \sin\theta) + C_2, \tag{2.17}$$

where C_2 is a second arbitrary constant. If we choose $\theta = 0$ when $x = 0$, then $C_2 = 0$. Setting $C_1 = 2A$ for convenience, the equations

$$x = A\,(\theta - \sin\theta), \quad y = A\,(1 - \cos\theta) \tag{2.18}$$

are just the parametric equations for a *cycloid*, the curve traced out by a point on the rim of a wheel rolling on the x-axis. The curve which minimizes the time of descent from O to B is just a portion of an inverted cycloid. The precise shape depends on the values of b and c which can be used to obtain A.

<div align="center">∗∗∗</div>

Both our examples involved answers expressed in terms of elementary functions. The nonlinear spring equation (2.3) with which we began this chapter can also be solved analytically but the answer involves a *special function*, the *Jacobian elliptic function*. Since the mathematics is more involved, we will postpone tackling the nonlinear spring problem until Chapter 5, the *World of Motion*.

2.3 Fixed Points and Phase-Plane Analysis

Consider an ODE system of the so-called *standard* form,

$$\dot{x} = P(x,y), \quad \dot{y} = Q(x,y), \tag{2.19}$$

where P and Q are specified nonlinear functions of x and y. Because P and Q do not depend explicitly on the independent variable t, the system is said to be *autonomous*. Otherwise, it is *nonautonomous*. It should be noted that all ODE systems arising from Newton's second law of mechanics of the structure $\ddot{x} = F(x, \dot{x})$, where F is the force, can be put into the standard form, by setting $\dot{x} = y$, viz.,

$$\dot{x} = y \equiv P, \quad \dot{y} = F(x,y) \equiv Q. \tag{2.20}$$

For example, for the nonlinear spring equation (2.3), one has $Q = -\alpha\,x - \beta\,x^3$. Other systems, such as the Lotka–Volterra equations (1.23), are naturally of the standard form. In this case, one can identify $P = a\,x - b\,x\,y$ and $Q = -c\,y + d\,x\,y$.

The *fixed*, or *stationary*, *points* of Equations (2.19) correspond to the points in the x–y plane (the *phase plane*) where $\dot{x} = 0$ and $\dot{y} = 0$. The number and locations of the fixed points in the phase plane are found by solving the simultaneous nonlinear equations

$$P(x,y) = 0, \quad Q(x,y) = 0. \tag{2.21}$$

Unlike the situation for linear ODEs, if P and Q are nonlinear functions, more than one fixed point is possible as illustrated in the following example.

Example 2-4: Rats and Cats

The rat and cat populations on Erehwon evolve with time as follows:

$$\dot{R} = 3\,R - R\,C/2, \quad \dot{C} = -C + R\,C/10.$$

Locate the fixed points of this ODE system.

Solution: Identifying $P(R, C) = R\,(3 - C/2)$ and $Q(R, C) = C\,(-1 + R/10)$, there are two fixed points, located at $(R = 0, C = 0)$ and $(R = 10, C = 6)$.

<div align="center">***</div>

The next step is to determine the behavior of the solution curve, or trajectory, in the vicinity of each fixed point in the phase plane. Since P and Q do not explicitly depend on t, the time can be eliminated by dividing the two equations in (2.19), yielding

$$\frac{dy}{dx} = \frac{Q(x,y)}{P(x,y)}. \tag{2.22}$$

This is just the slope of the trajectory at an arbitrary point (x, y) in the phase plane. At a fixed point, one has $P = Q = 0$, so $dy/dx = 0/0$ and the slope is indeterminate. At any other point (called an *ordinary* point), the slope has a definite unique[4] value

---

[4] As a consequence of uniqueness, trajectories cannot cross at ordinary points.

ranging in magnitude from 0 to ∞. As time advances, the solution will advance along the trajectory determined by the initial values of x and y.

Graphically, one can see **all** possible trajectories of the standard ODE system by creating a *tangent field.* Forming a systematic grid in the phase plane, the ratio $Q(x, y)/P(x, y)$ is calculated at each grid point. A small arrow with slope $dy/dx = Q/P$ is then drawn at each grid point, i.e., tangent to the trajectory at that grid point. The arrowhead should point in the direction of increasing t. Although tangent fields can be drawn by hand, it is recommended (especially if several fixed points are present) that you use a CAS such as *Maple* or *Mathematica* to quickly and accurately do the job.

Example 2-5: Tangent Field

Draw the tangent field for the rats–cats ODE system over the range $R = -5$ to $+15$, $C = -5$ to $+15$. Place small circles at the fixed points. Discuss the possible behavior.

Solution: Let's divide the range in both the R and C directions into 25 equally spaced grid points. The slope $dR/dC = (3\,R - R\,C/2)/(-C + R\,C/10)$ is calculated at each grid point (C, R). The sense of the arrowheads is determined at each point from the time-dependent ODEs. The resulting tangent field is shown in Figure 2.2. The fixed points at the origin and at $R = 10$, $C = 6$ are represented by the small circles.
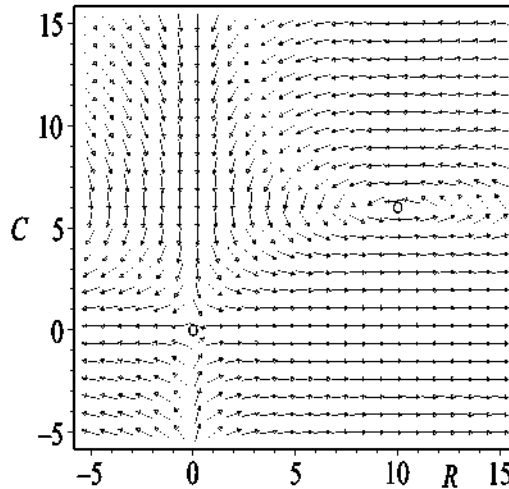
Figure 2.2: Tangent field for the rats–cats ODE system.

Since the rat and cat populations cannot be negative, only the quarter-plane region $R > 0, C > 0$ is of physical interest. In this quarter-plane, the tangent field arrows form a counterclockwise "whirlpool" or "vortex" around the fixed point ($R = 10, C = 6$). For this reason, this fixed point is called a *vortex* point. The behavior of the tangent field arrows tells us that the only possible physical solutions are cyclical.

For the fixed point at the origin, the tangent arrows along the horizontal R axis point away from the fixed point and point toward it along the vertical C axis. This fixed point is an example of a so-called *saddle* point, the name arising from analogy with a saddle point at the pass between two neighboring mountain peaks with two valleys

in the transverse direction. In the mountain situation, increasing height plays the role of increasing time. Using arrows to represent the direction of increasing height, two arrows point away from the mountain saddle point to the two peaks and two arrows point toward the saddle point as one ascends the pass from the valleys.

<p align="center">***</p>

Let us now turn to the issue of systematically identifying the types of fixed points that are possible and the behavior of the trajectories near each type. We proceed as follows. Let's label the coordinates of a fixed point as $(\bar{x}, \bar{y})$. At a nearby ordinary point, the coordinates are $(x = \bar{x} + u, y = \bar{y} + v)$, where u and v are assumed to be small. At this ordinary point, the slope of the trajectory is

$$\frac{dy}{dx} = \frac{Q(\bar{x} + u, \bar{y} + v)}{P(\bar{x} + u, \bar{y} + v)}. \tag{2.23}$$

Since u and v are assumed to be small, the numerator and denominator on the right-hand side of (2.23) can be Taylor expanded about $(\bar{x}, \bar{y})$ in powers of u and v, so

$$\frac{dy}{dx} = \frac{dv}{du} = \frac{c\,u + d\,v + \cdots}{a\,u + b\,v + \cdots}, \tag{2.24}$$

where

$$a \equiv \left(\frac{\partial P}{\partial x}\right)_{\bar{x},\bar{y}}, \quad b \equiv \left(\frac{\partial P}{\partial y}\right)_{\bar{x},\bar{y}}, \quad c \equiv \left(\frac{\partial Q}{\partial x}\right)_{\bar{x},\bar{y}}, \quad d \equiv \left(\frac{\partial Q}{\partial y}\right)_{\bar{x},\bar{y}}.$$

Assuming that u and v are sufficiently small, only the linear terms in u and v are retained in (2.24), higher-order terms being neglected. In this case, Equation (2.24) can then be regarded as resulting from the pair of linear ODEs

$$\dot{u} = a\,u + b\,v, \qquad \dot{v} = c\,u + d\,v. \tag{2.25}$$
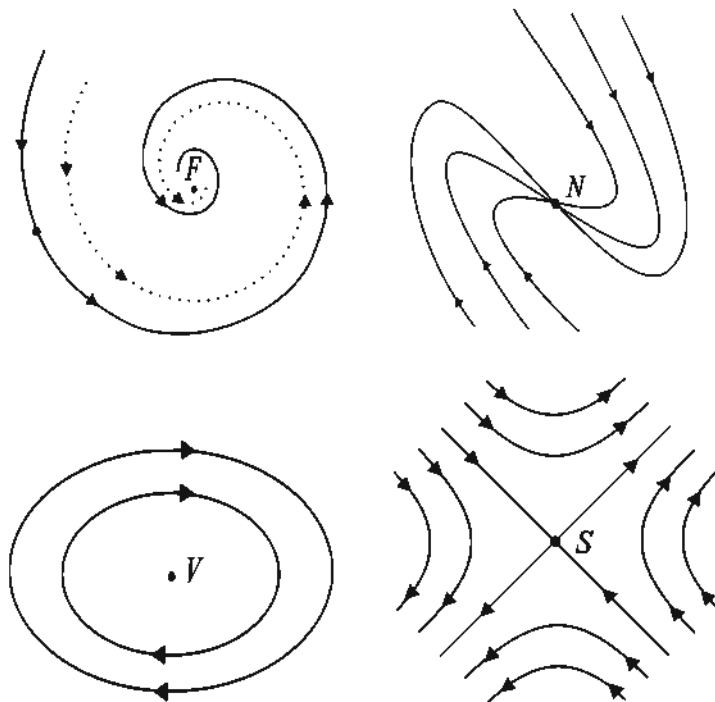
Assuming solutions of the form $(u, v) \sim e^{\lambda t}$, we obtain the two roots

$$\lambda = -\frac{p}{2} \pm \frac{1}{2}\sqrt{(p^2 - 4q)}, \quad \text{with} \quad p = -(a + d), \quad q = a\,d - b\,c.$$

Note that if $q = 0$, the roots are $\lambda = 0$ and $\lambda = -p$. In this case, higher-order terms in the Taylor expansion should be kept. For this reason, $q = 0$ corresponds to a *higher-order fixed point*. The fixed points which occur for $q \neq 0$ are referred to as *simple*. Detailed examination of the roots[5] for this case reveals that there are only four types of simple fixed points: the *saddle*, *focal* or *spiral*, *nodal*, and *vortex* points. In the neighborhood of these points, the trajectories are as qualitatively depicted in Figure 2.3, the arrows indicating the direction of increasing time. *Stable* focal and nodal points are shown, the trajectories approaching the fixed points as $t \to +\infty$. For *unstable* focal and nodal points, the arrow directions are reversed.

The ranges of q, p, and $p^2 - 4q$ dictate the type of fixed point and, in the case of the focal and nodal points, its stability. Table 2.1 summarizes all possibilities.

---

[5]For $p^2 = 4q$, $\lambda = -p/2$. In this degenerate case, a second solution of the form $t\,e^{\lambda t}$ is sought.

Figure 2.3: Trajectories near a focal (F), nodal (N), vortex (V), saddle (S) point.

Fixed Point	$q = a\,d - b\,c$	$p = -(a+d)$	$p^2 - 4\,q$
saddle	< 0	all p	> 0
higher-order	$= 0$	all p	≥ 0
stable focal		> 0	< 0
stable nodal		> 0	≥ 0
vortex or focal	> 0	$= 0$	< 0
unstable focal		< 0	< 0
unstable nodal		< 0	≥ 0

Table 2.1: Classification of fixed points.

For $q > 0$ and $p = 0$, note that either a vortex or focal point occurs. The "uncertainty" arises because of the neglect of higher-order terms in the Taylor expansion which may turn a closed loop (for the vortex) into a spiral. Although one can examine this situation on a case-by-case basis if desired, the following sufficient, but not necessary, *global* theorem due to Poincaré is often useful:

If $P(x, -y) = -P(x, y)$ and $Q(x, -y) = Q(x, y)$,
then the fixed point is a vortex, not a focal point.

Poincaré's theorem is easily proven using symmetry considerations.

The behavior of trajectories near a higher-order fixed point (when $q = 0$) is more complicated. Rather than tackling the issue analytically, a simple way of determining the behavior is to make a *phase-plane portrait* with one or more representative trajectories near the fixed point superimposed on the associated tangent field.

Example 2-6: Phase-Plane Analysis for Rats and Cats

Analytically identify the fixed points of the rats–cats ODE system.

Solution: Recalling that $P(R,C) = R(3 - C/2)$ and $Q(R,C) = C(-1 + R/10)$, the relevant partial derivatives for calculating a, b, c, and d are respectively

$$\partial P/\partial R = 3 - C/2, \quad \partial P/\partial C = -R/2, \quad \partial Q/\partial R = C/10, \quad \partial Q/\partial C = -1 + R/10.$$

For the fixed point at the origin, then $a = 3$, $b = 0$, $c = 0$, and $d = -1$, so that $p = -(a+d) = -2$ and $q = ad - bc = -3$. Since $q < 0$, Table 2.1 tells us that this fixed point is a saddle point. This is consistent with the tangent field shown in Figure 2.2.

For the other fixed point at $(R = 10, C = 6)$, we have $a = 0$, $b = -5$, $c = 6/10$, and $d = 0$. Since $p = -(a + d) = 0$, this fixed point is either a vortex or a focal point. To decide which it is, let's try applying Poincaré's theorem. We find that $P(R, -C) \neq -P(R, C)$ and $Q(R, -C) \neq Q(R, C)$, so the theorem is indecisive.

That the fixed point (probably) is a vortex follows from producing a phase-plane portrait combining a very accurate numerical calculation of the trajectory for a given initial condition with a background of tangent arrows. This is done in Figure 2.4 using
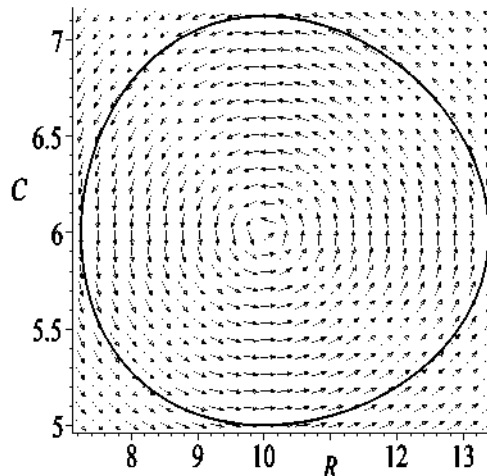

Figure 2.4: Phase-plane portrait for rats and cats.

the adaptive step RKF45 method for the initial condition $R(0) = 10$, $C(0) = 5$. The trajectory is a closed loop about the vortex point at $R = 10, C = 6$.

***

Example 2-7: Higher-Order Fixed Point

Newton's second law of mechanics for the displacement x of a unit mass experiencing a force $F = -x + 2\,x^2 - x^3$ yields the ODE, $\ddot{x} = -x + 2\,x^2 - x^3$. Determine the fixed points and produce a phase-plane portrait with a few trajectories and a tangent field. Discuss the result.

Solution: Setting $\dot{x} = y$, the second-order ODE is rewritten in standard form,

$$\dot{x} = y, \quad \dot{y} = -x + 2\,x^2 - x^3 = -x\,(1-x)^2.$$

We identify $P = y$ and $Q = -x\,(1-x)^2$. There are two fixed points, one at $(0,0)$ and a twofold degenerate one at $(1,0)$.

For the fixed point at the origin, $a = 0$, $b = 1$, $c = -1$, and $d = 0$. Then $p = -(a+d) = 0$ and $q = ad - bc = 1 > 0$. From Table 2.1, the fixed point is either a vortex or focal point. Applying Poincaré's theorem,

$$P(x, -y) = -y = -P(x, y), \quad Q(x, -y) = -x\,(1-x)^2 = Q(x, y).$$

The theorem is satisfied, so the fixed point at the origin is a vortex.

For the degenerate fixed point at $(1,0)$, we have $a = 0$, $b = 1$, $c = 0$, and $d = 0$. Then $p = 0$ and $q = 0$, so this fixed point is a higher-order fixed point.

To see what the topology looks like near this fixed point, a phase-plane portrait is produced with four trajectories corresponding to the initial conditions: $(x(0) = 0, y(0) = 0.35)$, $(-0.4, 0)$, $(-0.1, 0.394)$, and $(-0.1, 0.40)$. With the tangent field included, Figure 2.5 results. The tangent field near the origin and the innermost closed trajectory
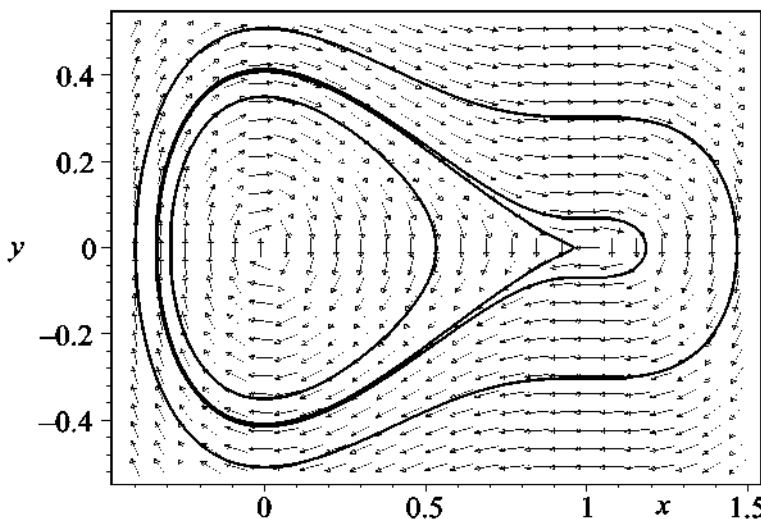

Figure 2.5: Phase-plane portrait for higher-order fixed point.

are consistent with the origin being a vortex. Examining the closest two trajectories to the higher-order fixed point at $(1,0)$, the one to the left of the fixed point is similar to

that near a saddle point, while the one to the right is characteristic of a vortex. The higher-order fixed point looks like the "coalescence" of a saddle and a vortex.

<div align="center">***</div>

In Problem 1-12 you were asked to numerically determine whether the gnus and sung on the planet Erehwon could coexist together. This question is now answered using phase-plane analysis and creating a phase-plane portrait with a few carefully selected trajectories. The example also introduces you to the concept of *basins of attraction*.

Example 2-8: Only the Lonely

On the bucolic planet of Erehwon, gnus and their backward relatives, the sung, are put together in a large enclosed pasture where they munch on the licorice-flavored clover, their favorite and only food supply. Suppose that the dynamical equations describing the gnu number $g(t)$ and sung number $s(t)$ (per unit area) at time t are

$$\frac{dg}{dt} = g\left(\frac{5}{2} - g\right) - 2\,g\,s, \quad \frac{ds}{dt} = s\,(2 - s) - \frac{3}{2}\,g\,s.$$

The first terms in each ODE are Verhulst-like to model the limited food supply available to both species. Since they are after the same food supply, the interaction between the species is detrimental to both, thus both interaction terms have a negative sign.

   a. Determine the number of fixed points, their locations, and their identity. Use the information to discuss the possible coexistence of the gnus and sung.

   b. Create a phase-plane portrait which includes the tangent field, trajectories which clearly indicate the possible outcomes as time evolves, and the locations of the fixed points. Use the figure to support your conclusion in part **a**.

Solution: a. Taking

$$P(g,s) = g\left(\frac{5}{2} - g\right) - 2\,g\,s, \quad Q(g,s) = s\,(2 - s) - \frac{3}{2}\,g\,s,$$

and setting them equal to zero yields four fixed points:

$$(g_0, s_0) \;=\; (0,0), \;\; (5/2, 0), \;\; (0, 2), \;\; (3/4, 7/8).$$

The relevant partial derivative for identifying the fixed points are

$$\frac{\partial P}{\partial g} = \frac{5}{2} - 2\,g - 2\,s, \quad \frac{\partial P}{\partial s} = -2\,g, \quad \frac{\partial Q}{\partial g} = -\frac{3}{2}\,s, \quad \frac{\partial Q}{\partial s} = 2 - 2\,s - \frac{3}{2}\,g.$$

Using these partial derivative, the quantities a, b, c, d, $p = -(a + d)$, $q = a\,d - b\,c$, and $\Delta \equiv p^2 - 4\,q$ are evaluated for each fixed point and Table 2.1 used to identify the nature of the fixed point. The results for each fixed point are given in the following table.

So, what can we conclude from the fixed points. The origin is an unstable nodal point, so any initial condition which starts near this point will produce a solution trajectory which moves away from the origin as time evolves. There are two stable nodal

Point	a	b	c	d	p	q	Δ	Type
$(0,0)$	$+\dfrac{5}{2}$	0	0	$+2$	$-\dfrac{9}{2}$	$+5$	$\dfrac{1}{4}$	*unstable nodal point*
$\left(\dfrac{5}{2},0\right)$	$-\dfrac{5}{2}$	-5	0	$-\dfrac{7}{4}$	$+\dfrac{17}{4}$	$+\dfrac{35}{8}$	$\dfrac{9}{16}$	*stable nodal point*
$(0,2)$	$-\dfrac{3}{2}$	0	-3	-2	$+\dfrac{7}{2}$	$+3$	$\dfrac{1}{4}$	*stable nodal point*
$\left(\dfrac{3}{4},\dfrac{7}{8}\right)$	$-\dfrac{3}{4}$	$-\dfrac{3}{2}$	$-\dfrac{21}{16}$	$-\dfrac{7}{8}$	$+\dfrac{13}{8}$	$-\dfrac{21}{16}$	$\dfrac{505}{64}$	*saddle point*

points which can attract trajectories as $t \to \infty$. The one at $(g = 5/2, s = 0)$ corresponds to only the gnus surviving, the sung becoming extinct, while the other at $(g = 0, s = 2)$ corresponds to the gnus becoming extinct, the sung being the survivors. Since the fourth fixed point is a saddle point, it appears that the gnus and sung cannot coexist.

b. A phase-plane portrait is now created showing the tangent field, small circles locating the four fixed points, and four trajectories corresponding to the initial conditions, $(g(0), s(0)) = (0.1, 0.15), (0.1, 0.2), (2.5, 2.4), (2.5, 2.5)$. The resulting picture is shown in Figure 2.6. The initial condition $(2.5, 2.5)$ produces a trajectory which heads toward the saddle point at $(3/4, 7/8)$, but suddenly veers upwards in the figure, asymptotically
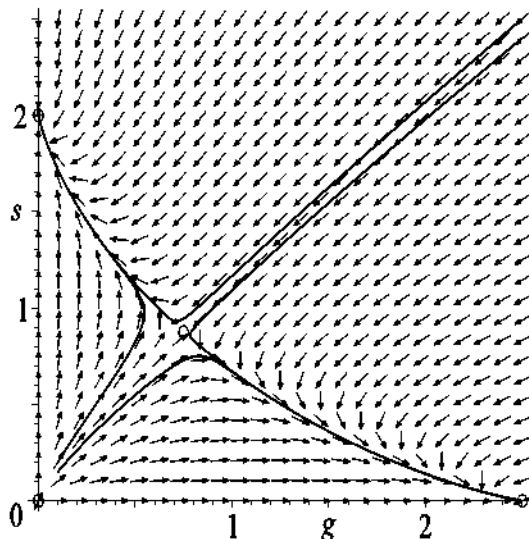

Figure 2.6: Phase-plane portrait for gnus and sung.

approaching the stable nodal point at $(0, 2)$. In this case the gnus become extinct.

Lowering the initial sung population density slightly from 2.5 to 2.4 generates a trajectory which again heads toward the saddle point, but suddenly veers downwards, approaching the other stable nodal point at $(5/2, 0)$. The sung become extinct. We see that the two trajectories approximately divide a portion of the phase plane into *basins of attraction*, the arrows in one basin being attracted to one of the stable nodal points, the arrows in the other basin being attracted to the other stable nodal point.

Similarly, the other two initial conditions, $(0.1, 0.15)$ and $(0.1, 0.2)$, also generate trajectories which approximately divide the remaining portion of the quarter-plane into basins of attraction, each trajectory approaching a different stable nodal point. The dividing lines between the basins are examples of *separatrixes*, these lines dividing or separating the phase plane into regions of different behavior. It is this possibility of different outcomes that makes nonlinear ODE systems so interesting.

Putting it all together, unfortunately the gnus and sung cannot coexist.

<div align="center">***</div>

Combining phase-plane analysis with numerically generated pictures is a very powerful approach to understanding nonlinear ODE systems. The approach can be generalized to systems of three first-order ODEs, but is too involved to present here. See, e.g., Jackson's *Perspectives of Nonlinear Dynamics* ([Jac90]) for the mathematical details.

2.4 Bifurcations

In general, as one or more "control" parameters in a nonlinear ODE model are changed, the location and character of the fixed points change, leading to changes in the topological nature of the possible solution curves. These changes in behavior are referred to as *bifurcations* and the values of the control parameter at which they change are called *bifurcation points*. We will now list and illustrate some[6] of the more common types of bifurcations that can occur as a single control parameter ε is changed.

a. Saddle-Node Bifurcation: An unstable saddle and a stable node (nodal point) are destroyed (or created) as ε passes through a saddle-node bifurcation point.

Example 2-9: Saddle-Node Bifurcation Point

Show that $\varepsilon = 1$ is a saddle-node bifurcation point for the real nonlinear ODE system

$$\dot{x} = y - 2x, \qquad \dot{y} = \varepsilon + x^2 - y.$$

Solution: The fixed points are

$$(\bar{x}, \bar{y}) = \ (1 + \sqrt{1 - \varepsilon},\ 2 + 2\sqrt{1 - \varepsilon}), \quad (1 - \sqrt{1 - \varepsilon},\ 2 - 2\sqrt{1 - \varepsilon}),$$

for which

$$p = 3, \quad q = \mp 2\sqrt{1 - \varepsilon}, \quad p^2 - 4q = 9 \pm 8\sqrt{1 - \varepsilon}.$$

---

[6]For a more complete listing and discussion, see either Verhulst ([Ver90]) or Strogatz ([Str94]).

The upper (lower) sign corresponds to the first (second) fixed point.

Now, consider what happens as ε is increased through $\varepsilon = 1$ from below. For $\varepsilon < 1$, we have $p = 3$ and $q < 0$ for the first fixed point, so it is a saddle. For the second fixed point, $p = 3$, $q > 0$, and $p^2 - 4q > 0$, so it is a stable node.

As $\varepsilon \to 1$, the two fixed points coalesce into the single degenerate fixed point $(1, 2)$. Since $p = 3$ and $q = 0$, it is a higher-order fixed point.

For $\varepsilon > 1$, there are no real fixed points. The saddle and node are "annihilated" as ε is increased through $\varepsilon = 1$. Conversely, the saddle and node are "born" as the parameter is decreased through the bifurcation point.

<div align="center">***</div>

b. Transcritical Bifurcation: Two fixed points (e.g., unstable saddle and a stable node) exchange their stability as ε passes through a transcritical bifurcation point.

Example 2-10: Transcritical Bifurcation Point

Show that $\varepsilon = 0$ is a transcritical bifurcation point for the nonlinear system

$$\dot{x} = x\,(\varepsilon - x), \qquad \dot{y} = x - y.$$

Solution: There are two fixed points

$$(\bar{x}, \bar{y}) = \quad (0, 0), \quad (\varepsilon, \varepsilon),$$

for which

$$p = 1 \mp \varepsilon, \quad q = \mp \varepsilon, \quad p^2 - 4q = (\varepsilon \pm 1)^2 \geq 0.$$

The upper (lower) sign applies to the first (second) point.

For $\varepsilon < 0$, we have $q > 0$, $p > 0$, and $p^2 - 4q \geq 0$ for the first fixed point, so it is a stable nodal point. The second fixed point is an unstable saddle point since $q < 0$.

For $\varepsilon > 0$, we have $q < 0$ for the first fixed point so it loses its stability, becoming a saddle. The second fixed point is a stable node, since now $q > 0$, $p > 0$, and $p^2 - 4q \geq 0$. The two fixed points have exchanged their stability as ε passes through 0.

<div align="center">***</div>

c. Pitchfork Bifurcation: As ε is increased through a pitchfork bifurcation point, a stable fixed point loses its stability, but two other stable fixed points are born. When either of the fixed point coordinates (e.g., x) is plotted versus ε, the stable branches (plotted as solid curves) resemble the handle and two prongs of a pitchfork.

Example 2-11: Pitchfork Bifurcation Point

Show that $\varepsilon = 0$ is a pitchfork bifurcation point for the nonlinear system

$$\dot{x} = x\,(\varepsilon - x^2), \qquad \dot{y} = x - y.$$

Solution: There is a single real fixed point $(0, 0)$ for $\varepsilon < 0$, but three fixed points

$$(\bar{x}, \bar{y}) = \quad (0, 0), \quad (\sqrt{\varepsilon}, \sqrt{\varepsilon}), \quad (-\sqrt{\varepsilon}, -\sqrt{\varepsilon})$$

for $\varepsilon > 0$.

For the fixed point, $(0,0)$, one has

$$p = 1 - \varepsilon, \quad q = -\varepsilon, \quad p^2 - 4q = (\varepsilon + 1)^2 \geq 0.$$

For $\varepsilon < 0$, then $p > 0$ and $q > 0$, so the fixed point is a stable node. For $\varepsilon > 0$, the fixed point is an unstable saddle since $q < 0$. The fixed point loses its stability as ε is increased through $\varepsilon = 0$.

For both fixed points $(\sqrt{\varepsilon}, \sqrt{\varepsilon})$ and $(-\sqrt{\varepsilon}, -\sqrt{\varepsilon})$, which only exist for $\varepsilon > 0$, we obtain

$$p = 2\varepsilon + 1, \quad q = 2\varepsilon, \quad p^2 - 4q = (2\varepsilon - 1)^2 \geq 0.$$

For $\varepsilon > 0$, one has $p > 0$ and $q > 0$, so they are both stable nodal points. Thus, two symmetrically located stable fixed points are born as ε increases through the critical point $\varepsilon = 0$. If, say, the x-coordinate of the stable fixed points is plotted as a function of ε, the pitchfork shown in Figure 2.7 results.
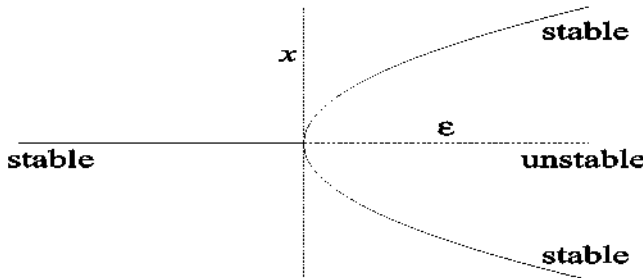

Figure 2.7: Pitchfork bifurcation.

More precisely, this is referred to as a *supercritical* pitchfork bifurcation. A *subcritical* bifurcation occurs at $\varepsilon = 0$ if the term $x(\varepsilon - x^2)$ is replaced with $x(\varepsilon + x^2)$ in the $\dot{x}$ equation. This case is left as a problem.

$$***$$

d. Hopf Bifurcation: A Hopf bifurcation involves the change of stability of a focal or spiral point as the control parameter passes through the bifurcation point.

Example 2-12: Hopf Bifurcation Point

Show that a Hopf bifurcation occurs at $\varepsilon = 0$ for the ODE system

$$\dot{x} = y, \qquad \dot{y} = -x + \varepsilon(1 - x^2)y.$$

Solution: The only fixed point is $(0,0)$, for which $p = -\varepsilon$, $q = 1$, and $p^2 - 4q = \varepsilon^2 - 4$. Since $q > 0$, the origin is a stable focal or nodal point for $\varepsilon < 0$ and an unstable focal or nodal point for $\varepsilon > 0$. For $0 < |\varepsilon| < 2$, it is a focal point since then $p^2 - 4q < 0$. So as ε increases through zero from small negative values, the phase-plane trajectory changes from a stable spiral (spiraling into the origin) to an unstable spiral (spiraling outwards). This is an example of a Hopf bifurcation.

$$***$$

2.5   Hysteresis and the Jump Phenomena

In a typical undergraduate electromagnetism course, students encounter the concept of a *hysteresis* cycle or loop when the flux density B is plotted as a function of the magnetic induction H for a ferromagnet. If H is increased, then decreased, B does not move back down the same curve but, instead, traces out a new path. The reason for this behavior is that the underlying mechanism in a ferromagnet is magnetic domain formation, a process which is nonlinear. As H is decreased, the magnetic domains that are formed are not the same as those when H was increased.

Hysteresis occurs in other contexts (e.g., the current–voltage relation for the superconducting Josephson junction ([Jos62], [Str94]), the Duffing oscillator (introduced shortly)) as well and, as with the ferromagnet, is an indicator that the underlying mechanism is such that the mathematical description is nonlinear. Generally, this mathematics is quite involved so we will be content here to illustrate hysteresis for a simple nonlinear ODE system. This system will also illustrate the so-called *jump phenomena* which are associated with the hysteresis loop that is generated.

Consider the following nonlinear ODE system:

$$\dot{x} = \varepsilon\, x + 2\, x^3 - x^5, \qquad \dot{y} = x - y, \tag{2.26}$$

with ε a real control parameter which can be varied from negative to positive values.

Setting $\dot{x} = \dot{y} = 0$, it is easy to find the fixed points $(\bar{x}, \bar{y})$ of this ODE system, as well as determine the ranges for which they are real, and establish their stability. The results are summarized in Table 2.2.

$(\bar{x}, \bar{y})$	Range	Stability
$(0,0)$	all ε	$\varepsilon < 0$: stable; $\varepsilon > 0$: unstable
$\pm\left(\sqrt{1 + \sqrt{1+\varepsilon}},\ \sqrt{1 + \sqrt{1+\varepsilon}}\right)$	$-1 < \varepsilon$	stable
$\pm\left(\sqrt{1 - \sqrt{1+\varepsilon}},\ \sqrt{1 - \sqrt{1+\varepsilon}}\right)$	$-1 < \varepsilon < 0$	unstable

Table 2.2: Fixed points, ranges for which they are real, and stability.

In a similar manner to what was done for the pitchfork bifurcation in the previous section, let's plot $\bar{x}$ versus ε over a range of ε which includes all the ranges listed in the table, say from $\varepsilon = -2$ to $+2$. The stable branches will be plotted as solid lines, the unstable branches as dotted lines. The curves will further be labeled as stable or unstable for absolute clarity. The resulting picture is shown in Figure 2.8.

For $\varepsilon < -1$, there is only one stable branch, $\bar{x} = 0$. Irrespective of the initial condition, the ODE system will approach the origin as $t \to +\infty$.
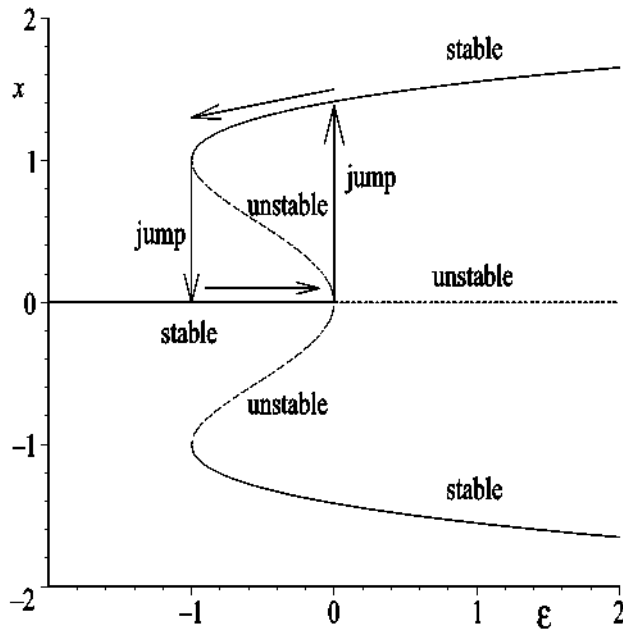
Figure 2.8: Hysteresis loop with jumps.

Now increase ε so that one is in the range $-1 < \varepsilon < 0$. There are three stable branches,

$$\bar{x} = 0, \quad \sqrt{1 + \sqrt{1 + \varepsilon}}, \quad -\sqrt{1 + \sqrt{1 + \varepsilon}},$$

and two unstable branches,

$$\bar{x} = \sqrt{1 - \sqrt{1 + \varepsilon}}, \quad -\sqrt{1 - \sqrt{1 + \varepsilon}}.$$

Which stable branch the system approaches as $t \to +\infty$ now depends on the choice of initial point. If this point is close to the zero-amplitude branch, the system will evolve toward it, but if it is closer to one of the two non-zero-amplitude branches it will evolve toward the closest of these branches.

Finally, for $\varepsilon > 0$, there are two stable branches, $\bar{x} = \pm \left(\sqrt{1 + \sqrt{1 + \varepsilon}} \right)$, and one unstable branch, $\bar{x} = 0$. Again, which stable branch the system evolves toward depends on the location of the initial point.

So, how does a hysteresis loop occur? Suppose that we start the system in the state $\bar{x} = 0$ for $\varepsilon < -1$ and continuously increase the value of ε. Because this state is stable, the system remains at the origin until $\varepsilon = 0$ is reached at which point the origin loses its stability. Then, the slightest "nudge" will cause the system to "jump" to one of the two non-zero-amplitude branches, e.g., the upper one. Increasing ε further, the system will move to the right along the upper branch. If ε is decreased, the system will remain on the stable upper branch even as ε is decreased through 0. As ε decreases through -1, the system will jump downwards to the lower stable branch, $\bar{x} = 0$. The hysteresis loop is depicted in Figure 2.8 by arrows with the associated up- and down-jumps indicated.

2.6 Limit Cycles

In considering autonomous nonlinear ODE systems of the standard form ($\dot{x} = P(x, y)$, $\dot{y} = Q(x, y)$, with P and Q nonlinear functions), we have encountered *point attractors* such as the stable focal and nodal points. Another extremely important type of attractor is the stable *limit cycle*, which is an isolated closed trajectory having the property that all other trajectories in its neighborhood wind onto the limit cycle as $t \to +\infty$.

Why are stable limit cycles important? As we shall see in later chapters, stable limit cycles model systems that display self-sustained oscillations, even in the absence of an external periodic force. The examples range from electronic and chemical oscillators to the beating of the human heart. If the system is perturbed slightly away from a stable limit cycle, it is always attracted back to it.

As a simple mathematical illustration, let's use polar coordinates and consider

$$\dot{r} = r\,(1 - r), \quad \dot{\theta} = 1, \tag{2.27}$$

where $r \geq 0$ is the radial distance and θ is the angle measured from the positive x-axis of the x–y phase plane. Taking the initial radius and angle to be $r(0) = r_0$ and $\theta(0) = \theta_0$, the ODEs are easily solved. The angular solution is $\theta(t) = t + \theta_0$. Recognizing that the radial equation is just the previously solved logistic ODE, we obtain

$$r(t) = \frac{r_0\,e^t}{1 + r_0\,(e^t - 1)}. \tag{2.28}$$

For any $r_0 < 1$ or $r_0 > 1$, we see that $r(t) \to 1$ as $t \to +\infty$. For $r_0 = 1$, then $r(t) = 1$. The circle of radius $r = 1$ is a stable limit cycle. The angular solution tells us that any trajectory starting off the limit cycle will wind onto it in a counterclockwise fashion.

The complete time evolution of a trajectory starting off the limit cycle can be displayed in the x–y phase plane by setting $x = r\cos\theta$ and $y = r\sin\theta$.
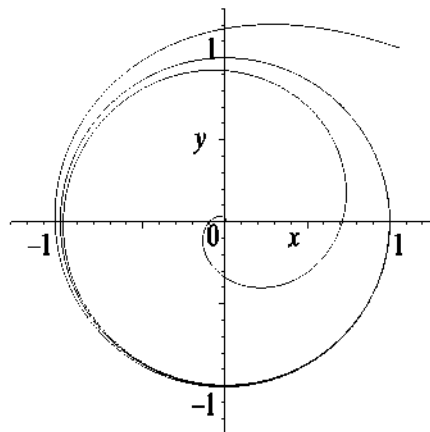

Figure 2.9: Two trajectories approaching the circular limit cycle of radius $r = 1$.

Figure 2.9 shows two trajectories winding onto the stable limit cycle for the two initial radii, $r_0 = 0.01$ and 1.5, and initial angle $\theta_0 = \pi/4$ radians.

Mathematical models can also be created which display *unstable* and *semistable* limit cycles. For the former, a slight perturbation away from the limit cycle produces trajectories which move away from the limit cycle as $t \to +\infty$. For the semistable case, trajectories are stable on one side (inside or outside) and unstable on the other. Here's a mathematical example of an unstable limit cycle.

Example 2-13: Unstable Limit Cycle

Consider the nonlinear ODE system

$$\dot{x} = y + x\left(x^2 + y^2 - 1\right), \quad \dot{y} = -x + y\left(x^2 + y^2 - 1\right).$$

- **a.** By converting the system to polar coordinates and analytically solving the resulting equations, show that the system has an unstable limit cycle of radius $r = 1$.

- **b.** Plot trajectories over the time range $t = 0$ to 10 for the two initial radii $r_0 = 0.99$ and 1.01 and initial angle $\theta_0 = \pi/4$. Superimpose the tangent field on the plot.

Solution: a. Multiplying the $\dot{x}$ equation by x, the $\dot{y}$ equation by y, and adding the resultant equations yields

$$x\dot{x} + y\dot{y} = \frac{1}{2}\frac{d}{dt}\left(x^2 + y^2\right) = \left(x^2 + y^2\right)\left(x^2 + y^2 - 1\right).$$

But $x^2 + y^2 = r^2$, so that this becomes

$$\frac{1}{2}\frac{d}{dt}\left(r^2\right) = r\dot{r} = r^2\left(r^2 - 1\right), \quad \text{or} \quad \dot{r} = r\left(r^2 - 1\right).$$

Separating variables, and integrating with $r(0) = r_0$ at $t = 0$, yields the radial solution

$$r(t) = \frac{r_0}{\sqrt{r_0^2 + \left(1 - r_0^2\right)e^{2t}}}.$$

For $r_0 = 1$, $r(t) = 1$ for all t. For $r_0 < 1$, $r(t) \to 0$ as $t \to +\infty$. For $r_0 > 1$, $r(t) \to \infty$ in a *finite* time. The circle of radius 1 is an unstable limit cycle.

The angular sense of the trajectories is found as follows. Multiply the $\dot{y}$ equation by x, the $\dot{x}$ equation by y, and subtract the second equation from the first, again noting that $x^2 + y^2 = r^2$. This yields

$$\dot{\theta} = -1,$$

with the solution

$$\theta(t) = \theta_0 - t.$$

The trajectories wind off the limit cycle in a clockwise sense.

b. The two trajectories winding off the unstable circular limit cycle of radius $r = 1$ are shown in Figure 2.10. Consistent with the tangent field, the inner trajectory winds onto a stable focal point at the origin. The outer trajectory diverges to infinity.
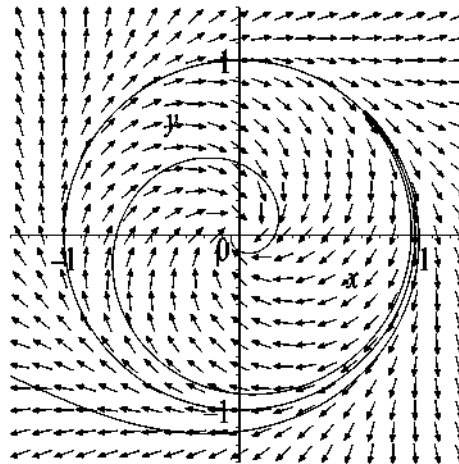
Figure 2.10: Phase-plane portrait for the unstable limit cycle.

***

A great deal of mathematical effort has gone into deriving general theorems which establish the analytic existence or nonexistence of limit cycles for a given set of nonlinear ODEs of the standard form $\dot{x} = P(x, y)$, $\dot{y} = Q(x, y)$. Two of the more well-known theorems are *Bendixson's negative criterion* and the *Poincaré–Bendixson theorem*.

Bendixson's negative criterion states:

If $\partial P / \partial x + \partial Q / \partial y \neq 0$ doesn't change its sign within a simply connected region of the phase plane, no periodic motions can exist in that region.

A simply connected planar region is one in which any closed curve lying in the region can be shrunk continuously to a point without passing outside the region. That is, a simply connected region has no holes. A proof of this theorem may be found in [EM00].

Example 2-14: Successful Application

Using Bendixson's negative criterion, show that the nonlinear system

$$\dot{x} = -x + y^2, \qquad \dot{y} = -y^3 + x^2$$

has no periodic solutions for real x and y, and hence no limit cycles.

Solution: Identifying $P \equiv -x + y^2$ and $Q \equiv -y^3 + x^2$, then

$$\frac{\partial P}{\partial x} + \frac{\partial Q}{\partial y} = -1 - 3 y^2,$$

which cannot change sign for real y. So there are no periodic solutions.

***

The Poincaré–Bendixson theorem states:

Let $x(t)$, $y(t)$ be the parametric equations of a half-trajectory $(0 \leq t < +\infty)$ T which remains inside a finite domain D for $t \to +\infty$ without approaching any fixed point. Then, either T is itself a closed trajectory or T approaches such a trajectory.

The following example illustrates how this intuitively plausible theorem is applied.

Example 2-15: Existence Proven

Consider the nonlinear system

$$\dot{r} = r\,(1 - r), \quad \dot{\theta} = 1,$$

with which we began this section. Dividing the first equation by the second eliminates the time, yielding

$$\frac{dr}{d\theta} = r\,(1 - r).$$

Remembering that the radial coordinate cannot be negative, we have $dr/d\theta > 0$ for $r < 1$ and $dr/d\theta < 0$ for $r > 1$. We also know that $d\theta/dt > 0$.

Let's choose as our domain the annular region D between $r = 0.5$ and $r = 1.5$. There are no fixed points inside this domain or on its boundaries. The trajectories crossing the inner and outer circular boundaries must qualitatively look like those shown in Figure 2.11.
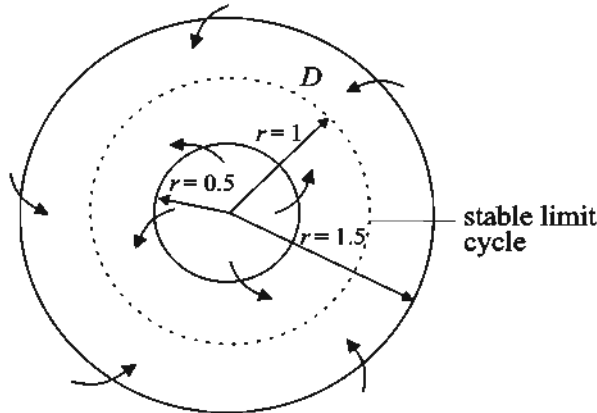

Figure 2.11: Application of the Poincaré–Bendixson theorem.

All the trajectories crossing in through either boundary must be trapped inside the domain, since no arrows leave D. There must exist a half-trajectory that remains inside D as $t \to \infty$ without approaching any fixed point. So, there is at least one stable limit cycle inside the domain. Of course, we know that there is a circular limit cycle at $r = 1$.

***

Limit cycles can also occur for autonomous three-dimensional ODE systems. Trying to establish global theorems for the existence or nonexistence of limit cycles in three-dimensional *phase space* is a difficult mathematical task which is beyond the scope of this text. For example, Bendixson's negative criterion doesn't generalize into three dimensions ([Ver90]).

As an example of a three-dimensional ODE system that can display limit cycles, consider the Lorenz model ([Lor63]) equations,[7]

$$\dot{x} = \sigma\,(y - x), \quad \dot{y} = r\,x - y - x\,z, \quad \dot{z} = x\,y - b\,z, \tag{2.29}$$

where mathematicians traditionally take $\sigma = 10$, $b = 8/3$, and r as the variable control parameter. Robbins ([Rob79]) and Sparrow ([Spa82]) have explored the bifurcation structure of this system as r is varied.

Sparrow has established ranges of r (e.g., $r = 145$ to 166) where stable limit cycles can occur. Figure 2.12 shows the numerically determined three-dimensional limit cycle
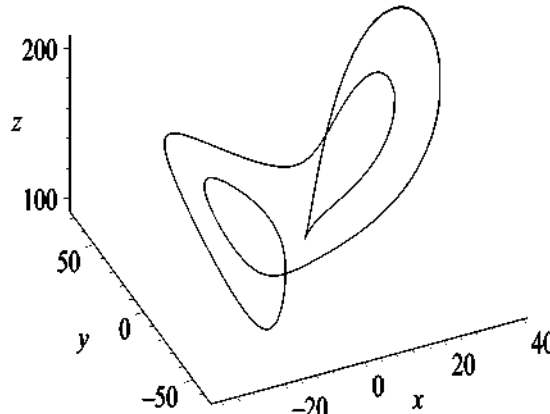

Figure 2.12: Three-dimensional limit cycle for the Lorenz model equations.

over the time range $t = 50$ to 100 for $r = 150$ and $x(0) = 20$, $y(0) = 50$, and $z(0) = 50$. The transient portion $t = 0$ to 50 of the solution curve has been omitted.

2.7 Strange Attractors and Chaos

Three-dimensional systems, such as the Lorenz model, can display still another type of attractor, referred to as a *strange attractor*. For a strange attractor, the solution curve is attracted not to a point or a closed loop, but to a localized region of phase space where

---

[7]The Lorenz equations arose out of Edward Lorenz's study of atmospheric dynamics. Physically, x is proportional to the convective velocity, y to the temperature difference between ascending and descending flows, and z to the mean convective heat flow. The coefficient σ is the *Prandtl number*, r the reduced *Rayleigh number*, and b is related to the wave number.

it traces out a nonrepeating or *chaotic* path. A strange attractor is characterized by a *fractal*, or noninteger, *dimension*, this concept being discussed shortly. Undoubtedly, the most famous strange attractor is the *butterfly* attractor of the Lorenz system. With σ and b the same as for the above limit cycle, taking $r = 28$ produces the beautiful butterfly strange attractor shown in Figure 2.13. The coordinate axes are omitted.
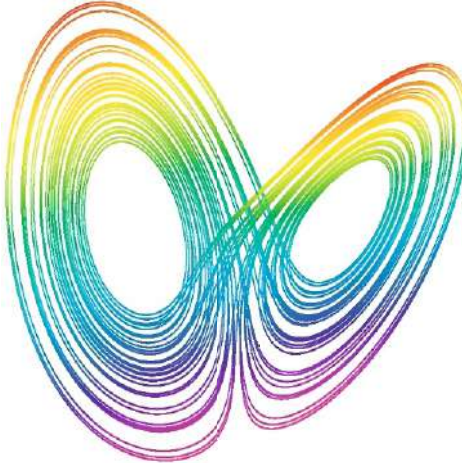

Figure 2.13: Chaotic butterfly strange attractor for the Lorenz system.

Strange attractors can also occur for nonautonomous two-dimensional ODE systems, such as *forced nonlinear oscillators*, because they can be reexpressed as autonomous three-dimensional systems. For example, let's consider the nonlinear mechanical system given by Equation (2.3) which is subjected to an external driving force $F \cos(\omega t)$ as well as a *drag*[8] *force* $-2\gamma\dot{x}$. F is the amplitude of the driving force, ω the driving frequency, and γ the damping coefficient. The equation of motion then is *Duffing's equation*,

$$\ddot{x} + 2\gamma\dot{x} + \alpha x + \beta x^3 = F \cos(\omega t). \tag{2.30}$$

Although nonautonomous in two dimensions, Duffing's equation can be recast into an autonomous three-dimensional system by setting $\dot{x} = y$, and $\dot{z} = \omega$ with $z(0) = 0$. Then,

$$\dot{x} = y, \quad \dot{y} = -2\gamma y - \alpha x - \beta x^3 + F \cos z, \quad \dot{z} = \omega. \tag{2.31}$$

To see an example of a strange attractor, let's take[9]

$$\alpha = -1, \ \beta = 1, \ \gamma = 0.25, \ \omega = 1, \ F = 0.42, \quad \text{and} \quad x(0) = y(0) = 2, \ z(0) = 0.$$

Because z simply increases linearly with time and is not very interesting, let's plot the trajectory in the x–y phase plane. Taking the time range to be from $t = 0$ to 500 and only plotting the interval $t = 100$ to 500 in order to remove any transient, Figure 2.14 results. The chaotic nature of this localized trajectory, which never approaches a fixed point or

---

[8]The assumed form (drag force proportional to the velocity) is *Stokes's law of resistance*. Although commonly assumed in elementary physics texts, it is inadequate to describe the motion of many familiar objects such as windmills and helicopter rotors as well as badminton birds and golf balls.

[9]The mathematical case where $\alpha < 0$ and $\beta > 0$ is known as the *inverted Duffing* oscillator.
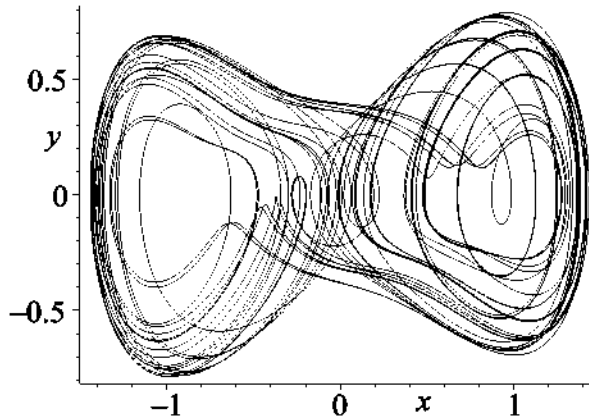
Figure 2.14: Strange attractor for the Duffing oscillator.

a limit cycle, is self-evident. It should be noted that the apparent crossings of the trajectories at ordinary points are an artifact resulting from projecting a 3-dimensional trajectory onto a 2-dimensional plane.

Unlike the situation when periodicity prevails, in the chaotic regime the solution is extremely sensitive to initial conditions, a general feature of nonlinear chaotic models. Figure 2.15 shows $x(t)$ corresponding to the strange attractor in the previous figure as
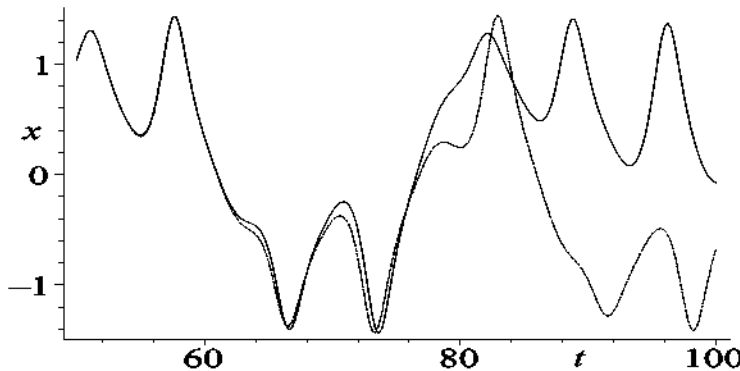
Figure 2.15: Sensitivity to initial conditions. Solid line: $z(0) = 0$; dashed: $z(0) = 0.001$.

well as the curve obtained by changing $z(0)$ very slightly from 0 to 0.001. Up to about $t = 50$, the solution curves for the two slightly different initial conditions are almost identical but, as seen from the figure, begin to deviate substantially at larger times.

The Lorenz model is a severely truncated version of the full nonlinear PDE system of atmospheric equations. However, the full system is also subject to this same sensitivity to initial conditions. This led Lorenz [Lor63] to conclude that, even for a perfect atmospheric model, the weather cannot be accurately predicted beyond a week or so.

2.8   Fractal Dimensions

Strange attractors are characterized by noninteger, or fractal, dimensions. For the butterfly attractor, for example, Lorenz found ([Lor84]) that it had a fractal dimension of 2.06 ± 0.01. Since we normally think of dimension taking on integer values, zero for a point, one for a smooth continuous line, two for a smooth continuous surface, and so on, the idea of a noninteger dimension may seem rather strange. It's not! One simply has to generalize the concept of dimension so that it reduces to our familiar cases, but can be used to characterize irregularly shaped lines (e.g., edges of snowflakes, ferns, coastlines, etc.) or lines, surfaces, and volumes (e.g., Swiss cheese) with holes in them.

There are several different ways that the usual concept of dimension can be generalized. We will only discuss the so-called *capacity dimension* D_C. Other types of fractal dimension are discussed in Parker and Chua ([PC89]). Whatever the type, the fractal dimension must reduce to an integer in situations where we would expect it to do so.

To introduce the capacity dimension, let's start by considering a smooth continuous line of length L. Divide the line into equal segments of length $\varepsilon = L/n$, where n is a positive integer (e.g., $n = 3$). Then, the number of segments is $N(\varepsilon) = n = L/\varepsilon$ (e.g., $N = 3 = L/(L/3)$). Now divide each of the n segments into n smaller segments, each of length $\varepsilon = (L/n)/n = L/n^2$. Then, $N(\varepsilon) = n^2 = L/\varepsilon$ (e.g., $N = 3^2 = 9 = L/(L/9)$). Clearly, $N(\varepsilon) = L/\varepsilon$ independent of how many times the subdivision takes place.

Next, consider a smooth continuous square of side L. Divide the square into smaller square boxes, each of length $\varepsilon = L/n$ on a side. The number of boxes to fill the square is $N(\varepsilon) = n^2 = L^2/\varepsilon^2$. If each new box is divided into even smaller boxes of length $\varepsilon = (L/n)/n = L/n^2$ on a side, then the number of boxes is $N(\varepsilon) = n^4 = L^2/\varepsilon^2$. Thus, $N(\varepsilon) = L^2/\varepsilon^2$, no matter how many times the original square is divided.

In three dimensions, the same reasoning leads to $N(\varepsilon) = L^3/\varepsilon^3$, independent of the number of subdivisions. Generalizing to D dimensions, we have $N(\varepsilon) = L^D/\varepsilon^D$. Taking the logarithm of this last expression and solving for D yields

$$D = \frac{\ln N(\varepsilon)}{\ln L + \ln(1/\varepsilon)}.$$

The dependence on the size L may be removed by taking the limit $\varepsilon \to 0$. Then $\ln(1/\varepsilon) >> \ln L$, and the capacity dimension is defined as

$$D_C = \lim_{\varepsilon \to 0} \frac{\ln N(\varepsilon)}{\ln(1/\varepsilon)}. \tag{2.32}$$

This definition is now applied to two examples of nonsmooth lines.

Example 2-16: Cantor Set

Consider a straight line of length $L = 1$. Divide the line into three equal segments and throw away the middle third. Repeat this process for each remaining line segment and determine for each subdivision the number $N(\varepsilon)$ of line segments remaining. Do not count the line segments that are thrown away. Use this result to calculate the capacity dimension D_C of the segmented line with gaps (called a *Cantor set*). Discuss the result.

Solution: Starting with the entire line shown at the top of Figure 2.16, divide the line into three equal parts ($\varepsilon = 1/3$) and throw away the middle segment. The segment
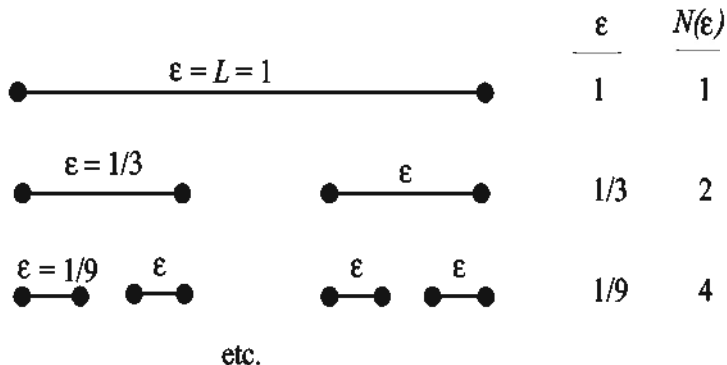

Figure 2.16: The Cantor set.

boundaries are denoted by dots. On this step, the number of remaining line segments is $N(\varepsilon) = 2$. Then divide the remaining two line segments into three equal parts, again throwing away the middle region. Then $\varepsilon = (1/3)^2 = 1/9$ and $N(\varepsilon) = 2^2 = 4$. Generalizing, on the nth step we have $\varepsilon = (1/3)^n$ and $N(\varepsilon) = 2^n$. The capacity dimension is

$$D_{\mathrm{c}} = \lim_{n \to \infty} (\ln 2^n / \ln 3^n) = \ln 2 / \ln 3 \approx 0.63.$$

The fractal (noninteger) dimension lying between 0 and 1 makes intuitive sense because the resulting line with holes in it is more than a point (zero dimension) but less than a continuous line (one dimension). The Cantor set is an example of a *self-similar* fractal. On each step, the new line segment is a scaled-down version of the old segment.

<div align="center">***</div>

Example 2-17: Koch Triadic Curve

Consider a line of length 1 unit. Instead of throwing away the middle third as in the Cantor set, form an equilateral triangle in the middle third as shown in Figure 2.17.
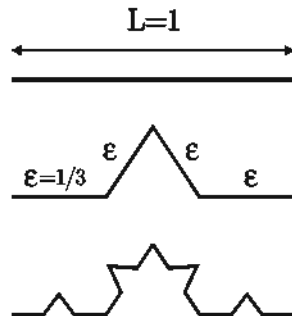

Figure 2.17: The Koch curve.

Each line segment is $\varepsilon = 1/3$. Repeat the process with each new line segment in step 1 to produce step 2. Each line segment now has length 1/9. Repeating this process indefinitely, determine D_C. Discuss the result.

Solution: On the first step, we have $\varepsilon = 1/3$ and $N(\varepsilon) = 4$. On the second step, $\varepsilon = (1/3)^2 = 1/9$ and $N(\varepsilon) = 4^2 = 16$. Generalizing, on the nth step, $\varepsilon = (1/3)^n$ and $N(\varepsilon) = 4^n$. The capacity dimension is

$$D_C = \lim_{n \to \infty} (\ln 4^n / \ln 3^n) = \ln 4 / \ln 3 \approx 1.26.$$

The dimension is intermediate to a smooth continuous line (dimension one) and a closed surface (dimension two), so it makes intuitive sense.

$$* * *$$

In experimental situations, where one doesn't have nice analytical formulas such as in our examples, a *box counting* estimate of the fractal dimension is made. Basically, the object whose fractal dimension is to be determined is covered with a one-, two-, or three-dimensional grid and the number of regions of the grid that are occupied are counted. To obtain a good estimate of D_C, finer and finer grids are taken until it appears that D_C is approaching a limit. For very fine grids, care must be taken to have a sufficient number of experimental points so as to not leave a grid region empty that should actually be occupied. The box counting approach was used by Lorenz in his estimate of the fractal dimension of the butterfly attractor.

2.9   Poincaré Sections

With five parameters and three initial coordinates available, the Duffing oscillator can exhibit a tremendous variation in possible behavior besides the strange attractor. A systematic way of numerically exploring the possible bifurcations is to hold all parameter values fixed except for one, e.g., the force amplitude F, which is allowed to change.

For example, let's vary F from 0.325 to 0.420, holding all other parameter values the same as in the previous subsection. As F is increased, one will observe a sequence of *period doublings* prior to reaching the chaotic attractor at $F = 0.42$. The period of the driving force is $T = 2\pi/\omega$. If the period of the solution (the response) is nT where $n = 1, 2, 3, 4, \ldots$, it is referred to as a period-1, period-2, period-3, period-4, etc., solution. The corresponding frequency of the solution is $\omega, \omega/2, \omega/3$, and in general ω/n for period n. The solutions for positive integer $n > 2$ are referred to as *subharmonics*.

A convenient way of graphically viewing the change in periodicity of the solution is to create a *Poincaré section*. One observes the y versus x phase plane at each multiple of the driving period, making sure to eliminate the transient solution. If $n = 1$ (period of solution same as driving period), the solution trajectory will pass through exactly the same point in the phase plane on each complete cycle of the driving force. So the Poincaré section then consists of a single point. For $n = 2$, the solution trajectory will pass through one point in the phase plane on completion of a driving force cycle, and

through a second point on completion of two cycles. This identical pattern will then repeat, so the Poincaré section displays two points. Similarly, period-4 produces four points, and so on. For the strange attractor, a new point is added to the phase plane picture on each cycle, the points however being confined to a localized region.

Returning to the Duffing oscillator, a period-1 solution occurs for $F = 0.325$, period-2 for $F = 0.350$, period-4 for $F = 0.357$, period-8 for $F = 0.358$, the period doubling continuing until the chaotic strange attractor is observed at $F = 0.420$. The Poincaré section, consisting of eight points, is shown on the left of Figure 2.18 for period-8, while the strange attractor is shown on the right.
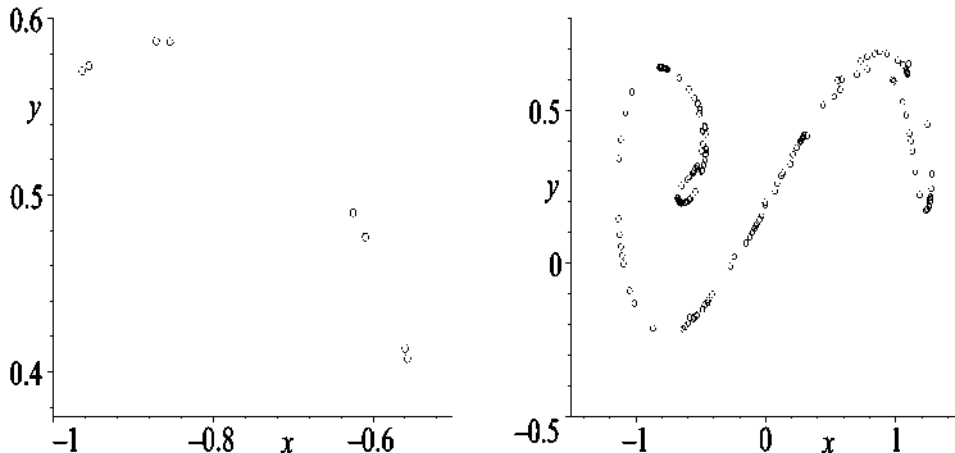

Figure 2.18: Poincaré sections for a (a) period-8 solution, (b) strange attractor.

2.10   Power Spectrum

Another diagnostic tool for studying the change in periodicity or frequency content of the solution $x(t)$ of a time-dependent nonlinear ODE such as Duffing's equation is to calculate the *power spectrum*. Assuming $-\infty < t < +\infty$, the *Fourier transform* $F(\omega)$ of $x(t)$ and its inverse are defined by the following relations:

$$F(\omega) = \int_{-\infty}^{\infty} x(t)\, e^{-i\omega t}\, dt, \quad x(t) = \int_{-\infty}^{\infty} F(\omega)\, e^{i\omega t}\, d\omega, \tag{2.33}$$

where $i = \sqrt{-1}$. From these definitions, Parseval's theorem, viz.,

$$\int_{-\infty}^{\infty} |x(t)|^2\, dt = \int_{-\infty}^{\infty} |F(\omega)|^2\, d\omega, \tag{2.34}$$

can be derived. If $x(t)$ is the instantaneous displacement, the left-hand side of (2.34) is proportional to the total energy. Since the right-hand side must have the same dimensions, $|F(\omega)|^2$ represents the energy per unit frequency interval. Aside from a

suitable normalization factor, $S(\omega) \equiv |F(\omega)|^2$ is called the *power spectrum*. It provides information on the distribution of energy as a function of frequency.

For nonlinear ODEs such as the Duffing oscillator, an analytic solution is not possible, so $x(t)$ is not known at every instant in time. A numerical solution must be sought which, because of computational time constraints, only evaluates x at a finite number of discrete time steps. This leads to a number of technical issues (replacing the continuous Fourier transform with the discrete Fourier transform, taking a sufficiently large number of time steps, etc.) in actually calculating $S(\omega)$. These issues are discussed, e.g., in Enns and McGuire ([EM00], [EM01], [EM07]), where *Maple* and *Mathematica* computer recipes for calculating the power spectrum are also provided.

If, for example, all the energy is in a single frequency, the power spectrum will consist of a single vertical "spike" at that frequency. For a period-1 solution, the spike will be at the driving frequency ω. This is illustrated on the left of Figure 2.19 for the Duffing
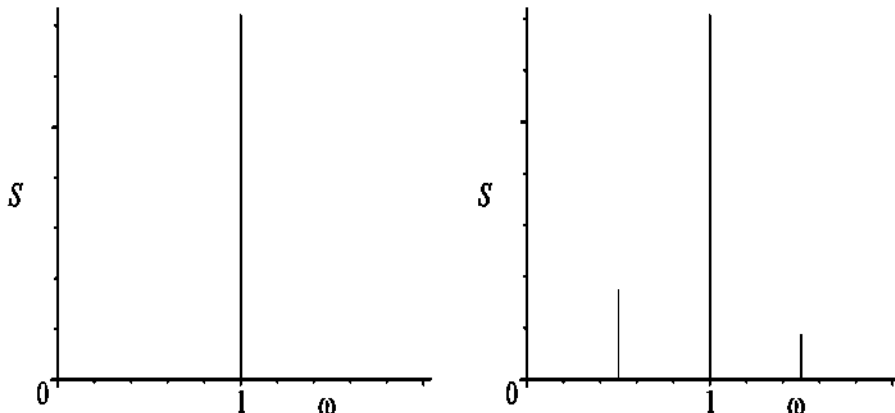

Figure 2.19: Power spectrum for period-1 (left) and period-2 (right).
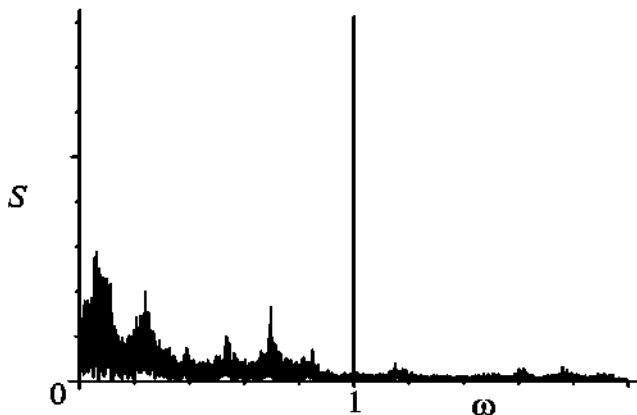

Figure 2.20: Power spectrum for the chaotic Duffing oscillator.

oscillator with $F = 0.325$ and frequency $\omega = 1$ radian/sec, all other parameters the same as in the previous section.

For $F = 0.350$, the power spectrum on the right of the figure results. In addition to the spike at the driving frequency, there is a smaller spike at the *subharmonic* frequency $\omega/2 = 0.5$ rad/sec, indicating that the solution is period-2. Note that there is also a spike in the spectrum at $3(\omega/2) = 1.5$ rad/sec, telling us that there is some energy in the *third harmonic* of the subharmonic frequency. The appearance of harmonics can complicate the power spectrum, but just remember that for period-n, the lowest frequency spike will be at ω/n.

When the solution is chaotic, the corresponding spectrum is spread over all frequencies. An example of such a spectrum, superimposed on the driving frequency spike at $\omega = 1$, is illustrated in Figure 2.20 for $F = 0.420$.

PROBLEMS

Problem 2-1: The Bernoulli ODE
The *Bernoulli* ODE is a first-order nonlinear ODE of the general structure

$$\dot{y} + f_1(t)\, y = f_2(t)\, y^n,$$

where n is a constant and f_1 and f_2 are arbitrary functions of t.

Show that the Bernoulli ODE may be reduced to a linear ODE by introducing the new dependent variable

$$z = \frac{1}{y^{n-1}}.$$

A sphere of unit mass falling from rest near the Earth's surface experiences an atmospheric drag force,

$$F_{drag} = -a\, v - b\, v^2, \quad a > 0, b > 0,$$

where v is the instantaneous speed. Analytically determine $v(t)$.

Problem 2-2: The Riccati ODE
The nonlinear *Riccati* ODE is a first-order nonlinear ODE of the form

$$\dot{y} + a\, y^2 + f_1(t)\, y + f_2(t) = 0,$$

where a is a constant and f_1 and f_2 are arbitrary functions of t.

Show that the Riccati ODE may be reduced to a linear ODE by introducing the new dependent variable

$$z = e^{a \int_0^t y\, dt}.$$
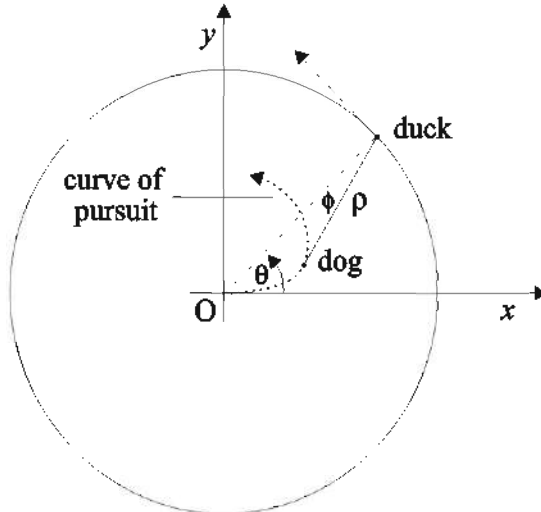
Making use of this result, solve the Riccati ODE for $y(t)$ if

$$f_1(t) = \frac{1}{t}, \quad f_2(t) = \frac{1}{a},$$

being sure to identify the functions which appear in the solution.

Problem 2-3: Circular pursuit

A much more difficult pursuit problem is that of circular pursuit, proposed by A. S. Hathaway ([Hat21]). Referring to the following figure, a dog initially at the center O of a circular pond of unit radius sees a duck swimming counterclockwise along the edge.

Both the dog and the duck swim at constant speed, the ratio of the dog's speed to that of the duck being r.

    a. If the dog always aims at the duck, show that the curve of pursuit is described by the coupled nonlinear ODE system

$$\rho\,\phi' = \cos\phi - \rho, \qquad \rho' = \sin\phi - r,$$

where prime denotes differentiation with respect to θ. This ODE system cannot be analytically solved in closed form.

    b. By numerically determining and plotting the paths traveled by the dog and the duck for some representative values of r, show that the duck eludes capture for $r < 1$ and is caught for $r > 1$.

Problem 2-4: Lane–Emden equation

Consider a spherical cloud of gas of radius R. In equilibrium, the gravitational attraction of the gas molecules is balanced by the pressure p. At a radius $r \leq R$, Newton's law of gravitation tells us that the acceleration g of gravity is

$$g = \frac{G\,M(r)}{r^2} = -\frac{d\phi}{dr}.$$

G is the gravitational constant, $M(r)$ the mass of cloud inside r, and ϕ the gravitational potential. The decrease in pressure between r and $r + dr$ is

$$dp = -\rho\,g\,dr,$$

where ρ is the gas density. Making use of the following assumptions,

- an adiabatic equation of state $p = k\,\rho^\gamma$ prevails where k is a positive constant and γ is the ratio of specific heat at constant pressure to that at constant volume;

- ϕ satisfies Poisson's equation,

$$\nabla^2 \phi = \frac{d^2\phi}{dr^2} + \frac{2}{r}\frac{d\phi}{dr} = -4\,\pi\,G\,\rho;$$

- the boundary conditions are $\phi(R) = \rho(R) = p(R) = 0$ and $\phi(0) = \phi_0$, $g(0) = 0$;

derive the *Lane–Emden* ([Lan70], [Emd07]) nonlinear *equation*,

$$\frac{d^2 y}{dx^2} + \frac{2}{x}\frac{dy}{dx} + y^n = 0.$$

Here

$$n = \frac{1}{(\gamma - 1)}, \quad y = \frac{\phi}{\phi_0}, \quad x = \sqrt{4\,\pi\,G\,C\,\phi_0^{(n-1)}}\,r, \quad C = \frac{1}{[(n+1)\,k]^n}.$$

The Lane–Emden equation has analytic solutions for $n = 0, 1, 5$. Derive these solutions. For other n values, the equation must be solved numerically. Solve Emden's equation using the fourth-order Runge–Kutta method for $\gamma = 5/3$ and $\gamma = 7/5$ and plot $y(x)$ for both γ values in the same figure. Discuss the result. What types of gas do the above γ values correspond to?

Problem 2-5: Fixed points of a nonlinear spring
Locate and identify all the fixed points of the nonlinear spring equation,

$$\ddot{x} + \alpha\,x + \beta\,x^3 = 0,$$

for the following cases: **(a)** hard spring $(\alpha > 0,\ \beta > 0)$; **(b)** soft spring $(\alpha > 0,\ \beta < 0)$; **(c)** inverted spring $(\alpha < 0,\ \beta > 0)$. Taking $|\alpha| = |\beta| = 1$, plot the tangent field for each case and discuss the possible solution trajectories.

Problem 2-6: Nonlinear superposition for the Riccati ODE
Show that if y_1, y_2, and y_3 are solutions of the Riccati equation introduced in Problem 2-2, then y will be a solution if it satisfies

$$\frac{y - y_2}{y - y_1} = C\,\frac{y_3 - y_2}{y_3 - y_1},$$

where C is an arbitrary constant. ([Zwi89], [Inc64])

Problem 2-7: Multitude of fixed points
Locate and identify the fixed points of the following ODE system (x and y are real and can be positive or negative):

$$\dot{x} = y\left(1 + x - y^2\right), \quad \dot{y} = x\left(1 + y - x^2\right).$$

Create a phase-plane portrait for this system with the tangent field included and some representative trajectories.

Problem 2-8: Saturable Lotka–Volterra model
To take into account the saturable effect of a large number of prey, the Lotka–Volterra
model equations can be extended ([Ver90]) as follows:

$$\dot{x} = a\,x - b\,\frac{x\,y}{1+s\,x}, \quad \dot{y} = -c\,y + d\,\frac{x\,y}{1+s\,x},$$

where $x, y \geq 0$ are the population numbers (or density) for the prey and predators,
respectively, and all coefficients are positive. Discuss the structure of the saturable
terms in the model. Determine and identify the fixed points of this system. Use this
information and suitable plots to discuss possible solution trajectories.

Problem 2-9: Bifurcation
Determine the type of bifurcation which occurs at the origin for the ODE system

$$\dot{x} = y + \varepsilon\,x, \quad \dot{y} = -x + \varepsilon\,y - x^2\,y$$

as the control parameter ε passes through 0.

Problem 2-10: Another predator–prey model
Consider the following (dimensionless) predator–prey system ([Ode80]):

$$\dot{x} = x^2\,(1-x) - x\,y, \quad \dot{y} = -\varepsilon\,y + x\,y,$$

with $x, y \geq 0$ and $\varepsilon \geq 0$ the control parameter.

    a. Which is the predator and which is the prey?

    b. Locate and identify all the fixed points of this system.

    c. Determine the types of bifurcations which can occur as ε is increased from zero.

    d. Support your analysis with appropriate phase-plane diagrams.

Problem 2-11: Symbiotic interaction
A *symbiotic* interaction between two species is one which is of advantage to both. A
simple model ([Mur02]) of symbiosis for two species with normalized population densities
x and y is given by the following ODE system:

$$\dot{x} = x\,(1 - x + a\,y),$$

$$\dot{y} = r\,y\,(1 - y + b\,x),$$

with the dimensionless parameters a, b, and r all positive. Locate and identify all the
physically realizable fixed points of this system. Use the fixed points to qualitatively
determine all possible solutions to the ODE system. Confirm your conclusions with
supporting tangent field plots.

Problem 2-12: Competing for the same food supply

A simple model ([Mur02]) for two species with normalized population densities x and y competing for the same food supply is given by the following ODE system:

$$\dot{x} = x\left(1 - x - a\,y\right),$$

$$\dot{y} = r\,y\left(1 - y - b\,x\right),$$

with the dimensionless parameters a, b, and r all positive. Locate and identify all the physically realizable fixed points of this system. Use the fixed points to qualitatively determine all possible solutions to the ODE system. Confirm your conclusions with supporting tangent field plots.

Problem 2-13: Chemostat

A *chemostat* is a device for harvesting bacteria. It consists of a bacterial culture chamber which has an inflow from a nutrient reservoir and an outflow which is adjusted so that the volume of the culture remains constant. In dimensionless form, the governing equations ([EK88]) for the bacterial density N and nutrient concentration C in the chemostat are

$$\dot{N} = \alpha\left(\frac{C}{1+C}\right)N - N,$$
$$\dot{C} = -\left(\frac{C}{1+C}\right)N - C + \beta,$$

where α and β are parameters.

a. Determine the fixed points of this nonlinear ODE system. What restrictions must be imposed on α and β so that N and C are never negative?

b. Determine the nature of the fixed points and discuss the possible behavior of the system.

Problem 2-14: Baleen whales and krill

Beddington and May ([BM82]) have proposed the following ODE system to model the interaction between baleen whales (population density y) and their main food source, krill (population density x):

$$\dot{x} = r\,x\left(1 - \frac{x}{K}\right) - a\,x\,y,$$
$$\dot{y} = s\,y\left(1 - \frac{y}{b\,x}\right).$$

Discuss the mathematical structure of this ODE system. Locate and identify all the fixed points.

Problem 2-15: Nested limit cycles
Consider the nonlinear ODE system

$$\dot{x} = -y + x\,(x^2 + y^2)\,\sin\left(\frac{1}{\sqrt{x^2 + y^2}}\right),$$

$$\dot{y} = x + y\,(x^2 + y^2)\,\sin\left(\frac{1}{\sqrt{x^2 + y^2}}\right).$$

Analytically show that "nested" circular limit cycles of radii $r = 1/(n\,\pi)$ exist, where $n = 1, 2, 3, \dots$. Show that the limit cycles are stable for even values of n and unstable for odd values.

Problem 2-16: Semistable limit cycle
Analytically show that the nonlinear ODE system

$$\dot{x} = x\,(x^2 + y^2 - 1)^2 - y, \qquad \dot{y} = y\,(x^2 + y^2 - 1)^2 + x$$

has a semistable limit cycle of radius $r = 1$, stable from the inside and unstable from the outside. Confirm your analysis with a tangent field plot.

Problem 2-17: Circular limit cycle
Consider the second-order nonlinear ODE

$$\ddot{x} + a\,\dot{x}\,(x^2 + \dot{x}^2 - 1) + x = 0,$$

with $a > 0$.

   a. Find and classify all the fixed points.

   b. Show that the ODE has a circular limit cycle and determine its amplitude, period, and stability.

Problem 2-18: Bendixson's negative criterion
Use Bendixson's negative criterion to demonstrate that the following nonlinear ODE systems ([Str94]) have no periodic solutions and, therefore, no limit cycles:

   a. $\dot{x} = -x + 4\,y, \ \ \dot{y} = -x - y^3$;

   b. $\dot{x} = -2\,x\,e^{(x^2 + y^2)}, \ \ \dot{y} = -2\,y\,e^{(x^2 + y^2)}$;

   c. $\dot{x} = y - x^3, \ \ \dot{y} = -x - y^3$.

Problem 2-19: Poincaré–Bendixson theorem
Consider the nonlinear ODE system

$$\dot{x} = -x - y + x\,(x^2 + 2\,y^2), \qquad \dot{y} = x - y + y\,(x^2 + 2\,y^2).$$

   a. Locate and identify all the fixed points.

b. Reexpress the ODEs in terms of polar coordinates. Choosing appropriate concentric circles of different radii centered on the origin, apply the Poincaré–Bendixson theorem to the annular region to demonstrate that the ODE system has at least one periodic solution.

c. Make a tangent field plot in the x–y plane which allows you to identify the nature of the periodic solution.

Problem 2-20: Rössler's strange attractor

By numerically integrating and plotting the solution, show that the 3-dimensional Rössler ODE system ([R76])

$$\dot{x} = -y - z, \quad \dot{y} = x + 0.2\,y, \quad \dot{z} = 0.2 + (x - \varepsilon)\,z$$

undergoes a series of period doublings between $\varepsilon = 2.5$ and $\varepsilon = 5.0$, at which point a chaotic strange attractor occurs. Take $x(0) = 4$, $y(0) = 0$, and $z(0) = 0$, and a sufficiently long time in each case to establish the nature of the solution.

Problem 2-21: Koch's snowflake

Consider an equilateral triangle with sides of unit length. Applying the same procedure as in the Koch triadic curve to each side, determine the capacity dimension of Koch's *snowflake* curve which results as the procedure is continued indefinitely.

Problem 2-22: Sierpinski's self-similar fractal gasket

Consider an upright equilateral black triangle with sides of unit length. Remove an inverted equilateral triangle inscribed inside the black triangle with vertex points bisecting the sides of the black triangle. One will now have an inverted white triangular hole with three smaller upright black triangles adjacent to its three sides. Repeat this removal process inside each of the three new black triangles. Repeating the process as many times as necessary and only counting the number of black triangles (i.e., not the white triangular holes), determine the capacity dimension of this geometrical shape, known as Sierpinski's gasket. Does your answer make intuitive sense? Explain.

Problem 2-23: A non-self-similar fractal

A black square of unit length on each side is divided into nine equal smaller black squares. One of the squares is then selected at random and thrown away, leaving a white square hole in its place. The same process is then applied to the remaining eight black squares, and so on. Counting only the black squares (i.e., not the holes), what is the capacity dimension of this non-self-similar fractal?

Problem 2-24: Modified Cantor set

Instead of removing the middle third as in the Cantor set, remove the middle x fraction from each remaining line segment. Show that the capacity dimension for this modified Cantor set is

$$D_C = \frac{\ln 2}{\ln 2 - \ln(1 - x)}.$$

Explain the limiting cases $x = 0$ and $x = 1$.
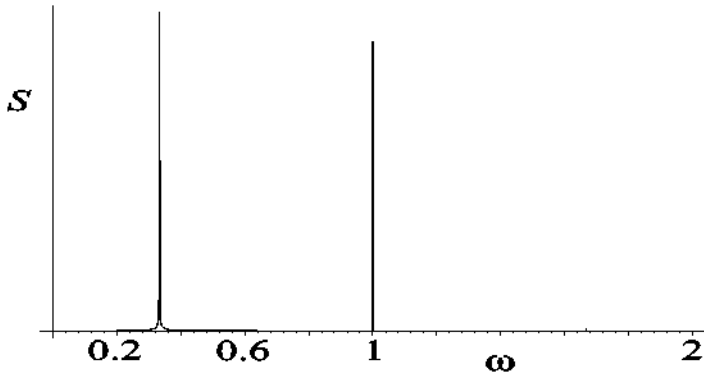
Problem 2-25: Poincaré section

Obtain the Poincaré section and determine the Duffing oscillator response for

a. $\alpha = 1$, $\beta = -1$, $\gamma = 0.25$, $\omega = 1$, $F = 0.34875$, $x(0) = 0.09$, $\dot{x}(0) = 0$;

b. $\alpha = 0$, $\beta = 1$, $\gamma = 0.04$, $\omega = 1$, $F = 0.2$, $x(0) = 0.25$, $\dot{x}(0) = 0$.

Problem 2-26: Power spectrum

The power spectrum for a certain Duffing oscillator with driving frequency $\omega = 1$ is given in the following figure. What does this spectrum tell us about the period of the oscillator response?

Problem 2-27: Pontryagin's maximum principle

Pontryagin's maximum principle, developed by the Russian mathematician Lev Semenovich Pontryagin (1908–1988) and his students, is a method for solving the following quite general *control problem* ([PBGM86], [LM67], [AF66]) which has many applications in our nonlinear world.

Consider the following system of ODEs describing the temporal evolution of the state variables $x_j(t)$ ($j = 1, \ldots, n$) over the time interval $0 \le t \le T$,

$$\dot{x}_1 = f_1(x_1, x_2, \ldots, x_n, u_1, u_2, \ldots, u_n),$$

$$\dot{x}_2 = f_2(x_1, x_2, \ldots, x_n, u_1, u_2, \ldots, u_n),$$

$$\cdots \cdots \cdots \cdots \cdots \cdots \cdots \cdots \cdots \cdots \cdots \cdots$$

$$\dot{x}_n = f_n(x_1, x_2, \ldots, x_n, u_1, u_2, \ldots, u_n),$$

with initial values $x_j(0) = x_j^0$. Here, the f_j are known functions while the $u_j(t)$ are time-dependent *control variables*. The objective is to find the *optimal* control variables $u_j^*(t)$ and the corresponding "path" $x_j^*(t)$ which maximizes the functional,

$$V(T) = c_1 x_1(T) + c_2 x_2(T) + \ldots + c_n x_n(T) + \int_0^T f_0(x_1, x_2, \ldots, x_n, u_1, u_2, \ldots, u_n)\, dt.$$

Here, the c_j are given coefficients.

Pontryagin's maximum principle provides a *necessary condition* to achieve this task. Construct the "Hamiltonian,"

$$H = \psi_1 f_1 + \psi_2 f_2 + \ldots + \psi_n f_n + f_0,$$

where the ψ_j are so-called *adjoint variables* which satisfy the adjoint equation,

$$\frac{d\psi_j}{dt} = -\frac{\partial H}{\partial x_j}, \quad j = 1, \ldots, n, \quad \left(\text{Note} : \frac{dx_j}{dt} = \frac{\partial H}{\partial \psi_j}, \quad j = 1, \ldots, n. \right)$$

For each fixed time t $(0 \leq t \leq T)$, choose the control variables $u_j^*(t)$ that maximize the Hamiltonian among all admissible u_j (ψ and x are fixed).

Making use of the Internet, discuss in some detail specific applications of Pontryagin's maximum principle. Here are some examples and the web sites on which they are discussed:

- Minimizing the landing time of a Mars probe; maximizing insect reproduction at the end of the summer season; minimizing the time for a ferry to cross a flowing river; optimal plan for harvesting fish.

  http://www.uccs.edu/ rcascava/Math448/PontryaginSP10.pdf

- Economics problem; optimal harvesting of fish.

  http://www.sjsu.edu/faculty/watkins/pontryag.htm

- Optimization of the flight phase in ski jumping ([UJ09]).

  http://www.gymnica.upol.cz/index.php/gymnica/article/ viewFile/156/143

- Allocation of energy between growth and reproduction in animal populations ([KT99]).

  http://ecology.genebee.msu.ru/3_SOTR/CV_Terekhin_publ/ 1999_Seasons_EER.pdf

Chapter 3

World of Nonlinear Maps

Two important characteristics of maps should be noticed. A map is not the territory it represents, but, if correct, it has a similar structure to the territory, which accounts for its usefulness.
Alfred Korzybski, Polish scientist (1879–1950)

Many of the concepts and mathematical tools introduced for analyzing and understanding nonlinear ODE models also apply to nonlinear difference equations. For example, fixed points which play such an important role in ODE models are also fundamental to understanding difference equation models. Because nonlinear difference equations "map" sets of points on one time step into another set on the next step, they are commonly referred to as *nonlinear maps*.

3.1 Fixed Points of One-Dimensional Maps

A first-order nonlinear difference equation has the general structure

$$x_{n+1} = f(x_n), \tag{3.1}$$

where f is a known nonlinear function. The action of the function f is to map the points x_n into new points x_{n+1}. A specific example of a one-dimensional nonlinear map is the logistic difference equation with which we began this text. In this case,

$$f = a\,x_n\,(1 - x_n), \tag{3.2}$$

with $0 < x_0 < 1$ and the control parameter a restricted to the range 0 to 4.

For the general first-order map, the fixed points $\bar{x}_k$ for period-k are obtained by forcing the kth iteration of the map (the kth-*iterate map*) to return the current value

$$x_{n+k} = x_n \equiv \bar{x}_k = f^{(k)}(\bar{x}_k), \tag{3.3}$$

where $f^{(k)}$ means to apply the function f a total of k times.

For example, the fixed points of the logistic map for period-1 are obtained from

$$x_{n+1} = x_n \equiv \bar{x}_1 = f(\bar{x}_1) = a\,\bar{x}_1\,(1 - \bar{x}_1). \tag{3.4}$$

Solving Equation (3.4) for $\bar{x}_1$ yields two roots,

$$\bar{x}_1 = 0, \ 1 - \frac{1}{a}. \tag{3.5}$$

Remembering that x is to remain between 0 and 1, the second root is rejected for $a < 1$, since it is then negative. So for $a < 1$, there is only one fixed point, namely, $\bar{x}_1 = 0$. At $a = 1$, the roots become degenerate indicating that a bifurcation is about to take place as a is increased further. For $a > 1$, both roots are positive, and two fixed points occur.

In a similar manner, the fixed points for period-2 are found from

$$x_{n+2} = x_n \equiv \bar{x}_2 = f^{(2)}(\bar{x}_2) = f(f(\bar{x}_2)) = a\,(a\,\bar{x}_2\,(1-\bar{x}_2))\,(1 - a\,\bar{x}_2\,(1-\bar{x}_2)), \tag{3.6}$$

which yields the following four roots:

$$\bar{x}_2 = 0, \ 1 - \frac{1}{a}, \ \frac{1}{2} + \frac{1}{2\,a} - \frac{\sqrt{(a^2 - 2\,a - 3)}}{2\,a}, \ \frac{1}{2} + \frac{1}{2\,a} + \frac{\sqrt{(a^2 - 2\,a - 3)}}{2\,a}. \tag{3.7}$$

The first two roots are the same as for period-1. The last two roots are imaginary for $a < 3$ and must be rejected, degenerate for $a = 3$ (a bifurcation point), and real and distinct for $a > 3$.

Example 3-1: Interpretation

Relate the above fixed point analysis to what was observed in Example 1-4 for the logistic map.

Solution: A period-1 solution occurred for $a = 2.8$, the solution asymptotically approaching the value 0.643 (quoted earlier to three significant figures). From Equation (3.5), there are two distinct real fixed points for $a < 3$, namely,

$$\bar{x}_1 = 0 \quad \text{and} \quad \bar{x}_1 = 1 - \frac{1}{2.8} = 0.6428571429 \approx 0.643.$$

It is the latter fixed point that the numerical solution approaches, so this must be a *stable* fixed point. The other fixed point at $\bar{x}_1 = 0$ must be *unstable*. This conclusion will be verified in the following section where we derive an analytic criterion for stability.

Next, we took $a = 3.2$ and observed a period-2 solution, the asymptotic numerical curve alternating between $x \approx 0.513$ and 0.799. For $a = 3.2$, Equation (3.7) yields the following four real fixed points:

$$\bar{x}_2 = 0, \ 0.6875, \ 0.5130445096, \ 0.7994554904.$$

The solution curve clearly oscillates between the last two fixed points which must therefore be stable, the other two being unstable.

<div align="center">***</div>

Before examining what happens as the control parameter a is increased further, let's turn to the general issue of analytically determining the stability of the fixed points.

3.2 Stability Criterion

What is the analytic criterion for stability of the fixed points? To answer this question, consider an initial point x_0 close to, say, the fixed point $\bar{x}_1$. We take

$$x_0 = \bar{x}_1 + \epsilon, \tag{3.8}$$

with ϵ very small. A single iteration yields, on Taylor expanding to first order in ϵ,

$$x_1 = f(x_0) = f(\bar{x}_1) + \epsilon \left(\frac{df}{dx}\right)_{\bar{x}_1} = \bar{x}_1 + (x_0 - \bar{x}_1)\left(\frac{df}{dx}\right)_{\bar{x}_1}, \tag{3.9}$$

or, on rearranging and taking the absolute value,

$$|x_1 - \bar{x}_1| = |(x_0 - \bar{x}_1)| \left|\left(\frac{df}{dx}\right)_{\bar{x}_1}\right|. \tag{3.10}$$

If the slope condition

$$\left|\left(\frac{df}{dx}\right)_{\bar{x}_1}\right| < 1 \tag{3.11}$$

holds, the iteration reduces the distance from the fixed point. Iterating again will reduce the distance further, and so on. Conversely, repeated iterations increase the distance if the slope magnitude is greater than 1. The same analysis can be applied to the fixed points of higher-iterate maps. Thus, the stability criterion for a fixed point is as follows:

If the magnitude of the slope at the fixed point is less (greater) than 1, the fixed point is stable (unstable).

This stability criterion is now applied to the logistic map.

Example 3-2: Stability of the Fixed Points of the Logistic Map

For the logistic map, analytically show that

  a. The origin is a stable fixed point for all $a < 1$ and unstable for $a > 1$.

  b. The fixed point $\bar{x}_1 = 1 - 1/a$ is stable for $1 < a < 3$ and unstable for $a > 3$.

  c. The bifurcations at $a = 1$ and $a = 3$ are transcritical and pitchfork, respectively.

Solution: a. For the logistic map, $f = a\,x\,(1 - x)$ so the slope at arbitrary x is

$$f'(x) \equiv \frac{df}{dx} = a\,(1 - 2\,x).$$

At $x = 0$, $|f'(0)| = |a|$. For $a < 1$, $|f'(0)| < 1$, so the fixed point is stable. The solution for any $a < 1$ decays to zero. For $a > 1$, $|f'(0)| > 1$, so the fixed point becomes unstable.

b. At the fixed point $\bar{x}_1 = 1 - 1/a$, we have

$$|f'(\bar{x}_1)| = |2 - a|.$$

For $1 < a < 3$, $|f'(\bar{x}_1)| < 1$, so the fixed point is stable. For $a > 3$, the slope magnitude exceeds 1, and the fixed point becomes unstable.

c. As a is increased through 1, the fixed point $\bar{x}_1 = 0$ loses its stability and the other fixed point $1 - 1/a$ becomes stable. This exchange of stabilities indicates that $a = 1$ is a transcritical bifurcation point.

As a is increased through 3, the fixed point $\bar{x}_1 = 1 - 1/a$ loses its stability and two symmetric stable fixed points, $\bar{x}_2 = 1/2 + 1/(2\,a) \mp \sqrt{a^2 - 2\,a - 3}/(2\,a)$, are "born." So $a = 3$ is a pitchfork bifurcation point.

<div align="center">***</div>

3.3   Cobweb Diagram

A *cobweb* diagram is a useful way of geometrically representing the influence of the fixed points on the behavior of a one-dimensional map as the control parameter is changed. The construction of such a diagram is now illustrated, using the logistic map.

In Figure 3.1 the parabola

$$y = f(x) = a\,x\,(1 - x)$$

with, say, $a = 3.2$ is plotted along with several other curves, which are now explained.
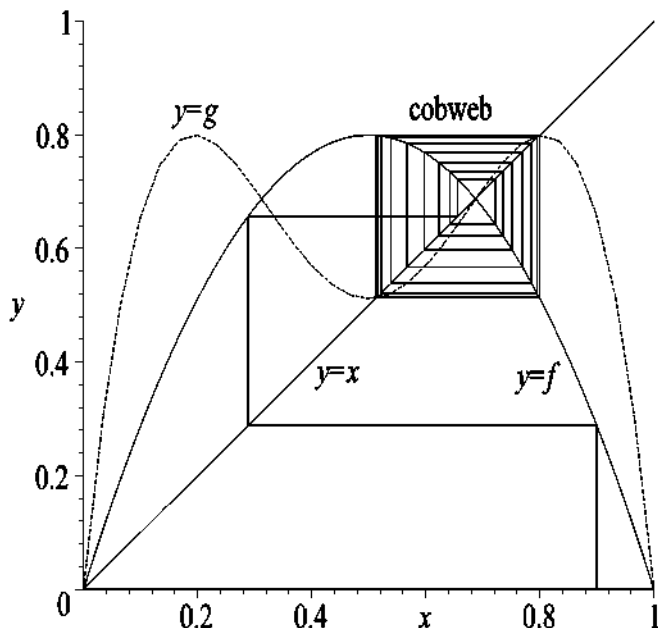
Figure 3.1: Cobweb diagram for period-2.

Since period-2 occurs for this a value, a 45° line (labeled $y = x$) is also plotted, corresponding to $x_{n+2} = x_n$. The second-iterate map,

$$y \equiv g = f^{(2)}(x_0) = f(f(x_0)),$$

which is the double-humped curve in the figure is also included.

The four fixed points (0, 0.6875, 0.5130, 0.7995) for period-2 are the intersections of the 45° line with the $y = g$ curve. Noting that 45° corresponds to a slope of 1, we see that the magnitude of the slope of the $y = g$ curve is less than at one $x = 0.5130$ and 0.7995, but more than one at $x = 0$ and 0.6875. The first two fixed points are stable and the latter two are unstable, as has already been analytically established.

To see the "cobweb" and the effect of the stable fixed points, let's iterate the logistic map taking, e.g., the initial value $x_0 = 0.9$. Substituting x_0 into the logistic map yields $x_1 = f(x_0) = 0.288$ for $a = 3.2$. $f(x_0)$ is the intersection of the vertical line from $x_0 = 0.9$ with the parabola $y = f$. Now $x_1 = 0.288$ becomes the new input value, so move horizontally to the 45° line. Using $x_1 = 0.288$, again move vertically to the parabola at which point $x_2 = f(x_1) = f^{(2)}(x_0) = 0.656\ldots$.

Repeating this procedure produces a "cobweb" which asymptotically winds onto a rectangle which cycles through the two stable fixed points. Cobweb diagrams can be created for other periodic solutions by replacing the second-iterate map with the appropriate iterate map for the given periodicity.

3.4 Period Doubling to Chaos

As a is further increased in the logistic model, additional bifurcations take place, corresponding to period doubling. If we label the a value at which period-2^n sets in as a_n, the following table shows that period-2 sets in at $a_1 = 3$, period-4 at $a_2 = 3.449490$,

a_n	Value	Period
a_1	3.000000	2
a_2	3.449490	4
a_3	3.544090	8
a_4	3.564407	16
a_5	3.568759	32
a_6	3.569692	64
a_7	3.569891	128
a_8	3.569934	256
$\vdots$	$\vdots$	$\vdots$
a_∞	$3.569946\cdots$	chaos

Table 3.1: Values of a at which period doubling occurs.

and so on, until "chaos" (period-∞) is reached. Notice that as the chaotic state is approached, the "windows" of periodicity (ranges of a) become narrower and narrower, thus making higher-periodic solutions difficult to discover.

The mathematician Mitchell Feigenbaum discovered that the above period doubling sequence satisfies the relation

$$a_k \approx a_\infty - \frac{C}{\delta^k}, \tag{3.12}$$

where C and δ are constants, the latter constant being called the *Feigenbaum number* after its discoverer. Its value is determined in the limit that $k \to \infty$.

Example 3-3: Evaluation of the Feigenbaum Number

Using Equation (3.12), show that the Feigenbaum number δ may determined from

$$\delta = \lim_{k \to \infty} \frac{(a_k - a_{k-1})}{(a_{k+1} - a_k)}. \tag{3.13}$$

Using Table 3.1, estimate the Feigenbaum number taking $k = 7$. Then estimate C.

Solution: From Equation (3.12), we have

$$a_k - a_{k-1} = -\frac{C}{\delta^k} + \frac{C}{\delta^{k-1}} = \frac{C}{\delta^k}(\delta - 1).$$

Similarly,

$$a_{k+1} - a_k = \frac{C}{\delta^k} \frac{(\delta - 1)}{\delta}.$$

Dividing the first equation by the second, and taking the limit as $k \to \infty$, yields the desired relation (3.13). For $k = 7$,

$$\delta = \frac{(a_7 - a_6)}{(a_8 - a_7)} = \frac{(3.569891 - 3.569692)}{(3.569934 - 3.569891)} \approx 4.63.$$

Using this estimate of δ, the constant $C = (a_\infty - a_7)\delta^7 \approx 2.51$.

$$***$$

In the limit that $k \to \infty$, Feigenbaum found that

$$\delta = 4.669201609\ldots, \quad C = 2.6327\ldots, \tag{3.14}$$

so our estimate of the Feigenbaum number was not too bad, the estimate of C being less accurate.

Even more importantly, Feigenbaum ([Fei79], [Fei80]) also found that the constant δ is a *universal property* of the period doubling route to chaos, not only applying to the logistic map but also to other 1-dimensional nonlinear maps of a similar shape.

The Feigenbaum number is a universal constant for the period doubling route to chaos for any one dimensional map which is unimodal. A unimodal map is one which is smooth, concave downward, and has a single maximum.

Returning to the logistic map, the bifurcations can be summarized by making a *bifurcation diagram*, which shows the asymptotic (large n) values of x as a function of a. The logistic map bifurcation diagram is shown in Figure 3.2.

We have already shown that the period-2 bifurcation is a pitchfork. From the figure, it is clear that as period doubling takes place, each "prong" of the pitchfork produces another smaller pitchfork. Also seen in the diagram are narrow windows of periodicity appearing as a is increased above a_∞. Can you spot period-3 in the figure?
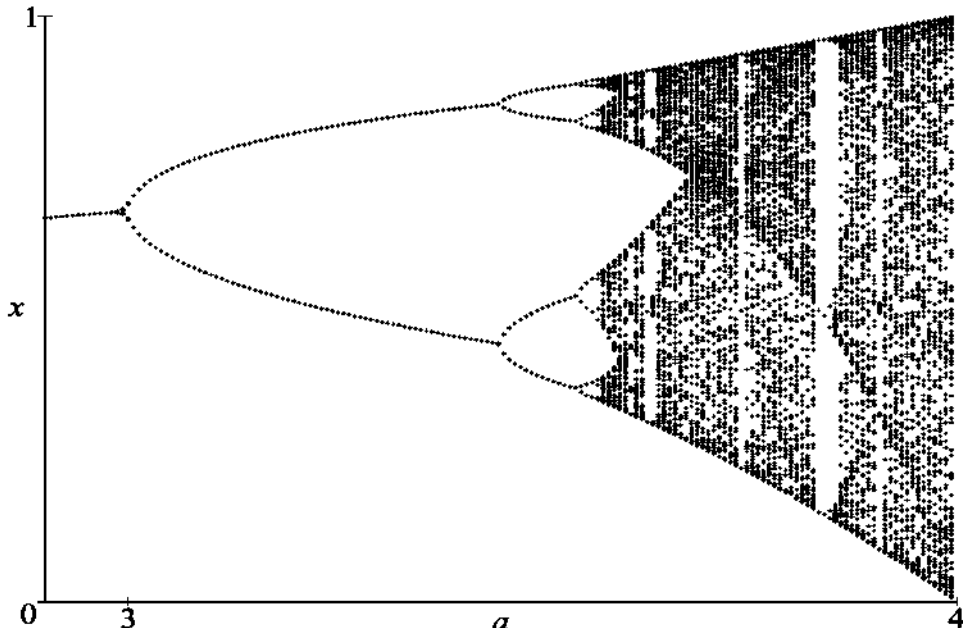
Figure 3.2: Bifurcation diagram for the logistic map.

Clearly, bifurcation diagrams can be created for other nonlinear maps. Some problems at the end of the chapter will give you the opportunity to generate your own bifurcation diagrams.

3.5 Creating Lorenz Maps

What does the period doubling route to chaos that occurs for one-dimensional unimodal maps have to do with the real world, where the physical, chemical, or biological processes are usually described by ordinary or partial differential equations? Period doubling has been observed not only for the forced Duffing oscillator when the force amplitude is increased but also in experiments involving fluid convection, nonlinear electronic circuits, laser feedback, and acoustics, when a relevant externally controllable parameter (e.g., the Rayleigh number for fluid convection) is changed.

Table 3.2 lists some of these latter experiments and the number N of observed period doublings. Using the observed bifurcation values of the relevant control parameter, in

Experiment	Reference	N	δ
Fluid convection:			
In water	Giglio et al. ([GMP81])	4	4.3 ± 0.8
In mercury	Libchaber et al. ([LLF82])	4	4.4 ± 0.1
Nonlinear circuit:			
Diode	Linsay ([Lin81])	4	4.5 ± 0.6
Driven oscillator	Testa et al. ([TPJ82])	5	4.3 ± 0.1
Transistor	Arecchi and Lisi ([AL82])	4	4.7 ± 0.3
Josephson	Yeh and Kao ([YK82])	3	4.5 ± 0.3
Laser feedback	Cvitanovic ([Cvi84])	3	4.3 ± 0.3
Acoustic: in helium	Cvitanovic ([Cvi84])	3	4.8 ± 0.6

Table 3.2: Experimentally observed period doublings and Feigenbaum number.

each case the Feigenbaum number δ was estimated along with an estimate of the error.

Although the estimates of δ are crude because of the limited number of period doublings, most of them are consistent with the value $\delta = 4.669$ for a nonlinear one-dimensional unimodal map. But, why should this be the case as the underlying mathematical description for all the experiments involved differential equations, not one-dimensional maps. The rigorous answer involves applying the so-called *renormalization theory* of statistical mechanics to period doubling. The mathematical level of this theory is beyond the scope of this text, the interested reader being referred to the works of Feigenbaum ([Fei79], [Fei80]), Collet and Eckmann ([CE80]), Schuster ([Sch89]), Drazin ([Dra92]), and Cvitanovic ([Cvi84]).

Qualitatively, the answer involves the fact that the governing differential equations in each experiment could be reduced, at least approximately, to a 1-dimensional nonlinear unimodal map, i.e., a map of the form $x_{n+1} = f(x_n)$ where f is a unimodal function. Such a map constructed from a nonlinear ODE system is called a *Lorenz map*. The construction of such a map is illustrated in the following example.

Example 3-4: Lorenz Map for the Rössler Strange Attractor

As an example of a nonlinear ODE system which can display a period doubling sequence culminating in a strange (chaotic) attractor, Rössler ([R76]) introduced the equations

$$\dot{x} = -y - z, \quad \dot{y} = x + a y, \quad \dot{z} = b + (x - c)\, z, \tag{3.15}$$

with x, y, and z real and the coefficients a, b, and c positive.

a. Taking $x(0) = -1$, $y(0) = z(0) = 0.1$, and $a = b = 0.2$, $c = 5.7$, numerically solve the Rössler equations and separately plot the trajectory in x-y-z space and x vs. t. Take $t = 0$ to 100. Discuss the plots.

b. Determine all the maxima of $x(t)$ in the range $t = 0$ to 800. Labeling the first maximum as x_1, the second as x_2, and so on, form the plotting points (x_n, x_{n+1}). Show that these points lie on a unimodal curve in the x_{n+1} vs. x_n plane.

Solution: a. Numerically solving the ODE system using the RKF45 method produces the trajectory in x-y-z space shown on the left of Figure 3.3. The trajectory traces out
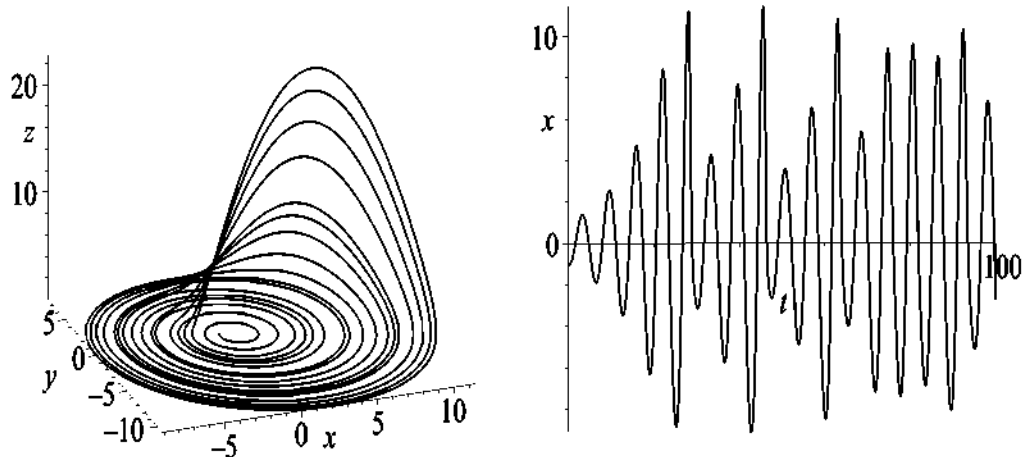
Figure 3.3: Left: Rössler's strange attractor. Right: Chaotic behavior of $x(t)$.

a nonrepeating (chaotic) "tophat" pattern in a localized region of the 3-dimensional space. This is referred to as Rössler's strange attractor. The chaotic behavior of $x(t)$ is shown on the right of Figure 3.3.
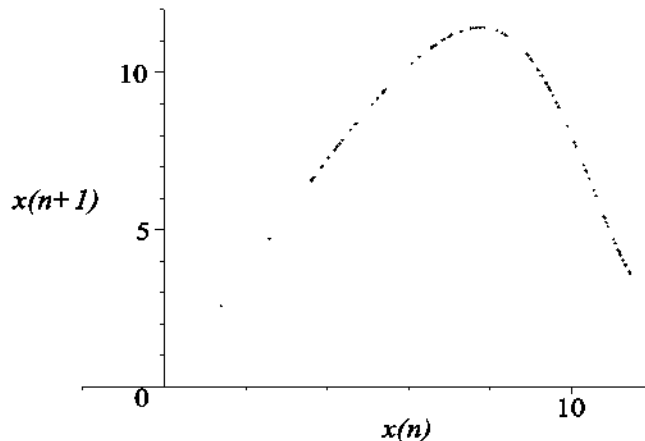
Figure 3.4: Lorenz map for the Rössler strange attractor.

b. By monitoring the slope of the $x(t)$ curve as t is increased and recording the x values (the x_n) at which the slope changes from positive to negative, there are 136 maxima in the range $t = 0$ to 800. Forming plotting points (x_n, x_{n+1}), Figure 3.4 is generated. The points lie fairly well on an inverted, skewed, parabolic curve. This suggests a 1-dimensional mapping of the form $x_{n+1} = f(x_n)$, with f a unimodal function whose form could be extracted by performing a least squares fit with a quadratic function.

<div align="center">***</div>

3.6 Lyapunov Exponent

Another diagnostic tool which complements the bifurcation diagram is the *Lyapunov exponent* L, introduced by the Russian mathematician Aleksandr Mikhailovich Lyapunov (1857–1918). It exploits the extreme sensitivity to initial conditions in the chaotic case and lack of sensitivity in the periodic situation.

Consider a general 1-dimensional map $x_{n+1} = f(x_n)$, and let x_0 and y_0 be two initial points which are very close to each other. For n iterations of the map for these initial points, we obtain

$$x_n = f^{(n)}(x_0), \quad y_n = f^{(n)}(y_0).$$

Because of their insensitivity (sensitivity) to initial conditions, the initial points will converge (diverge) for periodic (chaotic) solutions .

Following Lyapunov, one assumes for sufficiently large n that there is an (approximately) exponential dependence on n of the separation distance, i.e.,

$$|x_n - y_n| = |x_0 - y_0| e^{Ln},$$

with $L < 0$ for the periodic case and $L > 0$ for the chaotic situation. Solving for L and taking the limit of very large n, we have

$$L = \lim_{n \to \infty} \frac{1}{n} \ln \left| \frac{x_n - y_n}{x_0 - y_0} \right| = \lim_{n \to \infty} \frac{1}{n} \ln \left| \frac{f^{(n)}(x_0) - f^{(n)}(y_0)}{x_0 - y_0} \right|.$$

However, for a one-dimensional map such as the logistic difference equation, the range of x (and y) is restricted to a bounded region (e.g., $0 < x < 1$). So exponential separation in the logistic case cannot occur for very large n unless the limit $|x_0 - y_0| \to 0$ is also taken. Including this, and making use of the definition of a derivative, we have

$$L = \lim_{n \to \infty} \frac{1}{n} \lim_{|x_0 - y_0| \to 0} \ln \left| \frac{f^{(n)}(x_0) - f^{(n)}(y_0)}{x_0 - y_0} \right| = \lim_{n \to \infty} \frac{1}{n} \ln \left| \frac{df^{(n)}(x_0)}{dx_0} \right|.$$

Now, for example, $f(x_0) = x_1$, $f(x_1) = f^{(2)}(x_0) = x_2$, so that

$$\frac{df^{(2)}(x_0)}{dx_0} = \frac{df(x_1)}{dx_1} \frac{dx_1}{dx_0} = \frac{df(x_1)}{dx_1} \frac{df(x_0)}{dx_0},$$

and, generalizing,

$$\frac{df^{(n)}(x_0)}{dx_0} = \prod_{k=0}^{n-1} \frac{df(x_k)}{dx_k}.$$

Using this result, the Lyapunov exponent is finally given by

$$L = \lim_{n \to \infty} \frac{1}{n} \sum_{k=0}^{n-1} \ln\left(\left|\frac{df(x_k)}{dx_k}\right|\right). \tag{3.16}$$

In the following example, we calculate L for the logistic map for a specific value of a.

Example 3-5: L for the Logistic Map

Calculate the Lyapunov exponent L for the logistic map for $a = 2.8$ and confirm that the solution is periodic. You may take[1] $x_0 = 0.2$.

Solution: For the logistic map $f = a\,x\,(1-x)$, so $df/dx = a\,(1-2\,x)$. Taking $a = 2.8$ and $n = N = 10000$ as approximating the limit $n \to \infty$, the Lyapunov exponent is

$$L = \frac{1}{N} \sum_{k=0}^{N-1} \ln(|(2.8\,(1-2\,x_k)|)).$$

By iterating the logistic map, the values of x_k are determined, and L calculated using the above expression. We obtain $L \approx -0.223 < 0$, so the solution is periodic.

<p style="text-align:center">***</p>

To determine L for the logistic map over a range of a, one increments a in small steps Δa. This is done in Figure 3.5 (for $x_0 = 0.2$) for $a = 2.8$ to 4, with $\Delta a = 0.0025$. To detect very narrow windows of periodicity, the step size Δa should be further reduced. The regions where $L < 0$ correspond to periodic regions, and $L > 0$ to chaos.
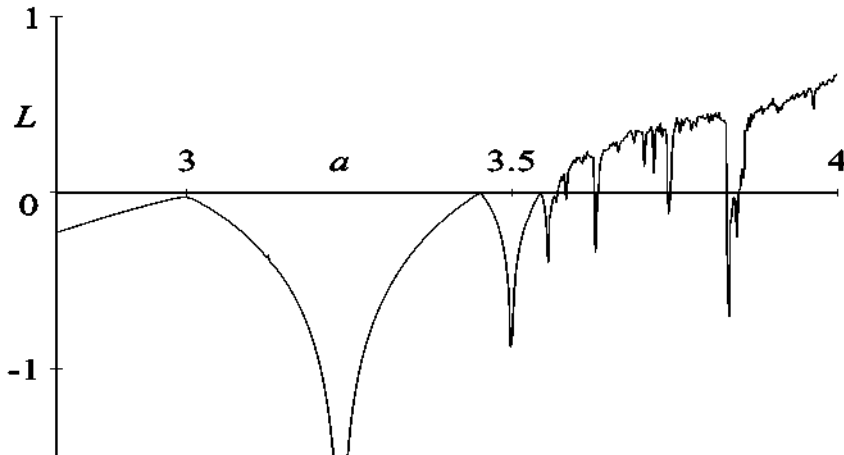
Figure 3.5: Lyapunov exponent for the logistic map.

---

[1]For periodic solutions, the choice of x_0 doesn't matter, but it does for chaotic trajectories, i.e., in general $L = L(x_0)$. If desired, one can define an average L, averaged over all initial points.

3.7   Two-Dimensional Maps

Recall that the mathematical structure of the 1-dimensional logistic map is built on the Verhulst idea that the growth of a population is limited due to "negative influences" (overcrowding, overeating, ...) in the previous generation. The *delayed logistic map*,

$$x_{n+1} = \epsilon\, x_n\,(1 - x_{n-1}), \qquad 0 < x_0 < 1, \tag{3.17}$$

with $\epsilon > 0$ the control parameter, models a negative influence in the population two generations ago. It is actually a *2-dimensional map*, since it can be rewritten as

$$x_{n+1} = \epsilon\, x_n\,(1 - y_n), \qquad y_{n+1} = x_n. \tag{3.18}$$

To analyze such a map, it is useful to once again find the fixed points. Paralleling our treatment of 2-dimensional nonlinear ODE systems, let's be quite general and consider the *standard* 2-dimensional map,

$$x_{n+1} = P(x_n, y_n), \qquad y_{n+1} = Q(x_n, y_n), \tag{3.19}$$

where P and Q are nonlinear functions. For the delayed logistic map, $P = \epsilon\, x_n\,(1 - y_n)$ and $Q = x_n$.

The fixed points correspond to

$$x_{n+1} = x_n \equiv \bar{x}, \quad y_{n+1} = y_n \equiv \bar{y}, \tag{3.20}$$

so that they are the solutions of $\bar{x} = P(\bar{x}, \bar{y})$ and $\bar{y} = Q(\bar{x}, \bar{y})$. For *ordinary* points very close to a fixed point, write

$$x_n = \bar{x} + u_n, \quad y_n = \bar{y} + v_n,$$

with u_n and v_n very small. To first order in u_n and v_n, the standard difference equations (3.19) reduce to the linear difference equations

$$u_{n+1} = a\, u_n + b\, v_n, \qquad v_{n+1} = c\, u_n + d\, v_n \tag{3.21}$$

with

$$a \equiv \left(\frac{\partial P}{\partial x}\right)_{\bar{x},\bar{y}}, \quad b \equiv \left(\frac{\partial P}{\partial y}\right)_{\bar{x},\bar{y}}, \quad c \equiv \left(\frac{\partial Q}{\partial x}\right)_{\bar{x},\bar{y}}, \quad d \equiv \left(\frac{\partial Q}{\partial y}\right)_{\bar{x},\bar{y}}.$$

Eliminating v from the system (3.21) yields the second-order difference equation

$$u_{n+2} + p\, u_{n+1} + q\, u_n = 0 \tag{3.22}$$

with $p = -(a+d)$ and $q = a\,d - b\,c$. Now assume a solution of the form $u_n \sim e^{r\,n} \equiv \lambda^n$, with $\lambda = e^r$. This yields the following quadratic equation for λ:

$$\lambda^2 + p\,\lambda + q = 0, \tag{3.23}$$

which, in general, has two roots λ_1 and λ_2. The general solution of (3.22) then is

$$u_n = A\,(\lambda_1)^n + B\,(\lambda_2)^n, \tag{3.24}$$

where A and B are arbitrary constants. If $|\lambda_1| < 1$ and $|\lambda_2| < 1$, then all trajectories in the x–y phase plane are attracted to the fixed point, so it is stable. If at least one λ has a magnitude greater than one, the fixed point is unstable. Analyzing the roots in detail, one finds that

- If λ_1 and λ_2 are real and $0 < \lambda_1 < 1$, $0 < \lambda_2 < 1$, the fixed point is a stable nodal point. If $\lambda_1 > 1$, $\lambda_2 > 1$, the fixed point is an unstable node.

- If $0 < \lambda_1 < 1$ and $\lambda_2 > 1$, the fixed point is a saddle.

- If at least one λ is negative, successive points of an orbit near the fixed point lie alternately on two distinct branches.

- If $\lambda_1 = \lambda_2^*$ (i.e., are complex conjugate), and $|\lambda_1| = |\lambda_2| \equiv |\lambda| \neq 1$, the fixed point is a focal point, stable if $|\lambda| < 1$ and unstable if $|\lambda| > 1$. If $|\lambda| = 1$, it is a vortex.

The nature of the fixed point when there are equal real roots is left as a problem.

Example 3-6: Fixed Points of the Delayed Logistic Map

Classify and discuss the fixed points of the delayed logistic map. Support your analysis with an appropriate plot of the trajectory in the x–y plane if necessary.

Solution: The fixed points are the solutions of

$$P = \epsilon \, \bar{x} \, (1 - \bar{y}) = \bar{x}, \quad Q = \bar{x} = \bar{y}.$$

For $\epsilon < 1$, there is only one fixed point at $\bar{x} = \bar{y} = 0$, while there are two at

$$\bar{x} = \bar{y} = 0, \quad \bar{x} = \bar{y} = 1 - \frac{1}{\epsilon},$$

for $\epsilon > 1$.

For the fixed point at the origin, we obtain $p = -\epsilon$ and $q = 0$, so Equation (3.23) yields the roots $\lambda = 0$ and ϵ. According to the classification scheme, this fixed point is a stable nodal point for $\epsilon < 1$. In this case, all trajectories are attracted to the origin, no matter what the initial values. For $\epsilon > 1$, the origin is a saddle, so all orbits avoid the origin. To see where they might go, let's examine the second fixed point.

For the second fixed point, we find that $p = -1$ and $q = \epsilon - 1$, so Equation (3.23) yields

$$\lambda = (1/2)\,(1 \pm \sqrt{5 - 4\epsilon}).$$

For $1 < \epsilon < 2$, $|\lambda| < 1$, so the second fixed point is stable. All trajectories must be attracted to this point, the exact topology in the neighbor of the fixed point depending on the value of ϵ. Below $\epsilon = 5/4$, it is a stable nodal point, while above this value it is a stable focal point.

For $\epsilon > 2$, the λs are complex conjugate and $|\lambda| > 1$, so the second fixed point is an unstable focal point. With two unstable fixed points, what happens to an orbit as ϵ is increased above 2 is a bit trickier. Figure 3.6 shows the trajectory for $\epsilon = 2.1$ and initial values $x_0 = 0.4$, $y_0 = 0.2$. The delay map has been iterated 5000 times.
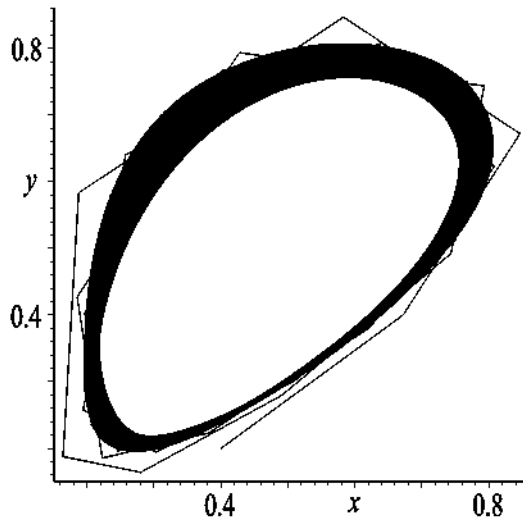
Figure 3.6: Trajectory for the delayed logistic map for $\epsilon = 2.1$.

The trajectory evolves along a path which eventually is confined to, and fills in, a closed elliptical region, somewhat reminiscent of a limit cycle. As ϵ is further increased, a point is reached at which all trajectories, not surprisingly, diverge to infinity.

<div align="center">***</div>

3.8   Mandelbrot and Julia Sets

Probably the most well-known 2-dimensional map is the mathematical extension of the logistic map into the complex plane by the Franco-American mathematician Benoît Mandelbrot, often referred to as the "father of fractal geometry."

With the substitution $x = (1/2) - z/a$, the logistic map becomes

$$z_{n+1} = z_n^2 + C, \tag{3.25}$$

with $C = a\,(2 - a)/4$.

The *Mandelbrot map* results on setting $z = x + i\,y$ and $C = P + i\,Q$ in Equation (3.25) and separating into real and imaginary parts, viz.,

$$x_{n+1} = x_n^2 - y_n^2 + P, \qquad y_{n+1} = 2\,x_n\,y_n + Q. \tag{3.26}$$

We shall not locate and classify the fixed points of the Mandelbrot map, leaving this aspect as a problem. Here we shall just comment on the interesting fractal geometrical patterns that can occur.

The *Mandelbrot set* of points is generated with the Mandelbrot map, the parameters P and Q being allowed to systematically vary over specified ranges, the initial point (x_0, y_0) being held fixed. As the map is iterated, there will be values of P and Q for

which the initial point will rapidly escape (i.e., iteration number n is small) to infinity, while for other values the point will escape very slowly or not all because it is attracted to a stable finite fixed point $(\bar{x}, \bar{y})$. Taking the number of iterations n as a third axis, one determines the number of iterations needed for $|z| = |x + i\,y| = \sqrt{x^2 + y^2}$ to reach some specified value, e.g., $|z| = 2$. It is assumed that if this value is exceeded, the initial point is heading off to infinity. A color-coded contour plot of the results can be plotted in the P vs. Q plane.

For example, let's take the range of P to be from -2.0 to $+0.8$ and Q from -1.2 to $+1.2$, with the initial point $(0, 0)$. The total number of iterations possible is taken to be 25. The resulting picture is shown in Figure 3.7.
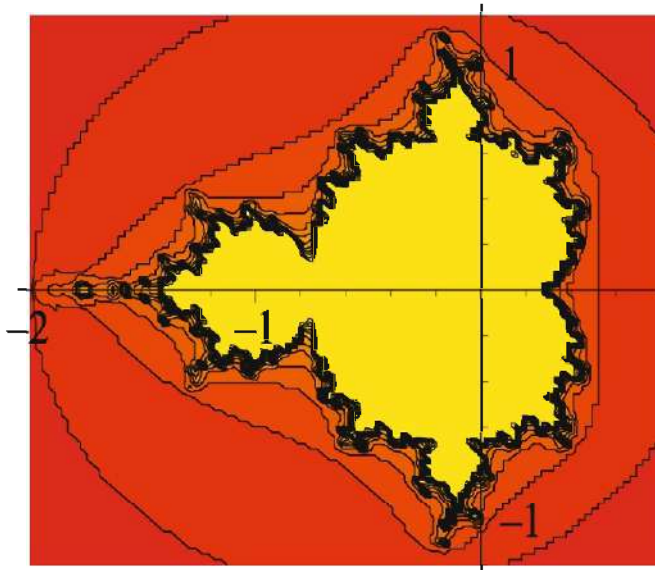
Figure 3.7: Mandelbrot set picture.

The central yellow region with the fractal contour boundary corresponds to the largest number of iterations n. Moving outwards from this "attractive" region are contours for decreasing n as the value $|z| = 2$ is more rapidly reached. Other interesting attractive fractal "shapes" can be generated by changing the ranges of P and Q.

The *Julia set*, named after the French mathematician Gaston Julia (1893 – 1978), is also generated with the Mandelbrot map, the parameters P and Q now being held fixed while the values of x_0 and y_0 are systematically varied over specified ranges. The procedure for generating the Julia set is similar to that for the Mandelbrot set, except if the value of $|z| = 2$ is exceeded before the maximum possible 25 iterations, a value of 1 is assigned, while if $|z| = 2$ is not reached, a value of 0 is allotted. The Julia set of points refers to the points which lie on the fractal boundary between regions of divergence (the region of ones) and convergence (region of zeros).

Example 3-7: Douady's Rabbit

Generate the Julia set of points and plot them for $P = -0.12$ and $Q = 0.74$. Take x_0 from -1.5 to $+1.5$ and y_0 from -1.2 to $+1.2$, with a grid of 150 by 150.

Solution: Figure 3.8 shows the fractal boundary (Julia set of points) between the region of convergence (inside the boundary) and divergence (outside). This Julia set is commonly known in the literature as Douady's "rabbit" because of its shape.
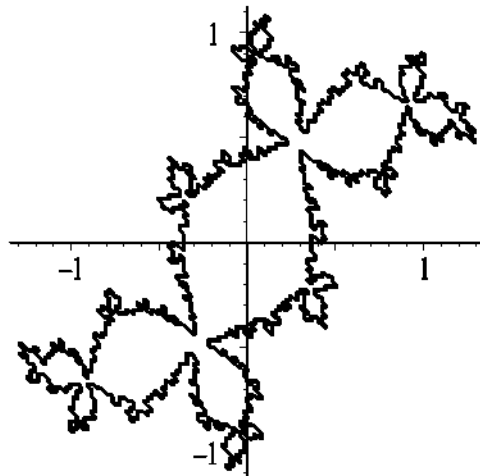

Figure 3.8: Douady's "rabbit."

Adrien Douady is a French mathematician who has specialized in *holomorphic dynamics*, the dynamics induced by the iteration of analytic maps in complex number space.

***

3.9   Chaos versus Noise

It is important not only for the scientist and engineer but also for the stock market trader to distinguish chaos from *noise*. Chaos refers to the irregular temporal behavior occurring for a *deterministic* nonlinear dynamical system. Noise, on the other hand, is *random*. Presented with time series data sampled at a regular time interval t_s, how can one determine whether there exists some underlying mathematical structure waiting to be discovered or one is simply dealing with noise? If the structure is known, it is possible to predict the future behavior of the system as the system parameters are changed.

Suppose that the data points, sampled at a time $t = nt_s$, with $n = 0, 1, \ldots$, are $x_0, x_1, x_2, \ldots, x_n, x_{n+1}, \ldots$. If the time series is deterministic, then x_{n+1} will be related somehow to previous data points, i.e., to x_n, x_{n-1}, etc. In the simplest situation, x_{n+1} will depend only on the previous value x_n. So assume that $x_{n+1} = f(x_n)$, with the mathematical function f not yet known.

As an example, consider the time series consisting of 100 data points, connected by straight-line segments, presented graphically in Figure 3.9.
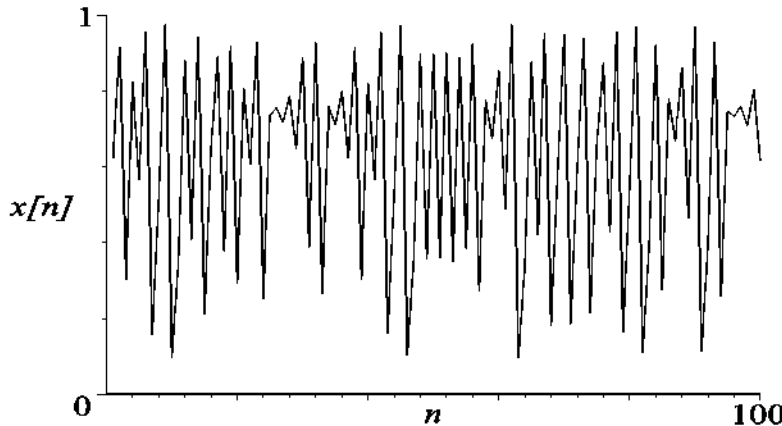
Figure 3.9: A time series.

Now let's make a plot of x_{n+1} versus x_n for the time series, each point in Figure 3.10 representing a value of (x_n, x_{n+1}). The points appear to lie on an inverted parabola,
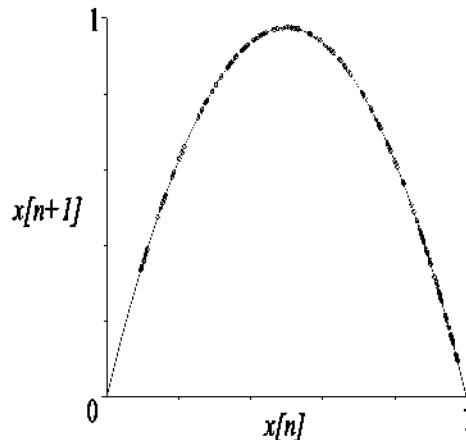
Figure 3.10: Extracting the mathematical form of the time series.

reminiscent of the mathematical form of the nonlinear logistic map. Assuming this to be the case, a least squares fit using the logistic map with $a = 3.9$ produces the solid curve. Knowing that the logistic map prevails, one can now use the map to predict other behavior as the parameter a is varied.

By contrast, let's look at what happens when we apply the same extraction technique to "noisy" time series data. Using a random number generator to generate 12-digit decimal numbers in the range $x = 0$ to 1, the time series shown in Figure 3.11 was produced, the numbers again being joined by straight lines.

At first glance, it is not obvious whether the time series is chaotic or noisy. When
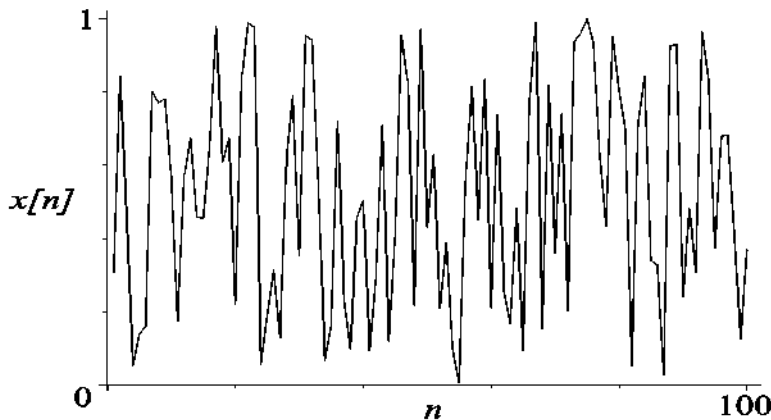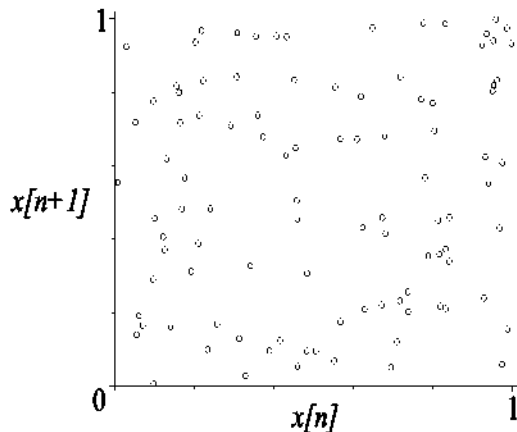
Figure 3.11: A second time series.

x_{n+1} is plotted versus x_n, Figure 3.12 results. The points appear to be randomly distributed, so no underlying mathematical form can be extracted.

Figure 3.12: Random distribution of (x_n, x_{n+1}) points for second time series.

For the first time series, the points (x_n, x_{n+1}) lay along a definite curve, implying that there could be an underlying 1-dimensional nonlinear map. If the points display more structure, which appears to be nonrandom, this could imply either experimental scatter in the data or that there may be an underlying two-dimensional map, namely,

$$x_{n+1} = f_1(x_n) + f_2(x_{n-1}), \quad \text{or} \quad x_{n+1} = f_1(x_n) + y_n, \ y_{n+1} = f_2(x_n),$$

where f_1 and f_2 are nonlinear functions. If the dimensionality of the underlying map is higher than two, the dimensionality of the space must be increased accordingly. To extract a 3-dimensional map, for example, one should use triplets of numbers, (x_n, x_{n+m}, x_{n+2m}) with $n = 0, 1, 2, \ldots$ and $m = 1$ or 2 or 3 or $\ldots$. The choice of m is dictated by what gives the best extraction of the underlying map.

3.10 Controlling Chaos

In recent years, there has been considerable interest in attempting to control chaotic behavior in nonlinear systems. For example, chaotic oscillations of the heart (cardiac arrhythmias) and in the brain (seizures) are highly undesirable so experimental methods are being developed to suppress the chaos and restore periodicity. See, for example, references ([GWDS95]) and ([SJD+94]) in the bibliography.

Conceptually, two of the basic methods for controlling chaos are:

- application of a small forcing term (e.g., [LP90], [BG91]) or modulation to the nonlinear system parameters to change the system dynamics;

- using proportional feedback such as that of Ott, Grebogi, and Yorke ([OGY90]), which has proven to be quite effective in numerical simulations (e.g., control of the chaotic pendulum ([Bak95])) as well as physical experiments (e.g., [DRS90]).

In this section, we will illustrate a simpler version of proportional feedback due to Flynn and Wilson ([FW98]) applied to the following two-dimensional *Hénon map* ([Hen76]):

$$x_{n+1} = a - x_n^2 + b y_n, \qquad y_{n+1} = x_n, \text{ with } a > 0, b > 0. \tag{3.27}$$

We will take $b = 0.3$ and let a be the control parameter. This parameter will be allowed to vary by a small amount about some value a_0 for which chaotic oscillations occur.

Example 3-8: Hénon Strange Attractor

Taking $x_0 = y_0 = 0.5$ and $a = a_0 = 1.29$, numerically iterate the Hénon map up to $n = N = 2500$ and plot the points in the x–y plane. Plot x_n versus n for $n = 500$ to 600 to further illustrate the chaotic nature of the solution.

Solution: Using small crosses to denote the numerical points in the x–y plane, the points produce the picture shown on the left of Figure 3.13. Although chaotic, the
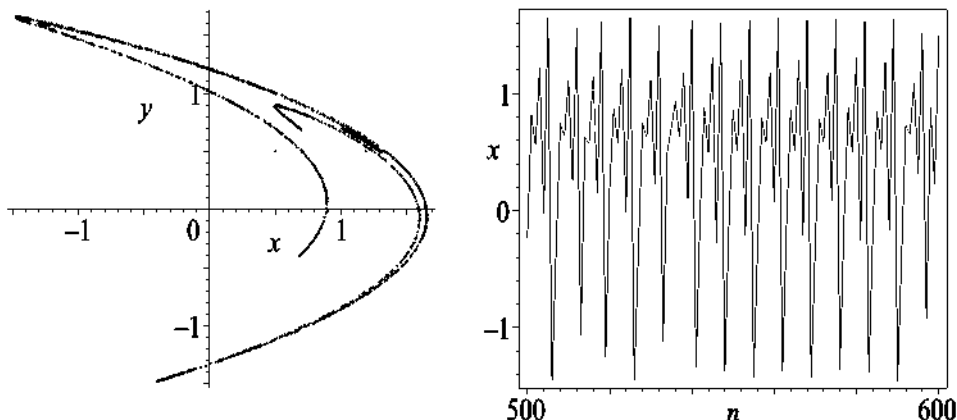
Figure 3.13: Left: Hénon strange attractor. Right: Chaotic oscillations.

points are attracted to a localized region, indicative of a strange attractor. For obvious reasons, this is referred to as the *Hénon strange attractor*. It has a fractal structure.

The behavior of x as a function of n is shown on the right of the figure. Since the plot begins at $n = 500$, the transient has been eliminated, so that these are truly chaotic oscillations. This can be checked by going to even higher n values.

<center>***</center>

Now we shall use feedback to change the chaotic oscillations in the above example into periodic behavior. First, it's necessary to determine the fixed points of the Hénon map. The fixed points are given by

$$y_{n+1} = y_n = \bar{y} = x_n = \bar{x}, \quad x_{n+1} = x_n = \bar{x} = a - \bar{x}^2 + b\bar{y} = a - \bar{x}^2 + b\bar{x}. \quad (3.28)$$

Next, taking $b = 0.3$, $a_0 = 1.29$, and $x_0 = y_0 = 0.5$, the a value will be allowed to vary slightly around a_0 according to the following procedure:

1. Iterate the Hénon map to find the next point x, y.

2. If $|x - y| < 0.01$, then this point is a fixed point $\bar{x} = \bar{y}$ for some particular a. Calculate a from $a = \bar{x}^2 + (1 - b)\bar{x}$ and label it as A.

3. If $|a_0 - A| < 0.2$, let $a = A$.

4. If $|a_0 - A| > 0.3$, let $a = a_0$. This condition prevents runaway.

5. Record the a value.

6. Loop back to step 1 and repeat until the iterations are completed.

The specified tolerances are those used by Flynn and Wilson but they can be adjusted.

Applying the above procedure to the chaotic oscillations of the last example yields the result shown in Figure 3.14. In less than 100 iterations, the chaotic oscillations have changed into a period-1 solution. The a value has changed from $a = a_0 = 1.29$ to $a = A = 1.167146373$.
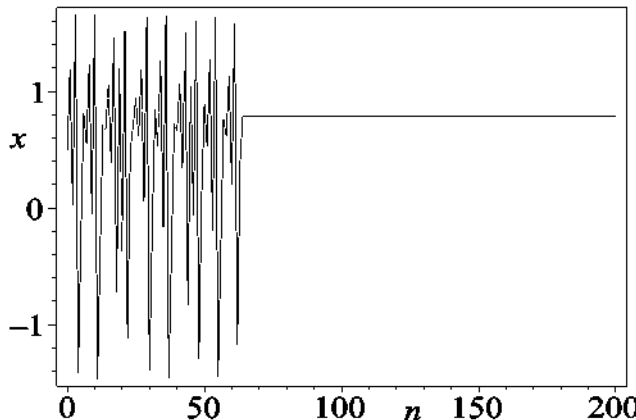
Figure 3.14: Applying the feedback procedure produces a period-1 solution.

PROBLEMS

Problem 3-1: Period-3 for the logistic map
Consider the logistic map with $a = 3.83$ and initial value $x_0 = 0.5$.

    a. Iterating the logistic map and plotting x_n versus n, show that a period-3 solution emerges for large n. What are the three possible steady-state values of x_n?

    b. By solving the third-iterate map for the fixed points and calculating the magnitudes of the slopes, show that there are three stable fixed points whose values are the same as those in part **a.**

    c. Generate a cobweb diagram which graphically supports the existence of period-3.

Problem 3-2: Intermittency in the logistic map
Intermittency is a term referring to almost periodic behavior interspersed with bursts of chaos. Taking $x_0 = 0.5$ and 300 iterations, show that intermittency occurs for $a = 3.82812$ in the logistic map. This a value is just below the onset of the period-3 window of the previous problem.

Problem 3-3: Period-3 to chaos
For the logistic map with $x_0 = 0.2$, a period-3 solution occurs for $a = 3.835$. As a is increased very slightly, a sequence of period doublings to chaos will occur. Explore and discuss this sequence by making an appropriate bifurcation diagram.

Problem 3-4: Cobweb diagram for the cubic map
Taking $a = 2.1$, $x_0 = 0.1$, and 100 iterations, form a cobweb diagram for the cubic map

$$x_{n+1} = x_n \left(a - x_n^2 \right).$$

Identify the periodicity of the solution by plotting the appropriate iterate map in the same figure.

Problem 3-5: Bifurcation diagram for the sine map
The *sine map* is given by

$$x_{n+1} = a \sin(\pi x_n),$$

with $0 \le a \le 1$ and $0 \le x \le 1$. Derive the bifurcation diagram for this map. Is this map unimodal? How does the bifurcation diagram for the sine map compare with that for the logistic map if only the range $a = 0.7$ to 1 is plotted.

Problem 3-6: Lyapunov exponent for the sine map
Calculate the Lyapunov exponent as a function of a ($0 \le a \le 1$) in steps of $\Delta a = 0.01$ for the *sine map*, defined in the previous problem. For what ranges of a do periodic solutions occur?

Problem 3-7: Equal real roots
For the general 2-dimensional nonlinear map, what is the nature of the fixed point if the two λ roots are real and equal?

Problem 3-8: Fixed points of the Mandelbrot map
Locate and classify the fixed points of the Mandelbrot map.

Problem 3-9: Fixed points of the Hénon strange attractor

For the Hénon map, consider the parameter values of the text example. Specifically locate the fixed points and establish their stability and nature. Discuss how the fixed points influence the evolution of the strange attractor.

Problem 3-10: Julia set for the San Marco attractor

Generate the Julia set of points for the Mandelbrot map corresponding to $p = -0.75$, $q = 0$. Take a sufficient range of x and y to completely reveal the shape of the attractor (called the *San Marco* attractor).

Problem 3-11: Predator–prey map

Consider the 2-dimensional nonlinear map

$$x_{n+1} = a\,x_n\,(1 - x_n - y_n), \quad y_{n+1} = a\,x_n\,y_n,$$

with $2 < a \le 4$.

  a. By discussing its mathematical structure, explain why this map can be considered as a model of a predator–prey interaction.

  b. Find and classify the fixed points of this map for: **(i)** $a = 2.40$; **(ii)** $a = 3.00$; **(iii)** $a = 3.43$; **(iv)** $a = 3.90$.

  c. Taking $x_0 = y_0 = 0.1$ and a sufficient number of iterations, plot the trajectories for each of the a values in part **b** and discuss the observed behavior in terms of the fixed points.

Problem 3-12: Chaos control

For the Hénon map, take $a = 1.4$, $b = 0.3$, and $x_0 = y_0 = 0$.

  a. Iterate the Hénon map 3000 times and plot the points in x–y space. Discuss the resulting picture.

  b. Show that the Flynn–Wilson feedback procedure will force the chaotic oscillations of part **a** to evolve into a periodic solution. Identify the period and determine the final a value.

Problem 3-13: Dissipative map

Consider the standard 2-dimensional map

$$x_{n+1} = P(x_n, y_n), \quad y_{n+1} = Q(x_n, y_n),$$

where P and Q are specified nonlinear functions.

Making use of a well-established result of calculus, applying such a mapping to an infinitesimal area $dx\,dy$ will produce a new area,

$$dx'\,dy' = |\text{determinant}(J(x,y))|\,dx\,dy,$$

$$\text{where} \quad J(x,y) = \begin{pmatrix} \dfrac{\partial P}{\partial x} & \dfrac{\partial P}{\partial y} \\[2mm] \dfrac{\partial Q}{\partial x} & \dfrac{\partial Q}{\partial y} \end{pmatrix} \quad \text{is the } \textit{Jacobian matrix.}$$

A nonconservative or dissipative map is one for which the mapping reduces the area, i.e., $|\text{determinant}(J(x, y))| < 1$. This reduction in area takes place because the map has either a fixed point (stable focal or nodal) or strange attractor which captures all trajectories with initial points within the attractor's "basin of attraction." Determine the condition for the Hénon map to be dissipative.

Problem 3-14: Density-limited population growth
The difference equation
$$N_{n+1} = \frac{r\,N_n}{(1 + a\,N_n)^b}$$
with positive parameters r, a, and b is often encountered in the biological literature (see, e.g., ([Has75])) as an empirical description of density-limited population growth. Find the fixed points of this difference equation and determine their stability.

Problem 3-15: Ricker's model for sockeye salmon populations
Salmon breed in specific freshwater lakes and river systems and migrate to the ocean where they mature for about 4 years before returning to the same lake or river where they spawn and then die. Table 3.3 shows the 4-year averages of the sockeye salmon (*Oncorhynchus nerka*) in the Skeena river system of northern British Columbia, Canada, for the period 1908 to 1948 ([SW58]). Each grouping of 4 years is a rough approximation of the offspring of the previous 4-year average of salmon.

Year	Population number (in thousands)
1908	1098
1912	740
1916	714
1920	615
1924	706
1928	510
1932	278
1936	448
1940	528
1944	639
1948	523

Table 3.3: Four-year averages of Skeena river sockeye salmon.

One finite-difference equation used by fishery management to model data such as that shown above is *Ricker's model* equation ([Ric58]). The population number in the nth 4-year cycle is given by
$$P_{n+1} = a\,P_n\,e^{-b\,P_n},$$
where a and b are positive constants. A nonlinear least squares fit of Ricker's model to the data of Table 3.3 yields $a = 1.535$ and $b = 0.000783$.

Taking $P_0 = 1098$, plot Ricker's model equation along with the data of Table 3.3 and discuss the plot. What is the asymptotic value of the population number of the sockeye salmon population for the Skeena river, assuming that there are no environmental changes or onsets of disease?

Problem 3-16: A fractal fern

Michael Barnsley ([Bar88])) has suggested a number of 2-dimensional nonlinear maps for mathematically "growing" various types of fractal-appearing ferns. To grow a fern resembling the *black spleenwort*, iterate the following piecewise-linear map $N = 40000$ times, starting at $x_0 = y_0 = 0$, and plot the points (x_n, y_n) (don't join them):

$$(x_{n+1}, y_{n+1}) = \begin{cases} (0, 0.16\,y_n), & 0 < r < p_1, \\ (0.2\,x_n - 0.26\,y_n,\ 0.23\,x_n + 0.22\,y_n + 0.2), & p_1 < r < p_2, \\ (-0.15\,x_n + 0.28\,y_n,\ 0.26\,x_n + 0.24\,y_n + 0.2), & p_2 < r < p_3, \\ (0.85\,x_n + 0.04\,y_n,\ -0.04\,x_n + 0.85\,y_n + 0.2), & p_3 < r < 1, \end{cases}$$

with the parameter r a random number between 0 and 1 and $p_1 = 0.01$, $p_2 = 0.08$, and $p_3 = 0.15$. Note that you will have to use a random number generator to generate a new value of r on each iteration. Also note that you will have to insert a conditional "if $\cdots$ then $\cdots$ else if" statement which selects the correct "branch" of the map depending on the value of r produced. If using *Maple* or *Mathematica*, you might wish to color the points in your fern an appropriate shade of green.

Problem 3-17: A fractal tree

By generating a new random number r between 0 and 1 on each iteration, show that the following piecewise-linear map produces a fractal-appearing tree when the points (x_n, y_n) are plotted:

$$(x_{n+1}, y_{n+1}) = \begin{cases} (0.05\,x_n,\ 0.60\,y_n), & 0 < r < p_1, \\ (0.05\,x_n,\ -0.50\,y_n + 1.0), & p_1 < r < p_2, \\ (0.46\,x_n - 0.15\,y_n,\ 0.39\,x_n + 0.38\,y_n + 0.60), & p_2 < r < p_3, \\ (0.47\,x_n - 0.15\,y_n,\ 0.17\,x_n + 0.42\,y_n + 1.1), & p_3 < r < p_4, \\ (0.43\,x_n + 0.28\,y_n,\ -0.25\,x_n + 0.45\,y_n + 1.0), & p_4 < r < p_5, \\ (0.42\,x_n + 0.26\,y_n,\ -0.35\,x_n + 0.31\,y_n + 0.70), & p_5 < r < 1. \end{cases}$$

Here, $p_1 = 0.1$, $p_2 = 0.2$, $p_3 = 0.4$, $p_4 = 0.6$, and $p_5 = 0.8$. Take $x_0 = 0.5$, $y_0 = 0.0$, and a total of $N = 25000$ iterations. Note that you will have to insert a conditional "if $\cdots$ then $\cdots$ else if" statement which selects the correct "branch" of the map depending on the value of r generated in each iteration. If using *Maple* or *Mathematica*, you might wish to appropriately color the points in your tree.

Problem 3-18: Lorenz map

Verify the Lorenz map for the Rössler attractor shown in Figure 3.3.

Problem 3-19: Renormalization

A simple introduction to renormalization theory is given in Section 10.7 of Steven Strogatz's *Nonlinear Dynamics and Chaos* ([Str94]). Consulting this reference discuss the renormalization concept in your own words.

Problem 3-20: Period doubling experiments

By consulting the given reference and any other references that you can find, discuss in detail one of the period doubling experiments listed in Table 3.2. If possible, qualitatively discuss how the underlying physical equations are reducible to a 1-dimensional unimodal map.

Problem 3-21: Atrioventricular conduction

The atrioventricular (AV) node in the heart is an area of specialized tissue which electrically connects the atria and the ventricles. Excitation produced by the normal pacemaker in the atria travels through the AV node to the ventricles, causing contraction of the heart and thus the pumping of blood to the lungs and the rest of the body.

Kaplan and Glass ([KG95]) have proposed the following problem based on a mathematical model of AV conduction in mammals due to Simson and coworkers ([SSM81]).

The AV conduction time x_{t+1} (in msec) on time step $n+1$ is related to the conduction time x_n on step n by the finite-difference equation

$$x_{n+1} = \frac{375}{x_n - 90} + 100, \quad x_n \geq 90.$$

a. Determine the fixed points of this difference equation and their stability.

b. How will x_n evolve if initially $x_0 = 200$ msec? Confirm your answer by iterating the difference equation with the given initial condition.

Problem 3-22: The tent map

The *tent map* has the mathematical form

$$x_{n+1} = 2\,a\,x_n, \qquad 0 < x \leq \frac{1}{2},$$

$$x_{n+1} = 2\,a\,(1 - x_n), \quad \frac{1}{2} \leq x < 1,$$

with $0 < a < 1$.

a. Derive the bifurcation diagram for the tent map, taking $x_0 = 0.2$, and discuss the result.

b. Analytically prove that the Lyapunov exponent for the tent map is $\lambda = \ln(2\,a)$. Discuss the result.

Problem 3-23: The universal sequence

A theorem due to Metropolis et al. ([MSS73]) states that for all unimodal maps of the form $x_{n+1} = a\,f(x_n)$, with $f(0) = f(1) = 0$ and a a positive parameter, the order in which stable periodic solutions appear is independent of the detailed structure of the map. The *universal sequence* will consist of period-1, period-2, period-4, period-6 (omitting the higher-order period 8, 16, . . .), period-5, period-3, ... Check this sequence for the logistic map and the sine map (introduced in an earlier problem).

Problem 3-24: The circle map
The *circle map* is given by

$$\theta_{n+1} = \theta_n + \Omega - \frac{K}{2\pi} \sin(2\pi\theta_n), \quad (\text{mod } 1),$$

where the parameters Ω and K are real and positive. Periodic boundary conditions prevail so that θ_n is restricted to the range 0 to 1. The inclusion of the mod 1 function indicates that if θ_n exceeds 1, the integer part must be subtracted to keep θ_n in the desired range. The circle map has been applied to the modeling of the heartbeat by Leon Glass and coworkers ([GP82], [GSB86]).

a. Take $K = 0.95$ and $\Omega = 0.4040040004\ldots$. Plot the right-hand side of the circle map in the θ_{n+1} vs. θ_n plane as θ_n is varied from 0 to 1. Applying the mod 1 condition, your graph should have two branches. Taking $\theta_0 = 0.2675$ and 13 iterations, create a cobweb diagram in the same plot with the trajectory confined between the two branches. You should see a periodic motion.

b. The *winding* number W is defined as

$$W = \lim_{n \to \infty} \frac{(\theta_n - \theta_0)}{n},$$

where θ_n is the actual value, not mod 1. What is the winding number for the above cobweb diagram? A rational winding number is an indication of periodic motion. Confirm that in the above case, it is the number of complete revolutions in the θ_{n+1} vs. θ_n plane divided by the number of iterations needed to produce those revolutions.

c. Plot the winding number W as a function of Ω as the latter is varied over the range 0 to 1. Take $K = 1.0$ and $\theta_0 = 0.2675$. This figure is referred to as the *Devil's staircase* because of the steps which appear in the curve.

Problem 3-25: The standard map
A perfectly elastic ball bounces vertically on a horizontal vibrating plate whose velocity is given by $v_{\text{plate}} = A \sin(\omega t)$. Let V_n be the speed of the ball prior to the nth bounce at time t_n.

a. Neglecting the vertical displacement of the plate relative to the flight of the ball, show that

$$V_{n+1} = V_n + 2A \sin\theta_n,$$

$$\theta_{n+1} = \theta_n + 2\left(\frac{\omega}{g}\right)V_{n+1},$$

where $\theta_n = \omega t_n$ is the phase at the nth bounce and g is the acceleration due to gravity.

b. By suitably scaling the variables, show that the above map may be rewritten in the form

$$x_{n+1} = x_n + \sin(2\pi y_n),$$

$$y_{n+1} = y_n + b x_{n+1}.$$

When x_n and y_n are evaluated mod 1, mathematicians refer to this 2-dimensional mapping as the *standard map*. The standard map also arises for the relativistic motion of an electron in a microtron accelerator and stellarator setups used in plasma fusion experiments ([Jac90]).

Problem 3-26: Marital interaction: divorce prediction and marriage repairs
In Chapter 5 of his text *Mathematical Biology: I. An Introduction* ([Mur03]), the mathematical biologist Jim Murray has developed a model involving nonlinear difference equations for the dynamics of marital interaction: divorce prediction and marriage repairs. Discuss in some detail Murray's marital interaction model.

Note: If you have no access to a library copy of Murray's book, Chapter 5 is available for reading as a Google book preview on the Internet.

Problem 3-27: Bass model for diffusion of new products and technologies
The *Bass diffusion formula* ([Bas69], [MMB90])[2] describes the rate of adoption (or purchase) of a new product, method, or technology, in the marketplace. Expressed as a nonlinear map, the Bass formula is

$$N_t = N_{t-1} + p(m - N_{t-1}) + q N_{t-1}\left(1 - \frac{N_{t-1}}{m}\right)$$

where

- N_t is the number of adopters at time t;

- m is the *market potential*: the total number of people who will eventually use the product;

- p is the *coefficient of innovation* (*external influence*): the likelihood that somebody who is not using the product will start using it because of mass media coverage or other external factors;

- q is the *coefficient of imitation* (*internal influence*): the likelihood that somebody who is not using the product will start using it because of "word of mouth" or other influence from those already using the product.

Explain the mathematical structure of the Bass formula. Taking $N_0 = 0$, $p = 0.03$ and $q = 0.38$, plot the Bass formula up to the time that N_t/m is within five percent of the asymptotic value.

---

[2][MMB90] ("New Product Diffusion Models in Marketing: A Review and Directions for Research") is available online at: **http://hitechproducts.net/files/MahajanMullerBass1990.pdf.**

It should be noted that many variations on the Bass model exist in the marketing literature. For example, the spread of hypertext use in the industrialized world since 1986 has been modeled by the following modified Bass formula,

$$N_t = N_{t-1} + p\,(m - N_{t-1}) + q\,(N_{t-1})^\delta \left(1 - \frac{N_{t-1}}{m}\right),$$

with $\delta \approx 1.5$. Taking $N_0 = 0$, $p = 0.03$ and $q = 0.38$, plot the modifed Bass formula up to the time that N_t/m is within five percent of the asymptotic value.

Chapter 4

World of Solitons

The universe may have a purpose, but nothing we know suggests that, if so, this purpose has any similarity to ours.
Bertrand Russell, English philosopher (1872–1970)

Figure 4.1: The Great Red Spot on Jupiter, a suspected soliton.

Most nonlinear PDE models that have been developed to describe the "universe," particularly those involving many coupled equations, must be solved numerically as general analytic solutions do not exist. The Navier–Stokes (NS) equations of fluid mechanics which are used to model the motion of the Earth's atmosphere and oceans provide a good example. The NS equations are PDE-based statements of conservation of mass, momentum, and energy and are the basis for numerically predicting future weather and climate change. These mathematical models are so complex that in order to make the predictions before the changes occur requires the use of a supercomputer.

However, there exist special analytic solutions to some nonlinear PDEs of physical

importance, the most famous being *soliton* solutions of nonlinear wave equations. A soliton is a stable *solitary wave*, which is a spatially localized pulse that can propagate at constant velocity without changing shape, a balance existing between different competing contributions to the governing nonlinear equation of motion.

A simple familiar example of a solitary wave is provided by the flame of a burning candle. The candle flame maintains its shape as it advances into the wax at constant velocity, balancing the diffusion of heat from the flame into the wax and the nonlinear energy release of the vaporizing wax ([Sco81]). The flame is soliton-like in sofar as it can withstand small air currents, flickering but preserving its basic shape.

A famous 3-dimensional soliton example is Jupiter's Great Red Spot which has been observed since the 17th century. The Great Red Spot is a vast (about 400,000 km in diameter), reddish-hued, cyclonic weather system which has remained stationary in Jupiter's turbulent atmosphere. A colored NASA photograph of the Red Spot is shown in Figure 4.1. Laboratory experiments ([ANST86]) and theoretical analysis ([Ing73]) support the idea that the Red Spot could be a soliton solution of the NS equations.

In this chapter we will confine our mathematical discussion to a single spatial dimension, the governing nonlinear PDE having an amplitude $\psi(x,t)$, where x is the spatial coordinate and t the time. To find a solitary wave, we assume that $\psi(x,t) = f(x - v\,t) = f(z)$, where v is the velocity of the wave. This assumed form ensures that a localized pulse will propagate along the x-axis unchanged in shape. Mathematically it reduces the nonlinear PDE to a nonlinear ODE which can be handled by the techniques of Chapter 2. Solitary wave solutions are special cases of *similarity solutions* wherein a functional relationship is assumed between x and t, thus reducing the PDE to an ODE.

The two most common shapes of 1-dimensional solitary waves are shown in Figure 4.2, those on the right (left) being called *topological* (*nontopological*) solitary waves. The topological variety are further subdivided into *kink* and *antikink* solitary waves.
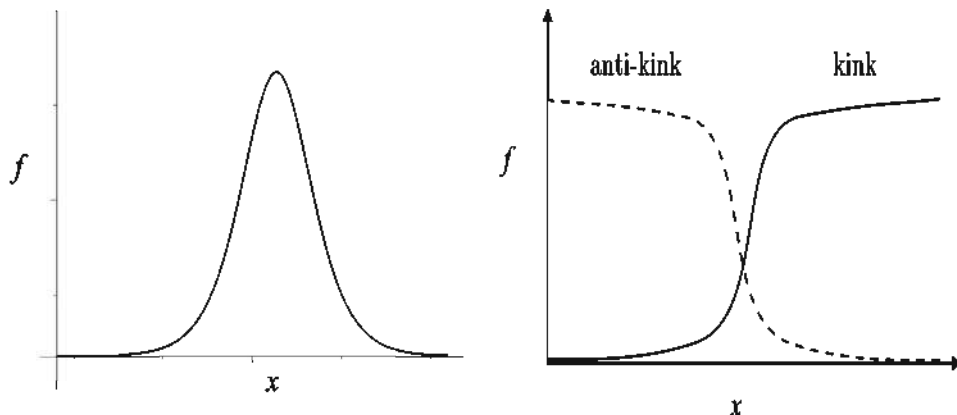
Figure 4.2: Solitary wave shapes. Left: nontopological. Right: topological.

In the following two sections, we shall give historically famous examples of both topological and nontopological solitons, starting with the nontopological variety.

4.1 Korteweg–deVries Solitons

The first scientifically recorded observation of a solitary wave was made by the great Victorian engineer and naval architect John Scott Russell ([Emm77]). As part of an investigation of which ship hull shapes encountered the least water resistance, he reported the following at the 14th meeting of the British Advancement of Science ([Rus44]):

I was observing the motion of a boat which was rapidly drawn along a narrow channel [1] *by a pair of horses, when the boat suddenly stopped — not so the mass of water in the channel which it had put in motion; it accumulated round the prow of the vessel in a state of violent agitation, then suddenly leaving it behind, rolled forward with great velocity, assuming the form of a large solitary elevation, a rounded smooth and well-defined heap of water, which continued its course along the channel apparently without change of form or diminution of speed. I followed it on horseback, and overtook it still rolling on at a rate of some eight or nine miles an hour, preserving its original figure some thirty feet long and a foot to a foot and a half in height. Its height gradually diminished, and after a chase of one or two miles I lost it in the windings of the channel. Such, in the month of August 1834, was my first chance interview with that singular and beautiful phenomenon . . .*

Several decades later, the Dutch mathematicians Diederik Korteweg and Gustav de Vries developed the nonlinear *Korteweg–de Vries* (KdV) *equation* in 1895 to describe Russell's solitary wave phenomenon. In suitably scaled units, the KdV equation for shallow water waves in a rectangular canal is

$$\frac{\partial \psi}{\partial t} + \psi \frac{\partial \psi}{\partial x} + \frac{\partial^3 \psi}{\partial x^3} = 0, \tag{4.1}$$

where ψ is the vertical displacement of the water surface from equilibrium, x the spatial coordinate in the direction of wave propagation, and t the time. The derivation of the KdV equation is beyond the scope of this text, the interested reader being referred to the text *Nonlinear Waves, Solitons, and Chaos* by Eryk Infeld and George Rowlands ([IR90]). Not only do the authors derive the KdV equation for water-surface gravity waves but also for ion acoustic waves in a plasma. The KdV equation also occurs in many other physical contexts (see [SCM73]).

To obtain Russell's solitary wave, which qualitatively has the shape on the left of Figure 4.2, we assume a solution of the form

$$\psi(x, t) = f(x - v t) \equiv f(z), \tag{4.2}$$

with $v > 0$ the velocity. This assumption reduces the PDE (4.1) to the following third-order nonlinear ODE:

$$\frac{d^3 f}{dz^3} + (f - v) \frac{df}{dz} = 0, \tag{4.3}$$

which is readily integrated. Assuming that f and $d^2 f/dz^2 \to 0$ for the solitary wave as

---

[1] The still-existing Union Canal linking Glasgow and Edinburgh in Scotland.

$|z| \to \infty$, the integration constant is zero, so we obtain

$$\frac{d^2 f}{dz^2} = v f - \frac{f^2}{2}. \tag{4.4}$$

At this stage, we can already establish the existence of a solitary wave solution by using phase-plane analysis, even if the nonlinear ODE (4.4) could not be solved analytically. The second-order ODE (4.4) can be written as two first-order ODEs,

$$\begin{aligned}
\frac{df}{dz} &= y \equiv P(f, y), \\
\frac{dy}{dz} &= v f - \frac{f^2}{2} \equiv Q(f, y),
\end{aligned} \tag{4.5}$$

the ODE system (4.5) having two fixed points,

$$(\bar{f}, \bar{y}) = \quad (0, 0) \quad \text{and} \quad (2v, 0). \tag{4.6}$$

Example 4-1: Types of Fixed Points

Applying the phase-plane analysis of Chapter 2, determine the nature of the fixed points.

Solution: Noting that

$$\frac{\partial P}{\partial f} = 0, \quad \frac{\partial P}{\partial y} = 1, \quad \frac{\partial Q}{\partial f} = v - f, \quad \frac{\partial Q}{\partial y} = 0,$$

for the first fixed point ($\bar{f} = 0$, $\bar{y} = 0$) we have (using the notation of Chapter 2)

$$a = 0, \quad b = 1, \quad c = v, \quad d = 0, \quad \text{so} \quad p = -(a + d) = 0, \quad q = a d - b c = -v < 0.$$

Consulting Table 2.1, this fixed point is identified as a saddle point.

For the second fixed point ($\bar{f} = 2v$, $\bar{y} = 0$) we obtain

$$a = 0, \quad b = 1, \quad c = -v, \quad d = 0, \quad \text{so} \quad p = 0, \quad q = +v > 0.$$

So this fixed point is either a vortex or a focal point. Applying Poincaré's theorem, we have

$$P(f, -y) = -y = -P(f, y), \quad Q(f, -y) = Q(f, y).$$

Since these two conditions are satisfied, the second fixed point is a vortex.

<div align="center">***</div>

Taking, say, $v = 1$, the tangent field picture shown in Figure 4.3 confirms the identification of the fixed points, the vortex being at $(2, 0)$. We have also included a trajectory which starts very close to the origin at ($f = 0.01, y = 0.01$). This trajectory approximates the separatrix which separates the trajectories cycling the vortex from those outside the separatrix, which diverge to infinity. The solitary wave corresponds to the separatrix, with $f = 0$ at $z = -\infty$, rising to a single maximum of magnitude $f = 3$, and then decreasing back to $f = 0$ as $z \to +\infty$.
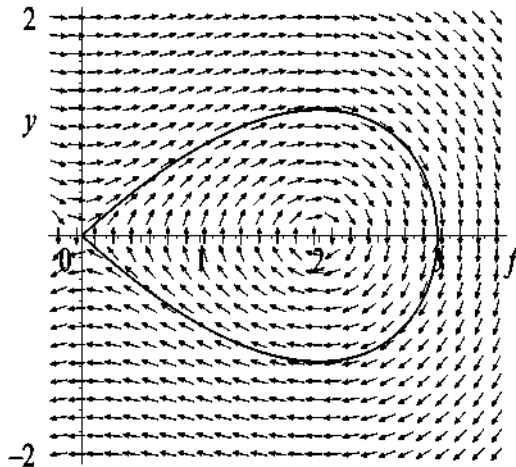
Figure 4.3: Phase-plane portrait for the KdV solitary wave.

Actually, the mathematical form of the KdV solitary wave can be found analytically.

Example 4-2: Analytic Solitary Wave Solution of the KdV Equation

Analytically solve Equation (4.4) for the KdV solitary wave solution. Discuss the result.

Solution: Multiplying Equation (4.4) by $2\,(df/dz)\,dz$, and integrating, yields

$$\left(\frac{df}{dz}\right)^2 = v\,f^2 - \frac{f^3}{3} + C,$$

with C the integration constant. For the solitary wave, both f and $df/dz \to 0$ as $|z| \to \infty$, so $C = 0$. Then,

$$\frac{df}{dz} = f\sqrt{v - \frac{f}{3}}.$$

This ODE is easily solved by separating variables and integrating, yielding

$$\psi(x,t) = f(z) = \frac{3\,v}{\cosh^2\left(\sqrt{v}\,z/2\right)} = 3\,v\,\mathrm{sech}^2\left(\frac{\sqrt{v}}{2}\,(x - v\,t)\right).$$

Note that the height (maximum amplitude at $z = 0$) of the solitary wave is proportional to the speed v, while its width is inversely proportional to $\sqrt{v}$. So a taller, narrower, solitary wave travels faster than a shorter, wider, one. This fact enables one to confirm that the solitary wave is a *soliton*. Although other criteria of stability can be adopted, mathematicians traditionally define a soliton as a solitary wave which, after undergoing a collision with another solitary wave solution of the same equation, emerges from the collision unchanged in shape.

***

Noting that the KdV solitary wave propagates in the positive x-direction for $v > 0$, one can numerically test collisional stability by placing a taller solitary wave initially to the left of a shorter one. As time evolves, the taller, faster, solitary wave overtakes the shorter, slower, one and a collision takes place. Figure 4.4 shows such a collision. A numerical scheme relevant to this solitary wave collision will be presented later in the chapter.
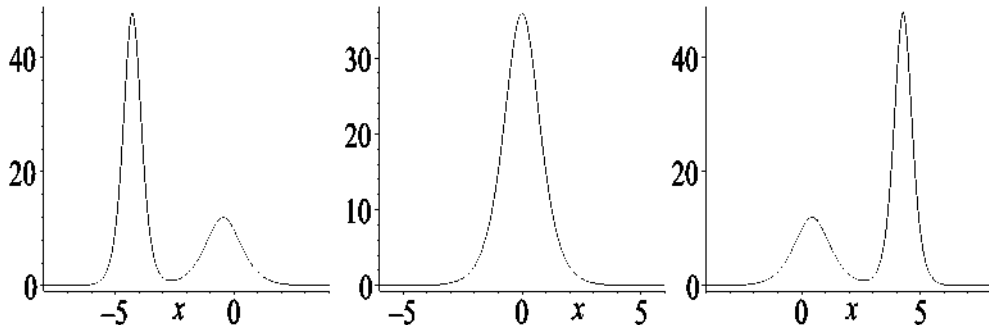
Figure 4.4: Collision of two KdV solitary waves.

The frame on the left of Figure 4.4 shows the taller solitary wave initially to the left of the shorter one. As time evolves, the taller one "collides" with the shorter one, complete overlap of the two pulses being shown in the middle frame. Noting the different vertical scale in this frame, we can see that linear superposition of the pulses doesn't hold here, the sum of the two overlapping pulses being less than the sum of the two separated pulses in the left frame. After the collision (far right frame), both the taller and shorter solitary waves emerge unchanged.

With the breakdown of linear superposition in nonlinear dynamics, mathematicians have developed various analytic techniques (e.g., *Bäcklund transformations*) for finding nonlinear superposition formulas. The reader who is interested in the details and examples of such techniques is referred to Daniel Zwillinger's *Handbook of Differential Equations* ([Zwi89]). For the KdV equation, e.g., if ψ_0, ψ_1 and ψ_2 are solutions, then

$$\psi_3 = \psi_0 + \frac{2\,(a_1 - a_2)}{\psi_1 - \psi_2} \tag{4.7}$$

is also a solution, where a_1 and a_2 are arbitrary parameters.

4.2   Sine-Gordon Solitons

A good example of a kink (or antikink) topological solitary wave is the motion of a *Bloch wall* (named after the Nobel physics laureate Felix Bloch) under the influence of an applied magnetic field. A Bloch wall is the narrow transition region between adjacent magnetic domains in a ferromagnet. In this transition region, the magnetization changes from its value in one domain to a different value in the adjacent domain. The governing

equation for the movement of a Bloch wall is the *sine-Gordon* equation (SGE),

$$\frac{\partial^2 \psi}{\partial x^2} - \frac{\partial^2 \psi}{\partial t^2} = \sin \psi, \tag{4.8}$$

where ψ is the (suitably scaled) magnetization.

To find a possible solitary wave solution to the SGE, let's again assume that the amplitude $\psi(x,t) = f(z = x - v\,t)$. This reduces the SGE to the nonlinear ODE

$$(1 - v^2) \frac{d^2 f}{dz^2} = \sin f,$$

or, assuming that $v \neq 1$ and setting $A = 1/(1 - v^2)$,

$$\frac{d^2 f}{dz^2} = A \sin f. \tag{4.9}$$

Example 4-3: Existence of a Sine-Gordon Solitary Wave

Using phase-plane analysis, demonstrate that kink and antikink solitary wave solutions to the SGE are possible.

Solution: The second-order ODE (4.9) is rewritten as

$$\frac{df}{dz} = y \equiv P(f, y), \quad \frac{dy}{dz} = A \sin f \equiv Q(f, y).$$

There are fixed points at

$$\bar{f} = n\,\pi, \quad \bar{y} = 0, \quad \text{with} \quad n = 0, \pm 1, \pm 2, \ldots.$$

Using the standard notation of phase-plane analysis, we obtain

$$p = 0, \quad q = (-1)^{n+1} A.$$

For the rest of the analysis, let's assume that $v < 1$ so that $A > 0$. The other case $A < 0$ (i.e., $v > 1$) is left as a problem.

For even integer n values, $q = -A < 0$, so the fixed points $(\bar{f} = 0, \pm 2\,\pi, \ldots, \bar{y} = 0)$ are saddle points.

For odd integer n values, $q = A > 0$, so the fixed points $(\bar{f} = \pm\,\pi, \pm 3\,\pi, \ldots, \bar{y} = 0)$ are either vortices or focal points. Applying Poincaré's theorem,

$$P(f, -y) = -y = -P(f, y), \quad Q(f, -y) = A \sin f = Q(f, y),$$

so they are vortices.

Thus, one has an alternating array of saddle points and vortices along the f-axis of the phase plane. This is a sufficiently simple pattern of fixed points that one can easily sketch the allowed trajectories in the phase plane without having to resort to a computer for assistance. The trajectories are qualitatively shown in Figure 4.5.

The saddle points are labeled S and the vortices V. Each vortex must be surrounded by a continuum of closed loops, corresponding to possible traveling wave solutions where
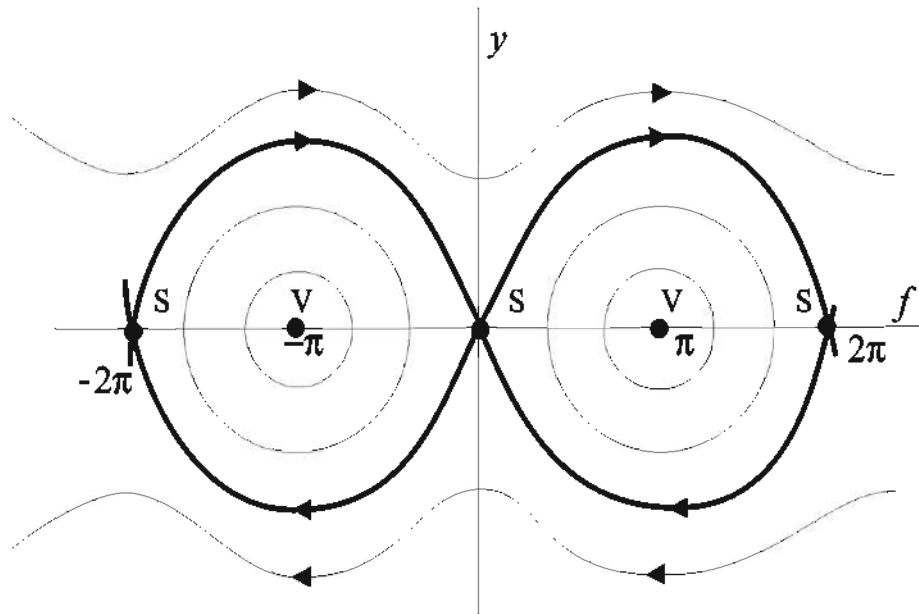
Figure 4.5: Trajectories in phase plane.

f oscillates up and down as z increases. Trajectories leaving a saddle point at $z = -\infty$ have no option but to approach an adjacent saddle point as $z \to \infty$. These trajectories, indicated by the heavy curves in the figure, act as separatrixes between the traveling wave solutions and unbounded solutions (f increasing indefinitely).

The separatrix trajectories correspond to possible kink and antikink solitary wave solutions. For example, the trajectory leaving S at the origin ($f = 0$) and asymptotically approaching S at $f = 2\pi$ corresponds to a kink solution, while the trajectory leaving S at $f = 2\pi$ and asymptotically approaching S at the origin is an antikink solution. Other kink and antikink solutions are clearly possible.

$$***$$

As with the KdV case, it is possible to derive analytic solutions for the sine-Gordon solitary waves.

Example 4-4: Sine-Gordon Solitary Waves

Derive the analytic form of a sine-Gordon kink solitary wave.

Solution: Multiplying Equation (4.9) by $2\,(df/dz)\,dz$, and integrating, yields

$$\left(\frac{df}{dz}\right)^2 = -2\,A\,\cos f + C,$$

where C is the arbitrary constant. Imposing the conditions that f and $df/dz \to 0$ for

$z \to -\infty$, the constant $C = 2A$. Then,

$$\left(\frac{df}{dz} \right)^2 = 2A \left(1 - \cos f \right) = 4A \sin^2 \left(\frac{f}{2} \right),$$

on using the trig identity, $\cos f = 1 - 2 \sin^2 (f/2)$. Taking the square root of the above ODE, separating variables, and integrating, yields

$$\int \frac{d(f/2)}{\sin(f/2)} = \ln(\tan(f/4)) = \sqrt{A}\, z,$$

where the integration constant has been set equal to zero without loss of generality. Finally, solving for f, the solitary wave solution is

$$f = 4 \arctan \left(e^{\sqrt{A}\,z} \right) = 4 \arctan \left(e^{(x-v\,t)/\sqrt{(1-v^2)}} \right).$$

That this is a kink solution is easily verified by plotting f versus z for a specific A value. For example, taking $A = 1/4$ generates the profile shown in Figure 4.6.
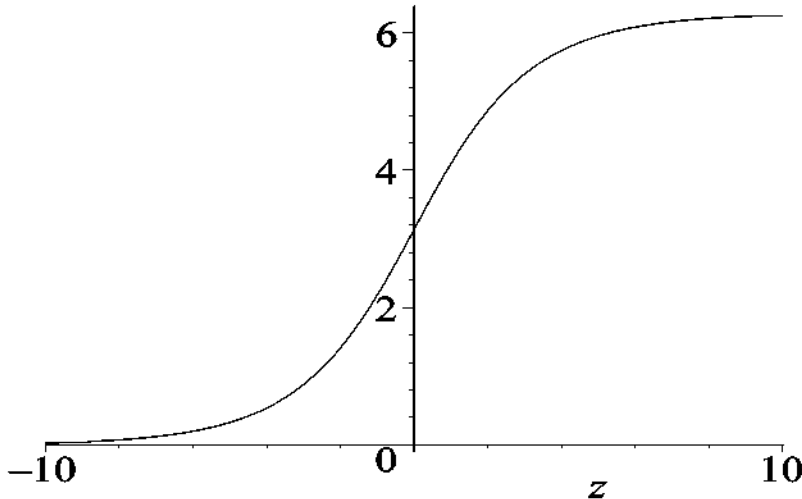
Figure 4.6: Kink solitary wave for the sine-Gordon equation.

***

4.3 Similarity Solutions

Solitary waves are the most famous members of the family of similarity solutions. The common denominator of this family is that new *similarity variables* are introduced which decrease the number of independent variables. For the 1-dimensional solitary waves the similarity variable is $z = x - vt$, which is a linear combination of the two independent variables x and t. Other functional combinations of x and t are possible

besides the linear one. General mathematical approaches, such as the *Lie group* method, to finding similarity variables are beyond the scope of this text. A systematic coverage is given, for example, in Bluman and Cole ([BC74]). Here, we will be content to give a physical example for which a similarity solution can be obtained by introducing a different similarity variable than that used in obtaining solitary waves.

With C the (scaled) liquid concentration, consider the following model equation introduced by Buckmaster ([Buc77]) to model the spreading of a thin liquid film on a flat, horizontal, surface under the action of gravity:

$$\frac{\partial C}{\partial t} = \frac{\partial}{\partial x}\left(C^3 \frac{\partial C}{\partial x}\right). \tag{4.10}$$

A similarity variable $z = x/t^{1/5}$ is introduced and a solution assumed of the form

$$C(x,t) \equiv \frac{f\left(x/t^{1/5}\right)}{t^{1/5}} \equiv \frac{f(z)}{t^{1/5}}. \tag{4.11}$$

Substituting (4.11) into the nonlinear PDE (4.10) yields

$$\frac{d}{dz}\left(f^3 \frac{df}{dz}\right) + \frac{1}{5} z \frac{df}{dz} + \frac{1}{5} f = 0, \tag{4.12}$$

or

$$5 \frac{d}{dz}\left(f^3 \frac{df}{dz}\right) + \frac{d}{dz}(z f) = 0. \tag{4.13}$$

Integrating, and setting the arbitrary constant equal to zero, yields

$$5 f^3 \frac{df}{dz} + z f = 0. \tag{4.14}$$

Finally, separating variables and integrating, we obtain

$$f = \left(A - \frac{3}{10} z^2\right)^{1/3}, \tag{4.15}$$

with A the integration constant. Since the concentration must be greater than or equal to zero, the above form is only valid for $|z| = |x/t^{1/5}| \le \sqrt{10\,A/3}$. The concentration outside this region can be taken to be zero, since $C = 0$ satisfies the original PDE. Thus, the complete solution for $t > 0$ is

$$C(x,t) = \begin{cases} \dfrac{\left(A - \dfrac{3}{10}\dfrac{x^2}{t^{2/5}}\right)^{1/3}}{t^{1/5}}, & |x| \le t^{1/5}\sqrt{\dfrac{10}{3}A}, \\[4mm] 0, & |x| > t^{1/5}\sqrt{\dfrac{10}{3}A}. \end{cases} \tag{4.16}$$

Taking, for example, $A = 1$, Figure 4.7 shows the evolution of the concentration over the time range $t = 1$ to $t = 1500$ (scaled) time units. The similarity solution captures the more important experimentally observed features of the spreading of thin liquid films, namely, the sharp boundary between zero and nonzero concentrations and the finite speed with which the boundary propagates.
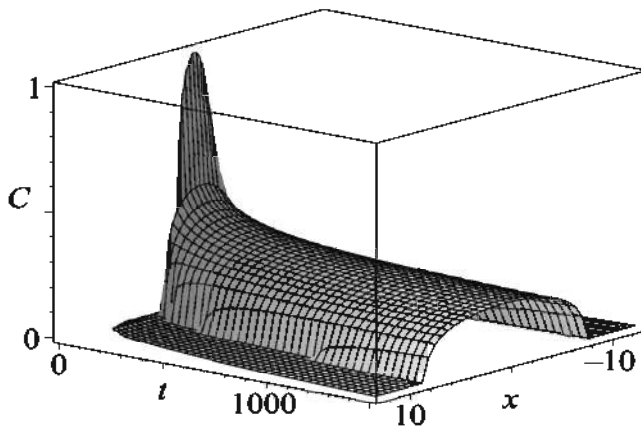
Figure 4.7: Similarity solution for a thin liquid film.

4.4 Numerical Simulation

In the introductory chapter, we mentioned that most nonlinear ODE systems of interest in the real world must be solved numerically on the computer, as analytic solutions do not exist. This is even more true for nonlinear PDE systems, especially for those involving time and more than one spatial dimension. As with nonlinear ODEs, the full set of PDEs must be replaced with finite difference approximations which are accurate and can be executed in a reasonable time on the computer. Again, this is a vast subject, so we shall only give you the flavor of it here, taking the KdV and sine-Gordon equations as simple examples. If you want to learn more about numerical algorithms for solving different classes of differential equations, a useful reference book is *Numerical Recipes* by Press, Flannery, Teukolsky, and Vetterling ([PFTV89]).

The KdV equation (4.1) contains a third spatial derivative, so what finite difference approximation should we use for it? A systematic approach to obtaining suitable approximations for derivatives of different orders is to make use of the Taylor expansion.

4.4.1 Finite Difference Approximations

Consider the general function $f(x \pm h)$, where x is an arbitrary spatial point and the spatial step $h = \Delta x$ is assumed to be sufficiently small that retaining a finite number of terms in the Taylor expansion of f in powers of h gives a good approximation to the derivative of f. The error in retaining a finite number of terms in the Taylor series is called the *truncation error*. The step size h cannot be made too small, not only because it will increase the computing time, but there is a danger of *round-off error* when working with a specified number of digits in the numerical calculation. For time derivatives, the spatial variable x is replaced with t and h with the symbol $k = \Delta t$.

Taylor expanding $f(x \pm h)$ in powers of h yields

$$f(x \pm h) = f(x) \pm h\,f'(x) + \frac{1}{2!}\,h^2\,f''(x) \pm \frac{1}{3!}\,h^3\,f'''(x) + \frac{1}{4!}\,h^4\,f''''(x) \pm \ldots \quad (4.17)$$

where a single prime indicates a first derivative with respect to x, two primes a second derivative, and so on. Taking the plus sign and neglecting terms of order h^2 ($O(h^2)$) and smaller yields the *forward difference approximation* to the first derivative,

$$f'(x) = \frac{f(x+h) - f(x)}{h} + O(h). \tag{4.18}$$

The forward difference approximation was used for the first time derivative in the explicit numerical schemes (forward Euler, RKF45) of Chapter 1.

If the minus sign is selected in (4.17) and terms of order h^2 are again neglected, the *backward difference approximation* results:

$$f'(x) = \frac{f(x) - f(x-h)}{h} + O(h). \tag{4.19}$$

As mentioned in Chapter 1, the backward difference approximation to the first time derivative is the basis of so-called *implicit* numerical schemes which we have not covered in this text.

Finally, a more accurate *central difference approximation* to the first derivative follows on subtracting the two expansions in (4.17) and neglecting terms of order h^3:

$$f'(x) = \frac{f(x+h) - f(x-h)}{2\,h} + O(h^2). \tag{4.20}$$

To reduce the numerical error, the Zabusky–Kruskal algorithm for the KdV equation actually uses this approximation for both the time and spatial first derivatives.

With different approximations available, the situation can get even more complicated for higher-order derivatives. However, the "traditional" difference approximation to the second derivative is obtained by adding the two expansions in (4.17) and neglecting terms of order h^4. The result is

$$f''(x) = \frac{f(x+h) - 2\,f(x) + f(x-h)}{h^2} + O(h^2). \tag{4.21}$$

Neglecting terms of order h^5, a commonly used difference approximation to the third derivative is

$$f'''(x) = \frac{f(x+2\,h) - 2\,f(x+h) + 2\,f(x-h) - f(x-2\,h)}{2\,h^3} + O(h^2). \tag{4.22}$$

This result is easily proved by Taylor expanding each of the functions in the numerator of the right-hand side. For other finite difference approximations to derivatives, you are referred to the *Handbook of Mathematical Functions* ([AS72]).

With this very brief introduction to finite difference approximations we can now develop the historically famous algorithm introduced by Norm Zabusky and Martin Kruskal ([ZK65]) to solve the KdV equation.

4.4.2 The Zabusky–Kruskal Algorithm

To numerically solve the KdV equation,

$$\frac{\partial \psi}{\partial t} + \psi \frac{\partial \psi}{\partial x} + \frac{\partial^3 \psi}{\partial x^3} = 0, \tag{4.23}$$

let's label the spatial step Δx as h and the time step Δt as k. The x–t plane is subdivided into a rectangular grid or "mesh" as shown in Figure 4.8, the coordinates of a typical mesh point P being $x = i\,h$, $t = j\,k$, with i, $j = 0$, 1, 2, …. With h and k specified, the mesh points may be labeled by their i, j values as well as any function depending on x and t, such as the displacement $\psi(x, t)$ in the KdV equation. That is to say, one writes $\psi(x = i\,h, t = j\,k)$ more compactly as $\psi_{i,j}$.
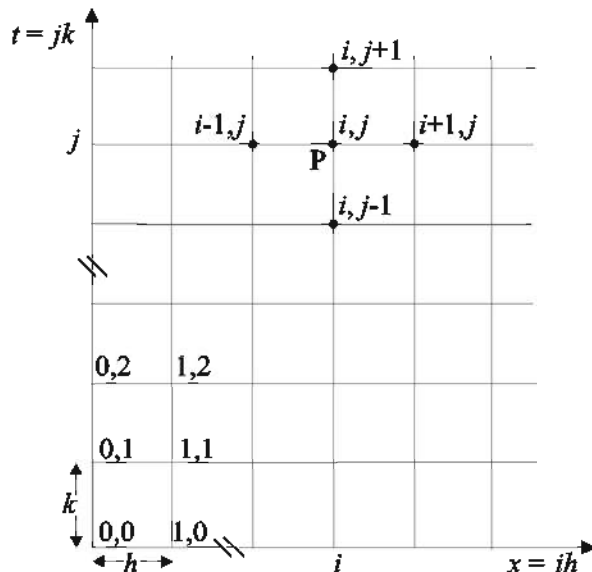
Figure 4.8: Subdividing the x–t plane with a numerical mesh.

With this notation, the difference approximation to $\partial^3 \psi / \partial x^3$ at P becomes

$$\left(\frac{\partial^3 \psi}{\partial x^3} \right)_P = \frac{\psi_{i+2,j} - 2\,\psi_{i+1,j} + 2\,\psi_{i-1,j} - \psi_{i-2,j}}{2\,h^3}. \tag{4.24}$$

Zabusky and Kruskal used the more accurate central difference approximation for the first-order spatial and time derivatives, viz.,

$$\begin{aligned}
\left(\frac{\partial \psi}{\partial x} \right)_P &= \frac{(\psi_{i+1,j} - \psi_{i-1,j})}{2\,h}, \\
\left(\frac{\partial \psi}{\partial t} \right)_P &= \frac{(\psi_{i,j+1} - \psi_{i,j-1})}{2\,k}.
\end{aligned} \tag{4.25}$$

Finally, they approximated the ψ term in $\psi \, \partial\psi/\partial x$ with an average over three adjacent spatial points centered on P, viz.,

$$\psi_P = \frac{\psi_{i+1,j} + \psi_{i,j} + \psi_{i-1,j}}{3}. \qquad (4.26)$$

As you may verify, this is more accurate than simply using $\psi_{i,j}$.

Putting all the above approximations together and rearranging, the KdV equation (4.23) is replaced with the Zabusky–Kruskal algorithm (with $j = 1, 2, \ldots$),

$$
\begin{aligned}
\psi_{i,j+1} = \psi_{i,j-1} &- \frac{k}{h} \left(\frac{\psi_{i+1,j} + \psi_{i,j} + \psi_{i-1,j}}{3} \right) (\psi_{i+1,j} - \psi_{i-1,j}) \\
&- \frac{k}{h^3} (\psi_{i+2,j} - 2\,\psi_{i+1,j} + 2\,\psi_{i-1,j} - \psi_{i-2,j}).
\end{aligned}
\qquad (4.27)
$$

As we shall show later, this algorithm, which connects time step $j + 1$ to the previous two time steps, $j - 1$ and j, is numerically stable for

$$\frac{k}{h^3} < \frac{2}{3\sqrt{3}} \approx 0.3849.$$

To iterate (4.27), the ψ values must be known at each mesh point on the $j = 0$ and $j = 1$ time steps. If the initial input shape is $f(x)$, then $\psi_{i,0} = f(x_i)$. For the first time step, the $\psi_{i,1}$ can be determined as follows:

If

$$\left(\frac{\partial\psi(x,t)}{\partial t} \right)_{t=0} = g(x),$$

the forward difference approximation yields

$$\frac{(\psi_{i,1} - \psi_{i,0})}{k} = g(x_i),$$

so

$$\psi_{i,1} = f(x_i) + k\,g(x_i). \qquad (4.28)$$

If desired, a more accurate approximation can be derived, but (4.28) will suffice for the illustrative example which follows.

Example 4-5: Evolution of an Amplified Solitary Wave

Recall that

$$\psi_{solitary} = 3\,v\,\operatorname{sech}^2 \left(\frac{\sqrt{v}}{2}\,(x - v\,t) \right)$$

is a solitary wave solution of the KdV equation.

Taking $v = 0.09$, $h = 1.0$, and $k = 0.25$, use the Zabusky–Kruskal algorithm (4.27) and (4.28) to numerically determine how an input pulse equal to $3\,\psi_{solitary}$ evolves. Discuss the result.

Solution: To apply the Zabusky–Kruskal algorithm, let's center the pulse at $x = 100$, taking the spatial range of the simulation to be from $x = 0$ to 200 and the step size $h = 1.0$. With $v = 0.09$, the input profile is

$$\psi(x, 0) = 3\,\psi_{solitary}(x, 0) = 0.81 \operatorname{sech}^2(0.15\,x - 15),$$

which is shown on the left of Figure 4.9.
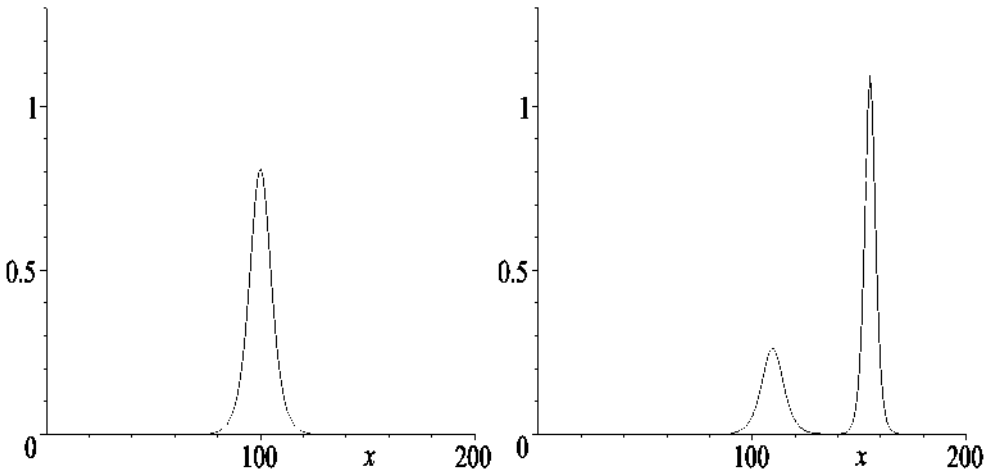
Figure 4.9: Right frame: evolution of the amplified solitary wave in the left frame.

Taking the time step size $k = 0.25$, then $k/h^3 = 0.25 < 0.3849$, so the simulation will be numerically stable. For greater accuracy, the step sizes and the ratio k/h^3 can be reduced. To avoid any possible unknown ψ values creeping into the calculation, the ψ values at all mesh points for $j \geq 2$ are initially set equal to 0.

After 600 time steps, the picture on the right of Figure 4.9 results. The original input pulse was not a soliton so, as it began to move, its shape changed. It apparently evolved into two differently sized solitary waves. Indeed, it can be demonstrated that taking $v = 0.087$ and $v = 0.365$ in the solitary wave solution provides a perfect fit to the two pulses. These pulses continue to propagate (not shown here) unchanged in shape as time is further increased. Because of their different velocities, these two solitons continue to separate as time increases.

***

For the KdV equation, a rectangular numerical mesh was used. For other nonlinear PDEs it may be more convenient to use a nonrectangular mesh. For example, for the sine-Gordon equation, a diamond-shaped mesh which follows the so-called *characteristic directions* of the SGE is preferable. Before outlining a numerical algorithm based on this approach, let's briefly look at the *method of characteristics* on which it is based.

4.4.3   Method of Characteristics

Consider a PDE of the general structure

$$a\frac{\partial^2 \psi}{\partial x^2} + b\frac{\partial^2 \psi}{\partial x \partial y} + c\frac{\partial^2 \psi}{\partial y^2} + f = 0, \tag{4.29}$$

where a, b, c, and f can be constants or functions of $\psi(x,y)$ and its first derivatives. Many linear and nonlinear PDEs of physical interest are just special cases of this equation. For example, the nonlinear sine-Gordon equation (4.8) results on setting $y = t$, $a = 1$, $b = 0$, $c = -1$, and $f = -\sin\psi$.

The so-called characteristic directions of the general PDE may be determined as follows. Let's set $U = \partial\psi/\partial x$ and $V = \partial\psi/\partial y$, so that (4.29) becomes

$$a\frac{\partial U}{\partial x} + b\frac{\partial U}{\partial y} + c\frac{\partial V}{\partial y} + f = 0. \tag{4.30}$$

But $U = U(x,y)$ and $V = V(x,y)$, so making use of the chain rule,

$$\frac{\partial U}{\partial x} = \frac{dU}{dx} - \frac{\partial U}{\partial y}\frac{dy}{dx}, \quad \frac{\partial V}{\partial y} = \frac{dV}{dy} - \frac{\partial V}{\partial x}\frac{dx}{dy}. \tag{4.31}$$

Substituting these expressions into (4.30), noting that $\partial V/\partial x = \partial U/\partial y$, multiplying by dy/dx, and finally rearranging, we obtain

$$\frac{\partial U}{\partial y}\left[a\left(\frac{dy}{dx}\right)^2 - b\left(\frac{dy}{dx}\right) + c\right] - \left[a\frac{dy}{dx}\frac{dU}{dx} + c\frac{dV}{dx} + f\frac{dy}{dx}\right] = 0. \tag{4.32}$$

The *characteristic directions* are those curves whose slopes satisfy

$$a\left(\frac{dy}{dx}\right)^2 - b\left(\frac{dy}{dx}\right) + c = 0. \tag{4.33}$$

Example 4-6: Characteristic directions for the SGE

Determine the characteristic directions for the SGE.

Solution: For the SGE, $a = 1$, $b = 0$, $c = -1$, so Equation (4.33) reduces to

$$\left(\frac{dy}{dx}\right)^2 - 1 = 0, \quad \text{so} \quad \frac{dy}{dx} \equiv \frac{dt}{dx} = \pm 1.$$

The characteristic directions in the x–t plane for the SGE are straight lines with slopes ± 1, i.e., $\pm 45°$. A numerical grid based on these characteristic directions will be diamond-shaped.

<center>***</center>

Along the characteristic directions, Equation (4.32) reduces to the differential relation

$$a \left(\frac{dy}{dx} \right) dU + c \, dV + f \, dy = 0. \tag{4.34}$$

Since $\psi = \psi(x, y)$, the change in ψ along the characteristic equations is given by

$$d\psi = \frac{\partial \psi}{\partial x} \, dx + \frac{\partial \psi}{\partial y} \, dy = U \, dx + V \, dy. \tag{4.35}$$

A numerical algorithm can now be developed for the SGE based on the method of characteristics.

4.4.4 Numerical Algorithm for the SGE

A diamond-shaped numerical grid is introduced as shown in Figure 4.10. Since the characteristic directions have slopes ± 1, we have $\Delta x = \Delta y = h$. The initial ($t \equiv y = 0$) values of ψ, U, and V are specified, i.e., $\psi(x, 0)$, $U(x, 0)$, and $V(x, 0)$ are known at each grid point along the bottom line of the numerical grid. To advance forward in time, we must advance along the characteristic directions. At a typical mesh point P, the values of U_P, V_P, and, most importantly, ψ_P can be calculated from the known values of these quantities at mesh points L and R.
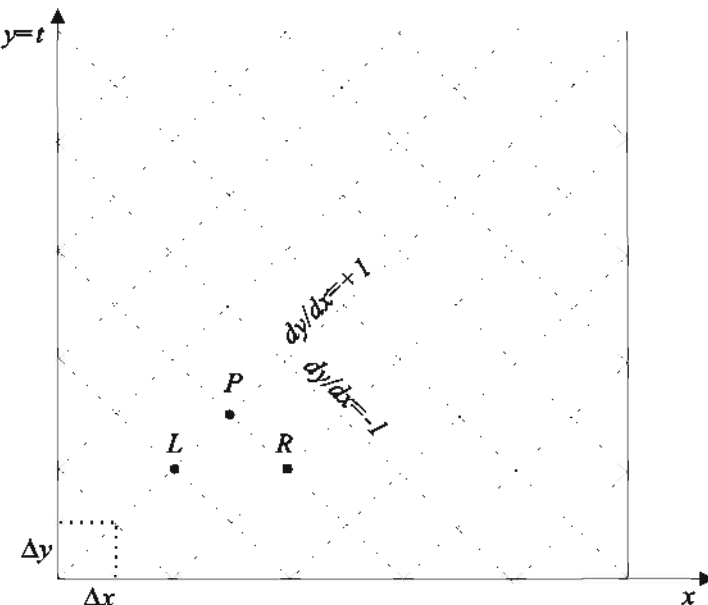
Figure 4.10: Diamond-shaped grid for numerically solving the SGE.

Along the lines of slope $dy/dx = \pm 1$, the differential relation (4.34) for the SGE, viz.,

$$\pm dU - dV = -f \, dy, \tag{4.36}$$

is replaced with the finite difference approximation

$$\pm \Delta U - \Delta V = -f\,\Delta y. \tag{4.37}$$

For $L \to P$ and $R \to P$, we then have the following equations:

$$(U_P - U_L) - (V_P - V_L) = -f_L\,h,$$
$$-(U_P - U_R) - (V_P - V_R) = -f_R\,h, \tag{4.38}$$

which can be solved for U_P and V_P:

$$U_P = \frac{1}{2}\,(U_R + U_L) + \frac{1}{2}\,(V_R - V_L) + \frac{1}{2}\,(f_R - f_L)\,h,$$
$$V_P = \frac{1}{2}\,(U_R - U_L) + \frac{1}{2}\,(V_R + V_L) + \frac{1}{2}\,(f_R + f_L)\,h. \tag{4.39}$$

With U_P and V_P known, the value of ψ_P can be determined. Replacing the differential relation $d\psi = U\,dx + V\,dy$ with the approximation

$$\Delta \psi = U\,\Delta x + V\,\Delta y, \tag{4.40}$$

we can calculate U_P starting with either L or R. Instead of just using the "old" values of U and V, the accuracy can be improved by averaging the old and "new" values of these quantities. Then for, say, $dy/dx = +1$, we have

$$\psi_P = \psi_L + \frac{1}{2}(U_L + U_P)\,(x_P - x_L) + \frac{1}{2}\,(V_L + V_P)\,(y_P - y_L)$$
$$= \psi_L + \frac{1}{2}\,h\,(U_L + U_P + V_L + V_P). \tag{4.41}$$

On the other hand, for $dy/dx = -1$ we obtain

$$\psi_P = \psi_R + \frac{1}{2}\,h\,(-U_R - U_P + V_R + V_P). \tag{4.42}$$

Since the numerical value calculated along the two different characteristics may not be the same, an average of the two values of ψ_P is taken.

In the following example, the above numerical scheme is applied to the collision of a kink and an antikink sine-Gordon solitary wave traveling in opposite directions.

Example 4-7: Collision of a Kink and an Antikink

The input profile for a widely separated kink (first term) and antikink (second term) traveling in opposite directions is

$$\psi = 4\arctan\left(e^{(x - x_1 - v_1 t)/\sqrt{1 - v_1^2}}\right) + 4\arctan\left(e^{-(x - x_2 + v_2 t)/\sqrt{1 - v_2^2}}\right),$$

evaluated at time $t = 0$. Taking $x_1 = -5$, $x_2 = +5$, and $v_1 = v_2 = 0.8$, this input profile is shown on the left of Figure 4.11 with the kink to the left of the antikink. As time progresses the kink and antikink will collide.

Taking $M = 600$ spatial steps between $x_{min} = -15$ and $x_{max} = +15$, determine the resulting profile after $N = 300$ time steps. Discuss the result.

Solution: The step size $h = (x_{max} - x_{min})/M = 0.05$. The derivatives $U = \partial\psi/\partial x$ and $V = \partial\psi/\partial t$ are determined. Then the initial values of ψ, U, and V are calculated at each grid point for $M = 0$. Implementing the algorithm for $N = 300$ steps produces the profile on the right-hand side of Figure 4.11. The kink–antikink hump has apparently
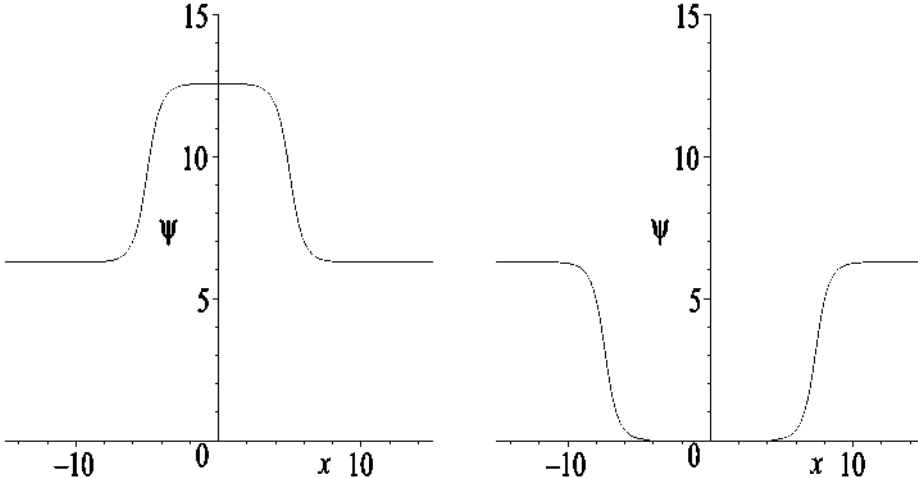
Figure 4.11: Left: input profile. Right: profile after collision.

flipped upside down. However, what has really happened is that the kink and antikink are still traveling in opposite directions and are unchanged in shape (indicating that they are solitons) except for a downshift of 2π in their amplitudes.

$$***$$

4.4.5 Numerical Stability

The issue of computational stability in numerically solving nonlinear PDEs with explicit schemes is a very important one. As noted earlier, the Zabusky–Kruskal algorithm, e.g., is numerically stable if the time (k) and spatial (h) steps satisfy the inequality $k/h^3 < 2/(3\sqrt{3})$. If this inequality is violated, increasingly large unphysical oscillations can occur in the numerical solution.

How is such a stability criterion established? One makes use of *Von Neumann stability analysis* ([PFTV89]). Suppose that ψ^0 is the exact solution of the proposed numerical scheme, while $\psi = \psi^0 + u$ is the actual solution where u is the error. For example, u can arise because of using a finite number of digits in the computer solution. Substituting ψ into the proposed algorithm, one retains only linear terms in u. Then

u can written as a Fourier series and, letting $I = \sqrt{-1}$ and i and j number the spatial and time steps, the behavior of a representative Fourier term $u_{i,j} = e^{I\,i\,\theta}\,e^{I\,j\,\lambda}$ examined as time (i.e., j) increases. Setting $\lambda = \alpha + I\,\beta$, with α and β real, then $u_{i,j} \sim e^{-\beta\,j}$. If $\beta < 0$, the proposed numerical scheme is unstable because then $u_{i,j} \sim e^{|\beta|\,j}$ will diverge as j increases. For stability, one must have $\beta > 0$.

We will now illustrate this method for the Zabusky–Kruskal algorithm (4.27).

Example 4-8: Stability Criterion for Zabusky–Kruskal Algorithm

Use Von Neumann stability analysis to show that the Zabusky–Kruskal algorithm is numerically stable for $r \equiv k/h^3 < 2/(3\sqrt{3})$. Assume that the spatial step $h \ll 1$ for simplicity of analysis.

Solution Setting $r = k/h^3$, the Zabusky–Kruskal algorithm is

$$
\begin{aligned}
\psi_{i,j+1} = \psi_{i,j-1} &- h^2\,r\,\left(\frac{\psi_{i+1,j} + \psi_{i,j} + \psi_{i-1,j}}{3}\right)\,(\psi_{i+1,j} - \psi_{i-1,j}) \\
&- r\,(\psi_{i+2,j} - 2\,\psi_{i+1,j} + 2\,\psi_{i-1,j} - \psi_{i-2,j}).
\end{aligned}
\tag{4.43}
$$

Substituting $\psi_{i,j} = \psi_{i,j}^0 + u_{i,j}$, retaining linear terms in u, and neglecting the $h^2\,r$ term compared to the r term, we obtain

$$
u_{i,j+1} = u_{i,j-1} - r\,(u_{i+2,j} - 2\,u_{i+1,j} + 2\,u_{i-1,j} - u_{i-2,j}).
$$

Setting $u_{i,j} = e^{I\,i\,\theta}\,e^{I\,j\,\lambda}$ and simplifying, we obtain

$$
e^{I\,\lambda} = e^{-I\,\lambda} - r\,\left(e^{2\,I\,\theta} - 2\,e^{I\,\theta} + 2\,e^{-I\,\theta} - e^{-2\,I\,\theta}\right)
$$

$$
= e^{-I\,\lambda} + 2\,I\,r\,[2\,\sin(\theta) - \sin(2\,\theta)].
$$

Multiplying this result by $e^{I\,\lambda}$ and solving the quadratic equation in $e^{I\,\lambda}$ yields

$$
e^{I\,\lambda} = I\,R \pm \sqrt{1 - R^2},
\tag{4.44}
$$

with

$$
R \equiv r\,[2\,\sin(\theta) - \sin(2\,\theta)] = r\,f(\theta).
\tag{4.45}
$$

Setting $\lambda = \alpha + I\,\beta$, with α and β real, and taking the absolute value of (4.44), we have

$$
|e^{I\,\lambda}| = e^{-\beta} = |I\,R \pm \sqrt{1 - R^2}|.
$$

For stability we require that $\beta > 0$, i.e., that $R^2 = r^2\,f^2(\theta) < 1$.

The maximum value of $f(\theta)$, namely, $f_{max} = 3\sqrt{3}/2$, occurs when $\theta = 2\,\pi/3$ radians. So the numerical scheme will be stable for

$$
r = \frac{k}{h^3} < \frac{1}{f_{max}} = \frac{2}{3\sqrt{3}}.
$$

***

4.5 Extension to Cellular Automata

To solve the KdV equation numerically, the continuous dependent variable ψ was evaluated at discrete spatial (x) and time (t) steps. Models for which not only the spatial and time variables take on discrete values, but also the dependent variable(s), are referred to as *cellular automata* (CA). CA were first investigated by Stan Ulam ([Ula62]) and John von Neumann, and have fascinated mathematicians and scientists ever since because they are easy to execute on the computer, can generate spatial patterns which resemble those observed in nature as well as other interesting behavior, and represent a mathematical frontier full of yet-to-be-discovered rules and properties.

Limiting our attention for the moment to one spatial dimension, we will now illustrate how a simple 1-dimensional CA is created, and then numerically solve it. Referring to the computational mesh in the x–t plane shown in Figure 4.8, let's concentrate on the "cells" which make up the mesh, rather than the intersection or mesh points. The cells can be labeled in a similar manner to that used for the mesh points, the cell labeled as (i, j) corresponding to the ith ($i = 1, 2, \ldots, N$) cell in the spatial direction and on the jth ($j = 0, 1, 2, \ldots, M$) time row.. An initial ($j = 0$) configuration of cells is specified for all values of i. For simplicity, we will only allow the initial state $S_{i,0}$ of the ith cell to be either 0 or 1, which will be colored black or white, respectively, in the graphical representation of the cell. A black cell is referred to as "dead," while a white cell is "alive." If the dependent state variable is allowed to take on more than two values, intermediate shades of gray can be included, or one can switch to distinct colors for the various states.

An algorithm is specified which dictates how all the cells on time step j evolve to the next time step, $j + 1$. In general, the algorithm will cause some live cells to die (become black) and some dead cells to (magically) be brought back to life (become white). In analogy with what we saw earlier for the finite difference approximation to the KdV equation, the evolution of a cell will depend not only on its previous state, but also on the previous states of neighboring cells. That is to say, if r is the *range* of interaction of cell i with its neighbors, then the state variable of cell i on time step $j + 1$ is related to the cells on step j within the interaction range by

$$S_{i,j+1} = f(S_{i-r,j}, \ldots, S_{i-2,j}, S_{i-1,j}, S_{i,j}, S_{i+1,j}, S_{i+2,j}, \ldots, S_{i+r,j}), \qquad (4.46)$$

where the function f remains to be specified. Various classes of functions have been considered in the research literature, with the most extensive cataloging and exploration of properties carried out by Stephen Wolfram ([Wol86], [Wol02]).

Example 4-9: Evolution of a One-Dimensional CA

E. Atlee Jackson ([Jac90]) has suggested the following polynomial form for f which includes next-nearest neighbors ($r = 1$):

$$f = \left((S_{i-1,j} - S_{i+1,j})^2 - S_{i,j} \right)^2. \qquad (4.47)$$

Determine the time evolution of a single live cell, all other cells initially being dead. Plot the spatial distribution of cells as a function of time, using the color white for a

live cell and black for a dead cell.

Solution: To avoid possible problems at the spatial boundaries, we take a large value for N, namely, $N = 200$, and place the live (1) cell in the middle (at $i = 100$) of the spatial range. All other cells are assigned the value 0, since they are dead. The upper limit on the time range is taken to be $j = M = 95$. If you wish to increase M, the value of N should be increased accordingly.

Iterating (4.47) with the given f, and assigning the color white to cells which have a state variable value of 1 and black to cells which have a value 0, produces Figure 4.12.
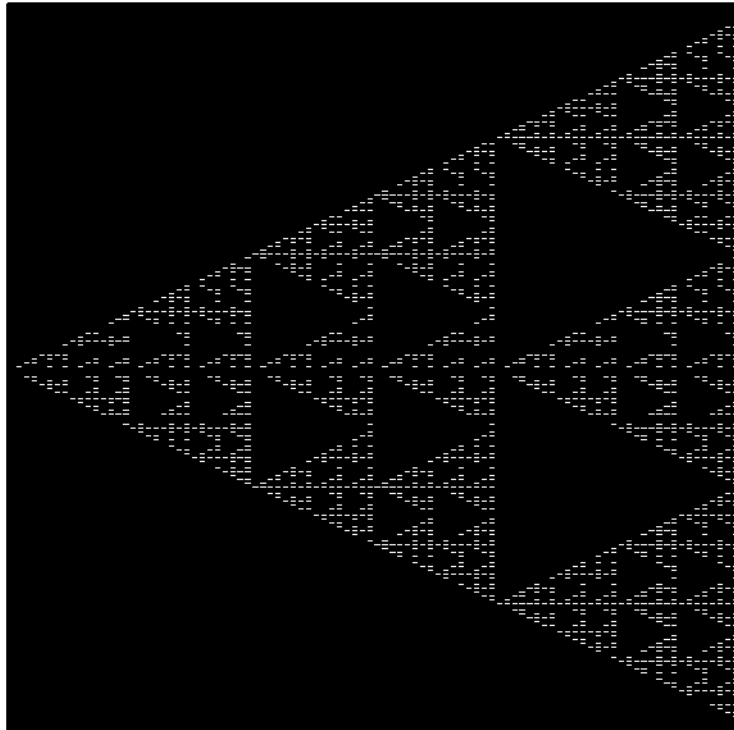
Figure 4.12: Evolution of a 1-dimensional cellular automata.

In this picture, the time index j runs horizontally from left to right, the spatial index i running vertically. The initial solitary white cell can be seen on the far left of the figure. As time progresses, the single white cell evolves as shown, generating a pretty geometric pattern involving triangles of different sizes.

<p style="text-align:center">***</p>

In the above example, for simplicity we chose to start with a single live (white) cell. However, we could have chosen some more complicated distribution of live and dead

cells taking care to avoid edge effects by concentrating the initial distribution far from the boundary or by using period boundary conditions.

It should be noted that triangular pigmentation patterns have been observed on certain molluscs and a CA approach used (see [WC69]) to mimic how these patterns are generated. This approach is a simple mathematical "proxy" for much more complicated nonlinear PDE reaction-diffusion activator-inhibitor models ([MK87]) based on real physical and chemical mechanisms. These models are discussed in Chapter 9.

One-dimensional CAs have been investigated in other contexts, e.g., soliton-like behavior (Aizawa and Nishikawa ([AN86]) and Park et al. ([PST86])), as well.

The extension to two-dimensional CAs is quite straightforward. Here's a simple mathematical example.

Example 4-10: 1 out of 8 Rule

Consider a 2-dimensional square lattice which has 61 cells to a side. The initial configuration is 4 live cells placed at (29,30), (30,30), (29,31), and (30,31), the remainder being dead. Using the rule that a cell becomes alive if exactly one of its eight neighbors is alive, otherwise it remains unchanged, what pattern emerges after 26 steps? Plot the resulting spatial pattern, coloring the live cells white and the dead cells black.

Solution: The resulting geometric pattern is shown in Figure 4.13.
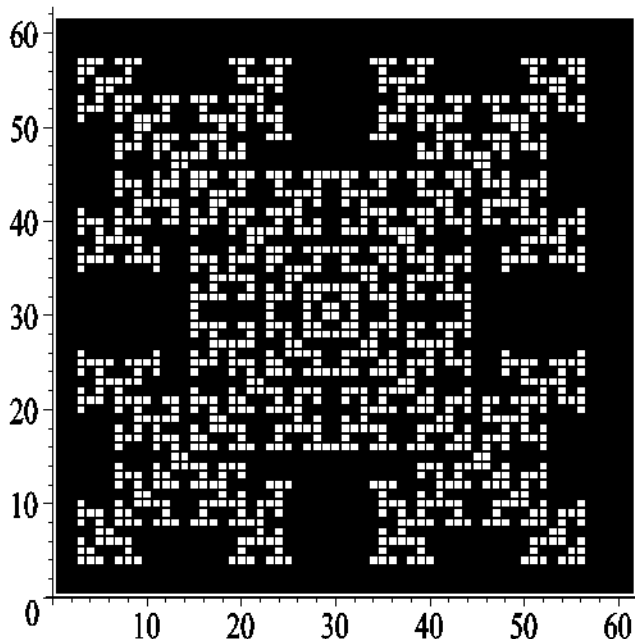
Figure 4.13: Resulting geometric pattern.

***

In the real world, Murray and Paola ([MP94]) have applied a two-dimensional non-linear CA model to the study of "stream braiding," i.e., how a broad sheet of water flowing over noncohesive sediment breaks up into a network of interconnected channels. A dramatic illustration of stream braiding can be found in the Mackenzie river delta of northern Canada as the Mackenzie river breaks up into a myriad of channels before entering the Beaufort Sea.

Another important application of two-dimensional CA is to *excitable media*. As opposed to a linear medium in which waves pass through each other, an excitable medium is a nonlinear medium in which colliding wavefronts annihilate each other and stop. Further, there is a *refractory time* during which no further wave action is possible. In an excitable medium of finite extent, eventually all wave action will stop until the medium "renews" itself. Here's a qualitative example of an excitable medium.

Example 4-11: Forest Fires

Consider the occurrence of several lightning strikes each of which starts a forest fire at different points in a forest. Assuming that there is no wind and the forest is homogeneous in its content, terrain, dryness, etc., describe the spreading of the fires. If each fire consumes the available fuel, what happens when the fire fronts meet? What is the refractory time if the forest is regarded as an example of an excitable medium?

Solution: Each lightning strike produces a circular wavefront of fire. When the fire fronts meet, the fires die out because the available fuel is exhausted. The refractory time is the time for the forest to renew itself.

<div align="center">***</div>

Application of a CA approach to wave propagation in an excitable planar medium, such as in the forest fire example, is easily implemented mathematically by considering, e.g., a square lattice with the cells having the following possible states:

- Quiescent (Q): These cells are not carrying a wave, but could do so if excited.

- Excited (E): A wave is passing through these cells at this instant.

- Refractory (R): These are cells that a wave has passed through and have not yet recovered to become excitable.

The CA rules for these cells are:

- If a cell is Q on a time step, it stays Q on the next step unless one of its neighboring cells is E. In this case, it becomes E.

- If a cell is E on a time step, it becomes R on the next step.

- If a cell is R on a time step, it becomes Q on the next step. If the refractory time is longer, it could take two or more steps to become Q.

A biological example of an excitable medium is cardiac tissue ([KG95]), while a chemical example involves the Belousov–Zhabotinskii reaction discussed in Chapter 9.

PROBLEMS

Problem 4-1: Solitary wave solution of the modified KdV equation

Derive a solitary wave solution for the modified KdV equation
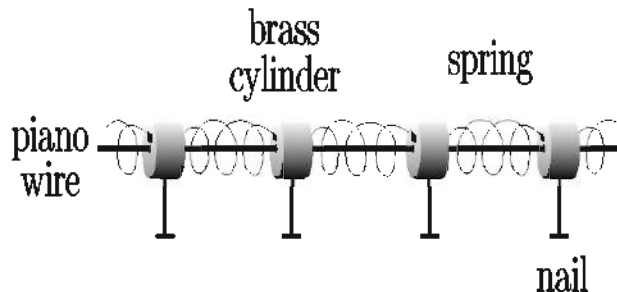
$$\frac{\partial \psi}{\partial t} + \psi^2 \frac{\partial \psi}{\partial x} + \frac{\partial^3 \psi}{\partial x^3} = 0,$$

which appears in theoretical models for:

- nonlinear wave propagation in certain electronic circuits ([Sco70]);
- propagating double layers in plasmas ([Tor81], [Tor86]);
- ion acoustic solitons in a multicomponent plasma ([Ver90]).

Problem 4-2: Mechanical model of the sine-Gordon equation

Barone, Esposito, Magee, and Scott ([BEMS71]) have constructed a mechanical model of the sine-Gordon equation, the physical setup being as shown in the following figure:

Letting ψ be the twist angle of a nail from the vertical, derive the equation of motion for ψ. You may assume that

- the brass cylinders and nail thickness are small so their masses can be ignored;
- the nail mass m is concentrated in the nail head a distance l from the piano wire;
- the restoring force on a given nail when it is twisted from the vertical only depends on the nearest-neighbor springs;
- Hooke's law applies to the spring restoring torque, the torque constant being k;
- the distance h between nails is sufficiently small that the restoring force can be Taylor expanded in powers of h;
- the acceleration due to gravity is g.

By suitable scaling out l, m, h, k, and g, show that the sine-Gordon equation results.

Problem 4-3: Sine-Gordon solitary waves

Redo the sine-Gordon examples 4-3 and 4-4 for the case $v > 1$ and discuss the results.

Problem 4-4: Nonlinear superposition

Confirm the nonlinear superposition result (4.7) for the KdV equation.

Problem 4-5: Similarity solution of nonlinear diffusion equation
Verify by direct substitution that the nonlinear diffusion equation

$$\frac{\partial C}{\partial t} = \frac{\partial}{\partial x}\left(C^n \frac{\partial C}{\partial x}\right),$$

for the concentration C, has a similarity solution of the form

$$C(x,t) = \begin{cases} \dfrac{\left(A - \dfrac{n}{2\,(n+2)}\,z^2\right)^{1/n}}{t^{1/(n+2)}}, & |z| \le \sqrt{\dfrac{2\,(n+2)}{n}\,A}, \\[3ex] 0, & |z| > \sqrt{\dfrac{2\,(n+2)}{n}\,A}, \end{cases}$$

where $z \equiv x/t^{1/(n+2)}$ and A is a constant. Shigesada ([Shi80]) has proposed a model for animal dispersion with $n = 1$. Muskat ([Mus37]) has used $n \ge 1$ to investigate the percolation of homogeneous fluids through porous media, while Larsen and Pomraning ([LP80]) have taken $n = 6$ in their study of radiative heat waves. Taking $A = 1$, plot and compare the evolution of the similarity solutions for $n = 1$ and 6.

Problem 4-6: Soliton collision
Consider two KdV solitary waves, one with $v = 0.95$ initially centered at $x = 60$ and a second with $v = 0.5$ initially centered at $x = 90$. Using the Zabusky–Kruskal algorithm with $h = 1.0$ and $k = 0.25$, numerically demonstrate that the two solitary waves survive the resulting collision intact and therefore are solitons.

Problem 4-7: Two-soliton solution of KdV equation
In 1971, Fred Tappert of Bell Laboratories derived the following expression for two interacting solitons for the KdV equation:

$$\psi(x,t) = 72\,\frac{[3 + 4\cosh(2\,x - 8\,t) + \cosh(4\,x - 64\,t)]}{[3\cosh(x - 28\,t) + \cosh(3\,x - 36\,t)]^2}.$$

Verify that this expression satisfies the KdV equation. Then confirm that it produces the sequence of plots shown in Figure 4.4. Hint: Take $t = -1/4$, 0, 1/4 and appropriate spatial ranges.

Problem 4-8: Courant stability condition
Using the traditional finite difference approximations for second derivatives, derive a numerical algorithm for integrating the linear wave equation

$$\frac{\partial^2 \psi}{\partial x^2} = \frac{1}{v^2}\frac{\partial^2 \psi}{\partial t^2},$$

where v is the wave velocity. Using Von Neumann stability analysis, show that the numerical scheme is stable if $r \equiv |v|\,k/h \le 1$. This is the *Courant stability condition*.

Problem 4-9: CA model of forest fires
Use the CA model in the text with varying refractory times and a computer program

of your own design to graphically simulate the spread of a number of fires initiated by simultaneous lightning strikes at separated points in a forest of large, but finite, extent. Discuss the results.

Problem 4-10: Fisher's equation

Fisher ([Fis37]) suggested the following nonlinear PDE for the spatial spread of a favored gene in a population:

$$\frac{\partial c}{\partial t} = \frac{\partial^2 c}{\partial x^2} + c\,(1 - c),$$

where c is the normalized concentration of the gene. Fisher's equation is just the logistic population growth equation to which a 1-dimensional diffusive term, $\partial^2 c/\partial x^2$, has been added to account for spatial spreading. Devise a finite-difference approximation scheme for numerically integrating Fisher's equation and use Von Neumann's stability analysis to determine the upper bound on the ratio $r = k/h^2$ for stability of the scheme.

Problem 4-11: A breather mode

Show that

$$\psi = 4 \arctan\left(\sqrt{\frac{m}{(1-m)}}\, \frac{\sin(\gamma\,\sqrt{(1-m)}\,(t - v\,x))}{\cosh(\gamma\,\sqrt{m}\,(x - v\,t))} \right),$$

with

$$\gamma = 1/\sqrt{1 - v^2}, \quad -1 < v < 1, \quad 0 < m < 1,$$

is a solution of the SGE.

By plotting ψ for $m = v = 1/2$ over a suitable range of x for a sequence of times, show that this solution represents a so-called *breather mode*.

Problem 4-12: Burgers's equation: The Hopf–Cole transformation

Burgers's equation is an important nonlinear PDE from fluid mechanics. Named after Johannes Burgers (1895–1981), it has been used in modeling the coupling between convection and diffusion in fluid dynamics and in modeling traffic flow.[2] Burgers's equation has the structure

$$\frac{\partial \psi}{\partial t} + \psi\,\frac{\partial \psi}{\partial x} = \sigma\,\frac{\partial^2 \psi}{\partial x^2},$$

where σ is a positive diffusion coefficient. Show that the *Hopf–Cole transformation*,

$$\psi = -2\,\sigma\,\frac{1}{\phi}\,\frac{\partial \phi}{\partial x}$$

discovered by E. Hopf ([Hop50]) and J. D. Cole ([Col51]), reduces Burgers's equation to the linear diffusion equation

$$\frac{\partial \phi}{\partial t} = \sigma\,\frac{\partial^2 \phi}{\partial x^2}.$$

---

[2]If you are interested in the subject of modeling traffic flow, see, e.g, the survey paper of Bellomo et al. ([BCD02]) and *The Physics of Traffic* by Kerner ([Ker04]).

Problem 4-13: Burgers's equation: Antikink solution
Derive an antikink solitary wave solution to Burgers's equation (see previous problem) and plot the result. How do the thickness of the antikink region and the velocity depend on the amplitude?

Problem 4-14: A kink–kink collision
Show that

$$\psi = 4 \arctan\left(v\, \frac{\sinh(x/\sqrt{1-v^2})}{\cosh(v\,t/\sqrt{1-v^2})}\right),$$

with $-1 < v < 1$ the velocity, satisfies the SGE. By taking $v = 0.5$ and plotting ψ over a suitable range of x for a sequence of times, show that the solution represents a kink–kink collision.

Problem 4-15: Dispersal of predators and prey
Consider the following Lotka–Volterra predator–prey system:

$$\frac{\partial X}{\partial t} = D_1 \frac{\partial^2 X}{\partial x^2} + A\,X\left(1 - \frac{X}{K}\right) - B\,X\,Y,$$

$$\frac{\partial Y}{\partial t} = D_2 \frac{\partial^2 Y}{\partial x^2} - C\,Y + F\,X\,Y,$$

where X and Y are the prey and predator population densities, respectively, and all coefficients (including the diffusion coefficients D_1 and D_2) are positive. If the dispersal of the predator is slow compared to that of the prey, i.e., $D_2 \ll D_1$, the diffusion term in the predator equation may be neglected. Assuming that this is the case, rewrite the predator–prey system in nondimensional form and investigate the possible existence of kink or antikink solitary waves solutions.

Problem 4-16: Kadomtsev–Petviashvili equation
The generalization of the KdV equation into two spatial dimensions is the *Kadomtsev–Petviashvili* (KP) equation ([KP70]). Without loss of generality, the KP equation may be written in the form

$$\frac{\partial}{\partial x}\left(\frac{\partial \psi}{\partial t} + 6\,\psi\,\frac{\partial \psi}{\partial x} + \frac{\partial^3 \psi}{\partial x^3}\right) + 3\,\lambda\,\frac{\partial^2 \psi}{\partial y^2} = 0,$$

where x and y are the longitudinal and transverse spatial directions, t is the time, ψ is the amplitude, and the parameter $\lambda = \pm 1$. The case $\lambda = +1$ has been used to model small-amplitude, long-wavelength, water waves with small surface tension. The equation then is referred to as the KPII equation. The other case, $\lambda = -1$, has been used to model waves in thin films with high surface tension. The equation is then labeled as the KPI equation.

Confirm by direct substitution that the KPII equation has the solitary wave solution

$$\psi = \frac{1}{2}\,k_x^2\,\text{sech}^2\left(\frac{1}{2}\,(k_x\,x + k_y\,y - v\,t)\right), \quad \text{with}\ \ v = k_x^3 + 3\left(\frac{k_y^2}{k_x}\right).$$

Sketch the above solitary wave solution at some instant in time.

Two-dimensional solitary waves similar in shape to this solution have been photographed in shallow ocean water off the coast of Oregon ([Kru91]).

Problem 4-17: Game of Life

A well-known 2-dimensional CA on a square lattice is the *Game of Life* invented by the Princeton mathematician John Conway. The Game of Life was featured ([Gar70, Gar71a, Gar71b]) by Martin Gardner in his Mathematical Games column, which regularly appeared in *Scientific American.*

Starting with an initial configuration of live (black) and dead (white) cells, each cell having 8 nearest neighbors, the rules are:

- Each cell only interacts with its nearest neighbors.

- A live cell stays alive on the next step if it has 2 or 3 live neighbors but otherwise dies (from loneliness for 0 and 1 live neighbors and from overcrowding for 4 or more live neighbors).

- A dead cell comes alive on the next step if it has exactly 3 live neighbors.

Experiment with different initial configurations and see what happens.

Problem 4-18: The Eden growth model

The Eden growth model ([Ede61]) attempts to replicate cell division, a single cell dividing into two cells, the two "daughter" cells then dividing, and so on. Specifically, Murray Eden considered a square lattice with initially $(t = 0)$ one live cell (colored black). On the next time step, $t = 1$, a second live cell is added randomly to one of the four positions adjacent to the initial live cell. On time step $t = 2$, a third live cell is added randomly to one of the six squares that are adjacent to the two live cells existing at $t = 1$. Continuing this process, generate the two-dimensional pattern of live cells produced after 100 time steps. Is the pattern fractal in nature? Explain.

Problem 4-19: Diffusion-limited aggregation

Diffusion-limited aggregation (DLA), introduced by Witten and Sander ([WS81]), is a computer simulation in which particles undergoing random diffusion cluster together to form aggregates or clusters which resemble real physical systems occurring in nature. Making use of the Internet, discuss DLA in detail, including:

- the details of how the computer simulations are carried out;

- the fractal nature of the clusters;

- a list of web sites which allow one to actively carry out DLA simulations;

- examples of physical systems to which DLA has been applied.

Problem 4-20: Solitary internal waves

According to the online Sci-Tech dictionary,[3] an internal wave is a gravity wave that

---

[3] http://www.answers.com/topic/internal-wave.

oscillates within, rather than on the surface of, a fluid medium. A simple example is a wave propagating at the interface between two fluids of different densities, such as oil and water.

Solitary internal waves have been observed and photographed in various parts of the world's oceans as well as in the atmosphere. Two good oceanic examples are provided by NASA satellite pictures, viz.,

- In the Sulu sea between Malaysia and the Philippines:

  http://visibleearth.nasa.gov/view_rec.php?id=6859

- In the Strait of Gibraltar:

  http://earthobservatory.nasa.gov/IOTD/view.php?id=4585

a. For each of the above satellite pictures discuss in detail the nature of the observed solitary internal waves, how they are generated, and how they are manifested at the ocean surface so that satellite pictures can be taken.

b. Performing an Internet search, discuss examples (e.g., the *Morning Glory* cloud which occurs in northern Australia's Gulf of Carpentaria) of solitary internal waves in the atmosphere.

Problem 4-21: Sand pile models

Making use of the Internet, discuss in some detail cellular automata models of sand piles. To get you started here are a few useful web sites:

- **http://www.econ.iastate.edu/classes/econ308/tesfatsion/ sandpilemodel.pdf**

- **http://carrot.whitman.edu/JavaApplets/SandPileApplet/**

- **http://www.csee.wvu.edu/~angela/cs418a/node2.html**

- **http://compmath.files.wordpress.com/2009/02/arfreport.pdf.**

Problem 4-22: Reducing prejudice

Patrick Grim and coworkers ([GSB+04]) have formulated a two-dimensional spatialized cellular automata model to investigate the following social science hypothesis on reducing prejudice:

Under the right circumstances,
prejudice between groups will be reduced with social contact.

Discuss the cellular automata prejudice reduction model in detail. A reprint of Grim's paper is available online at:

www.stonybrook.edu/philosophy/faculty/pgrim/vitanew10.pdf.

Part II

OUR NONLINEAR WORLD

Human history
is
highly nonlinear
and
unpredictable.

Michael Shermer,
Scientific American
columnist
and
author

Chapter 5

World of Motion

I can easily conceive, most Holy Father, that as soon as some people learn that in this book which I have written concerning the revolutions of the heavenly bodies, I ascribe certain motions to the Earth, they will cry out at once that I and my theory should be rejected.
Nicolaus Copernicus, Polish astronomer (1473–1543)

In the following two chapters, we will sample some of the nonlinear dynamical phenomena in the world of motion, a world where it is possible to verify and apply the nonlinear mathematical concepts that have been introduced. This chapter deals with more traditional nonlinear topics from the realm of physics and engineering, while examples from the world of sports are the theme of the following chapter.

5.1 Nonlinear Drag or Resistance

When an object moves with a velocity $\vec{v}$ through a viscous fluid such as air or water, the fluid exerts a retarding or *drag force* $\vec{F}_D$ on it which depends on:

- the speed v of the object;
- the size, shape, and surface roughness of the object;
- the properties (e.g., density ρ and viscosity coefficient η) of the fluid.

Drag plays an important role in the aerodynamics of airplanes and birds as well as golf balls and badminton birds. Minimizing drag is a major issue in reducing fuel consumption in modern jetliners as well as cars. The precise mathematical form of the drag force is in general quite complicated and is usually determined experimentally, e.g., by using wind tunnels for aircraft and cars, and large water tanks for ships. However, the simplest mathematical models which are usually considered assume that the drag force is some power or polynomial function of v, the coefficients then involving the other relevant factors cited above.

First, let's introduce the dimensionless *Reynolds number* ([Rey83]), proposed by the British fluid dynamics engineer Osborne Reynolds in 1883. The Reynolds number Re,

defined as

$$\text{Re} = \frac{\rho L v}{\eta}, \tag{5.1}$$

plays a key role in the study of viscous fluid drag, whether it's the drag on a major league fastball or the drag on blood flowing in a human artery. Here L is a *characteristic length* in the problem, e.g., the diameter of the ball or the artery.

Anticipating our future excursion into the world of sports, let's now determine the Reynolds number for a softball thrown by a recreational player.

Example 5-1: Reynolds Number for a Thrown Softball

A softball of diameter $d = 0.114$ m (about $4\frac{1}{2}$ inches) is thrown with a speed of 20 m/s (about 45 mph). Air at 20°C has a density $\rho_{air} = 1.21$ kg/m^3 and viscosity coefficient $\eta_{air} = 1.82 \times 10^{-5}$ N·s/m^2. Calculate the Reynolds number.

Solution:

$$\text{Re} = \frac{\rho_{air}\, d\, v}{\eta_{air}} = \frac{1.21 \times 0.114 \times 20}{1.82 \times 10^{-5}} = 1.5 \times 10^5.$$

✱✱✱

In itself, the above Reynolds number tells us nothing unless we have something to compare it against and some idea of how it is to be applied. Some representative Reynolds numbers for various bodies moving in water or air at their typical speeds are listed in the following table. The Reynolds number for blood flow in a human artery is also given.

Object	Reynolds number, Re
Bacterium	1×10^{-5}
Sea urchin sperm	3×10^{-2}
Blood flowing in an artery	500
Large dragonfly	3×10^4
Person swimming	4×10^6
Large whale	3×10^8
Large ship (e.g., QE2)	5×10^9

Table 5.1: Reynolds number for some moving objects ([Vog94]).

The Reynolds number is not only important in deciding what mathematical model of drag to use, but also allows a physically scaled-down model of, e.g., an aircraft to act as a surrogate for the full-sized aircraft in wind tunnel experiments. The experimental results for the scaled-down model will apply to the similarly shaped full-sized airplane, provided that Re is the same. This is extremely important to the design engineer.

For small Reynolds numbers, fluid flow tends to be smooth or *laminar*, moving in parallel layers with no mixing. When the Reynolds number is sufficiently large, turbulent flow occurs, the layers mixing chaotically with the formation of waves and eddies.

The upward flow of smoke from a cigarette, as shown in Figure 5.1, provides a nice visual example of the transition from laminar to turbulent flow. The hot smoke is lighter than the surrounding air and consequently by Archimedes buoyancy principle
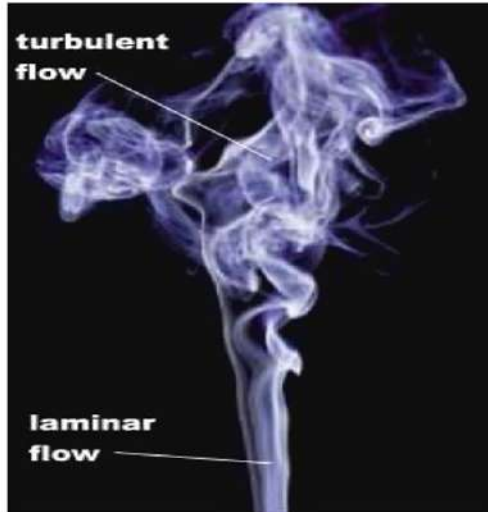
Figure 5.1: Transition from laminar flow to turbulence for rising cigarette smoke.

experiences an upward force. Initially, near the cigarette (located below the figure), the speed and therefore the Reynolds number is sufficiently low that the flow of smoke is laminar. The upward force acts continuously on the rising smoke, thus causing a progressive increase in speed as the smoke rises farther from the cigarette. Eventually, the speed and therefore the Reynolds number is sufficiently high that the flow becomes turbulent as illustrated in the figure.

Let's now return to the issue of the drag force on a moving object. The drag force $\vec{F}_D$ exerted on a body moving through a fluid medium of density ρ and viscosity η with a velocity $\vec{v} = v\,\hat{v}$ relative to the medium is given by

$$\vec{F}_D = -\frac{1}{2}\,\rho\,C_D\,A\,v^2\,\hat{v}. \tag{5.2}$$

Here A is the cross-sectional area of the body measured perpendicular to $\vec{v}$ and C_D is the *drag coefficient*. The value of C_D depends on the shape of the body and its surface roughness. Further, in general C_D is a function of the Reynolds number which can alter the speed dependence of the drag force from the quadratic form above.

One of the most extensively studied shapes is the sphere, a shape of great importance in the world of sports where many of the sports balls (tennis ball, golf ball, baseball, etc.) are spherical. For Reynolds numbers below about 1, a regime where the fluid flow past

the sphere is laminar, one can show that $C_D = 24/\text{Re}$. This result was first derived[1] in 1851 by the Anglo-Irish mathematician and physicist George Stokes (1819–1903).

In this case, taking L equal to the diameter d of the sphere, then $A = \pi \, (d/2)^2$ and the drag force (5.2) reduces to the *Stokes's drag law*,

$$\vec{F}_{Stokes} = -a \, v \, \hat{v}, \qquad a = 3 \, \pi \, \eta \, d. \tag{5.3}$$

Stokes's drag law is linear in the speed, rather than quadratic. This law can be applied to other shapes in the low Reynolds number regime, e.g., a thin circular disk of diameter d oriented with its flat side perpendicular to the velocity.

Example 5-2: A Falling Grain of Sand

A tiny spherical grain of sand of mass m falls vertically from rest under the influence of gravity (gravitational acceleration, g) through cold water in a settling pond. Assume that it experiences a viscous drag due to the water given by Stokes's law.

    a. Determine the raindrop's velocity v as a function of time t.

    b. In the limit $t \to \infty$, v approaches its terminal velocity v_t. Given that $g = 9.8$ m/s^2, sand has a density $\rho_{sand} = 2.6 \times 10^3$ kg/m^3, the grain of sand has a diameter $d = 5 \times 10^{-5}$ m, water at 5°C has a viscosity $\eta_{water} = 1.51 \times 10^{-3}$ N·s/m^2 and density $\rho_{water} = 10^3$ kg/m^3, determine v_t and the corresponding Reynolds number. Is the assumption that Stokes's law applies valid? Explain.

Solution: a. The equation of motion for the falling grain of sand is

$$m \frac{dv}{dt} = m \, g - a \, v.$$

This linear ODE is easily solved by separating variables and integrating. The result is

$$v(t) = \left(\frac{m \, g}{a} \right) \left(1 - e^{-(a/m) \, t} \right).$$

b. In the limit $t \to \infty$, $v(t) \to m \, g/a$, which is the terminal velocity v_t. In this limit, the downward pull of gravity is balanced by the upward viscous drag and $dv/dt = 0$. The spherical grain of sand has a mass

$$m = \rho_{sand} \left(\frac{4 \, \pi}{3} \right) \left(\frac{d}{2} \right)^3 = 1.70 \times 10^{-10} \text{ kg.}$$

The coefficient $a = 3 \, \pi \, \eta_{water} \, d = 0.712 \times 10^{-6}$, so

$$v_t = \frac{m \, g}{a} = 2.34 \times 10^{-3} \text{ m/s, and } \text{Re} = \frac{\rho_{water} \, d \, v_t}{\eta_{water}} = 0.0776.$$

Since Re $\ll 1$, Stokes's drag law is valid.

<div align="center">***</div>

---

[1]A derivation may be found in Batchelor ([Bat67]).

Keeping our attention on the sphere, as the Reynolds number increases, C_D continues to decrease albeit with a different functional dependence than that of Stokes. However, a region is reached for $1000 < \text{Re} < 10^5$, where the drag coefficient is approximately constant ($C_D \approx 0.5$). In this region, the boundary layer on the front of the moving sphere is laminar but a wide turbulent *wake* forms behind the sphere.

As Re further increases, C_D drops to a new approximately constant value, the critical value of Re depending on whether the surface of the sphere is smooth or rough. For a smooth sphere, the critical Reynolds number is $\text{Re}_{cr} = (3 \text{ to } 4) \times 10^5$ and $C_D \approx 0.1$ for $\text{Re} > \text{Re}_{cr}$. In this region, the boundary layer on the front of the moving sphere becomes turbulent, and the trailing wake becomes narrower but more turbulent. For a sphere with a rough surface, the boundary layer becomes turbulent faster, occurring for $\text{Re}_{cr} \approx 1 \times 10^5$. For $\text{Re} > \text{Re}_{cr}$, $C_D \approx 0.4$. It should be noted that a major league baseball is a rough sphere because of protruding stitches. Pitchers also alter the surface roughness by scuffing the baseball. See Adair ([Ada90]).

Returning to the thin circular disk of diameter d oriented with its flat side perpendicular to the velocity, the drag coefficient also drops with increasing Reynolds number to a plateau value when turbulence sets in. However, unlike the sphere a constant value, $C_D = 1.17$, prevails for all Re values above 1000.

When C_D can be taken to be constant, the fluid resistance law (5.2) is known as *Newton's drag law*, viz.,

$$\vec{F}_{Newton} = -b\, v^2\, \hat{v}, \quad b = \frac{1}{2}\rho\, C_D\, A. \tag{5.4}$$

Newton's drag law leads to a nonlinear equation of motion.

Example 5-3: A Falling Penny

A thin circular disk of mass m and diameter d falls vertically from rest under the influence of gravity (gravitational acceleration g). Assume that it falls with its flat face perpendicular to the vertical (i.e., does not tumble) and that Newton's drag law applies.

a. Determine the disk's speed as a function of time.

b. The disk is a U.S. penny, for which $m = 2.5 \times 10^{-3}$ kg and $d = 1.905 \times 10^{-2}$ m. Air has a density $\rho = 1.21$ kg/m^3 and viscosity coefficient $\eta = 1.82 \times 10^{-5}$ N$\cdot$s/m^2. The drag coefficient $C_D = 1.17$. Evaluate $v(t)$ and plot it for the first 4 seconds of fall.

c. Determine the Reynolds number when the penny has fallen for 0.1 s. What does this tell you about the assumed form of the drag law?

Solution: a. The equation of motion is given by the following nonlinear ODE:

$$m\frac{dv}{dt} = m\,g - b\,v^2.$$

When the terminal velocity v_t is reached, $dv/dt = 0$. So $v_t = \sqrt{m\,g/b}$. The ODE may be then rewritten in the form

$$\frac{dv}{dt} = g\left(1 - \frac{v^2}{v_t^2}\right).$$

Although nonlinear, this ODE is readily solved by separating variables and integrating subject to the initial condition $v(t = 0) = 0$. The result is

$$v(t) = v_t \tanh\left(\frac{t}{\tau}\right), \quad \text{with} \quad \tau = \sqrt{\frac{m}{b\,g}}.$$

b. Since a U.S. penny is circular, $A = \pi\,(d/2)^2$, and therefore,

$$b = \frac{1}{2}\,\rho\,C_D\,A = 2.018 \times 10^{-4}, \quad v_t = \sqrt{\frac{m\,g}{b}} = 11.02 \text{ m/s}, \quad \tau = \sqrt{\frac{m}{b\,g}} = 1.124 \text{ s}.$$

Thus,

$$v(t) = 11.02 \tanh\left(\frac{t}{1.124}\right),$$

which is plotted in Figure 5.2.
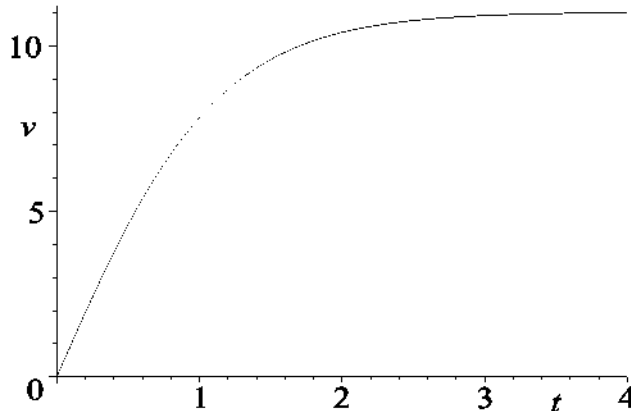
Figure 5.2: Velocity of a falling penny as a function of time.

c. Using the above formula, $v = 0.9774$ m/s at $t = 0.1$ s and the Reynolds number is

$$\text{Re} = \frac{\rho\,v\,d}{\eta} = 1238.$$

This value is larger than 1000, so the penny has very quickly entered the turbulent regime where C_D is constant. Thus, Newton's drag law is a very good approximation for the falling penny.

<div align="center">***</div>

In addition to the falling penny, many other moving objects in the real world can be characterized (at least approximately) by a constant C_D for the velocities with which they typically move. Some examples are listed in Table 5.2 with their drag coefficient values. For the dolphin the relevant area A is the wetted area, rather than the frontal area. For the racing and commuter cyclists, the relevant A in square meters is stated.

Object	C_D
Dolphin (wetted area)	0.0036
Supersonic fighter (Mach 2.5)	0.016
Modern car: Toyota Prius	0.26
Bullet	0.295
Bird	0.4
Old car: Model T Ford	$0.7 - 0.9$
Bike: Racing ($A = 0.35$ m^2)	0.88
Tractor trailer truck	0.96
Bike: Upright commuter ($A = 0.5$ m^2)	1.1
Upright person	$1.0 - 1.3$
Ski jumper	$1.2 - 1.3$
Parachute	1.5
Passenger train	1.8
Eiffel Tower	$1.8 - 2$

Table 5.2: C_D for some moving objects. Reference: **www.engineeringtoolbox.com**

Since Newton's drag force depends not only on the value of C_D but also on the frontal area A, engineers and automotive designers try to minimize the so-called *drag area* $C_D A$ to improve on fuel efficiency at freeway speeds. About 60% of the power required to cruise at these speeds is to overcome air drag. A solar racer has a drag area of about $0.07 \, \text{m}^2$, average full-size passenger cars about $0.79 \, \text{m}^2$, and the 2003 Hummer about $2.44 \, \text{m}^2$. Lists of drag coefficients and drag areas for cars and trucks can be found at various web sites, e.g., **www.bookrags.com/wiki/Automobile_drag_coefficients**.

5.2 Nonlinear Lift

In addition to nonlinear drag, *nonlinear lift* on an object due to fluid flow past it plays a key role in the aerodynamics of aircraft wings, helicopter rotors, wind turbines, and even baseballs and golf balls. Among the effects that create lift on a moving object are

- asymmetrical shape (e.g., aircraft wing) or orientation with respect to the flow;
- spin (e.g., rotating baseball, golf ball);
- uneven or rough surface (e.g., tennis ball, badminton birdie).

In terms of magnitude, the nonlinear lift force F_L is given by the same mathematical structure as the nonlinear drag force, the drag coefficient C_D being replaced by the lift coefficient C_L, viz.,

$$F_L = \frac{1}{2} \rho \, C_L \, A \, v^2. \tag{5.5}$$

Unlike the drag force, $\vec{F}_L$ is transverse to the direction of motion, i.e., to $\vec{v}$. In the case of a spinning ball, $\vec{F}_L$ is a *deflecting* force (called the *Magnus force*[2]) given by

$$\vec{F}_{Magnus} = \frac{1}{2}\rho\,C_L\,A\,v^2\,(\hat{\omega}\times\hat{v}), \qquad (5.6)$$

where $\vec{\omega}$ is the angular velocity vector which points along the spin axis. The sense of the spin is given by the "right-hand rule." Point the thumb of your right hand in the direction of $\vec{\omega}$. Your curled fingers will indicate the sense of the spin. The Magnus force is perpendicular to the plane containing $\hat{\omega}$ and $\hat{v}$, its direction given by the cross product. Thus for a ball moving horizontally with *backspin* in the horizontal plane, the Magnus force is vertically upwards (lift) as shown in Figure 5.3.
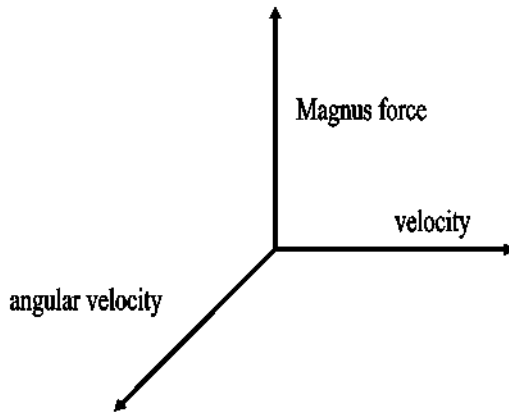
Figure 5.3: Magnus force for backspin.

The lift coefficient for moving objects, including spinning baseballs, tennis balls, etc., is usually determined experimentally. For a nonsmooth spinning baseball of radius r at a Reynolds number $\mathrm{Re}\approx 10^5$, LeRoy Alaways found[3] that

$$C_L \approx \frac{r\,\omega}{v} \quad \text{for} \quad \frac{r\,\omega}{v} < 1 \qquad \text{(baseball)},$$

while for a tennis ball at high Re, Antonin Stepanek ([Ste88]) obtained

$$C_L = \frac{1}{2.2 + 0.98\left(\frac{r\,\omega}{v}\right)} \qquad \text{(tennis ball)}.$$

In the following example, we calculate C_L and compare the Magnus force for a major league pitch with the gravitational force.

---

[2]Named after the German physicist Heinrich Magnus who described the effect in 1853, although Newton was also aware of this force some 180 years earlier after studying the flight of a tennis ball.

[3]LeRoy Alaways, *Aerodynamics of the Curveball*, Ph.D. thesis in Engineering, University of California (Davis), 1998. For his contribution to analyzing the aerodynamics of the curveball, Alaways received a lifetime pass to the National Baseball Hall of Fame.

Example 5-4: Magnus Force on a Major League Pitched Ball

A nonsmooth baseball (radius $r = 0.0366$ m and mass $m = 0.145$ kg) is thrown with a speed $v = 40$ m/s (90 miles/h) and a spin $S = 2000$ rpm. The density of air is $\rho = 1.21$ kg/m^3 and the gravitation acceleration $g = 9.8$ m/s^2. Calculate the lift coefficient and Magnus force and compare the latter with the gravitational force.

Solution: The angular velocity is

$$\omega = 2\pi \frac{S}{60} = 2\pi \frac{2000}{60} = 209.4 \text{ radians/s.}$$

Thus,

$$C_L = \frac{r\omega}{v} = \frac{0.0366 \times 209.4}{40} = 0.19.$$

The cross-sectional area of the ball is $A = \pi r^2 = 4.19 \times 10^{-3}$ m^2. So,

$$F_{Magnus} = \left(\frac{1}{2}\right) \rho C_L A v^2 = \frac{1.21 \times 0.19 \times 4.19 \times 10^{-3} \times (40)^2}{2} = 0.77 \text{ newton.}$$

The force of gravity is

$$F_G = mg = 0.145 \times 9.8 = 1.42 \text{ newtons.}$$

The Magnus force is slightly more than one-half the gravitational force so plays an important role in determining the trajectory of the baseball.

<div align="center">***</div>

For a moving airfoil (aircraft wing, wind turbine blade, kite, etc.) not only are shape and degree of surface roughness important, but also the *angle of attack*, i.e., the angle α (in radians) that the airfoil makes relative to the wind. Neglecting finite transverse edge effects (assuming infinite wing span to enable 2-dimensional analysis) for the moment, the lift coefficient is observed to increase linearly with the angle of attack, up to some maximum angle at which point C_L begins to decrease and the airfoil "stalls." In the linear regime, we can write $C_L = c_0 + s\alpha$. For a thin flat airfoil (e.g., a kite), *thin airfoil theory*[4] yields $c_0 = 0$ and $s = 2\pi$, i.e., the lift coefficient is zero for $\alpha = 0$. Most real wings are asymmetrically shaped so that there is uplift even at zero angle of attack. For example,[5] for a Boeing 747–200, $c_0 = 0.29$.

Real airfoils also do not have infinite wing spans, so edge effects must be included. Near the tips of an airfoil (wing) with finite wing span b, the air flow spills from the lower side to the upper because of higher pressure on the bottom. A *downwash* is created which changes the angle of attack and the lift coefficient. The factor which is used as a measure of this effect is called the *aspect ratio* AR, defined as AR $= b^2/A$, where A is the wing area.

---

[4]See, e.g., *Applied Aerodynamics: A Digital Textbook*, **www.desktopaero.com**.

[5]*Applying the Lift Equation*, **aerospaceweb.org**.

For a flat kite, for example, the "wing span" is generally small compared to the surface area, so a kite has a low aspect ratio. So does a modern fighter with swept back wings, e.g., the BAC Lightning. The effect of a low aspect ratio is to reduce the lift coefficient as a function of attack angle, i.e., effectively reduce the slope s. For the kite, in fact, the effect of downwash at the "wing tips" is to alter C_L to the following form[6]:

$$C_L = \frac{2\pi\alpha}{1 + (2\pi\alpha)/(\pi\,\mathrm{AR})}. \tag{5.7}$$

For the BAC Lightning, wind tunnel studies yield $C_L \approx 2.9\,\alpha$. The Boeing 747-200, on the other hand, with a wing span $b = 59.74$ m and area $A = 510.97$ m^2, has a large aspect ratio AR $= 6.98$. Its lift coefficient at a cruising altitude of 12000 m is $C_L = 0.29 + 5.5\,\alpha$. Higher aspect ratio, however, leads to a lower stall angle. For example, a Cessna 172 with a high aspect ratio stalls at about $15°$, while the Lightning stalls at $27°$.

Nonlinear lift and drag considerations also apply to the design of wind turbines, which convert the kinetic energy of the wind into useful shaft power. Vertical axis wind turbines were used as early as the 10th century in Persia to grind corn and pump water. Horizontal axis wind turbines, with typically two or three giant (50 m) blades, are more prevalent nowadays in generating electrical power. Denmark generates over 20% of its electricity with wind turbines.

For a horizontal axis wind turbine, the blades are constrained to move in a vertical plane with the rotor hub at the center connected to the main shaft which spins and drives a generator. The nonlinear lift force due to the wind causes rotation of the blades about the hub, while the nonlinear drag force impedes the motion. Since a blade varies in shape along its length to take advantage of variable wind speeds, the driving force on a blade due to the wind must be applied on each area element dA of the blade and the total force obtained by integrating over the entire blade. This is referred to in the engineering literature as *blade element theory* (see, e.g., "Wind Turbines" by Swift and Moroz ([SM96])). If ϕ is the angle of the rotor axis with the wind, V is the wind speed, Ω is the rotor speed (in rads/s), r is the radial distance of the element dA, and a is the *axial induction factor* (fraction by which the wind speed is reduced by the rotor blades), the force on an element of blade area dA is

$$F = \frac{1}{2}\rho\,[C_L \sin\phi - C_D \cos\phi]\,(dA)\,[(V(1-a))^2 + (r\,\Omega)^2]. \tag{5.8}$$

The maximum theoretical power extraction from the wind is 59.3% (called the *Betz limit* after the German physicist Albert Betz who discovered it in 1919), and occurs when the free stream wind velocity is slowed to 2/3 of its original value.

The same nonlinear lift and drag considerations that apply to wind turbines apply to helicopter rotors (the blades rotating horizontally with spin axis vertical), except here the blades are allowed to flap. The relevant nonlinear *blade flapping* differential equations may be found in *Rotary Wing Technology* by Richard Bennett[7] and are derived in *Helicopter Performance, Stability, and Control* by Raymond Prouty ([Pro95]).

---

[6]Kite lift equations from National Aeronautics and Space Administration, Glenn Research Center.
[7]Short course notes, The Boeing Company, Mesa, Arizona, September 19–23, 2007.

5.3 The Pendulum, Simple and Otherwise

5.3.1 The Simple Pendulum

A problem that almost every undergraduate engineering and physics student encounters but avoids solving is that of the oscillatory motion of a simple pendulum for large angles. This is because the full ODE is nonlinear in nature and the motion for large and small angles looks qualitatively the same. For these reasons, the motion is restricted to small angles, where the nonlinear ODE reduces to the linear simple harmonic oscillator (SHO) equation whose solution is well known. Here, we will show you that solving the full nonlinear ODE isn't difficult and that there are significant quantitative differences between the predictions of the exact solution and those of the SHO approximation.

As illustrated in Figure 5.4, the pendulum consists of a small mass m, attached to the bottom end of a thin, light, rigid rod of length L, which is allowed to swing along a circular arc in a vertical plane under the influence of the gravitational force $m\,\vec{g}$. All frictional forces are neglected for the moment.
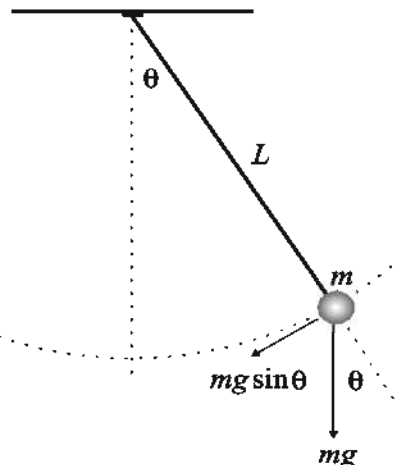
Figure 5.4: Simple pendulum.

If the pendulum rod is displaced by an angle θ from the vertical, the mass experiences a restoring force component $-m\,g\sin\theta$ along the arc direction. The minus sign is included because the restoring force is in the opposite direction to increasing θ. Noting that the acceleration tangent to the arc is $L\,\ddot{\theta}$, Newton's second law of motion applied in the arc direction yields

$$m\,L\,\ddot{\theta} = -m\,g\sin\theta, \tag{5.9}$$

or, on setting $\omega = \sqrt{g/L}$ and rearranging,

$$\ddot{\theta} + \omega^2 \sin\theta = 0. \tag{5.10}$$

Despite being nonlinear, an analytic solution to Equation (5.10) can be readily found.

Multiplying the ODE by $2\dot\theta\,dt$ and integrating yields

$$\dot\theta^2 = 2\,\omega^2\cos\theta + C, \tag{5.11}$$

where C is the integration constant. If the maximum angular displacement is θ_m, then $C = -2\omega^2\cos\theta_m$ since $\dot\theta = 0$ at this point. Taking the square root, (5.11) then becomes

$$\dot\theta = \omega\,\sqrt{2\,(\cos\theta - \cos\theta_m)} = 2\,\omega\,\sqrt{\sin^2(\theta_m/2) - \sin^2(\theta/2)}, \tag{5.12}$$

on using the trigonometric identity $\cos\theta = 1 - 2\sin^2(\theta/2)$. Separating variables, assuming that $\theta = 0$ at $t = 0$ and integrating, and finally solving for $\theta(t)$, yields

$$\theta(t) = 2\arcsin(k\,\mathrm{JacobiSN}(\omega\,t, k)), \tag{5.13}$$

for the pendulum solution, where $k \equiv \sin(\theta_m/2)$ and $\mathrm{JacobiSN}(u, k)$ is the *Jacobian elliptic sine function*. Although the notation varies,[8] the properties of elliptic functions are tabulated in standard reference texts such as Abramowitz and Stegun ([AS72]) or Gradshteyn and Ryzhik ([GR65]). In the limit that $k \to 0$, $\mathrm{JacobiSN}(u, k) \to \sin(u)$.

The pendulum period (time for one complete oscillation) is

$$T = \frac{4}{\omega}\,K(k), \quad\text{where}\quad K(k) \equiv \int_0^{\pi/2}\frac{d\phi}{\sqrt{1 - k^2\sin^2\phi}} \tag{5.14}$$

is called the *complete elliptic integral of the first kind.*

For θ_m sufficiently small that the approximation $\sin\theta = \theta$ can be made, the pendulum equation (5.10) reduces to the SHO equation, the solution (5.13) to $\theta = \theta_m\,\sin(\omega\,t)$, and the period (5.14) to $T = 2\pi/\omega$. For $\theta_m = 60°$ or approximately 1 radian, the error in using this approximation to the period is about 7%, but increases rapidly with increasing θ_m. Taking $\omega = 2\pi$ for convenience, the picture on the left of Figure 5.5 shows the correct period (solid curve) given by Equation (5.14) compared with the SHO approximation (horizontal dashed curve) over the maximum angular range 0 to π radians. As $\theta_m \to \pi$, the period approaches infinity. Classically, if the pendulum is standing on end, it will take an infinite time to move if not perturbed. Minimizing frictional forces as much as possible, the period formula (5.14) is readily verified for large θ_m in the laboratory with merely a stopwatch. See, e.g., Experimental Activity 11 in ([EM00])).

The solid curve on the right of Figure 5.5 shows the pendulum solution (5.13) for $\theta_m = 175°$, the period being 2.88, while the dotted curve is the SHO approximation.

To this point all frictional forces have been neglected. Let's now include viscous damping, including a drag force given by Stokes's drag law, $\vec F_D = -a\,\vec v$. Noting that $v = L\dot\theta$ along the arc direction, inclusion of $\vec F_D$ in the pendulum equation (5.9) yields

$$m\,L\,\ddot\theta = -m\,g\sin\theta - a\,L\,\dot\theta, \tag{5.15}$$

or, on setting $a/m = \gamma$,

$$\ddot\theta + \gamma\,\dot\theta + \omega^2\sin\theta = 0. \tag{5.16}$$

---

[8]A common notation is to suppress the argument k and write the elliptic sine function as $\mathrm{sn}(u)$. It should also be noted that, because they are related to the elliptic integral, elliptic function solutions are not "closed-form" solutions.
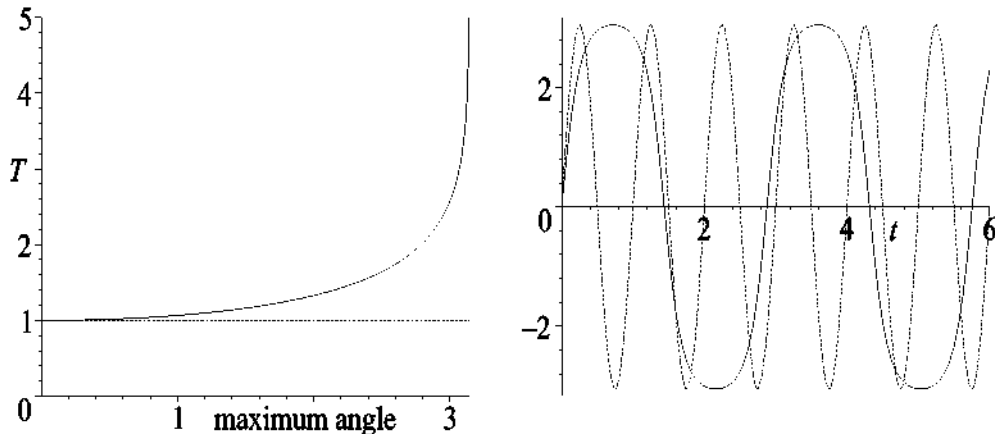
Figure 5.5: Pendulum (solid) vs. SHO (dash). Left: period. Right: solution.

In the small angle approximation, $\sin\theta \approx \theta$, this nonlinear ODE reduces to the linear damped SHO equation. Unlike for the damped SHO, a closed form analytic solution of Equation (5.16) doesn't exist, and the ODE must be solved numerically. Phase-plane analysis is a useful mathematical tool for determining all possible solutions of (5.16) as the parameters γ and ω are varied. This is illustrated in the following example.

Example 5-5: Phase-Plane Analysis of the Damped Pendulum

Locate and identify all the fixed points of the damped pendulum equation (5.16) and discuss what types of solutions can occur as γ is varied for fixed ω.

Solution: Setting $\dot{\theta} = y$, Equation (5.16) may be rewritten as

$$\dot{\theta} = y \equiv P(\theta, y), \quad \dot{y} = -\gamma\, y - \omega^2 \sin\theta \equiv Q(\theta, y),$$

which has fixed points at $y = 0$ and $\theta = n\,\pi$, with $n = 0, \pm 1, \pm 2, \ldots$.

To identify the fixed points, let's calculate the relevant partial derivatives, viz.,

$$\partial P/\partial\theta = 0, \quad \partial P/\partial y = 1, \quad \partial Q/\partial\theta = -\omega^2 \cos\theta, \quad \partial Q/\partial y = -\gamma.$$

Thus, using the phase-plane notation of Chapter 2,

$$a = 0, \quad b = 1, \quad c = -\omega^2 \cos(n\,\pi) = -\omega^2(-1)^n, \quad d = -\gamma,$$

so

$$p = -(a + d) = \gamma \geq 0, \quad q = a\,d - b\,c = \omega^2(-1)^n, \quad \text{and } p^2 - 4q = \gamma^2 - 4\,\omega^2(-1)^n.$$

For $\gamma = 0$ (no damping), we have $p = 0$ and $q = \omega^2 > 0$ for even integer values of n and $q = -\omega^2 < 0$ for odd integer values. Making use of Poincaré's theorem, the fixed points for even integer n are vortices, while saddle points occur for odd integer n. The vortex points correspond to the motionless pendulum hanging vertically downwards, the saddle

points to the pendulum standing vertically on end. In the vicinity of a vortex point, the trajectories are closed loops as expected for the cyclic motion discussed earlier.

As the damping coefficient γ is increased from 0, a bifurcation takes place, since then $p = \gamma > 0$. Saddle points remain saddle points, but the vortices turn into stable focal points, provided $p^2 - 4q < 0$, i.e., $\gamma < 2\omega$. This is the *underdamped* case in the jargon of classical mechanics.

As γ is further increased another bifurcation takes place, the stable focal points turning into stable nodal points for $\gamma \geq 2\omega$. This is *overdamping*. Figure 5.6 shows a phase plane portrait with two representative trajectories for the underdamped case ($\gamma = 1$, $\omega = 1$) and the corresponding $\theta(t)$.
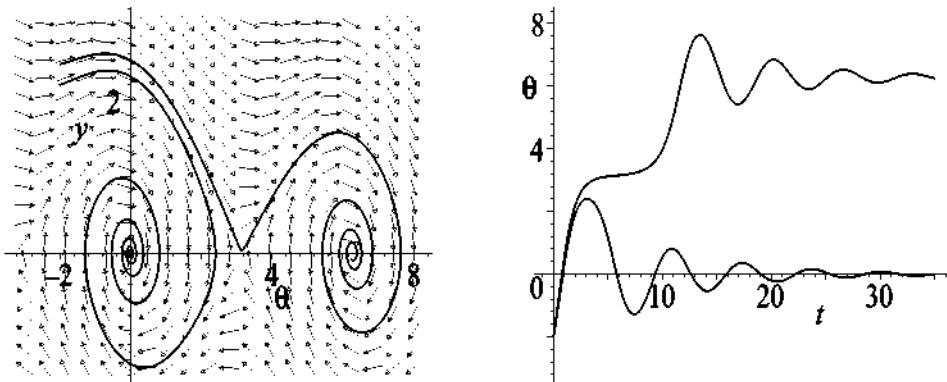
Figure 5.6: Left: Phase-plane portrait for underdamping. Right: Corresponding $\theta(t)$.

Both trajectories have the same initial angle $\theta(0) = -2$ rad, but different initial angular velocities. For $y(0) \equiv \dot\theta(0) = 2.20$ rad/s, the trajectory winds onto the stable focal point at the origin. On the other hand, for $y(0) = 2.47$ rad/s, the angular velocity is sufficiently large that although the pendulum slows down near the top of its arc (approaches close to the saddle point at $\theta = \pi$, $y = 0$), it goes over the top once before approaching the stable focal point at $\theta = 2\pi$, $y = 0$. If the initial velocity is increased further, the pendulum can go over the top more than once before asymptotically approaching the equilibrium position with the pendulum rod hanging vertically downwards.

<div align="center">***</div>

The decay of the oscillations for the damped pendulum can be overcome by applying a periodic driving force. The equation of motion (5.16) is generalized to

$$\ddot\theta + \gamma\dot\theta + \omega^2 \sin\theta = F_d \cos(\omega_d t), \tag{5.17}$$

where F_d is the driving force amplitude and ω_d the driving frequency. The nature of the oscillations that can then occur is sensitive to the coefficient values as well as the initial conditions. Here is a representative example.

Example 5-6: Forced Oscillations of the Damped Pendulum

Given that $\gamma = 0.5$, $\omega = 1$, $F_d = 1.51$, $\omega_d = 2/3$, and $\theta(0) = \dot{\theta}(0) = 0$, numerically solve Equation (5.17) for $\theta(t)$ over the time interval $t = 500$ to 700 and plot the result. Discuss the nature of the forced oscillations. What happens when the driving force amplitude is decreased slightly to $F_d = 1.50$?

Solution: Using the RKF45 method, the numerical solution for $F_d = 1.51$ is shown on
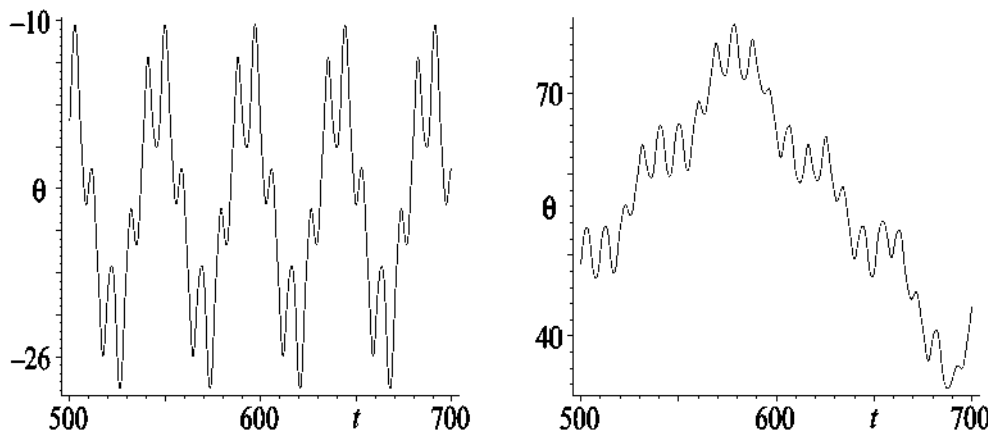
Figure 5.7: Periodically driven pendulum. Left: $F_d = 1.51$. Right: $F_d = 1.50$.

the left of Figure 5.7. The oscillations are periodic, the repetition interval being about 47.1. Since the driving period is $T_d = 2\pi/\omega_d = 9.425$, the period of the response is about 5 times this value, indicating a period-5 solution. When F_d is decreased to 1.50, the forced oscillations are as shown on the right of Figure 5.7. There is no readily observed periodicity to the oscillations, suggesting that the response is chaotic. This can be confirmed by taking a larger time interval and going to a large enough time to make sure any transient has been eliminated.

<div align="center">***</div>

On a historical note, while working on the design of the pendulum clock, the Dutch scientist Christian Huygens observed in 1666 that when he placed two such clocks on a wall near each other and swung the pendulums at different rates, they would eventually end up swinging at the same rate, i.e., have the same period. This synchronization phenomenon is called *entrainment* and applies to not only pendulum clocks but also to a wide variety of coupled oscillators, including those of the biological kind.

For example, individual pulsing heart cells will begin beating in synchrony when brought close to each other (the basis for electronic heart pacemakers), groups of fireflies will synchronize their flashing as part of their mating ritual, the human sleep–wake cycle has been entrained by the night–day light cycle which is governed by the rotation of the Earth,[9] and women who live in the same household will often find that their menstrual cycles will coincide.

---

[9]Such environmental time cycles are referred to as *Zeitgebers* (German for "time givers").

5.3.2 Parametric Excitation

Now suppose that the pivot point O of the undamped simple pendulum is jiggled up and down vertically as in Figure 5.8, its displacement at time t being $A \sin(\Omega t)$. This simple physical action will generate an equation of motion that cannot be solved analytically.
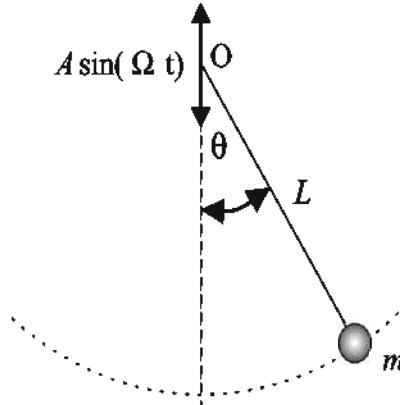
Figure 5.8: Pendulum with vertically oscillating pivot point.

To determine the relevant nonlinear ODE, it is more convenient to use Lagrange's equation of motion ([FC86]) for the *Lagrangian* $\mathcal{L} = T - V$,

$$\frac{d}{dt}\left(\frac{\partial \mathcal{L}}{\partial \dot{\theta}}\right) - \frac{\partial \mathcal{L}}{\partial \theta} = 0. \tag{5.18}$$

Here, T is the kinetic energy and V the potential energy. Taking the origin at the bottom $(\theta = 0)$ of the arc, the Cartesian coordinates of the mass m are

$$x = L \sin\theta, \quad y = L\left(1 - \cos\theta\right) + A \sin(\Omega t). \tag{5.19}$$

The potential energy is

$$V = m\,g\,y = m\,g\,L\left(1 - \cos\theta\right) + m\,g\,A \sin(\Omega t), \tag{5.20}$$

while, on making use of $\sin^2\theta + \cos^2\theta = 1$, the kinetic energy is

$$\begin{aligned}
T &= \frac{1}{2}\,m\,\left(\dot{x}^2 + \dot{y}^2\right) \\
&= \frac{1}{2}\,m\,L^2\,\dot{\theta}^2 + \frac{1}{2}\,m\,A^2\,\Omega^2\,\cos^2(\Omega t) + m\,L\,\sin\theta\,A\,\Omega\,\dot{\theta}\,\cos(\Omega t).
\end{aligned} \tag{5.21}$$

Substituting the Lagrangian $\mathcal{L} = T - V$ into Equation (5.18), performing the various derivatives, dividing by $m\,L^2$, and setting $g/L = \omega^2$, we obtain the so-called *parametric excitation* equation of motion,

$$\ddot{\theta} + \left(\omega^2 - \frac{A\,\Omega^2\,\sin(\Omega t)}{L}\right)\sin\theta = 0. \tag{5.22}$$

5.3.3 The Rotating Pendulum

Both the previous examples involved planar motion. Other pendula may involve motion not confined to a single plane such as the *rotating pendulum* shown in Figure 5.9.
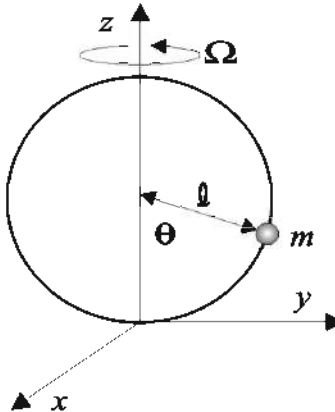
Figure 5.9: The rotating pendulum.

A vertically oriented, frictionless, circular wire of radius ℓ rotates with angular velocity Ω about the z-axis as in the figure. A point mass m is allowed to slide along the wire. Let's derive the governing equation of motion for the mass, assuming that the plane of the circular wire is oriented along the y-axis at time $t = 0$.

The Cartesian coordinates of the mass are

$$x = \ell \sin\theta \sin(\Omega t), \quad y = \ell \sin\theta \cos(\Omega t), \quad z = \ell (1 - \cos\theta).$$

The potential energy and kinetic energy are

$$V = m g z = m g \ell (1 - \cos\theta),$$

$$T = \frac{1}{2} m \left(\dot{x}^2 + \dot{y}^2 + \dot{z}^2 \right) = \frac{1}{2} m \ell^2 \left(\dot{\theta}^2 + \Omega^2 \sin^2\theta \right).$$

Substituting the Lagrangian $\mathcal{L} = T - V$ into Equation (5.18) and making use of the identity $2\sin\theta \cos\theta = \sin(2\theta)$, the desired equation is

$$\ddot{\theta} + \omega^2 \sin\theta - \frac{1}{2}\Omega^2 \sin(2\theta) = 0,$$

with $\omega = \sqrt{g/\ell}$. This nonlinear ODE must be solved numerically.

Still another interesting pendulum example is the *spherical pendulum* where the mass m is confined to move on the surface of a frictionless sphere. Deriving its equation of motion is left as a problem.

5.4   Nonlinear Springs

In Chapter 2, you were introduced to the "hard" and "soft" spring force laws. The following example illustrates how two linear springs can be combined to form a hard spring.

Example 5-7: A Hard Spring

Consider the spring configuration lying in a horizontal plane shown in Figure 5.10. A mass m is initially connected to two identical stretched linear (spring constant K) springs of length L, their unstretched lengths being $L_0 < L$. The mass, which is free to move on a smooth (negligible friction) horizontal surface, is then pulled away from the equilibrium position a distance x and allowed to oscillate.
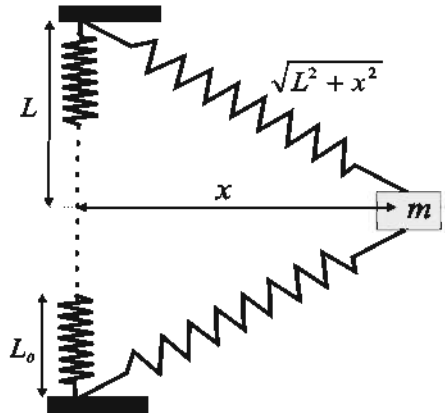
Figure 5.10: Nonlinear spring assembly.

a. Derive the restoring force F on m.

b. Assuming that $x \ll L$, Taylor expand F to order $(x/L)^3$ to obtain the hard spring force law. Estimate the error in neglecting the fifth-order term for $x/L = 1/4$.

c. Determine the period of the oscillations in the hard spring approximation.

Solution: a. Referring to Figure 5.10, when the mass is pulled aside a distance x, each spring is stretched by an amount $d = \sqrt{L^2 + x^2} - L_0$. The potential energy V associated with a linear spring of spring constant K which has been stretched by an amount d is $K d^2/2$. Since two springs are involved here, the total potential energy is twice this amount, i.e., $V = K d^2$. The restoring force F on the mass is then given by

$$F = -\frac{dV}{dx} = -2K \left(1 - \frac{L_0}{\sqrt{L^2 + x^2}} \right) x.$$

b. Assuming that $x \ll L$, we can Taylor expand F to order $(x/L)^3$, yielding

$$F \approx -2K \left(1 - \frac{L_0}{L} \right) x - K \left(\frac{L_0}{L^3} \right) x^3.$$

This is the hard spring force law,

$$F = -k\,x - k_2\,x^3,$$

with

$$k \equiv 2\,K\left(1 - \frac{L_0}{L}\right), \quad k_2 \equiv \frac{K\,L_0}{L^3}.$$

The ratio of the neglected fifth-order term to the third-order term is $(3/4)\,(x/L)^2$. For $x/L = 1/4$, the error in neglecting the fifth-order term is less than 5%.

c. Applying Newton's second law, the equation of motion for the mass m is

$$\ddot{x} + \alpha\,x + \beta\,x^3 = 0,$$

with $\alpha = k/m$ and $\beta = k_2/m$. To determine the period of the oscillations, let's use the same mathematical approach as for the simple pendulum ODE. Multiplying the second-order nonlinear ODE by $2\,\dot{x}\,dt$ and integrating yields

$$\dot{x}^2 + \alpha\,x^2 + \frac{\beta}{2}\,x^4 = E,$$

where the integration constant E is proportional to the total energy. If m is initially pulled out a distance $x = A$ and released from rest $(\dot{x} = 0)$, then $E = \alpha\,A^2 + (\beta/2)\,A^4$. Then, taking the positive square root, the above ODE becomes

$$\frac{dx}{dt} = \sqrt{\alpha\,(A^2 - x^2) + \frac{\beta}{2}\,(A^4 - x^4)} \equiv f(x).$$

Separating variables and integrating, the period is

$$T = 2\int_{-A}^{A} \frac{dx}{f(x)} = 4\,\frac{\mathrm{K}\left(\dfrac{\sqrt{\beta\,A^2/2}}{\sqrt{\alpha + \beta\,A^2}}\right)}{\sqrt{\alpha + \beta\,A^2}},$$

where K is the complete elliptic integral of the first kind.

<div align="center">***</div>

By taking the mass m to be an airtrack glider on a linear airtrack, one can actually create an experimental setup similar to that in Figure 5.10. By measuring the period of oscillations with a stopwatch, the theoretically predicted period T for the hard spring approximation can be confirmed.

In the above example, a specific form for the nonlinear restoring force was derived and a Taylor expansion applied for small displacements from equilibrium. Let's now look at a *general* restoring force $F(x)$ for a mechanical system undergoing small vibrations about its equilibrium position $x = 0$. Taylor expanding $F(x)$ about $x = 0$ yields

$$F(x) = F_0 + \left(\frac{dF}{dx}\right)_0 x + \frac{1}{2!}\left(\frac{d^2F}{dx^2}\right)_0 x^2 + \frac{1}{3!}\left(\frac{d^3F}{dx^3}\right)_0 x^3 + \cdots. \tag{5.23}$$

In equilibrium, $x = 0$ and the restoring force must also be zero, so $F_0 = 0$. Hooke's law, $F = -k\,x$ with spring constant $k = -(dF/dx)_0$, follows on neglecting quadratic and higher terms in x.

If the oscillations are symmetric about $x = 0$, then all even power terms in x must be omitted, because they do not change sign as x changes from positive to negative values. If terms of order x^5 and higher can be neglected, we have $F(x) = -k\,x - k_2\,x^3$ with $k_2 = -(1/3!)\left(d^3F/dx^3\right)_0$. We have just seen an example of a "hard" spring $(k_2 > 0)$. Both hard and "soft" $(k_2 < 0)$ oscillations can be produced experimentally (see [EM00]) with an *inverted pendulum* [10] (also called an *Euler strut*).

If the oscillations are asymmetric, some terms involving even powers of x must be present. For example, neglecting terms of $O(x^3)$ and higher, then $F(x) = -k\,x - \beta\,x^2$, with $\beta = -(1/2!)\left(d^2F/dx^2\right)_0$. For $k > 0$ and $\beta > 0$, the magnitude of the restoring force for $x > 0$ is larger than for $x < 0$, so the amplitude of the oscillations is different on opposite sides of the equilibrium position.

Simple nonlinear spring models are often the starting point for at least qualitatively understanding more complex situations in the physical and biological world. Two different examples illustrate the point.

The nonlinear nature of the ear has been known from the time of Helmholtz ([Hel95]) but it has only been in modern times that a physiologically correct explanation of the workings of the inner ear has been developed. If the input sound wave contains two tones or frequencies f_1 and f_2, the ear generates additional tones which are combinations (called *combination tones*) of these frequencies. In particular, the *cubic difference tone* $2f_1 - f_2$ is audible to the normal human ear as well as other test animals (e.g., guinea pigs ([AMS+98])). If, for example, the two input frequencies are $f_1 = 1000$ Hz and $f_2 = 1200$ Hz, the cubic difference tone is $2f_1 - f_2 = 800$ Hz. As the name suggests, the cubic difference tone can arise if a cubic nonlinearity is present.

Example 5-8: Cubic Difference Tone

If the input is $x = \cos(\omega_1 t) + \cos(\omega_2 t)$, show that if the response is proportional to x^3, the cubic difference tone $2\omega_1 - \omega_2$ is present in the output. Discuss the result.

Solution: Expanding x^3 and using the trig identities $\cos^3\theta = (3\cos\theta + \cos 3\theta)/4$, $\cos^2\theta = (1 + \cos 2\theta)/2$, and $\cos\theta_1 \cos\theta_2 = [\cos(\theta_1 - \theta_2) + \cos(\theta_1 + \theta_2)]/2$, we obtain

$$
\begin{aligned}
x^3 &= (\cos(\omega_1 t) + \cos(\omega_2 t))^3 \\[4pt]
&= \cos^3(\omega_1 t) + 3\cos^2(\omega_1 t)\cos(\omega_2 t) + 3\cos(\omega_1 t)\cos^2(\omega_2 t) + \cos^3(\omega_2 t) \\[4pt]
&= \frac{9}{4}\cos(\omega_1 t) + \frac{9}{4}\cos(\omega_2 t) + \frac{3}{4}\cos((2\omega_1 - \omega_2)\,t) + \frac{3}{4}\cos((2\omega_1 + \omega_2)\,t) \\[4pt]
&\quad + \frac{3}{4}\cos((2\omega_2 - \omega_1)\,t) + \frac{3}{4}\cos((2\omega_2 + \omega_1)\,t) + \frac{1}{4}\cos(3\omega_1 t) + \frac{1}{4}\cos(3\omega_2 t).
\end{aligned}
$$

The cubic difference tone $2\omega_1 - \omega_2$ is present. Other combination tones are possible in

---

[10] A stiff but flexible metal strip is clamped at its bottom end and allowed to undergo transverse vibrations at its top end.

principle along with third harmonics of the input frequencies. A detailed mathematical model of the ear is necessary to explain what output frequencies have sufficiently large amplitudes to actually be heard.

$$***$$

The previous example was of the hand-waving variety. Here's a quantitative example which illustrates the occurrence of cubic difference tones for a damped hard spring which is driven by a forcing term containing two different frequencies.

Example 5-9: Cubic Difference Tones for the Driven Hard Spring

Consider the forced hard spring ODE

$$\ddot{x} + \gamma \dot{x} + \alpha x + \beta x^3 = F_1 \cos(\omega_1 t) + F_2 \cos(\omega_2 t).$$

Taking $\gamma = 0.2$, $\alpha = 1$, $\beta = 1/4$, $\omega_1 = 1$, $F_1 = 0.2$, $\omega_2 = 1.2$, $F_2 = 0.2$, and the initial condition $x(0) = 0.25$, $\dot{x}(0) = 0$, numerically solve the ODE and plot the power spectrum. Interpret the result.

Solution: Using *Maple* or *Mathematica*, the ODE is solved using the adaptive step RKF45 method. To eliminate any transient behavior, the points for plotting are taken after the time $t = 50\pi$. The x values are sampled in time steps $\Delta t = \pi/2$ up to $t = 5050\pi$, i.e., 10000 values are used. The discrete Fourier transform $F(\omega)$ of these x values is then calculated. The power spectrum then is $S(\omega) = |F(\omega)|^2$. To emphasize any small peaks in the spectrum, we will plot $\sqrt{S}$, the result being shown in Figure 5.11.
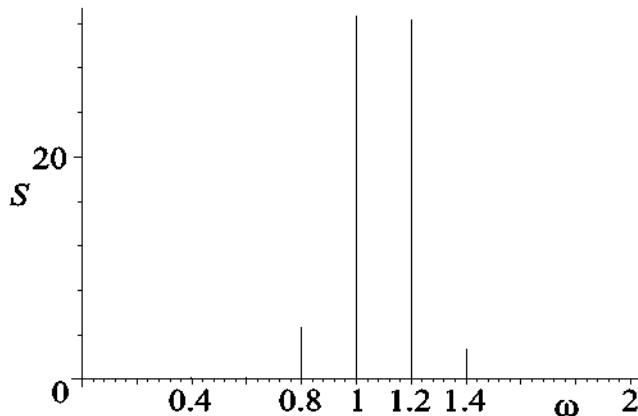
Figure 5.11: Power spectrum.

The two tallest spikes are at the input frequencies $\omega_1 = 1$ and $\omega_2 = 1.2$. In addition, two smaller peaks are clearly visible, located at the cubic difference frequencies $2\omega_1 - \omega_2 = 0.8$ and $2\omega_2 - \omega_1 = 1.4$.

$$***$$

5.4.1   Lattice Dynamics

Turning now to the world of solid-state physics, as early as 1914 the Dutch physicist Peter Debye pointed out that inclusion of some nonlinearity in the atomic forces is necessary if one is to understand at a more fundamental level the phenomenon of heat conduction in solids and the related zeroth law of thermodynamics. The zeroth law is a statement that for an isolated system an initially nonuniform temperature distribution will eventually evolve into a uniform temperature throughout the system.

Considering N identical, equally spaced, atoms arrayed on a 1-dimensional lattice, suppose that the interactive forces are sufficiently short range that only nearest-neighbor interactions need be considered. If the forces are given by Hooke's law, the vibrations of the atoms about equilibrium are then governed by a system of N coupled simple harmonic oscillator equations whose solution may be decomposed into N *normal modes*. It is well-known in classical mechanics that if, for example, all the energy resides in one of these modes, the energy will remain in that mode for all times. To have an energy exchange between modes, as required for heat flow, it is essential that additional nonlinear contributions to the force law be included.

The mathematical development of this idea had to wait until the era of the digital computer. After being used for the development of the atomic bomb, the Maniac I computer at Los Alamos was applied to the zeroth law problem in the early 1950s by the Nobel physics laureate Enrico Fermi and his collaborators, John Pasta and Stan Ulam (the trio hereafter referred to by the initials of their last names, i.e., FPU) ([FPU65]).

Using the Maniac I, FPU numerically solved Newton's equations of motion for $N = 64$ atoms (each of mass m), considering only nearest-neighbor interactions, and the "nonlinear spring" restoring forces,

$$F(x) = -m\,\omega^2\,x - \alpha\,x^2, \quad \text{and} \quad F(x) = -m\,\omega^2\,x - \beta\,x^3, \tag{5.24}$$

where x is the relative displacement of nearest neighbors from equilibrium, ω is frequency, and α and β are positive constants. The FPU numerical experiment was intended to verify that the introduction of small nonlinearities in the force law would ultimately lead to an equipartition of energy among the modes of the isolated coupled oscillators, i.e., energy would flow from one mode to another until all modes would have the same energy in a time-averaged sense. The evolution toward this equilibrium is expected from the zeroth law of thermodynamics. Much to their surprise, FPU found that energy fed into one of the low-frequency (long wavelength) modes didn't flow to the higher-frequency modes, but was only exchanged among a small number of low frequency modes, before flowing back almost exactly to the initial state. This counterintuitive result was referred to as the *FPU anomaly*.

Resolving the FPU anomaly is beyond the scope and level of this text, the interested reader being referred to a Los Alamos review article by David Campbell ([Cam87]) and the text *Theory of Nonlinear Lattices* ([Tod89]) by Morikazu Toda. Toda was able to study the FPU anomaly analytically, rather than numerically, by considering a lattice (referred to as the *Toda lattice*) described by the nearest-neighbor force,

$$F(x) = a\,(e^{-b\,x} - 1), \tag{5.25}$$

with the product $a\,b > 0$. Taylor expanding $F(x)$ for small x and keeping the first two terms in the expansion yields

$$F(x) = -a\,b\,x + (a\,b^2/2)\,x^2. \tag{5.26}$$

For $a < 0$ and $b < 0$, this is just the first (asymmetric) force law in Equation (5.24) explored by Fermi, Pasta, and Ulam.

Research still continues on the problem of heat conduction in FPU-like lattices in one and two dimensions. For a survey of what progress has been made and what issues are still open, you are referred to the review paper ([LLP05]) by Stefano Lepri et al.

5.5 Hysteresis and Jumps Revisited

In Chapter 2, we illustrated hysteresis and the jump phenomena with a simple mathematical example. As noted there, hysteresis occurs in the real world but in most cases the mathematical development is quite involved. However, the forced Duffing oscillator,

$$\ddot{x} = -2\,\gamma\,\dot{x} - \alpha\,x - \beta\,x^3 + F\,\cos(\omega\,t), \tag{5.27}$$

which can be experimentally tested ([EM00],[EM01]), is amenable to a simple analytic treatment when the nonlinear term is small.

The reader has probably studied the driven SHO equation which is a special case of Equation (5.27) with $\gamma = 0$ and $\beta = 0$. After a transient time interval the SHO responds at the driving frequency ω, the steady-state solution given by

$$x = A\,\cos(\omega\,t), \quad \text{with} \quad A = \frac{F}{(\omega_0^2 - \omega^2)}, \quad \omega_0 = \sqrt{\alpha}. \tag{5.28}$$

When $|A|$ is plotted versus ω for a given force amplitude F, the well-known *linear resonance curve* results with an infinitely high peak at $\omega = \omega_0$. For nonzero damping ($\gamma \neq 0$), the peak is rounded off to a finite value.

An approximate steady-state solution can be generated when $\beta \neq 0$ by using an *iteration procedure*. With $\gamma = 0$ for the moment, a first-order approximation to the steady-state solution is taken to be

$$x_1 = A\,\cos(\omega\,t), \tag{5.29}$$

but with A yet to be determined. To determine A, we generate a second-order solution x_2 by substituting x_1 into the rhs of Duffing's equation, using the trig identity

$$\cos^3(\omega\,t) = [\cos(3\,\omega\,t) + 3\,\cos(\omega\,t)]/4,$$

and integrating twice. This procedure yields

$$x_2 = C_1 + C_2\,t + A_2\,\cos(\omega\,t) + \frac{1}{36}\,\frac{\beta\,A^3}{\omega^2}\,\cos(3\,\omega\,t), \tag{5.30}$$

with C_1 and C_2 arbitrary constants and

$$A_2 = \frac{\left(\omega_0^2 A + \frac{3}{4} \beta A^3 - F\right)}{\omega^2}. \tag{5.31}$$

The $C_2 t$ term (called a *secular term*) grows with time and would destroy the periodicity of the solution if kept. So, we set $C_2 = 0$. Similarly $C_1 = 0$ to avoid the same problem in the next approximation. Also, for x_2 to be consistent with x_1, we take $A_2 = A$, so

$$x_2 = A \cos(\omega t) + \frac{1}{36} \frac{\beta A^3}{\omega^2} \cos(3\omega t), \tag{5.32}$$

with A satisfying the cubic equation

$$\left(\omega_0^2 - \omega^2\right) A + \frac{3}{4} \beta A^3 = F. \tag{5.33}$$

For this iteration procedure to be valid, one must have the third harmonic term in (5.32) much smaller than the harmonic term, i.e., $|\beta A^2/(36\omega^2)| \ll 1$.

What happens when $\gamma \neq 0$? Iteration still yields the form (5.32), but A satisfies

$$\left(\left[\left(\omega_0^2 - \omega^2\right) A + \frac{3}{4} \beta A^3\right]^2 + [2\gamma\omega A]^2\right)^{1/2} = F. \tag{5.34}$$

A *nonlinear resonance curve* results when (5.34) is used to plot $|A|$ versus ω for a given F.

Example 5-10: Nonlinear Resonance Curve

Plot $|A|$ versus ω for $\omega_0 = 1$, $\gamma = 0.2$, $\beta = 0.3$, and $F = 4$. Discuss the result.

Solution: Numerically solving (5.34) for A as a function of ω, and plotting $|A|$, we obtain the nonlinear resonance curve shown in Figure 5.12.
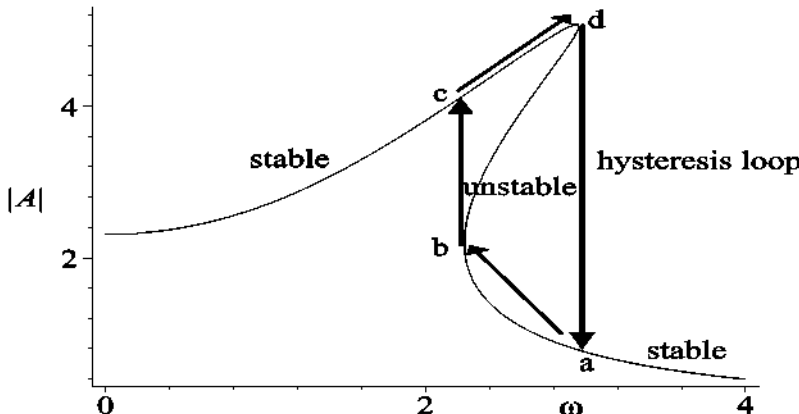
Figure 5.12: Nonlinear resonance curve.

The nonlinear resonance curve tilts to the right (for $\beta < 0$ it would tilt to the left) creating a range of ω where $|A|$ is a triple-valued function of ω. It can be shown (see, e.g., Cunningham ([Cun64])) that the underside of the resonance curve between the two infinite-slope points b and d is unstable. The remaining portions of the resonance curve are stable. Hysteresis can occur as follows. Starting at point a, decrease the frequency so the system moves along the lower stable branch to b. At b, an infinitesimal decrease in ω causes the system to jump vertically to the upper stable branch at c. Then increase the frequency. The system moves along the upper stable branch to d. At d, an infinitesimal increase in ω causes the system to jump vertically downwards to a, completing the hysteresis loop.

***

A hysteresis loop with jumps can also occur if $|A|$ is plotted versus F at a fixed frequency in the multivalued range. This is left as a problem.

The jump phenomena and hysteresis discussed in this section can be observed in mechanical, electrical, and magnetic experiments (see [EM00]).

5.6 Precession of Mercury

The orbit of a planet around the sun can be found to a good approximation by considering the two-body interaction of that planet with the sun through an inverse square law central force. This leads to the familiar closed elliptical orbits of the planets studied in undergraduate physics and engineering classes. However, the presence of other planets causes the orbit to be not quite closed, the apsides slowly rotating or precessing in the plane of the orbit. In the case of the planet Mercury, pictured in Figure 5.13, the pre-
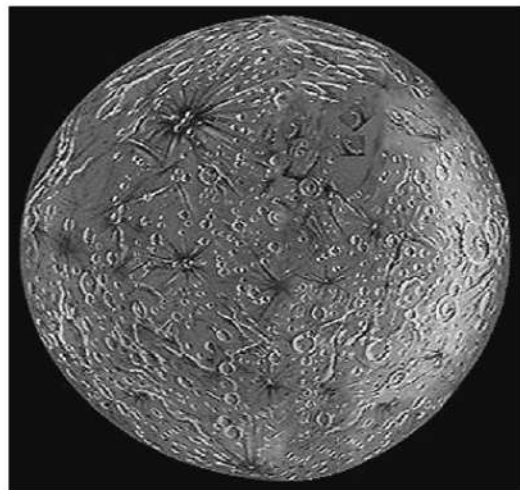
Figure 5.13: NASA photograph of Mercury.

dicted precession is 531 arcseconds per century. However, astronomical observations revealed that the precession was actually 574 arcseconds per century, a discrepancy of 43 arcseconds per century.

The discrepancy was not understood until Albert Einstein introduced his *general theory of relativity* which led to a relativistic correction to the central force law. In the plane of the orbit, the radial distance r of a planet of mass m from the sun (mass $M = 1.99 \times 10^{30}$ kg) is described by ([MT95])

$$\frac{d^2 u}{d\theta^2} + u = -\frac{m}{\ell^2 u^2}\, F(1/u), \tag{5.35}$$

where $u = 1/r$, θ is the polar angle, $\ell = $ constant is the first integral of the motion, and $F(1/u)$ is the force law. Including the relativistic correction, the force is given by

$$F = -G\, m\, M\, u^2 - \frac{3\, G\, M\, \ell^2}{m\, c^2}\, u^4, \tag{5.36}$$

where $G = 6.6726 \times 10^{-11}$ m^3/s^2 kg is the gravitational constant and $c = 3 \times 10^8$ m/s is the (vacuum) speed of light. The first term is the usual gravitational inverse square law, the second is the relativistic contribution.

Setting

$$\frac{1}{\alpha} = \frac{G\, m^2\, M}{\ell^2}, \text{ and } \delta = \frac{3\, G\, M}{c^2}, \tag{5.37}$$

reduces Equation (5.35) to the nonlinear ODE

$$\frac{d^2 u}{d\theta^2} + u = \frac{1}{\alpha} + \delta\, u^2. \tag{5.38}$$

This ODE cannot be solved exactly. However, since $\delta\, u^2 \ll 1/\alpha$, an approximate solution can be obtained as follows. Neglecting the $\delta\, u^2$ term, the first-order approximation to the solution u is $u_1 = (1/\alpha)\, (1 + \epsilon \cos\theta)$, which is easily confirmed by direct substitution. In terms of $r = 1/u$, this is the equation of a conic section [11] with one focus at the origin. The parameter ϵ is the *eccentricity*. For planetary motion $0 < \epsilon < 1$, and the orbit is an ellipse. In this case ([MT95]), $\ell^2 = \mu\, G\, m\, M\, a\, (1 - \epsilon^2)$, where $\mu = m\, M/(m + M)$ is the reduced mass and a is the semimajor axis of the ellipse.

To obtain the second-order approximation to u, we substitute u_1 into the right-hand side of (5.38) and use the trig identity $\cos^2\theta = (1 + \cos 2\theta)/2$:

$$\frac{d^2 u}{d\theta^2} + u = \frac{1}{\alpha} + \frac{\delta}{\alpha^2}\left[1 + 2\,\epsilon\cos\theta + \frac{\epsilon^2}{2}(1 + \cos 2\theta)\right]. \tag{5.39}$$

This equation has the solution

$$\begin{aligned} u = u_2 &= u_1 + \frac{\delta}{\alpha^2}\left[\left(1 + \frac{\epsilon^2}{2}\right) + \epsilon\,\theta\,\sin\theta - \frac{\epsilon^2}{6}\cos 2\theta\right] \\ &= \frac{1}{\alpha}\left[1 + \epsilon\cos\theta + \frac{\delta\,\epsilon}{\alpha}\,\theta\,\sin\theta\right] + \frac{\delta}{\alpha^2}\left[\left(1 + \frac{\epsilon^2}{2}\right) - \frac{\epsilon^2}{6}\cos 2\theta\right]. \end{aligned} \tag{5.40}$$

---

[11]A conic section is formed by the intersection of a plane and a cone.

All the terms in u_2 are periodic (or constant), except for the $\theta \sin \theta$ term which destroys the periodicity of the solution. This secular term prevents the ellipse from closing on each revolution, the perihelion slowly rotating. The angular displacement of the perihelion on each revolution can be determined as follows. Noting that $\delta \theta / \alpha$ is small, one can make use of the approximations $\cos(\delta \theta / \alpha) \approx 1$ and $\sin(\delta \theta / \alpha) \approx \delta \theta / \alpha$. Then, the terms inside the first square brackets of (5.40) become

$$1 + \epsilon \cos \theta + \epsilon \frac{\delta \theta}{\alpha} \sin \theta \approx 1 + \epsilon \left[\cos \left(\frac{\delta \theta}{\alpha} \right) \cos \theta + \sin \left(\frac{\delta \theta}{\alpha} \right) \sin \theta \right]$$

$$= 1 + \epsilon \cos \left(\theta - \frac{\delta \theta}{\alpha} \right).$$

In choosing the form of u_1, we chose to measure θ from the perihelion distance $r_{min} = u_{max}$ at $t = 0$, so the next perihelion will occur when the argument of the cosine term in the last mathematical line is 2π. Thus,

$$\theta = \frac{2\pi}{1 - \delta / \alpha} \approx 2\pi \left(1 + \delta / \alpha \right).$$

So the relativistic term causes an angular displacement of the perihelion in each revolution by an amount

$$\Delta = \frac{2\pi\delta}{\alpha} = 6\pi \left(\frac{GmM}{c\ell} \right)^2 \approx \frac{6\pi GM}{ac^2 (1 - \epsilon^2)}, \tag{5.41}$$

where the approximation $\mu \approx m$ (since $M \gg m$) was made in the last step. Since Mercury has the smallest a and largest ϵ, it has the largest value of Δ of all the planets.

Example 5-11: Calculation of Δ for Mercury

For Mercury, $a = 0.3871$ A.U. (1 Astronomical Unit (A.U.)$=1.495 \times 10^{11}$ m), $\epsilon = 0.2056$, and the time for one revolution is 0.2408 year ([MT95]). Calculate Δ, expressing the answer in arcseconds per century. Discuss the result.

Solution: Substituting the given parameter values into (5.41) yields

$$\Delta = \frac{6\pi \left(6.6726 \times 10^{-11} \right) \left(1.99 \times 10^{30} \right)}{\left(0.3871 \times 1.495 \times 10^{11} \right) \left(3 \times 10^8 \right)^2 \left(1 - 0.2056^2 \right)} = 5.02 \times 10^{-7} \text{ rad/rev}$$

or, on converting to arcseconds,

$$\Delta = \left(5.02 \times 10^{-7} \frac{\text{rad}}{\text{rev}} \right) \left(\frac{180}{\pi} \frac{\text{deg}}{\text{rad}} \right) \left(60^2 \frac{\text{arcsec}}{\text{deg}} \right) \left(\frac{1}{0.2048} \frac{\text{rev}}{\text{yr}} \right) \left(100 \frac{\text{yr}}{\text{century}} \right)$$

$$= 43 \text{ arcseconds/century}.$$

Einstein's relativistic contribution completely accounts for the discrepancy in the astronomical observations.

<div style="text-align:center">***</div>

5.7   Saturn's Rings: A "Toy" Model

Jan Froyland ([Fro92]) has developed what he refers to as a "toy" model of the rings of Saturn. The term "toy" refers to the fact that the model is not intended to capture all the details of the rings which would necessitate numerically solving a large and complex system of nonlinear differential equations. Instead, the model uses a modest amount of physical and mathematical reasoning to create a three-dimensional nonlinear map which can be iterated to generate a planar ring-like structure which resembles the actual rings. A NASA photograph of a segment of Saturn's rings is shown in Figure 5.14, the gaps between rings appearing as black bands.
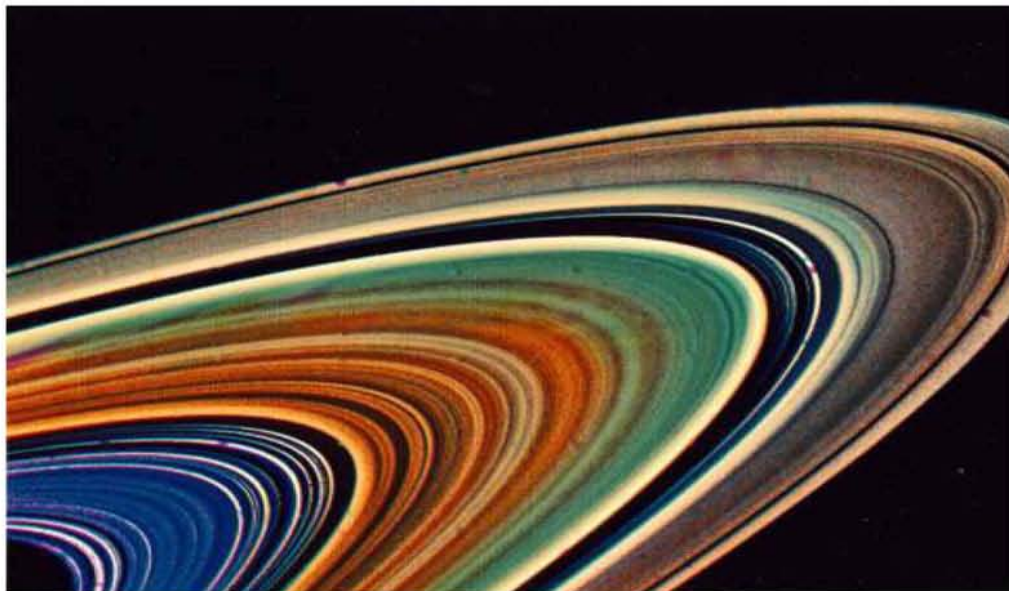
Figure 5.14: NASA photograph of the rings of Saturn.

That the rings are nearly planar follows from the fact that they span a distance of 250 thousand kilometers with a thickness of no more than $1\frac{1}{2}$ km, with some individual rings of the order of tens of meters in thickness.

Developing an accurate model of the rings is not a trivial task because one must not only include the interaction between Saturn and the ring "particles" (ranging in size from a few centimeters to several meters) but also take into account the effects of Saturn's very large number[12] of moons. These moons range in size from tiny Thrymr with a diameter of 5.6 km to Titan whose diameter is nearly a thousand times larger. The moons span a very large distance from Saturn's center, ranging from the innermost moon, Pan, at 133.6 thousand km to the outermost moon, Ymir, at 23.1 million km. Of course, because of their size and/or proximity some moons play a more important

---

[12]For a full listing of Saturn's moons, their distances, sizes, and estimated masses and densities, the reader is referred to the NASA web site.

role in "organizing" certain rings than others. For example, the "shepherd" moons
Prometheus and Pandora herd particles into Saturn's narrow F ring.

Froyland's toy model attempts to describe the formation of Saturn's inner rings from
a uniform radial distribution of particles lying between Saturn's surface ($r_S = 60.4$
thousand km) and the moon Mimas, located at a distance $r_M = 185.6$ thousand km
from Saturn's center. Mimas, the seventh farthest out of the inner moons, has a density
$\rho_M = 1140$ kg/m^3, which suggests that Mimas is made up mainly of ice with only a
small amount of rock. In the oversimplified model, all other moons are neglected, the
system thus consisting of Saturn, Mimas, and the particles. Furthermore, all orbits are
taken to be circular.

First, the effect of Saturn's gravitational force on Mimas and on a representative
particle is considered. Kepler's third law for planetary orbits tells us that for an object
orbiting Saturn (mass M_S) in a circular orbit of radius r, the period T is given by

$$T^2 = \frac{4\pi^2}{GM_S} r^3, \tag{5.42}$$

where G is the gravitational constant.

Now, each time Mimas completes an orbit of radius r_M with period T_M, its angular
position changes by 2π radians. A representative particle at a different radial distance
r_n after the nth orbit will have a different period T_n and thus its angular position will
have changed by a different amount on that orbit from Mimas. The angle (mod 2π)
θ_{n+1} that the particle makes on orbit $n+1$ with respect to Mimus will be related to
the angle θ_n on the nth orbit by

$$\theta_{n+1} = \theta_n + 2\pi\left(\frac{T_M}{T_n}\right) = \theta_n + 2\pi\left(\frac{r_M}{r_n}\right)^{3/2}. \tag{5.43}$$

A second equation is needed for updating the radial distance of the representative par-
ticle as the orbit number increases. This entails looking at the gravitational perturbing
effect of Mimas on the particle which causes its radial distance to change.

If F is the radial component of the gravitational force per unit mass exerted by
Mimas on a particle, by Newton's second law, the particle's radial acceleration is $\ddot{r} = F$.
To solve this ODE numerically, we could replace it on the nth time step with the finite
difference approximation

$$\frac{(r_{n+1} - 2r_n + r_{n-1})}{(\Delta t)^2} = F_n, \tag{5.44}$$

where Δt is the size of the time step. To obtain his second equation, Froyland took
$\Delta t = T_M$, i.e., averaged the radial acceleration over a complete period of Mimas, and
let n refer to the nth orbit. He further took $f_n \equiv T_M^2 F_n$ to be an attractive inverse
square law of the form

$$f_n = -A\frac{\cos\theta_n}{(r_M - r_n)^2}, \tag{5.45}$$

where A is a positive parameter. By symmetry the radial force must be an even function
of θ, the cosine function being just one possible choice.

Putting it all together, Froyland's second equation then is

$$r_{n+1} = 2\,r_n - r_{n-1} - A\,\frac{\cos\theta_n}{(r_M - r_n)^2}. \tag{5.46}$$

If one sets $h_{n+1} = r_n$, we have a 3-dimensional nonlinear map,

$$\theta_{n+1} = \theta_n + 2\,\pi\,\left(\frac{r_M}{r_n}\right)^{3/2},$$

$$r_{n+1} = 2\,r_n - h_n - A\,\frac{\cos\theta_n}{(r_M - r_n)^2}, \quad h_{n+1} = r_n. \tag{5.47}$$

Although A can be estimated if Mimas is the only moon considered, Froyland and Gould and Tobochnik ([GT96]) allowed for a large range of A to account for the omission of other moons and the crudeness of the model. With r_M and r_n expressed in thousands of kilometers, Figure 5.15 shows the ring structure which occurs on iterating Froyland's "toy" model equations for $A = 100$. Particles were inputted in steps of 5 thousand km between 70 and 170 thousand km, 4000 particles per step. To avoid numerical overflow and excessive computing time, particles that "drifted" beyond 350 thousand km were discarded. Particles that "penetrated" Saturn's radius were also rejected as unphysical. The solid black circle in the middle of the picture is Saturn and the outer circle is the orbit of Mimas. The horizontal and vertical lines are the Cartesian coordinate axes $x = r\cos\theta$, $y = r\cos\theta$. The gaps in the rings are clearly evident.
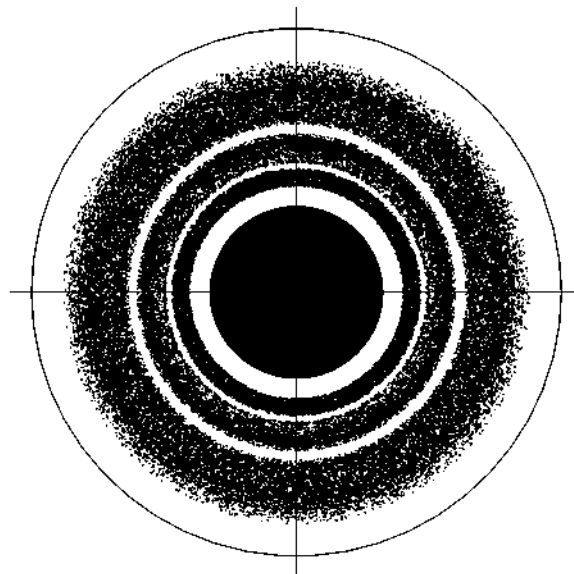
Figure 5.15: Rings of Saturn generated by Froyland's "toy" model.

5.8 Hamiltonian Chaos

One of the frontiers of nonlinear research in classical mechanics is the ongoing study of so-called *Hamiltonian chaos*. As a very simple illustrative example, Hénon and Heiles ([HH64]) considered the two-dimensional motion of a unit mass in the *conservative* (velocity independent and no explicit time dependence) potential,

$$V = x^2/2 + y^2/2 + x^2 y - y^3/3. \tag{5.48}$$

Figure 5.16 shows a contour plot of V, with $V = 0$ (the minimum potential) at $x = y = 0$ and increasing in steps of $\Delta V = 0.03$ up to $V = 0.24$ as one moves away from this point. Three saddle points can be seen in the figure, whose locations can be easily determined.
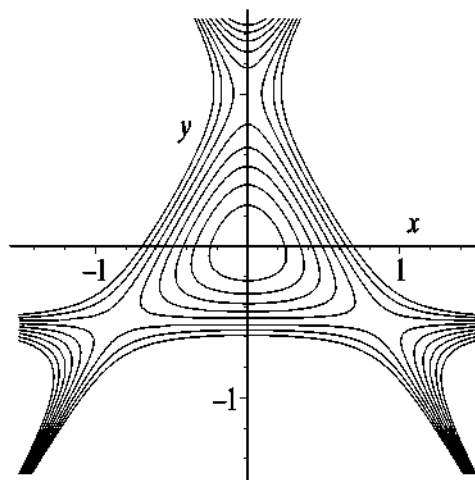
Figure 5.16: Hénon–Heiles potential.

Example 5-12: Saddle Points

Determine the location of the three saddle points and the value of V at these points. As the total energy E is varied, what general conclusion can you reach about the nature of the particle trajectory?

Solution: To locate the extrema (minima, maxima, and saddle points), we set

$$\frac{\partial V}{\partial x} = x + 2xy = 0, \qquad \frac{\partial V}{\partial y} = y + x^2 - y^2 = 0$$

and solve the equations for x and y. This yields the four solutions

$$(x, y) = (0, 0), \quad (0, 1), \quad \left(-\frac{\sqrt{3}}{2}, -\frac{1}{2}\right), \quad \left(\frac{\sqrt{3}}{2}, -\frac{1}{2}\right).$$

The first solution corresponds to the minimum, the other three to the saddle points. At each of the saddle points, $V = 1/6$. If the total energy E of the particle is such that $E < 1/6$, the particle will be trapped inside the potential well and trace out a bounded trajectory. If $E > 1/6$, the particle can escape and wander off to infinity.

$$***$$

Noting that the kinetic energy $T = p_x^2/2 + p_y^2/2$, where p_x and p_y are the x and y momentum components, respectively, the *Hamiltonian* for the motion is given by

$$H = T + V = \frac{p_x^2}{2} + \frac{p_y^2}{2} + \frac{x^2}{2} + \frac{y^2}{2} + x^2 y - \frac{y^3}{3}. \tag{5.49}$$

The Hamiltonian is a constant of the motion, so if $H = E$ is initially specified, the total energy will not change as time progresses. Our interest will be in $E < 1/6$.

With $q_1 = x$ and $q_2 = y$, Hamilton's equations of motion, namely,

$$\dot{q}_i = \frac{\partial H}{\partial p_i}, \quad \dot{p}_i = -\frac{\partial H}{\partial q_i}, \tag{5.50}$$

yield (setting $v = p_x$ and $z = p_y$ for notational convenience)

$$\dot{x} = \frac{\partial H}{\partial p_x} = p_x \equiv v, \quad \dot{y} = \frac{\partial H}{\partial p_y} = p_y \equiv z,$$

$$\dot{v} = \dot{p}_x = -\frac{\partial H}{\partial x} = -x - 2\,x\,y, \quad \dot{z} = \dot{p}_y = -\frac{\partial H}{\partial y} = -y - x^2 + y^2. \tag{5.51}$$

This system of four coupled first-order nonlinear ODEs cannot be solved analytically, so it must be numerically integrated forward in time for given values of $x(0)$, $y(0)$, $v(0)$, and $z(0)$. However, if E is specified, the initial values are not independent. If, say, $x(0)$, $y(0)$, and $z(0)$ are also specified, then $v(0)$ is given by

$$v(0) = \sqrt{2\,E - z(0)^2 - x(0)^2 - y(0)^2 - 2\,x(0)^2\,y(0)^2 + (2/3)\,y(0)^3}. \tag{5.52}$$

The energy constraint $H = E$ defines a 3-dimensional *hypersurface* [13] in the 4-dimensional phase space. The particle trajectory is confined to a 3-dimensional volume in the 4-dimensional space.

Hamilton's equations can be solved numerically for given E, $x(0)$, $y(0)$, and $z(0)$ and the particle trajectory plotted in the 3-dimensional x vs. y vs. z space. If desired, a Poincaré section can be created by taking a planar slice, e.g., $x = 0$, through the 3-dimensional volume.

The following example illustrates the generation of almost periodic (*quasi-periodic*) and chaotic trajectories for the Hénon–Heiles potential.

---

[13] Analogous to the constraint $x^2 + y^2 + z^2 = r^2$, where r is a specified radius, defining a 2-dimensional (spherical) surface in the 3-dimensional x-y-z space.

Example 5-13: Solving Hamilton's equations

Numerically solve Hamilton's equations for $x(0) = -0.2$, $y(0) = -0.2$, $z(0) = -0.06$, and (a) $E = 0.07$; (b) $E = 0.165$. In each case plot x vs. t and the trajectory in the x vs. y vs. z space. Discuss the results.

Solution: Using the constraint condition (5.52), we obtain $v(0) = 0.2589723280$ for $E = 0.07$ and $v(0) = 0.5070174225$ for $E = 0.165$. With all the initial values known, the system (5.51) is numerically solved using *Maple* or *Mathematica*.
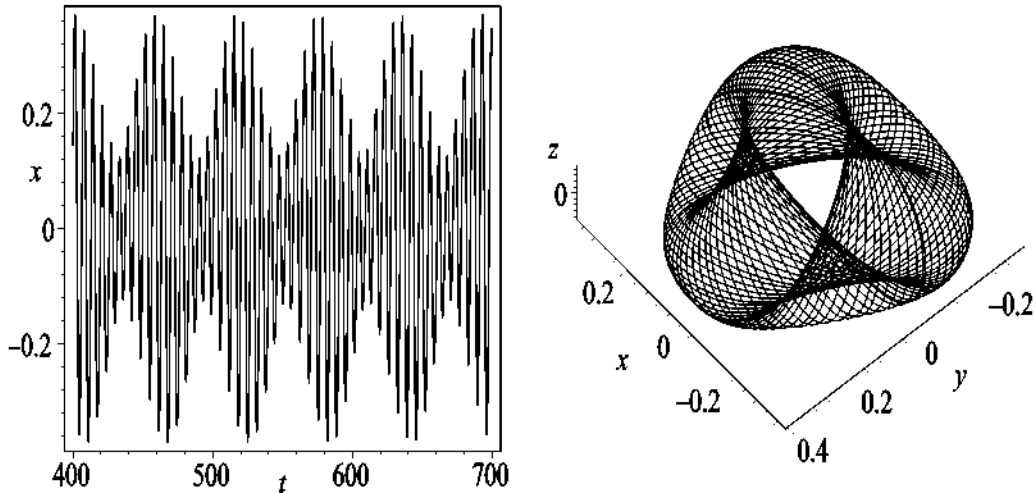
Figure 5.17: Left: x vs. t for $E = 0.07$. Right: Quasi-periodic trajectory.
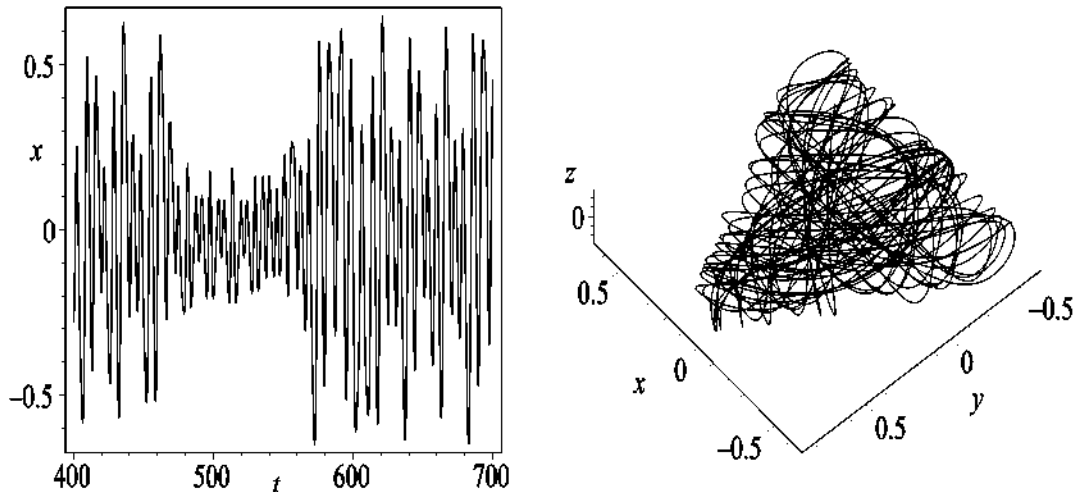
Figure 5.18: Left: x vs. t for $E = 0.165$. Right: Chaotic trajectory.

For $E = 0.07$, x vs. t is as shown on the left of 5.17. The motion is quasi-periodic. The

quasi-periodic trajectory is plotted in the 3-dimensional x vs. y vs. z space on the right of the figure. The trajectory resides on the surface of a twisted torus, commonly known as the *KAM (Kolmogorov–Arnold–Moser) torus.*

The corresponding plots for $E = 0.165$, which is just below the saddle point energy, are shown in Figure 5.18. The trajectory becomes chaotic, resembling a chaotically wrapped ball of yarn when plotted in the 3-dimensional space.

<div align="center">***</div>

PROBLEMS

Problem 5-1: World record swim
At the Beijing Olympics in 2008, Eamon Sullivan of Australia swam the 100-meter freestyle in a world record time of 47.05 seconds. Calculate the Reynolds number for this record-breaking swim, given that Sullivan is 189 cm tall and the viscosity of water is $\eta_{water} = 1 \times 10^{-3}$ N·s/m^2.

Problem 5-2: Reynolds number
Doing a literature/Internet search for representative sizes and speeds, calculate the Reynolds number for worms, bees, eagles, and whatever other moving creature or object that interests you.

Problem 5-3: Stokes's drag law
Consulting Batchelor ([Bat67]) or any other source, present a derivation of Stokes's drag law for a moving sphere.

Problem 5-4: Lift on a Boeing 747
Calculate the lift coefficient for a Boeing 747-200 flying at an altitude of 12 km with an angle of attack of 2.4 degrees.

Problem 5-5: Return speed
A small mass is thrown vertically upwards with an initial speed v_0 near the Earth's surface. If Newton's resistance law applies, show that the speed with which the mass passes its initial position is

$$v_{return} = \frac{v_0 \, v_t}{\sqrt{v_0^2 + v_t^2}},$$

where v_t is the terminal speed.

Problem 5-6: Sliding block
A small block of unit mass slides from rest down a smooth inclined plane which makes an angle θ with the horizontal. If the air resistance on the mass is given by Newton's drag law, $F_{drag} = -b\,v^2$, show that the time T required for the mass to slide a distance d is

$$T = \frac{\cosh^{-1}\left(e^{b\,d}\right)}{\sqrt{b\,g\,\sin\theta}},$$

where g is acceleration due to gravity.

Problem 5-7: Force on a wind turbine blade
Derive Equation (5.8) describing the force of the wind on a wind turbine blade.

Problem 5-8: Betz's limit
Consulting the Internet or any other source (e.g., [Bet66]), derive Betz's limit, stating any assumptions that are made.

Problem 5-9: Horizontal parametric excitation
Derive the equation of motion for a simple pendulum with a horizontally oscillating pivot point.

Problem 5-10: A parametrically excited spider
A small spider clings to the bottom end of a simple pendulum rod of length 1 m whose pivot point at the upper end undergoes vertical oscillations given by $0.1 \sin(\Omega t)$. Numerically solve the equation of motion for $\theta(t)$ for different values of Ω, given $\theta(0) = \pi/3$ radians, $\dot{\theta}(0) = 0$, and $g = 9.8$ m/s^2. Create plots of the spider's trajectory in the x–y phase-plane for each Ω value chosen. In each case, take a sufficiently long time interval that the nature of the spider's trajectory is revealed.

Problem 5-11: Time to descend
An undamped simple pendulum initially makes an angle of 175° with the vertical. If released from rest, how long does it take to descend to $\theta = 25$°?

Problem 5-12: Marble pendulum
Suppose that a solid spherical marble of radius r rolls back and forth without slipping on a circular arc of radius R. Show that the angle θ with the vertical satisfies the simple pendulum equation but with the frequency given by

$$\omega = \sqrt{\frac{5}{7}\frac{g}{(R-r)}},$$

where g is the acceleration due to gravity.

Problem 5-13: Spherical pendulum
A small spider of mass m clings to the lower end of a light connecting rod of length R which can swing freely in all directions from a fixed pivot point at the rod's upper end. Since the spider is constrained to move on a spherical surface, this is an example of a so-called *spherical pendulum*.
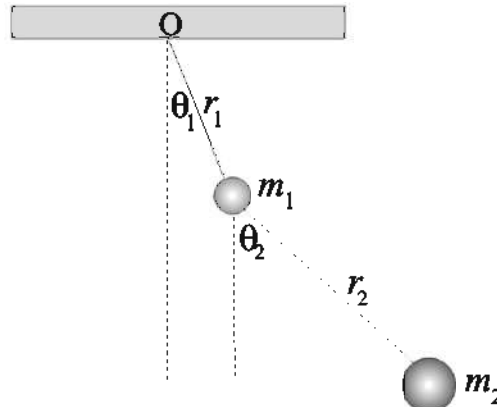
    a. Neglecting all frictional effects and taking the gravitational acceleration to be g, determine the equations of motion in terms of spherical polar coordinates r, θ, ϕ. Take the z-axis to point vertically downwards and let θ be the angle that the rod makes with the z-axis and ϕ the angle that its projection onto the x–y plane makes with the x-axis.

    b. Show that the spider's motion satisfies the nonlinear ODE

$$\ddot{\theta} - \frac{\ell^2 \cos\theta}{m^2 R^4 \sin^3\theta} + \omega^2 \sin\theta = 0,$$

where the constant ℓ is an angular momentum component and $\omega = \sqrt{g/R}$.

Problem 5-14: The double pendulum
The double pendulum consists of two small masses m_1 and m_2, with light connecting rods of lengths r_1 and r_2, free to execute planar motion about the pivot point O. Derive the equations of motion expressed in terms of the angles θ_1, θ_2.

Problem 5-15: Horizontal release of the simple pendulum
Show that for horizontal ($\theta_m = \pi/2$) release of the simple pendulum, the period is

$$T = \left(2\pi\sqrt{\frac{L}{g}}\right)\frac{\sqrt{\pi}}{\Gamma^2(3/4)},$$

where Γ is the Gamma function. How much longer, expressed as a percentage, is the period in this case than given by the small angle approximation?

Problem 5-16: Period of a pivoted meter stick
A meter stick of length L is pivoted at a distance r from its center of mass. Neglecting all frictional effects, show that the period of oscillations of the meter stick is given by

$$T = \left(\frac{2\sqrt{3}}{3}\right)\sqrt{\frac{(L^2 + 12r^2)}{rg}}\,K(k),$$

where g is the acceleration due to gravity and $K(k \equiv \sin(\theta_m/2))$ is the complete elliptic integral.

Problem 5-17: Relating the simple pendulum to the sine-Gordon soliton
Derive the "exact" closed-form solution for the simple pendulum that crosses $\theta = 0$ at time $t = 0$ and has $\theta = -\pi$ at $t = -\infty$ and $\theta = +\pi$ at $t = +\infty$. Relate this solution to the sine-Gordon soliton solution in Chapter 4.

Problem 5-18: Period of oscillation in an anharmonic potential
The simple harmonic oscillator is governed by Hooke's law which is derivable from the simple harmonic potential $U = Ax^2$, viz., the restoring force $F = -dU/dx = -2Ax \equiv -kx$. When the exponent in the potential differs from 2, the potential is referred to as

anharmonic. As discussed in the text, anharmonic potentials are important in discussing large amplitude vibrations of lattices. In this problem, we consider the symmetric anharmonic potential $U = A \mid x \mid^n$, where in general n is not equal to 2.

Show that the period of oscillation of a particle of mass m in this anharmonic potential is given by

$$T = \frac{2}{n} \sqrt{\frac{2\pi m}{E}} \left(\frac{E}{A}\right)^{1/n} \frac{\Gamma(1/n)}{\Gamma(1/2 + 1/n)},$$

where E is the total energy and Γ is the Gamma function. Taking $n = 2$ evaluate the Gamma functions and show that the period reduces to the normal expression for the simple harmonic potential.

Problem 5-19: The standard map
A perfectly elastic ball bounces vertically on a horizontal plate vibrating in the vertical direction with frequency ω and amplitude A. The velocity of the plate at time t is $A \sin(\omega t)$.
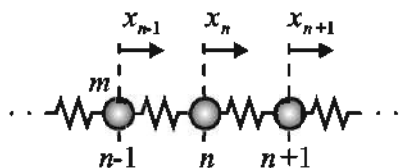
Let v_n be the speed of the ball prior to the nth bounce at time t_n. Neglecting the vertical displacement of the plate relative to the flight of the ball and air resistance, show that the motion of the ball may be described by the so-called *standard map*,

$$v_{n+1} = v_n + 2A \sin\theta_n, \quad \theta_{n+1} = \theta_n + 2\left(\frac{\omega}{g}\right)v_{n+1},$$

where $\theta_n = \omega t_n$ is the phase at the nth bounce.

Problem 5-20: Toda Solitons
Consider the infinitely long 1-dimensional lattice shown in the following figure, consisting of identical atoms of mass m connected by nonlinear springs. The displacement of the nth atom from equilibrium (vertical dashed line in figure) is x_n, and so on. The

Toda force between nearest-neighbor atoms is $F(r) = a\left(e^{-br} - 1\right)$, where r is the relative displacement of adjacent atoms from equilibrium, and the product $ab > 0$.

a. Sketch the Toda potential $V(r)$ for $a, b > 0$ and for $a, b < 0$.

b. Assuming nearest-neighbor interactions only and using Newton's second law of motion, derive Toda's equation of motion,

$$\ddot{y}_n(\tau) = 2e^{-y_n} - e^{-y_{n+1}} - e^{-y_{n-1}},$$

where $y_n \equiv br_n = b(x_{n+1} - x_n)$ and $\tau = \sqrt{(ab/m)}\, t$.

c. Show that Toda's equation of motion admits the solitary wave solution

$$e^{-y_n} - 1 = \beta^2 \operatorname{sech}^2[\kappa(n \pm c\tau)]$$

with $\beta \equiv \sinh \kappa$. Relate the speed c to the parameter κ.

Numerical experiments reveal that the above solitary wave solution is stable against collisions, i.e., is a (lattice) soliton.

Problem 5-21: Wing rock

Elzebda et al. ([ENM89]) have developed the following nonlinear ODE to model the behavior of the roll angle θ for subsonic *wing rock* of slender delta wings:

$$\ddot{\theta} + \gamma(\theta)\dot{\theta} + \omega^2\theta + \beta\theta^3 = 0,$$

with

$$\gamma(\theta) = A + B|\theta| + C|\dot{\theta}|.$$

The coefficients are functions of the angle of attack, α, of the wing. Table 5.3 gives the coefficients for two angles of attack, α_1 and $\alpha_2 > \alpha_1$:

Coefficient	α_1	α_2
ω^2	0.00362949	0.01477963
β	0.051880962	−0.016297021
A	0.00858295	−0.004170843
B	−0.02020694	0.02381943
C	0.0219083	−0.02977157

Table 5.3: Coefficient values for two angles of attack.

At a critical angle of attack, α_{cr}, between α_1 and α_2, the fixed point at the origin loses its stability due to a Hopf bifurcation. The ensuing oscillatory motion about the origin is called *wing rock*.

a. Discuss the structure of the model ODE in terms of nonlinear springs and damping.

b. Determine the fixed points and their stability for each angle of attack.

c. Construct phase-plane portraits for each angle of attack and discuss them.

Problem 5-22: Precessional rates for Earth and Venus

Estimate the precessional rates in seconds of arc per century for

- Earth: $a = 1.0000$ A.U., $\epsilon = 0.0167$, period=1.0000 year;

- Venus: $a = 0.7233$ A.U., $\epsilon = 0.0068$, period=0.6152 year.

How do your estimates compare with the observed rates of 5.0 ± 1.2 for Earth and 8.4 ± 4.8 for Venus?

Problem 5-23: Hysteresis loop

Plot $|A|$ versus F for Equation (5.34), given $\gamma = 0.2$, $\omega_0 = 1$, $\beta = 0.4$, and $\omega = 3$. Take the range of F to be from 0 to 20. You should obtain an S-shaped curve.

If the intermediate portion of the S between the infinite slope points is unstable and the remainder stable, explain how a hysteresis loop can be produced as F is varied.

Problem 5-24: Ballistic coefficient

The *ballistic coefficient* of a moving object is a measure of its ability to overcome air resistance in flight. Basically, it is a measure of the ratio of the kinetic energy of the object to the drag force exerted on it. Perform an Internet search to discuss the ballistic coefficient in detail, including its precise definition and its relevance to

- *bullet drop* of a bullet fired from a handgun or rifle;

- the flight of ballistic missiles;

- satellite reentry.

Note that there are a very large number of web sites run by hunting enthusiasts and gun manufacturers devoted to discussions of the ballistic coefficient.

Problem 5-25: Supersonic flight

The text discussion of the drag on an object moving through air was limited to subsonic (slower than the speed of sound) flight. For supersonic flight, so-called *wave drag* and *shocks* also contribute to the drag. By performing an Internet search, discuss in detail these additional factors. Include in your discussion examples of projectile flight in the supersonic range and the relative importance of the factors contributing to the drag.

A starting point for your search might be the web site:
www.adl.gatech.edu/classes/hispd/hispd03/sources_of_drag.html.

Problem 5-26: Poincaré sections

Construct Poincaré sections in the $x = 0$ plane for the two cases in Example 5-13.

Problem 5-27: Toy model of Saturn's rings

Taking input conditions similar to those in the text, iterate the finite difference equations for the toy model of the rings of Saturn for different values of A and plot the results. Discuss the effect of changing A on the ring structure.

Problem 5-28: Hamiltonian chaos

Consider the potential
$$V = x^2 + y^2/2 + x^4 y - y^3/4.$$

a. Construct a 2-dimensional contour plot for V in the energy range 0 to 0.36. Choose contours that clearly show the spatial behavior of V.

b. Locate the fixed points of V, identify their nature, and evaluate V at those points.

c. Numerically solve Hamilton's equations for $x(0) = -0.1$, $y(0) = -0.2$, $z(0) \equiv p_y(0) = -0.05$, and $E = 0.06$. Plot x vs. t and the trajectory in the x vs. y vs. $z \equiv p_y$ space. Discuss the result.

d. Create a Poincaré section in the $x = 0$ plane.

Problem 5-29: Roll angle of a ship in beam seas

Nayfeh and Khdeir ([NK86a], [NK86b], [NB95]) have modeled the roll angle θ (in radians) of a ship in beam seas [14] with the following nonlinear ODE:

$$\ddot{\theta} + D(\dot{\theta}) + \omega^2 f(\theta) = 0.15 \cos(\Omega t),$$

taking

- $\omega = 0.7037$ rad/s;

- $D(\dot{\theta}) = 0.0455\,\dot{\theta} + 0.2\,\dot{\theta}^3$ (nonlinear damping);

- $f(\theta) = (\theta - \theta_s) - 0.598\,(\theta^3 - \theta_s^3) - 0.939\,(\theta^5 - \theta_s^5)$ (nonlinear restoring force);

- $\theta_s = 0.12963$ rad (bias angle).

Create a phase plane portrait ($\dot{u}$ vs. $u = \theta - \theta_s$) for the following values of the ship–wave encounter frequency Ω and discuss the behavior in each case:

$$\Omega = 0.6260; \quad 0.6200; \quad 0.6130; \quad 0.6117; \quad 0.6116.$$

Problem 5-30: Nonlinear dynamics of ships in broaching

Broaching is a type of ship motion instability which can cause a sudden divergence of the ship from its initial course, sometimes leading to a rapid capsize. Kostas Spyrou has written several research papers on this topic, the article entitled "The nonlinear dynamics of ships in broaching" being available online at:

http://67.20.105.217/annals/volume1/spyrou.pdf.

Using this paper, or any other that you may find, discuss the topic of broaching.

Problem 5-31: Nonlinear dynamics of liquid drop formation

The detailed understanding of drop formation in free-surface liquid flow is not only important from a fundamental physics viewpoint but also from a technological perspective, e.g., in applications such as ink-jet printing, fiber spinning, and silicon chip technology.

A very readable, although lengthy, review paper on the topic is "Nonlinear dynamics and breakup of free-surface flows" by Jens Eggers ([Egg97]). A reprint of this paper is available at:

http://m.njit.edu/~kondic/capstone/2007/eggers_revmodphys97.pdf.

---

[14]In a *beam sea* the waves are moving in a direction approximately 90° to the ship heading.

Discuss the nonlinear dynamics of liquid drop formation, focusing on the main ideas that are presented in Eggers's article.

Problem 5-32: Pedal locomotion

Nonlinear dynamics plays an important role in the pedal locomotion of creatures of all sizes, from centipedes and cockroaches to dogs and cats to humans and robots. A Google search on the topic will turn up many research papers and articles on the subject. Here, e.g., are a few interesting topics with the associated web sites:

- *Biomimetic Control with a Feedback Coupled Nonlinear Oscillator: Insect Experiments, Design Tools, and Hexapedal Robot Adaptation Results*, Stanford Ph.D. thesis of Sean Bailey.

  http://www-cdr.stanford.edu/ baileys/thesis/2004_07_Bailey_thesis %20-%20Biomimetic%20control%20with%20a%20feedback%20coupled %20nonlinear%20oscillator%20-%20Insect%20experiments,%20design %20tools,%20and%20hexapedal%20robot%20adaptation%20results.pdf

- *Worm-like Locomotion as a Problem of Nonlinear Dynamics* by Klaus Zimmermann and Igor Zeidis ([ZZ07]).

  http://www.ptmts.org.pl/zimmer-z-1-07.pdf

- *Nonlinear Dynamical Model of Human Gait* by Bruce West and Nicola Scafetta ([WS03]).

  http://www.fel.duke.edu/ scafetta/pdf/PRE51917.pdf

- *Nonlinear Dynamics of the Human Motor Control* by Gentaro Taga

  http://robotics.mech.kit.ac.jp/amam/amam2000/papers/K02-taga.pdf

- *Adaptive Gait Pattern Control of a Quadruped Locomotion Robot* by Katsuyoshi Tsujita, Kazuo Tsuchiya and Ahmet Onat.

  http://www.kmu-f.jp/katsu/works/iros01.pdf

Select one of the above papers, or any other that you can find on the Internet of interest, and discuss the nonlinear aspects of locomotion.

Chapter 6

World of Sports

Football is not about life or death. It is more important than that.
Bill Shankly, manager of Liverpool (England) football club (1959–1974)

In this chapter, we will show that the motion of various moving objects in the world of sports is governed by nonlinear dynamics. Examples will include, but not be limited to, a curveball thrown by a major league pitcher, a soccer ball (football, outside North America) kicked by a professional footballer, a golf ball hit by a PGA player, auto racing, and archery. We begin by briefly looking at the aerodynamics of sports balls.

6.1 The Aerodynamics of Sports Balls

The sale of sports balls, such as tennis balls and golf balls, is a big business and much research has gone into investigating the aerodynamics of such balls in an attempt to improve their flight characteristics. Figure 6.1, for example, shows a photograph taken by Rabi Mehta of the air flow pattern (revealed with smoke) around a nonspinning tennis ball placed in a wind tunnel at the NASA Ames Research Center.
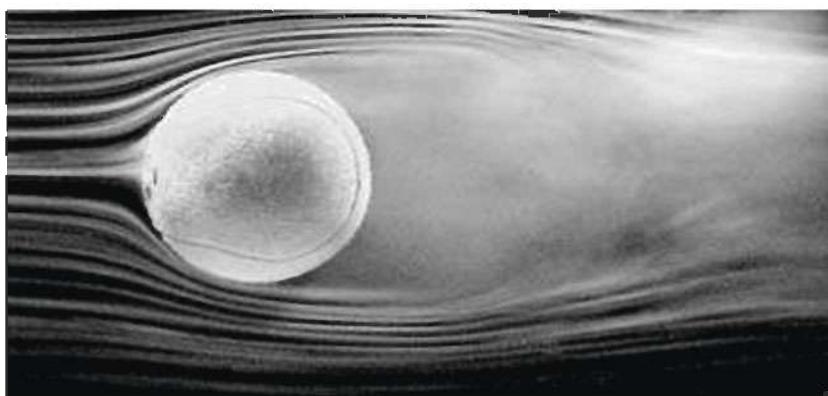
Figure 6.1: NASA photograph of smoke flow past a nonspinning tennis ball.

With the ball moving to the left in the picture, the smooth contours on the front side indicate laminar flow. As one moves toward the backside of the ball, the laminar flow detaches from the surface of the ball, leaving a turbulent *wake* in the rear. For the tennis ball, because of its very rough surface, the wake is as wide as the ball and extends several ball lengths behind it. The size of the wake plays an important role in determining the overall drag on a sports ball. This is because in addition to *skin friction drag* on the ball due to the "sticky" (viscous) nature of the air as it flows over the surface, the pressure differential between the laminar and wake regions creates an additional *pressure drag* which slows the ball down. For the tennis ball it's even more complicated as the "hair" or fuzz on the surface is made up of flexible filaments which change orientation as the speed changes. According to Mehta,[1] the large pressure and fuzz drags are the reason why tennis balls have a much higher drag coefficient ($C_D \approx 0.6$) than other sports balls. What makes the game of tennis interesting, he claims, is that as a game progresses the fuzz wears off, changing the drag coefficient.

Turning to a different sports ball, Figure 6.2 shows a famous wind tunnel photograph[2] taken by Frank Brown of the smoke flow past a dimpled golf ball with backspin.
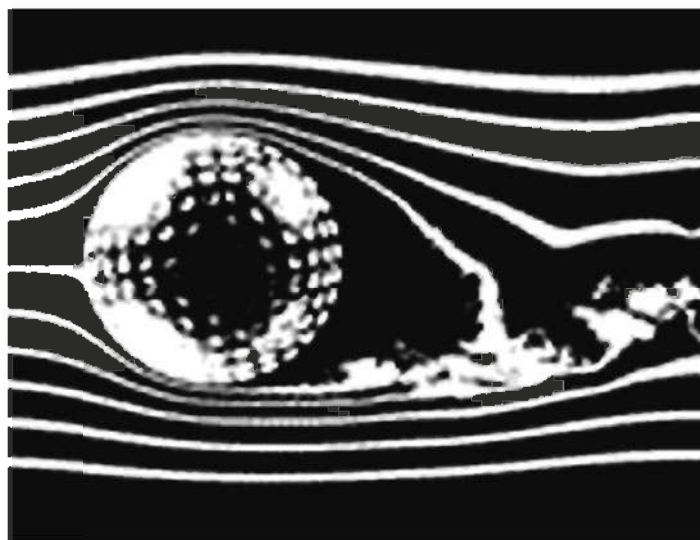
Figure 6.2: Flow over a golf ball with backspin.

As noted in the last chapter, a spinning ball with backspin has a Magnus force upwards, thus causing lift. The presence of this upward force is revealed in the picture by the crowding of the laminar flow lines above the ball relative to those below. I.e.,

---

[1]See **www.nasa.gov/centers/ames/news/releases/2000/00_58AR.html**.

[2]Available at several sites on the Internet. Frank Brown of Notre Dame University was a pioneer in flow visualization and more of his photographs may be found in Mueller ([Mue78]).

the airflow velocity across the top is greater (due to backspin) than across the bottom, a situation which produces a net upward force.

The turbulent wake (which is deflected downwards due to the backspin) behind the golf ball quickly narrows down in comparison to the wake of the tennis ball. This is due to the geometrical arrangement of recessed dimples on the surface of the golf ball. If the dimples were not present, the wake would be much larger and as a consequence so would the pressure drag. Adding the dimples reduces the overall drag so that the golf ball can fly farther than if it were perfectly smooth.

Wind tunnels are not the only way of studying the flight of sports balls. For example, radar guns are routinely used to monitor the speeds of baseball pitches and tennis serves. If you were asked to name in which sport the "ball" has the fastest speed, you might think that it's the baseball or the golf ball or the tennis ball. Actually it's none of these, as Table 6.1 reveals.

Ball	Fastest Speed (mph)
badminton shuttlecock	206
golf ball (drive)	204
pelota ball	188
jai alai ball	188
tennis ball (serve)	155
baseball (hit)	127
hockey puck (slapshot)	105
baseball (pitch)	103
volleyball (spike)	80
ping pong ball (smash)	70

Table 6.1: Fastest speeds of some sports balls (Ref: **www.listafterlist.com**).

Badminton claims to be the fastest racquet ball game in the world and its high listing in the above table certainly lends credence to this claim. But, you have to be a bit careful. From the viewpoint of the player, ping pong or table tennis as a game is much faster than it appears from its lowly listing. This is because the ping pong table is quite short and very fast reflexes are needed to return a smash when playing at the international level. To lengthen the time before returning a smash, the receiving player typically stands far back from the table. This, of course, leaves him or her vulnerable to softer shots which barely make it over the net.

Let us now turn our attention to some specific sports. A more extensive coverage of the role of physics and mathematics in describing the motion of sports balls may be found in Armenti's *Physics of Sports* ([PLA92]) and Palmer's *Physics for Game Players* ([Pal05a]). If you are interested in learning more about the aerodynamics of sports balls you should consult Rabi Mehta's lengthy article ([Meh85]) on the subject.

6.2   Bend It Like Beckham

Over the years, the English international footballer David Beckham has become well-known [3] for the curved trajectory that results when he takes a "free kick" on a stationary soccer ball. A free kick is awarded at the point on the field outside the penalty box [4] at which a player has been fouled by a member of the opposing team. The defenders of the offending team typically line up in a "wall" between that point and the goal so as to make it difficult to make a direct shot on goal. The wall must be a minimum distance of 10 yards from the ball. Skilled players like Beckham [5] are able to create a shot on goal by striking the ball with the outside of their foot so as to put sufficient spin on the ball that the ball bends over or around the wall of defenders.

As qualitatively analyzed in *Physics World* magazine ([Fea98]), an amazing free kick was executed by Roberto Carlos of Brazil in the 1997 Tournament of France, a friendly international football tournament held as a warmup to the 1998 FIFA World Cup [6] held in France. With the ball placed about 30 meters from the opposition goal and slightly to the right of it, Carlos hit the ball so far to the right that it cleared the wall of defenders by over a meter and caused a ball boy standing on the sideline meters from the goal to duck his head. To the astonishment of the media, the players, and particularly the goalkeeper, the ball then curved dramatically to the left and entered the top right-hand corner of the goal.

Qualitatively, what occurred is as follows. Carlos kicked the ball hard with the outside of his left foot to make it spin anticlockwise when looking down on the ball. The ball acquired a speed of about 30 meters per second (70 miles per hour) with a spin of about 10 revolutions per second. The critical value of the Reynolds number was exceeded so that the drag coefficient was low. Somewhere in the vicinity of the defending wall, the ball's velocity dropped sufficiently that the Reynolds number dropped below the critical value. The drag coefficient jumped substantially so the ball slowed even more. As the speed dropped, the sideways Magnus force which was bending the ball toward the goal became increasingly more important, ultimately producing enough of a bend for the ball to enter the goal.

It should be noted that a professional football is not a perfectly smooth sphere. Its surface consists of fairly smooth panels which are stitched together. Traditionally a hexagonal pattern of 26 or 32 panels has been used, but the 2006 World Cup ball designed by Adidas had 14 panels whose shape deviated from the traditional hexagonal pattern. Because of the paneling and stitching, the critical Reynolds number for a football is lower than for a smooth sphere of the same size. Figure 6.3 shows the drag coefficient as a function of Reynolds number for a nonspinning 32-panel football obtained in a wind tunnel experiment by Asai et al. ([ASKS07]).

---

[3] In fact, so well-known that *Bend It Like Beckham* was the title of a 2002 British movie.

[4] The penalty box is a rectangular area 18 yards deep in front of the goal. A foul in this area results in the awarding of a penalty kick from a spot 12 yards from goal.

[5] Another master of the free kick is the Real Madrid (formerly Manchester United) player Christiano Ronaldo, the international footballer of the year in 2008.

[6] The FIFA World Cup, held every 4 years, is a tournament to determine the top soccer nation in the world. Italy was the winner of the 2006 World Cup. The 2010 World Cup competition is in South Africa.
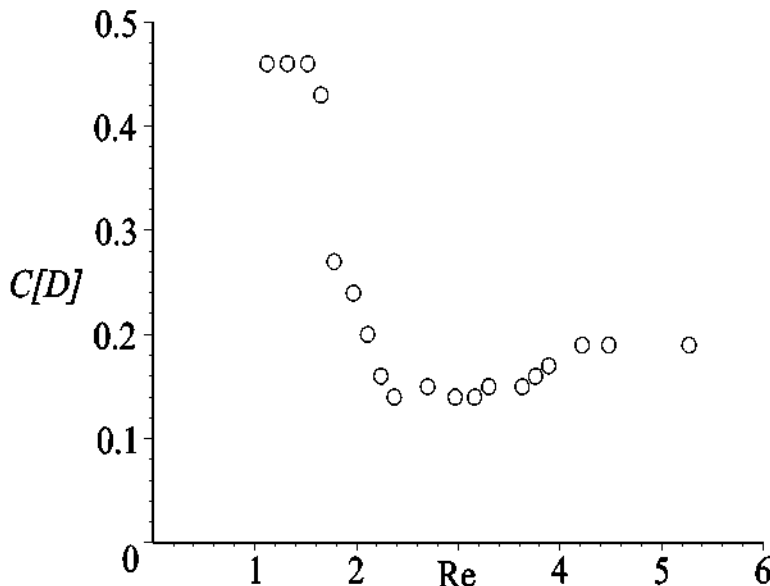
Figure 6.3: C_D versus Re ($\times 10^{-5}$) for a 32-panel football.

The exact shape of the drag curve and the critical Reynolds number varies with the number of panels and the brand of the football. Typically, the critical Reynolds number ranges from about $\text{Re}_{cr} = 2.2 \times 10^5$ to about $\text{Re}_{cr} = 3.0 \times 10^5$. The value of the drag coefficient in the lower plateau region for $\text{Re} > \text{Re}_{cr}$ varies from about 0.19 (for the 32-panel ball) to about 0.21.

Example 6-1: Jump in the Drag Coefficient

The diameter of a professional football is $d = 25.4$ cm. Air at 20°C has a density $\rho_{air} = 1.21$ kg/m^3 and a viscosity coefficient $\eta_{air} = 1.82 \times 10^{-5}$ N·s/m^2. Taking $\text{Re}_{cr} = 3.0 \times 10^5$, show that if Roberto Carlos kicked the ball with a speed of 30 m/s, it doesn't take much of a decrease in speed for the Reynolds number to decrease below Re_{cr} and therefore the drag coefficient to jump substantially.

Solution: Taking the characteristic length L to be the diameter d of the football and $v = 30$ m/s, the Reynolds number is

$$\text{Re} = \frac{\rho_{air}\, d\, v}{\eta_{air}} = \frac{1.21 \times 0.254 \times 30}{1.82 \times 10^{-5}} = 3.4 \times 10^5.$$

A decrease in speed of 12% will lower Re below Re_{cr}.

<div align="center">***</div>

In the following example, an estimate is made of how much Roberto Carlos's kick was bent by the time it reached the goal due to the spin imparted to the ball.

Example 6-2: Estimated Deflection Distance

The Magnus force F_{Magnus} on a football traveling about 30 m/s with a spin of 8 to 10 revolutions/second is about $3\frac{1}{2}$ newtons. If the free kick were taken 30 meters out from the goal and the time t of flight is about 1 second, estimate how much the ball deviates from a straight-line course when it reaches the goal. A professional football must have a mass m of 410 to 450 grams.

Solution: The acceleration a of the ball is given by $a = F_{Magnus}/m$. Since m can vary between 0.41 and 0.45 kg, the acceleration is between 7.8 and 8.5 m/s^2. The sideways deflection Δ of the ball is given by $\Delta = a\,t^2/2$, i.e., between 3.9 and 4.25 meters. A deflection of roughly 4 meters is enough to trouble any goalkeeper!

<div align="center">***</div>

A more precise estimate would involve numerically solving the nonlinear equation of motion for the football taking into account the change in the drag coefficient as the ball slows down. Although an extensive literature exists (see [GC09] and references therein) dealing with the trajectory of a soccer ball, we will look at an easier sports example where the drag coefficient can be taken to be constant throughout the flight of the ball.

6.3   A Major League Curveball

What better example of a nonlinear phenomenon in the real world is there than the curveball thrown in a baseball game by a major league pitcher. This is the true tale of one such pitch thrown by the Boston Red Sox lefthander John Lester in the August 3, 2007, ball game between Boston and the Seattle Mariners. In this tale, both nonlinear drag and lift (Magnus force) play important roles.

To analyze the trajectory of a baseball pitch having a linear velocity $\vec{v}$ and angular
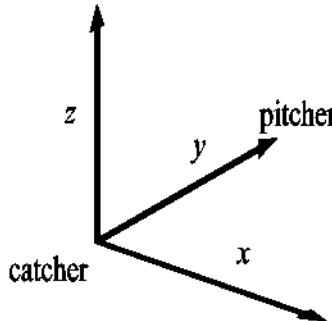
Figure 6.4: Coordinate system for the baseball pitch.

(spin) velocity $\vec{\omega}$, we can introduce a 3-dimensional coordinate system as in Figure 6.4. Home plate is at the origin with the catcher standing behind it, the positive y-axis

points to the pitcher, the positive z-axis points upwards, and the positive x-axis points to the catcher's right. The angular velocity $\vec{\omega}$ of the ball is assumed to lie in the x–z plane and make an angle ϕ with the x-axis, so the angular velocity unit vector

$$\hat{\omega} = \cos\phi\,\hat{x} + \sin\phi\,\hat{z}.$$

When $\phi = 0°$, the angular velocity points along the positive x-axis, and the ball has "topspin." When $\phi = 90°$, $\vec{\omega}$ points along the positive z-axis, and the ball has "sidespin".

Three forces act on the ball during its flight:

- the drag force, $\vec{F}_D = \dfrac{1}{2}\rho\,A\,C_D\,v\,\vec{v}$;

- the Magnus force, $\vec{F}_{Magnus} = \dfrac{1}{2}\rho\,A\,C_L\,v\,(\hat{\omega}\times\vec{v})$;

- the gravitational force, $\vec{F}_G = -m\,g\,\hat{z}$.

Here, ρ is the air density, A is the cross-sectional area of the ball, C_D is the drag coefficient, C_L is the lift coefficient, m is the ball mass, g is the gravitational acceleration, and the speed v of the ball is given by

$$v = \sqrt{v_x^2 + v_y^2 + v_z^2} = \sqrt{\dot{x}^2 + \dot{y}^2 + \dot{z}^2}.$$

For notational convenience, we will set $K \equiv (1/2)\,\rho\,A/m$ in the equations of motion.

Applying Newton's second law of mechanics with the drag, Magnus, and gravitational forces included, yields the following nonlinear ODEs for the (x, y, z) coordinates of the ball at time t:

$$\ddot{x} = -K\,C_D\,v\,\dot{x} - K\,C_L\,v\,\dot{y}\,\sin\phi,$$

$$\ddot{y} = -K\,C_D\,v\,\dot{y} + K\,C_L\,v\,(\dot{x}\,\sin\phi - \dot{z}\,\cos\phi), \qquad (6.1)$$

$$\ddot{z} = -K\,C_D\,v\,\dot{z} + K\,C_L\,v\,\dot{y}\,\cos\phi - g.$$

Example 6-3: Reynolds Number for a Fastball

A major league pitcher can throw a fastball at about 42 m/s (95 miles/hour). A baseball has a diameter $d = 0.073$ m, while air at 20°C has a density $\rho_{air} = 1.21$ kg/m^3 and viscosity coefficient $\eta_{air} = 1.82 \times 10^{-5}$ N·s/m^2. Calculate the Reynolds number and discuss the implication for the drag coefficient.

Solution: The Reynolds number is

$$\text{Re} = \rho_{air}\,d\,v/\eta_{air} = 1.21 \times 0.073 \times 42/(1.82 \times 10^{-5}) = 2 \times 10^5.$$

Because of the stitches in its surface a major league baseball can be treated as a rough sphere for which, recall, $\text{Re}_{cr} = 1 \times 10^5$. Since $\text{Re} > \text{Re}_{cr}$, the drag coefficient $C_D \approx 0.4$.

***

Using the PITCHf/x tracking system to measure the trajectories, the physicist Alan Nathan[7] has analyzed 99 baseball pitches made by Boston Red Sox lefthander John Lester in the August 3, 2007, game against the Seattle Mariners at Seattle's Safeco field. The following example is based on one of Lester's pitches.

Example 6-4: Trajectory of John Lester's Pitch

In non-SI units, Alan Nathan's data for one of Lester's pitches is as follows:

- $g = 32.2$ ft/s^2,

- $K = 5.44 \times 10^{-3}$ ft^{-1},

- $C_D \approx 0.40$ for $v = 90$ mph (132 ft/s),

- $C_L \approx 0.19$ for $\omega = 2000$ rpm,

- $\phi = 170°$.

Taking the initial conditions

- $x(t = 0) = 0$, $y(0) = 60$ ft (distance between home plate and where pitcher releases the ball), $z(0) = 5$ ft (approximate height at which ball is released),

- $v_x(0) = 0$, $v_y(0) = -132$ ft/s (ball thrown in the negative-y direction), $v_z(0) = 0$,

numerically solve the ODE system (6.1). Discuss the effect of drag and lift on the pitch.

Solution: Using the RKF45 algorithm, the numerical solution is shown in Figure 6.5,
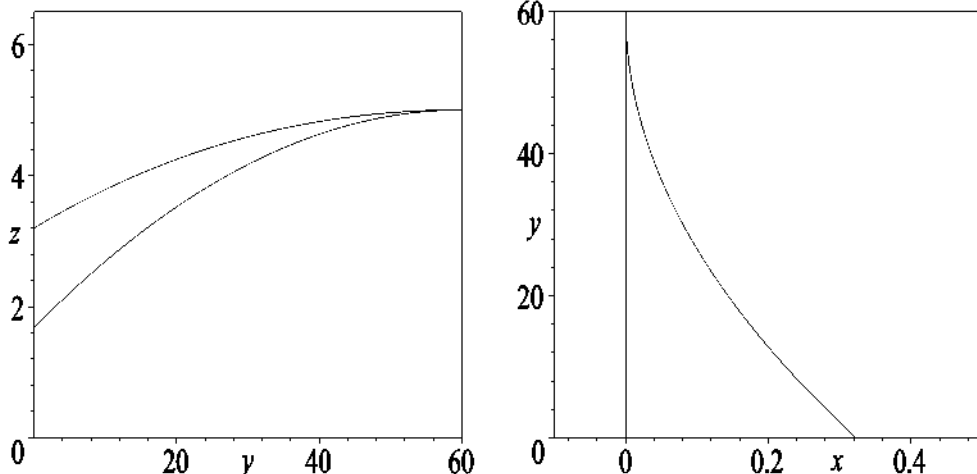
Figure 6.5: Left: bottom curve, no lift or drag; top curve, lift and drag. Right: straight line, no lift or drag; curved line, lift and drag.

---

[7]*Analysis of PITCHf/x Pitched Baseball Trajectories* by Alan M. Nathan, Department of Physics, University of Illinois, Urbana, IL 61801, September 9, 2007.

along with the curves which would result for zero drag and zero Magnus (lift) force. Note that the z and x scales are exaggerated compared to the scale in the y-direction.

Referring to the left picture which shows the height z of the ball versus distance y, the effect of nonlinear drag and lift for this pitch is to cause the ball to drop about 1.5 feet or 18 inches less than it would under the influence of gravity alone as it crosses home plate. Referring to the right picture which shows the deflection x in the horizontal plane versus distance y, the effect of nonlinear drag and the Magnus force is to cause the ball to be deflected about 1/3 feet or 4 inches in the positive x-direction, i.e., to the catcher's right. This particular pitch was a *curveball*, which would break away slightly from a right-hand batter and in to a left-handed hitter. Reducing ϕ from 170° toward 90° increases the deflection, but decreases the rise.

<div align="center">***</div>

If you wish to learn more about the physics of baseball, see Alan Nathan's web site, **http://webusers.npl.illinois.edu/a-nathan/pob**. Examples of topics on this site, with numerous hyperlinks, are:

- aerodynamics of the baseball;

- the effect of spin and spin decay on the flight of a baseball;

- the Pitchf/x system;

- scattering of a baseball by a bat;

- aluminum versus wooden bats;

- vibrational analysis of a bat;

- dynamics of the baseball–bat collision;

- physics and acoustics of bats;

- hitting and pitching mechanics.

Not all topics on Nathan's web site are nonlinear (the central theme of this text), but the site is a rich source for information on the physics of baseball. If you prefer tennis to baseball, there is even a link to research on tennis rackets.

6.4 Golf Ball Trajectory

In elementary physics and engineering classes, the drag and lift on a golf ball are traditionally neglected, the trajectory then being an inverted parabola. In the real world, these effects cannot be ignored. To see what happens we can borrow some of the mathematical modeling that was used in examining the path traveled by the thrown baseball.

Due to the golf club's loft (the angle between the club face and the vertical plane) and parallel grooves, backspin is imparted to almost every shot in golf. Due to the Magnus force, a backspinning ball experiences an upward lift force which makes the

ball fly higher and longer than a ball without spin. If the club face is not oriented perpendicularly to the direction of the swing, sidespin will also occur causing the ball to curve to one side or the other (just like the baseball). In the language of golf, a *hook* is a golf ball trajectory in which the ball starts out to the right, for a right-handed golfer, but then curves drastically back to the left and missing the intended target to the left. (The directions are reversed for a left-handed golfer.) A *slice* is the opposite of a hook.

Quoting from the web site, **golf.about.com/cs/golfterms/g/bldef_hook.htm**, hooks are often the the bane of amateur golfers and, for amateurs, can be tough to straighten out. A popular golf saying is

> *You can talk to a slice but a hook won't listen.*

Well, we will listen and for simplicity assume that the golf ball in our analysis has only backspin ($\phi = 90°$ in the notation of the baseball equations) and that there is no transverse (x) component of initial velocity.

Taking the y direction to be horizontal and in the direction of flight and the z direction to be vertical, we have (from the baseball equations) the following ODE system governing the golf ball trajectory:

$$\ddot{y} = -K\,C_D\,v\,\dot{y} - K\,C_L\,v\,\dot{z},$$

$$\ddot{z} = -K\,C_D\,v\,\dot{z} + K\,C_L\,v\,\dot{y} - g,$$

(6.2)

with $v = \sqrt{\dot{y}^2 + \dot{z}^2}$ the speed, C_D and C_L the drag and lift coefficients, g the gravitational acceleration, and $K = (1/2)\,\rho\,A/m$, with ρ the air density, A the ball's cross-sectional area, and m its mass.

The drag coefficient for a golf ball is shown in Figure 6.6 for a Reynolds number in
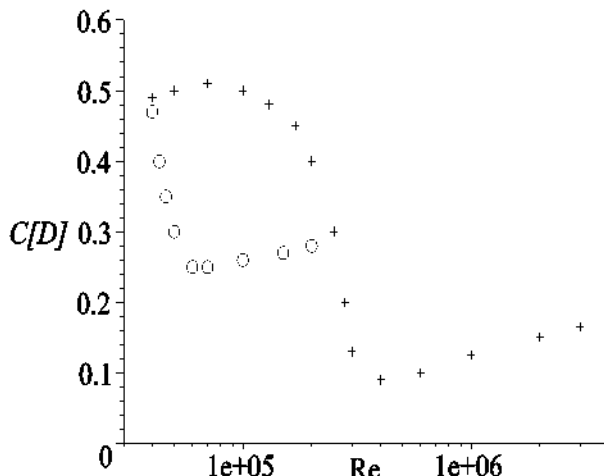
Figure 6.6: Drag coefficient for a dimpled golf ball (circles) and a smooth sphere (crosses). (**www.aerospaceweb.org/question/aerodynamics/q0215.shtml**)

the neighborhood of its critical Reynolds number. The drag coefficient for a smooth sphere is shown for comparison. Note that the horizontal scale is logarithmic with Re

ranging from $= 3 \times 10^4$ to 4×10^6. The critical Reynolds number for the golf ball occurs at a much lower value than for the smooth sphere because of the golf ball's dimpled surface. The golf ball is designed so that for a typical drive, the Reynolds number is such that $\text{Re} > \text{Re}_{cr}$ and the drag coefficient is small. The *Rules of Golf*, adhered to by the U.S. Golf Association, stipulate that the maximum mass of a golf ball can be 45.93 grams and the minimum diameter d can be 42.67 mm.

Example 6-5: Reynolds Number for a Golf Ball Drive

Typically, a golf ball driven off a tee has an initial speed $v(0) \approx 70$ m/s and an initial angle $\theta \approx 16°$ with the horizontal. The density of dry air at 1 atmosphere pressure and $20°C$ is $\rho_{air} = 1.21$ kg/m^3 and the viscosity coefficient $\eta_{air} = 1.82 \times 10^{-5}$ N·s/m^2. Calculate the Reynolds number and use Figure 6.6 to determine C_D for this drive.

Solution: The Reynolds number is $\text{Re} = \rho_{air} v(0) d / \eta_{air} = 1.99 \times 10^5$. From Figure 6.6, the drag coefficient $C_D \approx 0.28$. It should be noted that the spin on a golf ball is typically such that the lift coefficient C_L has about the same value.

<p align="center">***</p>

Example 6-6: Golf Ball Trajectory

Taking $C_D = C_L = 0.28$, $g = 9.81$ m/s^2, $\rho_{air} = 1.21$ kg/m^3, $d = 4.267 \times 10^{-2}$ m, $m = 4.593 \times 10^{-2}$ kg, $v(0) = 70$ m/s, and $\theta(0) = 16°$, numerically solve the golf ball ODE system and plot the trajectory. Approximately how long is the golf ball in the air, assuming level ground? The height of the tee can be taken to be 3 cm.

Solution: Noting that $A = \pi (d/2)^2$, we obtain $K = 0.0188$. The initial conditions are $y(0) = 0$, $z(0) = 0.03$ m, $\dot{y}(0) = v(0) \cos\theta(0) = 67.3$ m/s, and $\dot{z}(0) = v(0) \sin\theta(0) = 19.3$ m/s. Using the RKF45 numerical method, Equations (6.2) are solved over the time
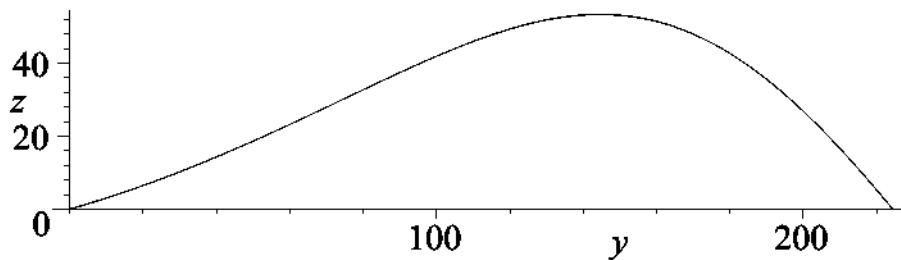
Figure 6.7: Trajectory of the golf ball. Scale is in meters.

interval $t = 0$ to 8.14 seconds and the trajectory is plotted in Figure 6.7. The golf ball is in the air for about 8.14 seconds before striking the ground.

<p align="center">***</p>

6.5   A Falling Badminton Bird

Peastrel, Lynch, and Armenti ([PLA92]) have experimentally investigated the effect of air drag on the motion of a badminton shuttlecock or bird. In particular, they measured the distance (in meters) that a badminton bird, falling vertically from rest, drops as a function of time (in seconds). Their data is given in Table 6.2.

time	0.347	0.470	0.519	0.582	0.650	0.674	0.717	0.766
distance	0.61	1.00	1.22	1.52	1.83	2.00	2.13	2.44
time	0.823	0.870	1.031	1.193	1.354	1.501	1.726	1.873
distance	2.74	3.00	4.00	5.00	6.00	7.00	8.50	9.50

Table 6.2: Experimental data for the falling badminton bird.

The question is, which air resistance force law best explains the experimental observations, Stokes's or Newton's drag law? To answer this question, they solved the equation of motion for the badminton bird falling under the influence of the gravitational force and subject to each of the force laws. This is easily done as follows:

- *Stokes's drag law* ($F_{Stokes} = -a\,v$): The equation of motion for a badminton bird of mass m falling under the influence of gravity (gravitational acceleration g) is

$$m\,\frac{dv}{dt} = m\,g - a\,v. \tag{6.3}$$

Integrating with respect to time, and taking the initial velocity to be zero, yields

$$v(t) = \left(\frac{m\,g}{a}\right)\left(1 - e^{-(a/m)\,t}\right) = v_T\left(1 - e^{-g\,t/v_T}\right), \tag{6.4}$$

where v_T is the terminal velocity. Integrating $v(t)$ with respect to time yields the distance formula,

$$d_{stokes} = \frac{v_T^2}{g}\left(e^{-g\,t/v_T} - 1 + \frac{g\,t}{v_T}\right). \tag{6.5}$$

As a check, note that for $a \to 0$, one has $v_T \to \infty$ and, on Taylor expanding,

$$d_{stokes} = \frac{v_T^2}{g}\left(1 - \frac{g\,t}{v_T} + \frac{1}{2}\frac{(g\,t)^2}{v_T^2} + \cdots - 1 + \frac{g\,t}{v_T}\right) = \frac{1}{2}\,g\,t^2,$$

as expected.

- *Newton's drag law* ($F_{Newton} = -b\,v^2$): Integrating twice with respect to time, subject to the initial conditions $v(0) = 0$ and $d(0) = 0$, one obtains

$$d_{newton} = \frac{v_T^2}{g}\ln\left(\cosh\left(\frac{g\,t}{v_T}\right)\right), \tag{6.6}$$

with $v_T = \sqrt{m\,g/b}$.

Example 6-7: Terminal Velocity of Falling Badminton Bird

Using the last two data points in Table 6.2, the terminal velocity is

$$v_T = \frac{(9.50 - 8.50)}{(1.873 - 1.726)} = 6.80 \text{ m/s}.$$

That the ball has dropped sufficiently far for the terminal velocity to be reached can be checked by plotting the ball's velocity, calculated in the same way as above, throughout its flight. This is left as a problem.

<div align="center">*** </div>

For the badminton experiment, Peastrel et al. measured $g = 9.81$ m/s^2. Using the above value of v_T, the two model formulas, d_{stokes} and d_{newton}, for the distance can be plotted and compared with the experimental data of Table 6.2.

The result is shown in Figure 6.8, the circles representing the experimental data. The upper solid curve is for d_{newton}, the lower curve for d_{stokes}.
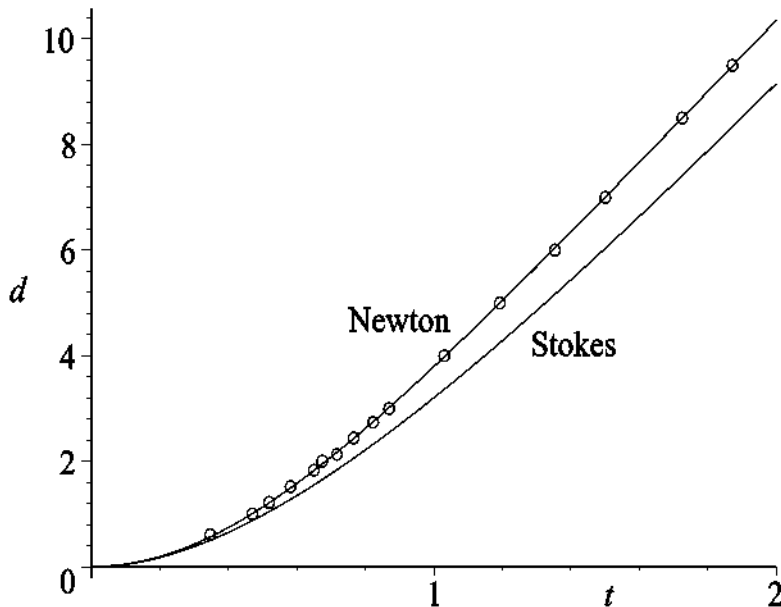
Figure 6.8: Circles: data. Upper (lower) curve: Newton's (Stokes's) drag law.

Newton's drag law fits the data almost perfectly. The drag law is nonlinear because the flow of air through the feathers of the badminton bird is turbulent, rather than laminar.

The method of measuring the distance through which a sports ball falls from rest is an easy way of determining the drag law on that ball.

Now let's turn our attention away from the nonlinear flight dynamics of sports balls to another sport, car racing.

6.6 Car Racing

The same fundamental physics principles that allow an airplane to fly apply to car racing as well, whether it be on the Formula 1 racing circuits of Europe or at the Indianapolis Speedway. As already noted in Chapter 5, in the case of the airplane wing, the wing is designed so that the air flows more quickly over the top than over the bottom. The Bernoulli effect then tells us that the upward pressure on the bottom of the wing is greater than the downward pressure on the top, thus producing a net lift force.

Racing cars are designed so as to be an upside down airfoil or wing, the air rushing faster under the car chassis than over the top. This produces a net downward force or negative lift on the racing car. Airfoils are also used on the front and rear of the car to create even more downward force.

With the aid of front and rear wings, an Indy "ground effect" car such as that schematically depicted in Figure 6.9 can reach speeds of over 240 mph. The Venturi on the bottom of the car forces air through a narrow region, thus speeding up airflow and increasing the downward force.
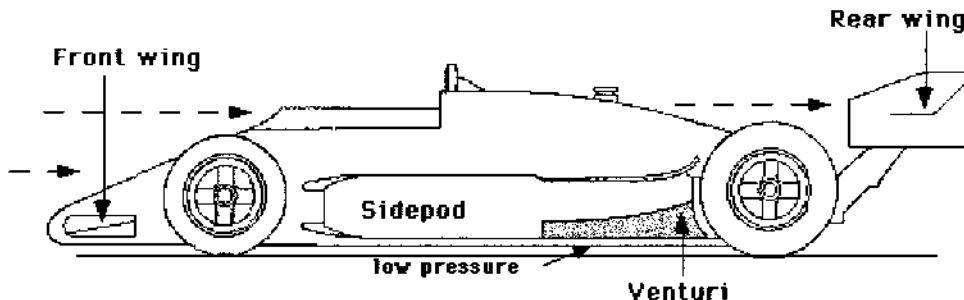
Figure 6.9: Ground effect car (Ref: **www.nas.nasa.gov**).

The design enables the car to achieve higher cornering speeds as the car is "sucked" to the road with a downward force of more than twice its weight. The frontal area of the car is reduced in size so as to reduce the drag coefficient. Racing teams use track testing and wind tunnels to determine the most efficient downward force-to-drag ratio. For example, for the Galmer G-92 (driven by Al Unser, Jr.) that won the 1992 Indianapolis 500 mile race, the measured downward force at a speed of 352 km/h (220 mph) was 12,610 newtons, the drag force 4323.5 newtons, so the downward force-to-drag ratio was 2.92. The airflow past the car was governed by Newton's drag law with a drag coefficient $C_D = 0.669$. (Reference: **www.nas.nasa.gov**.)

6.7 Medieval Archery

Although now relegated to a sporting event, the bow and arrow (particularly the English longbow) was an extremely effective weapon in medieval wars.[8] Probably the most decisive military use of the longbow was in the battle of Agincourt (France) which took place on the 24th of October in the year 1415. In this battle, about 6000 English soldiers under Henry V faced 50,000 French troops. The English army consisted of about 80% longbow-men, whereas the French army was mainly cavalry with virtually no bowmen.

Aiming high to maximize the range, the 5000 English bowmen fired at a rate of about 10 arrows each per minute. With 50,000 arrows raining down on them per minute, the French cavalry was completely routed, the survivors fleeing back through the front columns of their infantry. The remaining French troops were then chopped to pieces by the English soldiers with their hatchets and billhooks.[9]

Neglecting air resistance completely, the maximum range (obtained by aiming at 45° to the horizontal) of an arrow would be $R_0 = v^2/g$, where v is the speed with which the arrow is fired and g is the acceleration due to gravity. The initial speed of a medieval war arrow has been estimated ([Ree95]) to have been about 58 m/s. Taking $g = 9.81$ m/s^2, then $R_0 = 343$ m.

Actually, air resistance cannot be neglected. Wind tunnel experiments reveal that the air resistance on an arrow is given by Newton's drag law, $F_{drag} = c\,v^2$, where the proportionality constant c depends on the particular type of arrow. According to Gareth Rees, the maximum range R then is given to an accuracy of a few percent by the formula

$$R = R_0 \left(1 + \frac{c\,v^2}{m\,g}\right)^{-0.74}, \tag{6.7}$$

where m is the mass of the arrow.

Example 6-8: Maximum Range of a Medieval War Arrow

For a typical medieval war arrow, $m \approx 60$ grams and $c \approx 10^{-4}$ N s^2/m^2. Taking $g = 9.81$ m/s^2 and $v = 58$ m/s, estimate the maximum range of a medieval war arrow with air resistance included.

Solution: Using the range formula (6.7),

$$R = 343 \left(1 + \frac{(10^{-4} \times 58^2)}{(0.06 \times 9.81)}\right)^{-0.74} = 245 \text{ m}.$$

Air resistance reduces the range to about 71% of that when air resistance is neglected.

<center>***</center>

We have concentrated on the flight of the arrow. What about the bow? The best wood for the English longbow was obtained from the yew tree, this wood having a

---

[8]For a more complete account of the physics of medieval archery see the review paper by Gareth Rees ([Ree95]).

[9]Originally used as a farming tool, the billhook was a weapon which originated as a cross between a broad curved knife which was hook shaped at the end and an axe.

maximum elastic energy storage per unit mass of about 700 joules per kilogram. This is as good as spring steel! These early bows could be reasonably approximated by a Hooke's law relation between the applied force F and the string displacement x from equilibrium.

For a modern compound bow, a nonlinear relation exists between F and x. A compound bow uses a levering system of cables and pulleys to bend the limbs which are much stiffer than those of a longbow. In the United States the compound bow, which was first developed and patented by Holless Wilbur Allen in Missouri in 1967, is the dominant form of bow. For the Realtree Masterbucks compound bow manufactured by Bear Archery of Gainesville, Florida,

$$F = 5133.7\,x^3 - 6748.7\,x^2 + 2223.6\,x,$$

where F is in newtons and x is in meters.[10]

Example 6-9: Advantages of the Compound Bow

For the Realtree Masterbucks compound bow, plot the applied force F versus the string displacement x over the range $x = 0$ to 90 cm. What is the x value at which the first peak in F occurs? What are the advantages of drawing the bow string to a somewhat larger x than this value before releasing it?

Solution: The applied force versus string displacement is as shown in Figure 6.10.
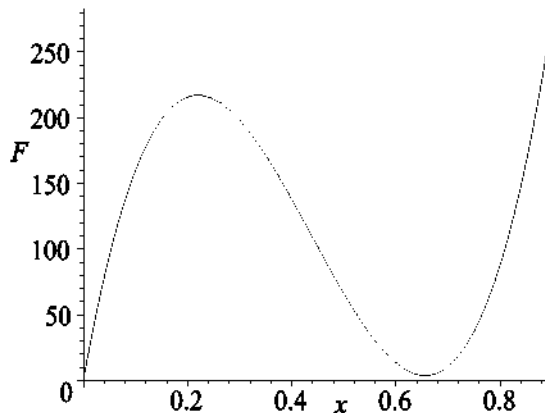
Figure 6.10: Applied force versus displacement for Realtree Masterbucks bow.

The first peak in F occurs for x slightly larger than 0.2 meters. A more precise value is obtained by differentiating F with respect to x, viz.,

$$\frac{dF}{dx} = 15401.1\,x^2 - 13497.4\,x + 2223.6$$

---

[10]See *Archer's Compound Bow-smart use of Nonlinearity* by Randall Peters, Dept. of Physics, Mercer University, which is available at **http://physics.mercer.edu/petepag/combow.html.**

and setting this result equal to zero. Solving for x yields $x \approx 0.22$ and 0.66 m. The first peak in F occurs at $x = 0.22$ m, the value $x = 0.66$ m corresponding to a minimum in the curve. For a draw somewhat larger than 22 cm, the reduced force that is needed to hold the string stationary permits the archer to more easily aim, thus leading to greater precision in the shot. The compound bow is also little affected by changes of temperature and humidity, thus contributing to superior accuracy, velocity, and distance in comparison to other bows.

<div align="center">***</div>

PROBLEMS

Problem 6-1: Newton's distance formula
Show that Newton's distance formula (6.6) yields $d = (1/2)\,g\,t^2$ in the limit that the coefficient $b \to 0$.

Problem 6-2: Indy car on a short oval track
Figure 6.11 shows the negative lift or down force (squares) and the drag force (circles) for an Indy car on a short (less than a mile) oval track as a function of speed. (Reference: **www.nas.nasa.gov.**) The force F is in thousands of pounds and the speed v is in miles per hour.
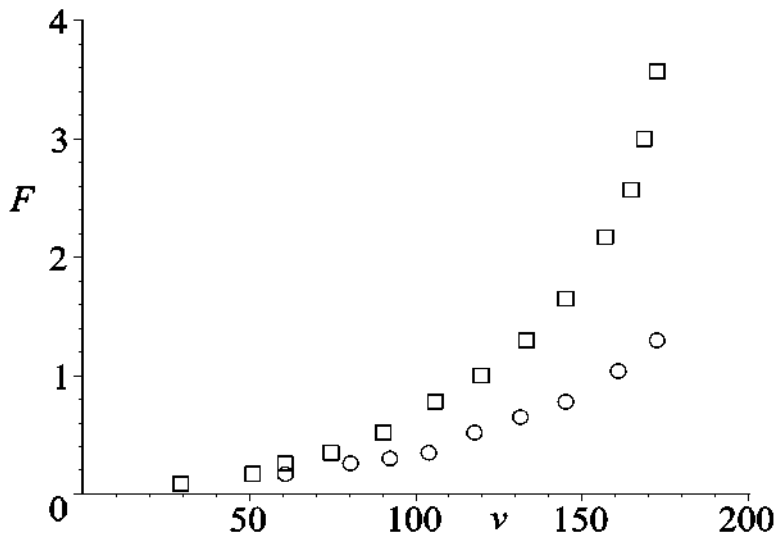
Figure 6.11: Squares (circles): down (drag) force F vs. speed v.

Assuming that the down force can be modeled approximately by a force law of the form $F = k\,v^2$, determine the value of k for each data point. Plot k versus the speed and determine an approximate constant k value which best fits the data. Repeat this procedure for the drag force. Then, determine the (approximate) down force (negative lift)-to-drag ratio.

Problem 6-3: Indy car on a speedway oval

Figure 6.12 shows the negative lift or down force (squares) and the drag force (circles) for an Indy car on a speedway (between 1 and 2 miles) oval track as a function of speed. The force F is in thousands of pounds and the speed v is in miles per hour. (Reference: **www.nas.nasa.gov**.)
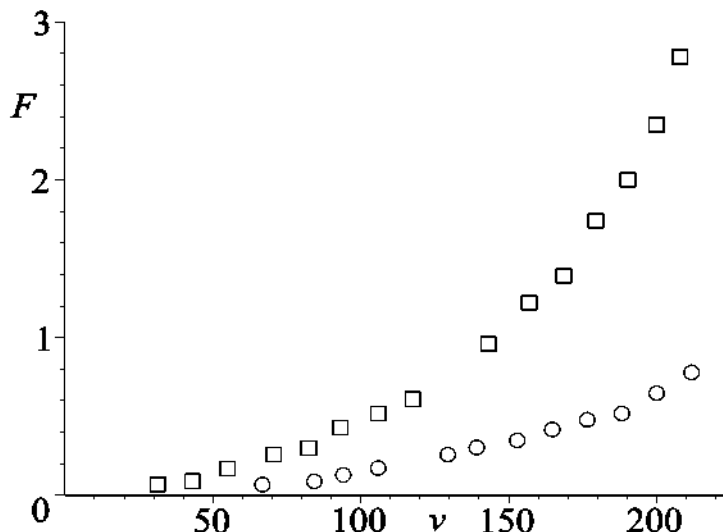
Figure 6.12: Squares (circles): down (drag) force F vs. speed v.

Assuming that the down force can be modeled approximately by a force law of the form $F = k v^2$, determine the value of k for each data point. Plot k versus the speed and determine an approximate constant k value which best fits the data. Repeat this procedure for the drag force. Then, determine the (approximate) down force (negative lift)-to-drag ratio.

Problem 6-4: Lift coefficient for a spinning tennis ball

The lift coefficient for a spinning tennis ball ([Ste88]) is given by

$$C_L = \frac{1}{2.2 + 0.98 \left(\dfrac{r\,\omega}{v} \right)},$$

where r is the radius, ω is the angular velocity, and v is the linear velocity. For a tennis ball, $r = 3.3$ cm.

    a. Assuming that the tennis ball is spinning at 2000 rpm and has a velocity equal to the fastest speed for a serve given in Table 6.1, calculate the lift coefficient.

    b. If $\rho_{air} = 1.21$ kg/m^3, calculate the lift force on the tennis ball.

    c. Calculate the drag force on the tennis ball.

Problem 6-5: Lift on a soccer ball

According to Palmer ([Pal05a]), experiments have been carried out at the University of Sheffield (England) to determine the effect of spin on the flight of a soccer ball. A soccer ball was fired at a constant velocity of 18 m/s and the lift coefficient determined for different spin rates. The data can be fitted with a lift coefficient of the form

$$C_L = 0.385 \left(\frac{r\,\omega}{v}\right)^{0.25},$$

where r is the radius of the ball, ω is the angular velocity, and v is the linear velocity. Given that a soccer ball has a diameter of 25.4 cm, what is the lift coefficient on the ball for $v = 18$ m/s if the angular velocity is 10 revolutions per second? If the density of air is 1.21 kg/m^3, what is the Magnus force on the ball?

Problem 6-6: Check on badminton bird's terminal velocity

Using the experimental data of Table 6.2, plot the badminton bird's velocity as a function of time and confirm that the terminal velocity calculated in the text is a good approximation to the terminal velocity.

Problem 6-7: Coefficient b for the badminton bird

If the badminton bird in the experiment of Peastrel et al. had a mass of 5 grams, what is the value of the coefficient b in Newton's drag law for the badminton bird?

Problem 6-8: Air drag on a hockey puck

Consulting the web site **www.thephysicsofhockey.com**, discuss the effect of altitude on the air drag on a hockey puck. By what percentage is the drag force on a hockey puck moving at 100 mph reduced in Denver compared to Toronto?

Problem 6-9: Effect of altitude on baseball trajectories

Quantitatively discuss what the effect would have been on John Lester's pitch if he had been pitching at Coors Field in Denver, instead of at Seattle's Safeco Field. What about other spin angles? Plot the trajectory in each case.

Problem 6-10: Range of a medieval war arrow

Explain why Newton's drag law is applicable to the flight of an arrow. By numerically solving the equation of motion for the flight of a medieval war arrow subject to Newton's drag law, show that the expression (6.7) is a good approximation to the maximum range of the arrow.

Problem 6-11: Heart rate response to treadmill walking exercise

Discuss the paper "A nonlinear dynamic model for heart rate response to treadmill walking exercise"[11] by Teddy Cheng, Andrey Savkin, Branko Celler, Lu Wang, and Steven Su. A reprint of this paper is available at:

www.bsl.unsw.edu.au/docs/2007/A%20nonlinear%20dynamic %20model%20for%20heart%20rate%20response%20to%20treadmill %20walking%20exercise.pdf.

---

[11]Proceedings of the 29th Annual International Conference of the IEEE EMBS, Cit Internationale, Lyon, France, August 23-26, 2007.

Problem 6-12: Aging affects variability during gait

Discuss the paper "Nonlinear dynamics indicates aging affects variability during gait" by Ugo Buzzi and coworkers ([BSK⁺03]). A reprint of this paper is available at:

www.unomaha.edu/biomech/pdf/Buzzi%20nonlinear%2003%20CB.pdf.

Problem 6-13: How boxers decide to punch a target

Discuss the paper "How boxers decide to punch a target: Emergent behaviour in nonlinear dynamical movement systems" by Robert Hristovski et al. ([HDAB06]). A reprint of this paper is available at:

www.jssm.org/combat/1/10/v5combat-10.pdf.

Problem 6-14: Curling rock dynamics

The game of curling is a popular wintertime team sport played in northern countries. The objective of the game is to slide a 20-kg granite "rock" a distance of some 25 to 30 m and place the rock as close as possible to the center of a circular bulls-eye painted on the flat ice surface. Attached to the top of the rock is a handle which by twisting during the delivery allows the player to make the rock *curl* (follow a curved trajectory) as it travels along the ice. Typically, a rock which moves 25 m forward will undergo a transverse displacement of about 1 ± 0.5 m.

Mark Denny ([Den98]) has derived the nonlinear equations of motion for a curling rock. A reprint of the paper is available online at:

http://article.pubs.nrc-cnrc.gc.ca/ppv/RPViewDoc?issn=1208-6045 &volume=76&issue=4&startPage=295.

Making use of this paper, derive the equations of motion of a curling rock and discuss how the predicted results compare with experimental reality.

An argument exists in the literature as to the relative importance of dry friction and wet friction in accounting for the curl of a curling rock. You should look at the article "Comment on "The motion of a curling rock"" ([Den03]), a reprint being available at:

http://article.pubs.nrc-cnrc.gc.ca/ppv/RPViewDoc?issn=1208-6045 &volume=81&issue=6&startPage=877.

Problem 6-15: Point shaving in college basketball

The field of *forensic economics* applies price-theoretic models to uncover evidence of corruption. As an example, Justin Wolfers has investigated ([Wol06]) "how the structure of gambling on college basketball yields pay-offs to gamblers and players that are both asymmetric and nonlinear, thereby encouraging mutually beneficial effort manipulation through point shaving."[12]

Discuss Wolfers's paper. A reprint is available online at:

http://bpp.wharton.upenn.edu/jwolfers/Papers/PointShaving.pdf.

---

[12]Point shaving: The illegal practice of deliberately limiting the number of points scored by one's team in an athletic contest, as in return for a payment from gamblers to ensure winnings. (American Heritage Dictionary of the English Language, Fourth Edition, published by Houghton Mifflin Company)

Chapter 7

World of Electromagnetism

Why, sir, there is every possibility that you will soon be able to tax it!
Michael Faraday, English physicist (1791–1867),
to Prime Minister William Gladstone on the usefulness of electricity.

In this chapter, we shall sample some of the nonlinear phenomena that can occur in electromagnetism, beginning with electrical circuits containing nonlinear components.

7.1 Nonlinear Electrical Circuits

7.1.1 Nonlinear Inductance

An inductance coil of N turns with an air core and carrying a current I has a linear relationship between the current and the flux ϕ threading through one turn, namely, $I = N\phi/L_0$, where L_0 is the self-inductance. A nonlinear inductor can be created by inserting an iron core inside the coil. Then, qualitatively, the current–flux relation looks like that shown in Figure 7.1. The deviation away from linear behavior as the
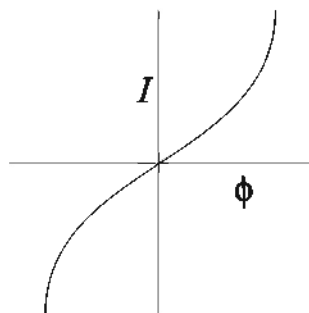
Figure 7.1: Nonlinear current–flux relation with iron core present.

magnitude of ϕ is increased occurs because as the current is increased the inductor's iron core will approach the magnetic saturation limit. Increasing the current further

will produce very little increase in the flux. The mathematical form of the current–flux relation in Figure 7.1 may be written as

$$I = \frac{N\phi}{L_0} + b\phi^3, \tag{7.1}$$

with $b > 0$. The iron core inductor is now connected in series to a resistor R and a capacitor C (see Figure 7.2) which is initially fully charged with no current flowing. As the capacitor discharges, a current I flows in the circuit.
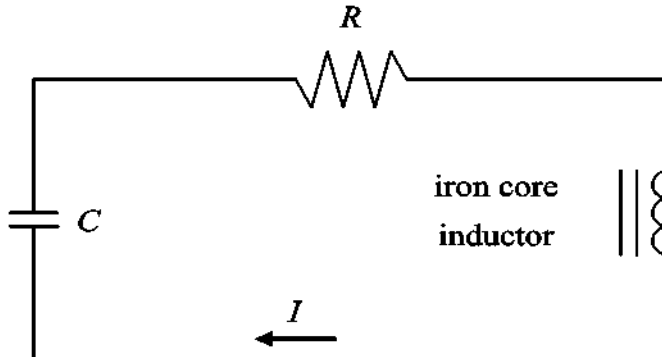
Figure 7.2: Circuit consisting of resistor, capacitor, and nonlinear iron core inductor.

If $q(t)$ is the charge on the capacitor at time t, then Kirchhoff's rule that the algebraic sum of the potential drops around the circuit is zero yields

$$\frac{q}{C} + IR + N\frac{d\phi}{dt} = 0. \tag{7.2}$$

The potential drop $\Delta V = IR$ is just *Ohm's law* for a *linear resistor*. In later examples, we shall encounter *nonlinear resistors* where Ohm's law is not applicable.

Differentiating (7.2) with respect to t, noting that (by definition) $I = dq/dt$, and using Equation (7.1), we obtain

$$\ddot{\phi} + \gamma(1 + B\phi^2)\dot{\phi} + \alpha\phi + \beta\phi^3 = 0, \tag{7.3}$$

with

$$\gamma = \frac{R}{L_0}, \quad B = \frac{3bL_0}{N}, \quad \alpha = \frac{1}{L_0C}, \quad \beta = \frac{b}{NC}.$$

For $R = 0$, we have $\gamma = 0$ so (7.3) reduces to the undamped hard spring ODE.

The flux is difficult to measure experimentally, so usually the current is measured as a function of time. The current is related to the flux through the relation (7.1).

Example 7-1: Time Dependence of Current in Nonlinear Circuit

Taking $\gamma = 0.05$, $B = 1$, $\alpha = 1$, and $\beta = 1$, numerically solve the flux equation (7.3) for the initial condition $\phi(0) = 0$, $\dot{\phi}(0) = 10$. Then plot $I(t)/(N\,C) = \alpha\,\phi(t) + \beta\,\phi(t)^3$ over the range $t = 0$ to 30 and discuss the result.

Solution: Using *Maple* or *Mathematica*, the nonlinear ODE (7.3) is solved with the given parameter values and initial condition for $\phi(t)$ using the adaptive step RKF45 method. Then, $I(t)/(N\,C)$ is plotted, the result being shown in Figure 7.3.
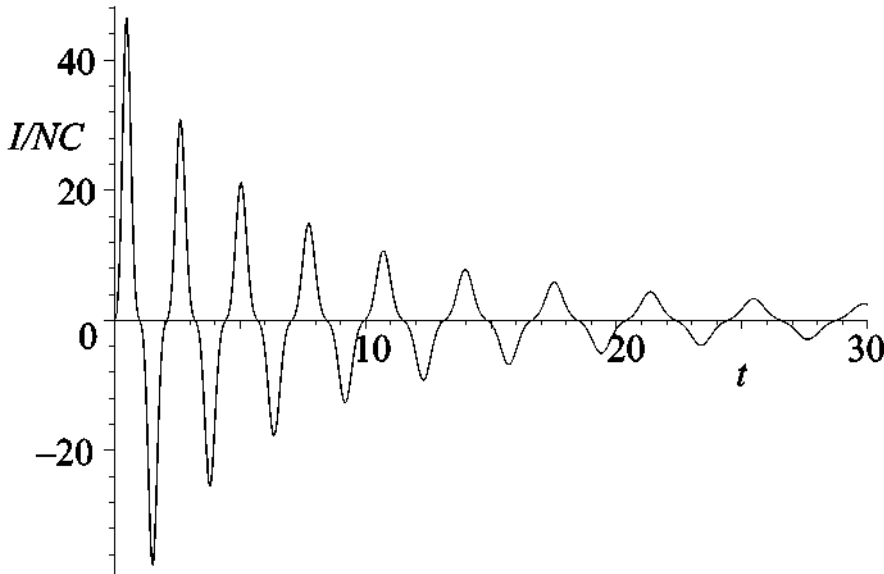
Figure 7.3: Time dependence of the current.

The oscillations decay because of energy dissipation in the resistor, i.e., R and therefore γ is not equal to zero. If the iron core were not present, one would have $b = 0$ and the equation would reduce to the well-known linear LRC circuit equation which displays decaying sinusoidal oscillations with the period of the oscillations fixed. For b nonzero, the oscillations deviate away from the sinusoidal shape and the period becomes amplitude dependent. As can be seen in Figure 7.3, the period of the oscillations increases with decreasing amplitude.

<center>***</center>

The circuit featured in this section is easily created in the laboratory and the nonlinear behavior illustrated in Figure 7.3 verified. The reader who is interested in experimentally studying nonlinear electrical circuits is referred to the experimental section of either ([EM00]) or ([EM01]). The former text makes use of *Maple* in the theory section, while the latter uses *Mathematica*.

7.1.2   Nonlinear Capacitance

By appropriately grouping linear circuit elements together, it is possible to introduce *piecewise-linear* behavior into electrical circuits. Piecewise linearity provides a simple way of creating nonlinear circuits. We will illustrate how this is done by inserting a piecewise linear capacitance into an LRC circuit.

The circuit, shown on the left of Figure 7.4, contains an inductor L (no iron core present here), a resistor R, two capacitors C_1 and C_2, and two diodes. The diodes are in parallel with C_2 and oriented as shown.
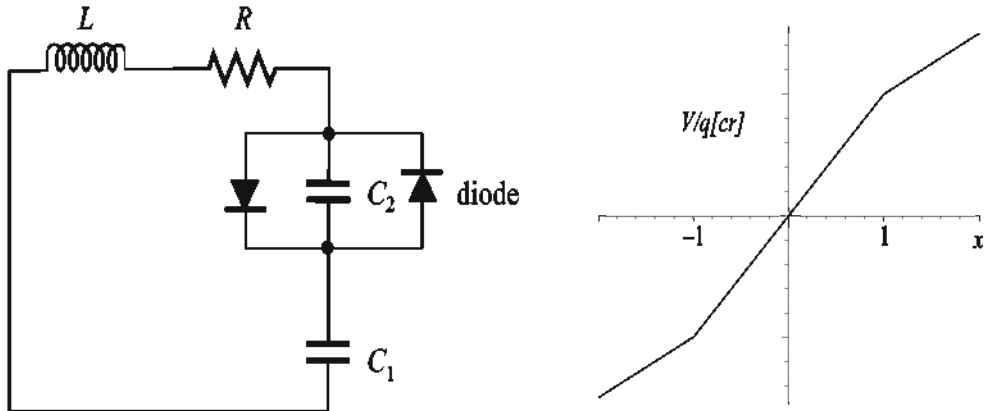
Figure 7.4: Left: Piecewise-linear capacitance circuit. Right: Voltage–charge curve.

Applying Kirchhoff's potential law to the circuit, we have

$$L\frac{dI}{dt} + RI + V_C = L\ddot{q} + R\dot{q} + V_C(q) = 0, \tag{7.4}$$

where q is the electric charge and V_C is the potential drop across both capacitors.

Because of the diodes, the value of V_C depends on the voltage drop across the capacitor C_2. If the potential drop across C_2 is less than a critical voltage V_{cr} (about 0.7 V for silicon diodes), the diodes do not conduct, and the capacitance of the circuit is simply that of the two capacitors in series. The equivalent capacitance C is given by $1/C = 1/C_1 + 1/C_2$. When the potential drop is greater than V_{cr}, the diodes conduct and effectively remove C_2 from the circuit. In this case, the capacitance is simply C_1.

If $q = q_{cr}$ when $V = V_{cr}$, then on setting $x = q/q_{cr}$, V_C is given by

$$\frac{V_C}{q_{cr}} = \begin{cases} (x+1)/C_1 - 1/C, & x \leq -1, \\ x/C, & |x| < 1, \\ (x-1)/C_1 + 1/C, & x \geq 1, \end{cases} \tag{7.5}$$

or, more compactly,

$$\frac{V_C}{q_{cr}} = \frac{x}{C_1} + \frac{1}{2}\left(\frac{1}{C} - \frac{1}{C_1}\right)(|x+1| - |x-1|). \tag{7.6}$$

Noting that $1/C > 1/C_1$, the V_C/q_{cr} curve has the piecewise shape shown on the right of Figure 7.4. Setting

$$\frac{R}{L} = 2\gamma, \quad \omega_1 = \frac{1}{\sqrt{(LC_1)}}, \quad \omega = \frac{1}{\sqrt{(LC)}}, \tag{7.7}$$

and using (7.6), the governing ODE (7.4) for the circuit reduces to

$$\ddot{x} + 2\gamma\dot{x} + \omega_1^2 x + \frac{1}{2}(\omega^2 - \omega_1^2)(|x+1| - |x-1|) = 0. \tag{7.8}$$

Because Equation (7.8) is a piecewise-linear ODE, it can be solved analytically. The possible behavior exhibited by solutions of this ODE is left as a problem.

7.1.3 Chua's Circuit: Piecewise-Linear Negative Resistance

A much more famous example of a piecewise-linear circuit is Leon Chua's circuit in which a piecewise-linear *negative resistance* is introduced. This circuit gains its fame for the richness of nonlinear behavior that it exhibits when the parameter values are changed. It is one of the simplest electronic circuits to display the period doubling route to chaos, as well as some other well-known bifurcation phenomena. Because the governing ODE is piecewise linear, it also has the advantage that it readily lends itself to rigorous mathematical analysis.

The circuit diagram ([Chu92],[Chu94], see also Chua circuit from Scholarpedia on the Internet) for the Chua circuit is shown on the left of Figure 7.5. It contains four linear elements (inductor L, resistor R, and two capacitors C_1 and C_2) and a piecewise-linear negative resistance contained in the "black box" labeled Chua's "diode." The current (I_R)–voltage (V_R) curve for Chua's diode is shown on the right of Figure 7.5. Because the slope is negative, the resistance is negative. The Chua diode can be realized (see [GMR07]) by using two Operational Amplifiers (Op Amps) and six linear resistors.
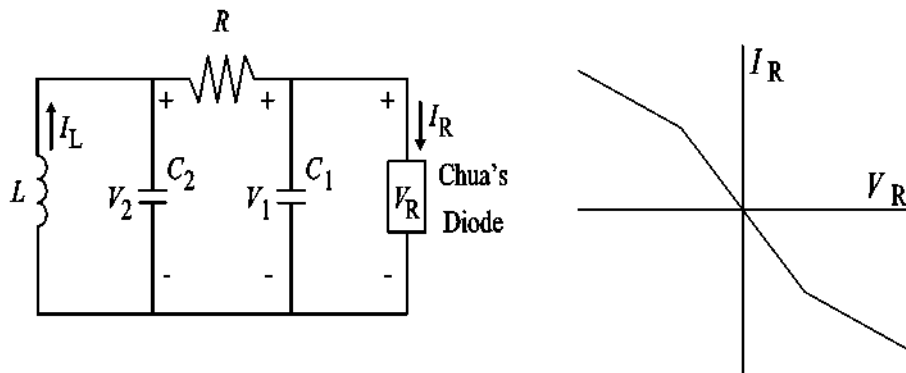
Figure 7.5: Left: Chua circuit. Right: Current–voltage curve for Chua diode.

Taking V_1 to be the voltage across C_1 (and the nonlinear resistance), V_2 to be the voltage across C_2 (and the inductor), and I_L to be the current through L, application of Kirchhoff's current and potential laws to the circuit yields

$$C_1 \frac{dV_1}{dt} = \frac{(V_2 - V_1)}{R} - g(V_1),$$
$$C_2 \frac{dV_2}{dt} = -\frac{(V_2 - V_1)}{R} + I_L, \tag{7.9}$$
$$L \frac{dI_L}{dt} = -V_2,$$

where $g(V)$ is the current–voltage characteristic for the Chua diode. If V_b is the voltage at the bend in the Chua diode current–voltage curve, then the dimensionless voltages

$$x = \frac{V_1}{V_b}, \quad y = \frac{V_2}{V_b} \tag{7.10}$$

can be introduced. Setting

$$z = \frac{R\,I_L}{V_b}, \quad \tau = \frac{t}{R\,C_2}, \quad \alpha = \frac{C_2}{C_1}, \quad \beta = \frac{R^2\,C_2}{L}, \tag{7.11}$$

the circuit equations (7.9) may be written as

$$\dot{x}(\tau) = \alpha(y - x - G(x)),$$

$$\dot{y}(\tau) = x - y + z,$$
$$\tag{7.12}$$
$$\dot{z}(\tau) = -\beta\,y,$$

$$\text{with} \quad G(x) = m_1\,x + \frac{1}{2}\,(m_0 - m_1)\,(|x + 1| - |x - 1|).$$

The dimensionless parameters m_0 and m_1 refer to the slopes of inner and outer segments of the piecewise-linear function shown on the right of Figure 7.5. These parameters have negative values because the slopes are negative.

In the following example, the parameters for the Chua circuit are chosen so as to produce a chaotic strange attractor.

Example 7-2: Double Scroll Attractor

Numerically solve the dimensionless Chua equations (7.12) with

$$m_0 = -8/7, \quad m_1 = -5/7, \quad \alpha = 15.6, \quad \beta = 25.58,$$

and initial condition $x(0) = 0.1$, $y(0) = z(0) = 0$. Make a 3-dimensional plot of the trajectory in x–y–z space for $\tau = 400$ to 600.

Solution: Using *Maple* or *Mathematica*, the nonlinear ODE system is solved for $x(t)$, $y(t)$, and $z(t)$, using the adaptive step RKF45 method. Over the time interval $\tau = 400$ to 600, the trajectory is as shown in Figure 7.6, the coordinate axes being suppressed. The trajectory winds onto a chaotic attractor with two "lobes," somewhat reminiscent of the Lorenz butterfly attractor. It is commonly referred to as the *double scroll attractor*.
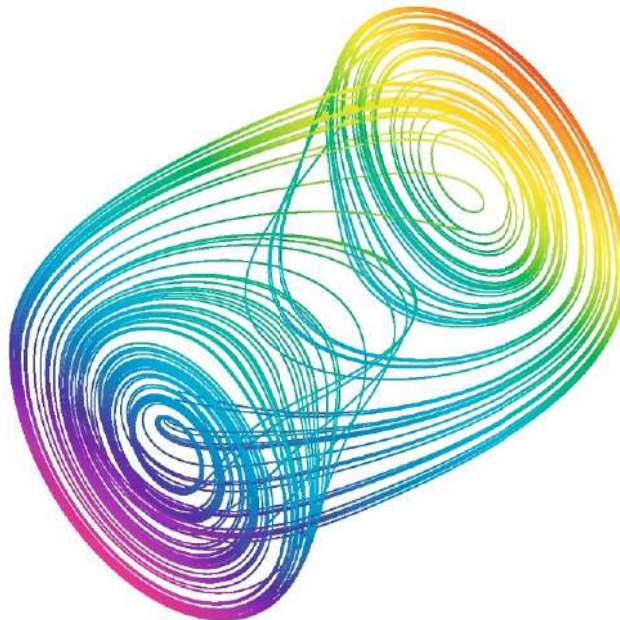
Figure 7.6: Chua's chaotic double scroll attractor.

$*{*}*$

If, in the above example, one varied the parameter β from $\beta = 50$ down to $\beta = 25.58$, one would observe a period-doubling route to chaos. Verifying this behavior is left as a problem for you to attempt.

7.1.4 Tunnel Diode Oscillator

Another electrical circuit element that has a nonlinear negative resistance region in its current–voltage curve is the *tunnel diode*. Introduced by Leo Esaki[1] in 1958, the tunnel diode differs from an ordinary or "normal" diode in that the doping concentration in a *p-n* semiconductor junction is sufficiently large that suitable forward biasing causes the electrons to quantum mechanically tunnel through the junction barrier rather than jump over it. Although capable of acting as very fast switching devices, tunnel diodes

---

[1]Esaki shared the 1973 Nobel physics prize with Ivar Giaever and Brian Josephson for their work on quantum mechanical tunneling in semiconductors.

suffer from the problem of being susceptible to unwanted signals from stray capacitances and inductances contained in the wires and contact points.

Typically, the I–V curve for a tunnel diode is as shown on the left of Figure 7.7, the negative slope region corresponding to negative resistance. Qualitatively, the current–voltage curve of a normal diode does not display the first "hump," instead jumping at some critical voltage to the upper positive slope (positive resistance) branch.
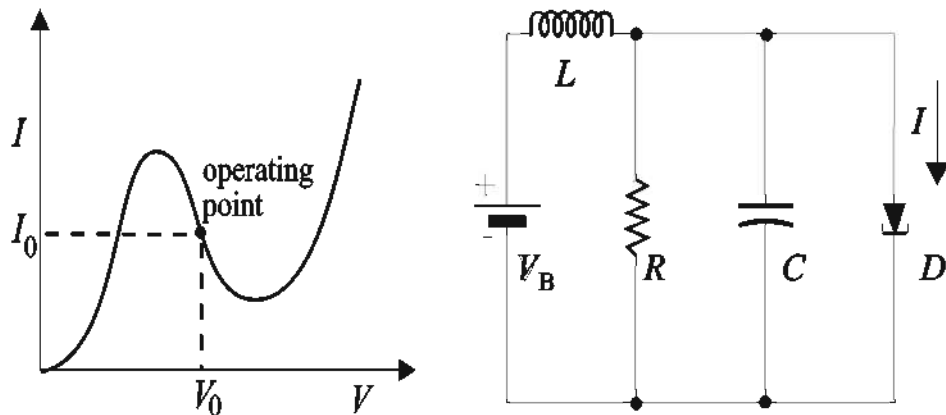
Figure 7.7: Left: Tunnel diode current–voltage curve. Right: Oscillator circuit.

A tunnel diode oscillator circuit may be created by inserting the tunnel diode D in the circuit shown on the right of the figure and operating in the negative resistance region about the inflection point (I_0, V_0) of the curve. This is done by adjusting the battery voltage V_B to be equal to V_0. Letting $i(t) = I(t) - I_0$ and $v(t) = V(t) - V_0$ be the current and voltage at time t relative to the operating point, the current i is given to a good approximation by the cubic polynomial $i = -a\,v + b\,v^3$, where a and b are positive coefficients which depend on the particular tunnel diode. For example, with i and v measured in amperes and volts, respectively, $a = 0.05$ and $b = 1.0$ for the tunnel diode 1N3719.

Letting I_L, I_R, I_C, and I be the currents through the inductor L, resistor R, capacitor C, and diode, Kirchhoff's current law yields

$$-I_L + I_R + I_C + I = 0. \tag{7.13}$$

The voltage drops V_C and V_R across the capacitor and resistor are equal to the drop across the diode, so $V_C = V_R = V = V_0 + v$. The voltage drop V_L across the inductor is related to that across the diode by $V_L = V_B - V = V_0 - V = -v$. Taking the time derivative of Equation (7.13) and noting that $I = I_0 + i = I_0 - a\,v + b\,v^3$, $I_R = V_R/R$ from Ohm's law, $I_C = C\,(dV_C/dt)$ from the definition of capacitance, and $dI_L/dt = V_L/L$ from the definition of inductance, we obtain

$$\frac{v}{L} + \frac{1}{R}\frac{dv}{dt} + C\,\frac{d^2v}{dt^2} - a\,\frac{dv}{dt} + 3\,b\,v^2\,\frac{dv}{dt} = 0,$$

or, on collecting terms and dividing by C,

$$\frac{d^2v}{dt^2} + \frac{1}{C}\left(\frac{1}{R} - av + 3bv^2\right)\frac{dv}{dt} + \frac{v}{LC} = 0. \tag{7.14}$$

This ODE can be cast into a dimensionless form by setting

$$\omega = \frac{1}{\sqrt{LC}}, \quad \epsilon = \frac{(a-1/R)}{\omega C}, \quad \tau = \omega t, \quad \text{and} \quad x = \frac{\sqrt{(3b)}\,v}{\sqrt{(a-1/R)}}. \tag{7.15}$$

The resulting dimensionless nonlinear ODE, called the *van der Pol* equation, is

$$\ddot{x}(\tau) - \epsilon\left(1 - x(\tau)^2\right)\dot{x}(\tau) + x(\tau) = 0. \tag{7.16}$$

The Dutch electrical engineer and physicist Balthasar van der Pol ([vdP26]) discovered this equation in 1926 while working with electrical circuits containing vacuum tubes. The van der Pol equation arises in many different applications:

- lasers (Lamb ([Lam64]));

- Q machines used in experimental plasma physics (Lashinsky ([Las69]));

- arc discharge (Keen and Fletcher ([KF70]));

- oil film journal bearings (Jain and Srinivasan ([JS75]));

- flutter of plates and shells (Fung ([Fun55]); Nayfeh and Mook ([NM79]));

- vehicle dynamics (Beaman and Hedrick ([BH80]); Cooperrider ([Coo80]));

- electrical activity in gastrointestinal tracts (Linkens ([Lin74], [Lin76])).

Note that mathematically the van der Pol equation is just the simple harmonic oscillator equation with a nonlinear variable damping term. If the parameter $\epsilon > 0$, i.e., $R > 1/a$, one has *negative damping* when $x < 1$ and the more familiar positive damping when $x > 1$. Thus, if initially x is a very small oscillation (e.g., thermal "noise" in the electrical circuit), it will grow in amplitude as time proceeds. The circuit will spontaneously begin to oscillate, even though the energy source (the battery) is nonoscillatory. When $x > 1$, positive damping will tend to decrease the amplitude of the oscillations.

An important feature of the van der Pol equation is that for $\epsilon > 0$ it displays a limit cycle, i.e., evolves onto a closed loop fixed by ϵ in the x vs. $y \equiv \dot{x}$ phase plane, no matter what the initial condition. It also displays so-called *relaxation oscillations* when $\epsilon \gg 1$. A relaxation oscillation is characterized by fast changes in $x(\tau)$, interspersed with relatively slowly varying $x(\tau)$ in between. Both features are now illustrated.

Example 7-3: Van der Pol Limit Cycle and Relaxation Oscillations

Consider the van der Pol electronic circuit of Figure 7.7 with the tunnel diode 1N3719 ($a = 0.05$, $b = 1.0$) and $L = 25$ mH, $C = 0.5$ μF, and $R = 60$ Ω.

a. Evaluate the parameter ϵ.

b. Demonstrate that a relaxation oscillation occurs for this ϵ by numerically solving the van der Pol equation for $x(\tau)$ for the initial condition ic1 = $x(0) = 0.1$, $y(0) = 0$, and plotting the solution.

c. Choosing a second initial condition, e.g., ic2 = $x(0) = 3$, $y(0) = -10$, show that a limit cycle occurs when the solution trajectory is plotted in the phase plane for the two initial conditions.

Solution: a. First, evaluating the frequency ω,

$$\omega = 1/\sqrt{(LC)} = 1/\sqrt{(25 \times 10^{-3} \times 0.5 \times 10^{-6})} = 8944.27\,\mathrm{s}^{-1},$$

we obtain

$$\epsilon = \frac{(a - 1/R)}{\omega C} = \frac{(0.05 - 1/60)}{(8944.27 \times 0.5 \times 10^{-6})} = 7.45.$$

Since $\epsilon \gg 1$, $x(\tau)$ should display a relaxation oscillation.

b. Using *Maple* or *Mathematica*, the van der Pol ODE is solved numerically using the RKF45 method for $x(\tau)$, subject to ic1, over the time interval $\tau = 0$ to 30. The solution is shown on the left of Figure 7.8. The oscillatory motion is punctuated by very rapid changes in x with relatively slowly varying regions in between. This is an example of a relaxation oscillation.
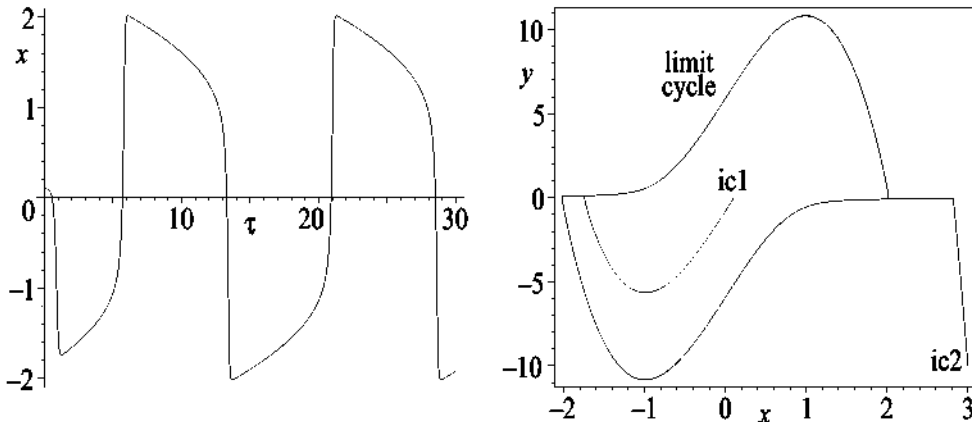
Figure 7.8: Left: Relaxation oscillation. Right: Two trajectories wind onto limit cycle.

c. Setting $\dot{x} = y$, the van der Pol equation becomes $\dot{y} = \epsilon\,(1 - x^2)\,y - x$. Numerically solving the coupled ODE system for $x(\tau)$ and $y(\tau)$ over the time interval $\tau = 0$ to 30 for the two initial conditions and plotting the two trajectories in the phase plane produces the picture shown on the right of Figure 7.8. Both trajectories wind onto the same closed loop, the stable limit cycle.

***

Oscillations characterized by long dormant periods between changes are well known in nature. For example, the geyser Old Faithful in Yellowstone National (U.S.A.) Park currently erupts about every 65 minutes (with an error of 10 minutes) for eruptions lasting less than $2\frac{1}{2}$ minutes. and about every 92 minutes for longer-lasting eruptions. The human heartbeat was recognized as early as 1928 by van der Pol and van der Mark ([vdPvdM28]) as being an example of a relaxation oscillator. Electrocardiogram recordings of a normal heartbeat may be found on the Internet, as well as those for hearts that are diseased in some way.

In the world of toys, an inexpensive mechanical toy called the Drinking Bird demonstrates relaxation oscillations. The "bird" consists of a hollow tube "body" with a hollow "head" at the top end and a "tail" at the bottom consisting of a glass reservoir containing a volatile fluid. The initially moist head is poised above a beaker of water. As the head slowly dries out, it cools, causing the air pressure inside it to be reduced. When the air pressure differential between the head and the tail is sufficient to overcome gravity, the fluid rises through the body to the head. The additional weight causes the head to dip into the water and remoisten the head. The head quickly bobs up, the pressure difference between head and tail goes to zero, and gravity pulls the liquid back into the tail. Toys, such as this one, illustrating a particular nonlinear concept, may be found in scientific toy stores.

7.1.5   Josephson Junction

A Josephson junction is formed by inserting a very thin (30 angstroms[2] or less) insulating[3] layer between two superconductors. To understand how such a junction works, let's review some relevant features of superconductivity. If you cool many metals and alloys toward absolute zero, a critical temperature T_{cr} (typically[4] around 20 Kelvin or less) is reached at which a phase transition occurs. For $T > T_{cr}$, the metal is in its "normal" state, with electrical resistance present because the moving electrons which make up the normal electrical current are scattered by the ionic lattice. For $T < T_{cr}$, it is in its "superconducting" state, pairs of electrons (called *Cooper pairs*) interacting with the lattice in such a way that they encounter no ionic scattering, and therefore no electrical resistance as they flow. The current associated with the flow of Cooper pairs is referred to as the *supercurrent.* There is, however, an upper bound I_{cr} to the permitted supercurrent. If it exceeds I_{cr}, the metal reverts back to its normal state. Depending on the superconductor, I_{cr} can vary from about $1\,\mu$A to $1\,$mA.

In 1962, Brian Josephson ([Jos62]) predicted that quantum mechanical tunneling of Cooper pairs, and thus a current, could occur through the intermediate insulating layer even if there was no voltage difference between the superconductors. This so-called *Josephson effect* would be impossible classically. Josephson received a Nobel prize[5] for

---

[2]1 angstrom=1.0×10^{-10} m.

[3]A normal metal or a semiconductor could also be used instead of an insulator. For the normal metal, the layer can be several microns thick.

[4]For "high-temperature superconductors" made of cuprate-perovskite ceramic materials, T_{cr} can be in excess of 90 Kelvin.

[5]The previously mentioned 1973 physics prize shared with Esaki and Giaever.

his theoretical prediction, a prediction which was experimentally verified by Anderson and Rowell ([AR63]).

In this section, we will look at a simple electrical circuit, consisting only of a battery (or some other dc source) connected to a Josephson junction. The battery provides a constant *bias* current I_b which, for a given junction, will act as the control parameter. The junction has a capacitance C and resistance R and the potential drop across the junction at time t is $V(t)$. The current through the junction is made up of three current contributions in parallel, the relative importance of each depending on details of the junction and the value of the control parameter. The three current contributions are:

- Supercurrent: The derivation of the form of the supercurrent necessitates the use of quantum mechanics. More specifically, it involves solving the Schrödinger equation for the quantum mechanical wave function $\psi = \sqrt{\rho}\, e^{i\theta}$ describing the state of the Cooper pairs in each superconductor. Here, ρ is the density of Cooper pairs, θ the phase angle, and $i = \sqrt{-1}$. All Cooper pairs in a given superconductor have the same wave function, those on one side of the insulating barrier described by $\psi_1 = \sqrt{\rho_1}\, e^{i\theta_1}$, those on the other side described by $\psi_2 = \sqrt{\rho_2}\, e^{i\theta_2}$. As shown, for example, in Volume III of *The Feynman Lectures on Physics* ([FLS65]), the supercurrent contribution is given by

$$I_s = I_{cr} \sin\theta, \quad \text{with} \quad \theta = \theta_1 - \theta_2. \tag{7.17}$$

- Normal current through the resistor: $I_n = \dfrac{V}{R}$.

- Displacement current through the capacitor: $I_d = C\,(dV/dt)$.

By Kirchhoff's first rule, the bias current provided by the battery must equal the sum of the three parallel currents through the junction, viz.,

$$I_b = I_d + I_n + I_s = C\,\dot{V} + \frac{V}{R} + I_{cr}\,\sin\theta. \tag{7.18}$$

A second quantum mechanical result relates the voltage V across the junction to the rate of change of phase angle difference between the two superconductors on opposite sides of the insulating barrier. The relation, also derived in Feynman, is

$$V = \frac{\hbar}{2\,e}\,\dot{\theta} \tag{7.19}$$

where $\hbar = h/(2\,\pi)$, with h being Planck's constant, and e is the electron charge. Substituting this relation into Equation (7.18) yield an equation for θ alone,

$$\frac{\hbar\,C}{2\,e}\,\ddot{\theta} + \frac{\hbar}{2\,e\,R}\,\dot{\theta} + I_{cr}\,\sin\theta = I_b. \tag{7.20}$$

This second-order nonlinear ODE can be cast into a nondimensional form by introducing the new variables

$$\tau = \sqrt{\left(\frac{2\,e\,I_{cr}}{\hbar\,C}\right)}\,t, \quad I = \frac{I_b}{I_{cr}}, \quad \gamma = \sqrt{\left(\frac{\hbar}{2\,e\,I_{cr}\,R^2\,C}\right)}. \tag{7.21}$$

This reduces Equation (7.20) to

$$\ddot{\theta} + \gamma \dot{\theta} + \sin \theta = I, \tag{7.22}$$

with the time derivatives now with respect to τ. Mathematically, Equation (7.22) is just the damped (damping coefficient $\gamma > 0$) simple pendulum equation with a constant torque. To understand the behavior of the Josephson junction connected to a battery, we must investigate this equation as, say, I is varied for a given value of γ. Without loss of generality, we can take $I \geq 0$.

Example 7-4: Fixed Points of the Josephson Junction Circuit

Locate and determine the nature of the fixed points of Equation (7.22) in the θ versus $\dot{\theta}$ phase plane. Since the sine function mathematically repeats as θ increases by 2π, we need only consider the "fundamental" range 0 to 2π for the analysis.

Solution: Setting $\dot{\theta} = y$, (7.22) may be written as the two first-order ODEs

$$\dot{\theta} = y \equiv P(\theta, y), \quad \dot{y} = I - \sin \theta - \gamma y \equiv Q(\theta, y).$$

The fixed points are given by

$$\bar{y} = 0, \quad \sin \bar{\theta} = I.$$

For $I > 1$, i.e., $I_b > I_{cr}$, the second relation cannot be satisfied for any $\bar{\theta}$, so there are no fixed points for this range of I.

For $0 < I < 1$, there are two values of $\bar{\theta}$ in the range 0 to 2π which will satisfy $\sin \bar{\theta} = I$, so there are two fixed points. Using the phase-plane analysis procedure and notation of Chapter 2, we find that

$$a = 0, \quad b = 1, \quad c = -\cos \bar{\theta} = \pm\sqrt{1 - I^2}, \quad d = -\gamma,$$

so

$$p = -(a + d) = \gamma, \quad q = ad - bc = \mp\sqrt{1 - I^2}, \quad \Delta = p^2 - 4q = \gamma^2 \pm 4\sqrt{1 - I^2}.$$

Consulting Table 2.1, the fixed point corresponding to $q < 0$ is a saddle point. Since $p > 0$, the other fixed point with $q > 0$ is either a stable nodal or focal point depending on whether $\Delta > 0$ or $\Delta < 0$.

Since the saddle and nodal/focal points vanish as I is increased through 1, $I = 1$ is a saddle-node bifurcation point.

<div align="center">***</div>

For $I > 1$, there are no fixed points of Equation (7.22). So what is the behavior of the Josephson junction in this regime? If we consider the phase plane to be wrapped into a cylinder which is infinitely long in the y direction and with a circumference of 2π in the θ direction, all trajectories will asymptotically wind onto the same closed loop on the cylindrical surface independent of the initial values of θ and y. That is to say, they will wind onto a stable limit cycle. This is illustrated in the following example.

Example 7-5: Stable Limit Cycle for $I > 1$

Taking $\gamma = 0.5$ and $I = 2$, numerically solve Equation (7.22) for the three initial conditions: (i) $\theta(0) = 0$, $y(0) = 0.5$; (ii) $\theta(0) = 0$, $y(0) = 2.0$; (iii) $\theta(0) = 0$, $y(0) = 5.0$. Plot $y(\theta)$ for all three initial conditions in the same figure over a θ interval of 2π at a time sufficiently long that all transients have died away. Discuss the result.

Solution: Using the RKF45 method, Equation (7.22) is solved for t sufficiently large ($\tau > 150$) that the transient has died away for all three initial conditions. The numerical results are then plotted in Figure 7.9 for the angular interval $\theta = 598$ to $\tau = 598 + 2\pi$.
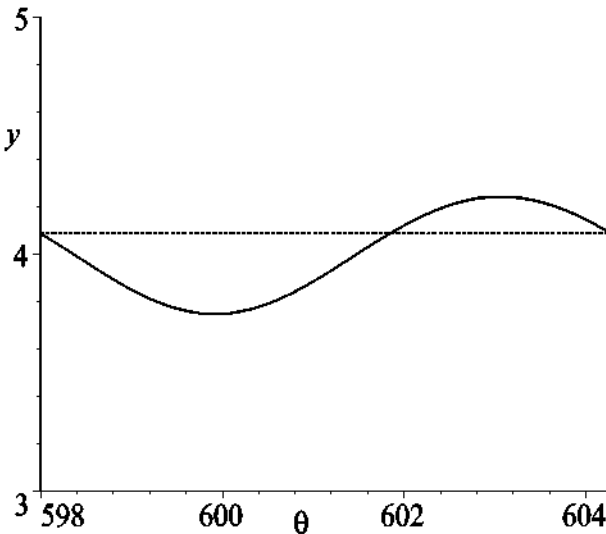
Figure 7.9: Indication of a stable limit cycle.

Independent of the initial conditions, all three curves lie on top of each other in the figure. The horizontal line is included to show that the trajectory closes on itself after an increase of 2π in θ. Thus one has a closed loop on the cylindrical surface and the same loop for all three initial conditions. One has a stable limit cycle. This result can be confirmed for other values of $I > 1$. Since the voltage V is proportional to y, the voltage is periodic in time.

<div align="center">***</div>

For $I < 1$, the behavior of the Josephson junction is slightly trickier, because we have two fixed points, a stable fixed point (node or focus) and a saddle point. Exactly what happens depends on the values of I and γ. Two different scenarios can occur:

- All trajectories approach the stable fixed point, so $V \to 0$.

- A bistable situation exists, with both a stable limit cycle and a stable fixed point present. Depending on the initial conditions, either V becomes periodic or approaches 0.

Example 7-6: Behavior of Josephson Junction for $I < 1$

Numerically solve Equation (7.22) for the following two cases, each of which has three initial conditions:

  a. $I = 0.2$, $\gamma = 0.5$, $\theta(0) = 0$ and (i) $y(0) = -2$; (ii) $y(0) = 2$; (iii) $y(0) = 5$;

  b. $I = 0.5$, $\gamma = 0.25$, $\theta(0) = 0$ and (i) $y(0) = 1.4$; (ii) $y(0) = 1.6$; (iii) $y(0) = 3$.

For each case, plot the 3 trajectories together in the same figure and discuss the results.

Solution: a. The three trajectories are shown on the left of Figure 7.10.
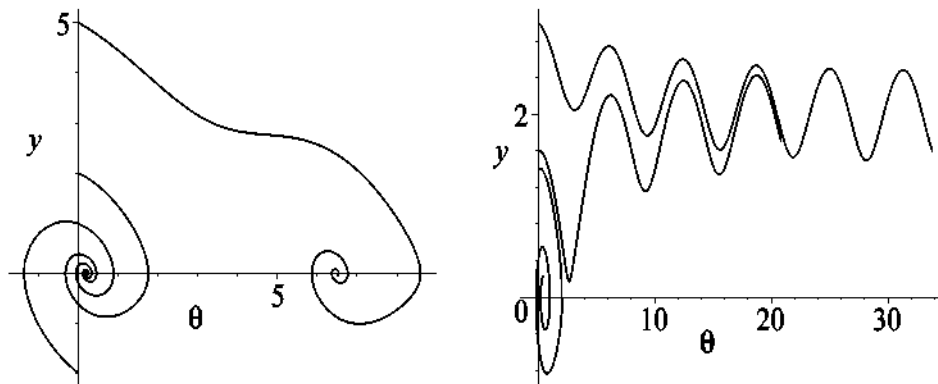
Figure 7.10: Left: Approach to stable fixed points. Right: Bistable situation.

The curves corresponding to $y(0) = -2$ and $+2$ wind onto a stable focal point at $(\bar{\theta} = \arcsin(0.2) = 0.20, \bar{y} = 0)$. The curve corresponding to $y(0) = 5$ winds onto a stable focal point at $(\bar{\theta} = 0.201 + 2\pi = 6.48, \bar{y} = 0)$. This is easily understood if one thinks of the equation describing a simple pendulum acted on by a constant torque. The "velocity" y is sufficiently large that the pendulum goes over the top and completes one revolution before approaching the focal point. Although mathematically this second fixed point is one revolution further along than the first fixed point, it is really the same angular position in space.

b. The relevant trajectories are shown on the right of Figure 7.10. The curve corresponding to $y(0) = 1.4$ winds onto the stable focal point $(\bar{\theta} = \arcsin(0.5) = 0.524, \bar{y} = 0)$. Increasing $y(0)$ slightly to 1.6, the curve no longer approaches the fixed point, but instead evolves into a periodic oscillation. Increasing $y(0)$ still further to 3, we find that the trajectory evolves onto the same periodic oscillation as for $y(0) = 1.6$, confirming that it is a stable limit cycle. With two possible stable states, we have a bistable situation.

$$***$$

The Josephson junction can be used to make useful devices such as the SQUID magnetometer for measuring extremely small magnetic fields.

7.1.6   SQUID Magnetometer

Invented in 1964 by Arnold Silver, Robert Jaklevic, John Lambe, and James Mercereau of Ford Research Labs, a dc SQUID (acronym for Superconducting **QU**antum Interference **D**evice) magnetometer consists of two Josephson junctions arranged in parallel as shown in Figure 7.11, subjected to a constant biasing current. The superconductors are labeled **sc** and the insulating layers are colored white. The voltage across the SQUID is monitored and is sensitive to any changing magnetic flux Φ passing through the inside region of the loop formed by the two junctions.
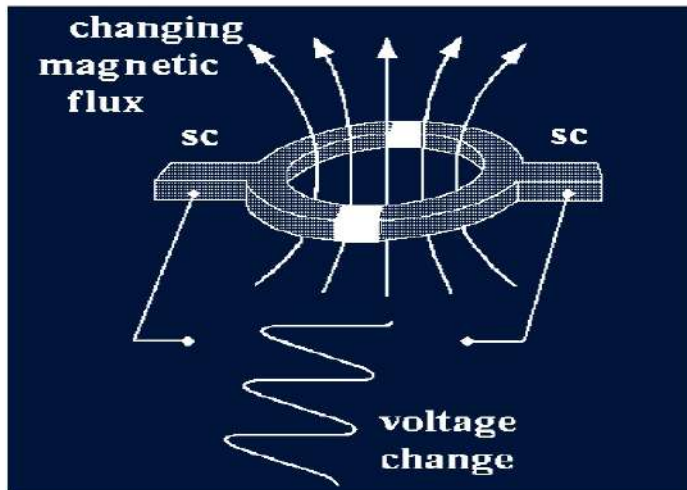
Figure 7.11: Schematic diagram of a SQUID magnetometer.

Suppose that Φ is changed. The voltage change across the junctions then is oscillatory as schematically indicated in the figure. These oscillations were first experimentally observed by Jaklevic et al. ([JLSM64]).

As shown, e.g., in Feynman, one period of voltage oscillation corresponds to a change in magnetic flux by one flux quantum,

$$\Phi_0 = \frac{\pi \hbar}{e} = 2.0687 \times 10^{-15} \ \text{tesla} \cdot \text{m}^2. \tag{7.23}$$

By counting the number n of oscillations and knowing the area A, the change ΔB in magnetic field can be calculated using $\Delta B = n \Phi_0 A$. SQUIDs can typically detect magnetic field changes of the order of 10^{-14} tesla, with specialized types and techniques allowing even smaller fields to be measured.

SQUIDs have found many practical uses, e.g., in studying the magnetic fields associated with electrical activity in the heart and brain. Typical magnetic fields in the heart and the brain are of the order of 10^{-10} and 10^{-13} tesla, respectively. For further information on the use of SQUIDs in *magnetocardiography*, see, e.g., ([Coh67], [BM63]), while their use in *magnetoencephalography* is discussed in ([Coh72]) and ([OIKO05]).

7.2   Nonlinear Optics

High-intensity light sources such as ruby and neodymium-glass lasers can generate ultrashort (nanosecond (10^{-9} s) to picosecond (10^{-12} s)) duration light pulses with large electric fields (10^6 V/m, or larger). When such intense light pulses propagate through solids, liquids, gases, or plasmas, nonlinear optical effects can occur associated with nonlinear electric field terms being induced in the polarization $\vec{P}$ or magnetization $\vec{M}$ of the medium. The field of *nonlinear optics* embodies the theoretical and experimental study and application of such effects. For the technically minded reader, a general treatment of the elements of nonlinear optics may be found, e.g., in Butcher and Cotter ([BC90]).

The starting point for any nonlinear optical modeling is Maxwell's equations:

1. Coulomb's law: $\nabla \cdot \vec{D} = \rho$, with $\vec{D}$ the displacement and ρ the free charge density.

2. Magnetic flux conservation: $\nabla \cdot \vec{B} = 0$, with $\vec{B}$ the magnetic flux density.

3. Faraday's law: $\nabla \times \vec{E} = -\partial \vec{B}/\partial t$, with $\vec{E}$ the electric field vector.

4. Maxwell–Ampere law: $\nabla \times \vec{H} = \vec{J} + \partial \vec{D}/\partial t$, with $\vec{H}$ the magnetic field vector and $\vec{J}$ the free current density.

In addition, one has the auxiliary relations

$$\vec{D} = \epsilon_0 \vec{E} + \vec{P} = \epsilon_0 \epsilon_r \vec{E} = \epsilon \vec{E}, \quad \vec{B} = \mu_0 (\vec{H} + \vec{M}) = \mu \vec{H}, \quad \vec{J} = \sigma (\vec{E} + \vec{v} \times \vec{B}),$$

where ϵ_0 and μ_0 are the vacuum *permittivity* and *permeability*, ϵ_r is the relative permittivity or *dielectric constant* of the medium, and ϵ and μ are the medium permittivity and permeability. The vacuum speed of light $c = 1/\sqrt{\mu_0 \epsilon_0}$. The coefficient σ is the electrical *conductivity* (zero for a dielectric) and $\vec{v}$ is the velocity of the medium if it is moving (e.g., for gas or liquid flow). See, e.g., Jackson's *Classical Electrodynamics* ([Jac75]).

For simplicity, let's confine our interest to nonlinear optical effects involving transversely polarized electromagnetic pulses traveling in an isotropic, nonmagnetic ($\vec{M} = 0$ so $\vec{B} = \mu_0 \vec{H}$), dielectric ($\rho = \vec{J} = 0$) medium. In this case, Coulomb's law reduces to

$$\nabla \cdot \vec{D} = 0, \quad \text{or} \quad \epsilon_0 \nabla \cdot \vec{E} = -\nabla \cdot \vec{P} = 0. \tag{7.24}$$

Maxwell–Ampere's law yields

$$\nabla \times \vec{B} = \mu_0 \epsilon_0 \frac{\partial \vec{E}}{\partial t} + \mu_0 \frac{\partial \vec{P}}{\partial t}. \tag{7.25}$$

Taking the curl of Faraday's law and using a well-known vector identity, we have

$$\nabla \times (\nabla \times \vec{E}) = -\frac{\partial}{\partial t}(\nabla \times \vec{B}),$$
$$\nabla(\nabla \cdot \vec{E}) - \nabla^2 \vec{E} = 0 - \nabla^2 \vec{E} = -\mu_0 \epsilon_0 \frac{\partial^2 \vec{E}}{\partial t^2} - \mu_0 \frac{\partial^2 \vec{P}}{\partial t^2} = -\mu_0 \epsilon_0 \frac{\partial^2}{\partial t^2} \left(\epsilon_r \vec{E} \right), \tag{7.26}$$

or

$$\nabla^2 \vec{E} = \frac{1}{c^2} \frac{\partial^2}{\partial t^2} \left(\epsilon_r \, \vec{E} \right). \tag{7.27}$$

For weak light beams propagating through a dielectric, ϵ_r is independent of $\vec{E}$ (i.e., is a constant) and (7.27) is just the linear wave equation for the electric field inside the dielectric. This is the domain of *linear optics*, the domain which dominates almost all undergraduate electromagnetic and optics courses.

For intense laser pulses, the electric fields inside the dielectric are sufficiently large that ϵ_r (and therefore the *refractive index* $n = \sqrt{\epsilon_r}$) will be electric field dependent. Equation (7.27) then is a nonlinear PDE for the electric field. This is the domain of *nonlinear optics*, the precise nonlinear optical effect depending on the electric field dependence of ϵ_r or n. We will now look at two nonlinear optical examples involving dielectric media, viz., optical soliton propagation in a glass fiber and stimulated Brillouin scattering in a liquid cell.

7.2.1 Optical Soliton Propagation

Our first example involves optical soliton propagation in a straight, transparent, glass fiber. Akira Hasegawa and Fred Tappert ([HT73]) first predicted stable solitary wave solutions to the governing *nonlinear Schrödinger equation* (NLSE) in 1973. Instead of deriving the NLSE directly from Equation (7.27), we shall use a mathematically simpler approach which glosses over some of the technical details. The reader who is interested in these details should consult Hasegawa's *Optical Solitons in Fibers* ([Has90]) or Govind Agrawal's *Nonlinear Fiber Optics* ([Agr89]).

The refractive index n of the glass fiber is given by the intensity-dependent[6] *Kerr index* ([Has90]),

$$n = \frac{c\,k}{\omega} = n_0(\omega) + n_2 \,|E|^2, \tag{7.28}$$

where k is the wave number, ω is the frequency, $n_0(\omega)$ is the linear refractive index, and the coefficient n_2 (whose frequency dependence can be neglected) of the nonlinear electric field term is positive.

Assuming that the diameter of the fiber is much larger than the wavelength of the laser pulse, the electric field of the pulse can be written as a product of a slowly varying complex amplitude Φ times a plane wave propagating in the fiber (x) direction, viz.,

$$E(x,t) = \Phi(x,t)\, e^{i(k_0 \, x - \omega_0 \, t)}. \tag{7.29}$$

Here k_0 and $\omega_0 = 2\,\pi\,c/\lambda_0$ are the central wave number and frequency, respectively, with λ_0 the central wavelength. The observable electric field is obtained by taking the real part of $E(x,t)$. For the laser pulse the frequency ω is limited to a small range around ω_0, thus allowing us to use $(\omega - \omega_0)$ as an expansion parameter.

---

[6]The time-averaged light intensity I is given by $I = (1/2)\,\epsilon_0 n_0 \,c\,|E|^2$.

Taylor expanding $k = k(\omega, |E|^2)$ around ω_0 and zero electric field, we obtain

$$k - k_0 = k_0' \, (\omega - \omega_0) + \frac{1}{2} \, k_0'' \, (\omega - \omega_0)^2 + \frac{2 \, \pi \, n_2}{\lambda_0} \, |E|^2 + \cdots, \tag{7.30}$$

where

$$k_0' \equiv \left(\frac{\partial k}{\partial \omega} \right)_0 = \frac{c}{n_0 + \omega_0 \, (\partial n_0 / \partial \omega)_0} \equiv \frac{1}{v_g} \tag{7.31}$$

and

$$k_0'' \equiv \left(\frac{\partial^2 k}{\partial \omega^2} \right)_0 = \left(\frac{\partial}{\partial \omega} \right) \left(\frac{1}{v_g} \right) = -\frac{1}{v_g^2} \, \frac{\partial v_g}{\partial \omega}. \tag{7.32}$$

Here v_g is the *group velocity* and k_0'' is a measure of the *group velocity dispersion*.

Let's now write the electric field in its Fourier integral form,

$$E(x,t) = \frac{1}{2 \, \pi} \int_{-\infty}^{+\infty} \int_{-\infty}^{+\infty} \varepsilon(k, \omega) \, e^{i \, (k \, x - \omega \, t)} \, dk \, d\omega. \tag{7.33}$$

Equating the two forms, (7.29) and (7.33), the amplitude $\Phi(x,t)$ is given by

$$\Phi(x,t) = \frac{1}{2 \, \pi} \int_{-\infty}^{+\infty} \int_{-\infty}^{+\infty} \varepsilon(k, \omega) \, e^{i \, [(k - k_0) \, x - (\omega - \omega_0) \, t]} \, dk \, d\omega. \tag{7.34}$$

Then, making use of (7.30) with higher-order terms neglected, we obtain

$$i \left(\frac{\partial \Phi}{\partial x} + \frac{1}{v_g} \, \frac{\partial \Phi}{\partial t} \right) - \frac{1}{2} \, k_0'' \, \frac{\partial^2 \Phi}{\partial t^2} + \frac{2 \, \pi \, n_2}{\lambda_0} \, |\Phi|^2 \, \Phi = 0. \tag{7.35}$$

Introducing the dimensionless variables

$$\zeta = s \, \frac{x}{\lambda_0}, \quad \tau = \frac{\sqrt{s}}{\sqrt{-\lambda_0 \, k_0''}} \left(t - \frac{x}{v_g} \right), \quad q = \frac{\sqrt{2 \, \pi \, n_2}}{\sqrt{s}} \, \Phi, \tag{7.36}$$

where s is a suitably chosen numerical scale factor, Equation (7.35) reduces to the *nonlinear Schrödinger equation*,

$$i \frac{\partial q}{\partial \zeta} + \frac{1}{2} \, \frac{\partial^2 q}{\partial \tau^2} + |q|^2 \, q = 0. \tag{7.37}$$

Note that we have assumed that $k_0'' < 0$ in introducing the dimensionless variable τ. In typical glass fibers, $k_0'' = 0$ at about 1.3 μm. Negative group velocity dispersion (called *anomalous* dispersion) occurs for wavelengths larger than 1.3 μm. Further note that in introducing τ, one has transformed from the laboratory frame of reference to a frame moving with the group velocity.

Typically for optical soliton propagation in a glass fiber,

$$\lambda_0 \approx 1.5 \ \mu\text{m}, \quad -\lambda_0 \, k_0'' \approx 3.2 \times 10^{-32} \ \text{s}^2, \quad n_2 \approx 1.2 \times 10^{-22} \ (\text{m/V})^2.$$

If the numerical scale factor is taken be $s = 10^{-9}$, then a scaled distance $\zeta = 1$ corresponds to 1.5 km, $\tau = 1$ to 5.7 ps, and $q = 1$ to 1.6×10^6 V/m.

The mathematical form of the solitary wave solution to the NLSE is now derived.

Example 7-7: Optical Solitary Wave

Derive a nontopological solitary wave solution for the NLSE, assuming that $q(\zeta, \tau) = Q(\tau) e^{i\beta\zeta}$ where β is a real parameter. This is referred to as a *stationary solution*, since it is stationary with respect to the frame moving with the group velocity. The light intensity is proportional to $|E|^2 = |\Phi|^2$ and therefore to $|q|^2 = Q^2$. Plot Q^2 for $\beta = 1/2$.

Solution: Substituting the assumed form of q into the NLSE yields the nonlinear ODE

$$\frac{d^2 Q}{d\tau^2} - 2\beta Q + 2Q^3 = 0.$$

Multiplying this ODE by $2\,(dQ/d\tau)$ and integrating with respect to τ, we obtain

$$\left(\frac{dQ}{d\tau}\right)^2 = 2\beta Q^2 + Q^4 + \text{constant}.$$

For a nontopological solitary wave both Q and $dQ/d\tau \to 0$ for $|\tau| \to \infty$ so that the integration constant is zero. Taking the square root, separating variables, and integrating yields

$$Q = \sqrt{2\beta}\, \text{sech}(\sqrt{2\beta}\,\tau).$$

The maximum value of Q is $\sqrt{2\beta}$, occurring at $\tau = 0$. The pulse width scales as $1/\sqrt{2\beta}$. Taking $\beta = 1/2$, $Q^2 = \text{sech}^2\tau$ is plotted in Figure 7.12.
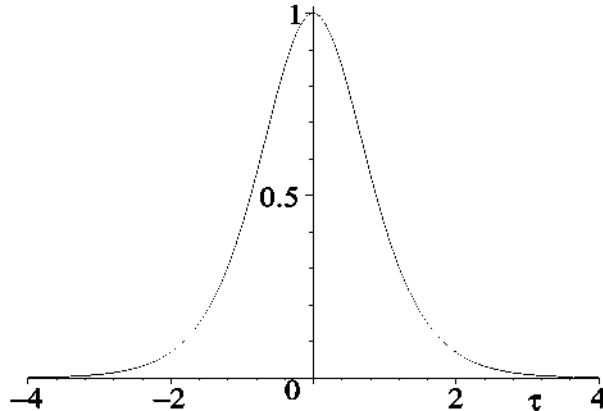
Figure 7.12: Plot of Q^2 (aside from a scale factor, the light intensity).

That the above solitary wave is a soliton can be established by carrying out numerical collision simulations similar to those for the KdV solitary waves.

***

Although their existence had been predicted by Hasegawa and Tappert in 1973, optical solitons were not experimentally observed until 1980 when a laser became available at the appropriate wavelength (≈ 1.5 μm) and the fiber loss (neglected in the above analysis) was sufficiently reduced to allow the pulses to propagate. Mollenauer, Stolen, and Gordon ([MSG80]) were able to propagate a 10-ps optical soliton with a wavelength of 1.5 μm and a peak power of a few watts through a 700-meter low-loss fiber. They showed that the pulse width decreases with increasing peak power. In 1988, Mollenauer's group ([MNE+88]) was able to transmit optical solitons over a 10,000-km distance in a fiber, using periodic amplifiers to reboost the solitons which slowly decay with increasing distance.

Since the soliton pulse widths are very narrow, one could envision using optical solitons as very-high-bit-rate carriers of digitized information in glass fibers. A stream of solitons separated by gaps could be used to represent a series of ones and zeros in the binary representation, the solitons being the ones and the gaps the zeros.

If the laser wavelength is in the *normal* dispersion range where $k_0'' > 0$, the nonlinear Schrödinger equation is modified to

$$i\frac{\partial q}{\partial \zeta} - \frac{1}{2}\frac{\partial^2 q}{\partial \tau^2} + |q|^2 q = 0. \tag{7.38}$$

In this case, *dark solitons* are possible, the solitons obtained earlier for anomalous dispersion being called *bright solitons*. A dark soliton is a localized dip in intensity in a bright background. Dark solitons have been experimentally confirmed by Weiner and co-workers ([WHH+88]).

The optical NLSE has been generalized to higher dimensions. For example, Edmundson and Enns have numerically investigated 3-dimensional spherical optical solitons (so-called *light bullets* ([Sil90])) for the generalized NLSE which involves a saturable Kerr index ([EE95]). Animated light bullet collisions and other interesting spherical soliton behavior may be seen on the Internet (**www.sfu.ca/~renns/lbullets.html**).

7.2.2 The Navier–Stokes Equations

Our second example in nonlinear optics will involve intense laser beams propagating in a fluid. The basic dynamical equations governing fluid flow are the nonlinear *Navier–Stokes* (NS) *equations*, developed by the French engineer Claude-Louis Navier (1785–1836) and Irish physicist George Stokes. These equations have been used to model all sorts of fluid phenomena ranging from engineering applications in aerodynamics and car design to research on fundamental physics questions about atmospheric and oceanic circulation (the sources of the weather and, on a longer time scale, climate change) and, when augmented with Maxwell's equations, the motion of the Earth's molten outer core.

The NS equations provide a mathematical description of the physics of fluid motion. In fluid mechanics, the fluid is treated as a continuum, its particle nature being ignored. Continuous variables such as the pressure p, temperature T, and density ρ, as well as the velocity $\vec{v}$ of a fluid volume element, are used to describe the fluid at every point $\vec{r}$ at each instant t in time.

In many applications, it is assumed that one is dealing with a *Newtonian* fluid. This is a fluid for which the shear (drag) force per unit area (the *stress*) exerted by a moving fluid layer on an adjacent layer is proportional to the gradient of $\vec{v}$ perpendicular to the direction of shear. The proportionality constant is the *viscosity coefficient* η. Despite widely different η values, air, water, and honey are all examples of Newtonian fluids.

Non-Newtonian fluids such as ketchup, blood, yogurt, gravy, and mud, to name a few, behave differently. A nonlinear relationship exists between doubling the speed that layers slide past each other and the shear force. For ketchup, for example, the shear force less than doubles when the speed is doubled.

The NS fluid equations are a statement of three conservation laws:

- Conservation of mass (the *continuity* equation):

$$\frac{\partial \rho}{\partial t} + \nabla \cdot (\rho \vec{v}) = 0. \tag{7.39}$$

In many applications, a fluid can be approximated as being *incompressible*, i.e., ρ is constant. Then (7.39) reduces to $\nabla \cdot \vec{v} = 0$. For example, water is treated as incompressible for flow through a pipe. On the other hand, compressibility must be considered for sound wave propagation through water.

- Conservation of momentum (Newton's second law per unit volume):

$$\rho \frac{d\vec{v}}{dt} = \rho \left(\frac{\partial \vec{v}}{\partial t} + (\vec{v} \cdot \nabla)\vec{v} \right) = -\nabla p + \eta \nabla^2 \vec{v} + \vec{F}. \tag{7.40}$$

The left-hand side is just mass (per unit volume) times acceleration. The acceleration is made up of two terms, the $\partial \vec{v}/\partial t$ term taking into account any explicit time variation of the velocity at a given point, while the nonlinear $(\vec{v} \cdot \nabla)\vec{v}$ term describes "convective" acceleration associated with flow of the fluid from point to point. On the right-hand side are the various forces (per unit volume), the pressure gradient, viscous drag (for a Newtonian fluid), and $\vec{F}$ representing all other forces that might be present. For example, these could include:

  - Gravitational force: $\vec{F}_{gravity} = \rho \vec{g}$.
  - Coriolis force on a spinning fluid (e.g., the Earth's atmosphere and oceans): $\vec{F}_{Coriolis} = -2\rho (\vec{\Omega} \times \vec{v})$, where $\vec{\Omega}$ is the angular velocity.
  - Electromagnetic force on a conducting fluid (e.g., the Earth's molten core): $\vec{F}_{em} = \vec{J} \times \vec{B}$, with $\vec{J}$ the current density and $\vec{B}$ the magnetic field.
  - Electrostrictive force on a dielectric fluid (e.g., stimulated Brillouin scattering): $\vec{F}_{electro} = C \nabla(E^2)$, with E the electric field and the constant $C > 0$.

- Conservation of energy:

$$\rho c_v \frac{dT}{dt} = K \nabla^2 T - p \nabla \cdot \vec{v} + S. \tag{7.41}$$

Here c_v is the specific heat per unit volume and K is the thermal conductivity. The first term on the right is the heat flux, while the second is associated with the work of compression. S represents any energy sources or sinks (losses).

Only with simplifying assumptions can exact closed form results be obtained for the NS equations.[7] For example, in undergraduate fluid dynamics courses a standard problem is to consider the steady *irrotational flow* of an incompressible fluid past a stationary sphere or very long cylinder. For irrotational flow, the *vorticity vector* $\vec{\omega} = \nabla \times \vec{v} = 0$, i.e., vortices or whirlpools are not present. This implies that a *velocity potential* ϕ can be introduced, with $\vec{v} = \nabla \phi$, since $\nabla \times \nabla \phi = 0$ for any scalar function ϕ. If the fluid is incompressible, then $\nabla \cdot \vec{v} = \nabla \cdot (\nabla \phi) = \nabla^2 \phi = 0$, which is *Laplace's equation* for the velocity potential. Because Laplace's equation is a linear PDE, a wide variety of standard mathematical methods (e.g., separation of variables) are available to solve it in different coordinate (e.g., spherical polar) systems.

It should be noted that the *Bernoulli equation*, $p + (1/2)\rho v^2 =$ constant, can be derived from the momentum conservation equation (7.40) for steady, incompressible, irrotational fluid flow and used to obtain the lift force on, e.g., an aircraft wing.

Example 7-8: Bernoulli Equation and the Lift Force

   a. Taking $\vec{F} = 0$, express (7.40) for an incompressible fluid in terms of $\vec{\omega}$.

   b. Show that Bernoulli's equation results for steady irrotational fluid flow and use it to explain the mathematical structure of the lift force on an aircraft wing.

Solution: a. We make use of the following two vector identities and set $\nabla \times \vec{v} = \vec{\omega}$:

$$(\vec{v} \cdot \nabla)\vec{v} = \frac{1}{2}\nabla(v^2) - \vec{v} \times (\nabla \times \vec{v}) = \frac{1}{2}\nabla v^2 - \vec{v} \times \vec{\omega},$$

$$\nabla^2 \vec{v} = \nabla(\nabla \cdot \vec{v}) - \nabla \times (\nabla \times \vec{v}) = \nabla(\nabla \cdot \vec{v}) - \nabla \times \vec{\omega}. \tag{7.42}$$

For an incompressible fluid, ρ is constant and $\nabla \cdot \vec{v} = 0$, so (7.40) becomes

$$\rho \frac{\partial \vec{v}}{\partial t} + \nabla \left(p + \frac{1}{2}\rho v^2 \right) = \rho(\vec{v} \times \vec{\omega}) - \eta(\nabla \times \vec{\omega}). \tag{7.43}$$

b. For steady flow, $\partial \vec{v}/\partial t = 0$. If the flow is also irrotational, then $\vec{\omega} = 0$, and we have

$$\nabla \left(p + \frac{1}{2}\rho v^2 \right) = 0, \quad \text{so} \quad p + \frac{1}{2}\rho v^2 = \text{constant}. \tag{7.44}$$

Consider the wing to be horizontal with a zero angle of attack with the wind. Let the pressure and air speed on the top side of the wing be p_t and v_t, respectively, and p_b and v_b on the bottom. The (Bernoulli) pressure difference $p_b - p_t = (1/2)\rho(v_t^2 - v_b^2)$. If the wing is shaped so that $v_t > v_b$, then $p_b > p_t$ and there is a net pressure upwards on it. If the incident wind speed is V and we set $v_t = aV$ and $v_b = bV$, with the constant $a > b$, then the lift force on a wing of area A is $F_L = (p_b - p_t)A = (1/2)\rho(a^2 - b^2)V^2 A \equiv (1/2)\rho C_L A V^2$, where C_L is the lift coefficient.

<p style="text-align:center">∗∗∗</p>

---

[7]The Clay Mathematics Institute of Cambridge, Massachusetts, has offered a 1 million dollar prize for proof of the existence of a smooth solution to the exact NS equations in 3 dimensions.

7.2.3   Stimulated Scattering of Light

Using the experimental setup schematically depicted in Figure 7.13, one can create a predator–prey interaction between two intense pulsed laser beams having different frequencies. The linearly polarized output of a ruby laser (the "pump" beam with frequency ω_L) is split into two beams with a beam splitter and then, using reflect-
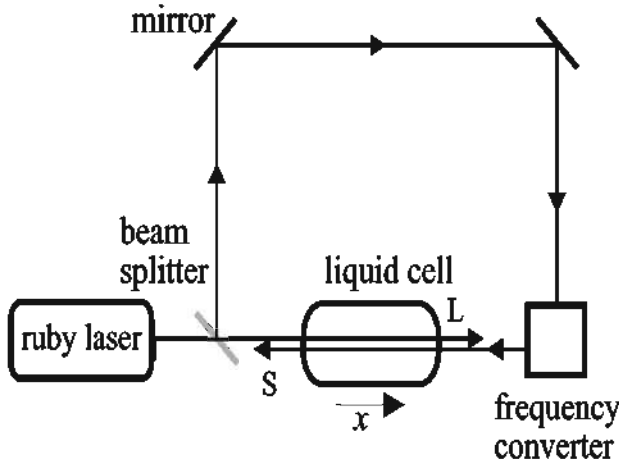
Figure 7.13: Experimental setup for the stimulated scattering of light.

ing mirrors, sent in opposite directions through each other in a glass cell of length ℓ containing a transparent liquid with a large thermal expansion coefficient, e.g., carbon tetrachloride. One of the beams (called the "signal" (S) beam) is sent through a frequency converter, which alters its frequency slightly from ω_L to $\omega_S < \omega_L$. Let the speed of sound in the liquid be v_{sound}, the intensity and wave number of the direct laser (pump) beam be I_L and k_L, and the intensity and wavenumber of the signal beam be I_S and k_S. The input intensities $I_L(x = 0)$ and $I_S(x = \ell)$ and output intensities $I_L(\ell)$ and $I_S(0)$ are experimentally determined quantities.

If the frequency difference is adjusted so that $\omega_L - \omega_S = \omega \approx v_{sound}\,k$, with $k = k_L + k_S$, the interacting beams produce an electrostrictive force (per unit volume) in the region of overlap which generates coherent sound waves (density fluctuations) with frequency ω and wave number k. The sound waves, in turn, cause light to be scattered from the pump to the signal beam, thus amplifying the latter at the expense of the former. This nonlinear optical phenomenon, first experimentally observed by Raymond Chiao, Charles Townes, and Boris Stoicheff in 1964 ([CTS64]), is called *stimulated Brillouin scattering* (SBS).[8]

If a small amount of absorbing dye (absorption coefficient α), e.g., iodine, is added to the transparent liquid, a thermally induced sound wave contribution also occurs which produces additional light scattering. This phenomenon is referred to as *stimulated thermal Brillouin scattering* (STBS). By combining Maxwell's wave equation for

---

[8]Leon Brillouin predicted the scattering of light by sound waves as early as 1922.

the interacting light beams with the Navier–Stokes equations (continuity equation, momentum equation with an electrostrictive force term, energy equation with an energy absorption source term proportional to αE^2) for the liquid, the following governing equations can be derived [9] for the light intensities in STBS:

$$\frac{dI_L}{dx} = -g\,I_L\,I_S - \alpha\,I_L,$$
$$\frac{dI_S}{dx} = -g\,I_L\,I_S + \alpha\,I_S,$$
(7.45)

with $g(\omega)$ the analytically determined *gain coefficient* expressed in terms of the known (independently measured) liquid parameters. In deriving these equations, use is made of the fact that the light pulse durations (typically of the order of 20 nanoseconds) are much longer than the induced sound wave lifetimes (of the order of a nanosecond) so that steady state prevails, thus removing all time derivatives. Order-of-magnitude arguments are also invoked to drop small spatially varying, and certain other, terms.

The STBS gain equations (7.45) cannot be solved exactly. If the initial pump intensity $I_L(0) \gg I_S(\ell)$ and the amplification of the signal beam small ($g\,I_L(0)\,\ell$ small), the depletion of the pump beam can be ignored to a first approximation, i.e., $I_L(x) \approx I_L(0)$. Then,

$$\frac{dI_S}{dx} \approx (-g\,I_L(0) + \alpha)\,I_S,$$

which is readily integrated to yield a signal output (at $x = 0$) given by

$$I_S(0) = I_S(\ell)\,e^{(g\,I_L(0)-\alpha)\ell} \approx I_S(\ell)\,[1 + g\,I_L(0)\,\ell]\,e^{-\alpha\ell}.$$
(7.46)

For SBS, $\alpha = 0$ and only electrostriction contributes to the gain coefficient. In this case, $g(\omega = \omega_L - \omega_S)$ has the shape shown on the left of Figure 7.14, the peak being center-
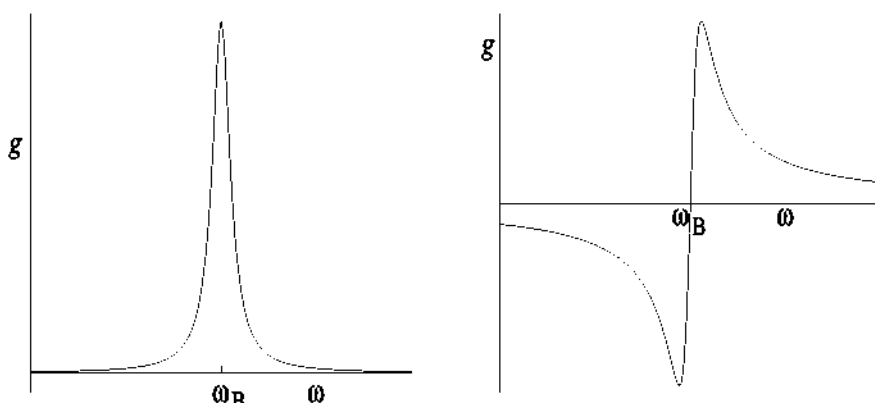
Figure 7.14: Electrostrictive (left) and absorptive (right) contributions to $g(\omega)$.

[9]See the review paper by Batra, Enns, and Pohl ([BEP71]) for the gory details.

ed at the *Brillouin frequency*, $\omega_B = v_{sound}\,k$. Since $g(\omega)$ is positive, the signal beam is amplified as it passes through the liquid cell. The analytically determined gain coefficient is in excellent agreement (see [BEP71]) with the measured $g(\omega)$, confirming the correctness of the theory.

For STBS, $\alpha \neq 0$, and an absorptive contribution to g must also be included. The qualitative shape of this contribution is shown on the right of the above figure. The total gain coefficient for STBS is the sum of the electrostrictive and absorptive contributions. The STBS gain coefficient has been measured experimentally by Pohl, Reinhold, and Kaiser ([PRK68]) and found to be in excellent agreement with theory (see also [BEP71]).

7.3   The Earth's Magnetic Field

To round off our small sampling of interesting nonlinear phenomena from the world of electromagnetism, we will finish with examples involving the Earth's magnetic field.

7.3.1   Aurora Borealis

The *Aurora Borealis* or northern lights is produced by charged particles from the sun spiraling down the Earth's magnetic field lines in the vicinity of the North Magnetic Pole and striking molecules in the atmosphere causing them to glow. A similar phenomenon occurs near the South Magnetic Pole and is called *Aurora Australis*.

In this section, we will solve the nonlinear ODEs which describe this spiraling motion. Spherical polar coordinates (r, θ, ϕ) will be used, with the origin at the center of the Earth and the positive z-axis pointing in the direction of magnetic North. Here r is the radial distance from the origin, θ is the angle that the radius vector makes with the z-axis, and ϕ is the angle its projection in the x–y plane makes with the x-axis.

Although quite complicated in the interior, the Earth's magnetic field $\vec{B}$ on the outside is approximately that of a magnetic dipole, i.e., similar to the external field of a bar magnet. The radial and angular field components are given by ([Gri99])

$$B_r = -\frac{\mu_0}{4\pi}\frac{2\,m\cos\theta}{r^3}, \quad B_\theta = -\frac{\mu_0}{4\pi}\frac{m\sin\theta}{r^3}, \quad B_\phi = 0, \qquad (7.47)$$

where m is the magnetic dipole moment and μ_0 is the permeability of free space. For $\theta = 0$, the magnetic field lines point radially *inwards* to the North Magnetic Pole. The field lines at other points outside the Earth are easily determined. Noting that $dr/(r\,d\theta) = B_r/B_\theta$, the field lines satisfy the relation

$$\frac{dr}{r} = d(\ln r) = \frac{B_r}{B_\theta}\,d\theta = 2\,\frac{\cos\theta}{\sin\theta}\,d\theta = d(\ln(\sin^2\theta)),$$

which is easily integrated to yield

$$r = C\sin^2\theta, \qquad (7.48)$$

where C is an arbitrary constant. Choosing various values of C will produce the magnetic dipole field lines.

Example 7-9: Magnetic Field Lines for the Earth

Taking the Earth to be of unit radius, make a planar plot of some representative magnetic field lines outside the Earth's surface.

Solution: The field lines are plotted in Figure 7.15 for $C = \pm 15$, ± 12.5, ± 10, ± 7.5, ± 5. The Earth is plotted as a solid black circle of radius 1 unit.
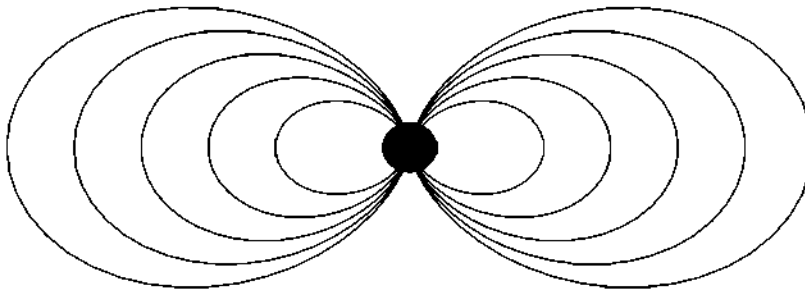
Figure 7.15: Magnetic dipole field outside the Earth.

***

It is convenient to introduce the *vector potential* $\vec{A}$, related to $\vec{B}$ by $\vec{B} = \nabla \times \vec{A}$. In spherical polar coordinates, it is straightforward to confirm that a vector potential which produces the magnetic dipole field (7.47) is

$$\vec{A} = -\frac{\mu_0}{4\pi} \frac{m \sin\theta}{r^2} \hat{\phi}, \tag{7.49}$$

where $\hat{\phi}$ is the unit vector in the ϕ direction.

The motion of a charged particle (charge Q, mass M, velocity $\vec{v}$) in the magnetic dipole field can be determined by making use of Lagrange's equations of motion,

$$\frac{d}{dt}\left(\frac{\partial L}{\partial \dot{q}_i}\right) - \frac{\partial L}{\partial q_i} = 0, \quad \text{with } q_1 = r, \ q_2 = \theta, \ q_3 = \phi, \tag{7.50}$$

where $L = T - V$ is the Lagrangian, T the kinetic energy of the particle, and V its potential energy. In spherical polar coordinates, the Lagrangian is ([GPS02])

$$L = \frac{1}{2} M v^2 + Q(\vec{v} \cdot \vec{A}) = \frac{1}{2} M (\dot{r}^2 + r^2 \dot{\theta}^2 + r^2 \sin^2\theta \, \dot{\phi}^2) - \frac{\mu_0}{4\pi} \frac{Q m}{r} \sin^2\theta \, \dot{\phi}. \tag{7.51}$$

Noting that L contains no explicit ϕ dependence, taking $q_i = q_3 = \phi$ in (7.50) yields

$$M r^2 \sin^2\theta \, \dot{\phi} - \frac{\mu_0}{4\pi} \frac{Q m}{r} \sin^2\theta = C, \tag{7.52}$$

where C is a constant of the motion. A second constant of the motion is the speed v. This follows because the *Lorentz force* $\vec{F} = Q\,(\vec{v} \times \vec{B})$ exerted by the magnetic field on Q is perpendicular to the velocity, so that the energy delivered by the field to the charge per unit time is $\vec{F} \cdot \vec{v} = 0$.

Taking $q_i = q_1 = r$ and $q_2 = \theta$ in (7.50) yields the following coupled nonlinear ODEs, which must be solved numerically:

$$\ddot{r} - r\dot{\theta}^2 - r\,\sin^2\theta\,\dot{\phi}^2 - \frac{\mu_0}{4\pi}\frac{Q\,m}{M\,r^2}\,\sin^2\theta\,\dot{\phi} = 0,$$
$$r^2\,\ddot{\theta} + 2\,r\,\dot{r}\,\dot{\theta} - r^2\,\sin\theta\,\cos\theta\,\dot{\phi}^2 + \frac{\mu_0}{4\pi}\frac{2\,Q\,m}{M\,r}\,\sin\theta\,\cos\theta\,\dot{\phi} = 0. \tag{7.53}$$

Example 7-10: Proton Trajectory in the Earth's Dipole Field

The Earth has a radius $R_E = 6.37 \times 10^6$ m and a magnetic dipole moment $m = 7.94 \times 10^{22}$ A·m², while the permeability of free space $\mu_0 = 4\pi \times 10^{-7}$ N/m. Take the particle to be a proton with rest mass $M_0 = 1.67 \times 10^{-27}$ kg and charge $Q = 1.6 \times 10^{-19}$ C. Initially, $r(0) = 2\,R_E$, $\theta(0) = \pi/2$, $\phi(0) = 0$, $\dot{r}(0) = 0$, $\dot{\theta}(0) = 17$, and $\dot{\phi}(0) = 0$.

a. Calculate the initial speed $v(0)$ of the proton and then its mass $M = M_0/\sqrt{1 - \beta^2}$, where $\beta = v/c$. Here, $c = 3 \times 10^8$ m/s is the vacuum speed of light.

b. Solve the coupled ODE system and plot the 3-dimensional trajectory in units of the Earth's radius, including a sphere to represent the earth. Discuss the result.

Solution: a. We have $v(0) = 2\,R_E\,\dot{\phi}(0) = 2.17 \times 10^8$ m/s. The ratio $\beta = 0.72$, so the relativistic mass $M = M_0/\sqrt{1 - \beta^2} = 2.41 \times 10^{-27}$ kg.

b. Figure 7.16 shows a portion of the proton's trajectory in the Earth's magnetic di-
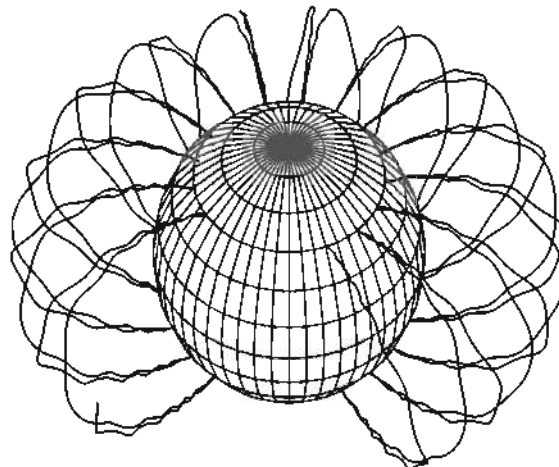
Figure 7.16: Trajectory of a proton moving in the Earth's magnetic dipole field.

pole field. The spherical Earth is also shown, with the north pole at the top. In this idealized model calculation which neglects all energy losses, the proton spirals along the lines of force, reversing direction in the vicinity of the poles and eventually circumnavigating the globe. The aurora occur in the vicinity of the turning points near the North and South Magnetic Poles.

<p align="center">***</p>

7.3.2   The Drifting North Magnetic Pole

Although the North Magnetic Pole is close to the geographic north pole (fixed by the Earth's spin axis), it is shifting with time and as a consequence the location of the northern lights is also shifting. Scientists have known for a long time that the North Magnetic Pole moves. The British explorer James Ross located the pole for the first time in 1831 in the vicinity of the Boothia Peninsula in northern Canada. This is position 1 in Figure 7.17, the figure covering the region from (about) 90° to 115° W and 65° to 85° N.
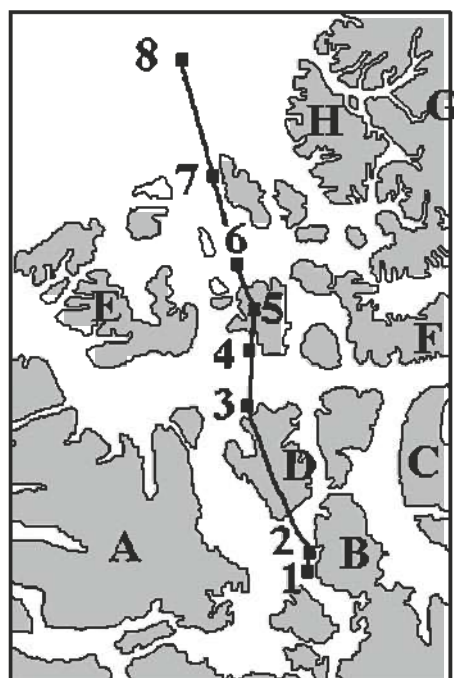
Figure 7.17: Track of the North Magnetic Pole, 1831–2001 (Geological Survey of Canada). Dates: 1 = 1831, 2 = 1904, 3 = 1948, 4 = 1962, 5 = 1973, 6 = 1984, 7 = 1994, 8 = 2001. Landmarks: A=Victoria Island, B=Boothia Peninsula, C=Baffin Island, D=Prince of Wales Island, E=Melville Island, F=Devon Island, G=Ellesmere Island, H=Axel Heiberg Island. (**www.nrcan.gc.ca**)

When Roald Amundsen found the North Magnetic Pole again in 1904, it had moved 50 kilometers farther north to position 2. The pole kept drifting northerly and westerly during the 20th century, averaging about 10 km per year. Lately, it has speeded up to 40 km/year according to Larry Newitt of the Geological Survey of Canada. Predicted to be at about 85° N and 133° W in 2010, the North Magnetic Pole will exit North America and reach Siberia in a few decades.

This drifting of the North Magnetic Pole is mild compared to the chaotic flipping of the poles (north becoming south and vice versa at irregular times) observed in the paleomagnetic records. The last magnetic pole reversal occurred about 780 thousand years ago. To understand the behavior of the Earth's magnetic field, one has to examine the geodynamo action which occurs in the Earth's molten iron outer core. Because this region is difficult to study experimentally, one must rely on numerically solving Maxwell's electromagnetic equations coupled to the nonlinear Navier–Stokes equations describing the Earth's liquid iron core.

7.3.3   The Geodynamo Origin of the Earth's Magnetic Field

On the basis of seismic wave propagation through the Earth and other geophysical evidence, we have a good idea of the Earth's layered structure as well as reasonable estimates of the parameter values for each layer ([CHT97]).

The outermost layer of the Earth is the *crust* which is from 10 to 70 km thick and consists of solid moving plates which are being pushed apart along the ocean ridges (e.g., the mid-Atlantic ridge between North America and Europe) and colliding along the ocean trenches (e.g., the Aleutian trench off Alaska). The plates are driven by the *subduction* (gravity-controlled sinking) of cold, denser oceanic slab material along the trenches. This *slab pulling* drags the rest of the plate with it. As the slab material sinks, it heats up and begins to soften and flow, forming a convective cell in the underlying *mantle*, the mantle extending down to 2900 km below the Earth's surface. The convective cells produce upwelling along the ocean ridges. As the ejected molten ridge material cools below the *Curie temperature* for permanent magnetism, the magnetic field of the Earth is "recorded" in it. These paleomagnetic recordings reveal that the Earth's magnetic field has existed for over 3 billion years and that the north and south poles have reversed with time in an unpredictable (chaotic) manner. The subduction zones, on the other hand, are regions where substantial volcanic activity occurs (e.g., the volcanic *ring of fire* around the Pacific ocean) due to melting of the subducted plates.

Below the mantle is the liquid *outer core* composed of an iron–nickel alloy (by weight, about 80% iron, 5% nickel) along with some less dense elements. The outer core extends from 2900 km to 5080 km with the temperature ranging from about 4400°C at the core–mantle boundary (CMB) to about 6100°C at the inner core boundary (ICB). Remarkably, the *kinematic viscosity*, $\nu = \eta/\rho$, of the liquid iron–nickel outer core is comparable to that of water ([dWKV$^+$98]). This permits vigorous (by geological standards) convection in the outer core with fluid velocities on the order of 10 km per year ([BJ91]), sufficiently fast to sustain the Earth's magnetism through a *geodynamo* mechanism.

Despite being at an estimated temperature of 7000°C, the iron *inner core* is solid because of the immense pressure exerted by the overlying material. The inner core

spans from 5080 km to 6371 km. The reason for the high concentration of iron in the inner and outer cores is that during the formation of the Earth most of the heavier iron sank, leaving the lighter silicates and oxides to predominate in the mantle and crust.

Let us now outline some of the basic ideas of *geodynamo* theory ([Buf00], [GOC04], and references therein) and the conclusions reached by numerically solving the Navier–Stokes and Maxwell equations ([GR95b], [GR96]). In the latter equations, the *magnetohydrodynamic* (MHD) *approximation* is made, i.e., the conducting fluid is taken to be electrically neutral (set $\rho = 0$) and the displacement current contribution ($\partial \vec{D}/\partial t$) in the Maxwell–Ampere law is neglected ([Jac75]).

The Earth's magnetic field is thought to be generated by a dynamo process in the outer core. Liquid iron and nickel flowing in this region due to temperature and concentration gradients and the Coriolis force due to the Earth's spin provide a moving fluid conductor capable of generating a magnetic field. It has long been known that the core cannot be a permanent magnet, because the temperature of the core is well above the Curie temperature (about 1000 K for iron) for permanent magnetism. It can be shown that the magnetic field would decay away in about 15 thousand years if it were not being continually regenerated. To confirm this, let's first derive a single PDE for the magnetic field from the MHD approximation to Maxwell's equations and then apply it to the Earth's core.

Example 7-11: Magnetic Field Equation

Taking the permeability μ and electrical conductivity σ of a moving fluid (velocity $\vec{v}$) as constants and using the MHD approximation to Maxwell's equations, show that $\vec{B}$ satisfies the *magnetic field equation*,

$$\frac{\partial \vec{B}}{\partial t} = \nabla \times (\vec{v} \times \vec{B}) + \lambda \nabla^2 \vec{B},$$

where $\lambda = 1/(\mu \sigma)$ is called the *magnetic diffusivity*. The first term on the right is called the *advection* term, the second is the *diffusion* term.

Solution: In the MHD approximation, the Maxwell–Ampere law yields

$$\nabla \times (\vec{B}/\mu) = \vec{J} = \sigma (\vec{E} + \vec{v} \times \vec{B}).$$

Taking the curl of this equation and setting $1/(\mu \sigma) = \lambda$, we have

$$\lambda \nabla \times (\nabla \times \vec{B}) = (\nabla \times \vec{E}) + \nabla \times (\vec{v} \times \vec{B}).$$

But, on the left-hand side,

$$\nabla \times (\nabla \times \vec{B}) = \nabla(\nabla \cdot \vec{B}) - \nabla^2 \vec{B} = -\nabla^2 \vec{B},$$

since $\nabla \cdot \vec{B} = 0$. On the right-hand side, the first term $\nabla \times \vec{E} = -\partial \vec{B}/\partial t$ from Faraday's law. Putting it all together and rearranging yields the magnetic field equation.

$$***$$

If L is the characteristic distance over which $\vec{B}$ varies appreciably, the ratio of the advection term to the diffusion term in the magnetic field equation is of order $(v\,B/L)/(\lambda\,B/L^2) = v\,L/\lambda$. This ratio is called the *magnetic Reynolds number*,

$$\mathrm{Re_M} = \frac{v\,L}{\lambda}. \tag{7.54}$$

For $\mathrm{Re_M} \ll 1$, the advection term is relatively unimportant and the magnetic field satisfies the linear diffusion equation with magnetic diffusion constant λ. If the Earth were a permanent solid magnet, then $\mathrm{Re_M} = 0$. An initial magnetic field distribution would obey the magnetic diffusion equation, decaying away in a time of order

$$\tau = \frac{L^2}{(\pi^2\,\lambda)}. \tag{7.55}$$

Example 7-12: Magnetic Field Decay in the Earth's Core

Calculate τ for the Earth's core. The core parameter values ([Buf00]) are $\lambda = 2$ m^2/s and radius $r = 3000$ km. Discuss the result in light of the paleomagnetic evidence that the Earth's field has existed for over 3 billion years.

Solution: Taking $L \approx r = 3 \times 10^6$ m, then $\tau = r^2/(\pi^2\,\lambda) = 4.56 \times 10^{11}$ seconds, or about $14\frac{1}{2}$ thousand years. The implication is that there must be some mechanism in the core which replenishes the magnetic field or else the magnetic field of the Earth would have disappeared long ago.

<div align="center">***</div>

For $\mathrm{Re_M} \gg 1$, diffusion is relatively unimportant on the length scale L. In the case of the Earth's core, the magnetic flux lines are advected (carried along) with the fluid flow until such time as the magnetic field gradients are concentrated into regions of short enough L that diffusion balances advection.

The Earth is cooling and the resulting drop in temperature with increasing radius through the fluid outer core leads to thermal convection. Also, as the outer liquid core cools down, iron is preferentially plated onto the solid inner core at the ICB, releasing latent heat and leaving behind a higher concentration of lighter elements which tend to rise aiding the convection process. Additional heating may exist in the fluid core due to radioactive decay, potassium-40 being the best candidate.

Due to the Coriolis force caused by the spinning Earth, the convecting fluid in the outer core doesn't simply move radially outwards, but rather follows curved (helical) trajectories. Differential rotation shears the existing poloidal (north–south and radial) magnetic field into toroidal (east–west) magnetic field and the 3-dimensional helical motion twists toroidal into poloidal field. The more twisted and sheared the magnetic field, the faster it decays away, magnetic diffusion tending to smooth the field. To have a self-sustaining field, new magnetic fields must be continuously generated to balance this decay. These new magnetic fields arise from the flow of the conducting fluid through the existing magnetic field which produces an electromotive force that drives large electrical currents which in turn generate the new magnetic fields.

To go beyond these qualitative ideas, one actually has to self-consistently solve the Navier–Stokes and Maxwell equations which describe the dynamo action of the fluid outer core for Earth-like parameter values. The first 3-dimensional MHD dynamo models of the geodynamo that successfully produced a dominantly dipolar field at the model Earth's surface and which showed flipping of the poles were not produced until 1995 by Garry Glatzmaier and Paul Roberts ([GR95a], [GR95b]), and Kageyama et al. ([KSW⁺95]) and Jones et al. ([JLH95]). A "snapshot" of the magnetic field structure between reversals, simulated with the Glatzmaier–Roberts (GR) geodynamo model, is shown on the left of Figure 7.18.
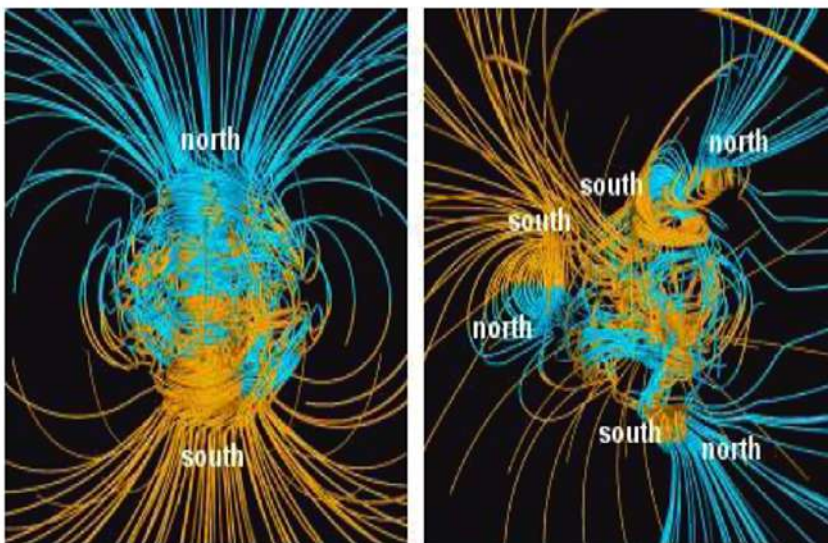
Figure 7.18: Magnetic field generated with the Glatzmaier–Roberts model ([GR95a]). Left: between reversals. Right: during a reversal.

At this instant in time, the predominantly dipole field outside the Earth's surface is clearly seen, the magnetic field lines inside being highly twisted and convoluted. Improvements and refinements of the GR dynamic model have been produced, although many questions remain to be answered. Some features of the simulations are robust, like the dominance of the dipolar field outside the core and the chaotic flipping of the poles, while detailed features inside the core depend on approximations in the model equations, assumed boundary conditions at the ICB and CMB, parameter values, and numerical resolution in the computer simulations.

For example, in the Glatzmaier–Roberts MHD geodynamo model the *anelastic approximation* was made. See ([GR96]) and ([GOC04]). In the Earth's outer core, the acoustic velocities are seven orders of magnitude larger than the fluid flow velocities. In the anelastic approximation, the acoustic velocity is taken to be infinite and compressibility of the conducting fluid ignored. As to numerical resolution, simulations that

span hundreds of thousands of years, involving tens of millions of numerical computations, have been run at very low spatial grids (e.g., 33 radial, 32 latitudinal, and 64 longitudinal levels). Higher resolutions have been used, resulting in shorter simulated times (tens of thousands of years). The computer code was run on massively parallel computers at the Pittsburgh Supercomputing Center and at the Los Alamos National Laboratory.

In addition to those features already mentioned, several other results arising in the GR simulations, and in others, are worth mentioning. Although predominantly dipolar at the Earth's surface, the magnetic field has a nondipolar part which drifts westward at a rate of 0.2° per year, a feature which has been observed (e.g., [BJ92]) in the geomagnetic field over the past couple of hundred years. The inner core, on the other hand, displays a drift in the opposite direction. Confirmation of this rotation of the inner core has been inferred from several seismic analyses (e.g., [SR96]) but estimates of the actual rotation rate vary from close to zero up to 3° eastward per year. The GR model further shows that in the inner core the magnetic field has an opposite polarity to the outer core which stabilizes the field against a tendency to reverse more frequently. During a magnetic flip of the poles, which takes a few thousand years to complete, the magnetic field doesn't vanish at the Earth's surface but becomes more complicated, with magnetic poles popping up in "odd" places. According to Glatzmaier, a south magnetic pole might pop up over Africa or a north pole over Tahiti. Further, as shown on the right of Figure 7.18, several north pole-south pole combinations can occur.

A limitation of the GR model is that it doesn't really take into account the strongly turbulent convection which probably exists in the Earth's outer core, so critical dynamical phenomena could be missing. Another problem is the coarse spatial resolution in the simulations, which can only be made finer with the development of faster parallel computers and improved computer codes. Nevertheless, the successes already achieved with the GR and other magnetohydrodynamic models are a strong confirmation of the general validity of the Navier–Stokes equations and the nonlinear origin and behavior of the Earth's magnetic field. However, even with a perfect model of the fluid core and the fastest of supercomputers, the nonlinear chaotic nature of the core precludes accurately predicting the time of the next pole reversal.

The following example illustrates chaotic pole reversal for an earlier, simpler, disk dynamo model of the Earth's magnetic field.

Example 7-13: Chaotic Magnetic Field Reversal

Prior to the Glatzmaier–Roberts geodynamo model, Chillingworth and Holmes ([CH80]) introduced a modified *disk dynamo model* of the Earth's magnetic field which displayed chaotic magnetic field reversals. The full magnetohydrodynamic PDE system was truncated to yield the simpler nonlinear ODE system,

$$\dot{x} = a\,(y - x), \quad \dot{y} = -y - x\,z, \quad \dot{z} = b - x\,y - c\,z,$$

where a, b, and c are positive constants, and $b > a\,c\,(a + c + 3)/(a - 1 - c)$. The variable x is related to the poloidal potential, y to the toroidal magnetic field, and z to the moment of angular momentum.

a. Taking the nominal (artificial) parameter values $a = 3$, $b = 25$, $c = 1$, and initial condition $x(0) = 0.2$, $y(0) = 1$, $z(0) = 0$, numerically solve the ODE system and demonstrate the chaotic nature of the solution with a suitable plot.

b. Illustrate the sensitivity of the results to small changes in the initial condition. For example, you might take $z(0) = 0.00001$.

Solution: a. Using the RKF45 method, the ODE system is solved numerically with the given parameter values and initial condition for the time range $t = 0$ to 200. To eliminate the transient, only the interval $t = 100$ to 200 will be plotted. Considering, say, the toroidal magnetic field variable y, the behavior of y as a function of time t is shown on the left of Figure 7.19. We can see that the toroidal magnetic field undergoes
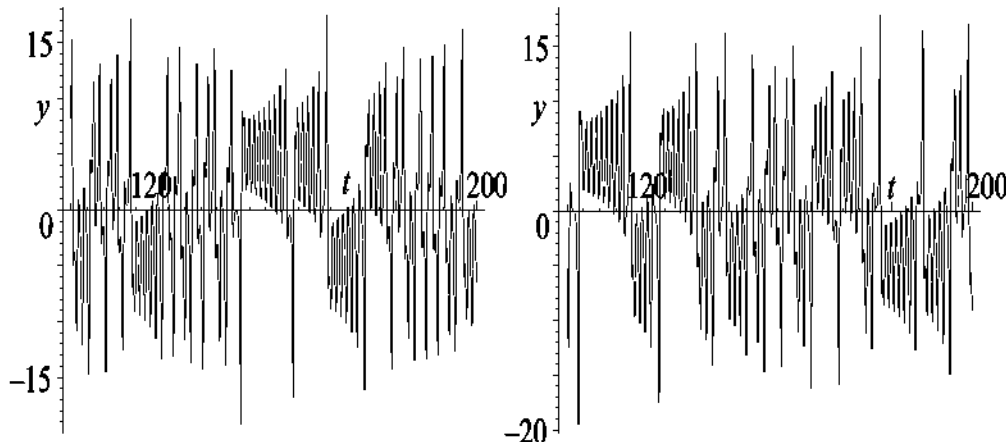
Figure 7.19: y vs. t for $z(0) = 0$ (left) and $z(0) = 0.00001$ (right).

abrupt changes of sign, corresponding to sudden field reversals. The pattern of these reversals is highly irregular (chaotic) over the time interval shown. If even longer time intervals are considered, no periodic behavior is revealed.

b. Taking $z(0) = 0.00001$ produces the result shown on the right of Figure 7.19. Comparing the plots on the left and right, the slight change in the value of $z(0)$ has produced a completely different behavior of y with time, thus illustrating the sensitivity to the initial condition.

<p align="center">***</p>

PROBLEMS

Problem 7-1: Piecewise-linear capacitance
Analytically solve the piecewise-linear ODE (7.8). Discuss the behavior of the solution as the frequency parameters are varied.

Problem 7-2: Josephson effect
Consulting Feynman ([FLS65]) or some other source, derive the basic quantum mechanical equations (7.17) and (7.19) for the Josephson effect.

Problem 7-3: A tunnel diode oscillator circuit
Consider the circuit diagram shown in Figure 7.20 which contains a battery with voltage V_B, a resistor R, an inductor L, a capacitor C, and a tunnel diode D.
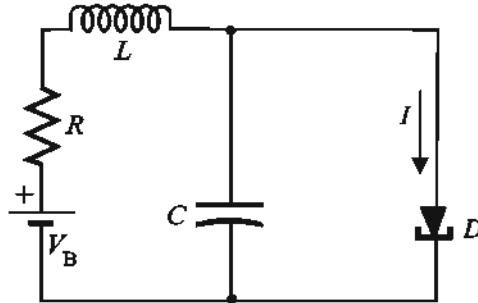
Figure 7.20: Tunnel diode circuit.

The current I through D is related to the potential drop V across it by

$$I = a V \left(V^2 - \frac{3}{4}V + \frac{1}{7} \right), \quad a > 0.$$

a. Taking $V_B = \frac{1}{4}$ volt, use Kirchhoff's current and voltage rules to show that the relevant dimensionless circuit equation is

$$\ddot{x}(\tau) - \epsilon \left(1 - x^2\right) \dot{x} + f(x) + x = 0,$$

with

$$x = \frac{V - \frac{1}{4}}{b}, \quad \tau = \frac{t}{\sqrt{LC}},$$

$$b = \sqrt{\frac{5}{336} - \frac{RC}{3La}}, \quad \epsilon = 3 a b^2 \sqrt{\frac{L}{C}}.$$

The mathematical structure of the function $f(x)$ is to be determined.

b. Taking $a = 1.2$ amperes/volt, $L = 20$ henry, $C = 0.01$ farad, $R = 1$ ohm, and $x(0) = \dot{x}(0) = 0$, numerically solve the ODE for $x(\tau)$ and plot the result over a suitable time range. Discuss the result.

c. Analytically determine the critical value of the resistance above which the oscillations die away. Numerically confirm the existence of this critical resistance.

Problem 7-4: Period-doubling route to chaos
In the dimensionless Chua equations, take $m_0 = -8/7$, $m_1 = -5/7$, $\alpha = 15.6$, and

initial condition $x(0) = 0.1$, $y(0) = z(0) = 0$. Numerically solve the equations for $\beta = 50, 35, 33.8$ and graphically demonstrate that period-1, period-2, and period-4 solutions occur. In this period-doubling sequence to chaos (to the double scroll attractor), for what β value does period-8 occur?

Problem 7-5: Vector potential for magnetic dipole field
Confirm that the vector potential $\vec{A}$ given by (7.49) yields the correct magnetic dipole field (7.47).

Problem 7-6: SQUID physics
By consulting Feynman ([FLS65]) or some other source, discuss in mathematical detail the underlying physics for the voltage oscillations in a SQUID as the magnetic field through the SQUID loop changes.

Problem 7-7: SQUID applications
By doing an Internet search, determine some other applications that SQUIDs have in the "real" world. Discuss each application in some detail.

Problem 7-8: Neon tube circuit
The electrical circuit shown in Figure 7.21 contains a battery B with voltage V_B, a resistance R, an inductance L, a capacitance C, and a neon tube. The voltage drop V across the neon tube is related to the current I through it by the relation

$$V = V_0 + A\,(I - I_0)^2,$$

with A, V_0, and I_0 all positive constants.
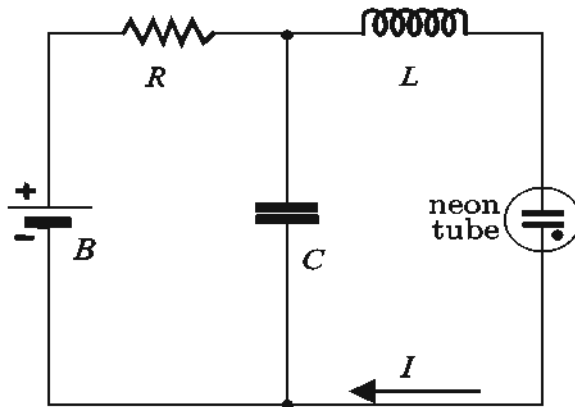
Figure 7.21: A circuit containing a neon tube.

Using Kirchhoff's current and voltage rules, derive the equation of motion for the circuit, expressed in terms of the time-dependent variable $x = I - I_0$.

Problem 7-9: The three-wave problem
The three-wave problem ([ER79]) in nonlinear optics refers to the nonlinear interaction of two intense electromagnetic waves (subscripts 0, 1) and a sound wave (subscript 2)

propagating in, say, the x direction with velocities $v_2 \ll v_0, v_1$. In the slowly varying amplitude approximation, and neglecting all damping, the real amplitudes satisfy the following coupled nonlinear ODE system:

$$\frac{\partial \phi_0}{\partial t} + v_0 \frac{\partial \phi_0}{\partial x} = -\beta_0\, \phi_1\, \phi_2,$$

$$\frac{\partial \phi_1}{\partial t} + v_1 \frac{\partial \phi_1}{\partial x} = \beta_1\, \phi_0\, \phi_2,$$

$$\frac{\partial \phi_2}{\partial t} + v_2 \frac{\partial \phi_2}{\partial x} = -\beta_2\, \phi_0\, \phi_1.$$

The coupling parameters β are all real and positive. Derive solitary wave solutions for ϕ_0, ϕ_1, and ϕ_2 that propagate together with a common velocity $c < v_2$ along the x-axis. Sketch their shapes in the same figure. It can be shown that these solitary waves are solitons ([Kau76], [KRB79]).

Problem 7-10: Dark solitary wave

By using phase-plane analysis, demonstrate that a dark solitary wave solution to Equation (7.38) can exist. Derive the analytic form of the dark solitary wave and plot the intensity for a representative parameter value.

Problem 7-11: Numerically solving the STBS equations

Using the fourth-order Runge–Kutta method, numerically solve Equations (7.45) for the normalized intensities $I_L(x)/I_L(0)$ and $I_S(x)/I_S(\ell)$ over the cell range $x = 0$ to $x = \ell = 10\,\text{cm}$. Plot the normalized intensities in the same figure. The parameter values are: $g\, I_L(0) = 1\,\text{cm}^{-1}$, $I_S(\ell)/I_L(0) = 0.05$, and $\alpha = 0.02$. How does the numerically-derived normalized signal intenstiy output at $x = 0$ compare with that given by the approximate formula (7.46)?

Problem 7-12: Analytically solvable laser beam interaction

The laser beam interaction equations given by Equations (7.45) cannot be solved analytically. However, if the signal (S) and pump (L) beams travel in the same direction, an analytical solution can be found. In this case, the coupled nonlinear ODE system is given by

$$\frac{dI_L}{dx} = -g\, I_L\, I_S - \alpha\, I_L,$$

$$\frac{dI_S}{dx} = +g\, I_L\, I_S - \alpha\, I_S.$$

a. If the inputs at $x = 0$ are $I_L(0)$ and $I_S(0)$, derive the analytic forms of $I_L(x)$ and $I_S(x)$ at arbitrary $x > 0$.

b. If $I_S(0)/I_L(0) = 0.01$, $g\, I_L(0) = 1\,\text{cm}^{-1}$, plot $I_S(z)/I_S(0)$ for $0 \le z \le 10\,\text{cm}$ for $\alpha = 0$ and $0.5\,\text{cm}^{-1}$. Discuss the results.

Problem 7-13: Disk dynamo model

Confirm the graphical results for the disk dynamo model shown in Figure 7.19. Also plot

$x(t)$ and $z(t)$ and discuss the results. Explore the behavior of the toroidal magnetic field variable $y(t)$ as the parameter values are changed and discuss any interesting features.

Problem 7-14: Geodynamo theory and simulations

The review paper *Geodynamo Theory and Simulations* by Paul Roberts and Garry Glatzmaier ([RG00]) is available at the Internet address:

http://www.ipp.mpg.de/~emp/ulm/earth/earth.pdf.

Elaborate in detail on the MHD model equations used in the geodynamo simulations, the limitations of the model, and the numerical results obtained.

Problem 7-15: Vibrations of a straight current-carrying wire

Suppose that a very long conducting wire carrying a constant current I_b is fixed in a vertical straight line as shown in Figure 7.22. A small wire of length ℓ and mass m and carrying a current I_a is placed parallel to the long one and attached to a linear spring with spring constant k. When the spring is unstretched $x = 0$ and the separation of the two wires is a. The small wire is put into motion in the x direction, its orientation remaining parallel to the long conductor. Damping is negligible.
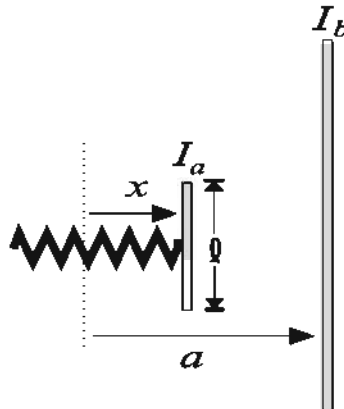
Figure 7.22: Parallel current-carrying wires.

a. Show that the equation of motion of the small conducting wire is

$$\ddot{x} - \frac{k}{m} \frac{x^2 - a\,x + \lambda}{a - x} = 0,$$

where λ remains to be identified.

b. Locate and identify the physically allowable fixed points. Note that λ can be positive or negative. Explain why.

c. Sketch the phase plane for various values of λ and discuss the motion of the small wire.

Hint: The force F per unit length between two parallel wires carrying currents I_a and I_b separated by a distance d is $F = \mu_0\, I_a\, I_b/(2\,\pi\,d)$, where μ_0 is the permeability of free space. The force is attractive if the currents are in the same direction, repulsive if they are in opposite directions.

Problem 7-16: Neon lamp
By doing a literature or Internet search, discuss in detail the nonlinear nature of the current–voltage curve for the neon lamp.

Problem 7-17: Second harmonic generation
Second harmonic generation (SHG) is a nonlinear optical phenomenon in which an electromagnetic wave is generated in a medium at twice the optical frequency (half the wavelength) of the input ("pump") wave. By doing a literature or Internet search, discuss SHG in some detail.

Problem 7-18: Four-wave mixing
Four-wave mixing involves the interaction in a medium of four coherent optical fields through the third-order nonlinear susceptibility. Consulting the review paper of C. W. Thiel available at:

http://staff.mbi-berlin.de/bfreyer/fwmixing.pdf,

or any other that you can find, discuss the nonlinear optical phenomenon of four-wave mixing and its applications.

Problem 7-19: Electrical circuit simulation of the Duffing–Holmes oscillator
The *Duffing–Holmes* (DH) ([Hol79]), or inverted Duffing, oscillator equation is given by

$$\ddot{x} + b\,\dot{x} - x + x^3 = a\,\sin(\omega\,t),$$

where the damping coefficient b, the amplitude a, and frequency ω are all positive.

Taking $b = 0.1$, $\omega = 1.3$ and initial condition $x(0) = 1$, $y(0) \equiv \dot{x}(0) = 0$, numerically solve the DH oscillator equation over the time interval $t = 600$ to 900 for each of the following a values. In each case, plot $x(t)$ and y versus x and identify the periodicity (i.e., period-1, period-2, period-4, chaotic, or ?) of the oscillation.

   a. $a = 0.200$;

   b. $a = 0.250$;

   c. $a = 0.300$;

   d. $a = 0.305$;

   e. $a = 0.450$.

Tamaševičiutė et al. ([TTM$^+$08]) have presented an electrical circuit which simulates the DH equation in a linear-piecewise approximation. Discuss this electrical circuit in detail, deriving the circuit equations and numerically verifying the plotted results in the paper for the given circuit parameters. A reprint is available at:

http://www.lana.lt/journal/29/Tamaseviciute.pdf.

Problem 7-20: Aurora

Consulting the following website of the Geophysical Institute of the University of Alaska,

http://odin.gi.alaska.edu/FAQ/,

or any other source that you can find, discuss the phenomenon of aurora in some detail.

Chapter 8

World of Weather Prediction

Perhaps some day in the dim future it will be possible to advance the computations faster than the weather advances and at a cost less than the saving to mankind due to the information gained. But that is a dream.
Lewis Fry Richardson, *Weather Prediction by Numerical Process* (1922)

As another example of fluid flow and the application of the nonlinear Navier–Stokes (NS) equations, we will now move outwards from the Earth's molten core to its circulating atmosphere. Specifically, in this chapter we will look at the problem of numerically predicting the weather. Although numerical weather prediction models can be generalized into climate[1] prediction models, we shall not delve into the latter models here. One reason is that because of the much shorter time scale involved, predicting the weather several days or a week in advance is mathematically easier than predicting how the climate will change 30 years, 100 years, or longer, from now. Fully developed climate models for the Earth involve the interaction of the atmosphere and oceans with each other as well as with the land/ice surface. Furthermore, the role of solar radiation from the Sun in driving the atmosphere–ocean–land system is extremely important. On a much longer time scale, the orbital dynamics, precession, and wobble of the Earth play an important role in climate change, e.g., in the onset and waning of *ice ages*.

On the other hand, in attempting to predict the weather, we can concentrate mainly on the behavior of the atmosphere, subject to specified boundary conditions at the Earth's surface. The atmospheric boundary layer at this surface is of the order of a kilometer or so in thickness. Above this boundary layer, topographical and surface frictional effects can be neglected and the mathematical treatment is much easier, with approximate analytic results being derivable. After a brief history of early weather prediction, this mathematical treatment will be presented, followed by a qualitative discussion of the results obtainable by numerically solving the complete nonlinear weather prediction problem using supercomputers.

---

[1]The *climate* of a region refers to the weather of that region averaged over many years ([Tho05]), the standard averaging period adopted by the World Meteorological Organization being 30 years. The quantities that are typically employed to characterize climate are average surface temperature, precipitation, and wind. The definition of climate involves a time average, but this average also varies over longer periods. This variation in climate with time is referred to as *climate change*.

8.1   Early History

The British mathematician Lewis Fry Richardson (1881–1953) was the first to attempt to forecast the weather in 1910, not by analyzing past historical records, but by numerically solving a simplified version of the nonlinear NS equations governing the dynamics of the Earth's fluid atmosphere. The fundamental idea, the basis of modern weather prediction, was to tabulate atmospheric pressure, temperature, velocity, etc., on a 3-dimensional grid (latitude, longitude, and altitude) to give a description of the atmosphere at an initial instant in time. A numerical algorithm then is applied to the relevant equations to advance the data by small finite time steps until a forecast can be made for several days or weeks in the future.

Specifically, Richardson used initial data at 7 am on May 20, 1910, and attempted to predict the surface pressures at two points in central Europe 6 hours later. Doing the numerical calculations by hand in this precomputer era, he forecast an unrealistically high pressure change over the 6-hour period, which was not borne out as the day evolved. Richardson, himself, recognized ([Ric95]) that the problem probably lay in the fact that the initial data was not suitably smoothed[2] or, in modern jargon, not properly *initialized*. Because of his failed attempt, the true significance of what Richardson had tried to achieve was not adequately recognized at the time. However, meteorologists now know that Richardson's work is the foundation upon which modern weather forecasting is built. To honor this fact, the European Geophysical Union has established the Lewis Fry Richardson Medal for exceptional contributions to nonlinear geophysics.

In the decades following Richardson's pioneering work a number of key developments occurred which laid the groundwork for modern numerical weather forecasting:

- the development of stable numerical algorithms for integrating forward in time;

- the invention of the *radiosonde* (a balloon-borne instrument package with radio transmitting capabilities) and its introduction into the global weather network;

- the development of the digital computer.

A discussion of these developments may be found in "Weather Forecasting: from Woolly Art to Solid Science"[3] by Peter Lynch ([Lyn01]).

Making use of the ENIAC[4] computer and a simplified model of the atmosphere based on the NS equations, the meteorologists Jules Charney and Ragnar Fjörtoft, and the renowned applied mathematician John von Neumann, made the first successful numerical weather forecast ([CFvN50]) in 1950. They predicted the movement of midlatitude (around 45° N) patterns of lows and highs in the troposphere, the *troposphere* being the lower portion of the atmosphere up to about 11 km.

---

[2]Peter Lynch ([Lyn99], [Lyn06]) has reworked Richardson's calculations with suitably filtered initial data and obtained a realistic result for the 6-hour pressure change.

[3]Lynch's papers available at **www.maths.tcd.ie/~plynch/Publications/Publications.html**.

[4]ENIAC is an acronym for Electronic Numerical Integrator and Computer. It was originally designed and built to calculate artillery firing tables for the U.S. Army's Ballistic Research Laboratory.

8.2 The Barotropic Vorticity Equation

Rather than solve the full 3-dimensional atmospheric flow problem, which was beyond the computational capability of ENIAC, Charney and coworkers reduced the problem to a computationally more-manageable 2-dimensional flow. Assuming that the atmosphere is approximately a *barotropic fluid* (equation of state is $\rho = \rho(p)$, with ρ the density and p the pressure) and making simplifying approximations, they reduced the NS momentum equation to the *barotropic vorticity equation*,

$$\frac{\partial \xi}{\partial t} + U \frac{\partial \xi}{\partial x} + V \frac{\partial \xi}{\partial y} + V \frac{\partial f}{\partial y} = \kappa \left(\frac{\partial^2 \xi}{\partial x^2} + \frac{\partial^2 \xi}{\partial y^2} \right). \tag{8.1}$$

Here,

- x and y are the horizontal coordinates in the east–west and north–south directions in the tangent plane to the Earth's surface at latitude ϕ;

- U and V are the x and y components of the atmospheric wind velocity $\vec{v}$;

- ξ is the component of vorticity, $\vec{\omega} = \nabla \times \vec{v}$, perpendicular (the z-direction) to the Earth's surface, called the *relative vorticity*;

- $f = 2\,\Omega \sin\phi$ is the *Coriolis parameter* with Ω the Earth's angular speed;

- κ is the *eddy viscosity* (or diffusivity) coefficient.

To properly account for energy dissipation in the *synoptic-scale* (of the order of a thousand kilometers) weather patterns which characterize high- and low-pressure regions in the troposphere, the small *kinematic viscosity coefficient* $\nu = \mu/\rho$ in the NS momentum equation was replaced by κ, which is several orders of magnitude larger.

It is instructive to derive the barotropic vorticity equation and then discuss some meteorological concepts [5] relevant to the Charney–Fjörtoft–von Neumann (CFVN) weather forecast. Including both the *Coriolis acceleration* $\vec{a}_c = 2\,(\vec{v} \times \vec{\Omega})$ and gravitational acceleration $\vec{g}$, and replacing ν with κ, the NS momentum equation (7.40) for the atmospheric wind velocity becomes

$$\frac{d\vec{v}}{dt} = \frac{\partial \vec{v}}{\partial t} + (\vec{v} \cdot \nabla)\,\vec{v} = -\frac{1}{\rho}\,\nabla p + \kappa\,\nabla^2 \vec{v} + \vec{a}_c + \vec{g}. \tag{8.2}$$

Treating the Earth as a sphere spinning around the North–South axis, let's take a tangent plane to the sphere at latitude ϕ, ϕ ranging from $-\pi/2$ radians at the South Pole to $+\pi/2$ radians at the North Pole. The *tangent plane approximation* to the spherical Earth for treating atmospheric air flow is quite good for weather patterns, such as high- and low-pressure regions, whose horizontal range extends up to the order of 1000 km. At the tangent point of the plane with the sphere, introduce a local Cartesian coordinate system with the positive x and y axes pointing horizontally due

---

[5] If you wish to expand your knowledge of meteorological concepts see, e.g., *An Introduction to Dynamic Meteorology* by Holton ([Hol04]).

east and north, respectively, in the plane, and the positive z-axis pointing upwards (i.e., radially outwards from the center of the sphere).

Then, the gravitational acceleration $\vec{g} = -g\,\hat{z}$ and the angular velocity ([MT95]) of the tangent point at latitude ϕ is

$$\vec{\Omega} = \Omega\left(\cos\phi\,\hat{y} + \sin\phi\,\hat{z}\right). \tag{8.3}$$

At the North Pole, $\phi = +\pi/2$ and $\vec{\Omega}$ points along the positive z-axis (i.e., outwards), while at the Equator, $\phi = 0$ and $\vec{\Omega}$ points along the positive y-axis (i.e., northwards).

Taking the wind velocity to be, quite generally,

$$\vec{v} = U\,\hat{x} + V\,\hat{y} + W\,\hat{z}, \tag{8.4}$$

then the Coriolis acceleration is

$$\vec{a}_c = 2\left(\vec{v}\times\vec{\Omega}\right) = 2\,\Omega\left[\left(V\sin\phi - W\cos\phi\right)\hat{x} - U\sin\phi\,\hat{y} + U\cos\phi\,\hat{z}\right]. \tag{8.5}$$

For tropospherical air flow at a sufficient altitude that topological features such as mountains can be ignored,[6] a good approximation is to assume that the vertical wind velocity component $W \ll U, V$. Further, $(\vec{a}_c)_z \ll g$, so

$$\vec{v} \approx U\hat{x} + V\,\hat{y} \quad\text{and}\quad \vec{a}_c \approx f\left(V\,\hat{x} - U\,\hat{y}\right), \tag{8.6}$$

where $f \equiv 2\,\Omega\sin\phi$ is the Coriolis parameter. We will also make the barotropic fluid approximation, $\rho = \rho(p)$, and take g as a constant.

Taking the curl of (8.2) and introducing the vorticity $\vec{\omega} = \nabla\times\vec{v}$, we obtain

$$\frac{\partial\vec{\omega}}{\partial t} + \nabla\times\left(\vec{v}\cdot\nabla\right)\vec{v} = -\nabla\times\left(\frac{1}{\rho}\nabla p\right) + \kappa\,\nabla^2\vec{\omega} + \left(\nabla\times\vec{a}_c\right). \tag{8.7}$$

Example 8-1: Barotropic Approximation

Prove that for a barotropic fluid, the first term on the rhs of (8.7) is equal to zero.

Solution: Taking $\phi = 1/\rho$ and $\vec{A} = \nabla p$, we use the vector identity

$$\nabla\times\left(\phi\vec{A}\right) = \left(\nabla\phi\times\vec{A}\right) + \phi\left(\nabla\times\vec{A}\right) = -\frac{1}{\rho^2}\,\nabla\rho\times\nabla p + \frac{1}{\rho}\left(\nabla\times\nabla p\right).$$

For a barotropic fluid, $\rho = \rho(p)$ so the cross-product $\nabla\rho\times\nabla p = 0$. We also have $\nabla\times\nabla p = 0$, since the curl of the gradient of any scalar function is zero.

<div align="center">***</div>

The z-component of the vorticity,

$$\xi(x,y) \equiv (\vec{\omega})_z = (\nabla\times\vec{v})_z = \partial V/\partial x - \partial U/\partial y, \tag{8.8}$$

---

[6] As air rushes over a mountain, the vertical component of wind velocity is often not negligible compared to the horizontal velocity components. This is also true for Antarctic winds associated with extremely cold and therefore dense air dropping off ice fields.

is relevant to air flow in the tangent plane, so let's take the z component of (8.7), viz.,

$$\frac{\partial \xi}{\partial t} + (\nabla \times (\vec{v} \cdot \nabla) \vec{v})_z = \kappa \left(\frac{\partial^2 \xi}{\partial x^2} + \frac{\partial^2 \xi}{\partial y^2} \right) + (\nabla \times \vec{a}_c)_z . \tag{8.9}$$

If f only varies in the y-direction and the fluid flow is assumed to be nondivergent ($\nabla \cdot \vec{v} = \partial U/\partial x + \partial V/\partial y = 0$), then on using (8.6), we obtain

$$(\nabla \times (\vec{v} \cdot \nabla) \vec{v})_z = U \frac{\partial \xi}{\partial x} + V \frac{\partial \xi}{\partial y}, \quad (\nabla \times \vec{a}_c)_z = -V \frac{\partial f}{\partial y}. \tag{8.10}$$

Substituting (8.10) into (8.9) yields the desired barotropic vorticity equation, (8.1).

8.3 Some Meteorological Concepts

To justify the nondivergence approximation for the fluid velocity in the tangent plane that was made in deriving the barotropic vorticity equation, we must develop a few simple meteorological concepts. For synoptic-scale weather patterns at midlatitudes and above the surface friction layer, the pressure gradient force in the x–y plane and the Coriolis force nearly balance. If the balance is taken to be exact, this is referred to as *geostrophic*[7] balance and the wind is referred to as the *geostrophic wind*. It should be noted that geostrophic balance is not possible between about 15°S and 15°N latitudes because the Coriolis force is too weak.

Letting $\vec{v}_g = U_g \, \hat{x} + V_g \, \hat{y}$ be the geostrophic wind velocity, geostrophic balance yields

$$\rho \, f \, (V_g \, \hat{x} - U_g \, \hat{y}) = \frac{\partial p}{\partial x} \, \hat{x} + \frac{\partial p}{\partial y} \, \hat{y}. \tag{8.11}$$

Equating the coefficients of $\hat{x}$ and $\hat{y}$, the geostrophic wind velocity components are

$$U_g = -\frac{1}{\rho f} \frac{\partial p}{\partial y}, \quad V_g = \frac{1}{\rho f} \frac{\partial p}{\partial x}. \tag{8.12}$$

Thus, the geostrophic wind velocity is

$$\vec{v}_g = \frac{1}{\rho f} \, (\hat{z} \times \nabla p). \tag{8.13}$$

Since the pressure gradient is perpendicular to the constant pressure contours (*isobars*), Equation (8.13) tells us that the *geostrophic wind velocity is tangent to the isobars*.

What about the sense of $\vec{v}_g$? Let's first assume that we are in the northern hemisphere where $f > 0$. As we move away from a center of low pressure, the pressure is increasing so $\nabla p > 0$. Then, Equation (8.13) tells us that the geostrophic wind velocity is *counterclockwise* (called *cyclonic*) about a low. Conversely, as one moves away from a center of high pressure, $\nabla p < 0$, so the air flow around a center of *high pressure* is

---

[7]Geo=earth, strophe=turning.

clockwise (anticyclonic). In the southern hemisphere, $f < 0$ and the geostrophic winds at midlatitudes are reversed compared to those in the northern hemisphere.

Since the geostrophic air flow cannot cross isobars,[8] the isobars act like the banks of a river. The air flow speeds up when the "banks" (isobars) are closer together and slows down when they are farther apart.

Example 8-2: Geostrophic Wind Speed

At 40°S, the density of air over the open ocean is 1.2 kg/m³. The distance between isobars drawn for every 4 millibars is 90 nautical miles. Determine the geostrophic wind speed in km/h and in knots (nautical miles per hour).

Solution: The Earth turns through 2π radians in 24 hours or $24 \times 60 \times 60 = 86,400$ seconds. Thus, the angular speed of the Earth is

$$\Omega = \frac{2\pi}{86400} = 7.27 \times 10^{-5} \text{ s}^{-1}.$$

The Coriolis parameter at 40°S is

$$f = 2\,\Omega \sin\phi = 2 \times 7.27 \times 10^{-5} \times \sin(40 \times \pi/180) = 9.35 \times 10^{-5} \text{ s}^{-1}.$$

We will convert pressure and distance to SI units by noting that 1 millibar=100 pascals and 1 nautical mile=1852 meters. The magnitude of the pressure gradient is

$$|\nabla p| = \frac{4 \times 100}{90 \times 1852} = 2.4 \times 10^{-3} \text{ Pa/m}.$$

From Equation (8.13), the geostrophic wind speed is

$$v_g = \frac{|\nabla p|}{\rho\,f} = \frac{2.4 \times 10^{-3}}{1.2 \times 9.35 \times 10^{-5}} = 21.4 \text{ m/s}$$

or 77 km/h, or about 42 knots.

<p style="text-align:center">***</p>

The density ρ, which is a difficult quantity to measure for the atmosphere, can be eliminated from $\vec{v}_g$ as follows. In general, an isobaric (e.g., 500 millibar pressure) surface will not be at a constant height, but varies in some manner as schematically indicated in Figure 8.1. The constant-pressure curve is $p = p_0$ and the constant-height line is $z = z_0$. The spatial increments are to be considered in the limit $\Delta x \to 0$ and $\Delta z \to 0$.

The gradient of the pressure in the x-direction between the points A and C is

$$\left(\frac{\partial p}{\partial x}\right)_z = \frac{p_C - p_A}{\Delta x} = \frac{p_C - p_0}{\Delta x},$$

---

[8]Near the Earth's surface, *surface winds* can cross the isobars (typically at angles of 20° to 30°) due to frictional losses slowing the wind and therefore reducing the Coriolis force. In the northern hemisphere, the surface winds blow counterclockwise into a surface low and clockwise out of a surface high. The opposite occurs in the southern hemisphere.
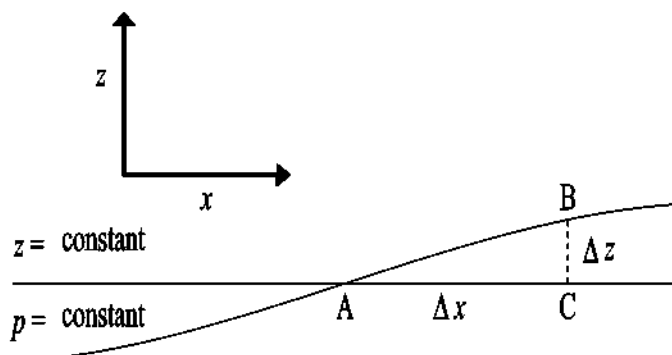
Figure 8.1: Constant-pressure and constant-height surfaces.

while the gradient of the height in the x-direction between the points A and B is

$$\left(\frac{\partial z}{\partial x}\right)_p = \frac{z_B - z_A}{\Delta x} = \frac{z_B - z_0}{\Delta x}.$$

Then,

$$\frac{p_C - p_0}{z_B - z_0} = \frac{p_C - p_B}{z_B - z_C} = \frac{(\partial p/\partial x)_z}{(\partial z/\partial x)_p} = -\frac{\partial p}{\partial z}. \tag{8.14}$$

But, making the *hydrostatic balance* approximation of the forces in the z-direction,

$$-\frac{\partial p}{\partial z} = \rho\, g, \tag{8.15}$$

so Equation (8.14) yields

$$\left(\frac{\partial p}{\partial x}\right)_z = \rho\, g \left(\frac{\partial z}{\partial x}\right)_p. \tag{8.16}$$

Similarly,

$$\left(\frac{\partial p}{\partial y}\right)_z = \rho\, g \left(\frac{\partial z}{\partial y}\right)_p. \tag{8.17}$$

Substituting the last two results into Equation (8.12), the geostrophic wind velocity components are quite generally given by

$$U_g = -\frac{g}{f}\left(\frac{\partial z}{\partial y}\right)_p, \quad V_g = \frac{g}{f}\left(\frac{\partial z}{\partial x}\right)_p, \tag{8.18}$$

i.e., in terms of height contours at constant pressure.

More commonly, since g varies slightly with height in the troposphere, *geopotential heights* are used rather than actual heights. The *geopotential* function Φ is introduced through the relation

$$d\Phi = g\, dz, \tag{8.19}$$

and the geopotential height defined as

$$Z = \frac{\Phi}{g_0} = \frac{1}{g_0} \int_0^z g\, dz, \qquad (8.20)$$

where $g_0 = 9.80665$ m/s^2 is the *standard gravity* at mean sea level. Ignoring the very small variation of g with height on a constant-pressure surface, then

$$Z = \left(\frac{g}{g_0}\right) z, \qquad (8.21)$$

so

$$U_g = -\frac{g_0}{f}\left(\frac{\partial Z}{\partial y}\right)_p, \quad V_g = \frac{g_0}{f}\left(\frac{\partial Z}{\partial x}\right)_p. \qquad (8.22)$$

As an example of a constant-pressure surface, Figure 8.2 shows the 96-hour (4-day) 500-mbar geopotential height contours predicted for the northern Pacific Ocean for January 24, 2008. The horizontal scale of this chart, issued to mariners by the Ocean Prediction
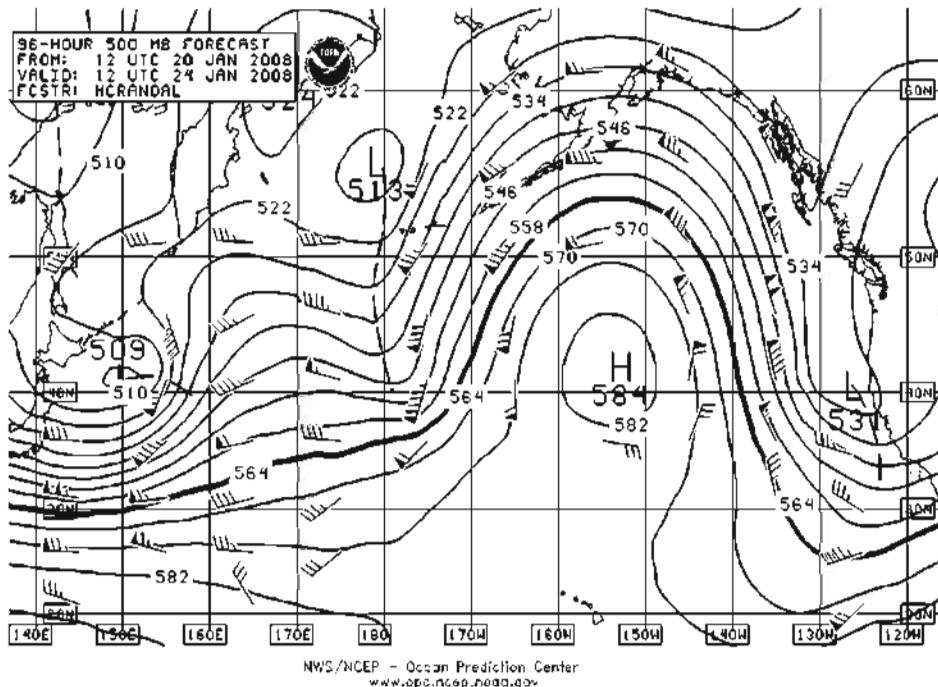
Figure 8.2: 500-mbar constant-geopotential-height contours.

Center, U.S. National Oceanic and Atmospheric Administration (NOAA), is from 140°E to 120°W longitude, the vertical scale from 20° to about 60°N latitude. The heights are given in dekameters (dm) above sea level. For example, the height contour labeled 564 corresponds to a geopotential height of 5640 m (about 18,000 feet). The highest

altitude (labeled H) on the contour is 584 dm, while there are several localized lows (labeled L). Overall, the 500-mbar surface tends to decrease in height from south to north because the northern air is cooler and therefore more dense.

Also indicated on the chart are wind direction arrows, the shaft pointing in the wind direction, the one-sided tail "feathers" indicating the speed in knots. The wind scale is as follows: half feather: 3 to 7 knots; one full feather: 8 to 12 knots; $1\frac{1}{2}$ feathers: 13 to 17 knots; two full feathers: 18 to 22 knots; and so on. A filled-in "flag" indicates a wind speed of 48 to 52 knots.

Similar to the situation for the isobars, the wind directions tend to be parallel to the constant-height contours because these contours are *stream lines* for the air flow. Taking f values typical of midlatitudes, a *stream function*,

$$\psi = \frac{g_0 Z}{f},\tag{8.23}$$

can be introduced. Then,

$$U_g = -\frac{\partial \psi}{\partial y}, \qquad V_g = \frac{\partial \psi}{\partial x},\tag{8.24}$$

and the geostrophic velocity is parallel to the stream lines. On the 500-mbar surface, the wind velocity is generally close to geostrophic and the wind speed is higher the tighter the height contours.

Returning, finally, to the velocity divergence issue, it is easy to show that the geostrophic wind is nondivergent, viz.,

$$\nabla \cdot \vec{v} = \nabla \cdot \vec{v}_g = \frac{\partial U_g}{\partial x} + \frac{\partial V_g}{\partial y} = -\frac{\partial^2 \psi}{\partial x \partial y} + \frac{\partial^2 \psi}{\partial y \partial x} = 0.\tag{8.25}$$

The successful weather forecast of Charney et al. was to predict the time evolution of the 500-mbar surface. To understand how this was achieved, we now note that the relative vorticity can be related to the stream function, viz.,

$$\xi = \frac{\partial V_g}{\partial x} - \frac{\partial U_g}{\partial y} = \frac{\partial^2 \psi}{\partial x^2} + \frac{\partial^2 \psi}{\partial y^2} = \nabla^2 \psi.\tag{8.26}$$

This is the 2-dimensional *Poisson equation*, the relative vorticity acting as a "source" function in the equation.

One now has all the ingredients to understand how the successful weather forecast at midlatitudes in the troposphere was made. Given the initial wind velocity distribution (i.e., U and V are known at $t = 0$ at each spatial grid point) on the 500-mbar surface, one proceeds as follows:

- Numerically solve the barotropic vorticity equation (8.1) for the ξ values at each spatial grid point a small time step Δt later;

- With ξ known, numerically solve Poisson's equation (8.26) (subject to spatial boundary conditions) for ψ at each spatial grid point at Δt;

- With ψ known, the new wind velocities at time step Δt are then determined at each spatial grid point using (8.24).

This procedure then is repeated for each successive time step.

8.4   Modern Numerical Weather Forecasting

A modern supercomputer has a computational speed that is of the order of 10^9 faster than the primitive ENIAC computer used by Charney, Fjörtoft, and von Neumann, and a memory 10 orders of magnitude larger. With the aid of such powerful supercomputers, modern numerical weather forecasting need not rely on solving such simplified models as the barotropic vorticity equation. Instead mathematical models involving the fully 3-dimensional NS atmospheric equations are run by the weather forecasting agencies (e.g., the National Center for Environmental Prediction (NCEP), part of NOAA) in the United States and the Met office in Britain) of various governments to predict regional, national, and global weather patterns. For surface pressure, temperature, wind, and precipitation maps, topographical features can be taken into consideration. Other physical processes, such as those involved in the nonlinear coupling of the ocean to the atmosphere, can also be included. This latter coupling is used in global forecast models to take into account such ocean events as El Niño and La Niña. These events correspond to an oscillation of the ocean–atmosphere system in the tropical Pacific region having important consequences for global weather. Whereas El Niño is characterized by unusually warm ocean temperatures in this region, La Niña generates colder than normal ocean temperatures.

NOAA provides a chart of the so-called Oceanic Niño Index (ONI), the time frame between 1979 and 2010, being shown in Figure 8.3. The ONI is defined as the 3-month running mean of the sea surface temperature anomaly in the tropical Pacific region 5°N to 5°S and 120° to 170°W. The base period for the temperature anomaly is 1971 to 2000. The last running mean shown in Figure 8.3 is for November–December–January 2009–10. El Niño events occur when the ONI is above +0.5° C (the upper horizontal dashed line), while La Niña occurs when the ONI is below −0.5° C (lower dashed line).
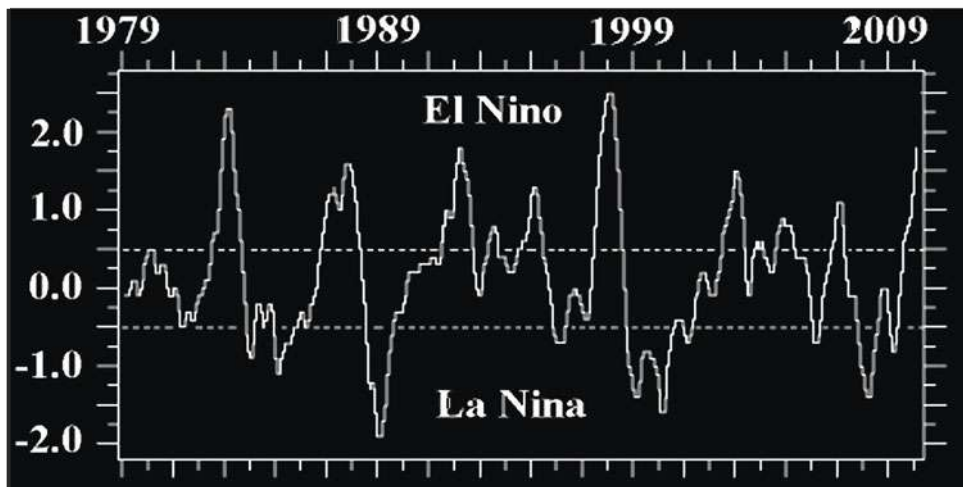
Figure 8.3: Oceanic Niño Index (vertical scale in °C) for the period 1979 to 2010.

What effects El Niño and La Niña have on the weather depends on what region is being considered. For example, El Niño produces increased rainfall across the southern half of the United States and in Peru, often accompanied with destructive flooding and mudslides. El Niño was responsible for the unusually warm weather that occurred during the 2010 Winter Olympics in Vancouver, threatening cancellation of some snowboarding events on a local mountain because of lack of snow. On the other side of the Pacific, El Niño can bring drought to Australia, often causing devastating brush fires such as the one that burned down part of Canberra, the national capital, in 2003. On the other hand, when La Niña occurs winter temperatures in the United States are warmer than usual in the Southeast, and cooler than normal in the Northwest.

Returning to the atmospheric model equations, it should be emphasized that they are not an exact description of the atmosphere, many physical processes and small-scale weather elements (boundary layer processes, heat exchange, cloud cover, etc.) being *parametrized*. For example, instead of dealing with each individual cloud which can vary in type, size, albedo,[9] duration, etc., one uses parameters such as average "cloudiness" to represent the cloud cover in a computational cell. Without such an approximation, even a supercomputer could not complete the weather prediction calculation quickly enough to be useful.[10]

Not only have computers been vastly improved in the last 50 years, but so has data acquisition with the development of weather satellites and other instruments. Since the model algorithms usually run on an evenly spaced 3-dimensional grid, initial data is required for all the grid points. This is not feasible, so mathematical interpolation methods are used to generate input data for grid points where observational data is not available (for example, over great portions of the oceans). For regional models, more data is required since finer spatial grids are used in order to resolve small-scale meteorological phenomena. For global models, the grid is usually coarser. For example, for the NOAA global numerical weather prediction model, the earth's surface is divided into squares of 35 or 70 km on a side and the atmosphere into 64 layers.

The NOAA runs its global numerical weather prediction model four times a day to produce forecasts up to 16 days in advance. A forecast is generated every 3rd hour for the first 7 days, and every 12th hour after that. The output of the NOAA model is the basis for most U.S. web-based forecast services, e.g., Weather Channel, Accuweather.

The NOAA puts out 500-mbar charts such as the one previously shown in Figure 8.2, as well as surface weather maps. What happens at the surface of the Earth is strongly influenced by the interaction between the lowest level in the atmosphere and mid and upper levels. An excellent measure of this interaction is the 500-mbar geopotential height field. An experienced weather forecaster can use the predicted temporal evolution of the 500-mbar height contours to infer changes in the surface weather. For a simple discussion of how this is done see, e.g., the article "Mariner's Guide to the 500-Millibar Chart"[11] by the meteorologists Joe Sienkiewicz and Lee Chesneau.

Due to the nonlinear nature of the atmosphere and the fact that the initial temper-

---

[9]Ratio of diffusely reflected to incident radiation.

[10]It should be noted that the inadequate representation of clouds is also a weakness in current climate change models. (2007 Intergovernmental Panel on Climate Change (IPCC) Report, [Pal05b])

[11]Available at Lee Chesneau's Marine Weather web site: **www.marineweatherbylee.com**.

ature, pressure, etc., to be used in the model calculations cannot be precisely measured and that kilometer-scale weather elements, such as clouds, are not accurately taken into account, a single weather forecast generally becomes increasingly inaccurate after 3 or 4 days. To push this limit out to about 2 weeks, *ensemble forecasts* are generated by weather forecasting agencies such as the NCEP and the British Met office. Instead of just running a single forecast (the *control* forecast based on the known input values), the model equations are run a number of times with slightly different initial conditions grouped around the known values to represent the uncertainties and errors in the observations and parametrizations. The complete set of forecasts is called the *ensemble*, and the individual forecasts the *ensemble members.*

The NCEP global model, for example, uses 17 ensemble members. By choosing an appropriate *probability density function* (e.g., Gaussian-like) for the distribution of ensemble members around the control, an *ensemble mean* of the forecasts can be calculated. This will represent the most probable weather forecast. If the ensemble members stay grouped closely around the ensemble mean, one will have reasonable confidence in the accuracy of the forecast. If they do not not, the forecast will be more uncertain. A measure of the uncertainty is the *ensemble spread*, which is just the standard deviation of the ensemble members from the mean. For detailed information on NCEP ensemble forecasting, see the papers of Toth and Kalnay ([TK93b], [TK93a]).

The NCEP makes available a number of forecast products daily on the Internet. One of the tools that they use is the so-called *spaghetti plot*, which is a snapshot at some instant in time of the spatial distribution of ensemble members for one or two geopotential heights on a constant-pressure surface, in particular the 500-mbar surface. The height contours for the ensemble members resemble strands of spaghetti, the strands grouped close together originally, but becoming increasingly spread as time evolves.

Spaghetti plots are available at the following NOAA web sites:

- **www.emc.ncep.noaa.gov/gmb/ens/fcsts/ensframe.html**.
  These animated plots are for North America and contain 40 ensemble members plus two controls split evenly with the Global Ensemble Forecast System at NCEP and the Canadian Ensemble Forecast System at the Canadian Meteorological Center.

- **www.cdc.noaa.gov/map/images/ens/spag_f360_nh.html**.

As an example, Figure 8.4 is a black-and-white version of the colored NCEP spaghetti plot for two geopotential heights on the 500-mbar surface over North America for Sunday, January 27, 2008, the starting day for the weather forecast.[12] The upper band shows the ensemble member "spaghetti strands" for 5460 m, the lower band (and the oval) the strands for 5640 m.

Spaghetti plot forecasts are made each day in 24-hour intervals up to 360 hours (15 days) in the future. The control strands lie at the center of each band. For greater accuracy, NCEP uses two controls at 00:00 and 12:00 hours for each height. In the colored Internet version of the plot, the control and other strands have different colors

---

[12]By going to the cited web sites, you can look at an up-to-date weather forecast.

Figure 8.5: Predicted spaghetti plot for Wednesday, January 30, 2008.

For each day of the forecast, an ensemble mean plot is determined for the geopotential height contours on the 500-mbar surface. Figure 8.6 shows such a plot for January 30, 2008, i.e., the same day as in Figure 8.5. For clarity here in the text, the outline of North America has been omitted from the plot. You should be able to pick out the ensemble mean contours for 5460 and 5640 meters.

A standard deviation plot is also provided by NCEP, along with ensemble mean plots for predicted precipitation and temperatures. To learn more about ensemble averaging and spaghetti plots used in weather forecasting, go to the Internet where you will have access to a large number of useful web sites besides those already provided.

In closing, although we shall not deal with the highly complex and still unsettled topic of climate change in this text, we should comment on one important aspect of the

Figure 8.5: Predicted spaghetti plot for Wednesday, January 30, 2008.

For each day of the forecast, an ensemble mean plot is determined for the geopotential height contours on the 500-mbar surface. Figure 8.6 shows such a plot for January 30, 2008, i.e., the same day as in Figure 8.5. For clarity here in the text, the outline of North America has been omitted from the plot. You should be able to pick out the ensemble mean contours for 5460 and 5640 meters.

A standard deviation plot is also provided by NCEP, along with ensemble mean plots for predicted precipitation and temperatures. To learn more about ensemble averaging and spaghetti plots used in weather forecasting, go to the Internet where you will have access to a large number of useful web sites besides those already provided.

In closing, although we shall not deal with the highly complex and still unsettled topic of climate change in this text, we should comment on one important aspect of the

Figure 8.6: Ensemble mean heights predicted for Wednesday, January 30, 2008.

generalization of numerical weather models (NWMs) into climate models. As already noted, because of their nonlinear nature, NWMs are sensitive to initial conditions which are never precisely known. This leads to increasing inaccuracy of weather predictions as the initially tightly bound strands of spaghetti in the spaghetti plot spread out with time.

So how can climate models, which are even more complex and highly nonlinear and make predictions much further out in time, be expected to make reasonable predictions of the future climate, both globally and regionally? The answer is that climate is weather averaged over a long period of time, i.e., it is a statistical result.

To draw a loose analogy, consider the repeated flipping of a coin into the air. Because the initial conditions vary slightly from one flip to the next, we cannot predict whether

the coin will land heads or tails. But, statistically, we can accurately predict the result of a very large number of coin tosses. Similarly, making use of past statistics, we might plan our next winter vacation in, say, Maui based on the average high and low temperatures and average rainfall for the month of January. Of course, when the time comes, we might be disappointed by uncharacteristically bad weather. To quote the American humorist Mark Twain, "Climate is what we expect, weather is what we get."

So initial conditions are unimportant to climate scientists in formulating their models of climate change. What they concentrate on is the response of the climate to external forcings such as changes in solar radiation, greenhouse gas[13] concentrations, etc. "What if" scenarios are posed, e.g., "What happens if the carbon dioxide concentration in the atmosphere is doubled?" A discussion of climate change models and scenario outcomes is given in the 2007 IPCC report which is available online.

PROBLEMS

Problem 8-1: Early history of weather forecasting
Consulting Peter Lynch's review paper "Weather Forecasting: from Woolly Art to Solid Science" cited in the text and available on the Internet at:

www.maths.tcd.ie/~plynch/Publications/Publications.html,

flesh out the early history of weather forecasting. For example, include the pioneering contribution of the Norwegian scientist Vilhelm Bjerknes.

Problem 8-2: Thermal wind
Consulting the Internet, define the *thermal wind* and discuss its usefulness and some rules that apply to it.

Problem 8-3: Geostrophic wind speed
At 60°S, the density of air over the open ocean is 1.2 kg/m^3. The distance between isobars drawn for every 4 millibars is 44 nautical miles. Determine the geostrophic wind speed in km/h and in knots (nautical miles per hour).

Problem 8-4: Katabatic wind
Performing an Internet search, discuss what is meant by a *katabatic wind* and provide some specific examples. You might wish to look at the videos of Antarctic katabatic winds available at:

www.youtube.com.

Problem 8-5: Gradient wind
In deriving the geostrophic wind velocity in the text, the role of centripetal acceleration which is relevant to wind flow tangent to curved isobars around a low or a high has been completely neglected. The *gradient wind velocity* takes centripetal acceleration

---

[13] Although they make up a small fraction of the Earth's atmosphere, the so-called *greenhouse gases* control the retention of heat by the atmosphere. Without their presence, the mean temperature at the Earth's surface would be far less than the present 15°C. In decreasing order of relative abundance, the greenhouse gases are: water vapor (up to 4% by volume), carbon dioxide (0.036%), methane (0.00017%), nitrous oxide (0.00003%), and ozone (0.000004%).

into account. By carrying out an Internet search, discuss the gradient wind velocity in some detail.

Problem 8-6: Marine weather forecasters' rules of thumb

Consulting the *Mariner's Guide to the 500-Millibar Chart*, state some "rules of thumb" that marine weather forecasters use based on the 500-millibar chart, in particular the 5640 contour. The Internet web site is:

www.marineweatherbylee.com.

Problem 8-7: North Atlantic Oscillation index

In addition to the oceanic Niño index, another index of importance in predicting regional weather is the North Atlantic Oscillation (NAO) index. Consulting an appropriate web site such as, e.g.,

http://www.cpc.noaa.gov/products/precip/CWlink/pna/nao_index.html,

http://www.ldeo.columbia.edu/res/pi/NAO/,

discuss the NAO index and its use in predicting winter weather in Europe and the eastern United States and Canada.

Problem 8-8: Ensemble forecasts

Discuss in detail the various NCEP ensemble forecast products available at:

http://www.esrl.noaa.gov/psd/map/images/ens/ens.html

Problem 8-9: Okta

By consulting a text on meteorology or the Internet, explain the unit of measurement called an *okta* used to describe cloud cover. Does this unit completely describe cloud cover? Explain.

Problem 8-10: Hadley cell

By consulting a text on meteorology or the Internet, discuss in detail the atmospheric circulation pattern known as the *Hadley cell*. Include in your discussion a history of its discovery.

Problem 8-11: Hurricane tracking

Consulting the Internet, discuss the use of spaghetti plots in hurricane tracking, providing spaghetti plots for specific historical hurricanes.

Problem 8-12: Courant–Friedrich–Lewy stability condition

To avoid numerical instability, the time step Δt of any explicit scheme for numerically simulating the dynamics of the atmosphere or ocean is constrained by the *Courant–Friedrich–Lewy* (CFL) stability condition[14] ([CFL28], [PFTV89]):

If Δx is the grid spacing and V is the speed of the fastest traveling disturbance, then, for numerical stability, Δt should satisfy the inequality $\Delta t \leq \Delta x/V$.

The fastest meteorological disturbances in the atmosphere are large gravity waves and jet streaks (very high velocity regions in jet streams). Their velocity rarely exceeds 100

---

[14]The CFL criterion is simply an extension of the Courant stability condition for the linear wave equation whose derivation using von Neumann stability analysis was assigned as a problem in Chapter 4.

m/s (320 km/hour). Taking $V = 140$ m/s to be on the safe side, what is the maximum step size in minutes allowed according to the CFL criterion if the grid size is taken to be 70 km?

Problem 8-13: Mean surface temperature of the Earth

The mean surface temperature of the Earth is about 15°C. This estimate is based on balancing the incoming solar radiation from the Sun with the emitted radiation from the Earth. Assuming that the Earth is spherical and making use of the Stefan–Boltzmann radiation law of physics, show that the mean surface temperature T (in degrees Kelvin) of the Earth's surface is given by the formula,

$$T = \left(\frac{(1 - a)\, S}{4\,\epsilon\,\sigma} \right)^{1/4}.$$

Here S is the solar radiation from the Sun incident on the Earth per unit area (the *solar irradiance*), $\sigma = 5.67 \times 10^{-8}$ J/(K^4·m^2·s) is the Stefan–Boltzmann constant, and ϵ and a are the Earth's emissivity and average *albedo* (fraction of the incident solar radiation that is reflected),[15] respectively.

For the Earth, $S = 1366$ watts/m^2, $\epsilon \approx 0.61$, and $a \approx 0.3$. Using these values, numerically calculate the mean surface temperature of the Earth in degrees Celsius.

Problem 8-14: Percentage change in albedo

Using the simple energy balance model of the previous problem, determine what percentage change in the Earth's albedo would be required to produce a 1°C change in the Earth's mean surface temperature.

Problem 8-15: Percentage change in solar irradiance

Employing the simple energy balance model, determine the percentage change in the solar irradiance that would be required to produce a 1°C change in the Earth's mean surface temperature.

---

[15]The average albedo is estimated from the known albedos of different reflecting surfaces, viz.,

- worn asphalt, $a = 0.12$ (**heatisland.lbl.gov/Pavements/Albedo/**);
- coniferous forest, $a = 0.09$ to 0.15 (**ace.mmu.ac.uk/resources/gcc/**);
- deciduous forest, $a = 0.15$ to 0.18 (**ace.mmu.ac.uk/resources/gcc/**);
- bare soil, $a = 0.17$ ([MC03]);
- green grass, $a = 0.25$ ([MC03]);
- desert sand, $a = 0.40$ ([Tet83]);
- new concrete, $a = 0.55$ ([MC03]);
- ocean ice, $a = 0.5$ to 0.7 ([MC03]);
- fresh snow, $a = 0.80$ to 0.90 ([MC03]).

The albedo of the ocean surface is dynamic and highly variable, the four most sensitive and readily available parameters being the solar zenith angle (the angle between the local zenith (direction directly above a particular location) and the line of sight to the Sun), the wind speed, the aerosol/cloud optical depth, and the ocean chlorophyll concentration. An ocean surface albedo look-up table is provided at: **http://snowdog.larc.nasa.gov/jin/getocnlut.html**.

Problem 8-16: NOAA global climate model
Consulting the web site,

www.oar.noaa.gov/climate/t_modeling.html,

or any other source, discuss in detail the NOAA coupled global climate model.

Problem 8-17: Global climate models used in the 2007 IPCC Report
Discuss the predictions made by the global climate models used in the 2007 IPCC report. Also discuss their various features, strengths, and weaknesses. The IPCC report is available on the Internet.

Problem 8-18: Criticism of global climate models
David Douglass and coworkers claim ([DCPS08]) that the predicted trends in tropospheric temperature made with 22 global climate models do not agree with satellite observations. Discuss this paper, a reprint of which is available at:

www.pas.rochester.edu/~douglass/papers/Published%20JOC1651.pdf

Problem 8-19: Milankovitch cycles
As a result of cyclic changes in the orbital shape and orientation of the Earth, the solar radiation received by the Earth varies, resulting in climatic change. These cyclic changes are called the *Milankovitch cycles*, after the Serbian civil engineer and mathematician Milutin Milanković (1879–1958) who proposed them. Consulting the Internet or an appropriate text, discuss the Milankovitch cycles in some detail, citing experimental evidence (e.g., ice core data) for these cycles.

Problem 8-20: Sunspot activity
The physical connection of solar sunspot activity to the Earth's climate is not well understood and is a subject of ongoing research. Nevertheless, there is a correlation between sunspot activity and historical temperature records. Consulting the Internet, discuss this correlation, including such examples as the "little ice age" which occurred in northern Europe around 1675 during the *Maunder minimum*. Also, discuss the research of Mike Lockwood et al. on the connection of sunspot activity to European weather patterns, reported in the 24 April 2010 online issue of *Nature News*. The article "Ebbing sunspot activity makes Europe freeze" is available at:

www.nature.com/news/2010/100414/full/news.2010.184.html.

Chapter 9

World of Chemistry

Every attempt to employ mathematical methods in the study of chemical questions must be considered profoundly irrational and contrary to the spirit of chemistry .... if mathematical analysis should ever hold a prominent place in chemistry – an aberration which is happily almost impossible – it would occasion a rapid and widespread degeneration of that science.
Auguste Comte, *Cours de philosophie positive*, 1830

Fortunately for the world of chemistry and the world of nonlinearity, Auguste Comte was wrong about the employment of mathematical methods leading to the widespread degeneration of chemistry.

9.1 Chemical Reactions
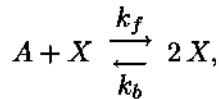
The nonlinear nature of chemistry arises from the fact that chemical reactions are governed by the *law of mass action*. Developed over the period 1864 to 1879 by the Norwegian scientists Cato M. Guldberg and Peter Waage ([GW64], [Waa64], [GW79]), this law (in its modern form) states:

The rate of a reaction is proportional to the product of the reactant concentrations.

This law can lead to a wide variety of nonlinear ODE models. As an example, let's first consider *autocatalysis*, a reaction in which a chemical X stimulates its own production.

9.1.1 Autocatalysis

Consider the following *reversible* autocatalytic chemical reaction:

$$A + X \underset{k_b}{\overset{k_f}{\rightleftharpoons}} 2\,X,$$

where one molecule of X combines with one molecule of A to produce two molecules of X (i.e., a net of one molecule of X), the *forward rate constant* being k_f. Eventually, the production is limited by a *back reaction*, where $2\,X$ combine to produce $A + X$, the

backward rate constant being k_b. Noting that $2X = X + X$ and using the same symbols A and X to denote the concentrations of A and X, applying the law of mass action leads to the following nonlinear ODE describing the production of X:

$$\dot{X} = k_f\, A\, X - k_b\, X^2. \tag{9.1}$$

Let's assume that the concentration of A is held constant, either by supplying this chemical to the reaction vessel to compensate for its depletion or by making its concentration so large that it remains essentially undepleted during the reaction. Setting $x = k_b\, X/(k_f\, A)$ and $r = k_f\, A$, Equation (9.1) reduces to the logistic ODE

$$\dot{x} = r\, x\, (1 - x), \tag{9.2}$$

which was solved in Chapter 1.

Example 9-1: Autocatalytic Reaction

For a certain autocatalytic reaction, the *molar concentrations* are $A = 0.06\,\mathrm{M}$ and, initially, $X(0) = 4.2 \times 10^{-4}\,\mathrm{M}$. If $k_f = 4800\,\mathrm{M^{-1}\,s^{-1}}$ and $k_b = 1200\,\mathrm{M^{-1}\,s^{-1}}$, determine the time T of maximum growth of x. What is the value of x when $t = 5\,T/4$?

Solution: From Equation (1.9), the time of maximum growth is

$$T = -\frac{\ln\left(\dfrac{x_0}{1 - x_0}\right)}{r}, \quad \text{where } x_0 \equiv x(t = 0).$$

Here,

$$x_0 = \frac{k_b\, X(0)}{k_f\, A} = \frac{(1200)\,(4.2 \times 10^{-4})}{((4800)\,(0.06))} = 1.75 \times 10^{-3}$$

and

$$r = k_f\, A = (4800)\,(0.06) = 288.0\,\mathrm{s^{-1}}.$$

Substituting these values into T, the time of maximum growth is $T = 0.022\,\mathrm{s}$.

From Equation (1.8), the solution of the logistic ODE (9.2) is

$$x(t) = \frac{x_0\, e^{r\,t}}{1 + x_0\,(e^{r\,t} - 1)}.$$

Substituting x_0 and $t = 5\,T/4$ into this expression yields $x = 0.83$.

$$\text{***}$$

An example of an autocatalytic transformation is *tin pest* (also known as *tin disease* or *tin leprosy*) which causes the disintegration of tin objects at temperatures below $13.2°\mathrm{C}$ ($56°\mathrm{F}$). Below this temperature, silvery, ductile *white tin* transforms into brittle *gray tin*, which eventually disintegrates into powder (tin pest). Tin pest was observed in the pipes of church organs in the cooler regions of medieval Europe and is conjectured to have been responsible for the disintegration of the buttons on Napoleon's soldiers' clothing in their bitterly cold winter retreat from Moscow. The reaction is autocatalytic

because even the presence of the tiniest amount of tin pest leads to more tin pest. To avoid tin pest, modern tin cans contain small amounts of other elements such as antimony, bismuth, silver, indium, or lead, to prevent decomposition.

Other important or interesting examples of autocatalytic reactions are:

- ozone depletion in the atmosphere: Measurements and modeling studies by Tang and McConnell ([TM96]) strongly suggest that springtime depletion of ozone in the Arctic planetary boundary layer is due to catalytic destruction by bromine atoms. Noting that the source of bromine is uncertain, they propose that the source of the bromine at polar sunrise is the snow pack on the ice covering the Arctic ocean and that it is released autocatalytically, stimulated by a bromine seed from one of the brominated organic compounds, such as CHBr3, by *photolysis*.

- binding of oxygen by hemoglobin: Hemoglobin is the iron-containing oxygen-transport metalloprotein in the red blood cells of vertebrates. Hemoglobin transports oxygen from the lungs or gills to the rest of the body where it releases the oxygen for cell use.

- spontaneous degradation of aspirin into salicylic acid and acetic acid. This causes very old aspirin in sealed containers to smell mildly of vinegar.

- Belousov–Zhabotinskii reaction: This interesting chemical reaction will be studied later in the chapter.

- evolution of life: The central role of autocatalysis in the evolution of life has been suggested by Robert Ulanowicz ([Ula97]) and Stuart Kauffman ([Kau02]).

9.1.2 Michaelis–Menten Enzyme Kinetics
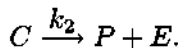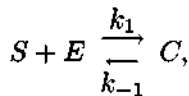
Enzymes, which are large protein molecules, are the catalysts which speed up chemical reactions in living things. They do work on specific molecules, called *substrates*. Without the presence of enzymes, the vast majority of chemical reactions that keep living things alive would be too slow to maintain life.

An example is the oxidation of *glucose* (a sugar) to give water, carbon dioxide, and energy. Left open to the air, the oxidation of glucose is extremely slow, no appreciable oxidation occurring after years of exposure. Yet in the human body, glucose is oxidized rapidly to provide the energy for us to walk and run.

Certain diseases, such as *phenylketonuria* (PKU), can occur when the body lacks a specific enzyme (*phenylalanine hydroxylase* in the case of PKU). If left untreated, PKU can cause problems with brain development, leading to progressive mental retardation and seizures. Although there is no cure, PKU is one of the few genetic diseases that can be controlled by diet.

One of the most important enzyme reactions was first proposed in 1913 by Leonor Michaelis and Maud Leonora Menten ([MM13]). It involves a substrate S reacting with an enzyme E to form a complex SE, this reaction being reversible with forward and backward rate constants k_1 and k_{-1}, respectively. The complex SE in turn is converted

irreversibly into a product P and the enzyme E. Labeling the complex SE as C for notational convenience, this autocatalytic reaction is

$$S + E \overset{k_1}{\underset{k_{-1}}{\rightleftharpoons}} C,$$

$$C \xrightarrow{k_2} P + E.$$

Using the same symbols to denote the concentrations and applying the law of mass action, the relevant chemical reaction equations are:

$$
\begin{aligned}
\dot{S} &= -k_1 \, E \, S + k_{-1} \, C, \\
\dot{E} &= -k_1 \, E \, S + (k_{-1} + k_2) \, C, \\
\dot{C} &= k_1 \, E \, S - (k_{-1} + k_2) \, C, \\
\dot{P} &= k_2 \, C,
\end{aligned}
\tag{9.3}
$$

with initial concentrations $S(0) = S_0$, $E(0) = E_0$, $C(0) = 0$, and $P(0) = 0$.

Example 9-2: Reduction of the Nonlinear ODE System

Show that the nonlinear ODE system (9.3) can be reduced to two coupled ODEs for $S(t)$ and $C(t)$. Write the relations down for determining $P(t)$ and $E(t)$, once $S(t)$ and $C(t)$ are known.

Solution: The last equation is uncoupled from the first three ODEs. Once $C(t)$ is known, $P(t)$ is determined from

$$P(t) = k_2 \int_0^t C(t') \, dt'. \tag{9.4}$$

Adding the second and third ODEs yields

$$\dot{E} + \dot{C} = 0, \quad \text{so} \quad E(t) = E_0 - C(t) \tag{9.5}$$

is the relation determining $E(t)$, once $C(t)$ is known.

Using this last result to eliminate $E(t)$, the first and third ODEs become

$$
\begin{aligned}
\dot{S} &= -k_1 \, E_0 \, S + (k_1 \, S + k_{-1}) \, C, \\
\dot{C} &= k_1 \, E_0 \, S - (k_1 \, S + k_{-1} + k_2) \, C.
\end{aligned}
\tag{9.6}
$$

$$***$$

The reduced ODE system (9.6) can be put into nondimensional form by setting

$$\tau = k_1 \, E_0 \, t, \quad x(\tau) = \frac{S(\tau)}{S_0}, \quad y(\tau) = \frac{C(\tau)}{E_0} \tag{9.7}$$

and

$$\lambda = \frac{k_2}{k_1 \, S_0}, \quad K = \frac{k_{-1} + k_2}{k_1 \, S_0} \equiv \frac{K_M}{S_0}, \quad \epsilon = \frac{E_0}{S_0}. \tag{9.8}$$

Then, (9.6) becomes

$$\dot{x}(\tau) = -x + (K - \lambda) \, y + x \, y, \quad x(0) = 1,$$

$$\epsilon \, \dot{y}(\tau) = x - K \, y - x \, y, \quad y(0) = 0. \tag{9.9}$$

The parameter K_M is called the *Michaelis constant*. It should be also noted that the coefficient $K - \lambda = k_{-1}/(k_1 \, S_0) > 0$.

An exact analytic solution to the nonlinear ODE system (9.9) doesn't exist but a useful approximation can be easily generated by noting that in most biological processes ([Mur02]), a very small amount of enzyme is needed in the reaction compared to the substrate, i.e., $\epsilon \ll 1$. The *steady-state approximation* (SSA) (more precisely, *quasi-steady-state*) consists of completely neglecting the term $\epsilon \, \dot{y}$ in (9.9). Then, we have

$$y = \frac{x}{K + x} \quad \text{and} \quad \dot{x} = -\frac{\lambda \, x}{K + x}. \tag{9.10}$$

Since $x(\tau = 0) = 1$, note that the SSA for y does not satisfy the initial condition $y(0) = 0$, so only applies to times not too close to $\tau = 0$ (called the *outer solution*). Separating variables in the above ODE and integrating subject to the initial condition $x(0) = 1$, we obtain an *implicit* solution for $x(\tau)$, viz.,

$$x(\tau) + K \ln x(\tau) = 1 - \lambda \tau. \tag{9.11}$$

Given the parameter values K and λ, this equation must be solved numerically for specified values of the normalized time τ. The following example compares the approximate (SSA) solutions for $x(\tau)$ and $y(\tau)$ to the exact (numerical) solutions.

Example 9-3: Comparison of the SSA with the Exact Solution

Taking $K = 8$, $\lambda = 0.1$, $\epsilon = 0.0001$, and $\tau = 0$ to 50, carry out the following steps:

   a. Numerically solve the ODE system (9.9) for $x(\tau)$ and $y(\tau)$;

   b. Numerically solve the implicit equation (9.11) for $x(\tau)$ in time steps $\Delta \tau = 2$. Then, calculate $y(\tau)$ using the SSA expression for the same time steps;

   c. In the same graph, plot the numerical solutions as solid curves and the SSA solutions as circles. How do the exact (numerical) and SSA results compare?

Solution: a. The ODE system (9.9) is solved numerically with $K = 8$, $\lambda = 0.1$, and $\epsilon = 0.0001$ over the time interval $\tau = 0$ to 50 using the RKF45 method.

b. The implicit equation (9.11) is solved with $K = 8$, $\lambda = 0.1$ for x at $\tau = 0, 2, 4, \ldots, 50$. Then $y = x/(K + x)$ is calculated at these time steps.

c. The numerical solutions are plotted as smooth curves and the SSA solutions as circles in Figure 9.1. The top results are for x, the bottom for y.
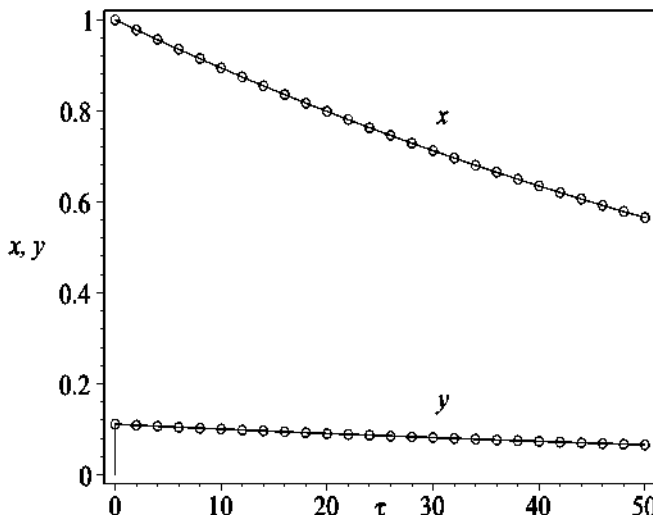
Figure 9.1: Solid curves: exact (numerical) results. Circles: SSA results.

The SSA result for $x(\tau)$ agrees extremely well with the exact (numerical) curve over the entire range of τ. Except extremely close to $\tau = 0$ where the exact curve jumps very rapidly, the SSA result for $y(\tau)$ also agrees very well with the exact result. By making a different approximation than the SSA, an analytic *inner solution* can be derived which captures this initial jump. See ([Mur02]) or ([EK88]) for the mathematical details.

$$***$$

Since $E(\tau)/E_0 = 1 - y(\tau)$ from Equation (9.5), there is an initial decrease in the enzyme concentration, but as $\tau \to \infty$ the SSA and exact result tell us that $y(\tau) \to 0$ so the enzyme concentration returns to its initial value.

Turning to the product P, the *Michaelis–Menten* (MM) *equation* for the so-called "velocity" $V = \dot{P}$ of the reaction can now be derived using the SSA. We have

$$V = \dot{P} = k_2\, C = k_2\, E_0\, y = \frac{k_2\, E_0\, x}{K + x} = \frac{k_2\, E_0\, S}{K_M + S}. \tag{9.12}$$

The maximum velocity V_{max} occurs in the limit $S \to \infty$, so $V_{max} = k_2\, E_0$. The MM equation then is

$$V = \frac{V_{max}\, S}{K_M + S}. \tag{9.13}$$

Experimentally one measures V as a function of S. The Michaelis constant K_M can be found by plotting $1/V$ versus $1/S$. Introduced by Hans Lineweaver and Dean Burk ([LB34]) in 1934, this plot is called a *Lineweaver–Burk* plot (also known as a *double reciprocal plot*). Inverting the MM equation, we have

$$\frac{1}{V} = \left(\frac{K_M}{V_{max}} \right) \frac{1}{S} + \frac{1}{V_{max}}. \tag{9.14}$$

Plotting $1/V$ against $1/S$, we obtain a straight line with slope K_M/V_{max} and intercept $1/V_{max}$. Thus K_M is equal to the ratio of the slope to the intercept. The rate constant $k_2 = V_{max}/E_0$. Some representative values of K_M and k_2 for different enzymes and substrates are given in Table 9.1.

Enzyme (E)	Substrate (S)	K_M (in M)	k_2 (in s^{-1})
Acetylcholine Esterase	Acetylcholine	9.5×10^{-5}	1.4×10^4
Carbonic Anhydrase	CO_2	1.2×10^{-2}	1.0×10^6
Carbonic Anhydrase	HCO_3^-	2.6×10^{-2}	4.0×10^5
Catalase	H_2O_2	2.5×10^{-2}	1.0×10^7
Fumerase	Fumerate	5.0×10^{-6}	800
Fumerase	Malate	2.5×10^{-5}	900
Urease	Urea	2.5×10^{-2}	1.0×10^4

Table 9.1: K_M and k_2 for some enzyme–substrate systems.

9.1.3 Lotka–Volterra Mechanism

In Chapter 1, you were introduced to the nonlinear Lotka–Volterra equations for interacting predator–prey systems, this system of equations having periodic solutions. The Lotka–Volterra mechanism can also occur for certain autocatalytic chemical reactions. Consider the following irreversible reactions, the first two of which are autocatalytic:

$$\begin{aligned} A + X &\xrightarrow{k_1} 2X, \\ X + Y &\xrightarrow{k_2} 2Y, \\ Y &\xrightarrow{k_3} B. \end{aligned} \tag{9.15}$$

The concentration of A is held fixed and B plays no part in the reaction once it has been produced. In practice, it would normally be removed. So, the only variables of

interest are the concentrations of X and Y. Applying the law of mass action yields the following Lotka–Volterra equations:

$$\dot{X} = k_1\, A\, X - k_2\, X\, Y \equiv P(X,Y),$$
$$\dot{Y} = k_2\, X\, Y - k_3\, Y \equiv Q(X,Y). \tag{9.16}$$

Although this system cannot be analytically solved for $X(t)$ and $Y(t)$, the relation between X and Y is easily found, thus allowing one to draw the trajectories in the X–Y phase plane. Dividing the second equation by the first to eliminate the time, then separating variables and integrating, yields the conservation law,

$$k_1\, A\, \ln Y - k_2\, Y - k_2\, X + k_3\, \ln X = C. \tag{9.17}$$

The integration constant C is fixed by the initial values of X and Y, i.e.,

$$C = k_1\, A\, \ln Y(0) - k_2\, Y(0) - k_2\, X(0) + k_3\, \ln X(0).$$

Example 9-4: Periodic Solutions

Taking $k_1\, A = k_2 = k_3 = 1$, plot the left-hand side of the conservation law (9.17) in the X–Y plane for $C = -2.01, -2.1, -2.5, -3, -4$. Discuss the results in terms of the fixed points of the ODE system.

Solution: The trajectories in the X–Y phase plane are shown in Figure 9.2. The
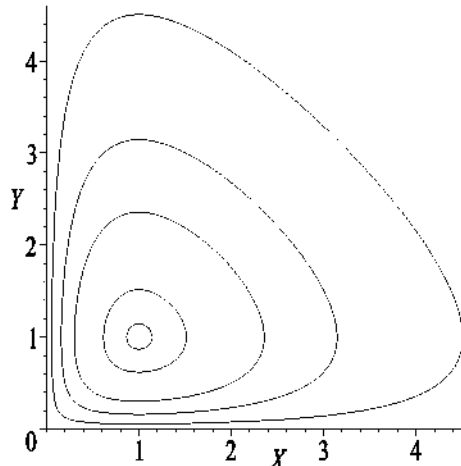
Figure 9.2: Periodic trajectories in phase plane.

innermost loop is for $C = -2.01$, the second innermost loop for $C = -2.1$, and so on, until $C = -4$ for the outermost loop. The trajectories are periodic as expected.

For the given parameter values, the ODE system has fixed points determined by

$$\dot{X} = 0 = \bar{X}\,(1 - \bar{Y}), \qquad \dot{Y} = 0 = \bar{Y}\,(-1 + \bar{X}).$$

So there are two fixed points, one at $(0,0)$ and the other at $(1,1)$. Noting that

$$\partial P/\partial X = 1 - Y, \quad \partial P/\partial Y = -X, \quad \partial Q/\partial X = Y, \quad \partial Q/\partial Y = -1 + X,$$

for the fixed point $(0,0)$, one has (using the notation of Chapter 2)

$$a = 1, \quad b = 0, \quad c = 0, \quad d = -1, \quad p = -(a+d) = 0, \quad \text{and} \quad q = ad - bc = -1.$$

Since $q < 0$, from Table 2.1 we conclude that this fixed point is a saddle point. This is consistent with the shape of the trajectory closest to the origin.

For the second fixed point, $(1,1)$, we obtain $p = 0$ and $q = 1 > 0$, so this is a vortex or focal point. Application of Poincaré's theorem is inconclusive but, from Figure 9.2, the fixed point is clearly a vortex.

<p align="center">***</p>

9.2 Chemical Oscillators

As mentioned earlier, autocatalysis can play an important role in oscillating chemical reactions, a situation where the concentrations of the reactants vary periodically in time or space. Chemical oscillators are the analogue of electrical oscillators, autocatalysis contributing to the positive feedback mechanism responsible for the oscillations. Oscillating reactions not only can be generated in the laboratory but also occur in some industrial processes. Oscillating reactions are also important in maintaining the beating of the heart, the cells of the heart acting as chemical reactors.
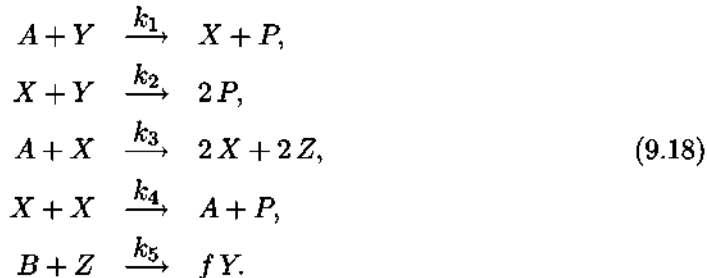
9.2.1 The Oregonator

Perhaps the best-known chemical oscillator is the Belousov–Zhabotinskii (BZ) chemical reaction ([Bel58],[ZZ70], [Zha91]). Historically, it is interesting to note that Belousov could not initially get his oscillator discovery published in any Soviet journal because it contradicted the then-current belief that all solutions of reacting chemicals must go monotonically to equilibrium. Only years later, when his work was confirmed by Zhabotinskii, was he given due recognition for his discovery. For his pioneering research work Belousov was awarded, along with Zhabotinskii, the Soviet Union's highest medal but the recognition was a bit late as he had died 10 years earlier.

What is the BZ reaction? When appropriate concentrations of malonic acid and cerium ammonium nitrate are dissolved and stirred in sulfuric acid, the resulting solution is initially yellow but turns clear after a few minutes. On then adding sodium bromate, the solution oscillates between yellow and clear with a period of about 1 minute. A more dramatic color change between red and blue can be achieved by adding a ferroin indicator (a 0.025 M solution of phenanthroline ferrous sulfate).

The full BZ reaction involves 18 steps and 21 different chemical species, but a simplified kinetic model which captures the observed oscillatory behavior makes use of only 5 steps. This is permitted because some reactions are very slow compared to others so

that the variation in concentrations of some species can be neglected on the time scale of the oscillations. This truncated model, developed by Richard Field and Robert Noyes ([FKN72], [FN74]) at the University of Oregon, is appropriately called the *Oregonator* model. It involves the following five reactions:

$$
\begin{aligned}
A + Y & \xrightarrow{k_1} X + P, \\
X + Y & \xrightarrow{k_2} 2P, \\
A + X & \xrightarrow{k_3} 2X + 2Z, \\
X + X & \xrightarrow{k_4} A + P, \\
B + Z & \xrightarrow{k_5} fY.
\end{aligned}
\tag{9.18}
$$

Here A is BrO_3^-, X is $HBrO_2$, Y is Br^-, Z is Ce^{4+}, B is $CH_2(COOH)_2$, and P is $HOBr$ or $BrCH(COOH)_2$. The concentrations of A, B, and P are sufficiently large that they may be treated as constants on the time scale of several oscillations. The parameter $f \approx 1/2$ is a compensating "fudge factor" introduced because of the drastic truncation of the full set of equations describing the reactions. Then using the same symbols to denote concentrations, the law of mass action leads to the following rate equations for producing X, Y, and Z:

$$
\begin{aligned}
\dot{X} &= k_1 A Y - k_2 X Y + k_3 A X - k_4 X^2, \\
\dot{Y} &= -k_1 A Y - k_2 X Y + f k_5 B Z, \\
\dot{Z} &= 2 k_3 A X - k_5 B Z.
\end{aligned}
\tag{9.19}
$$

The rate equations can be converted ([Tys85], [Sco95]) into a dimensionless form and the number of independent parameters reduced by setting

$$
x = \frac{k_4 X}{k_3 A}, \quad y = \frac{k_2 Y}{k_3 A}, \quad z = \frac{k_4 k_5 B Z}{2 k_3^2 A^2}, \quad \tau = (k_5 B) t
$$

and,

$$
\epsilon = \frac{k_5 B}{k_3 A}, \quad \epsilon' = \frac{k_4 k_5 B}{k_2 k_3 A}, \quad q = \frac{k_1 k_4}{k_2 k_3}.
$$

The Oregonator rate equations (9.19) then reduce to the form

$$
\begin{aligned}
\epsilon \dot{x}(\tau) &= q y - x y + x (1 - x), \\
\epsilon' \dot{y}(\tau) &= -q y - x y + 2 f z, \\
\dot{z}(\tau) &= x - z.
\end{aligned}
\tag{9.20}
$$

The following example solves this nonlinear ODE system using the experimentally determined values of the parameters.

Example 9-5: Oregonator Limit Cycle

For the Oregonator, the experimental parameter values (see "Oregonator", Richard J. Field (2007), *Scholarpedia*, 2(5):1386) are

$$\epsilon = 9.90 \times 10^{-3}, \quad \epsilon' = 1.98 \times 10^{-5}, \quad q = 7.62 \times 10^{-5}, \quad f = 1/2.$$

Taking the initial condition $x(0) = y(0) = z(0) = 0.1$, numerically solve the Oregonator ODE system (9.20) over the time interval $\tau = 0$ to 80 and show that the trajectory evolves onto a closed loop in the 3-dimensional x–y–z space. Confirm that this loop is a limit cycle by experimenting with other initial conditions. Plot the normalized $HBrO_2$ concentration, x, as a function of τ over the interval $\tau = 50$ to 80 .

Solution: Using *Maple* or *Mathematica*, the ODE system is solved over the time interval $\tau = 0$ to 80 using the adaptive step RKF45 method. The trajectory then is plotted in x–y–z space, the result being shown on the left of Figure 9.3. The trajectory winds
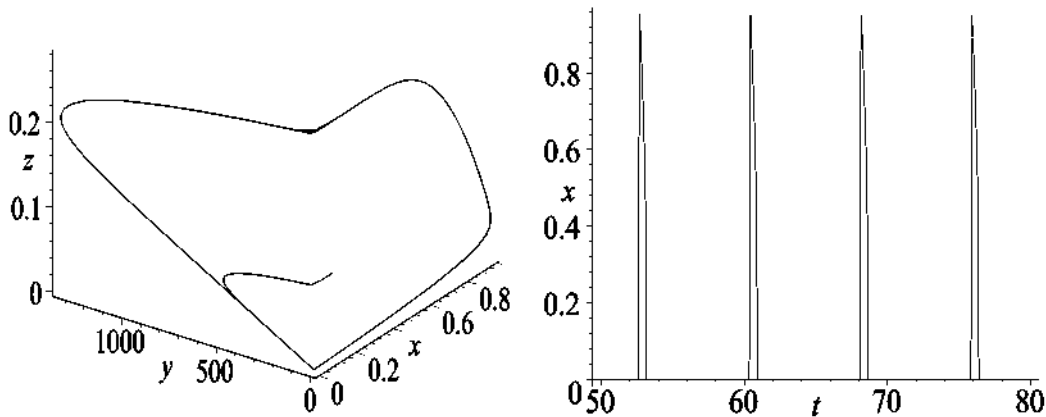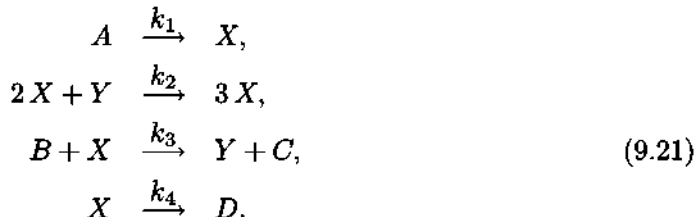
Figure 9.3: Left: evolution onto a limit cycle. Right: x versus (normalized) time.

onto a closed loop as expected for the chemical oscillator. The reader may confirm that changing the initial conditions produces the same closed loop, confirming the existence of the limit cycle.

The normalized $HBrO_2$ concentration is given by x, which is plotted as a function of (normalized) time τ on the right of the figure. The periodic spikes in x make the BZ reaction an example of a *chemical clock*.

***

9.2.2   The Brusselator

A second well-known example of a chemical oscillator involves the following set of hypothetical chemical reactions introduced by the Brussels researchers Ilya Prigogine and Rene Lefever ([PL68]):

$$A \xrightarrow{k_1} X,$$

$$2X + Y \xrightarrow{k_2} 3X,$$

$$B + X \xrightarrow{k_3} Y + C, \tag{9.21}$$

$$X \xrightarrow{k_4} D.$$

The concentrations of A and B are held fixed. Applying the law of mass action, the rate equations for the concentrations of X and Y in the above *Brusselator* model are

$$\dot{X} = k_1 A + k_2 X^2 Y - k_3 B X - k_4 X,$$

$$\dot{Y} = -k_2 X^2 Y + k_3 B X. \tag{9.22}$$

Setting $\tau = k_4 t$ and

$$x = \sqrt{\frac{k_2}{k_4}}\, X, \quad y = \sqrt{\frac{k_2}{k_4}}\, Y, \quad \tilde{a} = \sqrt{\frac{k_2}{k_4}}\, \frac{k_1}{k_4}\, A, \quad \tilde{b} = \frac{k_3}{k_4}\, B,$$

the Brusselator equations (9.22) reduce to

$$\dot{x}(\tau) = \tilde{a} + x^2 y - (\tilde{b} + 1)\, x \equiv P(x, y),$$

$$\dot{y}(\tau) = -x^2 y + \tilde{b}\, x \equiv Q(x, y). \tag{9.23}$$

Example 9-6: Brusselator Fixed Points

Locate and determine the nature of the fixed points of the reduced Brusselator equations. Show that a Hopf bifurcation occurs at $\tilde{b} = \tilde{a}^2 + 1$.

Solution Fixed points occur for $P = \tilde{a} + \bar{x}^2 \bar{y} - (\tilde{b} + 1)\bar{x} = 0$ and $Q = -\bar{x}^2 \bar{y} + \tilde{b}\, \bar{x} = 0$. There is only one fixed point, $\bar{x} = \tilde{a}$, $\bar{y} = \tilde{b}/\tilde{a}$. At this fixed point,

$$a = \left(\frac{\partial P}{\partial x}\right)_0 = \tilde{b} - 1, \ b = \left(\frac{\partial P}{\partial y}\right)_0 = \tilde{a}^2, \ c = \left(\frac{\partial Q}{\partial x}\right)_0 = -\tilde{b}, \ d = \left(\frac{\partial Q}{\partial y}\right)_0 = -\tilde{a}^2,$$

so $p = -(a + d) = \tilde{a}^2 + 1 - \tilde{b}$ and $q = a\, d - b\, c = \tilde{a}^2$. Noting that $q > 0$, there is clearly a Hopf bifurcation at $\tilde{b} = \tilde{a}^2 + 1$. For $\tilde{b} < \tilde{a}^2 + 1$, we have $p > 0$ so the fixed point is either a stable focal or nodal point. As the "control parameter" $\tilde{b}$ is increased above $\tilde{a}^2 + 1$, then $p < 0$ and the fixed point is an unstable focal or nodal point.

***

For $\tilde{b} > \tilde{a}^2 + 1$, the fixed point is an unstable focal or nodal point. A trajectory in the phase plane starting near this fixed point will move away from it. Where does the trajectory go? It winds onto a stable limit cycle as illustrated in the following example.

Example 9-7: Brusselator Limit Cycle

Taking $\tilde{a} = 1$ and $\tilde{b} = 3$, locate the fixed point for the Brusselator ODE system (9.23) and completely determine its nature. Then create a phase-plane portrait which shows the location of the fixed point, the tangent field, and the temporal evolution of the trajectories corresponding to the two initial conditions, $x(0) = y(0) = 0.1$ and $x(0) = 1.25$, $y(0) = 3.05$.

Solution: The fixed point is located at

$$\bar{x} = \tilde{a} = 1, \quad \bar{y} = \tilde{b}/\tilde{a} = 3.$$

It is either an unstable focal or nodal point since $\tilde{b} = 3 > \tilde{a}^2 + 1 = 2$. Making use of Example 8-6, we have

$$p = \tilde{a}^2 + 1 - \tilde{b} = -1, \quad q = \tilde{a}^2 = 1, \quad \text{and} \quad p^2 - 4q = -3 < 0.$$

So the fixed point is an unstable focal point.

The phase-plane portrait is shown in Figure 9.4, the small circle indicating the fixed point. The trajectories corresponding to both initial conditions follow the tangent field arrows and eventually wind onto a closed loop, which is the Brusselator limit cycle.
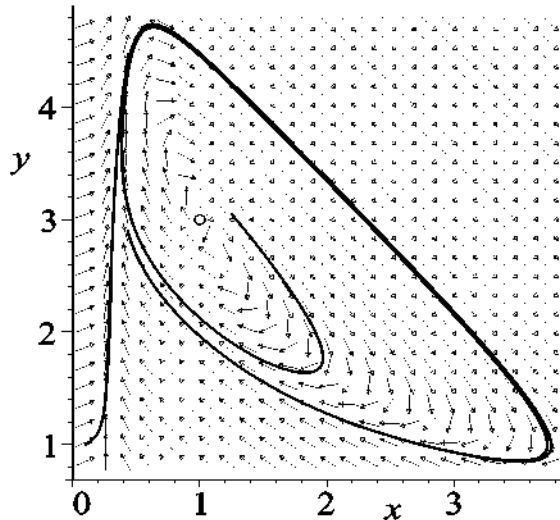
Figure 9.4: Trajectories wind onto the Brusselator limit cycle.

***

9.3   Chemical Waves and Patterns

Chemically oscillating solutions can generate waves and interesting spatial patterns when the solution is placed in a thin layer in a petri dish.

9.3.1   Target Patterns and Spiral Waves

Using an unstirred ferroin-catalyzed BZ reacting solution, Zaikin and Zhabotinskii ([ZZ70]) observed *bull's-eye* or *target patterns* involving the periodic propagation of concentric chemical waves generated by spontaneously occurring point chemical oscillators. Unlike the situation for small water waves which would pass through each other and linearly superimpose, when the chemical wave fronts collide they come to an abrupt halt, indicating that the chemical mixture is an *excitable medium*. That is to say, it is a nonlinear medium in which colliding wave fronts annihilate each other and stop, and for which there is a refractory time during which no further wave action is possible. Eventually, a static pattern, such as the one shown in Figure 9.5, is produced in the petri dish. When the petri dish is shaken, the process starts over again with, in general, a new final pattern being observed.
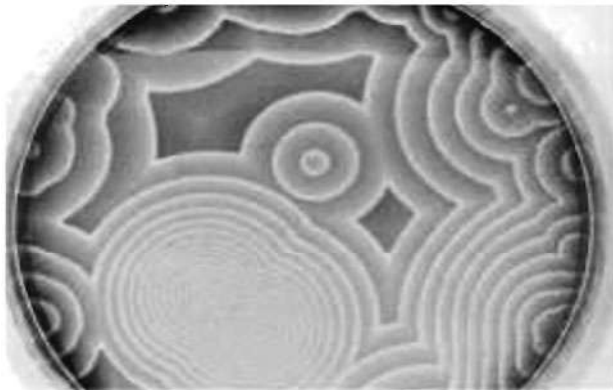
Figure 9.5: Target pattern.

Spiral wave patterns can be generated by tilting the petri dish in order to break some of the chemical wave fronts. The free ends of the wave fronts wrap around into spirals. Figure 9.6 shows an example of BZ spiral wave growth.

Spiral waves can also occur in biological examples of excitable media, for example, in cardiac tissue ([KG95], [BSG02]). This is relevant to sudden cardiac death which kills more than 300 thousand Americans a year. Normally, electrical impulses cause muscle fibers of the heart to contract. In a healthy heart, these electrical impulses pass through the cardiac tissue as a smooth wave. However, sometimes potentially dangerous spiral waves of electrical activity can form.

Leon Glass and co-workers have investigated these spiral waves in a sheet of chick-embryo cardiac cell tissue. Spiral waves often occur in the first 2 days of tissue growth.
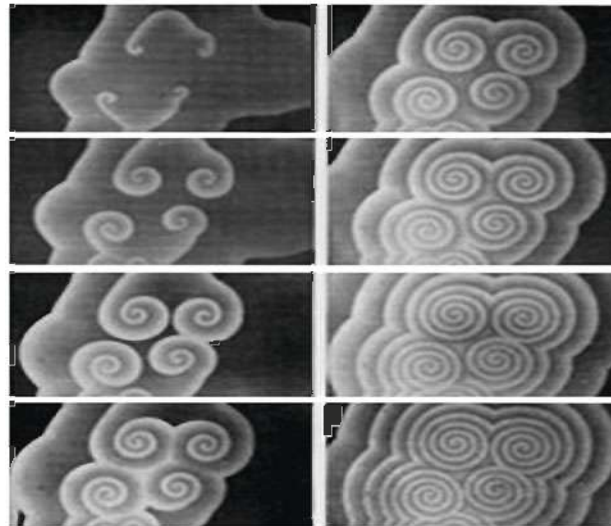
Figure 9.6: Spiral wave growth.

When the researchers administered a drug to the cardiac tissue to impair communication between cells, the rotating spiral waves broke up into multiple rotating spirals. This spiral wave breakup is believed to be similar to what occurs in ventricular fibrillation, a potentially fatal cardiac rhythm which occurs when communication between heart cells is impaired by a heart attack or other causes.

The mathematical description (see, e.g., ([Tys76]) and ([Mur02])) of target pattern and spiral wave formation involves the use of *reaction-diffusion* equations.

9.3.2 Reaction-Diffusion Equations

A reaction-diffusion system involving N reactants with concentrations c_1, c_2, etc., has the general mathematical structure

$$\frac{\partial c_i}{\partial t} = D_i \nabla^2 c_i + f_i(c_1, c_2, \ldots, c_N), \quad i = 1, 2, \ldots, N, \tag{9.24}$$

where D_i is the diffusion coefficient of the ith reactant and f_i is a nonlinear function describing its rate of production. Reaction-diffusion equations play a central mathematical role not only in explaining chemically produced spatial patterns but also in understanding the generation of biological and physical patterns as well as the spreading of different species and substances.

The simplest situation is when only a single chemical reactant or biological species or physical substance is involved. In this case, on dropping the subscript, we have

$$\frac{\partial c}{\partial t} = D \nabla^2 c + f(c). \tag{9.25}$$

Depending on the application, different (usually normalized) forms have been chosen historically for $f(c)$, for example:

- $f(c) = c\,(1 - c)$:

    The English statistician, evolutionary biologist, and geneticist Sir Ronald Fisher $(1890 - 1962)$ used this form of $f(c)$ to describe the spreading of an advantageous gene in a biological population. The 1-dimensional formulation, viz.,

    $$\frac{\partial c}{\partial t} = D\,\frac{\partial^2 c}{\partial x^2} + c\,(1 - c), \qquad (9.26)$$

is known as *Fisher's equation* ([Fis37]). This is just the linear diffusion equation to which the nonlinear logistic term has been added. Note that one can set $D = 1$ without loss of generality since a new spatial variable $x/\sqrt{D}$ could be introduced. Fisher's equation permits the existence of topological solitary waves.

Example 9-8: Fisher Solitary Wave

Show that Fisher's equation (9.26) allows for the existence of a topological solitary wave.

Solution: Assuming a solution for the concentration of the form $c(x, t) = U(z = x - v\,t)$, where $v > 0$ is the velocity, reduces the PDE (9.26) (with $D = 1$) to the nonlinear ODE

$$\frac{d^2 U}{dz^2} + v\,\frac{dU}{dz} + U\,(1 - U) = 0.$$

Setting $V = dU/dz$, this second-order ODE can be written as two first-order ODEs,

$$\frac{dU}{dz} = V, \qquad \frac{dV}{dz} = -v\,V - U\,(1 - U).$$

Dividing the second ODE by the first yields

$$\frac{dV}{dU} = \frac{-v\,V - U\,(1 - U)}{V} \equiv \frac{Q(U, V)}{P(U, V)}$$

which has the two fixed points $(\bar{U}, \bar{V}) = (0, 0)$ and $(1, 0)$. Using the phase-plane-analysis notation of Chapter 2, for the fixed point $(0, 0)$ we have $p = v > 0$, $q = 1$, and $p^2 - 4q = v^2 - 4$, so this is a stable nodal point for $v \geq 2$ and a stable focal point for $v < 2$. For the second fixed point, $q = -1 < 0$, so this is a saddle point.

On physical grounds, we cannot have $v < 2$ because the existence of a stable focal point at the origin would allow the concentration to be negative for certain ranges of z as the trajectory winds on to the focal point. Negative concentration is unphysical.

For $v \geq 2$, a separatrix trajectory leaving the saddle point at $(1, 0)$ can approach the stable nodal point at $(0, 0)$ as $z \to +\infty$ while keeping $U > 0$, so an antikink topological solitary wave can exist connecting $U = 1$ and $U = 0$. In general an analytic solitary wave solution doesn't exist for arbitrary values of v, but one exists for $v = 5/\sqrt{6}$. Determining the mathematical form of this special solution is left as a problem.

<div align="center">***</div>

- $f(c) = c\,(1 - c^2)$:

This choice yields the *Newell Whitehead Segel equation* ([NW69], [Seg69]) used to describe the evolution of *Rayleigh–Bénard convection* cells. Rayleigh–Bénard convection [1] involves the flow of heat energy upward through a fluid layer of infinite extension and finite thickness confined between two horizontal plates, the bottom plate being held at a higher temperature than the top one. Figure 9.7 schematically shows the heat inflow (bottom row of upright arrows) into the fluid at the lower, hotter, surface and the heat outflow (top row of upright arrows) at the cooler, upper, surface. For a small temperature difference, the fluid is at rest
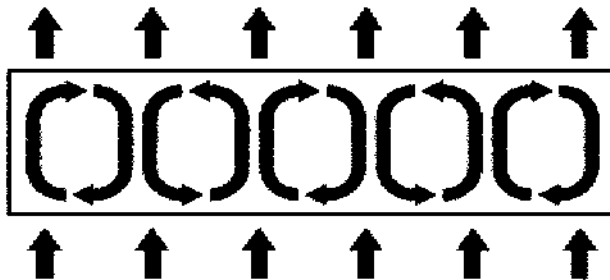
Figure 9.7: Rayleigh–Bénard convection rolls.

and the transfer of energy is via heat conduction. However, as the temperature difference is increased above a critical value, fluid convection occurs in the form of "rolls" as schematically depicted in the fluid. Hot fluid rises along a boundary between a pair of rolls, cools at the top surface, and then drops along the boundaries of adjacent rolls. As the temperature difference is further increased, more complex behavior occurs and ultimately chaotic convection (turbulence) is observed.

The next level of complexity, relevant to spatial pattern formation, involves two chemical species. Labeling their concentrations as A and B, the reaction-diffusion system is

$$\frac{\partial A}{\partial t} = D_A \nabla^2 A + f_A(A, B),$$
$$\frac{\partial B}{\partial t} = D_B \nabla^2 B + f_B(A, B).$$

$$(9.27)$$

Alan Turing ([Tur52]) suggested that if, for zero diffusion, A and B approach a linearly stable uniform steady state, then spatially inhomogeneous patterns can evolve under

---

[1] Originally studied by Lord Rayleigh ([Ray83]) and later by the French experimentalist Henri Bénard.

certain conditions if $D_A \neq D_B$. Basically one requires one of the reactants to be a short-range autocatalytic substance (called the *activator*) and the other a long-range antagonist (called the *inhibitor*).

To explain the activator–inhibitor idea, Jim Murray ([Mur02]) has suggested the following hypothetical scenario. Consider a uniform, dry, grassy field containing grasshoppers (G) which sweat a lot (thus providing copious amounts of moisture) if they get too warm. A fire (F) is set at some point in the field and a flame front begins to spread with a diffusion coefficient D_F through the dry grass. Here the fire is the activator and the grasshopper is the inhibitor. If there was no sweaty inhibitor to quench the flames, the fire would uniformly burn the whole field. With the grasshoppers present, the outcome would be different. When they feel the flame front coming, the grasshoppers having a much larger diffusion coefficient D_G move quickly ahead of it, sweating profusely and leaving the vacated area sufficiently wet that the grass cannot burn. In this way the burnt region is restricted to a finite area which depends on the diffusion coefficients of the reactants and various reaction parameters. If instead of a single fire, fires were set at random, it is clear that a final spatially inhomogeneous steady-state distribution of burnt and unburnt regions would occur in the field. If the grasshoppers and flame fronts diffused at the same speeds, no such spatial pattern would emerge.

The activator–inhibitor mechanism has been used to explain how the leopard got its spots ([Mur88]) as well as other coat patterns in the animal kingdom.

9.3.3 How the Leopard Got Its Spots

Why is the coat of a leopard spotted, whereas the coats of the tiger and zebra are striped? Why are the spots on a giraffe different and much larger than those on a leopard? Why do the coats of certain animals, such as the mouse and elephant, display no patterning? Why do the cheetah, jaguar, and leopard have spotted bodies and striped tails, but there are no known animals with striped bodies and spotted tails?

All of these questions can be answered by formulating a reaction-diffusion system describing how two different chemical products react and are propagated on the skin: one chemical (the activator) stimulating the production of the coloring agent *melanin* and the other chemical inhibiting this production. The activator–inhibitor equations show that the different coat patterns depend only on the size and form of the region where they are developed. For example, although they have similar bodies, tigers and leopards have different patterns because pattern formation doesn't take place at the same moment of growth of the embryo.

More precisely, the activator–inhibitor equations show that no pattern is formed if the embryo is very small (in the case of the mouse), that a striped pattern occurs if the embryo is a little bigger (for the tiger), a spotted pattern (for the leopard) if it is bigger yet, and no pattern whatsoever if it is too big (in the case of the elephant).

What's more, for surfaces of comparable areas, the shape of the surface makes a difference. Thus, if one considers a certain surface sufficiently large to permit the formation of spots, and gives it a long, cylindrical form (such as in an animal tail) without changing its total area, then the spots are transformed into stripes.

Because they are difficult to detect experimentally, lying in the epidermis or just

below, the chemical reactants responsible for patterning have not been directly observed, although there is indirect evidence for their existence.
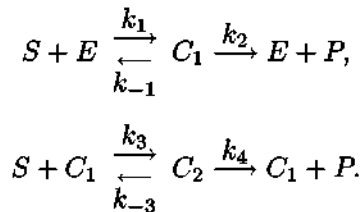
For the reader who is interested in the mathematical details of coat patterning in the animal kingdom see, for example, Jim Murray's text *Mathematical Biology* ([Mur02]) or Leah Edelstein-Keshet's *Mathematical Models in Biology* ([EK88]).

PROBLEMS

Problem 9-1: Cooperative phenomena

In the Michaelis–Menten enzyme reaction, one enzyme molecule combines with one substrate molecule, i.e., the enzyme has one binding site. Some enzymes, such as the oxygen-carrying protein *hemoglobin* (HB) in red blood cells, have more than one binding site for substrate molecules. HB has four binding sites for oxygen (O_2) molecules.

As an example, consider a cooperative phenomenon where the enzyme has two binding sites, the relevant chemical reactions being as follows:

$$S + E \underset{k_{-1}}{\overset{k_1}{\rightleftharpoons}} C_1 \overset{k_2}{\longrightarrow} E + P,$$

$$S + C_1 \underset{k_{-3}}{\overset{k_3}{\rightleftharpoons}} C_2 \overset{k_4}{\longrightarrow} C_1 + P.$$

In the first reaction, an enzyme molecule E binds a substrate molecule S to form a single bound substrate–enzyme complex C_1. Not only does the complex C_1 break down to form a product P and the enzyme E again, it can also combine (second reaction) with another substrate molecule to form a dual bound substrate–enzyme complex C_2. The C_2 complex breaks down to form a product P and the complex C_1.

    a. Using the law of mass action, write down the rate equations for the concentrations of S, C_1, E, C_2, and P. The initial conditions for the concentrations are $S(0) = S_0$, $E(0) = E_0$, $C_1 = C_2 = P = 0$.

    b. By deriving a conservation equation for the enzyme concentration, eliminate E from the equations for S, C_1, and C_2.

    c. Paralleling the procedure used in the text discussion of Michaelis–Menten kinetics, reduce the rate equation for S, C_1, and C_2 to nondimensional form.

Problem 9-2: Glycolysis

Glycolysis is the chemical process in which living cells obtain energy by breaking down sugar. For yeast cells, this process has an oscillatory time dependence, the period being a few minutes. Letting x and y be the normalized concentrations of *adenosine diphosphate* (ADP) and *fructose-6-phosphate* (F6P), respectively, Sel'kov ([Sel68]) proposed a simple model to describe the oscillations, the governing equations being

$$\dot{x} = -x + \alpha y + x^2 y,$$

$$\dot{y} = \beta - \alpha y - x^2 y,$$

where α and β are positive constants.

a. Show that the ODE system has a fixed point at $\bar{x} = \beta$, $\bar{y} = \beta/(\alpha + \beta^2)$ and that this fixed point is an unstable focal or nodal point if $(\beta^2 + \alpha)^2 < (\beta^2 - \alpha)$.

b. Taking $\alpha = 0.05$ and $\beta = 0.5$, check that the inequality in part **a** is satisfied. To establish the existence of a stable limit cycle onto which the trajectories wind, the Poincaré–Bendixson theorem of Chapter 2 can be applied to the domain schematically indicated in Figure 9.8.
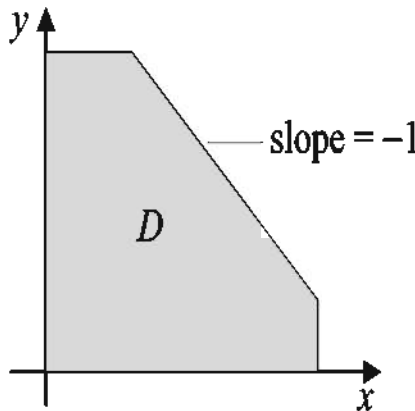
Figure 9.8: Domain for applying the Poincaré–Bendixson theorem.

Determine the mathematical form of the domain boundaries such that all trajectories cross the boundaries from the outside to the inside. Since the fixed point inside D is an unstable focal or nodal point, according to the Poincaré–Bendixson theorem a limit cycle must then exist within D.

c. Confirm the analysis of part **b** by creating a phase-plane portrait in the x–y plane showing several trajectories starting inside and outside D winding onto the limit cycle.

Problem 9-3: Fisher solitary wave
Setting $X = x/\sqrt{D}$ and taking the wave velocity $v = 5/\sqrt{6}$, show that Fisher's equation has the antikink analytic solitary wave solution
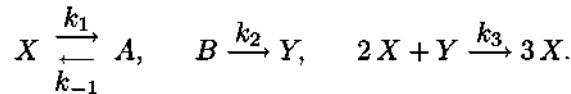
$$c = U(z = X + v\,t) = \frac{1}{\left(1 + A\,e^{-z/\sqrt{6}}\right)^2},$$

where A is an arbitrary constant. Discuss the balancing act between competing effects which allows this antikink to exist. Plot $U(z)$ over the range $z = -20$ to $+20$ for $A = 1$.

Problem 9-4: Schnakenberg reaction

Schnakenberg ([Sch79]) has considered the following set of chemical reactions:

$$X \underset{k_{-1}}{\overset{k_1}{\rightleftharpoons}} A, \qquad B \xrightarrow{k_2} Y, \qquad 2X + Y \xrightarrow{k_3} 3X.$$

    a. Using the law of mass action, determine the rate equations for X and Y.

    b. Introducing dimensionless variables $x \propto X$, $y \propto Y$, $a \propto A$, and $b \propto B$, write the rate equations in dimensionless form.

    c. Determine the location and nature of the fixed points of these equations.

    d. Show that a Hopf bifurcation occurs when $b - a = (a + b)^3$.

    e. Use the Poincaré–Bendixson theorem to show that a stable limit cycle can exist for a certain range of a and b.

    f. Create an appropriate phase-plane portrait which illustrates the existence of a stable limit cycle.

Problem 9-5: Spatial spreading of the spruce budworm

Considering one dimension for simplicity, the spatial spreading of the spruce budworm can be modeled by Equation (9.25) with

$$f(c) = r\, c \left(1 - \frac{c}{K}\right) - b\, \frac{c^2}{(a^2 + c^2)},$$

where c is the budworm concentration and r, K, b, and a are positive parameters.

    Taking $D = r = K = 1$, $a = 0.1$, and $b = 0.2$ and assuming a solution of the form $c(x, t) = U(z = x - v\,t)$, use phase-plane analysis to determine the possible solutions as the velocity v is increased from zero. Are solitary waves possible? Explain.

Problem 9-6: Oregonator limit cycle revisited

In Example 8-5, the parameter f was taken to be $1/2$. Explore and discuss how the limit cycle solution changes as f is varied from this value.

Problem 9-7: Autocatalysis in the real world

Using the Internet or any other source, cite other interesting or important examples of autocatalysis in the "real" world.

Problem 9-8: Chemotaxis

Chemotaxis is the phenomenon in which microorganisms such as bacteria direct their movements according to certain chemicals in their environment. This enables them to find food by moving toward the highest concentration of food molecules or to flee from poisons. For multicellular organisms such as spermatozoa, chemotaxis is responsible for their movement toward the egg in fertilization.

A model system ([Mur02]) for the chemotactically directed movement of bacteria (b) into a food source (nutrient n) is

$$\frac{\partial b}{\partial t} = \frac{\partial}{\partial x}\left(D\frac{\partial b}{\partial x} - \frac{\chi b}{n}\frac{\partial n}{\partial x}\right),$$

$$\frac{\partial n}{\partial t} = -Kb,$$

where the diffusion coefficient D and the parameters χ and K are all positive.

a. Establish the existence of a solitary wave solution as a function of $z = x - ct$, where c is the wave speed, with the asymptotic boundary conditions

$$b \to 0 \quad \text{as} \quad |z| \to \infty,$$

$$n \to 0 \quad \text{as} \quad z \to -\infty,$$

$$n \to 1 \quad \text{as} \quad z \to +\infty.$$

Note that here we are looking for a simultaneous nontopological solitary wave solution for the bacteria and a topological solitary wave solution for the nutrient.

b. Obtain a relationship between $b(z)$ and $n(z)$ for part **a**.

c. In the special case where $\chi = 2D$, show that the solitary wave solution is
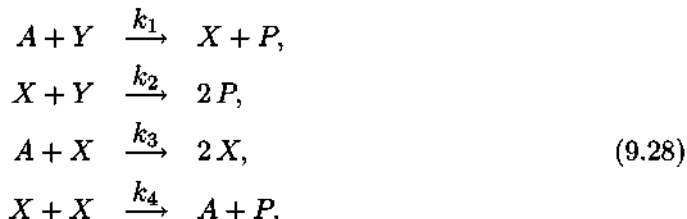
$$n(z) = \frac{1}{1 + Ce^{-cz/D}},$$

$$b(z) = \frac{c^2}{KD}\frac{e^{-cz/D}}{\left(1 + Ce^{-cz/D}\right)^2},$$

where C is an arbitrary positive constant.

d. Taking $C = 1$ in part **c**, sketch the solitary wave solution and explain what is happening biologically.

Problem 9-9: Traveling wave front in the BZ reaction
Jim Murray ([Mur76], [Mur02]) argues that for a traveling wave front involving the BZ reaction, Ce^{4+} plays a negligible role in the vicinity of the wave front so that the BZ reaction chain reduces to

$$\begin{aligned}
A + Y &\xrightarrow{k_1} X + P, \\
X + Y &\xrightarrow{k_2} 2P, \\
A + X &\xrightarrow{k_3} 2X, \\
X + X &\xrightarrow{k_4} A + P,
\end{aligned} \qquad (9.28)$$

where X and Y are $HBrO_2$ and Br^-, respectively.

a. Applying the law of mass action, using lowercase letters for the concentrations, letting ζ be the coordinate in the direction of propagation, and including diffusion of X and Y with diffusion constant D, write down the relevant PDEs for x and y.

b. Cast the PDE system in part **a** into nondimensional form by setting

$$u = \frac{k_1 \, x}{k_3 \, a}, \quad v = \frac{k_2 \, y}{k_3 \, a \, r}, \quad s = \sqrt{\frac{k_3 \, a}{D}} \, \zeta, \quad \tau = k_3 \, a \, t,$$

$$L = \frac{k_1 \, k_4}{k_2 \, k_3}, \quad M = \frac{k_1}{k_3}, \quad b = \frac{k_2}{k_4},$$

where r is a parameter which reflects the fact that the bromide ion concentration far ahead of the wave front can be varied experimentally.

c. Experimentally, $L \approx M = O(10^{-4})$, $b = O(1)$, and r varies from about 5 to 50. Write down the PDE system which results on neglecting terms in part **b** involving L and M.

d. Reduce the PDE system of part **c** to an ODE system by assuming that $u = f(z)$ and $v = g(z)$ with $z = s + c\,\tau$, where c is the wave front speed.

e. Taking $b = 1.25$, $r = 10$, $c = 0.096$, and boundary conditions $f(\infty) = g(-\infty) = 1$, $f(-\infty) = g(\infty) = 0$, numerically solve for $f(z)$ and $g(z)$ and plot these functions in the same figure.

Problem 9-10: Peroxidase-oxidase reaction

The peroxidase-oxidase (PO) chemical reaction is an important example of how oscillating reactions arise in living organisms. A model of the PO reaction, originally formulated by Olsen ([Ols83]), is discussed in detail on the following web site:

www.math.dartmouth.edu/archive/m53f07/public_html/proj/Karas.pdf.

Consulting this site, or any other source, discuss the PO reaction. In particular,

- write down the sequence of chemical reactions, identifying the chemicals involved;

- explain how the model equations are derived using the law of mass action;

- discuss in detail the types of behavior exhibited by the PO system.

Problem 9-11: Gierer–Meinhardt model of pattern formation

An activator–inhibitor model of pattern formation proposed by Alfred Gierer and Hans Meinhardt ([GM72])[2] is governed by the following reaction-diffusion equations:

$$\frac{\partial A}{\partial t} = r \, \frac{A^2}{I} - \mu_A \, A + D_A \, \frac{\partial^2 A}{\partial x^2} + r_A,$$

$$\frac{\partial I}{\partial t} = r \, A^2 - \mu_I \, I + D_I \, \frac{\partial^2 I}{\partial x^2} + r_I.$$

---

[2]Reprint available at: **http://www.eb.tuebingen.mpg.de/departments/former-departments/h-meinhardt/kyb.pdf**.

Here A and I are the activator and inhibitor concentrations, respectively, r is a production rate, μ_A and μ_I are decay rates, and D_A and D_I are diffusion coefficients. The A-independent term r_A is included so that activator autocatalysis can occur at very low concentrations of A. The term r_I is included so that a stable nonpatterned steady state is possible.

Making use of the web sites,

- http://www.scholarpedia.org/article/Gierer-Meinhardt_model
  —a review article with animations

- http://www.eb.tuebingen.mpg.de/departments/former-departments/
  h-meinhardt/Old%20Paper%20PDF/Generation%20of%20biological
  %20patterns.pdf
  —reprint of Gierer paper ([Gie81]) with corrections

and any other sources, discuss in detail various types of patterns that the Gierer–Meinhardt model can display.

Problem 9-12: Quasi-species model of RNA selection and evolution
Manfred Eigen[3] and co-workers have conjectured ([Eig71], [EGSWO81], [EMS88]) that RNA (ribonucleic acid) chemistry provided an environment for Darwinian selection and evolution in the primordial "soup" where life is thought to have begun.[4] In their proposed scenario, the first carriers of genetic information were primitive strands of RNA which could self-replicate, although imperfectly because of mutations. Slight errors in the nucleotide sequence making up a given RNA strand occurred, thus generating a "family" of closely related RNA species which competed for the available food and energy.

As a mathematical starting point to understanding selection and evolution of the RNA family, Eigen suggested a variety of simple nonlinear competition models, the best known being the *quasi-species model*. Making use of the cited references, present a detailed discussion of this model, clearly indicating what is meant by the term "quasi-species" and under what conditions quasi-species can occur. If you do not have library access to the cited journal papers, a reprint of the third article is available online at:

http://physwww.mcmaster.ca/ higgsp/3D03/Quasispecies.pdf

Problem 9-13: The Lennard-Jones potential
The *Lennard-Jones potential*, first proposed by John Lennard-Jones ([LJ24]) in 1924, is an anharmonic potential used in molecular dynamics to model the interaction between two identical uncharged atoms or molecules. It has the form

$$U = 4\epsilon \left[\left(\frac{\sigma}{r} \right)^{12} - \left(\frac{\sigma}{r} \right)^{6} \right],$$

---

[3] Awarded the 1967 Nobel prize in chemistry.
[4] See also *The RNA World* by Sidney Altman, 1989 Nobel laureate in chemistry, available online at: http://nobelprize.org/nobel_prizes/chemistry/articles/altman/index.html.

where r is the radial distance between the interacting particles and σ and ϵ are parameters that depend on the particle. The following table[5] gives the parameter values for some representative particles:

Particle	ϵ $(10^{-21}\,\text{J})$	σ $(10^{-10}\,\text{m})$
He	0.141	2.56
Ne	0.492	2.75
Ar	1.70	3.40
Kr	2.30	3.68
Xe	3.10	4.07
N_2	1.25	3.70
I_2	7.60	4.98
Hg	11.74	2.90
CCl_4	4.51	5.88

Table 9.2: Lennard-Jones parameters.

a. Consulting an appropriate chemistry or physics text or by going to the Internet, discuss the physical origin of the two terms that make up the Lennard–Jones potential.

b. Determine the radial distance at which the minimum in the potential occurs. What is the potential energy at this point?

c. Which particle in the table has the deepest potential well and what is the radial distance at the minimum? Plot the potential energy for this particle.

---

[5]www.diracdelta.co.uk/science/source/l/e/lennard-jones%20potential/source.html

Chapter 10

World of Disease

Medicine is learned by the bedside and not in the classroom. Let not your conceptions of disease come from words heard in the lecture room or read from the book. See, and then reason and compare and control. But see first.
William Osler, Canadian physician (1849–1919)

In this chapter, we shall look at nonlinear models for the spread and growth of diseases. We shall begin by looking at the spread of infectious diseases. An infectious disease such as influenza, for example, is of concern when an *epidemic*[1] of a new flu strain breaks out. The fear is that the new strain might mimic the horrific Spanish influenza outbreak of 1918. It should be noted that the naming of the 1918 flu outbreak as the *Spanish flu* is a misnomer, the flu having also created large numbers of deaths in other countries such as the United States, Great Britain, France, and Germany. However, these countries had imposed media censorship on these deaths because they were at war and did not want to reveal the information to their enemies. The deaths from flu of millions of Spaniards was first reported in the uncensored Spanish newspapers, and the rest of the world media picked up on it and called it the Spanish flu.

How bad was the Spanish flu? The Spanish flu was the greatest, most lethal, pandemic the world has ever known. According to James Armstrong[2] of the U.S. Navy Historical Center, between 22 and 40 million people perished worldwide in a ten-month period. In the United States, the death toll was over 675 thousand, with 22 million becoming ill. During the height of the flu pandemic, American children skipping rope were heard to chant the rhyme:

> *I had a little bird*
> *And its name was Enza*
> *I opened the window*
> *And in-flew-enza.*

Leading doctors of the time thought the infectious agent was a *bacterium*, but in fact it was something not yet discovered — a *virus*. The 1918 flu was not the flu that people of

---

[1] An epidemic is an unusually large, short-term (less than a year) outbreak of a disease.

[2] His interesting historical account is available on the Internet, as are many other accounts.

the time were familiar with. "Normal" flus were known to make you feel miserable for a few days with fever, muscle aches, and congestion. Although hundreds of thousands or even millions might become sick, deaths only tended to occur among the old, the young, and those in poor health.

In contrast, the Spanish flu struck victims in good health, with the highest death toll in the 15- to 40-year age group. The victims would be fine one moment and feverous and delirious the next, the skin turning bluish-black from lack of oxygen. Their lungs would fill with fluid and blood gush from their noses, death following quickly.

The purpose of epidemiological modeling is to understand how infectious diseases such as influenza spread among the population and devise methods for controlling or even preventing this spread. What control procedures should be used for a given infectious disease, inoculation, isolation, culling (e.g., in the case of rabid foxes), or some other method? Good mathematical models can be useful in implementing health policy and predicting what will happen. For example, based on nonlinear modeling, Herbert Hethcote ([Het83]) predicted that rubella will eventually disappear in the United States because the current vaccinations using the combined measles–mumps–rubella vaccine are significantly above the threshold required for "herd" immunity for rubella.

The models that will be presented here are the simplest prototypes of much more refined nonlinear models which have been applied to specific infectious diseases. A nice review paper on the more refined models is "The Mathematics of Infectious Diseases" by Hethcote ([Het00]). Hopefully, the prototypical models presented in this chapter will provide the reader with an interesting and useful glimpse into an exciting field of modern nonlinear research.

10.1 Classifying the Spread of Infectious Diseases

How do infectious diseases such as the Spanish flu spread? To answer this question, it is useful to classify infectious diseases by infectious agent and method of transmission. The four basic infectious agents are viruses, bacteria, protozoa, and helminths. *Protozoa* are microscopic one-celled animals, while *helminths* are worms (e.g., tapeworms and roundworms) or wormlike parasites.

There are also four basic methods of transmission:

- Human to human;

- Human to environment to human;

- Reservoir to vector to human;

- Reservoir to human.

The term *vector* refers to insects and *reservoir* to other nonhuman infectives (dogs and foxes for rabies, rats for the plague, etc.).

The classification of infectious diseases by infectious agent and transmission method has been given by Hethcote ([Het89]) and is reproduced in Table 10.1.

Infectious Agent	Human to Human	Human to Environment to Human	Reservoir to Vector to Human	Reservoir to Human
Virus	Measles Chickenpox Mumps Rubella Smallpox Influenza Poliomyelitis Herpes HIV (AIDS)		Yellow fever Dengue fever Encephalitis Tick fever Sandfly fever	Rabies
Bacteria	Gonorrhea Tuberculosis Pneumonia Meningitis Strep throat	Typhoid fever Cholera	Plague	Brucellosis Tularemia Anthrax
Protozoa	Syphilis	Amebiasis	Malaria Trypanosomiasis	
Helminths			Schistosomiasis Filariasis Onchocerciasis	Trichinosis

Table 10.1: Classification of infectious disease transmission ([Het89]).

10.2 Basic Models of Disease Transmission

We will now look at the three basic epidemiological models which are relevant to disease transmission. These models are the building blocks of more sophisticated models. Let us first state some assumptions and establish some useful concepts and notation relevant to the three models presented here.

In general, the total population can be divided into three classes or "compartments," the *susceptibles* (number S) who can get the disease but are not yet infective, the *infectives* (number I) who can transmit the disease to others, and the *removed* (number R) class who are removed from the susceptible–infective interaction because they recover with immunity or are isolated or die. The numbers S, I, and R are assumed to be sufficiently large that they can be treated as continuous variables. Otherwise, difference

equation models should be used. For the three basic epidemiological models, the total population number, $N = S + I + R$, is taken to be constant.

For some diseases, there is no removed class, no immunity being given on recovery, no deaths (normally) occurring, and no isolation being imposed. Although recovered, the victims of such diseases are susceptible to further infections. Models describing this situation are called *SIS* (susceptible to infectious to susceptible) *models*. If all three population classes are present, the models are called *SIR models*.

For epidemics (diseases which go through a population in less than a year), births and deaths (referred to as *vital dynamics*) need not be considered. For an *endemic* disease (one lasting more than 10 or 20 years), vital dynamics must be included. In this case, it is assumed ([Het89]) that births and natural deaths occur at equal rates and that all newborns are susceptible. The death rate in a population class is assumed to be proportional to the class size, the positive proportionality constant being μ.

It is assumed that the population is homogeneously mixing and that the rate of interaction between susceptibles and infectives is given by the mass action law, i.e., the interaction rate is $\beta S I$, where β is a positive constant.
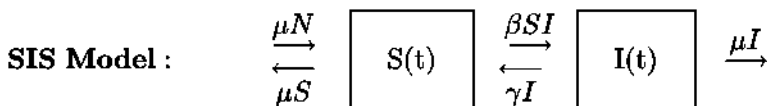
Finally, infectives are removed because of recovery at a rate proportional to the number of infectives, the positive proportionality constant being γ.

Let's first look at the simplest of the three basic models, the SIS model.

10.2.1   The SIS Model

The SIS model is relevant to a disease for which there is no removed class. SIS models are appropriate for some bacterial diseases such as gonorrhea, meningitis, and streptococcal sore throat, and for protozoan diseases such as malaria and sleeping sickness (trypanosomiasis).

Schematically, the SIS model has two compartments (the boxes in the following figure), the susceptible population number at time t being $S(t)$, the infective population number being $I(t)$. Since there are only two compartments and the total population number N is fixed, one has $S(t) + I(t) = N$. Including vital dynamics, the inputs and outputs are depicted by the arrows in the figure, the rate constants being as shown.

$$\textbf{SIS Model}: \quad \overset{\mu N}{\underset{\mu S}{\rightleftarrows}} \ \boxed{\ S(t)\ } \ \overset{\beta S I}{\underset{\gamma I}{\rightleftarrows}} \ \boxed{\ I(t)\ } \ \overset{\mu I}{\rightarrow}$$

The susceptible population grows because of births in the total population (rate μN) and infectives who recover, becoming susceptible again (rate γI). It decreases because of deaths of susceptibles (rate μS), and susceptibles becoming infected (contact rate $\beta S I$).

For the infectives, the population grows because susceptibles become infected, but decreases because infectives die (rate μI) and because recovered infectives become sus-

ceptible. Putting it all together the nonlinear rate equations for the SIS model are

$$
\begin{aligned}
\frac{dS}{dt} &= \mu N - \mu S + \gamma I - \beta S I, \\
\frac{dI}{dt} &= -\mu I - \gamma I + \beta S I,
\end{aligned}
\tag{10.1}
$$

or, if population fractions $s = S/N$ and $i = I/N$ are introduced and we set $\lambda = \beta N$,

$$
\begin{aligned}
\frac{ds}{dt} &= \mu - \mu s + \gamma i - \lambda s i, \\
\frac{di}{dt} &= -(\mu + \gamma) i + \lambda s i,
\end{aligned}
\tag{10.2}
$$

with $i + s = 1$. An analytic solution to this SIS system is easily derived by using the conservation relation to eliminate s from the infective equation and solving it.

However, let's first introduce some standard terminology. Setting $\tau = (\mu + \gamma) t \equiv t/T$ and $\sigma = \lambda T$, the infective equation can be cast into the dimensionless form

$$
\frac{di}{d\tau} = i(\sigma s - 1).
\tag{10.3}
$$

The time $T = 1/(\mu + \gamma)$ is the average period of infectivity before infectives are removed, either by death or by becoming susceptible once again. The infectious *contact number* ([Het89]) $\sigma = \lambda T$ is the average number of disease-transmitting contacts during this period. The product σs is the *replacement number*, i.e., the number of susceptibles infected by infectibles in the time interval T.

Finally, the *basic reproduction number* (or *basic reproduction rate*) $R_0 = \sigma s_0$ can be introduced, where $s_0 = s(t = 0)$. It is the average number of secondary infections that occur when one infective is introduced into a completely susceptible host population.

Now let's solve the SIS model equations.

Example 10-1: SIS Solution

Solve the SIS equations, given $i(0) = i_0$ and $s(0) = s_0$. Discuss what happen as $t \to +\infty$.

Solution: Substituting $s = 1 - i$ into Equation (10.3), the infective equation becomes

$$
\frac{di}{d\tau} = (\sigma - 1) i - \sigma i^2.
\tag{10.4}
$$

This ODE is a *Bernoulli* equation ([Zwi89]). Setting $i = 1/y$ reduces it to a linear ODE,

$$
\frac{dy}{d\tau} = -(\sigma - 1) y + \sigma.
\tag{10.5}
$$

For $\sigma \neq 1$, (10.5) is solved by multiplying it by the integrating factor $e^{(\sigma-1)\tau}$ and integrating, subject to $y(0) = 1/i(0) = 1/i_0$. Inverting y, we obtain

$$
i(t) = \frac{(\sigma - 1) i_0}{\sigma i_0 + [\sigma(1 - i_0) - 1] e^{-(\sigma-1)(\gamma+\mu)t}}.
\tag{10.6}
$$

For $\sigma = 1$, on the other hand,

$$i(t) = \frac{i_0}{1 + \lambda i_0 t}. \tag{10.7}$$

The fraction of susceptibles at time t is given by $s(t) = 1 - i(t)$.

As $t \to +\infty$,

$$i(t) \to \left\{ \begin{array}{cc} 1 - \dfrac{1}{\sigma}, & \sigma > 1 \\[2mm] 0, & \sigma \le 1 \end{array} \right\}.$$
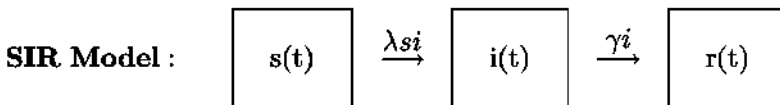
Thus, for a disease without immunity and any initial infective fraction greater than zero, the infective fraction approaches a constant value if the contact number exceeds 1. Otherwise, the disease dies out. There is a critical threshold for the disease to persist.

It should be noted that if vital dynamics (births and deaths) are omitted from the SIS model, the conclusion is the same except then $\sigma = \lambda/\gamma$ since $\mu = 0$.

<div align="center">***</div>

10.2.2   The SIR Model without Vital Dynamics

For epidemics which last a relatively short time (less than a year), vital dynamics can be neglected. The SIR model without dynamics was originally developed by Kermack and McKendrick ([KM27]) to describe the data for the deadly *Bombay plague* of 1906, but since then has been successfully used to model the dynamics of other diseases such as measles, mumps, rubella, and chickenpox.

In terms of population fractions, with $r(t) = R(t)/N$ being the fraction removed by death, permanent immunity, or isolation, the *compartmental diagram* for the SIR model[3] without vital dyamics is as follows:

$$\textbf{SIR Model}: \quad \boxed{\;s(t)\;} \xrightarrow{\;\lambda si\;} \boxed{\;i(t)\;} \xrightarrow{\;\gamma i\;} \boxed{\;r(t)\;}$$

The rate equations then are

$$\begin{aligned} \frac{ds}{dt} &= -\lambda s i, \\ \frac{di}{dt} &= \lambda s i - \gamma i, \\ \frac{dr}{dt} &= \gamma i, \end{aligned} \tag{10.8}$$

with $s(t) + i(t) + r(t) = 1$. Since this conservation law enables us to determine $r(t)$, knowing $s(t)$ and $i(t)$, we have to only consider the first two equations in the above ODE

---

[3]If the immunity is only temporary, the removeds can become susceptibles once again. This is the SIRS model. If the susceptibles are exposed to the disease but not immediately infectious, an *exposed* (E) compartment is also included in the compartmental diagram, leading to the SEIRS model.

system. Paralleling our treatment of the SIS model, a new time variable $\tau = \gamma t$ and contact number $\sigma = \lambda/\gamma$ are introduced, so that the first two ODEs in (10.8) become

$$\frac{ds}{d\tau} = -\sigma\, s\, i, \qquad \frac{di}{d\tau} = (\sigma\, s - 1)\, i. \tag{10.9}$$

The system (10.9) cannot be solved analytically, but a phase-plane portrait which reveals the behavior of the solution can be made for a specified value of σ.

Example 10-2: Phase-Plane Portrait

Taking $\sigma = 2$, create a phase-plane portrait for the SIR model without vital dynamics, showing the tangent field and several solution trajectories. Discuss the results.

Solution: The tangent field arrows for $\sigma = 2$ are shown in Figure 10.1.
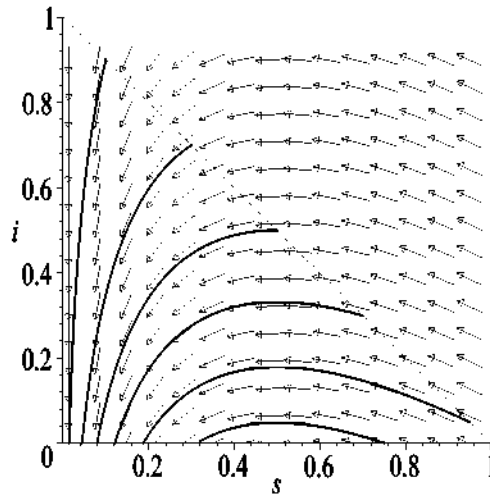
Figure 10.1: Phase-plane portrait for the SIR model without vital dynamics.

However, since the removed population number cannot be negative, one is restricted on physical grounds to the triangular range,

$$0 \le s(t) \le 1, \quad 0 \le i(t) \le 1, \quad s(t) + i(t) \le 1.$$

The bounding line $s + i = 1$ is plotted in the figure. As $\tau \to +\infty$, the population of infectives goes to zero no matter what the starting point inside the triangular region. Representative trajectories are also plotted in the figure for the six initial conditions: **(i)** $(s_0 = 0.1,\ i_0 = 0.9)$; **(ii)** $(0.3, 0.7)$; **(iii)** $(0.5, 0.5)$; **(iv)** $(0.7, 0.3)$; **(v)** $(0.75, 0.001)$; **(vi)** $(0.95, 0.05)$.

If the basic reproduction rate $R_0 = \sigma\, s_0 \le 1$, the infective fraction decreases directly to $i = 0$ as $t \to +\infty$. For $R_0 > 1$, the infective fraction first increases with time and then decreases to zero. This is the characteristic behavior of an epidemic. A representative *epidemic curve* is shown in Figure 10.2, the infective population fraction being plotted as a function of time for the initial condition **(vi)**.
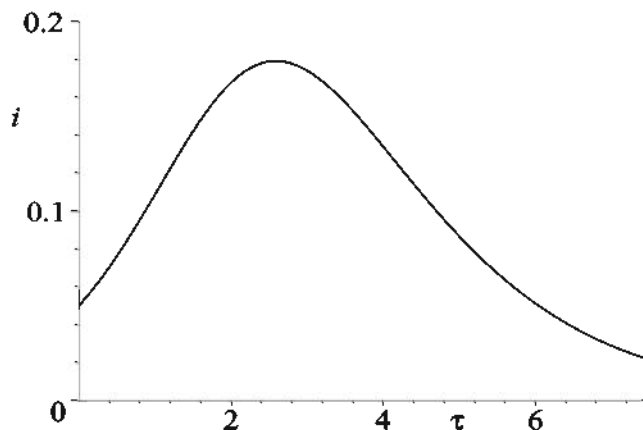
Figure 10.2: Example of an epidemic curve.

Data qualitatively consistent with the epidemic curve may be seen in Figure 10.3. The number of non-A, non-B hepatitis cases in a refugee camp in Tug Wajale, Somalia, is plotted for each week in the interval March 15 to October 25, 1986. The data is from
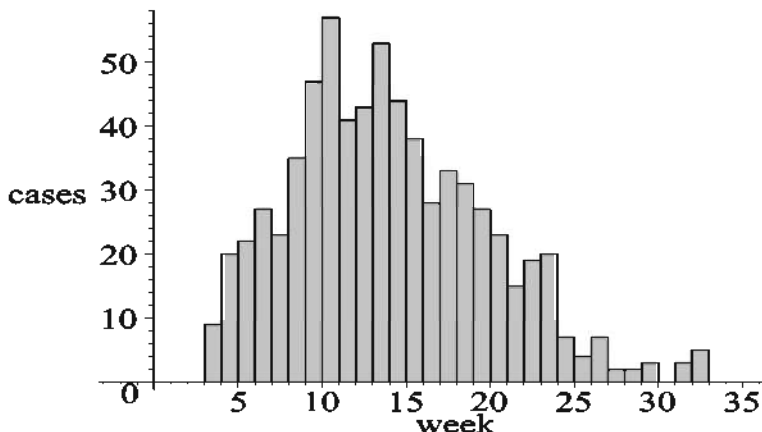
Figure 10.3: Hepatitis cases in a Somalia refugee camp.

a U.S. Centers for Disease Control Morbidity and Mortality Weekly Report ([fDC87]).

***

If an epidemic take place in a homogeneous population and no vaccination is applied during the epidemic, the contact number σ for that epidemic can be estimated ([HA87]) by testing the immune responses in the blood and measuring the susceptible fraction s before $(s(t = 0) = s_0)$ and after $(s(t = +\infty) = s_\infty)$ the epidemic. Then,

$$\sigma = \frac{\ln(s_0/s_\infty)}{s_0 - s_\infty}. \tag{10.10}$$

Example 10-3: Proof of Equation (10.10) and a Rubella Example

   a. Prove that the contact number is given by the relation (10.10). Assume that when the epidemic enters the population that $i(t = 0) = i_0$ is negligibly small.

   b. Tests (see Evans [Eva82]) on freshmen at Yale University for susceptibility to rubella at the beginning and end of their freshman year yielded $s_0 = 0.025$ and $s_\infty = 0.0965$. Estimate the contact number σ.

Solution: a. From Equations (10.9), we have

$$\frac{di}{ds} = \frac{\sigma s - 1}{-\sigma s} = -1 + \frac{1}{\sigma s}.$$

Separating variables and integrating from $t = 0$ to $t = \infty$, we obtain

$$i_\infty - i_0 = -s_\infty + s_0 + \frac{1}{\sigma} \ln(s_\infty/s_0).$$

But $i_\infty = 0$ and $i_0 \approx 0$. Solving the above relation for σ yields the desired result,

$$\sigma = \frac{\ln(s_0/s_\infty)}{s_0 - s_\infty}.$$

b. For the Yale University rubella data, the contact number is

$$\sigma = \frac{\ln(s_0/s_\infty)}{s_0 - s_\infty} = \frac{\ln(0.25/0.0965)}{(0.25 - 0.0965)} = 6.2.$$

<center>***</center>

Seasonal oscillations in the incidence and prevalence of some childhood diseases are known to occur. For example, the number of measles and rubella cases increases in the fall and winter due to children going back to school. For such diseases, one lets the contact parameter λ have a seasonal time dependence. See, e.g., London and Yorke ([LY73], [YL73]).

10.2.3 The SIR Model with Vital Dynamics

For an endemic disease, a SIR model with vital dyamics must be considered. That is to say, births must be included as a source of new susceptibles and natural deaths included in each class. The relevant rate equations for the susceptible, infective, and removed fractions are

$$\begin{aligned}
\frac{ds}{dt} &= -\lambda s\, i + \mu - \mu s, \\
\frac{di}{dt} &= \lambda s\, i - \gamma i - \mu i, \\
\frac{dr}{dt} &= \gamma i - \mu r.
\end{aligned} \tag{10.11}$$

Again, since one has the conservation law $s(t) + i(t) + r(t) = 1$, we need only consider the first pair of equations which, on setting

$$\tau = (\mu + \gamma)\, t, \quad \sigma = \frac{\lambda}{(\mu + \gamma)}, \quad \delta = \frac{\mu}{(\mu + \gamma)}, \tag{10.12}$$

may be rewritten as

$$\begin{aligned}
\frac{ds}{d\tau} &= -\sigma\, s\, i + \delta\, (1 - s), \\
\frac{di}{d\tau} &= (\sigma\, s - 1)\, i.
\end{aligned} \tag{10.13}$$

The behavior of the SIR model with vital dynamics can be ascertained by locating and determining the nature of the fixed points.

Example 10-4: Phase-Plane Analysis of SIR Model with Vital Dynamics

Determine the fixed points of the ODE system (10.13) and use Table 2.1 to classify their type. Use this information to predict the behavior of the solutions to the SIR model with vital dynamics as the contact number σ is varied.

Solution: Setting $ds/d\tau = 0$ and $di/d\tau = 0$, the possible fixed points (*FP*) of the ODE system (10.13) are:

- FP_1: $\bar{s} = 1$, $\bar{i} = 0$;

- FP_2: $\bar{s} = \dfrac{1}{\sigma}$, $\bar{i} = \dfrac{\delta\, (\sigma - 1)}{\sigma}$.

Using the fixed point notation of Chapter 2, for FP_1 we obtain

$$p = \delta + 1 - \sigma, \quad q = \delta\, (1 - \sigma), \quad p^2 - 4q = (\delta + \sigma - 1)^2.$$

For $\sigma < 1$, we have $p > 0$, $q > 0$, and $p^2 - 4q > 0$. Consulting Table 2.1, FP_1 is a stable nodal point for $\sigma < 1$. For $\sigma > 1$, $q < 0$ so then it is an unstable saddle.

Since the infectious fraction cannot be negative, FP_2 only applies for $\sigma > 1$. In this case, we obtain

$$p = \delta\, \sigma, \quad q = \delta\, (\sigma - 1), \quad p^2 - 4q = (\delta\, \sigma)^2 - 4\,\delta\, (\sigma - 1).$$

Since $p > 0$ and $q > 0$, FP_2 is either a stable focal or nodal point for $\sigma > 1$, depending on whether $p^2 - 4q$ is negative or positive.

The contact number σ has a bifurcation point at $\sigma = 1$. For $\sigma \leq 1$, the infective fraction asymptotically goes to zero (approaches FP_1) and the disease dies out. When the contact number is larger than 1, a small initial infective fraction will first grow to a maximum and then begin to decrease, just as with the SIR model without vital dynamics. However, the infective fraction does not go to zero as $t \to +\infty$. In the case where FP_2 is a focal point, there will be successive smaller bumps (smaller epidemics) in the infective fraction as the solution spirals into the fixed point.
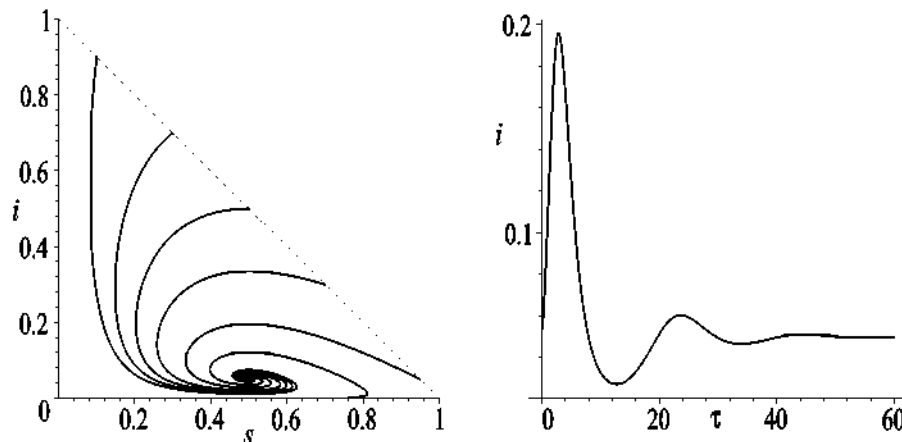
Figure 10.4: Left: Phase-plane trajectories. Right: Infective fraction vs. time.

This is illustrated in Figure 10.4, where we have taken $\sigma = 2$, $\delta = 0.1$, and the same six initial conditions as in Example 9-2 for the SIR model without vital dyamics.

On the left of the figure, the trajectories spiral into the focal point at $\bar{s} = 1/\sigma = 0.5$, $\bar{i} = \delta(\sigma - 1)/\sigma = 0.05$. The picture on the right illustrates the smaller secondary epidemic bumps for the initial condition $i(0) = 0.05$, $s(0) = 0.95$.

Since $s(t) \to s_\infty = 1/\sigma$ as $t \to +\infty$, the contact number σ can be estimated by measuring s_∞, i.e., testing immune responses in blood samples after the disease has reached an endemic equilibrium.

<center>***</center>

10.2.4 Herd Immunity and Vaccination

If enough people in a population are immune to the sudden introduction of a disease, the population is said to have *herd immunity*. Herd immunity may be achieved by vaccinating susceptibles in the population. To have herd immunity, the susceptible fraction s must be such that the replacement number $\sigma s < 1$, i.e., less than one person becomes infected by the average infective during the infectious period. If the fraction of the population which is immune due to vaccination is r, then since $s = 1 - r$ when the infective fraction is zero, herd immunity requires that

$$\sigma(1 - r) < 1,$$

or

$$r > r_{min} = 1 - \frac{1}{\sigma}. \tag{10.14}$$

Once the contact number is known, the value of r_{min} for herd immunity can be easily determined. For example, if $\sigma = 10$, then $r_{min} = 0.90$, i.e., at least 90% must be immune to have herd immunity.

Using data from a number of different countries and time periods, Anderson ([And82]) has estimated the contact number σ and thus r_{min} for herd immunity for a large number of childhood[4] diseases. The estimated values of σ and r_{min} are given in Table 10.2.

Disease	σ	r_{min}
Measles	$12 - 17$	$0.92 - 0.94$
Whooping cough	17	0.94
Chickenpox	11	0.91
Diphtheria	7.4	0.86
Scarlet fever	8.5	0.88
Mumps	8.1	0.88
Rubella	7.7	0.87
Poliomyelitis	$4.9 - 7.3$	$0.80 - 0.86$
Smallpox	5.2	0.81

Table 10.2: Estimated r_{min} for some diseases.

10.2.5   Geographic Spread of an Epidemic

The *Black Death*,[5] one of the deadliest pandemics in human history, spread from central Asia to Europe during the 1340s. In Europe, the disease first broke out in Venice, Italy, in 1347, killing three-fourths of the population. The epidemic wavefront then spread northwards to France, Germany, England, and Scandinavia at an estimated (see Langer ([Lan64])) speed of 320 to 640 km (200 to 400 miles) per year. It has been widely thought[6] to have been caused by the bacterium *Yersinia pestis* (bubonic plague) which was spread by fleas with the help of rats. It is estimated that the Black Death killed somehere between 30% and 60% of Europe's population at the time.

The geographic spread of an epidemic can be modeled (see Jim Murray's *Mathematical Biology* ([Mur02])) by incorporating the nonlinear interaction between susceptibles and infectives into one or more diffusion equations. For example, restricting ourselves to one spatial dimension, the spread of rabies in a fox population has been modeled by the following set of equations:

$$\frac{\partial S}{\partial t} = -r \, I \, S,$$
$$\frac{\partial I}{\partial t} = r \, I \, S - a \, I + D \, \frac{\partial^2 I}{\partial x^2}. \tag{10.15}$$

---

[4]For childhood diseases, the susceptible fraction decreases with age. Anderson made use of an age-structured model due to Dietz ([Die75]) to estimate σ. For this model $\sigma = 1 + L/A$ where L is the average lifetime and A is the average age at which the disease attacks.

[5]Its name derives from the fact that in the late stages of the disease, the afflicted individual's skin would blacken due to internal hemorrhaging.

[6]Some researchers have suggested other diseases.

Here S and I are the population densities of susceptibles and infectives (rabid foxes), respectively. In this model there are no recovereds as all rabid foxes die and it is assumed that only the infectives disperse. The parameter r is the rabies transmission coefficient, a the per capita death rate of rabid foxes, and D the diffusion coefficient.

If S_0 is the initial homogeneous susceptible population density, the above system can be put into a dimensionless form by setting

$$s = \frac{S}{S_0}, \quad i = \frac{I}{S_0}, \quad \tau = r\,S_0\,t, \quad y = \sqrt{\frac{r\,S_0}{D}}\,x, \quad \lambda = \frac{a}{r\,S_0}.$$

Then, Equations (10.15) become

$$\frac{\partial s}{\partial \tau} = -i\,s,$$

$$\frac{\partial i}{\partial \tau} = i\,s - \lambda\,i + \frac{\partial^2 i}{\partial y^2}. \tag{10.16}$$

Treating the epidemic wavefront as a kink solitary wave, we let $s(y, \tau) = s(z = y - c\,\tau)$ and $i(y, \tau) = i(z)$ where c is the solitary wave speed. This reduces Equations (10.16) to the nonlinear ODE system

$$c\,s' - i\,s = 0,$$

$$i'' + c\,i' + i\,(s - \lambda) = 0, \tag{10.17}$$

where the primes indicate derivatives with respect to z. The asymptotic boundary conditions are taken to be

$$s(+\infty) = 1, \ s'(-\infty) = 0, \ \text{and} \ i(-\infty) = i(+\infty) = 0.$$

Note that it is the derivative of s, not s itself, which vanishes as $z \to -\infty$, since we expect a residual number of susceptibles to survive the epidemic.

We can gain insight into the solution of this set of equations by linearizing them about $i = 0$ and $s = 1$. Setting $i = 0 + u$ and $s = 1 - v$ and keeping only linear terms in u and v, the second ODE in (10.17) becomes

$$u'' + c\,u' + u\,(1 - \lambda) = 0. \tag{10.18}$$

Assuming a solution of the form $u \sim e^{p\,z}$, we obtain the two roots

$$p = -\frac{c}{2} \pm \frac{1}{2}\sqrt{c^2 - 4\,(1 - \lambda)}. \tag{10.19}$$

To ensure that $u \to 0$ as $z \to +\infty$ and is nonnegative, we must have

$$\lambda < 1 \quad \text{and} \quad c \geq 2\sqrt{1 - \lambda}. \tag{10.20}$$

Thus, there is a minimum wave speed for the spread of the epidemic depending on the value of λ.

Because the model equations are simple, we can find the fraction of susceptibles which survive after the epidemic has passed, that is to say, we can determine $\sigma = s(-\infty)$. From the first ODE in Equations (10.17), we have $i = c\,s'/s$, so the second ODE may be rewritten as

$$i'' + c\,i' + \frac{c\,s'}{s}\,(s - \lambda) = 0.$$

Integrating yields

$$i' + c\,i + c\,s - c\,\lambda\,\ln(s) = \text{constant}.$$

As $z \to +\infty$, we have $i \to 0$, $i' \to 0$, and $s \to 1$. So the constant is equal to c. On the other hand, as $z \to -\infty$, we have $i \to 0$, $i' \to 0$, and $s \to s(-\infty) = \sigma$. This yields the transcendental equation

$$\sigma - \lambda\,\ln(\sigma) = 1, \quad \text{or} \quad \frac{(\sigma - 1)}{\ln(\sigma)} = \lambda, \quad \text{with } 0 < \lambda < 1. \tag{10.21}$$

A plot of σ over this range of λ is shown in Figure 10.5. For $\lambda = 0.4$, for example, one
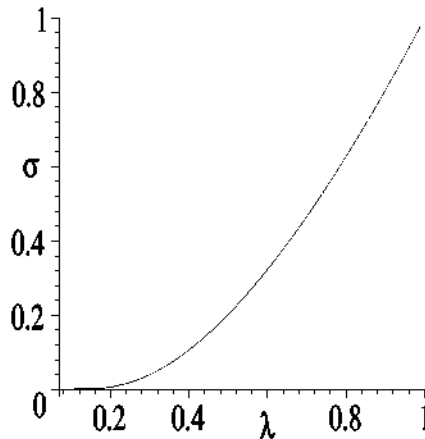
Figure 10.5: σ versus λ for the fox rabies epidemic.

has $\sigma = 0.1$, while for $\lambda = 0.7$, $\sigma = 0.5$. The smaller the value of λ is, the smaller the fraction of susceptibles which survive, i.e., the worse the epidemic. If $\lambda > 1$, there is no epidemic wave, since the death rate is higher than the influx of new infectives.

Example 10-5: Rabies Wavefront Solutions

Using *Maple* or *Mathematica*, numerically solve the nonlinear ODE system (10.17) for $s(z)$ and $i(z)$ over the range $z = -80$ to $z = +20$. Take $\lambda = 0.5$ and $c = \sqrt{2}$ and boundary conditions

$$s(-80) = \sigma, \quad i(-80) = 0.001, \quad i'(-80) = 0.0001.$$

Solution: Taking $\lambda = 0.5$, the transcendental equation (10.21) is numerically solved for σ, yielding $\sigma = 0.2031878700$ (to 10 digits). Writing the ODE system as three first-order equations, the system is solved subject to the given boundary conditions using the RKF45 algorithm. The resulting wavefront profiles for the susceptibles and infectives are plotted in Figure 10.6. The susceptible wavefront is a kink solitary wave moving to
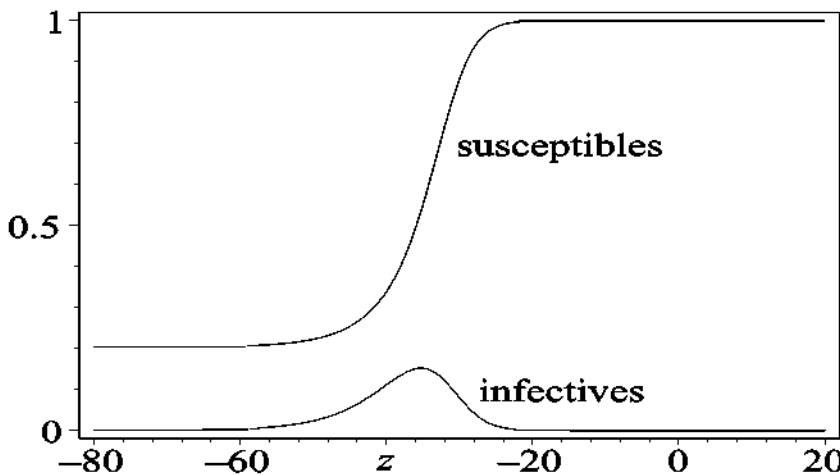
Figure 10.6: Wavefront curves for $s(z)$ (susceptibles) and $i(z)$ (infectives).

the right, while the susceptible profile is a localized peak moving with the kink.

$***$

Returning to the Black Death pandemic, Noble ([Nob74]) has modeled its geographic spread (in one dimension) by including the diffusion term $D \, \partial^2 S / \partial x^2$ in the susceptible equation of system (10.15). Since the infective equation is the same as in the rabies epidemic model, one still has the condition $\lambda < 1$ and wave speed $c \geq 2\sqrt{1-\lambda}$. In dimensional units, the wave speed V must satisfy the inequality

$$V \geq 2\sqrt{(r \, S_0 \, D)} \sqrt{1 - a/(r \, S_0)}. \tag{10.22}$$

Example 10-6: Estimate of Minimum Speed for Black Death Spread

Noble ([Nob74]) has estimated that the population density of susceptibles in Europe in 1347 was $S_0 = 50/\text{mile}^2$, the transmission coefficient $r = 0.4 \text{ mile}^2/\text{year}$, the mortality rate $a = 15/\text{year}$, and the diffusion coefficient $D = 10^4 \text{ miles}^2/\text{year}$. Estimate the minimum speed V_{min} in miles per year for the spread of Black Death. How does this speed compare with the experimental 200 to 400 miles/year range given by Langer?

Solution: The minimum speed is $V_{min} = 2\sqrt{(r \, S_0 \, D)} \sqrt{1 - a/(r \, S_0)}$. Substituting the given parameter values yields $V_{min} = 447.2$ miles per year. This speed is somewhat higher than the upper bound given by Langer.

$***$

Vicene Méndez ([Men98]) has shown that introducing a reasonable delay (incubation) time for the appearance of the infectious members brings the minimum speed down into the experimental range. In dimensional units,

$$V_{min} = \sqrt{2rS_0D} \left[\sqrt{\left(\lambda - \frac{1}{t_d rS_0} \right)^2 + \frac{4}{t_d rS_0}} - \lambda - \frac{1}{t_d rS_0} \right]^{1/2}, \qquad (10.23)$$

where t_d is the delay time.

Example 10-7: Méndez Estimate of Minimum Speed for Black Death Spread

Taking the same parameter values as in the previous example and $t_d = 15$ days, determine V_{min}. Discuss the result.

Solution: Converting the delay time into years, $t_d = 15/365$ years. Then, with all other parameters as before, we obtain $V_{min} = 339.5$ miles per year. This estimate of the minimum speed for the spread of black death lies in the experimental range.

<div align="center">***</div>

10.3   Examples of Disease Growth

In the previous section, we have briefly looked at how diseases spread. This is a subject with a vast literature covering a wide variety of diseases. A selection of case studies involving nonlinear models may be found in *Applied Mathematical Ecology*, including an article by May and Anderson ([MA89]) on *human immunodeficiency virus* (HIV)/AIDS transmission.

Now we will look at a few nonlinear models which attempt to describe how diseases grow, starting with mad cow disease.

10.3.1   Mad Cow Disease
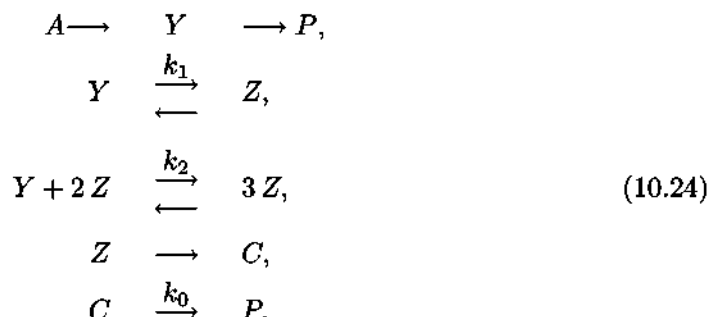
Chemical reactions can play an important role in the growth of certain diseases. *Prions* (short for *proteinaceous infectious particles*) are pathogens responsible for a variety of neurodegenerative diseases in animals as well as in humans. One of the more famous of the prion diseases is *bovine spongiform encephalopathy* (BSE) or, as it is more commonly known, *mad-cow disease* ([AW96], [AW97], [AW98]). BSE causes a spongy degeneration in the brains and spinal cords of affected cattle leading to their inevitable deaths. The worst-affected country for BSE is the United Kingdom, where 179,000 cattle have been infected and 4.4 million have been slaughtered as a precautionary measure.

Although quite rare, *Creutzfeldt–Jakob disease* (CJD) is the most common type of transmissible spongiform encephalopathy found in humans ([JC01]). It is incurable and ultimately fatal. A related brain disease to CJD, also believed to be caused by prions, is *kuru*. This disease caused an epidemic among the Fore tribe of Papua New Guinea in the middle of the twentieth century. The word *kuru* means "trembling with fear" in the Fore language. Kuru is also known as the laughing sickness because those afflicted displayed pathological outbursts of laughter.

In this section, we will outline a simple chemical kinetic model due to Vitagliano and D'Errico ([VD01]) for the possible progression of prion disease. Like the Belousov–Zhabotinskii chemical reaction, the model is a severe truncation of all the chemical processes which are believed to take place, attempting to capture some of the main observational features with a smaller set of chemical reactions. These features are the existence of a threshold for the prion diseases to progress and the long incubation period normally associated with prion diseases.

Since the chemical reactions involve prions, let us briefly say a bit more about them. Prions are glycosylated membrane proteins naturally occurring in neurons. Healthy "normal" prions are referred to as PrP^c (short for *prion protein cellular*). Infectious "rogue" prions are termed PrP^{sc} (the superscript sc stands for *scrapie*, the prion disease of sheep). The rogue prions have the ability to force the normal proteins to change shape, i.e., PrP^c and PrP^{sc} are the same chemical but with different shapes. It is the rogue prions which are responsible for the neurodegenerative diseases.

In the Vitagliano–D'Errico kinetic model which follows, Y will refer to the normal protein, PrP^c, and Z to the infectious protein, PrP^{sc}. The kinetic model reactions are:

$$
\begin{aligned}
A \longrightarrow \quad Y \quad &\longrightarrow P, \\
Y \quad &\underset{\longleftarrow}{\overset{k_1}{\longrightarrow}} \quad Z, \\
Y + 2Z \quad &\underset{\longleftarrow}{\overset{k_2}{\longrightarrow}} \quad 3Z, \\
Z \quad &\longrightarrow \quad C, \\
C \quad &\overset{k_0}{\longrightarrow} \quad P.
\end{aligned}
\tag{10.24}
$$

In the first reaction, the normal protein Y grows from a substrate A, whose concentration is taken to be constant, and is tranformed into products P. A includes all metabolic processes leading to Y. Since the authors were not interested in the abolute time scale, they took the rate constants here to be unity. Similarly, the rate constants for all other unlabeled arrows in the reaction scheme are equal to 1 as well.

Protein Y can change to Z through two different paths, given by the second and third reactions. In the second[7] reaction, Y is converted to Z in a *first-order* reversible reaction, the forward rate constant being k_1, the backward rate constant being unity. In the third reaction, Y is changed to Z in an autocatalytic reversible reaction, the forward rate constant being k_2. This *third-order*[8] reaction is included because it is known that more than one rogue prion is required to convert one healthy protein ([Lau97]).

In the fourth reaction, the prion Z infects cells C through a first-order irreversible process. The fifth, and last, equation represents the elimination of C in the form of the final metabolic products. This is a *zero-order* reaction. For a zero-order reaction, the

---

[7]The alternate reaction $A \overset{k_1}{\longrightarrow} Z$ is also considered by Vitagliano and D'Errico, but the results are similar to those presented here.

[8]Called third order since $3Z = Z + Z + Z$ so, e.g., a Z^3 term will appear in the rate equation for Y.

reaction rate is independent of the concentrations of the reactants, i.e., the contribution to $\dot{C}$ is simply $-k_0$.

Using the same symbols to denote concentrations, the rate equations for Y, Z, and C are:

$$\dot{Y} = A - Y - k_1\,Y + Z - k_2\,Y\,Z^2 + Z^3,$$

$$\dot{Z} = k_1\,Y - 2\,Z + k_2\,Y\,Z^2 - Z^3, \qquad\qquad (10.25)$$

$$\dot{C} = Z - k_0.$$

Note that the first two equations are independent of the third, the latter equation telling us the progression of the prion disease at time t, once $Z(t)$ is known. The general analysis of the fixed points of the first two equations is quite messy so, following Vitagliano and D'Errico, we will consider the representative parameter values

$$A = 5, \quad k_1 = 0.01, \quad k_2 = 0.8, \quad k_0 = 0.5.$$

Example 10-8: Fixed Points

For the representative parameter values, determine the number and locations $\bar{Y}$, $\bar{Z}$ of the fixed points of the first two rate equations.

Solution: Setting $\dot{Y} = 0$ yields

$$\bar{Y} = \frac{A + \bar{Z} + \bar{Z}^3}{1 + k_1 + k_2\,\bar{Z}^2}.$$

Setting $\dot{Z} = 0$, substituting $\bar{Y}$, and simplifying, generates a cubic equation for $\bar{Z}$,

$$\bar{Z}^3 - \left(\frac{k_2\,A}{1 + k_2}\right)\bar{Z}^2 + \left(\frac{2 + k_1}{1 + k_2}\right)\bar{Z} - \frac{k_1\,A}{1 + k_2} = 0.$$

Solving the cubic equation with $A = 5$, $k_1 = 0.01$, $k_2 = 0.8$ yields the following three fixed points (FP):

- FP_1: $\bar{Y} = 4.974$, $\bar{Z} = 0.026$;

- FP_2: $\bar{Y} = 4.285$, $\bar{Z} = 0.715$;

- FP_3: $\bar{Y} = 3.519$, $\bar{Z} = 1.480$.

<div align="center">***</div>

With the number of fixed points known and their locations determined, their nature can be determined, either analytically by carrying out a phase-plane analysis, or graphically by creating a phase-plane portrait as in the following example.

Example 10-9: Nature of the Fixed Points

By making an appropriate phase-plane portrait with some representative trajectories, determine the nature of the three fixed points in the previous example.

Solution: The Y and Z ODEs in (10.25) are numerically solved over the time interval $t = 0$ to 9 for the representative parameter values and the five initial conditions:

$$(Y(0), Z(0)) = (1.2, 2), \quad (1.5, 2), \quad (8, 0.373), \quad (8, 0.375), \quad (8, 0.45).$$

These initial conditions were selected by trial and error to best illustrate the nature of the fixed points.

The trajectories are then plotted in the phase plane, small circles being placed at the locations of the three fixed points. With the tangent field included, the phase-plane portrait then is as shown in Figure 10.7.
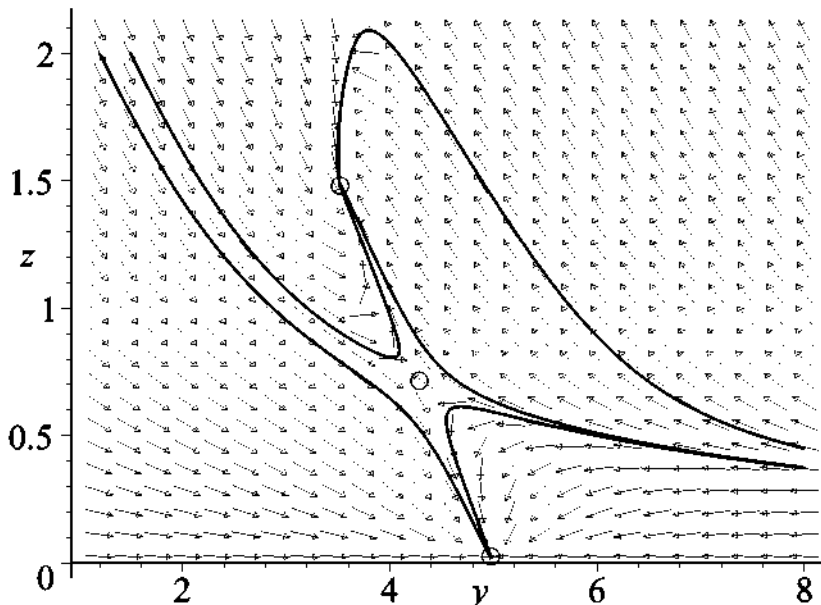
Figure 10.7: Phase-plane portrait for Y and Z equations in prion model.

From the figure, we can see that fixed points FP_1 and FP_3 are stable nodal points, the trajectories being attracted to these points along definite paths in the phase plane. The fixed point FP_2 is not stable, and is in fact a saddle point. Depending on the numerical value of $Y(0)$, there is clearly a threshold value for $Z(0)$, below which the ODE system evolves to FP_1, and above which it evolves toward FP_3.

<div align="center">***</div>

The change of C concentration depends on which stationary state is reached. With $k_0 = 0.5$, if the system approaches FP_1, then $Z \to \bar{Z} = 0.026$ which is less than k_0. Since C cannot be negative, C will go to zero. On the other hand, if it approaches

FP_3, then $Z \rightarrow \bar{Z} = 1.480$, and C will increase almost linearly. This is confirmed in the following example.

Example 10-10: Time Evolution of C

Taking $Y(0) = 5$, $C(0) = 0$, and the given parameter values, solve the system (10.25) for $C(t)$ over the range $t = 0$ to 8 for **(a)** $Z(0) = 0.6$, **(b)** $Z(0) = 0.63$, and **(c)** $Z(0) = 0.8$. Plot the three curves together and discuss the behavior of $C(t)$ as $Z(0)$ is increased. Remember that on physical grounds C cannot be allowed to go negative, i.e., only the range $C \geq 0$ should be plotted.

Solution: Using *Maple* or *Mathematica*, the nonlinear ODE system is solved for the three initial conditions over the time interval $t = 0$ to 8 using the adaptive step RKF45 method. Then, the three $C(t)$ curves are plotted, the resulting picture being shown in Figure 10.8. The bottom curve is for $Z(0) = 0.6$, the middle one for $Z(0) = 0.63$, and the top curve for $Z(0) = 0.8$.
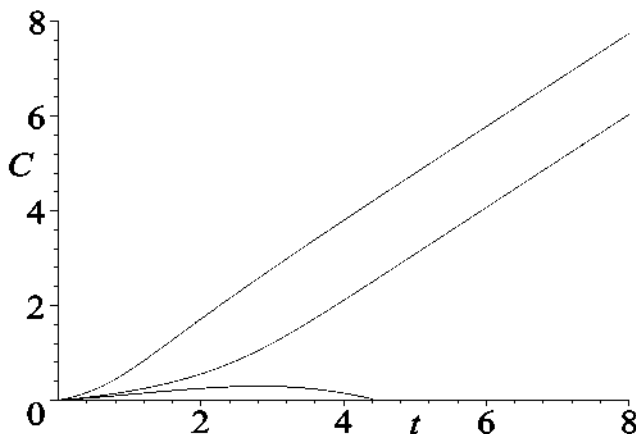
Figure 10.8: Growth of C with time.

For $Z(0) = 0.6$, C begins to grow but eventually dies away. For $Z(0) = 0.63$, the growth is initially close to that of the $Z(0) = 0.6$ curve but instead of dying away it begins to grow and approaches a linear increase with time. The threshold for growth is about $Z(0) = 0.62$. The initially lower slope of the growth curve is qualitatively associated with the incubation period before the appearance of the disease.

<div align="center">***</div>

Vitagliano and D'Errico point out that their kinetic model is only intended as a "test-bed" to understand how simple underlying nonlinear chemical reactions might explain some of the observed features of a quite complex disease.

10.3.2   Avascular Tumor Growth

Since cancer is one of the main causes of morbidity and mortality in the world, developed countries such as the United States and the United Kingdom are spending large sums

of money on research into the nature and treatment of this devastating disease. With a rapidly increasing amount of experimental data available, mathematicians are attempting to create realistic models of tumor growth with the hope that existing treatments can be improved, more successful treatments discovered, and, perhaps, cures achieved.

How exactly cancer is initiated in the body is still not settled but it is generally accepted that a normal cell is converted to a cancer cell through a series of gene mutations[9] which are triggered by both environmental and hereditary factors. One of the outcomes of these mutations is that the proliferation rate of the cancer cells is increased and the death rate decreased, thus allowing these cells to grow faster than the "host" (normal) cells.

As the cancer cells initially proliferate, in vitro experiments reveal that the cancerous tumor grows as a spheroidal clump ([Sut88]). However, the spheroidal tumor does not grow beyond a certain size without a blood supply because a balance is reached between the consumption of nutrients by the tumor and the inflow of vital nutrients (particularly oxygen) via diffusion into the tumor. This is called the *avascular* (without blood vessels) stage of cancer growth. Because diffusion is a relatively slow process, cell proliferation eventually only takes place near the surface of the spheroid where the nutrient level is sufficiently high. Deeper inside the tumor, the nutrient level drops sufficiently that the cancer cells are quiescent. Deeper yet, the nutrient level is sufficiently low that tumor cells begin to die. The center of the tumor (called the *necrotic* center) consists largely of dead cells.

The fact that diffusion limits tumor growth led to the *angiogenesis* hypothesis which has been experimentally verified. For tumors to grow larger, they need to obtain their own blood vessels. This stage, where a tumor develops its own blood supply, is called the *vascular* stage. One of the medical approaches currently being developed to fight cancer is to create drugs which target these tumor blood vessels and cut off the blood supply to the cancerous cells.

The third *metastatic* stage corresponds to when the cancer cells escape the primary tumor and set up secondary tumors elsewhere in the body.

From a clinical viewpoint, the last two stages are the most critical because vascular tumor growth and metastasis are what cause the patient to die. However, these stages are more difficult to mathematically model because so many factors are involved. The avascular stage is easier to model, yet has sufficient complexity that understanding this stage may lead to better models for the two more advanced stages. Experimentally, this stage is also more conducive to model testing because in vitro experiments can be easily and cheaply carried out for this stage. The other stages involve animal experiments in which it is often difficult to isolate individual effects.

Roose, Chapman, and Maini ([RCM07]) have written an excellent survey of nonlinear mathematical modeling of avascular tumor growth.[10] The two main approaches are:

- continuum models formulated in terms of reaction-diffusion-convection PDEs;

- discrete cell models with a cellular automata modeling of cell–cell interactions.

---

[9] A good review on this issue is given in ([MIN04]).

[10] Mathematical modeling of the vascular stage (angiogenesis) is discussed in ([MWO04]).

Here we will only outline one of the best parameterized of the continuum models due to Casciari, Sotirchos, and Sutherland ([CSS92]). The CSS model considers a spherical tumor of radius $r = R$ and the interaction of tumor cells with oxygen, glucose, carbon dioxide, and lactate, bicarbonate, chloride, and hydrogen ions. The aim of the model is to answer quantitative questions about the expected pH inside the tumor.

Letting C_i be the concentration of chemical species i inside the tumor, the conservation equation for the different chemical species is

$$\frac{\partial C_i}{\partial t} + \nabla \cdot \vec{N}_i = P_i, \tag{10.26}$$

where $\vec{N}_i$ is the flux of each of the chemical species inside the tumor spheroid and P_i is the net rate of consumption/production of the chemical species both by the tumor cells and due to chemical reactions with other species.

Table 10.3 shows the index i for the different chemical species and the functional dependence[11] of the P_i on the concentrations of these species.

i	Chemical Species	P_i
a	oxygen	$P_a = -\Omega \left(A_a + \dfrac{B_a}{C_b \, (C_g)^m} \right) \left(\dfrac{C_a}{C_a + K_{ma}} \right)$
b	glucose	$P_b = -\Omega \left(A_b + \dfrac{B_b}{C_a} \right) \left(\dfrac{1}{(C_g)^n} \right) \left(\dfrac{C_b}{C_b + K_{mb}} \right)$
c	lactate ion	$P_c = -(2\,P_b - P_a/3)$
d	carbon dioxide	$P_d = -k_f\,C_d + k_r\,C_e\,C_g$
e	bicarbonate ion	$P_e = k_f\,C_d - k_r\,C_e\,C_g - P_a$
f	chloride ion	$P_f = 0$
g	hydrogen ion	$P_g = k_f\,C_d - k_r\,C_e\,C_g - P_a + P_c$

Table 10.3: Index i and P_i for different chemical species.

C_a is the concentration of oxygen, C_b the concentration of glucose, and so on. The quantity Ω is the number of cells per unit volume of spheroid, assumed to be constant. The rate constants (k_f, etc.) and all other parameters in the P_i expressions are determined

---

[11] The P_i forms are obtained by considering the breakdown of glucose through glycolysis and the *Krebs cycle* (a sequence of 10 biochemical reactions ([You92])) and the detailed metabolic pathway for pH regulation on a single cell level. At low levels of oxygen and glucose, CSS use simpler forms for P_a and P_b.

from experimental data. Since the P_i are nonlinear functions of the concentrations, the PDEs (10.26) are also nonlinear.

For the uncharged oxygen, glucose, and carbon dioxide molecules, the flux is given by *Fick's law*,

$$\vec{N}_i = -D_i \nabla C_i, \tag{10.27}$$

where the D_i are positive diffusion coefficients. For the ionic species, electric-field-driven charge flow must be included as well as diffusion. Then,

$$\vec{N}_i = -z_i u_i F C_i \nabla \Phi - D_i \nabla C_i, \tag{10.28}$$

where z_i is the ionic charge of species i, u_i is the mobility, F is Faraday's constant, and Φ is the electric potential. For dilute solutions, CSS took the mobility to be given by the *Nernst–Einstein* equation,

$$u_i = D_i/(R_g T), \tag{10.29}$$

where R_g is the gas constant and T is the absolute temperature.

Assuming that there is zero net electrical current, so that $\sum_k z_k \vec{N}_k = 0$, Equation (10.28) can be rewritten as

$$\vec{N}_i = -D_i \left(\nabla C_i - z_i C_i \frac{\sum_k z_k D_k \nabla C_k}{\sum_k z_k^2 D_k C_k} \right). \tag{10.30}$$

So the flow of a specific ion species depends on the concentration gradients of all the ionic species present in the tumor.

The boundary condition at the surface of the spheroid is taken to be

$$\left(\hat{e}_r \cdot \vec{N}_i \right)_{r=R} = K_i \left(C_{i,out} - C_i \right)_{r=R}, \tag{10.31}$$

where $\hat{e}_r$ is the unit vector in the radial direction, K_i is the mass transfer coefficient of species i, and $C_{i,out}$ is the concentration of species i in the bulk medium outside the spheroid. To avoid any singularity at the origin, the condition

$$(\nabla C_i)_{r=0} = 0 \tag{10.32}$$

is also imposed.

The velocity $\vec{v}$ of cell movement is given by

$$\nabla \cdot \vec{v} = \lambda \mathcal{F}(C_i), \tag{10.33}$$

where λ is the maximum rate of cell proliferation and $\mathcal{F}(C_i)$ is an empirically determined function. CSS fitted the experimental data for the transient, preplateau phase of the spheroidal growth with the function

$$\mathcal{F}(C_i) = G_1 \left(\frac{C_a}{G_a + C_a} \right) \left(\frac{C_b}{G_b + C_b} \right) \left(\frac{1}{C_g} \right)^n, \tag{10.34}$$

where the Gs are fitting parameters. Because $\mathcal{F}$ is always positive, this implies that cells are proliferating everywhere and there cannot be a steady state for the tumor radius. To model growth saturation (i.e., a plateau), a cell death term should be included in $\mathcal{F}$.

Assuming a spherical tumor, the radial cell velocity at a radial distance r from the center of the tumor can be obtained from (10.33) and is given by

$$v_r(r) = \frac{\lambda}{r^2} \int_0^r \mathcal{F}(C_i) \, d^3r. \tag{10.35}$$

So the rate of increase of the tumor boundary at $r = R$ is

$$\frac{dR}{dt} = v_r(R) = \frac{\lambda}{R^2} \int_0^R \mathcal{F}(C_i) \, d^3r. \tag{10.36}$$

The system of Equations (10.26) to (10.36) was solved numerically by CSS, the model predicting that:

- The oxygen and glucose concentrations should fall in the middle of the spheroid, giving rise to a rim region near the surface of the spheroid of high cell proliferation. The measured thickness of this rim was found to be in reasonable agreement with the theoretically predicted thickness.

- The pH inside the tumor should differ from that on the outside, with higher acidity at the tumor center than near the boundary. This prediction was also experimentally confirmed.

The strength of the CSS model was not in how good a fit the model predictions were to experimental reality[12] but that it correctly captured (at least qualitatively) the complicated underlying biochemistry involved in avascular tumor growth. If you wish to learn more about modeling avascular tumor growth, see the review paper of Roose, Chapman, and Maini ([RCM07]), which is available on the Internet.

PROBLEMS

Problem 10-1: Seasonal variations in the SIS model
To account for seasonal variations, the contact number σ in the SIS model Equation (10.4) can be made periodic. Taking

$$\sigma = 2 - 1.8 \cos(5\tau)$$

and

$$i(0) = 0.8, \quad \mu = 0,$$

numerically solve Equation (10.4) for (i) $\gamma = 4$, (ii) $\gamma = 1$, and plot $i(\tau)$ in each case.

For each case, calculate the time-averaged (average over one period) contact number $\bar{\sigma}$ and relate the numerical results to whether $\bar{\sigma}$ is less than or greater than 1.

Problem 10-2: Improved fox rabies transmission model
To be of practical use in developing a control strategy for the transmission of fox rabies, a more realistic model is required than the simple one given in the text. Anderson,

---

[12]The fits were only satisfactory, far less accurate than in typical physics experiments.

Jackson, May, and Smith ([AJMS81]) have developed a three-species SIR model for the population dynamics of fox rabies in central Europe.

The fox population is divided into susceptible foxes, S, infected (but noninfectious) foxes, I, and infectious, rabid foxes, R. S, I, and R are in units of foxes/km^2. Note that there is no category of recovered immune foxes because very few, if any, survive after acquiring the rabies virus. Neglecting spatial spreading, the model equations are:

$$\dot{S} = a\,S - b\,S - \frac{(a-b)\,N\,S}{K} - \beta\,R\,S,$$

$$\dot{I} = -b\,I - \frac{(a-b)\,N\,I}{K} + \beta\,R\,S - \sigma\,I,$$

$$\dot{R} = -b\,R - \frac{(a-b)\,N\,R}{K} + \sigma\,I - \alpha\,R,$$

$$N = S + I + R.$$

The meaning of the coefficient symbols and their values are given in Table 10.4.

Symbol	Meaning	Value
a	average birth rate	1 per year
b	average intrinsic death rate	0.5 per year
K	carrying capacity	0.25 to 4.0 foxes/km^2
β	rabies transmission coefficient	80 km^2 per year
$1/\sigma$	average incubation time	28 days
$1/\alpha$	average duration of disease	5 days

Table 10.4: Symbol meaning and values for fox rabies ([AJMS81]).

Taking $K = 2$ foxes/km^2, numerically explore the solution of the fox rabies equations for different initial values of S, I, and R. Plot the solution curves and discuss the results.

The spatial spreading of fox rabies can be modeled by adding appropriate diffusion terms to the above model equations. For an extensive treatment of 1-dimensional spreading as well as some discussion of 2-dimensional spreading see Jim Murray's text ([Mur02]). The discussion includes examining such control mechanisms as vaccinating or killing foxes in a barrier region so as to reduce the population density below some critical value so that the rabies epidemic cannot jump the barrier.

Problem 10-3: Periodic cycles of infection
Anderson and May ([AM82]) have suggested a discrete model for the spread of disease which illustrates how periodic cycles of infection may arise in a given population. Let

the basic unit of time t be the average time interval for infection and let C_t and S_t be the number of disease cases and number of susceptible people at time t, respectively. The Anderson–May model assumes:

- the number of new cases C_{t+1} at time $t+1$ is some fraction f of the product of C_t and S_t;

- a case lasts for only one time unit;

- the susceptible number S_t is increased at each time interval by a fixed number of births $B \neq 0$ and decreased by the number of new cases;

- individuals who recover from the disease are immune.

a. Write the equations for C_{t+1} and S_{t+1} based on these assumptions.

b. Determine the fixed point(s) of the model.

c. In a third world country, typically $B = 36$ births per 1000 people and $f = 3 \times 10^{-5}$. Evaluate the fixed point(s).

d. By solving the model equations for the above parameter values and initial values $S_0 = 33300$ and $C_0 = 20$, show that a small deviation away from the fixed point(s) results in an oscillatory solution representing periodic cycles of disease incidence.

Problem 10-4: The SEIR model

For certain diseases, there is a significant period of time during which the individual has been exposed to the disease and has been infected, but is not yet infectious. For measles this latent period is about 8 days. The SEIR model incorporates this latent period into the SIR model with a fourth group of *exposed* individuals. Letting s, e, i, and r be the fractions of susceptible, exposed, infectious, and recovered (have become immune) individuals, respectively, the SEIR equations with vital dynamics are

$$\frac{ds}{dt} = -\lambda\, s\, i + \mu - \mu\, s,$$
$$\frac{de}{dt} = \lambda\, s\, i - (\mu + \alpha)\, e,$$
$$\frac{di}{dt} = \alpha\, e - (\mu + \gamma)\, i,$$

with $r(t) = 1 - s(t) - e(t) - i(t)$. Here $1/\alpha$ is the average latent period and all other coefficients are the same as in the SIR model. Show that the ODE system has two fixed points, one with $i = 0$ and one with $i > 0$. Defining $R_0 = (\alpha\, \lambda)/[(\mu + \alpha)(\mu + \gamma)]$, show that for $R_0 > 1$, the former fixed point is unstable and the latter is stable.

Problem 10-5: Prion disease fixed points

Using phase-plane analysis, determine the nature of the three fixed points FP_1, FP_2, and FP_3, in the prion disease example.

Problem 10-6: Onset of epileptic seizures

Letting x_n represent the fraction of neurons of a large neural network that fire on time step n, a simple finite-difference equation which models ([KG95]) the onset of epileptic seizures is

$$x_{n+1} = 4\,C\,x_n^3 - 6\,C\,x_n^2 + (1 + 2\,C)\,x_n,$$

where C is a positive constant and $0 \le x_n \le 1$.

  a. Determine the fixed points $\bar{x}_1$ corresponding to $x_{n+1} = x_n = \bar{x}_1$.

  b. Determine the stability of the fixed points and the C value at which they all become unstable.

  c. Determine the fixed points $\bar{x}_2$ corresponding to $x_{n+2} = x_n = \bar{x}_2$ and the C value at which they all lose their stability.

  d. Take $x_0 = 0.45$ and the following values $C = 1.5, 2.1, 2.5, 3.0, 3.3, 4.0$. In each case solve the model equation for n running from 0 to $n = N = 500$ and create a three-dimensional plot of n versus x_n versus x_{n+1}. Determine the periodicity in each case and relate the results to those in parts (a) to (c). Relate the results to the idea that increasing the value for C leads to the onset of uncontrolled neuron firings characteristic of an epileptic seizure.

Problem 10-7: AIDS

The *human immunodeficiency virus*, HIV, leads to *acquired immunodeficiency syndrome*, AIDS. By consulting Jim Murray's text ([Mur02]), or any other source,[13] discuss mathematical modeling of the transmission dynamics of HIV. A review of epidemiological data for AIDS is given in Anderson et al. ([AMMJ86]) and in May and Anderson ([MA87]).

Problem 10-8: Gompertz model for tumor growth

Provided that the number of tumor cells is sufficiently large, the *Gompertz growth function* does a good job of matching the growth of a tumor in the avascular stage ([Lai64], [ALSB73], [New80]). The growth function $G(N)$ is given by

$$G(N) = N\,(a - b\,\ln(N)),$$

where N is the number of tumor cells and a and b are constants determined by the experimental data for the tumor growth. It is assumed that the tumor has grown to a finite size before applying the formula, since the growth function is not defined at $N = 0$.

Simpson-Herren and Lloyd ([SHL70]) experimentally studied the growth of the C3H mouse mammary tumor, for which the best-fitting Gompertz curve yielded $a = 0.4126$ and $b = 0.0439$, with N in units of 10^6 tumor cells and G in units of 10^6 tumor cells/day.

  a. Plot G over the range $N = 10$ to 10^4. What is the maximum growth rate and at what value of N does this occur?

---

[13] *Modeling HIV Transmission and AIDS in the United States* by Herbert Hethcote and James Van Ark is freely available at http://biotech.law.lsu.edu/cphl/models/aids/index.htm

b. Analytically solve the Gompertz tumor growth ODE, $dN(t)/dt = G(N(t))$, for $N(t)$ given that $N(0) = N_0$. Plot $N(t)$ over the range $t = 0$ to 200 days for $N_0 = 10$. Assuming that angiogenesis does not occur, to what maximum value of N does the tumor cell population grow?

Problem 10-9: The SIR model and the Bombay plague

Kermack and McKendrick ([KM27]) were able to fit the removal rate dR/dt due to death for the Bombay plague epidemic of 1905–1906 with an expression of the form

$$\frac{dR}{dt} = A \operatorname{sech}^2(B\,t - C)$$

which they derived from the SIR model without vital dynamics. The best fit to the plague data was obtained with $A = 890$, $B = 0.2$, and $C = 3.4$, the time t being given in weeks from the onset of the plague.

a. Plot Kermack and McKendrick's expression for the removal (death) rate.

b. What was the maximum death rate and how many weeks after the onset of the plague did it occur?

c. Approximately how many weeks did it take for the plague to die out?

The derivation of the above Kermack–McKendrick removal rate expression is the subject of the following problem.

Problem 10-10: Deriving the Kermack–McKendrick removal rate expression

Derive the Kermack–McKendrick removal rate expression of the previous problem by carrying out the following steps:

a. Assuming that the initial susceptible and removed fractions are $s(0) = s_0$ and $r(0) = 0$, derive the following first-order ODE for $dr/d\tau$:

$$\frac{dr}{d\tau} = 1 - r - s_0\,e^{-\sigma\,r}.$$

Here $\tau = \gamma\,t$ is the normalized time and $\sigma = \lambda/\gamma$ is the contact number.

b. Following Kermack and McKendrick, assume that the epidemic is not severe (as was the case for the Bombay plague) so that $\sigma\,r < 1$. Taylor expand the exponential term in the above ODE in powers of $\sigma\,r$, keeping terms of order $(\sigma\,r)^2$.

c. Integrate the ODE in part (**b**) to obtain $r(\tau)$.

d. Using the analytic result for $r(\tau)$ obtained in part (**c**), calculate $dr/d\tau$.

e. Express your answer in terms of the unnormalized quantities and show that dR/dt is of the form

$$\frac{dR}{dt} = A \operatorname{sech}^2(B\,t - C),$$

where A, B, and C are to be determined in terms of the original parameters.

Problem 10-11: The SEIR model

Create a compartmental diagram for the SEIR model with vital dynamics, defining all the symbols. Then write out the rate equations for this model.

Problem 10-12: U.S. polio epidemic of 1949

The following table shows the cumulative number of polio cases diagnosed each month in the U.S. polio epidemic of 1949, the second worst in U.S. history (National Foundation for Infantile Paralysis, *12th Annual Report*, 1949).

January	February	March	April	May	June
494	759	1016	1215	1619	2964
July	August	September	October	November	December
8489	22377	32618	38153	41462	42375

   a. Does the data suggest that it might be fitted with a logistic curve? Explain.

   b. Using the least squares method of statistics, determine the best-fitting logistic curve and plot it along with the data.

   c. Discuss how well the curve fits the data, suggesting reasons for any deviation.

Problem 10-13: Flu virus pathogenicity

Discuss the biological basis for the 1918 influenza pandemic virus pathogenicity. A good starting point is the paper *1918 Influenza: the Mother of All Pandemics* by Jeffery Taubenberger and David Morens. This paper is available online at:

www.cdc.gov/ncidod/eid/vol12no01/05-0979.htm.

Problem 10-14: The Spanish flu epidemic of 1918

The following table shows the cumulative number of civilian deaths ([Cro03]) in 45 major U.S. cities due to the Spanish flu at the end of each week indicated in the fall of 1918. This was the second wave of three pandemic influenza waves which occurred within a year. This second wave was highly fatal, causing nearly 100 thousand deaths in 12 weeks.

Sept. 14	Sept. 21	Sept. 28	Oct. 5	Oct. 12	Oct. 19
68	517	1970	6528	17914	37853
Oct. 26	Nov. 2	Nov. 9	Nov. 16	Nov. 23	Nov. 30
58659	73477	81919	86957	90449	93641

   a. Using the least squares method of statistics, determine the best-fitting logistic curve and plot it along with the data.

   b. Discuss how well the curve fits the data, suggesting reasons for any deviation.

Problem 10-15: Other notable epidemics
By performing an Internet search, discuss in detail (type of disease, duration, how widespread, number of deaths, etc.) some of the other notable epidemics that have occured throughout recorded history. To get you started, here are three other deadly pandemics with the dates when they occurred:

- The Peloponnesian War Pestilence (431–404 B.C.);

- The Antonine Plague (165–189 A.D.);

- The Plague of Justinian (541–542 A.D.);

Chapter 11

World of War

War is an ugly thing, but not the ugliest of things. The decayed and degraded state of moral and patriotic feeling which thinks that nothing is worth war is much worse. The person who has nothing for which he is willing to fight, nothing which is more important than his own personal safety, is a miserable creature and has no chance of being free unless made and kept so by the exertions of better men than himself.
John Stuart Mill, English economist and philosopher (1806–1873)

Earlier in the text, we looked at simple nonlinear models of predator–prey (e.g., cats and rats, foxes and rabbits) interactions. Phrased differently, these were models of the *war* between physically different species. Although the examples that were presented involved oversimplified models of reality, better mathematical models can be created to describe these deadly wars.

Wars also occur within the same physical species, such as among different groups of humans. The war can be *hot* such as in the open armed conflict between different countries or alliances (e.g., World Wars I and II) or between factions within the same country (e.g., American Civil War, the Russian Revolution, etc.) or it can be a *cold war* (e.g., United States and its allies versus the Soviet Union and its satellites during a 35-year period after World War II) where enemies engage in angry rhetoric and "saber rattling" without actual physical conflict. Human "wars" can also be between different political parties within a country as each party attempts to seize more control or power, between different religious or moral belief systems as each attempts to attract more adherents, between different companies as each attempts to attract more customers, between different sports teams as each vies to be the champion, and so on.

Since all wars, whether human or otherwise, involve some sort of "conflict" between two or more "enemies," all mathematical models that attempt to describe them are inherently nonlinear, the law of "mass action" applying. This can often make attempting to predict the outcome of a given war extremely difficult, as nonlinear features, such as the sensitivity to initial conditions and to small parameter changes, can play an important role.

Wars are usually accompanied by an *arms race* between opponents, i.e., the development of more and/or better "weapons." We will now look at some arms race models.

11.1   The Coevolutionary Arms Race

What is meant by the term *coevolutionary arms race*? Although the research of Brodie and Brodie ([BJ99]) has concentrated on the evolutionary warfare between the poisonous, rough-skinned newt *Taricha granulosa* and the red-sided garter snake *Thamnophis sirtalis*, they have provided the following predator–prey metaphor to explain the term.

Consider the "predator" traffic cops who sit in their police cars or on their motorbikes behind or under freeway overpasses waiting to nab speeding motorists (the "prey"). As speeding drivers became more wary, the police employed radar guns to identify their prey. The prey responded by installing radar detectors in their cars. The police then switched to new frequencies, but radar detectors were rapidly modified to handle each new frequency. Then some jurisdictions passed laws to make the use of radar detectors illegal and police began using new technology to identify motorists with illegal radar detectors. Stealth and cloaking options were developed so that motorists could jam the police radar detectors. Law enforcement then introduced laser technology (Lidar detectors) to clock and record speed so quickly that the motorist had little time to react and reduce his or her speed. Driver defenses were improved once again with devices which could detect Lidar and jam the frequency to provide time for the driver to slow down and avoid getting a ticket. And on the arms race goes, evolving over "generations" of police and motorists, each technological step by one group being met by an escalating counterstep by the other. The penalty for failure by one group or the other to develop new "weapons" comes with a cost to that group (fortunately, only money).

Now, let's look at some real research examples of the coevolutionary arms race.

11.1.1   The Newt versus the Garter Snake

In the 1950s, three hunters were found dead at their Oregon campsite, no evidence of foul play being found by police investigators.[1] However, a boiled newt was discovered in the coffee remaining in the hunters' coffee pot. It is speculated that the newt was inadvertently included when water was scooped for coffee from a nearby stream.

This event piqued the interest of Edmund ("Butch") Brodie, Jr., then a young biology graduate student at the Oregon College of Education. Thus began a 40-year quest by Butch to fully understand the mystery of the hunters' deaths and ultimately learn how newts were involved in a form of evolutionary warfare with predatory garter snakes.

Butch began by studying rough-skinned newts (*Taricha granulosa*), like the one found in the coffee pot. These newts are brown backed, but with bright orange bellies. When disturbed or attacked, the newts curl their heads and tails toward each other, thus exposing their brightly colored bellies. Butch reasoned that perhaps the newts were warning potential predators that they are not good to eat, i.e., are poisonous. After all, some other brightly colored animals are poisonous (e.g., the Monarch butterfly) or venomous (e.g., the coral snake). To test this idea, he injected potential predators like birds and reptiles with different concentrations of newt skin solution as well as feeding them whole newts. All the predators became very sick or died as a result. Not long

---

[1]The narrative in this section is taken from the web site **www.evolution.berkeley.edu**.

afterwards, chemists identified the newt's poison as a *neurotoxin*, called *tetrodotoxin* or *TTX*. Neurotoxins are very dangerous. Some neurotoxins, such as the *tetanus toxin*[2], overstimulate nerve cells, causing the victim's muscles to contract all at once. The muscles can contract so much that the victim's bones are broken. TTX, on the other hand, causes nerves to stop functioning completely. Breathing stops and the untreated victim can die. To give some idea how potent TTX is, it is ten thousand times more toxic than cyanide and two or three times stronger than the venom of the world's deadliest snake, the Australian *Inland Taipan*.[3]

Butch suspected that natural selection had caused the newts to evolve this devastating weapon to combat their predators. However, he was puzzled by how loaded with TTX these newts were. The amount of TTX in one newt seemed like overkill. One newt could kill 200 herons or 2000 kingfishers.[4] Natural selection should cause newts to evolve their TTX level to just high enough to protect them from predators. Producing TTX requires energy. Newts that produce too much TTX have less energy to produce offspring and thus have fewer offspring. On the other hand, newts that produce too little TTX tend to get eaten by predators and thus produce no offspring. Natural selection should favor those newts that produce just enough TTX to kill their predators and no more. Butch reasoned that the TTX level was so high because there must exist a predator which had evolved a high resistance to TTX. This turned out to be the red-sided garter snake (*Thamnophis sirtalis*).

Butch reasoned that the two species had evolved in response to each other (*coevolution*). To prove this, he had to demonstrate that *natural selection* could operate on both newt toxicity and snake TTX resistance. The three requirements of natural selection are: variation, heritability, and differential reproductive success (*selection*). Brodie and his students were able to confirm that all three requirements were fulfilled.

To demonstrate that the snakes and newts coevolved, it was necessary to show that newt toxicity evolved in response to snake resistance and vice versa. To do this, Brodie's group studied the trade-offs between the costs and benefits of toxicity and resistance. TTX production is costly to newts in terms of their ability to produce offspring. But TTX resistance is similarly costly to snakes. Using a specially designed snake racetrack, Brodie's group measured the crawling speed of the garter snakes as a function of their TTX resistance. They found that more resistant snakes had a slower average crawling speed than less resistant ones. Since a slower crawling speed makes a snake more likely to be eaten by snake predators, one would expect that the snakes would have evolved to have just enough resistance to eat the local newts but no more.

It was then predicted that the newts and snakes would coevolve so that the newts would be just toxic enough to avoid predation and the snakes should be just resistant enough to eat the newts. By studying the newt and snake populations in different geographic locations, they found that this was the case. Newts in Tenmile, Oregon, are highly toxic and the snakes highly resistant. Moving eastwards to Benton, Oregon, the newts were less toxic and the snakes correspondingly less resistant to TTX. Moving northwards to the Olympic Peninsula of Washington, the newts were much less toxic

---

[2]Which can be picked up by stepping on a rusty nail carrying the tetanus bacteria.

[3]However, *botulinum toxin* found in contaminated food is ten thousand times stronger than TTX.

[4]Fortunately, humans don't eat newts as one newt could kill more than 100 people.

and the snakes much less resistant. Finally, on Texada Island, British Columbia, the newts had no TTX production and the snakes had no TTX resistance.

Butch Brodie's research on coevolution is not over as other questions have arisen. For example, within a population there are a few cases of mismatched traits, highly toxic snakes paired with low resistant snakes or mildly toxic snakes paired with highly resistant snakes. Some other factors must also play a role in the coevolution of the newts and snakes.

11.1.2 Biological Arms Race with a Dangerous Prey

Paul Waltman and James and Lorraine Braselton ([WBB02]) have introduced a nonlinear mathematical model which allows for the coevolution of a poisonous prey and resistant predator such as the newt and garter snake. The starting point in the mathematical development of their model is the following *Holling* predator–prey equations:

$$
\begin{aligned}
\dot{x} &= \alpha\, x \left(1 - \frac{x}{K}\right) - \frac{m\, x\, y}{a + x}, \\
\dot{y} &= \frac{m\, x\, y}{a + x} - s\, y,
\end{aligned}
\tag{11.1}
$$

where x and y are the prey and predator numbers (per unit area). The first term in the prey equation is of the standard logistic form, K being the carrying capacity to which the prey will grow if there are no predators, and α a positive rate constant. It is assumed that the predation rate term is of the *Holling Type* II form $m\, x\, y/(a + x)$, where the capture rate m and saturation constant a are positive.[5] Popular among ecologists, the term allows for a prey-handling (chasing, killing, eating, and digesting) time. It was introduced by C. S. Holling in the predation of small mammals on European pine sawflies, but such an interaction term has appeared in other contexts. In the predator equation, the positive constant s is the predator death rate in the absence of prey.

Example 11-1: Holling Type II Predation Rate

Derive the Holling Type II predation rate term, $m\, x\, y/(a + x)$, by considering that the predator spends its time T on searching for prey and then handling the captured prey.

Solution: Letting T_s and T_{ht} be the search and handling times, respectively, then $T = T_s + T_{ht}$. Assume that a predator attacks and captures x_c prey during time T. The handling time should be proportional to the number of prey captured, so

$$
T_{ht} = x_c\, T_{ht1},
$$

where T_{ht1} is the time spent on handling one prey.

Capturing prey is assumed to be a random process. A predator examines area A (the "area of discovery") per unit time while searching and captures all the prey found

---

[5]With the predation term of the general form $P(x)\, y$, Holling ([Hol59a], [Hol59b]) classified two other responses: Type I: $P(x) = m\, x$, for passive predators like spiders which catch flies in their webs; Type III: $P(x) = P_{max}\, x^2/(a^2 + x^2)$, for predators that increase their search activity with increasing prey density.

there. If x is the number of prey per unit area, then the number of prey captured in time T_s is $x_c = (A\,x)\,T_s$. So,

$$T = T_s + T_{ht} = \frac{x_c}{A\,x} + x_c\,T_{ht1}.$$

Solving for x_c, we have

$$x_c = \frac{A\,T\,x}{1 + A\,T_{ht1}\,x} = \frac{(T/T_{ht1})x}{1/(A\,T_{ht1}) + x} \equiv \frac{m\,x}{(a+x)}.$$

The predation term then is

$$x_c\,y = \frac{m\,x\,y}{(a+x)}.$$

$$* * *$$

The Holling predator–prey system (11.1) must be solved numerically.

Example 11-2: Holling Predator–Prey Solution

Taking the parameter values $m = 2.5$, $a = 0.37$, $s = 1.1$, $K = 1$, $\alpha = 1.2$ and initial conditions $x(0) = 0.05$, $y(0) = 0.1$, numerically solve the Holling predator–prey equations for $x(t)$ and $y(t)$ over the time interval $t = 400$ to $t = 430$. Plot $x(t)$ and $y(t)$ versus t and create a phase-plane plot of y versus x. Discuss the results. What happens when the parameter a is increased to $a = 0.7$, all other parameter values being unchanged?

Solution: Using the RKF45 numerical method, the coupled ODE system (11.1) is solved for $x(t)$ and $y(t)$ for the given parameter values, initial conditions, and time interval. The number densities are plotted as a function of time on the left of Figure 11.1.
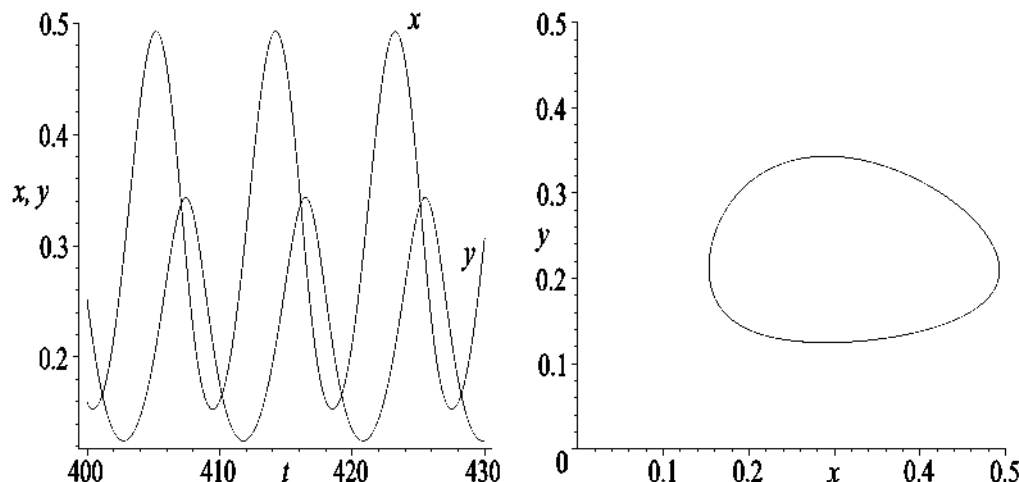
Figure 11.1: Left: Number densities versus time for $a = 0.37$. Right: Phase-plane plot.

Asymptotically, the predator and prey number densities are oscillatory, the phase-plane portrait shown on the right of the figure being a closed loop.

Increasing the parameter a to the value $a = 0.7$, and considering the time interval $t = 0$ to 100, generates the results plotted in Figure 11.2. In this case, both the predator and prey number densities approach constant values.
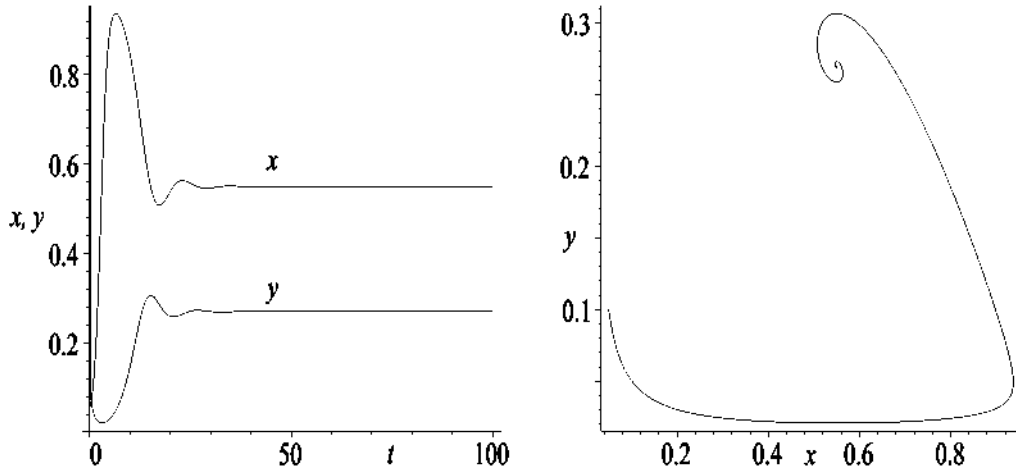
Figure 11.2: Left: Number densities versus time for $a = 0.7$. Right: Phase-plane plot.

***

Now, the full Waltman–Braselton arms race model incorporating genetic information for the prey and predators is developed. Starting with the prey, it is assumed that there are two *alleles* (forms of the gene), denoted by A and a, with one locus which are passed down in subsequent generations of prey. A *locus* is a given location on a chromosome which contains the blueprint instructions for a physical trait, e.g., TTX production.

Then, three genotype classes of prey are possible, namely, AA, Aa, and aa. Assuming that the mating is random and all genotypes are equally fit, the *Hardy–Weinberg law* ([EK88]) states that the relative frequencies of the gene classes will not change, i.e., no new stable distribution will appear.

The time evolution of the three genotypes (with 1 referring to AA, 2 to Aa, and 3 to aa) in the absence of any predator is given by ([NC74], [BFW81])

$$\dot{x}_1 = \frac{\alpha}{x}\left(x_1 + \frac{x_2}{2}\right)^2 - \frac{\alpha x_1 x}{K},$$

$$\dot{x}_2 = \frac{2\alpha}{x}\left(x_1 + \frac{x_2}{2}\right)\left(x_3 + \frac{x_2}{2}\right) - \frac{\alpha x_2 x}{K}, \qquad (11.2)$$

$$\dot{x}_3 = \frac{\alpha}{x}\left(x_3 + \frac{x_2}{2}\right)^2 - \frac{\alpha x_3 x}{K},$$

with $x = x_1 + x_2 + x_3$ and initial conditions $x_1(0) = x_{10}$, $x_2(0) = x_{20}$, $x_3(0) = x_{30}$.

If the three ODEs are added, the logistic equation for the total population number x is recovered. Reflecting the Hardy–Weinberg law in asymptotic form, Freedman and Waltman ([FW78]) have shown that as $t \to +\infty$, the three genotypes evolve in the ratio

$$(x_1 : x_2 : x_3) = (c^2 : 2\,c : 1),$$

where

$$c = \frac{(x_{10} + \frac{1}{2}\,x_{20})}{(x_{30} + \frac{1}{2}\,x_{20})}.$$

The ODE system (11.2) must be solved numerically.

Example 11-3: Evolution of Prey Genotypes in Absence of Predators

Taking $\alpha = 1.2$, $K = 1$, $x_{10} = 0.06$, $x_{20} = 0.1$, and $x_{30} = 0.02$:

a. Numerically solve Equations (11.2) for $x_1(t)$, $x_2(t)$, and $x_3(t)$ over the interval $t = 0$ to 10 and plot the three curves as well as the total x in the same graph;

b. Confirm that x saturates to the carrying capacity;

c. Confirm that $(x_1 : x_2 : x_3) = (c^2 : 2\,c : 1)$ in the asymptotic limit.

Solution: a. Using the RKF45 numerical method, the ODE system is solved and the numerical curves for x_1, x_2, x_3, and x are plotted in Figure 11.3.
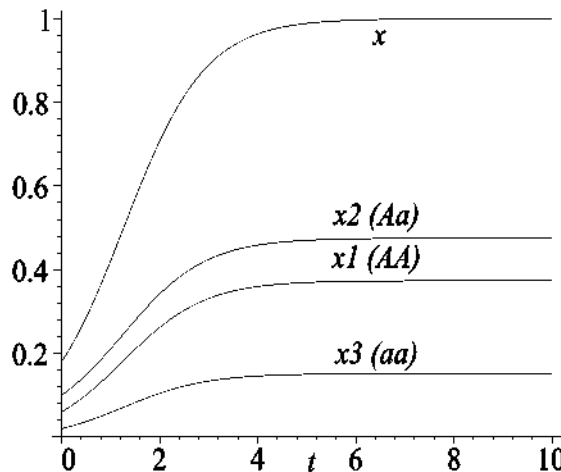
Figure 11.3: Time evolution of the three genotypes and the total number (x).

b. The total x saturates to the carrying capacity $K = 1$ as expected.

c. Using the initial values, we obtain $c = 1.571$, so the predicted asymptotic ratios of x_1/x_3 and x_2/x_3 are 2.469 and 3.143. As $t \to \infty$, we find numerically that $x_1 \to 0.37346$, $x_2 \to 0.47531$, and $x_3 \to 0.15123$. These produce ratios x_1/x_3 and x_2/x_3 in agreement with the theoretical prediction.

***

Now, predators are introduced into the full arms race model of coevolution involving a poisonous prey and resistant predator, e.g., the TTX-producing newt and TTX-resistant garter snake. For the prey, aa is taken as the dangerous (poisonous) prey. Complete dominance of A is assumed so that neither AA, or Aa, is dangerous, i.e., are nonpoisonous. For the predators, three genotypes are assumed, labeled as BB, Bb, and bb, with number densities y_1, y_2, and y_3, respectively. The genotype bb is assumed to be the resistant one, e.g., the TTX-resistant garter snake, while the other two genotypes are not.

Referring the reader to the Waltman–Braselton paper ([WBB02]) for the detailed reasoning and development of the coupled ODEs, the arms race equations are as follows:

$$\dot{x}_1 = \frac{\alpha}{x}\left(x_1 + \frac{x_2}{2}\right)^2 - \frac{\alpha\, x_1\, x}{K} - \frac{m_1\, x_1\, y}{a+x},$$

$$\dot{x}_2 = \frac{2\,\alpha}{x}\left(x_1 + \frac{x_2}{2}\right)\left(x_3 + \frac{x_2}{2}\right) - \frac{\alpha\, x_2\, x}{K} - \frac{m_2\, x_2\, y}{a+x}, \qquad (11.3)$$

$$\dot{x}_3 = \frac{\alpha}{x}\left(x_3 + \frac{x_2}{2}\right)^2 - \frac{\alpha\, x_3\, x}{K} - \frac{m_3\, x_3\, y}{a+x},$$

$$\dot{y}_1 = \frac{T(x_1,x_2,0)^2}{(a+x)\,T(x_1,x_2,x_3)\,y}\left(y_1 + \frac{y_2}{2}\right)^2 - \frac{m_3\, x_3\, y_1}{a+x} - s\,y_1,$$

$$\dot{y}_2 = 2\,\frac{\left(T(x_1,x_2,0)\,y_1 + \dfrac{1}{2}T(x_1,x_2,0)\,y_2\right)\left(T(x_1,x_2,x_3)\,y_3 + \dfrac{1}{2}T(x_1,x_2,0)\,y_2\right)}{(a+x)\,T(x_1,x_2,x_3)\,y}$$

$$\qquad -\frac{m_3\, x_3\, y_2}{a+x} - s\,y_2,$$

$$\dot{y}_3 = \frac{\left(T(x_1,x_2,x_3)\,y_3 + \dfrac{1}{2}T(x_1,x_2,0)\,y_2\right)^2}{(a+x)\,T(x_1,x_2,x_3)\,y} - s\,y_3,$$

$$\qquad\qquad (11.4)$$

with

$$x = x_1 + x_2 + x_3, \quad y = y_1 + y_2 + y_3 \qquad (11.5)$$

and

$$T(x_1,x_2,x_3) = m_1\, x_1 + m_2\, x_2 + m_3\, x_3. \qquad (11.6)$$

Here the parameter α controls the rate at which the prey approach the carrying capacity K (assumed to be the same for all three prey genotypes); s is the death rate of the predators (taken to be the same for all three predator genotypes); m_1, m_2, and m_3 measure the difficulty of prey capture by the three predator genotypes; and a takes into account the handling time.

The following example illustrates the coevolution of predators and prey for these model equations for some representative parameter values used by Waltman et al.

Example 11-4: Coevolution of Predators and Prey

For the biological arms race Equations (11.3)–(11.6),

  a. Numerically solve the equations using the parameter values

$$m_1 = m_2 = 2.5, \quad m_3 = 2.0, \quad a = 0.37, \quad s = 1.1, \quad \alpha = 1.2,$$

  and the initial conditions

$$x_{10} = 0.6, \quad x_{20} = 0.02, \quad x_{30} = 0, \quad y_{10} = 0.6, \quad y_{20} = 0.02, \quad y_{30} = 0.01.$$

  b. Plot the individual number densities and the totals x and y over the time interval $t = 0$ to 600. Discuss the results.

  c. What happens if the parameter m_3 is changed to $m_3 = 2.45$, all other parameter values remaining unchanged? Note that the time range must be increased.

Solution: a. Using either *Mathematica* or *Maple*, the ODE system (11.3)–(11.6) is solved with the RKF45 numerical method for the given parameter values and initial conditions.

b. The time evolution of the number densities y_1, y_2, and y_3, of predators and x_1, x_2, x_3, of prey is shown in the following sequence of figures. In Figure 11.4, we see the temporal evolution of x_1 and x_2, the number densities for the nonpoisonous prey AA and Aa, respectively. Both genotypes vanish at about 400 time units, although Aa actually grows considerably in number before "crashing" to zero.
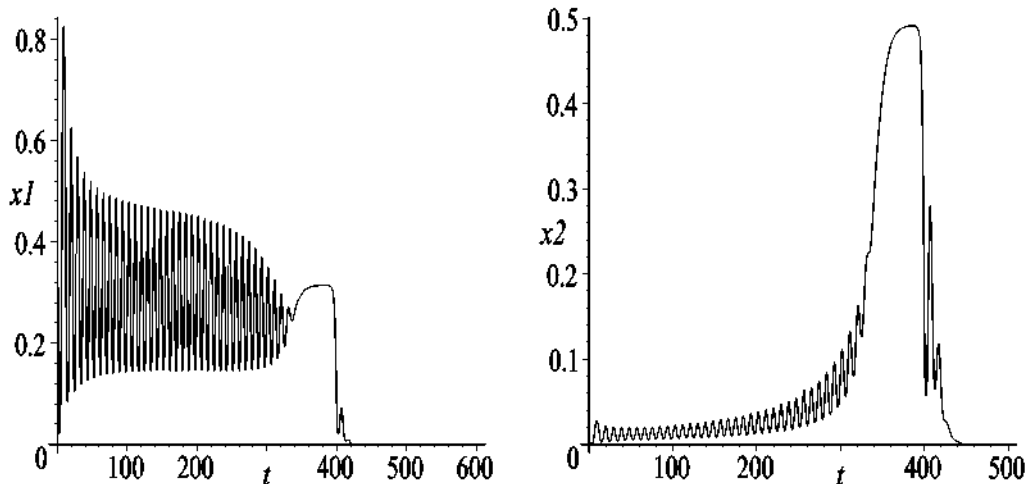
Figure 11.4: Evolution of the nonpoisonous prey AA (left) and Aa (right).

We next look at what happens to the nonresistant predators BB and Bb. The relevant number densities y_1 and y_2 are plotted in Figure 11.5.
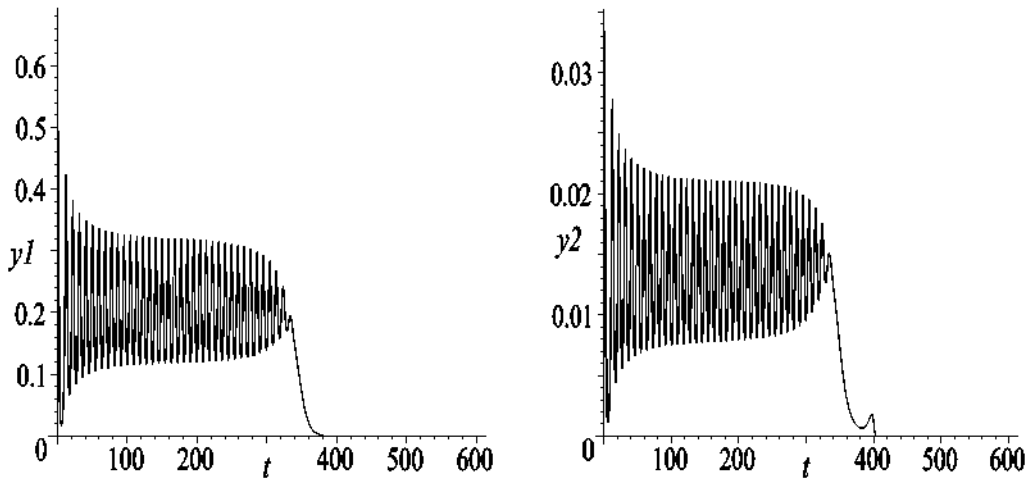
Figure 11.5: Evolution of the nonresistant predators BB (left) and Bb (right).

The nonresistant predators also vanish at about the same time as the nonpoisonous prey, a result which makes sense.

Turning to the poisonous prey aa and resistant predators bb, we see in Figure 11.6 that both survive, approaching constant values for the given parameters. The two genotypes, aa and bb, coevolve together. Note how their number densities dramatically increase at about the same time that the number densities of the nonpoisonous prey and nonresistant predators vanish.
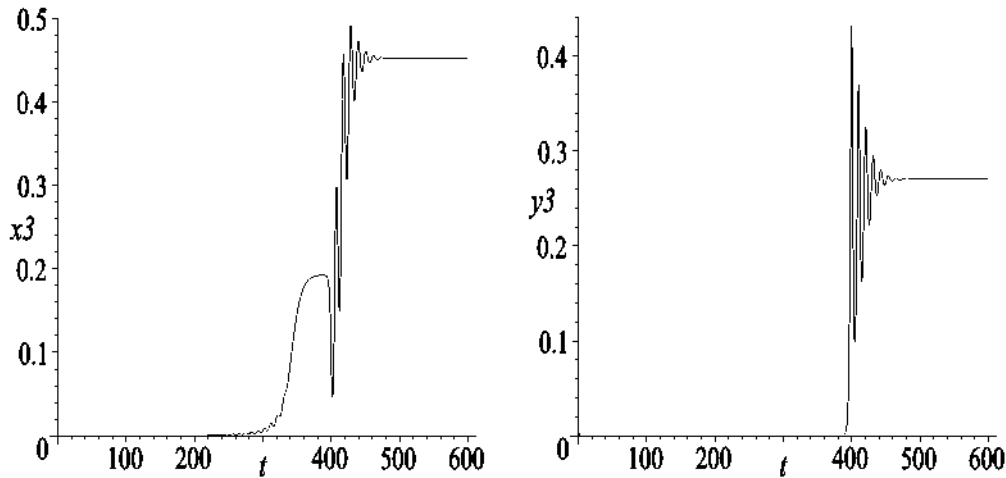
Figure 11.6: Evolution of poisonous prey aa (left) and resistant predators bb (right).

The time evolution of the total prey ($x = x_1 + x_2 + x_3$) and predator ($y = y_1 + y_2 + y_3$) number densities for $m_3 = 2.0$ is shown in the 3-dimensional plot of Figure 11.7.
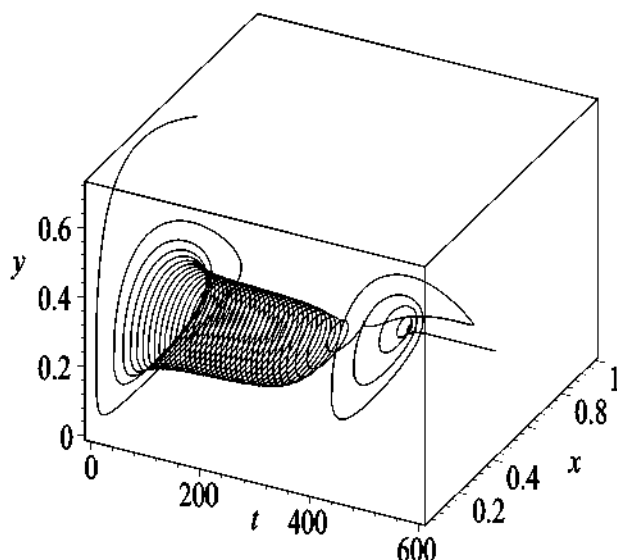
Figure 11.7: Time evolution of x and y for $m_3 = 2.0$.

c. For $m_3 = 2.45$, the nonpoisonous prey and nonresistant predator number densities still vanish, but at a much later time (about 4000 time units). The poisonous prey and
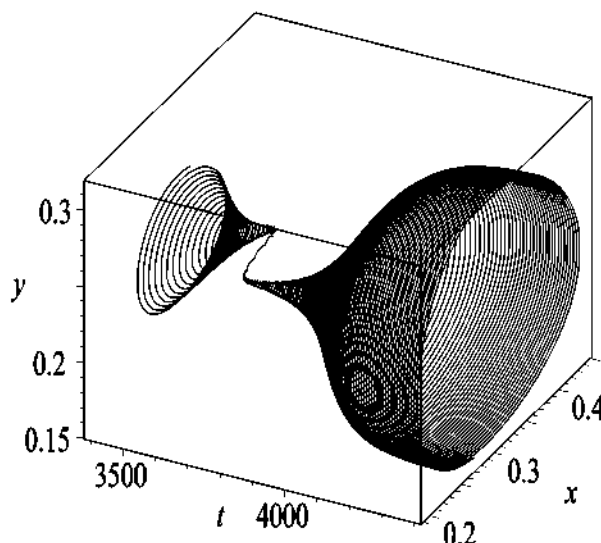
Figure 11.8: Time evolution of x and y for $m_3 = 2.45$.

resistant predator coevolve, eventually coexisting in an oscillatory regime. This is illustrated in Figure 11.8 where x and y are plotted versus t.

***

11.1.3   The Wild Parsnip and Geographic Mosaic Theory

Peter Kareiva has written an interesting commentary ([Kar99]) on war in the plant kingdom. As he states, "Plants are embattled in a war with rasping, sucking, and chewing insects, deadly viruses, debilitating bacteria, and castrating fungi. This war costs billions of dollars in crop losses each year, making the study of plant–pathogen and plant–herbivore interactions one of the most significant branches of applied biology."

Whether victory is ever possible in this ongoing war depends on learning about how plants interact with their predators. The idea of coevolution is popular in modern plant research, the idea being that herbivorous insects drive the evolution of plants, the evolved plants in turn causing the insects to adapt. However, even if true, coevolution could take place in different ways. For example, one could have:

- an escalating arms race in which plants relentlessly increase the weapons in their chemical arsenals and predatory herbivores respond by developing new defenses;

- cyclical selection in which highly defended plants are favored in times of severe attack, but which gradually decline in prevalence when not under attack because of the costs associated with resisting;

- a stasis in which little evolutionary change in either the plants or their enemies occurs, because of either the lack of genetic variation or the presence of constraints.

However, the observational or experimental evidence favoring one coevolutionary mode over another in a given plant population is rather slim. One of the most studied examples of coevolution in the plant kingdom involves the wild parsnip, *Pastinaca sativa*. This weed, which was introduced into eastern North America from Europe, has as its sole predator the parsnip webworm, *Depressaria pastinacella*. A decades-long study of this plant–predator system has been carried out by Berenbaum and Zangerl ([BZ98], [ZB03]).

Parsnips defend themselves by producing toxic *furanocoumarin* compounds, with heritabilities ranging from 0.54 to 0.62. But the webworms are able to metabolize these plant toxins, with heritabilities ranging from 0.33 to 0.45. In itself, this doesn't prove that coevolution has taken place. However, Berenbaum and Zangerl discovered two additional important facts:

- Both parsnips and webworms can be grouped into one of four phenotypic clusters, where each cluster corresponds to a particular mix of furanocoumarins being produced by the parsnips and an ability to metabolize the mix by the associated webworms. The four types of furanocoumarins involved are *bergapten, xanthotoxin, isopimpinellin,* and *sphondin.*

- When sampled along a latitudinal gradient, there is a remarkable match between the toxin-producing parsnips and toxin-resistant webworms. For example, plant clusters with a high bergapten production have associated webworm populations with a high bergapten metabolism.

Analyzing the data, Berenbaum and Zangerl suggest that geographical cyclical selection may be operating, each population slightly out of phase with each other. Alternative explanations do not appear to fit the facts. For example, there are no clear environmental

gradients underlying the geographic variation. Although the cyclic selection hypothesis is consistent with the facts, there is no direct evidence to support this model.

Further complicating the interpretation, there exist some sites such as one near Urbana, Illinois, where there is no matching whatsoever between the frequencies of plant phenotypes and herbivore phenotypes. This has led to the *geographic mosaic theory* of coevolution ([ZB03]). Selection intensity in interactions varies across a landscape, forming a selection mosaic; interaction traits match at coevolutionary "hotspots" where selection is reciprocal and mismatch at "coldspots" where reciprocity is not a factor. Consistent with the geographic mosaic theory, Zangerl and Berenbaum's research indicates that the presence of a chemically distinct alternate host plant can affect selection intensity in such a way as to reduce the likelihood of reciprocity in the coevolutionary interaction between wild parsnip and the parsnip webworm.

11.2 Human Conflict

11.2.1 Political Complexity: Nonlinear Models of Politics

Diana Richards has edited a text entitled *Political Complexity: Nonlinear Models of Politics* ([Ric00b]). Each of the contributing authors has attempted to use the ideas and methodology of nonlinear modeling to understand the political complexity we so often see in the world about us.

The various articles in the text deal with, and attempt to answer, questions such as:

- Why are U.S. congressional incumbents able to accumulate such large amounts of campaign funds ("war chests")? After posing this question, Walter Mebane, Jr. ([Meb00]) then asks why would a campaign contributor want to make an election noncompetitive. Mebane argues that there exists a nonlinear relationship among campaign contributions, district service, quality of the challenger, and election outcomes. Using a nonlinear game-theoretic model,[6] he finds, e.g., voter preferences only partially determine election outcomes.

- Can one explain and predict the kind of international environmental treaty that nations will agree to? Using a nonlinear games theory approach, Diana Richards ([Ric00a]) finds that even simple variables like the number of treaty participants or the presence of scientific consensus can have a counterintuitive effect on the stability of the players' interaction.

---

[6]Popularized by John von Neumann and Oskar Morgenstern in their book *Theory of Games and Economic Behavior* ([vNM44]), game theory is a branch of mathematics developed to study decision making by two or more competing "players" engaged in some sort of competition or "game." Game theory provides a mathematical process for a player to select an optimum strategy when faced with one or more opponents with strategies of their own. Game theory models are used in the social sciences, economics, evolutionary biology, engineering, political science, international relations, computer science, and philosophy. Numerous introductory and advanced texts are devoted to the foundations and applications of game theory, e.g., *Games and Information: An Introduction to Game Theory* by Eric Rasmusen ([Ras07]), *Game Theory: Mathematical Models of Conflict* by Antonia Jones ([Jon00].

- Can an artificial neural network[7] do a better job of forecasting the effects of economic sanctions than traditional statistical analysis? Using about 100 quantitative cases, David Bearce ([Bea00]) finds that the neural network model forecasts twice as well as the traditional statistical methods.

The mathematical details involved in using nonlinear models and methodology to deal with these and other questions of a political nature are left for the interested reader to explore in Richards's text.

11.2.2   Richardson Arms Race Model

The English physicist Lewis Fry Richardson (1881–1953), the father of numerical weather forecasting which will be discussed in the following chapter, is also well-known for his attempt to develop a mathematical model of the arms race between nations. A Quaker serving in the French medical corps during World War I, he was deeply troubled by the slaughter in this war and subsequently in World War II. Richardson conjectured that by studying the stability (or lack thereof) of an arms race between two nations (or two groups of nations), one could predict whether war would occur.

Letting $x(t)$ and $y(t)$ denote the arms expenditures at time t, Richardson proposed the following linear ODE system to model the arms race between countries X and Y:

$$\dot{x} = a\,y - m\,x + r,$$

$$\dot{y} = b\,x - n\,y + s. \tag{11.7}$$

Since arms expenditures cannot be negative, x and y are restricted to the domain $x \geq 0$, $y \geq 0$. The positive "fear" constants a and b represent the reactions of countries X and Y to the arms level of the other country. The positive "restraint" constants m and n represent the reluctance of countries to spend more of their budgets on arms, i.e., if they could, they would rather spend money on "butter" than guns. The "grievance/friendliness" constants r and s can be positive or negative, reflecting a country's hostile or peaceful intentions toward the other country. For, say, $r < 0$, nation X has peaceful intentions toward country Y, whereas for $r > 0$ it has hostile intentions. If the other terms in the $\dot{x}$ ODE are zero, x will decrease with time for $r < 0$ and increase for $r > 0$.

Different trajectories in the quarter phase plane $x \geq 0$, $y \geq 0$ can occur depending on the relative magnitudes of the various constants. A trajectory that asymptotically approaches the origin or the x- or y-axis is indicative of disarmament, while one diverging to infinity indicates a runaway arms race, a prelude to war. For some choices of the values of the constants, the outcome will depend on the initial condition. The following example illustrates these various possibilities.

---

[7]An artificial neural network (ANN) is an information processing model that is inspired by the way biological nervous systems, such as the brain, process information. An ANN is composed of a large number of highly interconnected processing elements ("neurons") working together to solve specific problems. Like the human brain, ANNs learn by example. For a brief introduction to ANN go to the following site: **http://www.doc.ic.ac.uk/~nd/surprise_96/journal/vol4/cs11/report.html#What is a Neural Network**.

Example 11-5: Richardson Arms Race

For the following coefficient values, (i) locate and identify the fixed point; (ii) create an appropriate tangent field plot revealing the possible trajectories; (iii) discuss the plot:

a. $a = 2$, $m = 5$, $r = 5$, $b = 2$, $n = 3$, $s = 5$;

b. $a = 2$, $m = 1$, $r = 3$, $b = 2$, $n = 2$, $s = 3$;

c. $a = 1$, $m = 4$, $r = -1$, $b = 1$, $n = 1$, $s = -2$;

d. $a = 2$, $m = 1$, $r = -3$, $b = 2$, $n = 1$, $s = -3$.

Solution: Using the notation of Chapter 2 for phase-plane analysis, we obtain

$$p = m + n, \quad q = mn - ab, \quad p^2 - 4q = (m - n)^2 + 4ab.$$

Now, let's consider each case:

a. The fixed point is at $x = 25/11$, $y = 35/11$ and $p = 8$, $q = 11$, and $p^2 - 4q = 20$. Therefore, referring to Table 2.1, the fixed point is a stable nodal point. The tangent field plot is shown on the left of Figure 11.9, all possible trajectories approaching the stable equilibrium point.
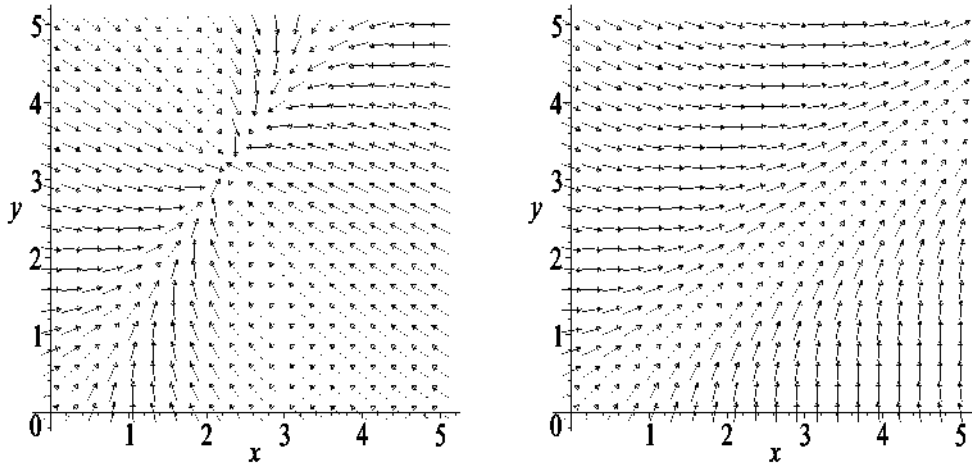
Figure 11.9: Tangent field for cases (a) (left) and (b) (right).

b. The fixed point lies outside the physical domain at $x = -6$, $y = -9/2$. In this case $p = 3$ and $q = -2 < 0$, so the fixed point is a saddle point. Despite lying outside the physical domain, the saddle point influences the trajectories in that domain. The tangent field is shown on the right of Figure 11.9. The tangent field arrows are heading toward infinity, indicating a runaway arms race for any real initial condition.

c. The fixed point is also outside the physical domain at $x = -1$, $y = -3$. In this case, $p = 5$, $q = 3$, and $p^2 - 4q = 13$, so the fixed point is a stable nodal point which attracts all trajectories toward it. The tangent field plot on the left of Figure 11.10 tells us that
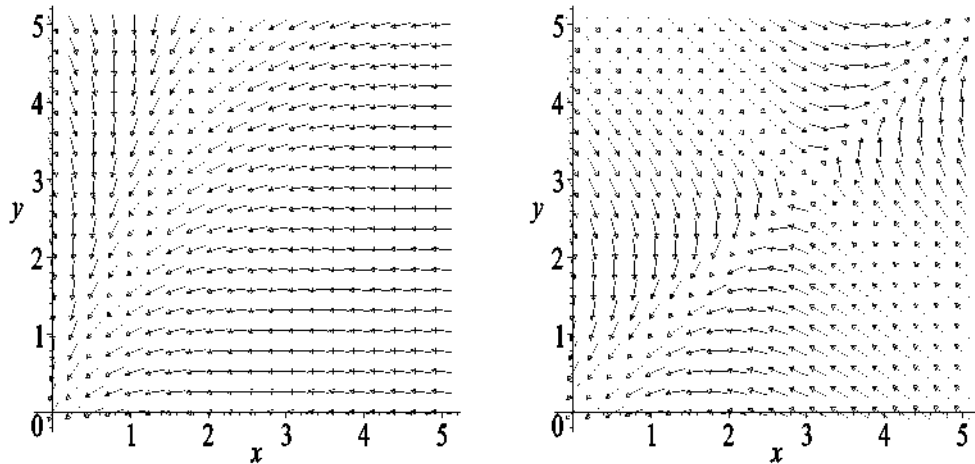
Figure 11.10: Tangent field for cases **(c)** (left) and **(d)** (right).

disarmament takes place.

d. The fixed point is at $x = 3$, $y = 3$. Since $q = -3 < 0$, it is a saddle point. Depending on the initial conditions, the plot on the right of Figure 11.10 tells us that either disarmament or a runaway arms race can occur.

<p align="center">***</p>

Dunne, Nikolaidou, and Smith ([DNS99]) have shown that the Richardson arms race model works well for the arms race between India and Pakistan, the arms race displaying a stable interaction with a well-determined equilibrium. However, the Richardson model has generally proven inadequate when applied to most real arms races.

Besides its general inadequacy, the Richardson model has a more fundamental defect. The possible existence of runaway solutions which diverge to infinity with increasing time runs counter to reality in our finite world. Linearity must eventually break down. Something like the quadratic term in the logistic model must become significant in any attempt to model the arms race in the real world. But once such a nonlinearity is present in the modeling, there is the possibility of bifurcations as one or more control parameters is changed and the possibility of chaos with its attendant unpredictability. In the following section, the transition to chaos is interpreted as the onset of war.

11.2.3   Chaos — a Model for the Outbreak of War

History is littered with conflicting examples where in some cases small perturbations or incidents have ignited massive armed conflicts or wars and in other situations to no appreciable change in the status quo. An example of the former is the assassination of Archduke Francis Ferdinand at Sarajevo in 1914. In this case, the killing of a single individual led to the declaration of World War I with its accompanying massive slaughter. On the other hand, the shooting down of Korean Airlines Flight 007 in September

1983, with the loss of 269 passengers (including a U.S. congressman) and crew, did not escalate into a major armed conflict. Trying to understand under what circumstances, small perturbations could produce a transition from stability (peace) to instability (war) led Alvin Saperstein ([Sap84], [SMK89], [KE96], [Sap99]) to formulate a number of increasingly more complex nonlinear models of the arms race between nations or groups of nations.

Saperstein's viewpoint is that the transition from stability to instability, from arms race to war, is analogous to the transition from laminar to turbulent (chaotic) fluid flow. In the nonchaotic regime, a reasonable estimate of initial conditions (which are never precisely known) allows one to confidently predict the future. Most historical evidence indicates that predictability and control are lost at the threshold between peace and war. Saperstein suggests that this threshold corresponds to the onset of chaos in the underlying nonlinear dynamical equations.

Because of its mathematical simplicity, rather than any attempt to model a given arms race accurately, we will look at one of Saperstein's early nonlinear models of the arms race, a model formulated in terms of nonlinear finite difference equations. The key dependent variable is the *devotion* of a nation to arms spending. Taking on a value between 0 and 1, devotion is the ratio of arms procurement expenditures to the gross national product (GNP) of that nation in a given budget cycle.

As a specific example, Table 11.1 shows the devotion of a number of European countries in the mid-1930s, countries that were soon to undergo the transition from peace to World War II. It should be noted that obtaining such information after the

Year	France	Germany	Italy	United Kingdom	USSR
1934	0.0276	0.0104	0.0443	0.0202	0.0501
1935	0.0293	0.0125	0.0461	0.0240	0.0552
1936	0.0194		0.0298	0.0296	0.0781
1937	0.0248		0.0359	0.0454	0.0947

Table 11.1: Devotion (fraction of arms expenditures to GNP) by country.

fact is much easier than trying to acquire accurate data before an impending conflict. When war looms, nations are not about to reveal how much they are spending on arms.

Saperstein's first model was a bilateral one, involving the arms race between two nations. Although an oversimplification for the situation in the 1930s where several major countries were involved and alliances were being formed, the model is a good starting point for understanding Saperstein's ideas.

Consider two nations X and Y that are involved in an arms race and let x_n and y_n be their respective devotions in budget cycle n. Increasing n corresponds to increasing time increments (e.g., yearly in Table 11.1). It is reasonable to assume that the devotion of nation X in budget cycle $n+1$ is proportional to Y's devotion in the previous budget cycle n, and vice versa, i.e.,

$$x_{n+1} \propto y_n \quad \text{and} \quad y_{n+1} \propto x_n. \tag{11.8}$$

As a further refinement, Saperstein assumed that if X's rival Y has such a high devotion that Y's resources are stretched to the breaking point in the previous budget cycle and no more resources are available, then X's devotion may be decreased (and vice versa). Saperstein's arms race model then takes the form (with $0 < a, b < 1$)

$$
\begin{aligned}
x_{n+1} &= 4\,a\,y_n\,(1 - y_n) \equiv F_a(y_n), \\
y_{n+1} &= 4\,b\,x_n\,(1 - x_n) \equiv F_b(y_n).
\end{aligned}
\tag{11.9}
$$

The range of the parameters a and b is such that the values of x_n and y_n will stay between 0 and 1 as n evolves. Notice how the right-hand sides of the model equations resemble those for the logistic model except they involve the devotions of the rival country.

The coupled equations (11.9) can be solved iteratively. For given a and b, suppose the devotions x_0 and y_0 are specified at $n = 0$. Then at $n = 1$, $x_1 = 4\,a\,y_0\,(1 - y_0)$ and $y_1 = 4\,b\,x_0\,(1 - x_0)$. Using x_1 and y_1, the values of x_2 and y_2 are calculated, and so on.

The values of a and b for the countries listed in Table 11.1 can be estimated as follows. Consider, for example, France (X) and Germany (Y) and take 1934 to correspond to $n = 0$ and 1935 to $n = 1$. Then, from Table 11.1,

$$x_0 = 0.0276, \quad y_0 = 0.0104, \quad x_1 = 0.0293, \quad y_1 = 0.0125,$$

so that

$$a = \frac{x_1}{4\,y_0\,(1 - y_0)} = 0.712 \quad \text{and} \quad b = \frac{y_1}{4\,x_0\,(1 - x_0)} = 0.116.$$

Table 11.2 shows the various a and b values calculated in a similar manner from the data of Table 11.1. Note that the estimated value of a for the USSR–Germany arms race exceeds the maximum value allowed in the model equations.

Before applying Saperstein's bilateral arms race model to the data of Tables 11.1 and 11.2, let's establish some basic ideas. First, we can eliminate the devotion variable y from Equations (11.9) by letting $n \to n+1$ in the first equation and using the second,

$$x_{n+2} = 4\,a\,y_{n+1}\,(1 - y_{n+1}) = 16\,a\,b\,x_n\,(1 - x_n)(1 - 4\,b\,x_n\,(1 - x_n)), \tag{11.10}$$

or, in more compact functional notation,

$$x_{n+2} = F_a(y_{n+1}) = F_a(F_b(x_n)) \equiv F_{ab}(x_n). \tag{11.11}$$

Countries	Years Used in Estimate	a	b
France–Germany	1934–35	0.712	0.116
France–Italy	1936–37	0.214	0.472
UK–Germany	1934–35	0.582	0.158
UK–Italy	1934–35	0.142	0.582
USSR–Germany	1934–35	1.34	0.0657
USSR–Italy	1936–37	0.819	0.125

Table 11.2: Estimates of model parameters a and b.

Of course, we could have eliminated the devotion variable x instead of y, obtaining

$$y_{n+2} = F_b(F_a(y_n)) \equiv F_{ba}(y_n). \tag{11.12}$$

The fixed points of Equations (11.11) and (11.12) correspond to $x_{n+2} = x_n$ and $y_{n+2} = y_n$. Referring back to the general discussion of the stability of nonlinear "maps" in Chapter 3, these fixed points are stable if the absolute magnitude of the derivative of $F_{ab}(x)$ (or $F_{ba}(y)$) is less than unity. It doesn't matter whether F_{ab} or F_{ba} is considered, since if one of the pair of fixed points is stable, then so is the other. There cannot be predictability in one of the devotion variables and unpredictability in the other. Both parties to the arms race will be at peace or at war simultaneously.

Similarly x_n can be mapped into x_{n+4}, i.e., x values four time steps apart are connected, by applying F_{ab} a second time:

$$x_{n+4} = F_{ab}(x_{n+2}) = F_{ab}(F_{ab}(x_n)) \equiv F_{ab}^{(2)}(x_n). \tag{11.13}$$

Similarly,

$$y_{n+4} = F_{ba}(y_{n+2}) = F_{ba}(F_{ba}(y_n)) \equiv F_{ba}^{(2)}(y_n). \tag{11.14}$$

The fixed points $x_{n+4} = x_n$ and $y_{n+4} = y_n$ are stable if the absolute magnitude of the derivative of $F_{ab}^{(2)}(x)$ (or $F_{ba}^{(2)}(y)$) is less than unity.

As the parameter b is increased from 0 for fixed a, the fixed points of F_{ab} and F_{ba} are stable. Increasing b further, these fixed points lose their stability and the fixed points of $F_{ab}^{(2)}$ and $F_{ba}^{(2)}$ become stable. Increasing b leads to a sequence of period doublings until a critical threshold is reached where the chaotic regime sets in. Since the parameter a can also be varied, the critical threshold is a curve in the a–b parameter plane.

In the periodic regime, the asymptotic evolution of the devotion variables for given initial conditions is entirely predictable and is not sensitive to small changes in these conditions. When chaos sets in, the outcome is extremely sensitive to changes in the initial values. The critical threshold at which chaos and unpredictablilty occur is interpreted as signaling the onset of war.

The following examples demonstrate how analysis of the stability of the fixed points may be used to predict the asymptotic (large n) behavior of the devotions and how the critical threshold is established.

Example 11-6: Stable Fixed Point

Taking $a = 0.8$, $b = 0.4$, $x_0 = 0.01$, and $y_0 = 0.05$, show that $x_{n+2} = x_n$ has two fixed points $\bar{x}$, one of which is stable, the other being unstable. Iterating the model equations (11.9) and plotting x_n versus n, show that x approaches the stable fixed point for large values of n. Confirm that y_n also approaches a fixed point.

Solution: From Equation (11.10), the fixed points $\bar{x}$ are the solutions of

$$F_{ab}(\bar{x}) = 16\,a\,b\,\bar{x}\,(1 - \bar{x})(1 - 4\,b\,\bar{x}\,(1 - \bar{x})) = \bar{x}.$$

Numerically solving this equation with $a = 0.8$ and $b = 0.4$ yields $\bar{x} = 0$ and $\bar{x} \approx 0.708$.

Calculating the slope $dF_{ab}(x)/dx$ for general a and b yields

$$\frac{dF_{ab}(x)}{dx} = 16\,a\,b\,(1 - x)\,(1 - 4\,b\,x\,(1 - x)) - 16\,a\,b\,x\,(1 - 4\,b\,x\,(1 - x))$$

$$+ 16\,a\,b\,x\,(1 - x)\,(-4\,b\,(1 - x) + 4\,b\,x).$$

With $a = 0.8$, $b = 0.4$, the first fixed point $(\bar{x} = 0)$ yields the slope 5.12, while the second fixed point $(\bar{x} = 0.708)$ yields the slope -0.722. The first fixed point has a
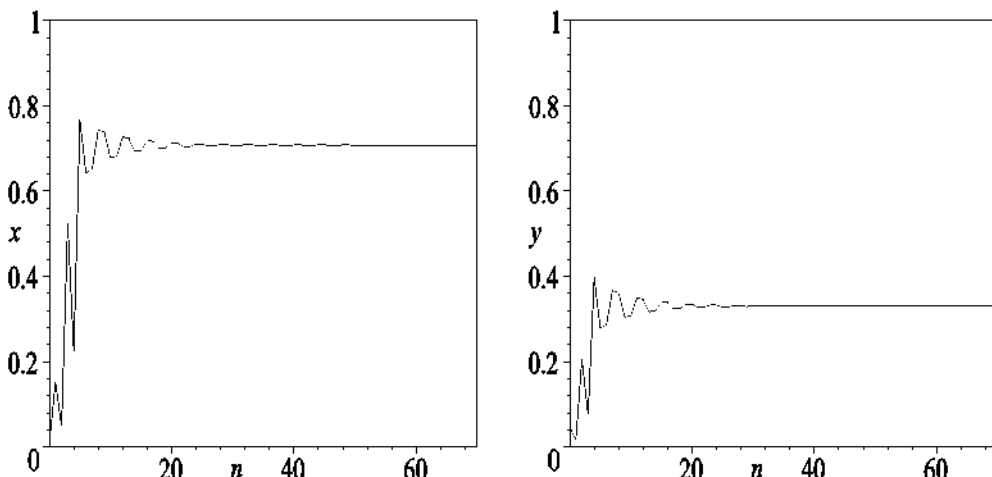
Figure 11.11: Left: Devotion of country X. Right: Devotion of country Y.

slope whose magnitude is greater than 1 so is unstable, while the second fixed point has a slope whose magnitude is less than 1, so is stable. As $n \to \infty$, we expect that $x \to 0.708$. To confirm that this prediction is correct, Equations (11.9) are iterated for $a = 0.8$, $b = 0.4$, $x_0 = 0.01$, and $y_0 = 0.05$ and the devotion of country X (i.e., x_n) plotted versus n for $n = 0$ to 70 on the left of Figure 11.11. This devotion approaches $\bar{x} = 0.708$, as expected. Similarly, referring to the plot on the right of Figure 11.11, the devotion of country Y approaches the fixed point $\bar{y} = 0.331$ (to three figures).

<div align="center">***</div>

Example 11-7: Period Doubling

If the parameter b is increased to $b = 0.86$ with all other parameter values and initial conditions the same as in the last example, show that a period doubling takes place, x_n asymptotically oscillating between two stable fixed points.

Solution: With $a = 0.8$ and $b = 0.86$, the fixed points of $F_{ab}(\bar{x}) = \bar{x}$ are $\bar{x} = 0$ and $\bar{x} \approx 0.427$ with respective slopes of (approximately) 11 and -1.1. Since the magnitudes of both slopes are larger than unity, these fixed points are unstable.

The fixed points $\bar{x}$ of $x_{n+4} = x_n = \bar{x}$ are obtained by numerically solving

$$F_{ab}^{(2)}(\bar{x}) = F_{ab}(F_{ab}(\bar{x})) = \bar{x},$$

with $a = 0.8$ and $b = 0.86$. There are four fixed points, whose $\bar{x}$ values are shown in the following table. The corresponding slopes $dF_{ab}^{(2)}(x)/dx$ at these fixed points are also given, along with the stability of the fixed point.

Fixed point ($\bar{x}$)	Slope	Stability
0	121.2	unstable
0.390	0.590	stable
0.427	1.21	unstable
0.476	0.590	stable

Asymptotically, x_n will oscillate between the two stable fixed points, indicative of period doubling. This can be confirmed by numerically solving the model equations (11.9) and plotting x_n versus n. This is left as a problem for the reader.

<div align="center">***</div>

As b is further increased with a held fixed at $a = 0.8$, a sequence of further period doubling takes place until around $b \approx 0.90$, chaos sets in. This is illustrated in the following example.

Example 11-8: Chaos

Increasing b further to 0.90 and holding all other parameter values and initial conditions the same as in the previous two examples, numerically solve Equations (11.9) and plot the devotion of country X over the range $n = 0$ to 150. Discuss the plot.

Solution: Iterating Equations (11.9) and plotting the values of x_n as a function of n, we obtain the result shown in Figure 11.12. There is no apparent periodic pattern to
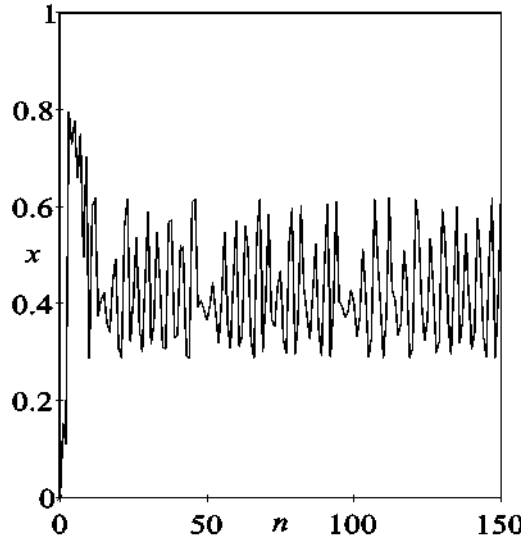
Figure 11.12: Devotion of country X for $a = 0.8, b = 0.90$.

the temporal evolution of country X's devotion. Taking even larger values of n confirms the chaotic behavior of the solution. If y_n were plotted versus n, it would also display chaotic behavior. This makes sense. One country can't slide into chaos (war) without its rival also doing so.

It should be noted that starting with $x_0 = 0.01$, $y_0 = 0.05$, the first iteration of the equations yields $x_1 = 0.1520$, $y_1 = 0.03564$. Country X has noted that Y spent 5 times as much on arms in the previous budget cycle and has increased its spending 15 times in the following budget. Country Y has actually cut back slightly but too late to prevent the *crisis instability* from developing. This acting too late to dampen a potentially explosive situation seems to happen all too often in human interactions, whether between countries or between individuals.

<div align="center">***</div>

Saperstein has obtained the approximate critical threshold curve for the onset of chaos in the bilateral arms race model, this curve being shown in Figure 11.13.
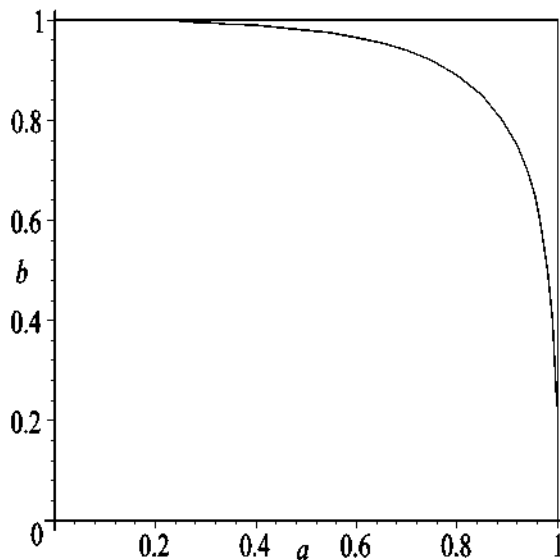
Figure 11.13: Threshold curve for the onset of chaos.

Referring to the a and b values of Table 11.2, Saperstein concluded that the USSR–Germany arms race was already in the chaotic regime and the France–Germany and Italian–Soviet arms races were close to the critical threshold. World War II broke out shortly thereafter.

Of course this calculation was done long after the onset of World War II and it is much easier to account for events in hindsight than to accurately predict the future. More importantly, the model suffers from being purely bilateral and should be generalized to include more countries.

Saperstein has created a tripolar (three-country) model which is a simple generalization of the bilateral one. Calling the third country Z, the tripolar equations are

$$x_{n+1} = 4\,a\,y_n\,(1 - y_n) + 4\,\epsilon\,z_n\,(1 - z_n),$$

$$y_{n+1} = 4\,b\,x_n\,(1 - x_n) + 4\,\epsilon\,c\,z_n\,(1 - z_n), \qquad (11.15)$$

$$z_{n+1} = 4\,\epsilon\,x_n\,(1 - x_n) + 4\,\epsilon\,c\,y_n\,(1 - y_n),$$

with two additional parameters ϵ and c. The stability analysis for a 3-dimensional nonlinear map is considerably more difficult than for a two-dimensional one, so no attempt will be made to present such an analysis here.

However, it is easy to iterate Equations (11.15) for given parameter and initial values. This is illustrated in the following example.

Example 11-9: Tripolar Model

Taking the same values

$$a = 0.8, \quad b = 0.86, \quad x_0 = 0.01, \quad y_0 = 0.05$$

as in the period doubling example, choose

$$\epsilon = 0.2, \quad c = 0.2, \quad z_0 = 0.02$$

in the tripolar model.

Then, iterate Equations (11.15) with these values and plot the devotion of country X as a function of increasing budget cycle n. Discuss the result.

Solution: We obtain Figure 11.14. For the bilateral case, a periodic solution emerged for $b = 0.86$. Including the third country lowers the threshold curve and chaos results instead. Inclusion of more countries leads to a greater chance of crisis instability.
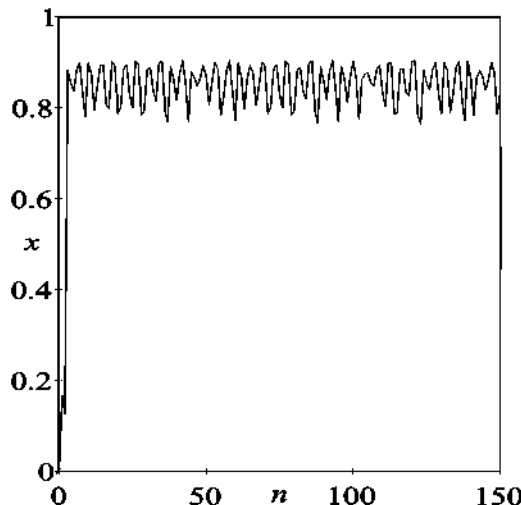
Figure 11.14: Chaotic evolution of country X's devotion in the tripolar model.

***

Saperstein applied the comparison of the bipolar and tripolar models to modern times and concluded that a tripolar world is more dangerous than a bipolar one. The latter was the prevailing situation when the world arms race was dominated by the United States and the Soviet Union.

11.2.4 The Dynamics of Warfare: Lanchester Equations

The English polymath and engineer Frederick W. Lanchester (1868–1946) made important contributions to automotive engineering,[8] aerodynamics, and co-invented the field of operations research. He was also among the first to attempt to mathematically model warfare with the goal of attempting to predict the outcome of military encounters ([Lan16], [Lan56]). Lanchester produced two famous laws, which bear his name:

- *Lanchester Square Law;*

- *Lanchester Linear Law.*

These laws were intended to apply to *aimed fire* encounters and *unaimed fire* situations, respectively.

Aimed fire describes the situation where the shooter aims directly at an enemy (e.g., rifle duels, tank combat, air-to-air combat). If/when that enemy is eliminated, the shooter then fires on a new target. As targets are eliminated, the firepower of the shooters is concentrated more and more on the remaining targets. The Lanchester "linear warfare" equations for estimating casualty rates for this situation are

$$\dot{R} = -k_B\, B(t), \quad R(0) = R_0,$$
$$\dot{B} = -k_R\, R(t), \quad B(0) = B_0, \tag{11.16}$$

where $R(t)$ and $B(t)$ are the numerical strengths of opposing Red and Blue forces at time t and k_B and k_R are the *killing rates* of Reds by Blues and Blues by Reds.

These equations led to the Lanchester square law,

$$k_R\, R^2 - k_B\, B^2 = k_R\, R_0^2 - k_B\, B_0^2. \tag{11.17}$$

Example 11-10: Lanchester Square Law

Derive the Lanchester square law. If $R_0 = 200$ soldiers, $B_0 = 100$ soldiers, $k_R = 0.01$, and $k_B = 0.03$, which force is the stronger side, Reds or Blues? How many soldiers remain on the stronger side when the weaker side is reduced to zero?

Solution: Multiplying the first ODE in (11.16) by $2\,k_R\,R$ and the second by $2\,k_B\,B$, and subtracting, yields

$$2\,k_R\,R\,\dot{R} - 2\,k_B\,B\,\dot{B} = \frac{d}{dt}\left(k_R\,R^2 - k_B\,B^2\right) = 0.$$

Integrating and applying the initial conditions yields the Lanchester square law.
  Using the given values we have

$$k_R\, R_0^2 = 0.01 \times (200)^2 = 400 \quad \text{and} \quad k_B\, B_0^2 = 0.03 \times (100)^2 = 300.$$

---

[8]His automobile inventions include the gas engine starter, rack-and-pinion steering, disk brakes, four-wheel drive, and fuel injection.

Since $k_R R_0^2 > k_B B_0^2$, the Red army is stronger. Although the blues have a higher killing rate, the strength scales with the *square* of the number of troops, thus giving the Reds the superiority.

The number of Red soldiers remaining when $B = 0$ is

$$R = R_0 \sqrt{1 - (k_B B_0^2)/(k_R R_0^2)} = 200 \sqrt{1 - 300/400} = 100.$$

<center>***</center>

According to Engel ([Eng54]), Lanchester's linear warfare equations, including a time-dependent reinforcement term on the American side (the Japanese were isolated and received no reinforcements), can be successfully applied to the Battle of Iwo Jima, one of the fiercest battles of World War II.

A well-known strategy of warfare is to divide the opposition troops in order to conquer them. This is now illustrated using the Lanchester square law.

Example 11-11: Divide and Conquer

The commander of the Blues in the previous example deceives the Reds commander into thinking that the Blues will attack from two different geographic locations. The Reds commander splits his army into two groups, sending off 50 Red troops to the other (erroneously) perceived point of attack. The Blues commander with his entire complement of 100 troops attacks the remaining 150 Reds. Assuming the square law applies and they all fight to the death, what happens in this encounter? What should the winning commander of this first encounter do?

Solution: In this case, we have $k_R R_0^2 = 0.01 \times (150)^2 = 225$, while $k_B B_0^2 = 300$ as before. Now the Blues have the superiority because of their greater killing ability. The number of Blues remaining after this battle will be

$$B = B_0 \sqrt{1 - (k_R R_0^2)/(k_B B_0^2)} = 100 \sqrt{1 - 225/300} = 50.$$

If the 50 remaining Blues now attack the remaining 50 Reds in the other group, the Blues will win because of their greater killing ability. As already mentioned, the concept of *divide and conquer* is a familiar strategy in warfare.

<center>***</center>

Turning now to unaimed fire, this refers to the situation when a shooter is firing upon an area in which the enemy is presumed to be. Unlike aimed fire, the shooter's fire remains directed at the area as a whole, the shooter not knowing the precise location of the targets and whether they have been hit. Examples of unaimed fire are artillery barrages and carpet bombing.

We shall now obtain Lanchester's linear law for unaimed fire. The basic ODEs (11.16) must be modified to reduce the attrition by the ratio of the numbers of remaining

live targets to the total initial targets. This yields the nonlinear ODE system

$$\frac{dR}{dt} = -k_B\, B(t) \left(\frac{R(t)}{R_0} \right), \quad R(0) = R_0,$$
$$\frac{dB}{dt} = -k_R\, R(t) \left(\frac{B(t)}{B_0} \right), \quad B(0) = B_0. \tag{11.18}$$

Multiplying the first ODE by $k_R\, R_0$, the second by $k_B\, B_0$, subtracting, and integrating, yields the Lanchester linear law,

$$k_R\, R_0\, (R - R_0) = k_B\, B_0\, (B - B_0). \tag{11.19}$$

It is called the linear law because R and B now only appear to the first power. It may seem a bit strange that Lanchester's linear model equations yield a law which is nonlinear (quadratic) in R and B, while the nonlinear model equations yield a linear law. Now let's redo Example 10-10 assuming that Lanchester's linear law is applicable.

Example 11-12: Lanchester Linear Law

If $R_0 = 200$ soldiers, $B_0 = 100$ soldiers, $k_R = 0.01$, and $k_B = 0.03$, how many soldiers remain in the Red army when the Blue army is reduced to zero? Compare the result to that predicted for the Lanchester square law.

Solution: When $B = 0$, we have

$$R = R_0 \left(1 - \frac{k_B\, B_0^2}{k_R\, R_0^2} \right) = 200 \left(1 - \frac{300}{400} \right) = 50 \text{ soldiers.}$$

Fewer Red soldiers survive here than when the square law is applied.

***

Chen and Chu ([CC01]) have applied Lanchester's linear law to the analysis of the World War II battle of Ardennes. Because human battles generally involve so many factors (varying terrain, elements of surprise and deception, morale and fatigue, retreats and advances, reinforcements and supplies, competent and incompetent leadership, and so on) it is not surprising that the simple Lanchester models are generally inadequate to describe the outcomes of most battles. The Lanchester models have been generalized[9] and even extended by Deitchman ([Dei62]) and Schaffer ([Sch67]) to include tactics employed in guerilla warfare.

11.2.5 War of the Fire Ants

To minimize or eliminate the many factors involved in human battles, Plowes and Adams ([PA05]) turned to nonhuman animals, carrying out controlled laboratory experiments involving battles of the fire ant *Solenopsis invicta*. Worker fire ants fight in groups with

---

[9] Artelli and Deckro (**www.scs.org/pubs/jdms/vol5num1/Artelli.pdf**.) and Jaiswal ([Jai97]).

lethal results, when defending territory or food resources. In replicated experiments, workers of various sizes from neighboring warring colonies were mixed in different ratios of initial numbers. The ants were place in plastic cups with high, steep, slippery sides so that they could not retreat or recruit new fighters. To identify the two warring groups, the ants on each side were sprayed with a different colored dye which could be identified under fluorescent light. The battles were allowed to go on for 24 hours and then the number of casualties (dead ants) on both sides counted.

Again calling the two opposing groups Reds and Blues, a generalization of the Lanchester equations was considered, the model equations taking the form

$$\dot{R} = -\alpha_R^{(1-n)} \alpha_B R^{(2-m)} B, \quad R(0) = R_0,$$
$$\dot{B} = -\alpha_R \alpha_B^{(1-n)} R B^{(2-m)}, \quad B(0) = B_0. \tag{11.20}$$

Here, R is the number of Reds surviving, α_R is their individual fighting ability, B is the number of Blues surviving, α_B is their individual fighting ability, and m and n are parameters. For Lanchester's square law, $m = 2$, while for Lanchester's linear law, $m = 1$.

Example 11-13: A Generalized Lanchester Law

Show that the following ratio r holds at any instant in time for the nonlinear ODE system (11.20):

$$r = \frac{R^m - (R_0)^m}{B^m - (B_0)^m} = \left(\frac{\alpha_B}{\alpha_R}\right)^n. \tag{11.21}$$

What condition must be satisfied for the Reds group to have the greater fighting ability and, hence, the lower per capita death rate?

Solution: Multiplying the first ODE in (11.20) by $(\alpha_R)^n R^{m-1}$, the second ODE by $(\alpha_B)^n B^{m-1}$, subtracting, and integrating subject to the initial conditions, yields

$$(\alpha_R)^n R^m - (\alpha_B)^n B^m = (\alpha_R)^n (R_0)^m - (\alpha_B)^n (B_0)^m.$$

The ratio given in (11.20) follows on rearranging the terms in the above equation.

The Reds have the greater fighting ability if $(\alpha_R)^n R^m > (\alpha_B)^n B^m$.

***

In the laboratory experiments, battles were carried out using different physical sizes of ants and different initial ratios of warring ants on the two opposing sides. For each case, the battles were replicated two or three times according to the number of available ants. The design of the experiment was such that m and r could be estimated by dead body counts. The parameter n could not be determined because the relative individual fighting abilities of different sizes of ants could not be conclusively determined.

The mean value of the estimates of m was 1.04, i.e., very close to the value of 1 to be expected if Lanchester's linear law prevails.

To complete this brief introduction to the dynamics of warfare, we should mention the interesting qualitative paper of Linda Beckerman available on the Internet (**www.calresco.org/beckermn/nonlindy.htm**). It provides many interesting historical examples which support the thesis that warfare can often be nonlinear in nature, with outcomes in battles and campaigns not linearly proportional to inputs (e.g., amount of manpower or number of weapons) and multiple possible states (a sign of nonlinearity) available which commanders must choose from to maximize their chance of success.

PROBLEMS

Problem 11-1: Period-two solution for Saperstein's arms race model
For Saperstein's arms race model, solve the model equations for $a = 0.8$, $b = 0.86$ and initial conditions $x_0 = 0.01$, $y(0) = 0.05$. Taking a sufficient number n of iterations, demonstrate that a period-two solution occurs. Plot the devotion of each country as a function of n.

Problem 11-2: The OODA loop
The OODA (acronym for "Observe, Orient, Decide, and Act") loop is a nonlinear feedback loop that has been applied to the combat operations process, often at the strategic level in both military and commercial operations. The OODA loop concept was developed by the American fighter pilot and military strategist Colonel John Boyd (1927–1997). To win in any engagement, one must execute one's own OODA loop faster than one's opponent. By going to the Internet (there are numerous web sites) discuss the OODA loop in detail, providing a flow diagram indicating the detailed pathways of the feedback loop. Provide some real-world examples.

Problem 11-3: Richardson arms race model with a carrying capacity
Budget constraints can be placed on nations X and Y in the Richardson arms race model by introducing carrying capacity terms for each country. The modified Richardson model is given by the equations

$$\dot{x} = \left(1 - \frac{x}{x_{max}}\right)(a\,y - m\,x + r),$$
$$\dot{y} = \left(1 - \frac{y}{y_{max}}\right)(b\,x - n\,y + s).$$

a. Taking $a = 1.0$, $b = 1.2$, $m = 0.9$, $n = 0.8$, $r = 1.0$, $s = -2.0$, $x_{max} = 7.0$, and $y_{max} = 9.0$, create a phase-plane portrait for this arms race model with several different trajectories. Discuss the results.

b. By creating a tangent field plot for $x_{max} = y_{max} = \infty$ and comparing with the plot in part (a), discuss how including a finite capacity affects the results.

c. Explore other values of the parameters and discuss the results.

Problem 11-4: Lower Slobovia versus Upper Slobovia
The armies of two warring countries, Lower Slobovia (X) and Upper Slobovia (Y), are

modeled by the following competition equations:

$$\dot{x} = a\,x - b\,x\,y,$$

$$\dot{y} = (a+1)\,y - \gamma\,b\,x\,y,$$

with a and b both positive and $\gamma > 1$. Here x and y are the numbers of troops in the armies of Lower and Upper Slobovia, respectively.

a. Discuss the structure of the equations and suggest how improvements could be made in the model.

b. Locate and identify all the fixed points of this system.

c. Make a tangent field plot which includes both fixed points and some representative trajectories. Take $a = 5$, $\gamma = 1.15$, and $b = 1/2500$.

d. Discuss possible outcomes on the basis of the above picture.

Problem 11-5: Estimating Holling type II parameters
In a controlled experiment, predators were kept in large cages (cage area 10 m^2), one predator per cage. Different numbers of prey were released in these cages and the number of surviving prey in each cage counted at the end of the experiment. The duration of the experiment was $T = 2$ days. To reduce the error, more replications were carried out at low prey densities than at high densities. The experimental data is as follows:

Number of prey per cage	Number of replications	Total prey killed	Average number of prey killed (x_c)	$Y \equiv 1/x_c$	$X \equiv 1/(x\,T)$ m^2/days
5	20	50	2.5	0.400	1.000
10	10	40	4.0	0.250	0.500
20	7	55	?	?	?
40	5	45	?	?	?
80	3	38	?	?	?
160	3	35	?	?	?

a. Complete the table by filling in the question marks.

b. Plot the experimental points $\left(X \equiv \dfrac{1}{(x\,T)},\, Y \equiv \dfrac{1}{x_c}\right).$

c. Setting $\alpha = 1/A$ and $\beta = T_{ht1}/T$ we have, from Example 10-1, the straight-line relation

$$Y = \alpha X + \beta.$$

Determine α and β by using the least squares method to find the best-fitting straight line to the experimental points.

d. Plot the best-fitting straight line in the same figure as the experimental points.

e. Determine the handling time, T_{ht1}, for one prey and the area of discovery, A.

f. Finally, determine the parameters m and a in the Holling type II predation term.

Problem 11-6: Holling type III predation

Repeat the steps in Example 10-2, for Holling type III predation, taking the same parameter values and initial conditions as in the example. Compare the results for the two different types of predation. Explore other parameter values and initial conditions to see if any interesting differences occur for the two different predation types.

Problem 11-7: Holling type I Predation

Example 10-2 reduces to type I predation if one sets $a = 0$. Taking all other parameter values and the initial conditions to be the same, repeat the steps in the example. Compare the results for the two different predation types.

Problem 11-8: Attrition warfare

Attrition warfare refers to the attempt by one side in a war to wear down its enemy to the point of collapse through continual losses in manpower and material. Such was the successful strategy of Ulysses Grant of the Union army in defeating the Confederate army in the latter part of the American Civil War.

By performing an Internet or literature search, cite other historic wars/battles where attrition warfare strategy was used. For which of the cited wars/battles was this strategy successful? unsuccessful? Suggest reasons in each case for the success, or lack of success, of an attrition warfare approach. You should consider such factors as killing power, maneuverability, divide-and-conquer strategy, the Lanchester laws, and so on.

Problem 11-9: Modeling the Lanchester laws with systems dynamics

Discuss in some detail the main ideas and examples contained in the paper entitled "Modeling the Lanchester Laws with Systems Dynamics" by Artelli and Deckro available at:

www.scs.org/pubs/jdms/vol5num1/Artelli.pdf.

Problem 11-10: Coevolutionary arms race

By performing an Internet or literature search, cite and discuss other examples in nature of the coevolutionary arms race.

Problem 11-11: The nonlinear dynamics of war

Discuss in some detail the main ideas and examples contained in the paper entitled "The Nonlinear Dynamics of War" by Linda Beckerman available on the Internet at:

www.calresco.org/beckermn/nonlindy.htm.

Problem 11-12: International relations

In the paper "Control Mechanisms for a Nonlinear Model of International Relations," Áron Péntek, Jim Kadtke, Suzanne Lenhart, and Vladimir Protopopescu apply control mechanisms to a discrete nonlinear model of a multination arms race. They consider two control mechanisms: a short-range reactive control based on the chaos control idea and a long-term strategic control based on an optimal control algorithm.

Discuss this paper in some detail. It is available online at:

www.osti.gov/bridge/servlets/purl/541860-7Usbf0/webviewable/.

Problem 11-13: Swarming and the future of warfare

Quoting from Sean Edwards's doctoral thesis ("Swarming and the Future of Warfare," Sept. 2004, Pardee Rand Graduate School):

Whenever military operations are non-linear, dispersed, and decentralized, swarming is an effective tactic. Today insurgents are employing swarming as a form of asymmetric warfare against superior conventional armies from the mountains of Afghanistan to the cities of Iraq. Swarming occurs when several units conduct a convergent attack on a target from multiple axes.

Consulting Edwards's thesis which is available online at:

www.rand.org/pubs/rgs_dissertations/RGSD189/index.html,

discuss swarming theory with historical examples. Include in your discussion the five primary variables that the author considers to be the most important to successful swarming.

Problem 11-14: Mathematical models of civil war

Quoting from the research work "The Devil's Calculus: Mathematical Models of Civil War" by Ajay Shenoy:

In spite of the movement to turn political science into a real science, various mathematical methods that are now the staples of physics, biology, and even economics are thoroughly uncommon in political science, especially the study of civil war. This study seeks to apply such methods - specifically, ordinary differential equations (ODEs) - to model civil war based on what one might dub the capabilities school of thought, which roughly states that civil wars end only when one side's ability to make war falls far enough to make peace truly attractive. I construct several different ODE-based models and then test them all to see which best predicts the instantaneous capabilities of both sides of the Sri Lankan civil war in the period from 1990 to 1994 given parameters and initial conditions.

Consulting Shenoy's paper which is provided online by the Munich Personal RePEc Archive,

http://mpra.ub.uni-muenchen.de/8895/1/MPRA_paper_8895.pdf,

discuss the mathematical models that are provided and the conclusions that are drawn.

Problem 11-15: The battle of Britain
The application of a Lanchester-type model to data available for the World War II battle of Britain has been published in *Naval Research Logistics* (published online: 16 Dec. 2008) by Ian Johnson and Niall MacKay. A reprint of the paper is available on the web site:

http://www-users.york.ac.uk/~nm15/LanchBoBv3.pdf

and a discussion at:

http://www.ima.org.uk/Conferences/defence09_mackay.pdf.

Discuss this paper in detail.

Problem 11-16: The drug war
Discuss and critique the paper "Using Dynamic Models to Investigate Drug Propagation" by Bradley Boven, Michael Pflug, and Travis Robey available online at:

http://max.cs.kzoo.edu/~bboven/drug_dynamics.pdf.

Problem 11-17: Evolution of cooperation
An important application of game theory is to the evolution of cooperation between potentially conflicting parties (people, businesses, nations, ...). The basic question is: "When should a party cooperate, and when should a party be selfish?"

According to Robert Axelrod, a good example is the situation where two industrial nations have set up trade barriers to each other's exports. Quoting from his paper[10] "Evolution of Cooperation":

Because of the mutual advantages of free trade, both countries would be better off if these barriers were eliminated. But if either country were to eliminate its barriers unilaterally, it would find itself facing terms of trade that hurt its own economy. In fact, whatever one country does, the other country is better off retaining its own trade barriers. Therefore, the problem is that each country has an incentive to retain trade barriers, leading to a worse outcome than would have been possible had both countries cooperated with each other.

Consulting Axelrod's paper as well as the following,

- "The Evolution of Cooperation" by Axelrod and William Hamilton ([AH81]):

  citeseerx.ist.psu.edu/iewdoc/download?doi=10.1.1.147.9644.pdf,

- *The Evolution of Cooperation* ([Axe06]),

discuss the evolution of cooperation in detail, citing specific examples, and general conclusions. Be sure to include the game theory model, "Prisoner's Dilemma."[11]

---

[10]Available at: citeseerx.ist.psu.edu/viewdoc/download?doi=10.1.1.117.7463.pdf

[11]The origin of this game, involving two players, is attributed to Merrill Flood and Melvin Dresher of the Rand Corporation in 1950. The name "prisoner's dilemma" and the version with prison sentences as payoffs are due to Albert Tucker. Each player (prisoner) in the game has two choices, either remain silent ("cooperate") or inform on each other ("defect"). Each player must make the choice without knowing what the other will do.

Problem 11-18: Conflict resolution model

Whether referring to the work place or the student dormitory or international negotiations, a "hot" topic in the current literature and on the Internet is how to resolve conflict. Discuss the conflict resolution model presented at the following web site:

http://www.latrobe.edu.au/psy/research/eris/docs/conflict_res_model.pdf.

Explain what the term BATNA stands for in the model and cite specific examples of BATNA. The above conflict resolution model is based on comprehensive research-based information gathered by Eleanor Wertheim and her coworkers and presented in the text *Skills for Resolving Conflict* ([WLPL06]).

Problem 11-19: Conflict resolution for air traffic management

Because of technological advances, air traffic management of the future could allow the possibility of *free flight* in which aircraft choose their own optimal routes, altitude, and velocities. In a paper entitled "Conflict Resolution for Air Traffic Management: a Study in Multi-Agent Hydbrid Systems," Claire Tomlin, George Pappas, and Shankar Sastry ([TPS98]) deal with the issue of safe and fair resolution of trajectory conflicts between aircraft in free flight. Discuss this paper which is available online at Claire Tomlin's web site:

http://sun-valley.stanford.edu/~tomlin/.

Problem 11-20: Insurgencies

A mathematical model developed by Bohorquez et al. ([BGD⁺09]) suggests that human insurgencies have a common underlying pattern that may allow the timing of attacks and the number of casualties to be predicted. Consulting the cited reference, discuss this model.

Bibliography

[Ada90]   R. K. Adair. *The Physics of Baseball.* Harper and Row, New York, 1990.

[AF66]   M. Athans and P. L. Falb. *Optimal Control. An Introduction to the Theory and its Applications.* McGraw-Hill, New York, 1966.

[Agr89]   G. P. Agrawal. *Nonlinear Fiber Optics.* Academic Press, New York, 1989.

[AH81]   R. Axelrod and W. D. Hamilton. The evolution of cooperation. *Science,* 211:1390, 1981.

[AJMS81]   R. M. Anderson, H. C. Jackson, R. M. May, and A. M. Smith. Population dynamics of fox rabies in Europe. *Nature,* 289:765, 1981.

[AL82]   F. T. Arecchi and F. Lisi. Hopping mechanism generating $1/f$ noise in nonlinear systems. *Phys. Rev. Lett.,* 49:94, 1982.

[ALSB73]   J. Aroesty, T. Lincoln, N. Shapiro, and G. Boccia. Tumor growth and chemotherapy: mathematical methods, computer simulations, and experimental foundations. *Math. Biosc.,* 17:243, 1973.

[AM82]   R. Anderson and R. May. The logic of vaccination. *New Scientist,* November, 1982.

[AMMJ86]   R. M. Anderson, G. F. Medley, R. M. May, and R. M. Johnson. A preliminary study of the transmission dynamics of the human immunodeficiency virus (HIV), the causative agent of AIDS. *IMA J. Math. Appl. Med. Biol.,* 3:229, 1986.

[AMS+98]   P. Avan, P. Magnan, J. Smyrzynski, R. Probst, and A. Dancer. Direct evidence of cubic difference tone propagation by intercochlear acoustic pressure measurements in the guinea-pig. *Eur. J. Neurosci.,* 10:1764, 1998.

[AN86]   Y. Aizawa and I. Nishikawa. Toward the classification of the patterns generated by one-dimensional cell automata. In G. Ikegami, editor, *Dynamical Systems and Nonlinear Oscillations.* World Scientific, Singapore, 1986.

[And82]   R. M. Anderson. Directly transmitted viral and bacterial infections of man. In R. M. Anderson, editor, *Population Dynamics of Infectious Diseases, Theory and Applications*. Chapman and Hall, New York, 1982.

[ANST86]   S. V. Antipov, M. V. Nezlin, E. N. Snezhkin, and A. S. Trubnikov. Rossby autosoliton and stationary model of the Jovian Great Red Spot. *Nature*, 323:238, 1986.

[AR63]   P. W. Anderson and J. M. Rowell. Probable observation of the Josephson superconducting tunneling effect. *Phys. Rev. Lett.*, 10:230, 1963.

[AS72]   M. Abramowitz and I. A. Stegun. *Handbook of Mathematical Functions (AMS 55)*. National Bureau of Standards, Washington, DC, 1972.

[ASKS07]   T. Asai, K. Seo, O. Kobayashi, and R. Sakashita. Fundamental aerodynamics of the soccer ball. *Sports Eng.*, 10:101, 2007.

[AW96]   A. Aguzzi and C. Weissmann. Bovine spongiform encephalopathy: a suspicious signature. *Nature*, 383:666, 1996.

[AW97]   A. Aguzzi and C. Weissmann. Prion research: the next frontiers. *Nature*, 389:795, 1997.

[AW98]   A. Aguzzi and C. Weissmann. Spongiform encephalopathies: the prions perplexing persistence. *Nature*, 392:763, 1998.

[Axe06]   R. Axelrod. *The Evolution of Cooperation (revised edition)*. Basic Books, New York, 2006.

[Bak95]   G. Baker. Control of the chaotic driven pendulum. *Am. J. Phys.*, 63:832, 1995.

[Bar88]   M. Barnsley. *Fractals Everywhere*. Academic Press, San Diego, 1988.

[Bas69]   F. M. Bass. A new product growth model for consumer durables. *Management Science*, 15:215, 1969.

[Bat67]   G. K. Batchelor. *An Introduction to Fluid Dynamics*. Cambridge University Press, Cambridge, 1967.

[BC74]   G. W. Bluman and J. D. Cole. *Similarity Methods for Differential Equations*. Springer-Verlag, New York, 1974.

[BC90]   P. N. Butcher and D. Cotter. *The Elements of Nonlinear Optics*. Cambridge University Press, Cambridge, 1990.

[BCD02]   N. Bellomo, V. Coscia, and M. Delitala. On the mathematical theory of vehicular traffic flow I. Fluid dynamic and kinetic modelling. *Math. Models Methods Appl. Sci.*, 12:1801, 2002.

[Bea00]   D. H. Bearce. Economic sanctions and neural networks: forecasting effectiveness and re-considering cooperation. In Diana Richards, editor, *Political Complexity: Nonlinear Models of Politics.* University of Michigan Press, Ann Arbor, 2000.

[Bel58]   B. P. Belousov. Oscillation reaction and its mechanism. In *Collection of Abstracts on Radiation Medicine.* Medgiz, Moscow, 1958.

[BEMS71]   A. Barone, F. Esposito, C. J. Magee, and A. C. Scott. Theory and applications of the sine-Gordon equation. *Riv. Nuovo Cim.*, 1:227, 1971.

[BEP71]   I. P. Batra, R. H. Enns, and D. Pohl. Stimulated thermal scattering of light. *Physica Status Solidi*, (b) 48:11, 1971.

[Bet66]   A. Betz. *Introduction to the Theory of Flow Machines* (D. G. Randall, Trans.). Pergamon Press, Oxford, 1966.

[BF89]   R. L. Burden and J. D. Faires. *Numerical Analysis.* PWS-Kent Publishing Company, Boston, 4th edition, 1989.

[BFW81]   G. J. Butler, H. I. Freedman, and P. Waltman. Global dynamics of a selection model for the growth of a population with genotypic fertility differences. *J. Math. Biol.*, 12:25, 1981.

[BG91]   Y. Braiman and I. Goldhirsch. Taming chaotic dynamics with weak periodic perturbations. *Phys. Rev. Lett.*, 66:2545, 1991.

[BGD$^+$09]   J. C. Bohorquez, S. Gourley, A. R. Dixon, M. Spagat, and N. F. Johnson. Common ecology quantifies human insurgency. *Nature*, 462:911, 2009.

[BH80]   J. J. Beaman and J. K. Hedrick. Freight car harmonic response: a simplified nonlinear method. In R. V. Ramnath, J. K. Hedrick, and H. M. Paynter, editors, *Nonlinear System Analysis and Synthesis, Vol. 2.* ASME, 1980.

[BJ91]   J. Bloxham and A. Jackson. Fluid flow near the surface of Earth's outer core. *Rev. Geophys.*, 29:97, 1991.

[BJ92]   J. Bloxham and A. Jackson. Time-dependent mapping of the magnetic field at the core–mantle boundary. *J. Geophys. Res.*, 97:19537, 1992.

[BJ99]   E. D. Brodie and E. D. Brodie Jr. Predator-prey arms races. *Bioscience*, 49:557, 1999.

[BM63]   G. M. Baule and R. McFee. Detection of the magnetic field of the heart. *Am. Heart J.*, 66:95, 1963.

[BM82]   J. R. Beddington and R. M. May. The harvesting of interacting species in a natural ecosystem. *Sci. Am.*, November:62, 1982.

[BSG02]   G. Bub, A. Shrier, and L. Glass. Spiral wave generation in heterogeneous excitable media. *Phys. Rev. Lett.*, 88:Feb. 4, 2002.

[BSK+03]   U. H. Buzzi, N. Stergiou, M. J. Kurz, P. A. Hageman, and J. Heidel. Nonlinear dynamics indicates aging affects variability during gait. *Clin. Biomech.*, 18:435, 2003.

[Buc77]   J. Buckmaster. Viscous sheets advancing over dry beds. *J. Fluid Mech.*, 81:735, 1977.

[Buf00]   B. A. Buffett. Earth's core and the geodynamo. *Science*, 288:2007, 2000.

[BZ98]   M. R. Berenbaum and A. R. Zangerl. Chemical phenotype matching between a plant and its insect herbivore. *Proc. Natl. Acad. Sci. USA*, 95:13743, 1998.

[Cam87]   D. Campbell. Nonlinear science—from paradigms to practicalities. *Los Alamos Sci.*, 15:218, 1987.

[CC01]   P. S. Chen and P. Chu. Applying Lanchester's linear law to model the Ardennes campaign. *Naval Res. Logist.*, 8:653, 2001.

[CE80]   P. Collet and J. P. Eckmann. *Iterated Maps of the Interval as Dynamical Systems*. Birkhauser, Boston, 1980.

[CFL28]   R. Courant, K. Friedrichs, and H. Lewy. Uber die partiellen differenzengleichungen der mathematischen physik. *Math. Ann.*, 100:32, 1928.

[CFvN50]   J. G. Charney, R. Fjörtoft, and J. von Neumann. Numerical integration of the barotropic vorticity equation. *Tellus*, 2:237, 1950.

[CH80]   D. R. J. Chillingworth and R. J. Holmes. Dynamical systems and models for reversals of the earth's magnetic field. *Math. Geol.*, 12:41, 1980.

[Cha39]   S. Chandrasekhar. *An Introduction to the Study of Stellar Structure*. Dover Reprint, Chicago, 1939.

[Chr69]   M. Chrichton. *The Andromeda Strain*. Alfred A. Knopf, New York, 1969.

[CHT97]   B. M. Clement, A. Holzheid, and A. Tilgner. Core geophysics. *Proc. Natl. Acad. Sci. USA*, 94(24):12472, 1997.

[Chu92]   L. O. Chua. The genesis of Chua's circuit. *Arch. Electron. Ubertragungstechnik*, 46:250, 1992.

[Chu94]   L. O. Chua. Chua's circuit: an overview ten years later. *J. Circuits Syst. Comput.*, 4:117, 1994.

[Coh67]   D. Cohen. Magnetic fields around the torso: production by electrical activity of the human heart. *Science*, 156:652, 1967.

[Coh72]   D. Cohen. Magnetoencephalography: detection of the brain's electrical activity with a superconducting magnetometer. *Science*, 175:664, 1972.

[Col51]   J. D. Cole. On a quasi-linear parabolic equation occurring in aerodynamics. *Q. Appl. Math.*, 9:225, 1951.

[Coo80]   N. K. Cooperrider. Nonlinear behavior in rail vehicle dynamics. In J. Holmes, editor, *New Approaches to Nonlinear Problems in Dynamics*. SIAM, Philadelphia, 1980.

[Cro03]   A. W. Crosby(Jr). *America's Forgotten Pandemic: The Influenza of 1918 (originally published in 1976 as Epidemic and Peace, 1918, by Greenwood Press)*. Cambridge University Press, Cambridge, 2003.

[CSS92]   J. J. Casciari, S. V. Sotirchos, and R. M. Sutherland. Mathematical modeling of microenvironment and growth in EMT6/Ro multicellular tumour spheroids. *Cell Proliferation*, 25:1, 1992.

[CTS64]   R. Y. Chiao, C. H. Townes, and B. P. Stoicheff. Stimulated Brillouin scattering and coherent generation of intense hypersonic waves. *Phys. Rev. Lett.*, 12:592, 1964.

[Cun64]   W. J. Cunningham. *Introduction to Nonlinear Analysis*. McGraw Hill, New York, 1964.

[Cvi84]   P. Cvitanovic. *Universality in Chaos*. Adam Hilger, Bristol, 1984.

[Dav62]   H. T. Davis. *Introduction to Nonlinear Differential and Integral Equations*. Dover, New York, 1962.

[DCPS08]   D. H. Douglass, J. R. Christy, B. D. Pearson, and S. F. Singer. A comparison of tropical temperature trends with model predictions. *Int. J. Climatol.*, 27:1519, 2008.

[Dei62]   S. J. Deitchman. A Lanchester model of guerilla warfare. *Oper. Res.*, 10:818, 1962.

[Den98]   M. Denny. Curling rock dynamics. *Can. J. Phys.*, 76:295, 1998.

[Den03]   M. Denny. Comment on "The motion of a curling rock". *Can. J. Phys.*, 81:877, 2003.

[Die75]   K. Dietz. Transmission and control of arborvirus diseases. In D. Ludwig and K. L. Cooke, editors, *Epidemiology, SIMS 1974 Utah Conference Proceedings*. SIAM, Philadelphia, 1975.

[DNS99]   J. P. Dunne, E. Nikolaidou, and R. P. Smith. Arms race models and econometric applications. In *The Arms Trade, Security and Conflict, Conference at Middlesex University Business School*. Middlesex University Business School, 1999.

[Dra92]   P. G. Drazin. *Nonlinear Systems*. Cambridge University Press, Cambridge, 1992.

[DRS90]   W. L. Ditto, S. N. Rauseo, and M. L. Spano. Experimental control of chaos. *Phys. Rev. Lett.*, 65:3211, 1990.

[dWKV⁺98]   G. A. de Wijs, G. Kress, L. Vocadlo, D. Dobson, A. Alfe, M. J. Gillan, and G. D. Price. The viscosity of liquid iron at the physical conditions of the earth's core. *Nature*, 392:805, 1998.

[Ede61]   M. Eden. A two-dimensional growth process. In J. Neyman, editor, *Proceedings of the Fourth Berkeley Symposium on Mathematical Statistics and Probability, Volume IV: Biology and Problems of Health*. University of California Press, Berkeley, 1961.

[EE95]   D. E. Edmundson and R. H. Enns. Particle-like nature of colliding 3-dimensional optical solitons. *Phys. Rev. A*, 51:2491, 1995.

[Egg97]   J. Eggers. Nonlinear dynamics and breakup of free-surface flows. *Rev. Mod. Phys.*, 69:865, 1997.

[EGSWO81]   M. Eigen, W. Gardiner, P. Schuster, and R. Winkler-Oswatitsch. The origin of genetic information. *Scientific American*, April:88, 1981.

[Eig71]   M. Eigen. Self-organization of matter and evolution of biological macromolecules. *Die Naturwissenschaften*, 58:465, 1971.

[EK88]   L. Edelstein-Keshet. *Mathematical Models in Biology*. Random House, New York, 1988.

[EM00]   R. H. Enns and G. C. McGuire. *Nonlinear Physics with Maple for Scientists and Engineers*. Birkhauser, Boston, 2000.

[EM01]   R. H. Enns and G. C. McGuire. *Nonlinear Physics with Mathematica for Scientists and Engineers*. Birkhauser, Boston, 2001.

[EM06]   R. H. Enns and G. C. McGuire. *Computer Algebra Recipes: An Introductory Guide to the Mathematical Models of Science*. Springer, New York, 2006.

[EM07]   R. H. Enns and G. C. McGuire. *Computer Algebra Recipes: An Advanced Guide to Scientific Modeling*. Springer, New York, 2007.

[Emd07]   R. Emden. *Gaskugeln: Anwendungen der Mechanischen Wärmetheorie auf Kosmologische und Meteorologische Probleme*. B. G. Teubner, Berlin, 1907.

[Emm77]   G. S. Emmerson. *John Scott Russell—A Great Victorian Engineer and Naval Architect*. John Murray, London, 1977.

[EMS88]   M. Eigen, John McCaskill, and Peter Schuster. Molecular quasi-species. *J. Phys. Chem.*, 92:6881, 1988.

[Eng54]   J. H. Engel. A verification of Lanchester's law. *Oper. Res.*, 2:163, 1954.

[ENM89]   J. M. Elzebda, A. H. Nayfeh, and D. T. Mook. Development of an analytical model of wing rock for slender delta wings. *J. Aircraft*, 26:737, 1989.

[ER79]   R. H. Enns and S. S. Rangnekar. The 3-wave interaction in nonlinear optics. *Physica Status Solidi*, (b) 94:9, 1979.

[Eva82]   A. S. Evans. *Viral Infections of Humans*, 2nd edition. Plenum Medical Book Company, New York, 1982.

[FC86]   G. R. Fowles and G. L. Cassiday. *Analytical Mechanics*. Saunders College Publishing, Orlando, 1986.

[fDC87]   U. S. Centers for Disease Control. Enterically transmitted non-A, non-B hepatitus–East Africa. *Morbidity and Mortality Weekly Report*, 36:241, 1987.

[Fea98]   Physics World Features. The physics of football. *Phys. World Mag.*, June 1:25, 1998.

[Fei79]   M. J. Feigenbaum. The universal metric properties of nonlinear transformations. *J. Stat. Phys.*, 21:69, 1979.

[Fei80]   M. J. Feigenbaum. Universal behavior in nonlinear systems. *Los Alamos Sci.*, 1:4, 1980.

[Fis37]   R. A. Fisher. The waves of advance of advantageous genes. *Ann. Eugenics*, 7:353, 1937.

[Fit61]   R. FitzHugh. Impulses and physiological states in theoretical models of nerve membrane. *Biophys. J.*, 1:445, 1961.

[FKN72]   R. J. Field, E. Körös, and R. M. Noyes. Oscillations in chemical systems, Part 2. Thorough analysis of temporal oscillations in the bromate–cerium-malonic acid system. *J. Am. Chem. Soc.*, 94:8649, 1972.

[FLS65]   R. P. Feynman, R. B. Leighton, and M. Sands. *The Feynman Lectures on Physics*. Addison-Wesley, Reading, MA, 1965.

[FN74]   R. J. Field and R. M. Noyes. Oscillations in chemical systems, IV. Limit cycle behavior in a model of a real chemical reaction. *J. Chem. Phys.*, 60:1877, 1974.

[FPU65]   E. Fermi, J. Pasta, and S. Ulam. Studies of nonlinear problems. In *Collected Papers of E. Fermi, Vol. 2*. University of Chicago Press, Chicago, 1965.

[Fro92]   J. Froyland. *Introduction to Chaos and Coherence*. CRC Press, New York, 1992.

[Fun55]   Y. C. Fung. *An Introduction to the Theory of Aeroelasticity*. John Wiley, New York, 1955.

[FW78]   H. I. Freedman and P. Waltman. Predator influence on the growth of a population with three genotypes. *J. Math. Biol.*, 6:367, 1978.

[FW98]   C. Flynn and N. Wilson. A simple method for controlling chaos. *Am. J. Phys.*, 66:730, 1998.

[Gar70]   M. Gardner. Mathematical games. *Sci. Am.*, 223 (10):120–0, 1970.

[Gar71a]   M. Gardner. Mathematical games. *Sci. Am.*, 224 (2):112, 1971.

[Gar71b]   M. Gardner. Mathematical games. *Sci. Am.*, 224 (4):117, 1971.

[Gau69]   G. F. Gause. *The Struggle for Existence*. Hafner, New York, 1969.

[GC09]   J. E. Goff and M. J. Carre. Trajectory analysis of a soccer ball. *Am. J. Phys.*, 77:1020, 2009.

[Gie81]   A. Gierer. Generation of biological patterns and form: Some physical, mathematical, and logical aspects. *Progr. Biophys. molec. Biol.*, 37:1, 1981.

[GM72]   A. Gierer and H. Meinhardt. A theory of biological pattern formation. *Kybernetik*, 12:30, 1972.

[GM79]   L. Glass and M. C. Mackey. Pathological conditions resulting from instabilities in physiological control systems. *Ann. N. Y. Acad. Sci.*, 316:214, 1979.

[GMP81]   M. Giglio, S. Musazzi, and V. Perini. Transition to chaotic behavior via a reproducible sequence of period-doubling bifurcations. *Phys. Rev. Lett.*, 47:243, 1981.

[GMR07]   G. Gandhi, B. Muthuswamy, and T. Roska. Chua's circuit for high school students. *Int. J. Bifurcation Chaos*, page 12, 2007.

[GOC04]   G. A. Glatzmaier, D. E. Ogden, and T. L. Clune. Modeling the earth's dyanamo. In R. S. J. Sparks and C. J. Hawkesworth, editors, *State of the Planet: Frontiers and Challenges in Geophysics*. IUGG, 2004.

[GP82]   L. Glass and R. Perez. Fine structure of phase locking. *Phys. Rev. Lett.*, 48:1772, 1982.

[GPS02]   H. Goldstein, C. Poole, and J. Safco. *Classical Mechanics,* 3rd edition. Addison Wesley, New York, 2002.

[GR65]   I. S. Gradshteyn and I. M. Ryzhik. *Tables of Integrals, Series, and Products.* Academic Press, New York, 1965.

[GR95a]   G. A. Glatzmaier and P. H. Roberts. A three-dimensional convective dynamo solution with rotating and finitely conducting inner core and mantle. *Phys. Earth Planet. Int.*, 91:63, 1995.

[GR95b]   G. A. Glatzmaier and P. H. Roberts. A three-dimensional self-consistent computer simulation of a geomagnetic field reversal. *Nature*, 377:203, 1995.

[GR96]   G. A. Glatzmaier and P. H. Roberts. An anelastic evolutionary geodynamo simulation driven by compositional and thermal convection. *Physica D*, 97:81, 1996.

[Gri99]   D. Griffiths. *Introduction to Electrodynamics,* 3rd edition. Prentice Hall, Upper Saddle River, NJ, 1999.

[GSB86]   L. Glass, A. Schrier, and J. Bélair. Chaotic cardiac rhythms. In A. V. Holden, editor, *Chaos.* Princeton University Press, Princeton, 1986.

[GSB⁺04]   P. Grim, E. Selinger, W. Braynen, R. Rosenberger, R. Au, N. Louie, and J. Connolly. Reducing prejudice: A spatialized game-theoretic model for the contact hypothesis. In J. Pollack, M. Bedau, P. Husbands, T. Ikegami, and R. A. Watson, editors, *Artificial Life IX: Proceedings of the Ninth International Conference on Artificial Life.* MIT Press, Cambridge, 2004.

[GT96]   H. Gould and J. Tobochnik. *An Introduction to Computer Simulation Methods.* Addison-Wesley, Reading, MA, 1996.

[GW64]   C. M. Guldberg and P. Waage. Studies concerning affinity. *C. M. Forhandlinger: Videnskabs-Selskabet i Christiana*, page 35, 1864.

[GW79]   C. M. Guldberg and P. Waage. Concerning chemical affinity. *Erdmann's J. Pract. Chem.*, 127:69, 1879.

[GWDS95]   A. Garfinkel, J. N. Weiss, W. L. Ditto, and M. L. Spano. Chaos control of cardiac arrhythmias. *Trends Cardiovasc. Med.*, 5:2, 1995.

[HA87]   H. W. Hethcote and J. W. Van Ark. Epidemiological models for heterogeneous populations: proportionate mixing, parameter estimation and immunization programs. *Math. Biosci.*, 84:85, 1987.

[Has75]   M. P. Hassell. Density dependence in single-species populations. *J. Anim. Ecol.*, 44:283, 1975.

[Has90]   A. Hasegawa. *Optical Solitons in Fibers.* Springer-Verlag, New York, 2nd edition, 1990.

[Hat21]   A. S. Hathaway. Pursuit in a circle. *Am. Math. Monthly*, 27:93, 1921.

[HDAB06] R. Hristovski, K. Davids, D. Araújo, and C. Button. How boxers decide to punch a target: Emergent behavior in nonlinear dynamical movement systems. *J. Sports Sci. Med.*, Combat Sports Special Issue:60, 2006.

[Hel95] H. Helmholtz. *Sensation of Tone.* Longmans Green, London, 1895.

[Hen76] M. Henon. A two-dimensional mapping with a strange attractor. *Commun. Math. Phys.*, 50:69, 1976.

[Het83] H. W. Hethcote. Measles and rubella in the United States. *Am. J. Epidemiol.*, 117:2, 1983.

[Het89] H. W. Hethcote. Three basic epidemiological models. In S. A. Levin, T. G. Hallam, and L. J. Gross, editors, *Applied Mathematical Ecology.* Springer, New York, 1989.

[Het00] H. W. Hethcote. The mathematics of infectious diseases. *SIAM Rev.*, 42:599, 2000.

[HH64] M. Hénon and C. Heiles. The applicability of the third integral of motion: some numerical experiments. *Astrophys. J.*, 69:73, 1964.

[HNKC09] Derke R. Hughes, Albert H. Nuttall, Richard A. Katz, and G. Clifford Carter. Nonlinear acoustics in cicada mating calls enhance sound propagation. *J. Acoust. Soc. Amer.*, 125:958, 2009.

[Hol59a] C. Holling. The components of predation as revealed by a study of small mammal predation of the European pine sawfly. *Can. Entomol.*, 91:293, 1959.

[Hol59b] C. Holling. Some characteristics of simple types of predation and parasitism. *Can. Entomol.*, 91:385, 1959.

[Hol79] P. Holmes. A nonlinear oscillator with a strange attractor. *Phil. Trans. Roy. Soc. London A*, 292:419, 1979.

[Hol04] J. R. Holton. *An Introduction to Dynamic Meteorology.* Academic Press, New York, 3rd edition, 2004.

[Hop50] E. Hopf. The partial differential equation $u_t + u\,u_x, = u_{xx}$. *Commun. Pure Appl. Math.*, 3:201, 1950.

[HT73] A. Hasegawa and F. D. Tappert. Transmission of stationary nonlinear optical pulses in dispersive dielectric fibers. 1. Anomalous dispersion. *Appl. Phys. Lett.*, 23:142, 1973.

[Inc64] E. L. Ince. *Ordinary Differential Equations.* Dover, New York, 1964.

[Ing73] A. P. Ingersoll. Jupiter's Great Red Spot: A free atmospheric vortex. *Science*, 182:1346, 1973.

[IR90]   E. Infeld and G. Rowlands. *Nonlinear Waves, Solitons and Chaos*. Cambridge University Press, Cambridge, 1990.

[Jac75]   J. D. Jackson. *Classical Electrodynamics*, 2nd edition. John Wiley, New York, 1975.

[Jac90]   E. A. Jackson. *Perspectives of Nonlinear Dynamics*. Cambridge University Press, Cambridge, 1990.

[Jai97]   N. K. Jaiswal. *Military Operations Research*. Kluwer Academic, New York, 1997.

[JC01]   G. S. Jackson and J. Collinge. The molecular pathology of CJD: old and new variants. *J. Clin. Pathol.*, 54:393, 2001.

[JLH95]   C. A. Jones, A. Longbottom, and R. Hollerbach. A self-consistent convection driven geodynamo model, using a mean field approximation. *Phys. Earth Planet Int.*, 92:119, 1995.

[JLSM64]   R. C. Jaklevic, J. Lambe, A. H. Silver, and J. E. Mercereau. Quantum interference effects in Josephson tunneling. *Phys. Rev. Lett.*, 12:159, 1964.

[Jon00]   A. J. Jones. *Game Theory: Mathematical Models of Conflict*. Horwood Publishing, Chichester, U. K., 2000.

[Jos62]   B. D. Josephson. Possible new effects in superconductive tunneling. *Phys. Lett.*, 1:251, 1962.

[JS75]   P. C. Jain and V. Srinivasan. A review of self-excited vibrations in oil film journal bearings. *Wear*, 31:219, 1975.

[Kar99]   P. Kareiva. Coevolutionary arms races: Is victory possible? *Proc. Natl. Acad. Sci. USA*, 96:8, 1999.

[Kar03]   V. P. J. Karmeshu. Nonlinear models of social systems. *Economic and Political Weekly*, 38:No.35, 2003.

[Kau76]   D. J. Kaup. The three–wave interaction: A nondispersive phenomenon. *Stud. Appl. Math.*, 55:9, 1976.

[Kau02]   S. Kauffman. *Ecology, the Ascendant Perspective*. Oxford University Press, New York, 2002.

[KE96]   L. D. Kiel and E. Elliot. *Chaos Theory in the Social Sciences*. University of Michigan Press, Ann Arbor, 1996.

[Ker04]   B. Kerner. *The Physics of Traffic*. Springer, New York, 2004.

[KF70]   B. E. Keen and W. H. W. Fletcher. Suppression of a plasma instability by the method of asynchronous quenching. *Phys. Rev. Lett.*, 24:130, 1970.

[KG95]   D. Kaplan and L. Glass. *Understanding Nonlinear Dynamics.* Springer-
            Verlag, New York, 1995.

[KM27]   W. O. Kermack and A. G. McKendrick. Contributions to the mathematical
            theory of epidemics-I. *Proc. R. Soc.*, 115A:700, 1927.

[KP70]   B. B. Kadomtsev and V. I. Petviashvili. On the stability of solitary waves
            in weakly dispersive media. *Sov. Phys. Dokl.*, 15:539, 1970.

[KRB79]   D. J. Kaup, A. Rieman, and A. Bers. Space-time evolution of nonlinear
            three-wave interactions. *Rev. Mod. Phys.*, 51:275, 1979.

[Kru91]   J. A. Krumhansl. Unity in the science of physics. *Phys. Today*, 44, No.3:33,
            1991.

[KSW+95]   A. Kageyama, T. Sato, K. Watanabe, R. Horiuchi, and T. Hayashi. Com-
            puter simulation of a magnetohydrodynamic dyanamo II. *Phys. Plasmas*,
            2:1421, 1995.

[KT99]   J. Kozlowski and A. T. Teriokhin. Allocation of energy between growth
            and reproduction: The pontryagin maximum principle solution for the
            case of age- and season-dependent mortality. *Evolutionary Ecology Res.*,
            1:423, 1999.

[Lai64]   A. K. Laird. Dynamics of tumor growth. *Brit. J. Cancer*, 18:490, 1964.

[Lam64]   W. E. Lamb. Theory of an optical maser. *Phys. Rev. A*, 34:1429, 1964.

[Lan70]   J. H. Lane. On the theoretical temperature of the sun under the hypoth-
            esis of a gaseous mass maintaining its volume by its internal heat and
            depending on the laws of gases known to terrestrial experiment. *Am. J.
            Sci. and Arts*, 50:57, 1870.

[Lan16]   F. W. Lanchester. *Aircraft in Warfare: The Dawn of the Fourth Arm.*
            Constable and Co., London, 1916.

[Lan56]   F. W. Lanchester. Mathematics in warfare. In J. R. Newman, editor, *The
            World of Mathematics, Vol. 4.* Simon and Schuster, New York, 1956.

[Lan64]   W. L. Langer. The black death. *Sci. Am.*, 210:114, 1964.

[Las69]   H. Lashinsky. Periodic pulling and the transition to turbulence in a sys-
            tem with discrete modes. In John Fox, editor, *Turbulence of Fluids and
            Plasmas.* Wiley, New York, 1969.

[Lau86]   H. A. Lauwerier. One-dimensional iterative maps. In A. V. Holden, editor,
            Chaos. Princeton University Press, Princeton, 1986.

[Lau97]   M. Laurent. Autocatalytic processes in cooperative mechanisms of prion
            diseases. *FEBS Lett.*, 407:1, 1997.

[LB34]   H. Lineweaver and D. Burk. The determination of enzyme dissociation constants. *J. Am. Chem. Soc.*, 56:658, 1934.

[Lin74]   D. A. Linkens. Analytic solutions of large numbers of mutually coupled nearly sinusoidal oscillators. *IEEE Trans. Circuit Syst.*, 21:294, 1974.

[Lin76]   D. A. Linkens. Stability of entrainment conditions for particular form of mutually coupled van der Pol oscillators. *IEEE Trans. Circuit Syst.*, 23:113, 1976.

[Lin81]   P. Linsay. Period doubling and chaotic behavior in a driven anharmonic oscillator. *Phys. Rev. Lett.*, 47:1349, 1981.

[LJ24]   J. E. Lennard-Jones. On the determination of molecular fields. *Proc. R. Soc. Lond. A*, 106:463, 1924.

[LJH78]   D. Ludwig, D. D. Jones, and C. S. Holling. Qualitative analysis of insect outbreak systems: the spruce budworm and forest. *J. Anim. Ecol.*, 47:315, 1978.

[LLF82]   A. Libchaber, C. Laroche, and S. Fauve. Period doubling cascade in Mercury, a quantitative measurement. *J. Phys. Lett.*, 43:L211, 1982.

[LLP05]   S. Lepri, R. Livi, and A. Politi. Studies of thermal conductivity in Fermi–Pasta–Ulam-like lattices. *Chaos*, 15:118, 2005.

[LM67]   E. B. Lee and L. Markus. *Foundations of Optimal Control Theory*. John Wiley and Sons, New York, 1967.

[Lor63]   E. N. Lorenz. Deterministic nonperiodic flow. *J. Atmos. Sci.*, 20:130, 1963.

[Lor84]   E. N. Lorenz. The local structure of a chaotic attractor in four dimensions. *Physica D*, 13:90, 1984.

[Lot56]   A. J. Lotka. *Elements of Mathematical Biology*. Dover reprint, New York, 1956.

[LP80]   E. W. Larsen and G. C. Pomraning. Asymptotic analysis of nonlinear marshak waves. *SIAM J. Appl. Math.*, 39:201, 1980.

[LP90]   R. Lima and M. Pettini. Suppression of chaos by resonant parametric perturbations. *Phys. Rev. A*, 41:726, 1990.

[LSW77]   J. Lewis, J. M. W. Slack, and L. Wolpert. Thresholds in development. *J. Theor. Biol.*, 65:579, 1977.

[LY73]   W. A. London and J. A. Yorke. Recurrent outbreaks of measles, chickenpox, and mumps. I. *Am. J. Epidemiol.*, 98:453, 1973.

[Lyn99]   P. Lynch. The life cycles of extratopical cyclones. In M. A. Shapiro and S. Gronas, editors, *Richardson's Marvellous Forecast*. American Meteorological Society, Boston, 1999.

[Lyn01]   P. Lynch. Weather forecasting: from woolly art to solid science. In R. P. Pearce, editor, *Meteorology at the Millenium*. Academic Press, San Diego, 2001.

[Lyn06]   P. Lynch. *The Emergence of Numerical Weather Prediction*. Cambridge University Press, Cambridge, 2006.

[MA87]   R. M. May and R. M. Anderson. Transmission dynamics of HIV infection. *Nature*, 236:137, 1987.

[MA89]   R. M. May and R. M. Anderson. The transmission dynamics of human immunodeficiency virus (HIV). In S. A. Levin, T. G. Hallam, and L. J. Gross, editors, *Applied Mathematical Ecology*. Springer, New York, 1989.

[May75]   R. May. *Stability and Complexity in Model Ecosystems*, 2nd edition. Princeton University Press, Princeton, 1975.

[May76]   R. M. May. Simple mathematical models with very complicated dynamics. *Nature*, 261:459, 1976.

[May80]   R. M. May. Nonlinear phenomena in ecology and epidemiology. *Ann. N.Y. Acad. Sci.*, 357:267, 1980.

[MC03]   T. Markvart and L. Castaner. *Practical Handbook of Voltaics*. Elsevier, New York, 2003.

[Meb00]   W. R. Mebane. Congressional campaign contributions, district service, and electoral outcomes in the United States: Statistical tests of a formal game model with nonlinear dynamics. In D. Richards, editor, *Political Complexity: Nonlinear Models of Politics*. University of Michigan Press, Ann Arbor, 2000.

[Meh85]   R. D. Mehta. Aerodynamics of sports balls. *Annu. Rev. Fluid Mech.*, 17:151, 1985.

[Men98]   V. Mendéz. Epidemic models with an infected-infectious period. *Phys. Rev. E*, 57:3622, 1998.

[MG77]   M. C. Mackey and L. Glass. Oscillations and chaos in physiological control systems. *Science*, 197:287, 1977.

[MIN04]   F. Michor, Y. Iwasa, and M. A. Nowak. Dynamics of cancer progression. *Nature Rev. Cancer*, 4:197, 2004.

[Mit77]   J. M. Mitchison. Cell cycle control models. In B. Drewinko and R. M. Humphrey, editors, *Growth Kinetics and Biochemical Regulation of Normal and Malignant Cells*. Williams and Wilkins, Baltimore, 1977.

[MK87]   H. Meinhardt and M. Klingler. A model for pattern formation on the shells of molluscs. *J. Theor. Biol.*, 126:63, 1987.

[MM13]   L. Michaelis and M. I. Menten. Die kinetik der invertinwirkung. *Biochem. Z.*, 49:333, 1913.

[MMB90]   V. Mahajan, E. Muller, and F. M. Bass. New product diffusion models in marketing: A review and directions for research. *J. of Marketing*, 54:1, 1990.

[MNE+88]   L. F. Mollenauer, M. J. Neubelt, S. G. Evangelides, J. P. Gordon, J. R. Simpson, and L. G. Cohen. Experimental study of soliton transmission over more than 10,000 km in dispersion-shifted fibers. *Opt. Lett.*, 15:1203, 1988.

[MP94]   A. B. Murray and C. Paola. A cellular model of braided rivers. *Nature*, 371:54, 1994.

[MPD+07]   N. Moll, E. Pascal, D. Dinh, J. Pillot, B. Bennetau, D. Rebiere, D. Moynet, Y. Mas, D. Mossayayib, J. Pistre, and C. Dejous. A Love wave immunosensor for whole E. coli bacteria detection using an innovative two-step immobilisation approach. *Biosens. Bioelectron.*, 22:2145, 2007.

[MSG80]   L. F. Mollenauer, R. M. Stolen, and J. P. Gordon. Experimental observation of picosecond pulse narrowing and solitons in optical fibers. *Phys. Rev. Lett.*, 45:1095, 1980.

[MSS73]   N. Metropolis, M. L. Stein, and P. R. Stein. On finite limit sets for transformations on the unit interval. *J. Combin. Theor.*, 15:25, 1973.

[MT95]   J. B. Marion and S. T. Thornton. *Classical Dynamics of Particles and Systems.* Saunders College Publishing, Orlando, 1995.

[Mue78]   T. J. Mueller. *Smoke Visualization of Subsonic and Supersonic Flow (The Legacy of F. N. M. Brown).* National Technical Information Service, U.S. Dept. of Commerce, Springfield, VA, 1978.

[Mur76]   J. D. Murray. On travelling wave solutions in a model for the Belousov-Zhabotinsky reaction. *J. Theor. Biol.*, 52:329, 1976.

[Mur88]   J. D. Murray. How the leopard gets its spots. *Sci. Am.*, March:80, 1988.

[Mur02]   J. D. Murray. *Mathematical Biology*, 2nd edition. Springer-Verlag, Berlin, 2002.

[Mur03]   J. D. Murray. *Mathematical Biology: I. An Introduction*, 3rd edition. Springer-Verlag, Berlin, 2003.

[Mus37]   M. Muskat. *The Flow of Homogeneous Fluids Through Porous Media.* McGraw Hill, New York, 1937.

[MWO04]   N. Mantzaris, S. Webb, and H. G. Othmer. Mathematical modeling of tumor-induced angiogenesis. *J. Math. Biol.*, 95:111, 2004.

[NAY62]   J. S. Nagumo, S. Arimoto, and S. Yoshizawa. An active pulse transmission line simulating nerve axon. *Proc. IRE*, 50:2061, 1962.

[NB95]   A. H. Nayfeh and B. Balachandran. *Applied Nonlinear Dynamics.* Wiley, New York, 1995.

[NC74]   T. Nagylaki and J. F. Crow. Continuous selection models. *J. Theor. Popul. Biol.*, 5:267, 1974.

[New80]   C. M. Newton. Biomathematics in oncology: modelling of cellular systems. *Annu. Rev. Biophys. Bioeng.*, 9:541, 1980.

[Nic57]   A. J. Nicholson. The self adjustment of populations to change. *Cold Spring Harbor Symp. Quant. Biol.*, 22:153, 1957.

[NK86a]   A. H. Nayfeh and A. A. Khdeir. Nonlinear rolling of biased ships in regular beam seas. *Int. J. Shipbldg. Prog.*, 33:84, 1986.

[NK86b]   A. H. Nayfeh and A. A. Khdeir. Nonlinear rolling of ships in regular beam seas. *Int. J. Shipbldg. Prog.*, 33:40, 1986.

[NM79]   A. H. Nayfeh and D. T. Mook. *Nonlinear Oscillations.* Wiley, New York, 1979.

[Nob74]   J. V. Noble. Geographic and temporal development of plagues. *Nature*, 250:726, 1974.

[NW69]   A. C. Newell and J. A. Whitehead. Finite bandwidth, finite amplitude convection. *J. Fluid Mech.*, 38:279, 1969.

[Ode80]   G. M. Odell. Qualitative theory of systems of ordinary differential equations, including phase plane analysis and the use of the Hopf bifurcation theorem. In L. A. Segel, editor, *Mathematical Models in Molecular and Cell Biology.* Cambridge University Press, Cambridge, 1980.

[OGY90]   E. Ott, C. Grebogi, and J. A. Yorke. Controlling chaos. *Phys. Rev. Lett.*, 64:1196, 1990.

[OIKO05]   Y. Ono, A. Ishiyama, N. Kasai, and A. Odawara. Development of mice biomagnetic measurement system using DC-SQUID magnetometer. *IEEE Trans. Appl. Supercond.*, 15:640, 2005.

[Ols83]   L. F. Olsen. An enzyme reaction with a strange attractor. *Phys. Lett. A*, 94:454, 1983.

[PA05]   N. J. R. Plowes and E. S. Adams. An empirical test of Lanchester's square law: mortality during battles of the fire ant Solenopsis invicta. *Proc. Ry. Soc. B*, 272:1809, 2005.

[Pal05a]   G. Palmer. *Physics for Game Players*. Apress, New York, 2005.

[Pal05b]   T. Palmer. Global warming in a nonlinear climate–can we be sure? *Europhysics News*, March/April:42, 2005.

[PBGM86]   L. S. Pontryagin, V. G. Boltyanskii, R. V. Gamkrelidze, and E. F. Mischenko. *The Mathematical Theory of Opitmal Processes*. Gordon and Breach, New York, 1986.

[PC89]   T. S. Parker and L. O. Chua. *Practical Numerical Algorithms for Chaotic Systems*. Springer-Verlag, Berlin, 1989.

[PFTV89]   W. H. Press, B. P. Flannery, S. A. Teukolsky, and W. T. Vetterling. *Numerical Recipes*. Cambridge University Press, Cambridge, 1989.

[PL68]   I. Prigogine and R. Lefever. Symmetry breaking instabilities in dissipative systems, II. *J. Chem. Phys.*, 48:1695, 1968.

[PLA92]   M. Peastrel, R. Lynch, and A. Armenti. Terminal velocity of shuttlecock in vertical fall. In A. Armenti, editor, *The Physics of Sports*. American Institute of Physics, New York, 1992.

[PRK68]   D. Pohl, I. Reinhold, and W. Kaiser. Experimental observation of stimulated thermal Brillouin scattering. *Phys. Rev. Lett.*, 20:1141, 1968.

[Pro95]   R. W. Prouty. *Helicopter Performance, Stability, and Control*. Krieger, Malablar, FL, 1995.

[PST86]   J. K. Park, K. Steglitz, and W. D. Thurston. Soliton-like behavior in automata. *Physica D*, 19:423, 1986.

[PT69]   J. J. Pella and P. K. Tomlinson. A generalized stock production model. *Bull. Inter-Am. Trop. Tuna Comm.*, 13:419, 1969.

[R76]   O. E. Rössler. An equation for continuous chaos. *Phys. Lett.*, 57A:397, 1976.

[Ras07]   E. Rasmusen. *Games and Information: An Introduction to Game Theory, 4th ed.* Blackwell, Malden, MA, 2007.

[Ray83]   Lord Rayleigh. On maintained vibrations. *Philos. Mag.*, 15:229, 1883.

[RCM07]   T. Roose, S. J. Chapman, and P. K. Maini. Mathematical models of avascular tumor growth. *SIAM Rev.*, 49:179, 2007.

[Ree95]   G. Rees. The physics of medieval archery. *Physics Rev.*, January, 1995.

[Rey83]   O. Reynolds. An experimental investigation of the circumstances which determine whether the motion of water shall be direct or sinuous, and of the law of resistance in parallel channels. *Philos. Trans. R. Soc.*, page 935, 1883.

[RG00]   P. H. Roberts and G. A. Glatzmaier. Geodynamo theory and simulations. *Rev. Mod. Phys.*, 72:1081, 2000.

[Ric58]   W. E. Ricker. *Handbook of Computations for Biological Statistics of Fish Populations.* Fisheries Research Board of Canada, 1958.

[Ric95]   L. F. Richardson. *Weather Prediction by Numerical Process.* Cambridge University Press, Cambridge, 1922. Reprinted by Dover Publications, 1995.

[Ric00a]   D. Richards. Nonlinear dynamics in games: convergence and stability in international environmental agreements. In D. Richards, editor, *Political Complexity: Nonlinear Models of Politics.* University of Michigan Press, Ann Arbor, 2000.

[Ric00b]   D. Richards, editor. *Political Complexity: Nonlinear Models of Politics.* University of Michigan Press, Ann Arbor, 2000.

[Rob79]   K. A. Robbins. Periodic solutions and bifurcation structure at high R in the Lorenz model. *J. Appl. Math.*, 36:457, 1979.

[Rus44]   J. S. Russell. Report on waves. Rep. 14th, *Brit. Assoc. Adv. Sci.*, 1844.

[Sap84]   A. M. Saperstein. Chaos—a model for the outbreak of war. *Nature*, 309:303, 1984.

[Sap99]   A. M. Saperstein. *Dynamical Modeling of the Onset of War.* World Scientific, Singapore, 1999.

[Sch67]   M. B. Schaffer. Lanchester models of guerilla engagements. The RAND Corporation, Santa Monica, CA, RM-5053-ARPA, DTIC No. AD648863, 1967.

[Sch79]   J. Schnakenberg. Simple chemical reaction systems with limit cycle behavior. *J. Theor. Biol.*, 81:389, 1979.

[Sch89]   H. G. Schuster. *Deterministic Chaos.* VCH, Weinheim, Germany, 1989.

[SCM73]   A. C. Scott, F. Y. F. Chu, and D. W. McLaughlin. The soliton: A new concept in applied science. *Proc. IEEE*, 61:1443, 1973.

[Sco70]   A. C. Scott. *Active and Nonlinear Wave Propagation in Electronics.* Wiley-Interscience, New York, 1970.

[Sco81]   A. C. Scott. Introduction to nonlinear waves. In R. H. Enns, B. L. Jones, R. M. Miura, and S. S. Rangnekar, editors, *Nonlinear Phenomena in Physics and Biology.* Plenum, New York, 1981.

[Sco95]   S. K. Scott. *Oscillations, Waves and Chaos in Chemical Kinetics.* Oxford University Press, New York, 1995.

[Seg69]   L. A. Segel. Distant sidewalls cause slow amplitude modulation of cellular convection. *J. Fluid Mech.*, 38:203, 1969.

[Sel68]   E. E. Sel'kov. Self-oscillations in glycolysis. *Eur. J. Biochem.*, 4:79, 1968.

[Shi80]   N. Shigesada. Spatial distribution of dispersing animals. *J. Math. Biol.*, 9:85, 1980.

[SHL70]   L. Simpson-Herren and H. H. Lloyd. Kinetic parameters and growth curves for experimental tumor systems. *Cancer Chemother. Rep. Part I*, 54:143, 1970.

[Sil90]   Y. Silberberg. Collapse of optical pulses. *Opt. Lett.*, 15:1282, 1990.

[SJD$^+$94] S. J. Schiff, K. Jerger, D. H. Duong, T. Chang, M. L. Spano, and W. L. Ditto. Controlling chaos in the brain. *Nature*, 370:615, 1994.

[SM96]   A. Swift and E. Moroz. Wind turbines. In R. C. Dorf, editor, *The Engineering Handbook*. CRC Press, Boca Raton, FL, 1996.

[SMK89]   A. M. Saperstein and G. Mayer-Kress. Chaos versus predictability in formulating national strategic security policy. *Am. J. Phys.*, 57:217, 1989.

[Spa82]   C. Sparrow. *Bifurcations in the Lorenz Equation*. Springer-Verlag, Berlin, 1982.

[SR96]   X. Song and P. Richards. Seismological evidence for differential rotation of the earth's inner core. *Nature*, 382:221, 1996.

[SSM81]   M. B. Simson, J. F. Spear, and E. N. Moore. Stability of an experimental atrioventricular reentrant tachycardia in dogs. *Heart Circ. Physiol.*, 9:H947, 1981.

[Ste88]   A. Stepanek. The aerodynamics of tennis balls–the topspin lob. *Am. J. Phys.*, 56:138, 1988.

[Str94]   S. H. Strogatz. *Nonlinear Dynamics and Chaos*. Addison-Wesley, Reading, MA, 1994.

[Sut88]   R. M. Sutherland. Cell and environment interactions in tumor microregions. *Nature Rev. Cancer*, 4:177, 1988.

[SW58]   M. P. Shepard and F. C. Withler. Spawning stock size and resutant production for Skeena sockeye. *J. Fish. Res. Board Can.*, 15:1007, 1958.

[Tet83]   G. Tetzlaff. Albedo of the Sahara. *Cologne Univ. Satellite Meas. of Radiation Budget Parameters*, October:60, 1983.

[Tho05]   A. J. Thorpe. Climate change prediction, a challenging scientific problem. *Institute of Physics Report*, 2005.

[TK93a]   Z. Toth and E. Kalnay. Ensemble forecasting at NMC: Operational implementation. *Weather Forecasting*, 8:379, 1993.

[TK93b]   Z. Toth and E. Kalnay. Ensemble forecasting at NMC: The generation of perturbations. *Bull. Am. Meteoro. Soc.*, 74:2317, 1993.

[TM96]   T. Tang and J. C. McConnell. Autocatalytic release of bromine from Arctic snow pack during polar sunrise. *Geophys. Res. Lett.*, 23:2633, 1996.

[Tod89]   M. Toda. *Theory of Nonlinear Lattices*. Springer-Verlag, Berlin, 2nd edition, 1989.

[Tor81]   S. Torvén. Modified Korteweg-De vries equation for propagating double layers in plasmas. *Phys. Rev. Lett.*, 47:1053, 1981.

[Tor86]   S. Torvén. Weak double layers in a current carrying plasma. *Phys. Scr.*, 33:262, 1986.

[TPJ82]   J. S. Testa, J. Perez, and C. Jeffries. Evidence for universal chaotic behavior of a driven nonlinear oscillator. *Phys. Rev. Lett.*, 48:714, 1982.

[TPS98]   C. Tomlin, G. J. Pappas, and S. Sastry. Conflict resolution for air traffic management: a study in multi-agent hybrid systems. *IEEE Transactions on Automatic Control*, 43, April 1998.

[TTM+08]   E. Tamaševičiutė, A. Tamaševičius, G. Mykolaitis, S. Bumelienė, and E. Lindberg. Analogue electrical circuit for simulation of the Duffing–Holmes equation. *Nonlinear Analysis: Modelling and Control*, 13:241, 2008.

[Tur52]   A. M. Turing. The chemical basis of morphogenesis. *Philos. Trans. Ry. Soc. London*, B237:37, 1952.

[Tys76]   J. J. Tyson. The Belousov–Zhabotinskii reaction. In *Lecture Notes in Biomathematics, Vol. 10*. Springer-Verlag, New York, 1976.

[Tys85]   J. J. Tyson. A quantitative account of oscillations, bistability, and traveling waves in the Belousov-Zhabotinsky reaction. In R. J. Field and M. Burger, editors, *Oscillating and Traveling Waves in Chemical Systems*. Wiley, New York, 1985.

[UJ09]   R. Uhlář and M. Janura. Pontragin's maximum principle and optimzation of the flight phase in ski jumping. *Acta Univ. Palacki. Olomuc., Gymn*, 39:61, 2009.

[Ula62]   S. M. Ulam. On some mathematical problems connected with patterns of growth of figures. *Proc. Symp. Appl. Math.*, 14:215, 1962.

[Ula97]   R. Ulanowicz. *Ecology, the Ascendant Perspective*. Columbia University Press, New York, 1997.

[VD01]   V. Vitagliano and G. D'Errico. A simple kinetic model to describe the progression of prion disease. *Phys. Chem. Chem. Phys.*, 3:4547, 2001.

[vdP26]   B. van der Pol. On relaxation oscillations. *Philos. Mag.*, 2:978, 1926.

[vdPvdM28]   B. van der Pol and J. van der Mark. The heart beat considered as a relaxation oscillator and an electrical model of the heart. *Philos. Mag.*, 6:763, 1928.

[Ver90]   F. Verhulst. *Nonlinear Differential Equations and Dynamical Systems.* Springer-Verlag, Berlin, 1990.

[vNM44]   J. von Neumann and O. Morgenstern. *Theory of Games and Economic Behavior.* Princeton University Press, Princeton, 1944.

[Vog94]   S. Vogel. *Life in Moving Fluids.* Princeton University Press, Princeton, 1994.

[Vol26a]   V. Volterra. Fluctuations in the abundance of a species considered mathematically. *Nature*, 118:558, 1926.

[Vol26b]   V. Volterra. Variazioni e fluttuazioni del numero d'individui in specie animali conviventi. *Mem. R. Accad. Naz dei Lincei*, 2:31, 1926.

[Waa64]   P. Waage. Experiments for determining the affinity law. *C. M. Forhandlinger i Videnskabs-Selskabet i Christiana*, page 92, 1864.

[WBB02]   P. Waltman, J. Braselton, and L. Braselton. A mathematical model of a biological arms race with a dangerous prey. *J. Theor. Biol.*, 218:55, 2002.

[WC69]   C. H. Waddington and R. J. Cowe. Computer simulation of a mulluscan pigmentation pattern. *J. Theor. Biol.*, 25:219, 1969.

[WHH+88]   A. M. Weiner, J. P. Heritage, R. J. Hawkins, R. N. Thurston, E. M. Kirsschner, and D. E. Experimental observation of the fundamental dark soliton in optical fibers. *Phys. Rev. Lett.*, 61:2445, 1988.

[WLPL06]   E. Wertheim, A. Love, C. Peck, and I. Littlefield. *Skills for Resolving Conflict.* Eruditions Publishing, Melbourne, Australia, 2006.

[Wol86]   S. Wolfram, editor. *Theory and Applications of Cellular Automata.* World Scientific, Singapore, 1986.

[Wol02]   S. Wolfram. *A New Kind of Science.* Wolfram Media, Champaign, IL, 2002.

[Wol06]   J. Wolfers. Point shaving: Corruption in ncaa basketball. *Amer. Econ. Rev.*, 96:279, 2006.

[WS81]   T. A. Witten and L. M. Sander. Diffusion limited aggregration: A kinetic critical phenomenon. *Phys. Rev. Lett.*, 47:1400, 1981.

[WS03]   B. J. West and N. Scafetta. Nonlinear dynamical model of human gait. *Phys. Rev. E*, 67:051917, 2003.

[YK82]   W. J. Yeh and Y. H. Kao. Universal scaling and chaotic behavior of a Josephson junction analog. *Phys. Rev. Lett.*, 49:1888, 1982.

[YL73]   J. A. Yorke and W. A. London. Recurrent outbreaks of measles, chicken-pox, and mumps. II. *Am. J. Epidemiol.*, 98:469, 1973.

[You92]   R. M. Youngson. *Collins Dictionary of Medicine*. Collins, UK, 1992.

[ZB03]   A. R. Zangerl and M. R. Berenbaum. Phenotype matching in wild parsnip and parsnip webworms: causes and consequences. *Evolution*, 57:806, 2003.

[Zha91]   A. M Zhabotinskii. A history of chemical oscillations and waves. *Chaos*, 1:379, 1991.

[ZK65]   N. J. Zabusky and M. D. Kruskal. Interaction of "solitons" in a collisionless plasma and the recurrence of initial states. *Phys. Rev. Lett.*, 15:240, 1965.

[Zwi89]   D. Zwillinger. *Handbook of Differential Equations*. Academic Press, New York, 1989.

[ZZ70]   A. N. Zaikin and A. M Zhabotinskii. Concentration wave propagation in two-dimensional liquid-phase self-organizing system. *Nature*, 225:535, 1970.

[ZZ07]   K. Zimmermann and I. Zeidis. Worm-like locomotion as a problem of nonlinear dynamics. *J. Theor. Appl. Mech.*, 45:179, 2007.

Index